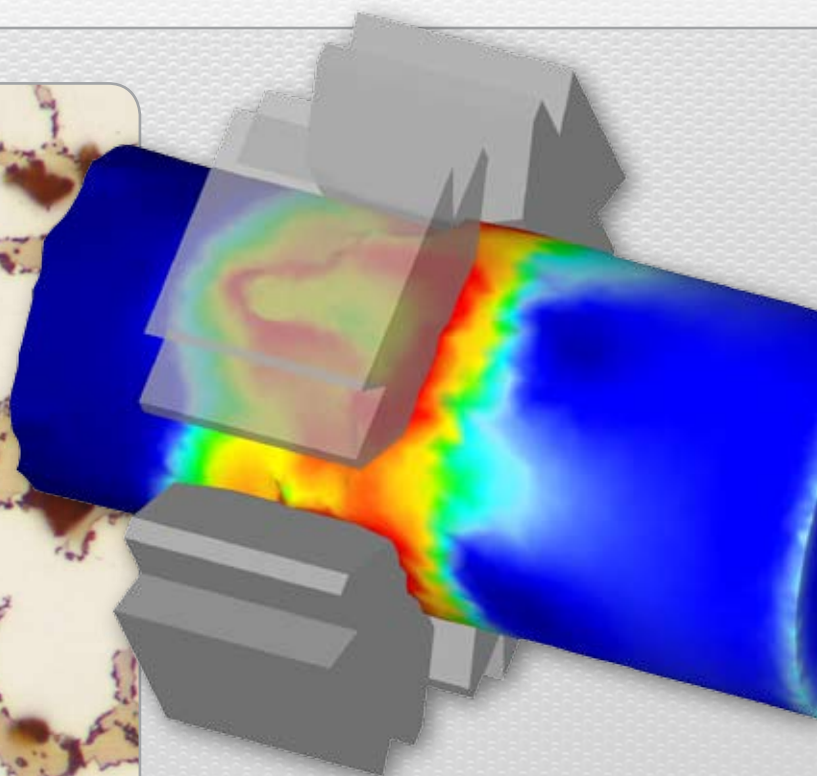
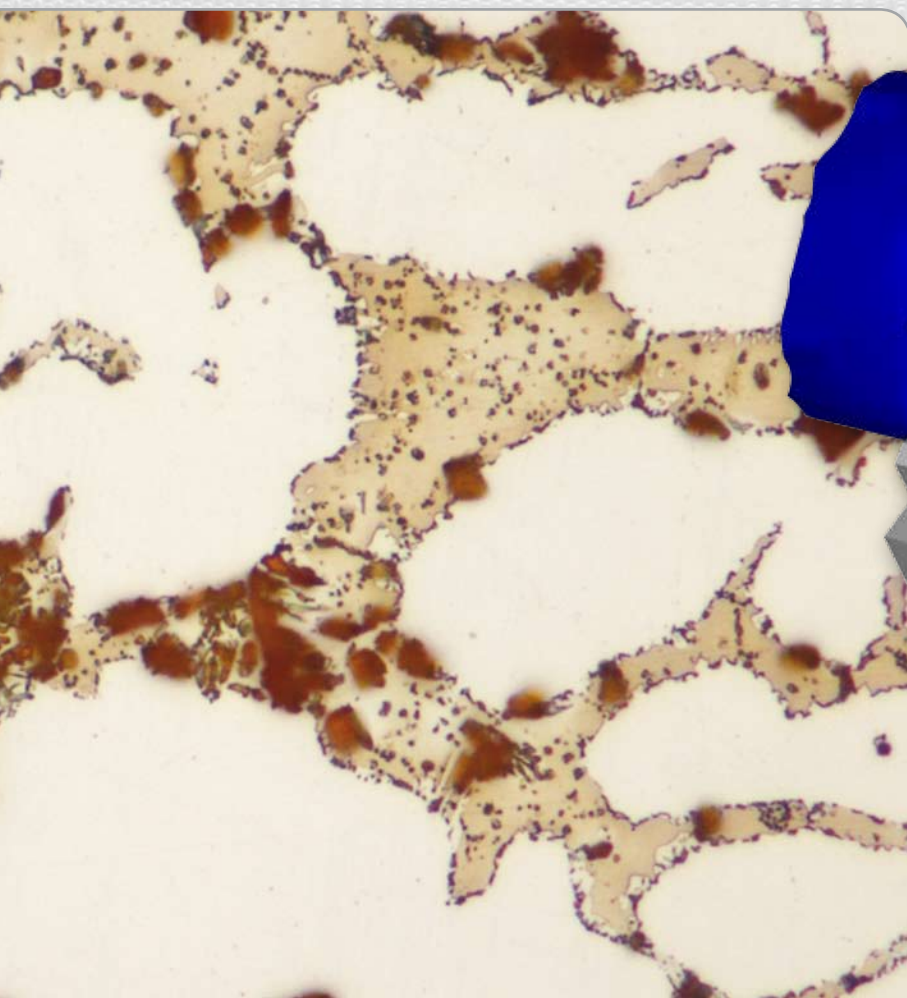


1st International Conference about Recent Trends in Structural Materials

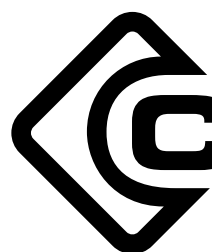


Conference proceedings

25–26th November 2010
PRIMAVERA Hotel & Congress centre
Pilsen / Czech Republic



1st International Conference about Recent Trends in Structural Materials

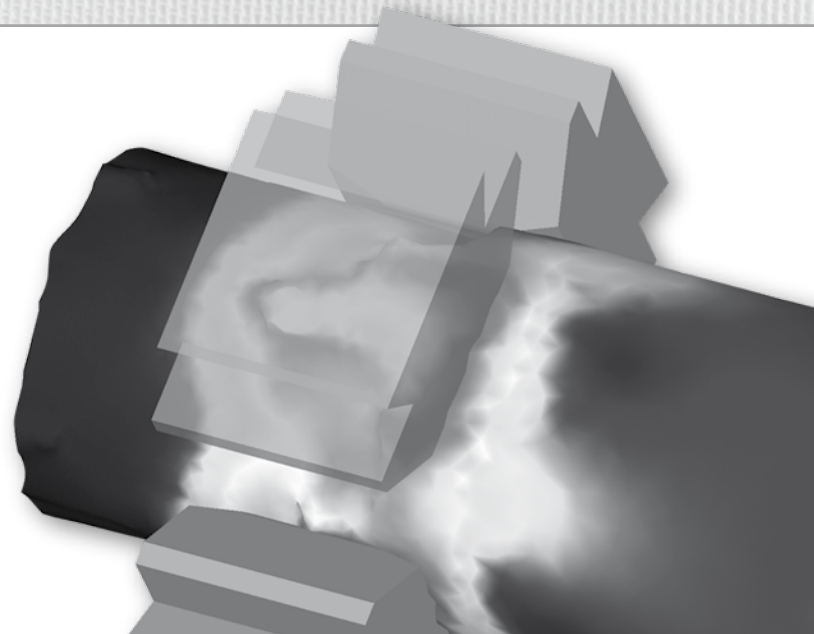


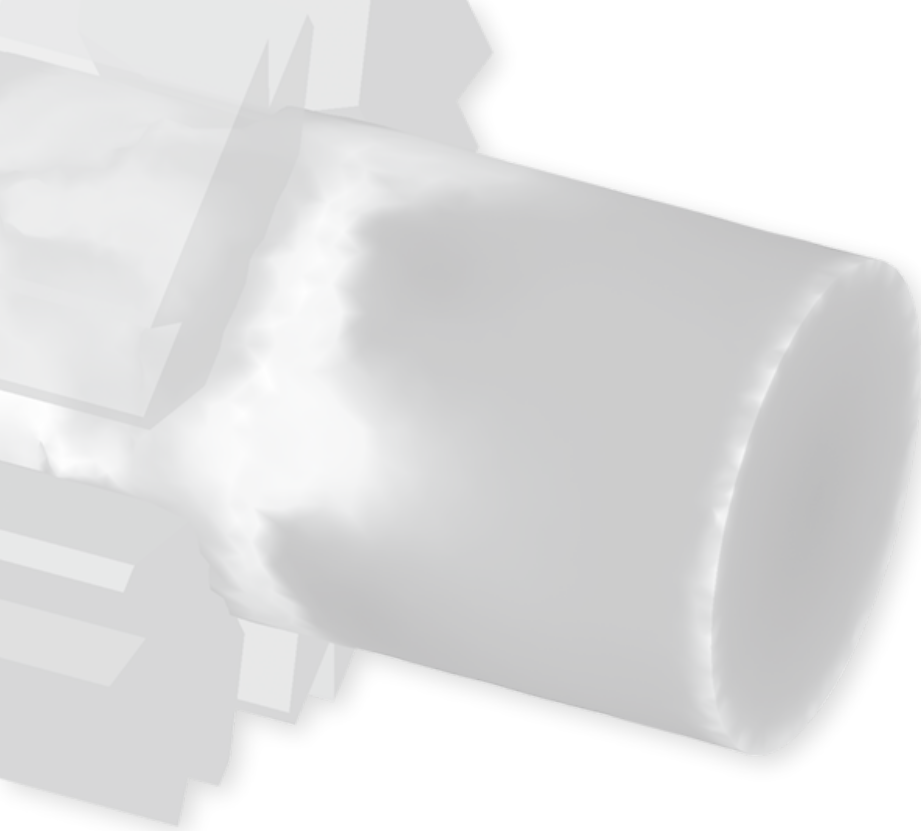
COMAT 2010

Recent trends in structural materials

Conference proceedings

25–26th November 2010
PRIMAVERA Hotel & Congress centre
Pilsen / Czech Republic





© COMTES FHT a. s. 2010

COMAT 2010

1st International Conference
about Recent Trends in Structural Materials

Conference proceedings

25-26th November 2010
PRIMAVERA Hotel & Congress centre
Pilsen / Czech Republic

Publisher: COMTES FHT a.s.
Průmyslová 995, 334 41 Dobřany
Czech Republic

1st Edition

Printed by: TYPOS, tiskařské závody, s.r.o.
Podnikatelská 1160/14, 320 59 Plzeň

Price: 1000 CZK

CD-ROM with full papers is part of the proceedings.
This publication is in its original form without editorial and stylistic correction.

ISBN 978-80-254-8683-2

Scientific committee / Odborní garanti

prof. Dr. Ing. Lothar Werner Meyer
Nordmetall GmbH, Adorf Gde, Neukirchen, Germany

Dr. Ing. Tomasz Babul
Institute of Precisions Mechanics, Warsaw, Poland

prof. Ing. Petr Louda, CSc.
Technical University of Liberec, Czech Republic

prof. Dr. Ing. Bohuslav Mašek
University of West Bohemia in Pilsen, Czech Republic

doc. Ing. Karel Šperlink, CSc.
Czech Society for New Materials and Technologies, Czech Republic

prof. Ing. Jozef Zrník, CSc.
COMTES FHT a.s., Czech Republic

Organising committee / Organizační výbor

Ing. Libor Kraus

Dr. Ing. Zbyšek Nový

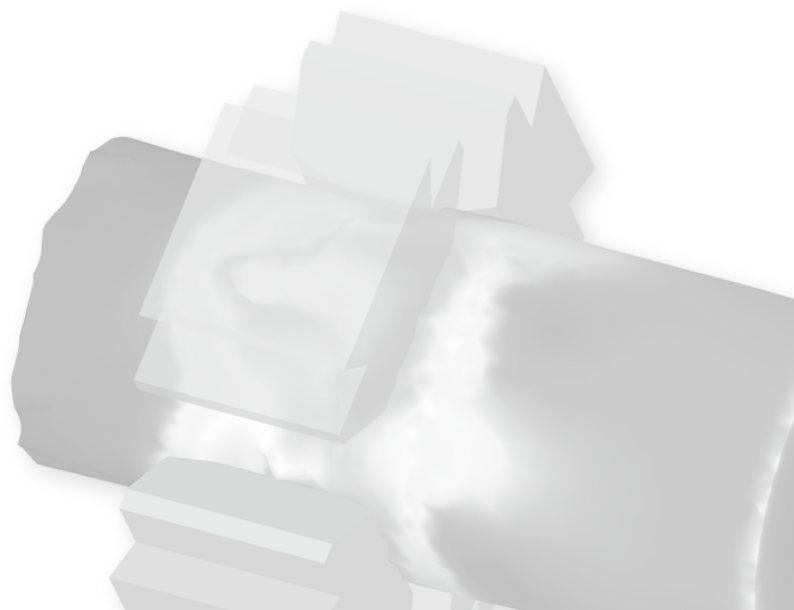
Ing. Jan Džugan, PhD.

Ing. Pavel Podaný

Ing. Jana Škalová

Ing. Pavel Šuchman

Ing. Michal Zemko, PhD.



Plenary talks

Kraus L., Nový, Z., Šuba J. / 10 years of the company COMTES FHT	8
Meyer L. W., Pursche F. / Modern high strength low alloyed steels	13
Valiev R. Z. / Bulk nanostructured metallic materials for innovation applications	19

Materials for Transport Equipment

Louda P., Rožek Z. / Applications of nanocrystalline thin coatings produced by plasma methods	25
Kasl J. / The analysis of failed locomotives wheel	29
Novák, S., Mráček J. / The experience from welding of high-strength fine-grained steels	34
Očenašek V., Karas V. / The effect of aluminium contents on structure and properties of CuAl9Fe3 forgings	44
Rusz S., Čížek L., Kedroň J., Tyšlar S., Žmija Z. Influence of heat treatment on structure and properties of brass after DRECE processing	50
Schieck F., Paul A., Pröhl M. / Forming technologies in automotive industry by application of light weight materials	54
Skrbek B., Nosek V., Kysel M., Sláma P. / Solution of modern pair of guide and valve of piston engines	60

Materials for Power Engineering

Zrník J., Strunz P., Maldini M., Wiedenmann A. Structure degradation of nickel base single crystal alloy under creep condition	70
Adolf Z., Bažan J., Socha L. / Conditions for formation of boron oxide and nitride in boron-alloyed steels	78
Balcar M., Novák J., Sochor L., Fila P., Martínek L. ASTM A694 F60 heat treatment and mechanical properties	83
Greger M., Kander L., Mašek V., Kočiščíková P. Structure and properties of ultra-fine grain titanium used for special applications	88

Hosnedl P., Nový Z., Konopík P., Džugan J., Tikal F. Structural materials and fluoride salts for high temperature applications	94
Martínek P., Podaný P., Poláková I. / Open-die forging of duplex steels	103
Nový Z., Motyčka P., Podaný P., Dlouhý J. / Recrystallization of nickel superalloys	110

Advanced Materials Processing Technologies

Kliber J. / Selected modern operations and research subject matters in material forming	120
Mašek B. / Steel and what we still do not know about it	129
Aišman D., Jirková H., Mašek B. / Mini-thixoforming tool steel X210CR12	135
Hauserová D., Dlouhý J., Nový Z., Zrník J. / Influence of carbides spheroidisation on mechanical properties in medium carbon steel	140
Jeleńkowski J., Ciski A., Babul T. / Substructure of deep cryogenically treated HS6-5-2 high speed steel	148
Kusý M., Behúlová M., Grgač P. / Solidification microstructures in the powder particles of hypereutectic iron based alloy	160
Malina J., Jirková H., Mašek B. / Influence of initial pearlite morphology on the resulting structure and distribution of deformation after cold flow forming process	167
Mašek B., Jirková H., Klauberová D., Petrenec M., Beran P. Unconventional thermomechanical treatment of advanced high strength low-alloyed steel	173
Němeček S., Mužík T., Urbánek M., Nový Z. / Laser welding of high strength steels	180
Olszar M., Olszar M., Koňář P., Hermann R. Treatment of ultra fine-grained steels using the strad method	186
Šuchmann P., Krejčík J., Fila P., Psík E., Jelen L. Development of new tool steels for forging dies	192
Urbánek M., Nesvadba P., Mašek B., Hronek P. Alternative explosion-formed joint of high-strength tube and sleeve	199

Zemko M., Matušek P., Martínková J., Fedorko M., Pětvaldský L. Modelling the process of forming railway wheels	205
--	-----

Analysis and Testing of Materials

Doig A. / Some metallurgical aspects of main battle tank armour and anti-armour warheads	212
Švejcar J. / Current potentials of structure analysis	218
Viehrig H. W. / The master curve approach as an approved fracture mechanics test method for more than one decade	228
Černý I. / The use of DCPD method for measurement of growth of physically short fatigue cracks	242
Ďuriš R. / A geometric nonlinear thermo-elastic analysis with the sandwich bar element	248
Džugan J., Konopík P. / Small punch tests for tensile properties and fracture toughness determination	256
Große-Heilmann N., Peters A., Šuchmann P. Characterisation of low alloyed steels using jominy-phase-diagrams	267
Hrušák D., Hájková L., Dluhoš L. / Morphological and functional pattern of cells cultured on nanostructured titanium	273
Matocha M. / The evaluation of circumferential weld of reheater header by small punch tests	278
Růžička J., Prantl A., Španiel M. / Ductile damage parameters identification in Fe program Abaqus	284
Sláma P., Macháčková K. / Influence of heat treatment on structure and properties of the CUAL10Ni5Fe4 alloy rods	288
Slováček M., Kovařík J., Tejc J., Bárta J., Pustějovský P. Heat treatment numerical simulation of sleeved roll	296
Wiedemeier B., Sander M., Richard H. A., Peters A. Fracture-mechanical characterization of steel tubes using arc-shaped specimens	303

10 YEARS OF THE COMPANY COMTES FHT

Libor Kraus¹, Zbyšek Nový², Jan Šuba³

Abstract

In the paper the history and development of COMTES FHT a.s. company is described. There are stated important milestones in the history, organizational structure, achievements, the most important areas of activities and future development.

Keywords: comtes fht, history, company activities

The company COMTES FHT s.r.o. was established in 2000 as an engineering consultancy firm with seven employees. Its headquarters were two rented offices in a block of flats, equipped with office PCs and DEFORM software licence for simulations of forming and heat treatment processes.



Figure 1 COMTES FHT s.r.o. in Plzeň, 2000

The business plan even became part of the company's name: COMplete TEchnological Service for Forming and Heat Treatment. From the outset and for the whole decade, the company focused on research into metallic materials and their processing by forming, heat treatment and thermomechanical treatment. In 2002, an additional two offices were rented in order to establish the company's first metallographic laboratory. COMTES DFM s.r.o., a daughter company, was formed jointly by COMTES FHT and an Austrian firm for the purpose of selling and providing consultancy for DEFORM software in the Czech and Slovak Republics. A workshop for manufacturing samples was equipped in 2003. The company's development gained momentum in 2004. We succeeded in winning a public tender called by the Czech Ministry of Education for a research plan which included funding for procuring

equipment, and we purchased our first research facilities in Lobežská Street in Plzeň. In addition to offices, the premises were gradually adapted to include laboratories for forming, heat treatment, light and electron microscopy, sample preparation and a mechanical workshop. To guarantee the level of quality of work and results, a certified quality management system according to ČSN EN ISO 9001 was introduced in 2005. In 2006, the material testing laboratory was accredited according to ČSN EN ISO/IEC 17025:2005.



Figure 2 COMTES FHT s.r.o. in Plzeň, 2004

The year 2006 saw another important step – establishing cooperation with the German company Benteler Stahl Rohr GmbH. In 2004, we were convinced that the new premises would be sufficient for our company's operations for several years to come. However, due to a lack of space for experiments, we were forced to rent a new hall outside Plzeň for a mechanical testing shop no later than 2006.

The continuing successful development of the company brought the need for new laboratory space for instruments and equipment, and greater requirements for utilities. The company management considered relocating the company to more suitable premises as early as in 2006. Conditions for green field construction were investigated at three available locations in Plzeň and its surroundings. Eventually, production premises became available for sale at an affordable price in the town of Dobřany, about 12 kilometres from Plzeň and with good access to the D5 motorway. One of the first EU structural funds projects in 2007 allowed us to purchase, adapt and equip it with cutting edge instruments. By the end of 2007, the entire company had relocated to the new headquarters and its research capacity was greatly expanded. The former private limited-type company then transformed into a joint-stock company and a non-profit research organisation under the rules of the European Community Framework. Investing all profits into research, development, instruments and equipment, which has been taking place since the establishment of the company, thus became an official principle and part of the company's articles of association. For its capital projects, COMTES FHT a.s. received an important award in 2008: 3rd place in the Investor of the Year 2008 competition in the category "Investment with the greatest innovation potential".



Figure 3 COMTES FHT a.s. in Dobřany, 2007

The core activities of the research organisation COMTES FHT a.s. consist in research and development of metallic materials, forming and heat treatment processes. The organisational structure of research and development is divided into four departments:

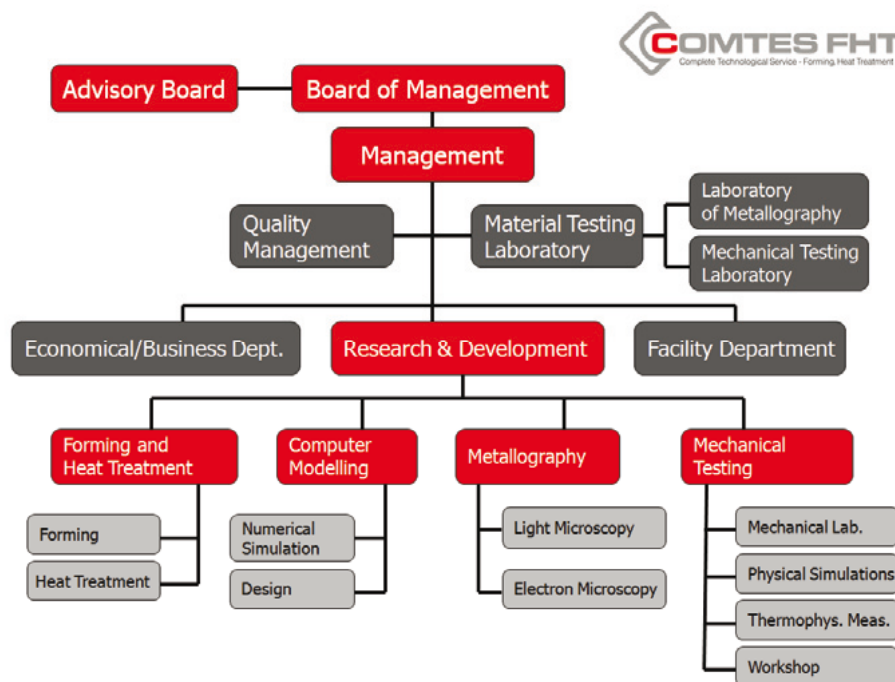


Figure 4 Organizational Structure

The main mission of the company is to provide comprehensive services to engineering and metallurgical enterprises in the above areas. The range of activities is very broad. In the mechanical testing shop and the metallographic laboratory, materials are analysed by techniques ranging from measurement of basic characteristics to special testing, such as fracture toughness measurement, high-cycle and low-cycle fatigue, high-temperature testing, testing at high strain rates, observation under an electron microscope at high magnification, EBSD phase analysis, EDX measurement of chemical composition and others.

As part of the materials and technology research, experimental materials with optimised chemical composition are being developed. These are then tested using various heat treatment and forming methods. The aim is to obtain the best possible combination of specific parameters. Optimisation of technological procedures is supported very effectively by numerical modelling. Using this discipline, predictions can be obtained for the most important process parameters of the technological procedure in question: temperature, strain and stress distributions in the work piece, the direction and intensity of material flow at any point, tool loads, failure probability and other factors.

The customers of COMTES FHT a.s. are, in most cases, companies engaged in metallurgical production, such as ironworks, rolling plants, non-ferrous metal works, wire mills and other industrial companies. They also include a number of engineering businesses which use formed or heat-treated metal products for further fabrication. The overwhelming majority of our partner companies are Czech businesses or corporations with a daughter company based in the Czech Republic. However, cooperation with foreign companies develops successfully as well. Those include German, Austrian, Polish and Slovak enterprises. Among the key partners are Benteler Stahl Rohr (today Benteler Steel Tube), ŽDAS, Pilsen Steel, ŠKODA POWER, ŠKODA JS, Kovárna VIVA Zlín, Pewag Austria, Bonatrans Group, MECAS ESI, ŠKODA AUTO and others.

COMTES FHT has created its niche in the research services market thanks to the experience of its employees and by offering experimental equipment which is difficult to find elsewhere. These are unique instruments, such as a simulator of thermomechanical cycles MTS with a range of working temperatures from -150°C to $+1,400^{\circ}\text{C}$, a scanning electron microscope with a field-emission cathode and EDS and EBSD diffractometers, a Schmetz vacuum furnace with nitrogen gas and liquid nitrogen cryogenic cooling, a CNC machining centre for manufacturing tools and specimens, equipment for special forming techniques ECAP, CGP and ASF, a Linseis quenching dilatometer, DEFORM 2D, 3D and HT packages, a drop tester with a maximum impact velocity of 18 m/s with a high-speed camera, and other equipment.

At present, the purchase of additional special forming equipment is being prepared: a device for continuous extrusion through an angular channel. This technique makes it possible to produce metal sections with extraordinary properties and ultrafine microstructure.

Typical research tasks carried out by COMTES FHT include:

- improving the microstructure and mechanical properties of existing metallic materials by efficient modification of their processing technology
- extending the life of tools for metal forming
- optimisation of shapes and materials of forging dies
- optimisation of open-die forging procedures
- development of materials and their processing procedures for heavy duty components of engineering complexes
- shortening heat treatment cycles
- replacement of conventional forming and heat treatment cycles with thermomechanical treatment

- correction of geometric deviations of structural parts by adapting their manufacturing processes
 - finding causes of failures of engineering components
- and other services.

COMTES FHT a.s. also cooperates with a number of universities and research institutions. The company offers topics for diploma and doctoral theses, its employees take part in teaching courses at the University of West Bohemia in Plzeň and act as supervisors or consultants for those theses. Students from Czech and foreign universities are offered internships in the company's laboratories.

Over the last three years, the company has been awarded two patents and eight industrial designs. Negotiations are underway to obtain international patents.

This year, 2010, COMTES FHT celebrates its 10th anniversary and faces another significant challenge. In the first half of 2010 our company succeeded in winning a public tender to build regional research centres. Now, the details of the agreement with the Czech Ministry of Education are being finalised. By 2013, new metallography and thermophysical measurement laboratories and a new metallurgy hall with state-of-the-art equipment for forming processes and the preparation of experimental materials should be erected on the neighbouring plot. This will be another important step towards building a modern comprehensive research centre.



Figure 5 The West-Bohemian Centre of Materials and Metallurgy

After only ten years of existence, COMTES FHT a.s. has become an important company on the regional, national and even Central European scale, pursuing materials research in the fields of forming and heat treatment of metals. A research centre was established in Dobřany which greatly contributes to the integration of the region into the European Research and Innovation Area.

¹ Ing. Libor Kraus, COMTES FHT a.s., Průmyslová 955, 334 41 Dobřany, Czech Republic, Tel.: +420 377 197 302, e-mail: libor.kraus@comtesfht.cz

² Dr. Zbyšek Nový, COMTES FHT a.s., Průmyslová 955, 334 41 Dobřany, Czech Republic, Tel.: +420 377 197 301, e-mail: zbysek.novy@comtesfht.cz

³ RNDr. Jan Šuba, COMTES FHT a.s., Průmyslová 955, 334 41 Dobřany, Czech Republic, Tel.: +420 377 197 3131, e-mail: jan.suba@comtesfht.cz

MODERN HIGH STRENGTH LOW ALLOYED STEELS

Lothar Werner Meyer¹, Frank Pursche²

Abstract

High Strength Low Alloyed Steels (HSLA) are weldable steels with an optimized relation between strength and toughness, used for protection applications. Using formerly Cr-Mo- or Cr-Ni-steel-types, today the Ni-Cr-Mo containing steels are dominant on the market.

Keywords: HSLA-steels, strength, toughness

1. Introduction

High strength low alloyed steels are used mostly for protection applications, which can be of civil or defense nature. Civil examples are the fast grown market of doors of tooling machines, which have to protect against tool fractures with velocities up to 200 m/s with usually "small" masses of up to 200 gr. or larger masses of 1-2 kg with 50-80 m/s. Both cases are severe threats and not easy to be handle.

Defense oriented targets have to sustain bullets, fragments, ammunitions, penetrators, self forging fragments or shape charges, IED or blast . Depending on the threat or loading condition, in all cases, the armor has to be as hard as possible and as safe as possible against fractures.

Regarding the time nature of an impact event it is clear, that the involved high velocities and energies are producing very high strains, high strain rates and multiaxial loading, similar to high speed machining operations. Therefore it can be started, that the levels of high strain rates of 10^3 to 10^5 1/s in civil or defense applications are very similar. Only the local concentrated energy input on the target, which have to be consumed without penetration, is much larger in defense applications, compared to civil scenarios as ship, railway or traffic crashes.

2. History of used steel types

In the years around 1935 in Germany a new battleship "Tirpitz" was constructed. It should get the "state of the art" of a high protection capability. Therefore a new steel alloy was developed with a high nickel content and with a large gradient of hardness all over the thickness, fig.1.

The challenge was the idea, to reach a high hardness on the striking surface combined with a tough back side to retard cracking. This was reached with a 20NiCr15-7-composition in a thickness of 150 mm. It is still today an open question, if the hardness profile was reached by quenching only from one surface after austenitisation or by quenching the complete plate and tempering only at the back face.

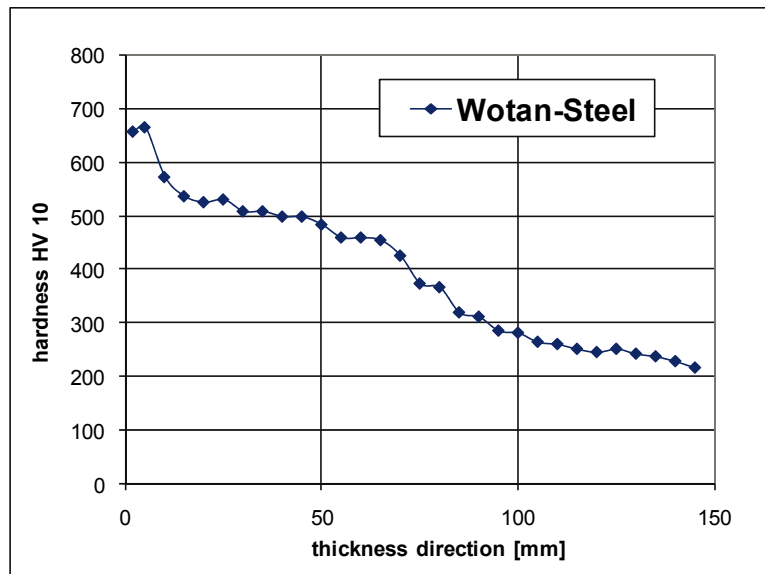


Figure 1: Hardness profile of thickness direction of Wotan-steel

The HSLA or Armor Steels of the seventies in Germany e. g. from Thyssen, named HZB-qualities, were alloyed mainly with Chromium and Molybdenum in equal relations. Vanadium was used as a particle inhibitor to reach a fine grain. To reach high hardnesses for better penetration resistances, the carbon content was increased, which led finally to a "HZB20 or HZB301" with 0,42 to 0,45% C and 1,5-2% Cr and Mo, named "45CrMo67", tab. 1.

Table 1: Types of HSLA-steels

year	origin name	description	note	
1935	Battleship "Tirpitz", Wotan-steel	20 Ni Cr 15-7	o	
1943	Skoda cannon tube	30 Cr Ni 7-2	o	
1980	Thyssen	HZB 20	42 Cr Mo V 6-7	+
		HZB 301	45 Cr Mo V 6-7	+
1984	Thyssen	XH 129 Ni1	30 Cr Ni Mo 5-5	+
		XH 129 Ni3	30 Ni Cr Mo 12-5	+
1990 ff	Thyssen	HZB 290	30 Cr Ni Mo 6-2-1	o
		HZB 293	30 Ni Cr Mo 15-4	o
		HZB 996	30 Cr Ni Mo 8	o
2000 ff	TKS	Secure 200	Mn Mo - type	+
		Secure 400	30 Cr Ni Mo 5-7-2	+
		Secure 450	20 Ni Cr Mo 9-4-7	+
		Secure 500 (<50mm)	30 Ni Cr Mo 7-5-2	+
		Secure 500 (>50mm)	30 Ni Cr Mo 14-5-6	+
		Secure 600	40 Ni Cr Mo 6-6-5	+
2000 ff	SSAB	Armox 370	30 Ni Cr Mo 7-4-7	+
		Armox 440T	20 Ni Cr Mo 10-4-7	+
		Armox 500	30 Ni Cr Mo 6-4-7	+
		Armox 600	45 Ni Cr Mo 6-6-5	+
2009	Creusot-Loire	Mars 240	30 Ni Cr Mo 7-6-6	+

+ nominal chemical composition
o measured content

The strength level of these steels were comparable to modern steel-products with a "long" Hooke's elastic region, fig. 2 followed by a work hardening up to 8 % strain. Furthermore is important, that these high strength low alloyed steels can be named as a "self protecting-steel" by a high energy consumption due to their rather high strain rate sensitivity of flow stresses, ultimate strength, shown in fig. 3, and fracture strain. That means, that the strength and the ductility is enhanced at high velocities.

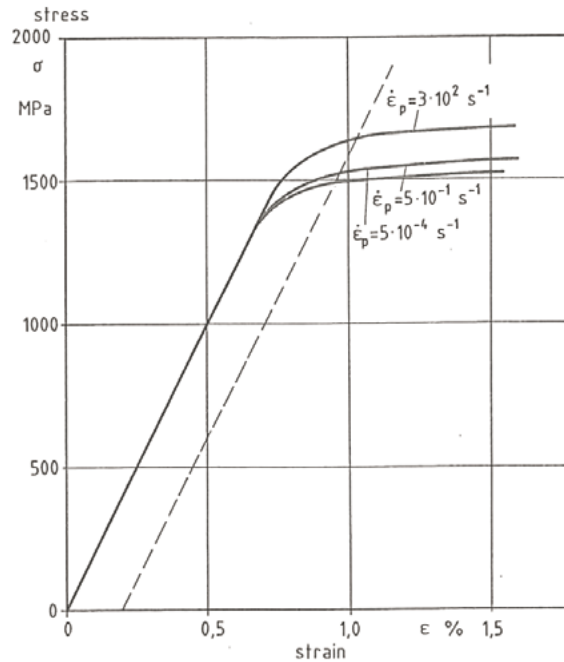


Figure 2: Stress-strain behaviour of base metal 45 Cr Mo V 6 7 with a hardness of 510 HV 30 at three rates of strain

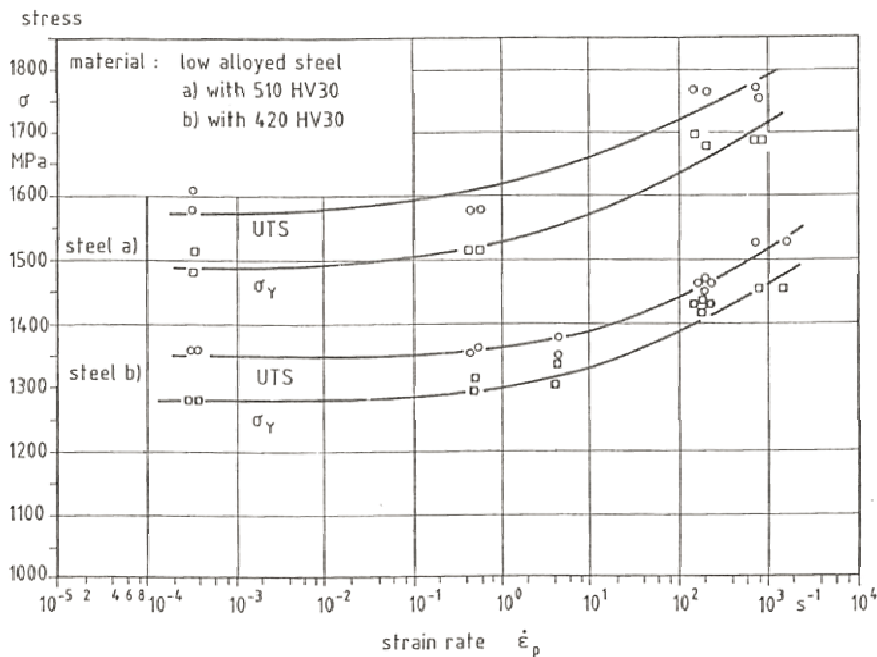


Figure 3: 0,2% yield strength and UTS versus strain rate of base metal 45 Cr Mo V 6 7 in two grades of hardness

Different hardnesses were adjusted by different tempering temperatures. Because formerly the tempering temperature and the reached hardness level was absolutely classified, still today that information is not free.

Due to the high carbon content and the following need of preheating and careful/costly welding procedures, the German steel producer Thyssen (Dr. Pircher) developed in the eighties a new generation of Q+T-steels with reduced carbon content and a lower tempering temperature, the XH-generation, tab.1, e.g. XH129 or XH129Cr. If needed with an additional Ni-content, tab. 1, as XH129Ni1 to XH129Ni3, related to different thicknesses to assure the full hardened state in the mid of the plates. Here first time the nickel-content exceeded the molybdenum-content in a "30CrNiMo55".

Later on, in the nineteen's, the new name XH-steel was replaced by the old world wide better known trademark "HQB" as e. g. HQB996 or HQB290, tab. 1.

Today the use of nickel for ballistic protection applications is the dominant alloying element, leading to Ni-Cr-Mo-steel-Types, above 200 Vickers hardnesses, tab. 1. Worth to note is too, that for each wished hardness level the carbon content and the alloying contents are changed to find the optimum behavior, not as noted before, by changing the tempering temperature after quenching.

This trend is valid for all European steel producers like TKS (Thyssen-Krupp-Stahl), SSAB Svenska Steel AB, or Creusot-Loire. Typically the carbon content is increased to reach higher hardnesses. An exception is obviously made for a steel type, named Secure 450 or ArmoX 440T, which has been optimized to reach a high dynamic toughness on a relatively high hardness level of 450 HB. This steel type has been reduced in carbon content to 0,2 % C, compensated by an enhanced nickel-content of 2 to 3 %. This assures a good welding usability and a high toughness. The reason for producing a high toughness as possible is, that a new threat is appearing on the battle fields, the blast mine or IED's, the improvised Explosive Devices. The blast pressure of the explosive is able to deform the armor structure in a severe manner. In order to reach the highest chance for the survival of the soldiers, the plates and the welding construction are not allowed to break in a brittle manner. This can be reached only with a preference to a high toughness on a relatively high hardness level. Normally, both properties do not correlate.

The dynamic fracture toughness $K_{I_{dyn}}$ was proven to be independent to strength or hardness, fig. 4 with the XH-steels. Even today you may find weak and brittle steels with a low toughness as well as high strengths steels, which exhibit a high, superior toughness, fig. 5.

What is the reason for a high toughness? In general, we have chemical or physical answers: Positive is a low phosphor and sulfur content, which is nearly normal in the modern steelplants. Or the addition of Calcium to prevent or reduce the manganese-sulfur inclusions, which was very successful in preventing lamellar tearing in offshore steels. Important too is a complete austenitisation before quenching to reach a homogenised distribution of the alloying elements and last not least a fine micro-structure.

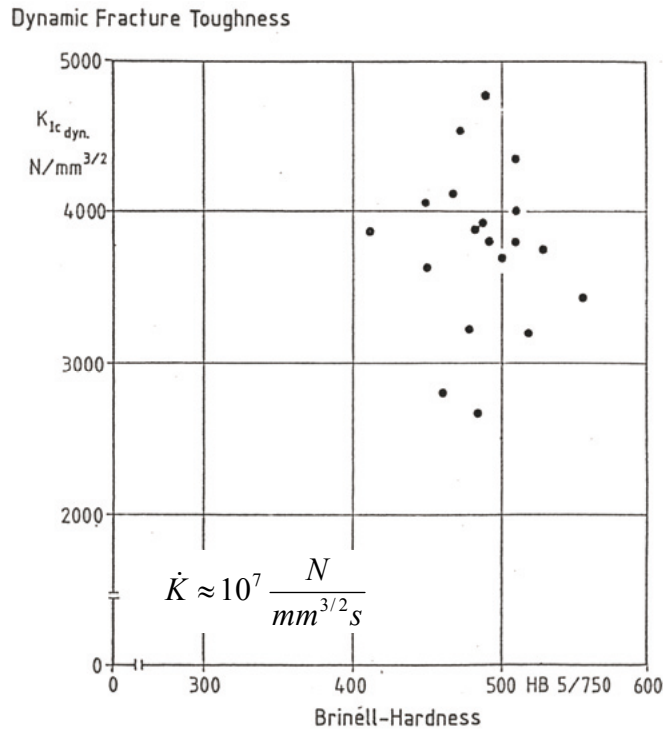


Figure 4: Fracture toughness of HSLA-armour plates versus the Brinell-Hardness of the plates

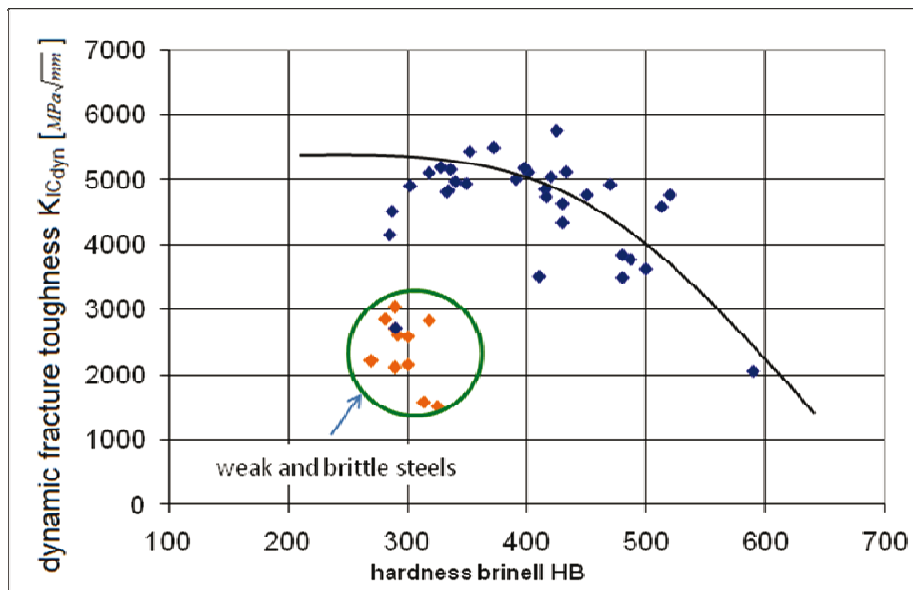


Figure 5: Dynamic fracture toughness vs. hardness of HSLA-steels

Important is, that from tensile testing exclusively we have little chance, to judge the deformability and nearly no chance to forecast the toughness. Toughness has always to do with the influence of the three-dimensional-stress field. The deformability is measured in a mono-axial tensile state or with a two-dimensional stress state e.g. in deep drawing situations. In the first case, the material is forced to elongate in one direction and is allowed to retract in the other both directions. For the second example of deep drawing, the material is able to stretch in two directions by reducing

the thickness. Under a three-dimensional stress field the local straining is limited by the geometry of the surrounding of a notch or a crack. Only the mechanical property of "strain hardening" or "work hardening" serves for a local "yielding zone", followed by a crack extension. The influence of a stepwise increased three dimensional stress state on the local true deformability of three steels is presented in fig. 6. One steel is a fine grained micro alloyed steel, and the other both are HSLA-steels, which possess nearly the same reduction in area under tensile loading.

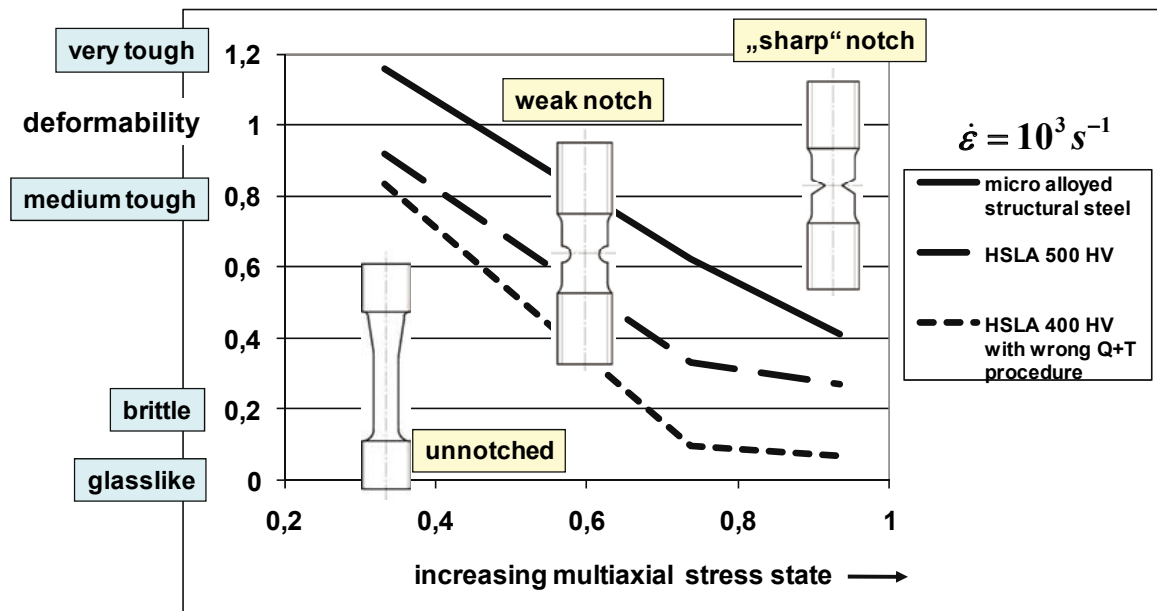


Figure 6: Deformability vs. multiaxial stress state of different steels

Surely, with increasing multiaxial loading, the deformability of all steels is reduced. Important and very meaningful for the intended use as a protective element, the embrittlement takes place very different:

The 500HV-high hardness steel remains comparable to the microalloyed steel, but the weaker 400HV-steel embrittles nearly completely to a few percent of deformability. The reason for this notch-sensitivity is a low toughness, probably due to a failed heat treatment.

3. Summary

It is obvious, that there is a common trend of the European steel producers of modern armor steels to be noted. All use the same or a very similar chemical composition as Ni-Cr-Mo steels with a few percent alloying elements, depending on the wished hardness and thickness.

¹ Prof. Dr.-Ing Dr. h. c. Lothar Werner Meyer, Nordmetall GmbH, Hauptstrasse 16, D-09221 Adorf / Gemeinde Neukirchen, Germany, phone: 0049-371-50349021, fax: 0049-371-50349011 e-mail: lothar.meyer@nordmetall.net

² Ing. Frank Pursche, Nordmetall GmbH, Hauptstrasse 16, D-09221 Adorf / Gemeinde Neukirchen, Germany, phone: 0049-371-50349023, fax: 0049-371-50349011 e-mail: frank.pursche@nordmetall.net

BULK NANOSTRUCTURED METALLIC MATERIALS FOR INNOVATION APPLICATIONS

Ruslan Z. Valiev¹

Abstract

During the last decade severe plastic deformation (SPD) has become a well established procedure of materials processing used for fabrication of bulk nanostructured materials (BNM) with attractive properties. Nowadays SPD processing is rapidly developing and is on the verge of a transition from lab-scale research to commercial production. This paper focuses on several new trends in the development of SPD techniques for effective grain refinement and properties enhancement. The paper also presents recent developments demonstrating the potential of using BNM for advanced and functional applications in engineering and medicine.

Keywords: severe plastic deformation, bulk nanomaterials, applications

1. Introduction

The processing of metallic materials through the application of severe plastic deformation (SPD) has now become of major importance in many research laboratories and technical centers around the world [1-3]. Today, SPD techniques are emerging from the domain of laboratory-scale research into commercial production of various ultrafine-grained materials. This change is revealed in several features. First, it is characterized by the fact that not only pure metals are investigated, but also commercial alloys for special applications; second, by the requirements of economically feasible production of ultrafine-grained metals and alloys. This paper considers these new trends in SPD processing and highlights several of our recent results on the development of BNM for innovation applications.

2. Developing SPD techniques for effective grain refinement

High-pressure torsion (HPT) and equal-channel angular pressing (ECAP) are the most popular SPD techniques but to date they have been usually used for laboratory-scale research.

The key to wide commercialization of UFG materials is to lower their processing cost and waste through continuous processing. Several attempts have been made to this end. For example, repetitive corrugation and straightening (RCS) [4, 5] has been recently developed to process metal sheets and rods in a continuous manner. The co-shearing process [6] and the continuous constrained strip shearing (C2S2) process [7] were recently also reported for continuously processing thin strips and

sheets to produce UFG structures. However, the question of further improvement of microstructure uniformity and properties remains topical in the development of these techniques.

In our studies we have worked on combining the Conform process with ECAP to continuously process UFG materials for large-scale commercial production. In this invention, the principle used to generate frictional force to push a work-piece through an ECAP die is similar to the Conform process [8], while a modified ECAP die design is used so that the work-piece can be repetitively processed to produce UFG structures.

We have designed and constructed an ECAP-Conform set-up which is schematically illustrated in Fig. 1 [9]. As shown in the figure, a rotating shaft in the center contains a groove, into which the work piece is fed. The work piece is driven forward by frictional forces on the three contact interfaces with the groove, which makes the work piece rotate with the shaft. The work-piece is constrained to the groove by a stationary constraint die. The stationary constraint die also stops the work piece and forces it to turn an angle by shear as in a regular ECAP process. In the current set-up, the angle is about 90° , which is the most commonly used channel intersection angle in ECAP. This set-up effectively makes ECAP continuous. Other ECAP parameters (die angle, strain rate, etc.) can also be used.

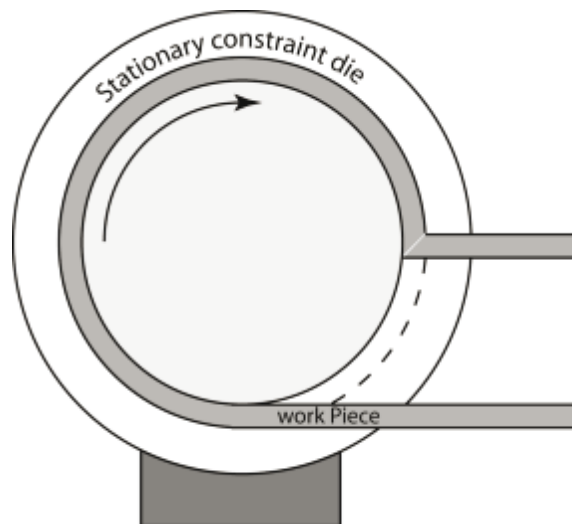


Figure 1 A schematic illustration of an ECAP-Conform set-up [9]

TEM observations showed that the ECAP-Conform led to microstructure evolution typical of the ECAP process [10, 11]. The tensile mechanical properties of the as-processed Al samples after 1 to 4 passes revealed that the ECAP-Conform has significantly increased the yield strength ($\sigma_{0.2}$) and the ultimate tensile strength (σ_u), while preserving a high elongation to failure (ductility) of 12-14%. These results are consistent those for with Al processed by conventional ECAP [10]. We also found that for CP Ti there is strength growth by more than 2 times after the processing as compared with the initial material, and this fact is also consistent with Ti subjected to conventional ECAP [12].

Thus, the recently developed continuous SPD technique, ECAP-Conform can successfully produce UFG materials. The continuous nature of the process makes it promising for production of UFG materials on a large scale, in efficient and cost

effective manner. Lately, the “NanoMeT” company located in Ufa (Russia) has set the first production line intended for the processing of rods 5-8 mm in diameter and up to 3 m in length from super-strong nanostructured Ti for its medical application (www.nanospd.ru).

When referring to the properties of BNM, it ought to be observed that the presence of ultrafine grains is an important but not exclusive structural parameter providing the enhancement of strength of metals and alloys subjected to SPD processing. As is known [2, 3], these materials may also possess specific nanostructural features, such as non-equilibrium grain boundaries, nanotwins, grain boundary segregations and nanoparticles. It has been demonstrated that the presence of grain boundary segregations and non-equilibrium boundaries can result in yield stress values that considerably exceed those predicted from the Hall-Petch relation for the given materials as it is exemplified in Fig. 2 [13, 14].

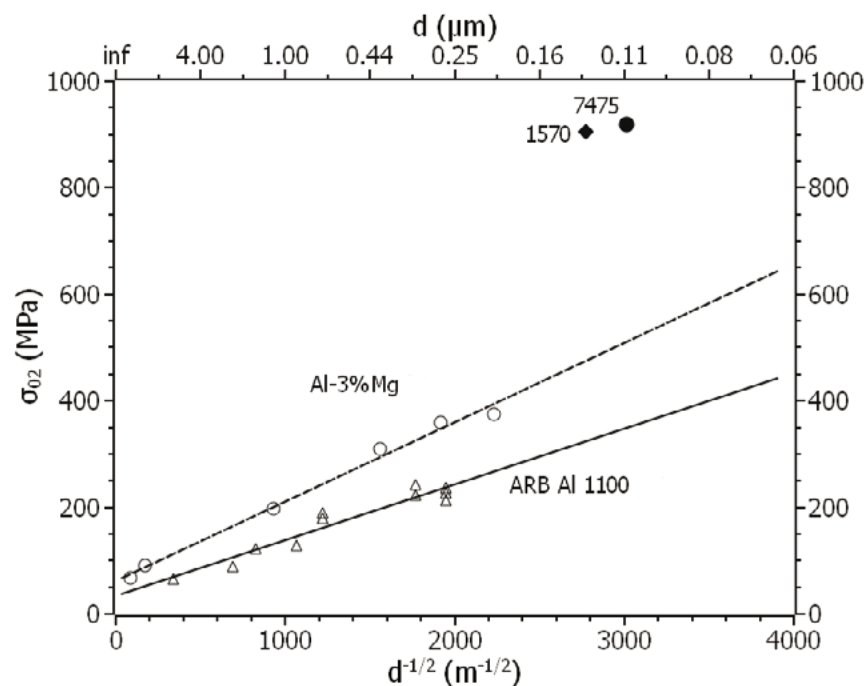


Figure 2 The Hall-Petch relation for the alloys 1100, Al-3%Mg and data on the yield stresses of the UFG alloys 1570 and 7475 [13, 14]

3. Innovation potential of bulk nanostructured materials

Recent reports documented more than 100 specific market areas for nanostructured metals [2, 15] and it is evident that many of these new structural applications involve extreme environments where exceptional strength is needed. Potential near-future applications are presented schematically in Fig. 3 demonstrating some specific examples [2].

Firstly, due to excellent biological compatibility combined with superior specific strength, it is probable that UFG titanium will enter the bio-medical market at an ever-increasing pace. Titanium and titanium alloys are currently used extensively as implant materials in traumatology, orthopaedics and dentistry [16]. This is due to several characteristics including their excellent biocompatibility, good corrosion resistance and specific strength compared with other metals. The implant materials

used in these areas are subjected to complex loads with additional biomedical and other technical requirements.

Significant progress may be achieved here by increasing the specific strength of the implant materials and thereby permitting the use of a smaller size with less invasive surgery. Recent investigations have shown that, due to nanostructuring, the fatigue strength of CP-Ti may be significantly increased to a level exceeding that of the coarse-grained Ti-6Al-4V alloy [17, 18].

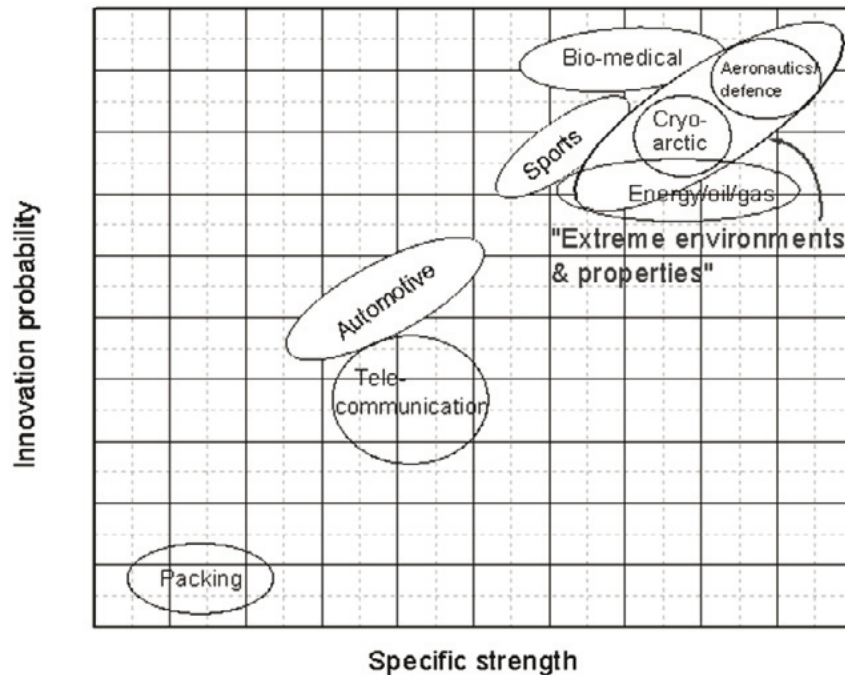


Figure 3 Assumed innovation probability in various sectors vs. specific strength. The highest potential may be seen in applications and products under "extreme environments and/or with extreme specific strength" requirements [2]

Hence, there is also the possibility to replace more expensive and less biocompatible alloys with commercial purity titanium that is more biocompatible [17]. Important requirements in all biomedical applications are corrosion resistance and excellent biocompatibility and both are fulfilled with titanium and most titanium alloys. Preliminary investigations of the corrosion behaviour of nano-titanium suggest that the corrosion resistance is improved by introducing a UFG microstructure [19]. A second example having a high innovative potential is the superplastic forming of light metals produced by SPD for the fabrication of products having both complex shapes and high specific strengths. It is anticipated that these products will have a wide range of applications in the aeronautic and automotive sectors as well as in the consumer product industry. The development of superplastic forming capabilities after SPD is now well established [20]. Numerous experiments show that these superplastic properties are retained when large billets processed by SPD are subsequently rolled into thin sheets during superplastic forming operations [21-23]. Furthermore, the ultrafine grain size is preserved after SPD forming and thus provides a very high strength at ambient temperatures which is an important consideration for many structural applications.

A third potential innovation lies in extreme low temperature applications as in arctic environments and in the special processing applications associated with the oil

and gas industries. This is especially important for low carbon and stainless ferritic steels where usually there is a sharp transition from ductile to brittle behavior with decreasing temperature. Extensive grain refinement due to SPD can significantly decrease the brittle-ductile transition temperature in these steels [24, 25] and this is especially important when undertaking construction work at high latitudes.

4. Summary

Processing by severe plastic deformation provides strong grain refinement and therefore an opportunity to enhance properties of metals and alloys making them attractive for new structural and functional applications. However, finding solutions to these problems is a complex challenge requiring individual approach to the choice of processing routes and regimes and formation of certain nanostructures. The limitation on the use of SPD-processed materials to date, which have arisen primarily from their processing costs and the inherent wastage in conventional processing methods, are now being overcome through the development of new and continuous processing techniques. It is reasonable to anticipate there will be significant advances in the use of nanomaterials in different areas of engineering and bio-medical applications in the coming years already.

References

- [1] Valiev RZ, Estrin Y, Horita Z, Langdon TG, Zehetbauer MJ, Zhu YT. *JOM* 2006;58(4):33.
- [2] Valiev RZ, Zehetbauer MJ, Estrin Y, Höppel HW, Ivanisenko Yu, Hahn H, Wilde G, Roven HJ, Sauvage X, Langdon TG. *Adv Eng Mater* 2007;9:527
- [3] Valiev RZ, Langdon TG. *Adv Eng Mater* 2010;12:677.
- [4] Huang J, Zhu YT, Jiang H, Lowe TC. *Acta Mater* 2001;49:1497.
- [5] Zhu YT, Jiang H, Huang J, Lowe TC. *Metall Mater Trans A* 2001;32:1559.
- [6] Saito Y, Utsunomiya H, Suzuki H, Sakai T. *Scripta Mater* 2000;42:1139.
- [7] Lee JC, Seok HK, Suh JY. *Acta Mat* 2002;50:4005.
- [8] Etherington CJ. *Eng. for Industry* 1974;8:893.
- [9] Raab GI, Valiev RZ, Lowe TC, Zhu YT. *Mater Sci Eng A* 2004;382:30.
- [10] Iwahashi Y, Horita Z, Nemoto M, Langdon TG. *Acta Mater* 1997;45:4733.
- [11] Furukawa M, Horita Z, Nemoto M, Langdon TG. *J Mater Sci* 2001;36:82.
- [12] Raab GI, Valiev RZ, Gunderov DV, Lowe TC, Misra A, Zhu YT. *Mater Sci Forum* 2008;584-586:80.
- [13] Valiev RZ, Enikeev NA, Murashkin MYu, Kazykhanov VU, Sauvage X. *Scripta Mater* 2010;63:949.
- [14] Valiev RZ, Enikeev NA, Langdon TG. *Kovove Mater (special issue on Bulk Nanostructured Materilas)* 2010; accepted for publication.
- [15] Lowe TC. *JOM* 2006;58(4):28
- [16] Brunette DM, Tengvall P, Textor M, Thomsen P. *Titanium in med.* Springer, Heidelberg, 2001.
- [17] Valiev RZ, Semenova IP, Latysh VV, Rack H, Lowe TC, Petruzelka J, Dluhos L, Hrusak D, Sochova J. *Adv Eng Mater* 2008;10:B15
- [18] Stolyarov VV, Zhu YT, Alexandrov IV, Lowe TC, Valiev RZ. *Mater Sci Eng A* 2003;343:43
- [19] Balyanov A, Kutnyakova J, Amirkhanova NA, Stolyarov VV, Valiev RZ, Liao XZ, Zhao YH, Jiang YB, Xu HF, Lowe TC, Zhu YT. *Scripta Mater* 2004;51:225
- [20] Horita Z, Furukawa M, Nemoto M, Barnes AJ, Langdon TG. *Acta Mater* 2000;48: 3633
- [21] Akamatsu H, Fujinami T, Horita Z, Nemoto M, Langdon TG. *Scripta Mater* 2001;44:759
- [22] Park KT, Lee HJ, Lee CS, Nam WJ, Shin DH. *Scripta Mater* 2004;51:479
- [23] Nikulin I, Kaibyshev R, Sakai T. *Mater Sci Eng A* 2005;07:62

- [24] Korznikov AV, Safarov IM, Nazarov AA, Valiev RZ. Mater Sci Eng A 1996;206:39
[25] Borisova MZ, Yakovleva SP, Ivanov AM. Sol St Phen 2006;14:97

¹ prof. Dr. Ruslan Z. Valiev, Institute of Physics of Advanced Materials, Ufa State Aviation Technical University, 12 K. Marx str., Ufa 450000 Russia, tel.: +7 347 2733422, e-mail: rzvaliev@mail.rb.ru

APPLICATIONS OF NANOCRYSTALLINE THIN COATINGS PRODUCED BY PLASMA METHODS

Petr Louda¹, Zbigniew Rożek²

Abstract

Recently, the thin coatings have been noticed as an attractive material for the widespread industrial application. Thin coatings deposited on the cutting tools or engine auto parts improve wear resistance and increase their service life. Carbon coatings with chemical inertness and high corrosion resistance are used in biomedical applications.

Keywords: plasma, thin layers, protective coatings

1. Introduction

Currently, it is known that the increases of the quality of products is related to development of new materials. Use of micrometric and nanometric materials in all fields of our life is growing exponentially, they play very important role in scientific revolution.

Thin coatings are deposited on the various types of substrates (metals, polymers ...) using PA CVD techniques. The application of thin coatings is ideal by means of deposition because it can be applied to modification of substrate surface properties, which often significantly affect the functional properties. Innovative coatings for protection against wear have recently attracted increasing interest from both academy and industry in many areas such as cutting and casting tools, mechanical components and also in biomedical applications. This review will describe some applications of thin coatings.

2. Thin coatings for machining applications

Use Currently, machine tools used in wood industry are characterised by high performance. Development of this industry has resulted in the full automation of the production process. However, cutting tools applied in this area do not fulfill all the requirements for full exploitation of the machines potential. In this case, the main problem is related to differences in physical and chemical structures between wood and material of cutting tool.

Wood and wood-like materials are characterized by specific properties. It is a multifunctional, multi-component, hydroscopic, anisotropic, fibrous, porous material. Furthermore, the surface defects present on this materials can cause blunting of the cutting edges. For this reasons this is exceptionally difficult material to machine.

Wood machining is characterized as very abrasive process, where the main mechanism of wear of cutting tool is erosion [1]. Because of this, coatings used in this field have to be very hard, adherent and smooth.

In the last few decades, many scientific centers have worked in the field of wood machining, and high wear resistant tools has been developed by applying carbides, nitrides and diamond based protective coatings [2,3].

Aluminium and its alloys are used in many different applications such as construction and structural materials, communications industries, transportation equipments, packaging. For this reason, the machining of aluminium is more and more widespread but the main problem is the necessity of using machining fluids. The fluids help dissipate heat created during the machining operations and minimize the adhesion of aluminum to the tool. Nevertheless, machining fluids increase machining costs and include strong degreasing agents which are harmful to the environments. Therefore, there is a need to find new kind of cutting tools with high wear and adhesion resistance. In the last few years it has been established that carbon based coatings or TiB_2/TiC multilayer coatings are well-suited for aluminium machining [4,5].

3. Thin coatings for the automotive industry

As in many other areas there is a tendency to reduction of products cost price in automotive industry and at the same time to apply innovative technology. Currently automotive production is determined chiefly by customer demand. They are primarily interested in low fuel consumption, so manufacturers are forced to build light vehicles. This is also related to the engine and for this reason aluminium cylinder walls are now becoming the norm. Cast iron has been replaced by lightweight and low-cost aluminum-silicon alloy. Unfortunately, the tribological properties of aluminium are poor. It has been established that piston skirt friction, piston rings and bearings account for 66% of total friction losses [6]. The remainder of the losses comes from crankshaft, transmission and gears. Materials for these applications have to fulfill the following requirements: high wear resistance and limp-home features in case of a lack of lubrication.

Application of DLC coatings with a high hardness and excellent lubricant properties implies many advantages for the automotive industry. Examples for DLC coatings used for automotive applications are as follow: piston rings [7], injector needles in diesel engines [8], camshafts and valves [9], gear boxes [10]. Use of carbon coatings in these applications makes possible to improve the mechanical stability, which means less wear, better gliding, less lubricants, longer service intervals and pronounced fuel saving.

4. Thin coatings for medical applications

Most common metal implants that are used in different biomedical applications are made from titanium alloys, stainless steel and cobalt-chromium alloys. The release of ions from these metals through corrosion processes and wear debris can lead to immunological reactions. For example stainless steel, a metal alloy widely used in biomedical applications, releases Ni ions and induces allergic reactions. This process leads to osteolysis (bone resorption) and aseptic loosening and failure of the implant [11].

Coating biomedical implants with protective films, which can increase corrosion and wear resistance, may prevent the problems described above. Diamond-like carbon films, which are characterized by chemical inertness, corrosion and wear resistance have demonstrated biocompatibility and have been shown to be effective as a diffusion barrier [12]. Thus, DLC coatings are used as protective coatings for improving the performance of orthopedic implants such as artificial knees, hip replacement and femoral heads [13].

In other cases, it has been established that the DLC coatings are characterized by good blood compatibility. They prevent interaction between implant and blood and thus prevent the occurrence of thrombosis [14]. For these reasons, DLC coatings has been suggested for application in blood contacting implants such as artificial hearts, mechanical heart valves, and coronary stents [15].

5. Conclusion

Friction, wear and adhesion play an important role in determining the performances of components of industrial devices. Performances of components of industrial devices are determined by friction, wear and adhesion. Nowadays, a great hope is directed to use of functional thin coatings providing high hardness and wear resistance, low friction and a many useful properties that improve the performances of devices.

Acknowledgements

This work was supported by FI-IM5/095 project

References

- [1] M.A. Djouadi, P. Beer, R. Marchal, A. Solokowska, M. Lambertin, W.P. Nouveau, "Antiabrasive coatings: application for wood processing", *Surface and Coatings Technology*, Vol. 116–119, 1999, pp 508-516.
- [2] A. Köpf, R. Haubner and B. Lux, "Double-layer coatings on WC–Co hardmetals containing diamond and titanium carbide/nitride", *Diamond and Related Materials*, Volume 9, No. 3-6, 2000, pp 494-501
- [3] M.G. Faga, L. Settineri, "Innovative anti-wear coatings on cutting tools for wood machining", *Surface and Coatings Technology*, Vol. 201, No. 6, 2006, pp 3002–3007.
- [4] G.R. dos Santos, D.D. da Costa, F.L. Amorim, R.D. Torres, "Characterization of DLC thin film and evaluation of machining forces using coated inserts in turning of Al–Si alloys", *Surface and Coatings Technology*, Vol. 202, No. 4-7, 2007, pp 1029–1033.
- [5] K.W. Lee, Y.-W. Chung, C. Korach, Le.M. Keer, "Tribological and dry machining evaluation of superhard TiB₂/TiC multilayer coatings deposited on Si(001), M2 steel, and C3 WC cutting tool inserts using magnetron sputtering", *Surface and Coatings Technology*, Vol. 194, No. 2-3, 2005, pp 184-189.
- [6] S.C. Tung, M.L. McMillan, "Automotive tribology overview of current advances and challenges for the future", *Tribology International*, Vol. 37, No. 7, 2004, pp 517-536.
- [7] A.M. Merlo, "The contribution of surface engineering to the product performance in the automotive industry", *Surface and Coatings Technology*, Vol. 174 –175, 2003, pp 21–26.
- [8] C.P.O. Treutler, "Industrial use of plasma-deposited coatings for components of automotive fuel injection systems", *Surface and Coatings Technology*, Vol. 200, No. 5-6, 2005, pp 1969-1975.

- [9] K. Bewilogua, G. Bräuer, A. Dietz, J. Gäbler, G. Goch, B. Karpuschewski, B. Szyszka, "Surface technology for automotive engineering", *CIRP Annals - Manufacturing Technology*, Vol. 58, No. 2, 2009, pp 608-627.
- [10] J. Vetter, G. Barbezat, J. Crummenauer, J. Avissar, "Surface treatment selections for automotive applications", *Surface and Coatings Technology*, Vol. 200, No. 5-6, 2005, pp 1962-1968.
- [11] S.K. Gupta, A. Chu, A.S. Ranawat, J. Slamin, C.S. Ranawat, "Review Article: Osteolysis After Total Knee Arthroplasty", *The Journal of Arthroplasty*, Vol. 22, No. 6, 2007, pp 787-799.
- [12] K. Mitura, P. Niedzielski, G. Bartosz, J. Moll, B. Walkowiak, Z. Pawłowska, P. Louda, M. Kieć-Świerczyńska, S. Mitura, "Interactions between carbon coatings and tissue", *Surface and Coatings Technology*, Vol. 201, No. 6, 2006, pp 2117-2123.
- [13] E.T. Uzumaki, C.S. Lambert, W.D. Belangero, C.M.A. Freire, C.A.C. Zavaglia, "Evaluation of diamond-like carbon coatings produced by plasma immersion for orthopaedic applications", *Diamond and Related Materials*, Vol. 15, No. 4-8, 2006, pp 982-988.
- [14] T. I. T. Okpalugo, A. A. Ogwu, P. D. Maguire, J. A. D. McLaughlin, D. G. Hirst, "In-vitro blood compatibility of a-C:H:Si and a-C:H thin films", *Diamond and Related Materials*, Vol. 13, No. 4-8, 2004, pp 1088-1092.
- [15] K. Gutensohn, C. Beythien, J. Bau, T. Fenner, P. Grewe, R. Koester, K. Padmanaban, P. Kuehnl, "In Vitro Analyses of Diamond-like Carbon Coated Stents, Reduction of Metal Ion Release, Platelet Activation, and Thrombogenicity", *Thrombosis Research*, Vol. 99, No. 6, 2000, pp 577-585.

¹ Prof. Ing. Petr Louda, CSc., Department of material Science, Technical University of Liberec, 2 Studentská Road, 461 17 Liberec 1, Czech Republic, Tel.: +420 485 353 116, e-mail: petr.louda@tul.cz

² Ing. Zbigniew Rożek, Institute for Nanomaterials, Advanced Technologies and Innovation, Technical University of Liberec, 2 Studentská Road, 461 17 Liberec 1, Czech Republic, Tel.: +420 485 353 342, e-mail: zbynekrozek@seznam.cz

THE ANALYSIS OF FAILED LOCOMOTIVES WHEEL

Josef Kasl¹

Abstract

Failure analysis of a broken locomotive wheel was performed using NDT, hardness and mechanical properties measurement, macrostructure and microstructure observation and fractographic analysis. The root cause of the wheel failure was an excessive thermal-deformation load of the tread during braking of the locomotive – i.e. an improper manner of braking or functions of the braking system.

Keywords: Failure analysis, locomotive wheel, thermal induced cracks

1. Introduction

This paper deals with a failure analysis of locomotive wheel. The wheel was installed in the locomotive on which a breakdown in consequence of a total breaking up of the wheel occurred in June 2010 in Egypt. According to the information by operator ENR the broken wheel was in operation approx 1.5 year [1].

Cast carbon steel Class B was used for production of the tested locomotive wheel. This class is designed for high-speed service with severe braking conditions and heavier wheel loads. Steel contains 0.67-0.77 weight % of carbon and 0.60 – 0.85 weight % of manganese. Heat treatment of the wheel consists of the following procedures: cooling to the temperature below the critical range and uniform reheating to the proper temperature to refine the grain, and then the rims of rotating wheels are quenched using water spraying. Following quenching, the wheels are tempered and subsequently cooled under the controlled conditions to meet the hardness requirement. Brinell hardness HB from 302 to 341 in the layer of depth of 25 mm copying the tread-flange contour should be reached [2,3].

Wheel failures have been the subject of intensive study since the beginning of the railroad industry. Railroad wheels may fail in different ways corresponding to the different failure mechanisms. Many experiences concerning railroad failures have been obtained which makes it possible to understand and classify various types of failures. In recent years, higher train speeds and increased axle loads have led to larger wheel/rail contact forces. This and optimization of the wheel and rail design tend to change the major wheel rim damage from wear to fatigue [4]. Unlike the slow deterioration process of wear, fatigue causes abrupt fractures in wheels or the tread surface material loss. The fatigue problem of a railroad wheel is often referred to as rolling contact fatigue [5] which is caused by repeated contact stress during the rolling motion. Authors of the work [6] divide the wheel fatigue failure modes into three different failure types corresponding to different initiations locations: surface

initiated, subsurface initiated and deep surface initiated fatigue failures. On the tread surface there are usually two types of cracks. One is caused by the repeated mechanical contact stress. The other one is initiated by thermal stresses arising from on-tread friction braking. The thermal cracks appear as short cracks oriented axially on the wheel tread [7]. Other causes of failures can be scrapes and gouges from mechanical damage, stampings used to identify the wheel and thermal events that create brittle martensite which easily cracks on application of mechanical or thermal stresses. The most important railroad wheel failures are caused by shattered rims, thermal cracking and vertical split rim. Thermal cracking usually breaks off a piece of the wheel tread, while shattered rim can destroy the integrity of the wheel.

In general, a catastrophic failure occurs as a result of a crack of a sufficient size that by fracture mechanics principles will cause complete failure on application of one specific load [8]. The size of the crack and the extent of the load at failure are interdependent and depend on the fracture properties under consideration and the rate of application of the load. So, properties of the material at the time of the failure (they can change during service), size and location of the crack and related circumstances are important. Stress required for a wheel failure is large, for above any service load. However, the stress at which a failure will occur is strongly reduced if there is development and a growth of a crack to a suitable size. When a crack is sufficiently large, with a minimum size of about 0.4 in., a catastrophic failure can occur as a result of the dynamic load of sufficient magnitude. However, the load must produce a fracture/critical level of local crack-opening stress at the site of the crack because of the rapid attenuation of a dynamic load away from the location on the rim of the wheel where the load is applied. The role of residual stresses in relation to wheel failure is not well established. However, it is supposed that it plays a minor role.

2. Results

A fragment of the wheel was supplied for the analysis. It represents approx. one quarter of the wheel circumference and a smaller part of the hub (Fig. 1).

The following works were carried out on the supplied wheel, actually on the fragment:

- non destructive testing - NDT by means of the magnetic particle method on the surfaces of the treads of the wheel with the aim to detect a possible occurrence of cracks;
- verification of the chemical composition of the wheel materials;
- verification of mechanical properties of the material based on the performed tensile and impact tests according to the specification [2];
- determination of hardness of the rim of the wheel on the side and on the cross-sections according to the specification [2];
- observing the microstructure of the wheel rims in the cross as well as longitudinal directions using light (LM) and scanning electron microscopy (SEM);
- a fractographic analysis of the fracture surfaces of the broken wheel;
- since during the defectoscopy inspection on the surfaces of the treads of both wheels there were detected indications of a crack nature, a specimen was cut out from the wheel and broken down using three-point bend at the temperature of liquid nitrogen to open the crack so that the fracture surfaces of the original cracks would be accessible for the fractographic analysis;

- observation of the surface of the treads of the wheels in as-received condition and after etching using a binocular microscope and SEM.

The defectoscopy test using the magnetic particle method revealed three indications of the size ranging from 10 to 15 mm on the tread surface. They lie in the axial direction on the taper side of the rim.

The composition of the wheel material corresponds to the specification for steel of Class B.

Brinell hardness was measured on the front face of the rim at the place of the edge determining a range of the hardened area and on the cross sections. The required value is only the one determined on the front face of the rim. The measured values lie just below the minimum hardness limit HB 302. It is evident from the values determined on the cross section that in the area under the tread on the side by the front face of the rim the hardness dropped to the values HB 261 to 268. This drop corresponds to the area with evident thermal affecting.

The specimen macrostructure was observed on the cross as well as circumferential sections of the rim. In the structure there is evident a considerable heat affected zone showing as differently etched area (Fig. 2). It lies between the edge of the front face of the rim and the tread and the flange. It reaches to the maximum depth of approx. 10 mm under the tread surface. The microstructure of the material in the area under the tread is formed of the pearlite nodules and ferrite which is eliminated mostly on the boundaries of the pearlitic nodules. In the centre of the heat affected zone the microstructure is considerably fine-grained in comparison with the non-affected material. This trend is kept as far as to the boundary of the heat affected zone.

Fractographic analysis was performed. Two cracks spread from the tread area in the radial direction. Several connected cracks lying approximately in the circumferential direction continue after them. Through these cracks the whole circumferential part of the wheel was broken off the hub. In addition to that several smaller fragments were broken off the center area of the wheel. The distance of both radial cracks is approximately one quarter of the circumference. One of the radial cracks was important for establishing the causes of the failure (Fig. 3). In the area under the tread there is a crack initiated on the tread surface and spreading in the radial direction to the wheel rim. It is of semi-elliptic shape and its center is 24 mm from the front face of the rim. Its total length is 18 mm; its depth is 5 mm. The crack surface is covered with a layer of oxides of black color. A defect of the size 18 x 30 mm lying on the edge of the tread surface and the front rim face developed from this crack. The surface of the fracture area of this defect is partially mechanically pressed, however, the microfractographic analysis carried out using SEM showed that the crack had spread by transcrystalline cleavage. The topography of the fracture surface in the surroundings of the defect shows that just from the defect the crack spread which led to the failure of the wheel. In fast fracture the crack spread by transcrystalline cleavage.

A specimen was cut out of the surrounding of one defect found during the defectoscopic test and broken so that the fracture surface of the original crack would be accessible for direct observation. The crack is of similar appearance and position as the crack described at the fracture surface of the fragment. It is of a semi-elliptic

shape (the length is 26 mm, the depth of penetration is 4 mm, the distance of the center from the front rim face is 24 mm). The crack is covered with black oxides.

On the tread surface in the circumferential direction by the front rim face there stretches a strip of the width approx. 100 mm formed of a thin black layer with a smooth surface. This strip is locally interrupted in the points where the layer was removed with the surface of metallic appearance with noticeable mechanic pressing. In this black layer there are tiny cracks oriented especially in the axial direction. From the layer they penetrate also to the metallic material lying under the layer.



Figure 1 Sample for analysis



Figure 2 Cross-section, HB valuesf

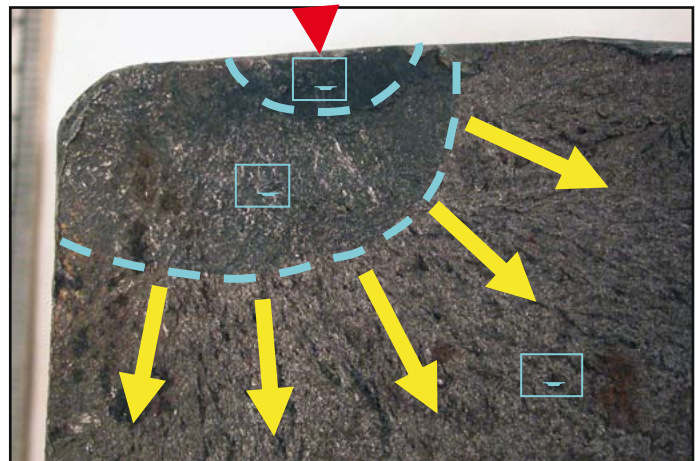


Figure 3 Fracture surface valuesf

3. Conclusions

1) The material of the wheel rim shows appearances of thermal damage which caused changes in the microstructure and the mechanical properties. The structure

change can be observed on macro level as differently etched area lying between the edge of the front rim face and the tread and the flange. Its depth is about 10 mm. There is considerably fine-grained microstructure in this heat affected zone in comparison with the non-affected material. The microstructure consists of the mixture of pearlite and ferrite on the boundaries of pearlite nodules. A significant decrease of hardness occurred in the heat affected zone.

2) There is a thin layer of iron oxides containing in addition to zinc, cuprum and also smaller amounts of calcium, magnesium, and aluminum on the tread. Small cracks were formed in this layer spreading into the metal material lying below this layer.

3) The presence of thermal cracks on the tread was found during NDT and fractographic analysis. Their sizes were approximately 15x5 mm.

4) During operation one of this crack expanded by cleavage to a defect of the size of 18x30 mm situated on the edge of the front rim face and the tread. This defect had a size above a critical value during a peak of the load and fast fracture occurred leading to the total destruction of the wheel.

5) The root cause of the wheel failure was obviously an excessive thermal-deformation load of the tread during braking of the locomotive – i.e. an improper manner of braking or functions of the braking system.

References

- [1] Picture documentation of a chassis with failed wheel taken in an engine house of ENR.
- [2] AAR Manual of Standards and Recommended Practices Wheels and Axles, Wheels, Carbon steel – specification M-107/M-208.
- [3] GE Rail Design Guides Section 3.1.10 Locomotive Wheel Design.
- [4] Turnay H.M., Mulder J.M.: The transition from the wear to the stress regime. *Wear* 1996; 191:107-12.
- [5] Johnson K.I.: The strength of surfaces in rolling contact. *Proc. Inst Mech Eng IMechE* 1989; 203: 151-63.
- [6] Ekberg A., Marais, J.: Effect of imperfections on fatigue initiation in railway wheels. *IMechE J Rail Rapid Trans* 1999; 214: 45-54.
- [7] Gordon J., Perlman A.B.: Estimation of residual stresses in railroad commuter car wheels following manufacture. *Proceedings of the international mechanical engineering congress and in Anaheim, CA, ASME RTD, vol. 15; 1998.*
- [8] Stone D.H., Fellini W.S., Harris W.J. Jr.: North American Wheel Failure Experience. In *Proceed. of 3rd Int. Heavy Haul Rwy Conf., Vancouver, BC, 1986, 10/13-10/17.*

¹ RNDr. Josef Kasl, CSc., ŠKODA VÝZKUM s.r.o., Tylova 1/57, 316 00 Plzeň. Czech Republic.
Tel.: +420 379 852 321, e-mail: josef.kasl@skodavyzkum.cz

THE EXPERIENCE FROM WELDING OF HIGH-STRENGTH FINE-GRAINED STEELS

Stanislav Novák¹, Jiří Mráček²

Abstract

The development of fine-grain materials with a higher yield limit (420, 460, 500, 550, 690 up to 1100 MPa) have boosted in recent years and have made them standard structure materials. In applications, high strength properties of these materials may bring both material savings and new solutions to loaded nodes. Although welding of these materials has been sufficiently researched and described, the main problem is the practical application of the findings in specific operating conditions. The requirements regarding welding and compliance with technological regulations during welding are much stricter for these steels than for usual structural materials, therefore, it is inevitable to adhere to all principles to produce a compliant welding seam. The study presents experience from the production of steel structures, equipment for vertical ore/ coal transportation in mines, etc.

Keywords: welding, high-strength, fine-grained steel

1. Introduction

The development and application of structural materials have recently resulted in a greater use of high-strength steels.

The practice is also leading up to a greater application of medium- and high-strength steels and wear resistant materials. The range of materials used for common structures can be extended with steels from S420 to S690 strength classes. Consumption of these steels has grown on both the global and local basis in the past six years and their use has become more and more common. Standards regulating this area have been already introduced. Moreover, the development of prices of these steels is also very positive, which makes their use more economic than the use of standard quality steels. They are suitable especially for large structures, such as bridges, vast halls, high-rise buildings, etc., but they can be effectively used for smaller structures, too. High-strength steels (above S500) can be used for stressed components of special structures for ore/coal mining or transportation equipment or their parts, such as skip buckets for vertical transportation of ore/coal, cages, skip cages, other components of mining equipment.

The production of fine-grained steels consists in thermomechanic treatment of steels during the rolling process. Essentially, they can be classified in four groups, see Table 1.

Table 1. Classification of thermomechanically treated steels

	<i>Hardened steels</i>	<i>Commercial brands</i>	<i>Basic mechanical properties</i>	<i>Other mechanical properties</i>	<i>Fundamental technological properties</i>
I.	High-strength structural steels	WELDOX DOMEX ALFORM	$R_e=700\div 1100$ MPa	Toughness	Weldability Bendability
II.	Wear-resistant steels	HARDOX XAR	Hardness 400÷600 HB	Toughness	Weldability Machinability Bendability
III.	Armour steel	ARMOX	Hardness 340÷600 HB	Toughness	Weldability
IV.	Tool steel	TOROX	Hardness 33 HRC 44 HRC		Machinability Thermal stability

Table 2 shows the main parameters of mechanical properties of DOMEX and WELDOX high-strength (Class I) materials.

Table 2. Mechanical properties of WELDOX, DOMEX steels

Brand	Thickness [mm]	Yield point and strength limit		Carbon equivalent
		$R_{p0,2}$ [MPa]	R_m [MPa]	CEV
WELDOX 355	8 ÷ 16	355	450 ÷ 610	0,39÷0,43
DOMEX 355 MC	(16) ÷ 25	345	450 ÷ 610	
WELDOX 420	6 ÷ 16	420	500 ÷ 660	0,37÷0,39
DOMEX 420 MC	(16) ÷ 40	400	500 ÷ 660	
	(40) ÷ 63	390	500 ÷ 660	
	(63) ÷ 80	380	480 ÷ 650	
WELDOX 460	6 ÷ 16	460	530 ÷ 720	0,37÷0,42
DOMEX 460 MC	(16) ÷ 40	440	530 ÷ 720	
	(40) ÷ 63	430	530 ÷ 720	
	(63) ÷ 80	420	510 ÷ 720	
WELDOX 500	6 ÷ 16	500	570 ÷ 720	0,37÷0,42
DOMEX 500 MC	(16) ÷ 40	480	570 ÷ 720	
	(40) ÷ 80	460	570 ÷ 720	
WELDOX 700	4 ÷ 50	700	780 ÷ 930	0,39÷0,64
DOMEX 700 MC	(50) ÷ 100	650	780 ÷ 930	
WELDOX 900	4 ÷ 50	900	940 ÷ 1100	0,56
	(50) ÷ 80	830	880 ÷ 1100	
WELDOX 960	4 ÷ 50	960	980 ÷ 1150	0,56÷0,64
WELDOX 1100	5 ÷ 50	1100	1200 ÷ 1500	0,68÷0,72

High-strength properties of these steels may in various applications bring both a number of material savings and new solutions to loaded nodes.

The following steels are used:

- normalized fine-grained steel (A)
- heat-treated fine-grained steel (Q) and
- thermomechanically treated fine-grained steels (M).

2. High-strength development trends

Mechanical properties of “traditional” non-alloyed structural steels are determined, in particular, by the content of carbon and manganese; generally speaking, they are reinforced through a substitution and interstitial mechanism.

The yield point and strength limit of non-alloyed structural steels can be increased by additional alloying with small contents of elements, such as Al, Ti, Nb and V, while retaining their good toughness and eliminating the impact of carbon on their weldability. Activity of these elements is enabled by formation of fine-grained structure, moreover, their bond to carbon and nitrogen taking form of precipitation strengthening increases strength properties of the materials. Such steels are called fine-grained. Considering very small amounts of the alloying elements, they are referred to as microalloyed fine-grained steels, being usually limited by the following figures – Al_{min}. 0.015 wt. %, Ti_{max}. 0.15 wt. %, V_{max}. 0.1 wt. % and Nb_{max}. 0.04 wt. % (the total amount of alloys ranges from 0.15 to 0.25%).

Low-alloyed fine-grained materials with higher strength were developed from traditional structural weldable steels, which gave rise to a group of weldable high-strength steels referred to by Anglo-Saxon literature as HSS (High-Strength Steels). These steels are incorporated in production portfolios of all global producers. Starting with Japanese producers, such as NIPPON, KAWASAKI, NKK, SUMITOMO STEEL, over British BSC, Swedish SSAB and AVESTA, German MANNESMANN, THYSSEN, to U.S. BENTHELEM STEEL and other e.g. MITTAL etc. Practically all known Czech steelworks manufacture these steels.

Future of high-strength “cheap” steel

The strength is growing due to higher proportion of hard phases compared to soft phases. Duplex steels consist of ferrite and up to 20% of martensite. TRIP steels refer to another direction of development. Transition to tensile-strength steels (over 800 MPa) lies in the use of multiphase steel. The structure of these steels consists of a higher proportion of hard phases with fine precipitates and soft phases. The entire microstructure is very fine.

Further development is represented by the concept of semi-martensitic steels. When the proportion of martensite exceeds 20%, the steels reach a relatively low yield point, but a high strength limit. The highest strength limit of 1400 MPa can be reached by pure martensitic steels.

The most realistic development trend is the reduction of grain size and a multiphase structure. However, an extreme reduction of the grain size may lead to a dangerous phenomenon when the yield point approximates the strength limit. This problem can be overcome by using a multiphase structure.

Wear-resistant thermomechanically hardened materials are widely applicable in the production of power industry equipment and ore/coal transportation equipment.

Hardness, which ranges from 400 to 600 HB, is the basic property of this group of thermomechanically hardened steels (wear-resistance of these plates is usually given

by their hardness). Production of the fine-grained, thermomechanically treated plates consists in intensive hardening of the entire plate cross-section. And it is the process of hardening of plates with a high primary purity of steel that is the decisive factor of the resulting properties of the plates. The essence of a rolling quench press consists in hot steel plate being dragged by cylinders through zones with water jets of different pressures. The plate is hardened while on the move and unlike the static quench press, hardening of the entire surface of the plate is uniform. Water pressure in hardening jets is so big that the water flow "blows out" a steam cushion, which forms in the first phase of hardening and thus substantially cuts the time to cool the plates. The plates obtain high wear-resistance properties due to this process adding just a small amount of alloying elements, which particularly enhances weldability of the steels. Up to the thickness of 25 mm, HARDOX 400, 450 and 500 steels show the same or better weldability than S355J2 steel. Mechanical properties and chemical composition of HARDOX plates, according to the producer (SAAB), are given in Table 3.

Table 3. Mechanical properties of HARDOX steels

Type	Hardness			Ductility	Toughness	Carbon equivalent		Bend diameter
	HB Brinell	R _{p0,2} [MPa]	R _m [MPa]	A5 [%]	KV _{-40°C} [J]	CEV	CET	Min. [mm]
HARDOX 400	370 – 430	1 000	1 250	12	45	0,37	0,26	3 × t
HARDOX 450	425 – 475	1 200	1 400	10	35	0,47	0,34	4 × t
HARDOX 500	470 - 530	1 300	1 550	8	30	0,60	0,42	5 × t
HARDOX 600	560 - 640	1 650	1 860	7	20	0,82	0,58	ne

3. Selection of base materials for loaded and heavily loaded parts (in power industry, ore/coal transportation and mining)

Designers and producers still tend to be somewhat reluctant when it comes to the application of high-strength fine-grained materials in power industry equipment and ore/coal transportation and mining equipment, however, a certain progress has been witnessed in the past 5 or 6 years.

For instance, a typical design of a skip bucket for ore/coal vertical transportation has a shape of a box. The load bearing structure is formed by vertical and horizontal "bars". The internal space of the bucket, i.e. the transported ore/coal container is encased with wear-resistant HARDOX materials, or the high-strength S690QL material. Due to technological reasons (being suitable for cold bending), the bars are mainly made of S420MC to S550MC materials (according to ČSN EN 10149-2).

The Table 4 shows examples of materials selected for the design of ore/coal transportation and mining equipment, namely the materials EN 10025-2 to -6 and EN 10149 that are produced under numerous brands.

Table 4. Materials selected for the design of ore/coal transportation and mining equipment

Material	Designation	Standard	Usage examples
S235	S235JR; St 37-2	EN 10025-2	Low-loaded components (covering sheets, ancillary equipment)
	S235J2; St 37-3		
	S235JRC; QSt 37-2		

	S235J2; QSte 37-3		
S355	S355J2; St 52-3	EN 10025-2	Loaded components – general use
	S355J2C; QSte 52-3		
S355MC až S700MC	S355MC, S420MC S460MC, S500MC S550MC, S600MC S650MC, S700MC	EN 10149-2 EN 10149-3	Cold-worked loaded components (bars), cage floors Plate thickness 1.5 to 20 mm, bends – diameter 0.5 to 2 thicknesses
S355N	S355N/ NL	EN 10025-3	Loaded components
S420	S420M; QSte 420 TM	EN 10025-4	Loaded components Bars, profiles, side plates
	DOMEX 420 MCD		
	WELDOX 420		
S460	S460M; QSte 460 TM	EN 10025-4	Loaded components Bars, profiles, side profiles Cage and skip top components
	DOMEX 460 MCD		
	WELDOX 460		
S500 S550	S500Q/QL; S550Q/QL	EN 10025-6	High-loaded components Bars Carrying side profiles, floors Cage and skip top components
	DOMEX 500/ 550 MCD		
	WELDOX 500/550		
	ALFORM 500M/550M		
S690	S690QL	EN 10025-6	High-loaded components Bars Carrying side profiles, floors Cage and skip top components
	WELDOX 700E		
	DOMEX 700 MC E		
	ALFORM 700 M		
Wear-resistant	HARDOX 400 HARDOX 450 HARDOX 500	Producers' standards	Surfaces highly loaded by attrition Side profiles filled with wear-resistant plate, charging components

4. Optimisation of filler materials selection

Parameters of fine-grained high-strength steel weld seams are affected namely by

- the selection of filler materials (FM) and protection gas (PG); FM is selected based on the required parameters of the specific welding metal and welding conditions – input heat, transition zone, heat treatment, etc.
- welding method
- execution of a perfect weld seam

The following methods are used, in particular, for welding of high-strength fine-grained materials:

- 111 (MMA) manual metal arc welding
- 135 (MAG) metal active gas welding
- 121 (SAW) submerged arc welding
-

From practical reasons (welding productivity), the preference is given to the method 135 or 111 (repairs, special seams).

The basic problem with welding of fine-grained high-strength materials is the prevention of damages, such as a cold crack or a hot crack.

In order to prevent hot cracks it is essential

- + to make sure that the welding metal is pure, especially when it comes to the content of sulphur, the minimum content of oxygen in the welding metal, the content of carbon below the peritectic point of primary ferrite solidification

- + optimum geometry of weld surfaces
- + optimum welding parameters

Cold cracks are caused by the impact of diffusion hydrogen as induced cracks. they occur in structures sensitive to hydrogen embrittlement (in martensite and bainite). Hydrogen enters the weld metal especially through humidity of the filler material and base material. Therefore, an emphasis is laid upon the preparation of weld surfaces (their cleanliness and welding conditions), storage of the filler materials and the levels of diffusion hydrogen in filler materials. To mitigate the risk of hot cracks it would be optimal to pre-heat the weld surfaces and keep them clean.

Filler materials for fine-grained high-strength materials are selected according to the required properties of the weld metal and welding method. Despite the wide range of filler materials offered by reputable producers, it is recommended to optimise the selection for the purposes of welding high-strength materials used for ore/coal mining. Selection is vital also due to the necessity to verify welding procedures (WPQR) and their applicability.

The following tables show filler materials from three renowned global companies recommendable for welding of high-strength materials applying 135 method (MAG) - Böhler Welding, Thyssen Weldin and ESAB companies.

The said filler materials offer the yield point $R_{e0,2}$ within the range of 480 to 930 MPa.

Table 5. 135(MAG) method F by Böhler Welding – for fine-grained high-strength materials

Böhler designation	EN standard	EN designation	AWS designation
NiCu 1-IG	EN ISO 14341-A (former EN 440)	G 42 4 M G0	A5.28-05: ER80S-G
		G 42 4 C G0	A5.28-05: ER90S-G
2.5 Ni-IG	EN ISO 14341-A (former EN 440)	G 46 8 M G2 Ni2	A5.28-05: ER80S-Ni2
		G 46 6 C G2 Ni2	
NiMo 1-IG	EN ISO 16834-A (former EN 12534)	G 55 6 M Mn3Ni1Mo	A5.28-05: ER90S-G
		G 55 4 C Mn3Ni1Mo	
NiCrMo 2.5-IG	EN ISO 16834-A	G 69 6 M Mn3Ni2.5CrMo	A5.28-05: ER110S-G
		G 69 4 C Mn3Ni2.5CrMo	
X 70-IG	EN ISO 16834-A	G 69 5 M Mn3Ni1CrMo	A5.28-05: ER110S-G
X 90-IG	EN ISO 16834-A	G 89 6 M Mn4Ni2CrMo	A5.28-05: ER120S-G

Table 6. 135(MAG) method F by Thyssen Welding – for fine-grained high-strength materials

Thyssen designation	EN standard	EN designation	AWs designation
UNION K 5 Ni	EN ISO 14341-A (former EN 440)	G 46 3 C G3Ni1	A5.28-05: ER80S-G
		G 50 5 M G3Ni1	
UNION Ni 2,5	EN ISO 14341-A	G 50 6 M G2Ni2	A5.28-05: ER80S-Ni2
UNION MoNi	EN ISO 16834-A	G Mn3Ni1Mo	A5.28-05: ER90S-G
UNION NiMoCr	EN ISO 16834-A	G Mn4Ni1,5CrMo	A5.28-05: ER100S-G ER100S-1 (mod.)
UNION X 85	EN ISO 16834-A	G Mn4Ni1,5CrMo	A5.28-05: ER110S-G
UNION X 90	EN ISO 16834-A	G Mn4Ni2CrMo	A5.28-05: ER120S-G
UNION X 96	EN ISO 16834-A	G Mn4Ni2,5CrMo	A5.28-05: ER120S-G

Table 7. 135(MAG) method F by ESAB – for fine-grained high-strength materials

ESAB designation	EN standard	EN designation	AWS designation
OK Autrod 13.23	---	---	A5.28-05: ER80S-Ni1
OK Autrod 13.28	EN ISO 14341-A	G 46 5 M G2Ni2	A5.28-05: ER80S-Ni2
OK Autrod 12.25	---	---	A5.28-05: ER100S-G
OK AristoRod 13.13	EN ISO 16834-A	G 56 3 M Mn3NiCrMo	A5.28-05: ER100S-G
OK AristoRod 13.29	EN ISO 16834-A	G 69 4 M Mn3Ni1CrMo	A5.28-05: ER100S-G
OK AristoRod 13.31	EN ISO 16834-A	G 79 3 M Mn4Ni2CrMo	A5.28-05: ER110S-G

Essentially, filler materials are offered in the following systems of alloys:

- **Mn**
- **MnNi**
- **MnMo**
- **MnNiMo**
- **MnCrNiMo**

Approximate composition of “solid wire” filler materials for the method 135 is given in Table 8.

Table 8. Approximate composition of high-strength ADs for the method 135

Alloying type	Composition	Minimum R _{p0,2} MPa (status after welding)	Impact work (status after welding)
Mn	1,0÷1,6 Mn	420 ÷ 460	> 60 J at -40 ⁰ C
MnNi	0,8÷1,4 Mn + 1,2÷2,5 Ni	440 ÷ 470	> 47 J at -80 ⁰ C
MnMo	0,8÷1,4 Mn + 0,4÷0,6 Mo	470 ÷ 490	> 40 J at -40 ⁰ C
MnNiMo	1,4÷1,5 Mn + 1,1÷1,2 Ni + 0,4÷0,6 Mo	510 ÷ 560	> 47 J at -60 ⁰ C
MnCrNiMo	1,4÷1,9 Mn + 0,4÷0,8 Cr + 2,2÷2,4 Ni + 0,4÷0,5 Mo	680 ÷ 890	> 47 J at -60 ⁰ C

The composition slightly differs with each producer.

4. Key principles of technological procedures of welding high-strength and wear-resistant steels

Fine-grained high-strength materials have low carbon equivalent, therefore they can be simply welded together and to all common structural materials using standard methods.

While welding fine-grained thermomechanically treated steels, the objective is:

- ◆ to minimize the input heat (to weld while complying with the given parameters); the recommended maximum heat input range from 5 to 15 (25) kJ/ cm; to comply with the maximum recommended input heat = adjust welding parameters (current, voltage, welding rate, potential pre-heating and interpass)
- ◆ Maintain hardness of the thermally affected zone (TAZ)
- ◆ Achieve recommended toughness of the zone

- ◆ The welding procedure should prevent detrimental tension in the structure; if possible, welds should be made in the direction towards loose ends and make it possible for the emerging tension to “escape” from the weld seam
- ◆ Pre-heating should be used for greater thicknesses only according to the metal plates producers
- ◆ Carefully prepare, clean and dry weld plates; make sure that humidity hydrogen does not enter the weld seam during welding, dry out any condensed humidity, remove any residual paint, grease and other impurities from the weld surface.
- ◆ Use filler materials with low-hydrogen content.

When designing weld seams from fine-grained, thermomechanically treated steels, further recommendations are:

- ◆ When designing loaded weld seams, butt welds (BW) should be preferred rather than fillet welds (FW)
- ◆ Minimise tension during contraction, particularly by precise positioning of the weld and by planning of an appropriate welding procedure
- ◆ When designing weld seams, consider the course of structure loading, eliminate inappropriate concentration of welds in loaded areas
- ◆ When designing weld nodes, appropriate butt weld angles must be chosen
- ◆ Weld seams must be placed in areas that are less exposed to wear load (considering HARDOX)
- ◆ Place the weld in the right angle to the abrasive material flow (considering HARDOX)
- ◆ Stress-relief annealing should not be used with HARDOX after welding, when annealed over 250 to 300°C these steels tend to lose hardness, and slack; post-heating is possible after welding in order to facilitate hydrogen evasion from the steel; post-welding temperature should be identical with the pre-heating temperature.

Verification of welding procedures

At present, EN ISO 126xx set of standards are used for approvals of welding procedures. In order to verify producer’s welding procedures, the ČSN EN ISO 15614-1, specification and qualification of welding procedures for metallic materials – Welding Procedure test Part 1: Arc and gas welding of steels and arc welding of nickel and nickel alloys. As to wear-resistant materials, such as HARDOX, not all requirements set out by the standard can be complied with, considering the material’s properties (e.g. execution of a transverse bend test), therefore, the welding procedure is verified using the ČSN EN ISO 15613 standard, Specification and qualification of welding procedures for metallic materials – Pre-production test based qualification.

5. Examples of technological instructions for welding of the main nodes and components for power industry and ore/coal transportations equipment

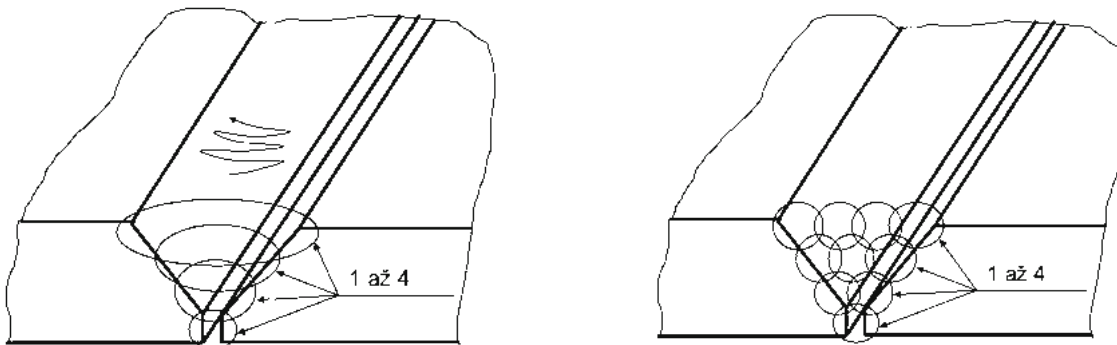
Although welding of these materials is an issue relatively well processed and described, the key problem consists in practical application of the experience in specific operating conditions. The requirements regarding welding and compliance with technological regulations during welding are much stricter for these steels than for usual structure materials, therefore, it is inevitable to adhere to all principles to produce a compliant welding seam.

An example of technological instructions for weld seams made during the fabrication of cages and skips:

- Minimize the input heat, adjust the technique of the bead deposition (comply with verified welding parameters according to PP – Production procedures)
- Ensure thorough preparation of weld surfaces (geometry, cleanliness, tack welding).
- Weld from the centre toward loose ends
- Weld beads may take a form of "stringer" beads in multiple- pass layers, see Fig. 1b – a narrow groove, "weave" beads (Fig. 1a) = a wide groove SHOULD NEVER BE USED

Figure 1a – A weave bead

1b – Multiple-pass layer of "stringer" beads



- Tacks must be of a low profile with a smooth transition from the base material, they shall be approx. 50 mm long with a 200 to 300 mm gap between each other. Tacks must not be made at the crossings. The minimum distance from a corner or a crossing must be 100 mm. high, non-uniform tacks with craters and cracks must be grinded or grinded off and re-welded elsewhere, if possible.
- Where multiple-layer welds are applied, the weld must be cleaned and grinded at both ends before deposition of the next layer, adjacent beads should not be connected in a single spot, they should be shifted so that the connection is re-melted and covered with the next layer.
- Welds should not be commenced in corners and at crossings with a minimum distance of 20 to 30 mm from these places.

- Make sure that the weld root is thoroughly welded through, or the weld area must be trimmed, the bad root must be grinded and re-welded.
- From time to time, back-step welds can be inlaid in long and longitudinal welds always starting towards the weld edges
- Transition between welds must be smooth without any grooves or extensive elevation, otherwise the weld must be grinded. This must especially be complied with at cage loaded places, such as the top, the floor, container location, etc.).
- A pulse welding source with appropriate parameters should be preferred for welding of bearing fine-grained bars in order to eliminate the input heat
- All identified imperfections must be repaired, reparations must be executed by an experienced welder according to the instructions of welding supervisor. Bearing bars can be repaired just once.
- Cracks, craters and grooves must not be repaired by depositing a weld on the damaged place. All cracks must be grinded off the damaged places and only then welded (it is recommended to perform a PT test).

The most important thing is to make sure that these principles are adhered to in real operating conditions (i.e. personnel expertise and technological equipment in the plant).

¹ Ing. Stanislav Novák, CSc., První železářská společnost Kladno, s.r.o., Huťská 160, 272 01 Kladno, Czech Republic, Tel.: +420 311 235 208, e-mail: stano@pzsk.cz

² Ing. Jiří Mráček, Ph.D., První železářská společnost Kladno, s.r.o., Huťská 160, 272 01 Kladno, Czech Republic, Tel.: +420 312 248 262, e-mail: pzsk@pzsk.cz

THE EFFECT OF ALUMINIUM CONTENTS ON STRUCTURE AND PROPERTIES OF CuAlFe3 FORGINGS

Vladivoj Očenášek¹, Vlastimil Karas²

Abstract

The present paper deals with the forgings made from aluminium bronze CuAl9Fe3. The effect of Al contents on final properties of forgings is evaluated with regard to technological forging parameters. It is investigated the influence of heat treatment including the cooling from the forging temperature on structure and properties at various contents of Al. Some technological measures to obtaining optimum properties are suggested.

Keywords: aluminium bronze, forgings, heat-treatment

1. Introduction

Aluminium bronzes are the alloys of special properties and use. Their density is the lowest of all copper alloys; they have very good corrosion resistance and fatigue properties and can be used at higher temperatures. Corrosion resistance increases with the increasing Al amount and reaches its maximum at 8% Al. These properties enable their application in corrosive environment. In addition to binary Cu-Al alloys, aluminium bronzes containing Fe, Ni, Mn and Si are also used. These elements affect some properties, production technology and heat-treatment and determine specific fields of their application. The properties of products made from aluminium bronzes are very sensitive to small changes of both chemical composition and heat-treatment. Thus, the appropriate type of alloy as well as the production parameters has to be chosen with regard to the conditions under which they will be used.

The present work deals with CuAl9Fe3 forgings that are used for urban mass transport overhead contact line components. Typical forgings are shown in Fig.1. Testing programme was initiated by quality variation of forgings that cause some problems during their processing and exploitation. Our work aims at the determination of the effect of Al contents on technological parameters of production and, in this way, to their final properties.



Figure 1 CuAl9Fe3 forgings used as overhead contact line components

2. Experimental material, results and discussion

2.1 Cu-Al-Fe system

Equilibrium diagram of Cu-Al binary alloys is shown in Fig.2. Maximum solubility of Al in the solid solution is 9.4 % at 565°C. The solubility does not change considerably with the decreasing temperature. In Cu alloys with 9 – 11 % Al the occurrence of γ_2 substantially influences the structure and properties as well. This phase originates from the eutectoidal decomposition of β phase at 565°C. The increasing amount of γ_2 phase is connected with the higher strength and lower plasticity.

The presence of Fe in binary Cu-Al alloys influences favourably their mechanical properties and grain refinement. Depending on Fe contents and cooling conditions from the liquid state, Fe occurs either in solid solution or in small grey particles of Fe_3Al (κ) phase which can contain Cu and Ni (providing that Ni is present in the structure). This phase occur in CuAl9Fe3 alloy after casting or pressing and does not solve at forging temperatures 750 – 800°C. The amount of 3 % Fe in the structure does not change practically the solubility limit of Al in Cu (in contrast to Ni) and that is why the account of the effect of temperature on structural changes can be based – in a quite good approximation- on Cu-Al binary diagram (Fig.2); the single-phase α field must be naturally replaced by ($\alpha+\kappa$) field.

2.2 CuAl9Fe3 forgings

Forgings made from this alloy are often brittle and it causes the failure either during their further processing (drilling or punching holes – Fig.3) or in the course of the assembly (short-term operation). Our results show that in the case of damaged forgings the chemical composition of the material used is conform with ČSN 42 3145 Standard.

Die forgings made from CuAl9Fe3 alloy can be forged either from precast semiproduct or from the extruded rod. In the case of blank, the forging can be carried out during the cooling of casting to spare the heating of material to the forging temperature. The disadvantage of this procedure is the necessity to harmonize casting and forging processes, i.e. to keep the cooling time of blank for a sufficiently long time to reach optimum forging temperature. After the forging, forgings are air-cooled in basket. However, cooling rate depends on the number of forging in basket and thus the forgings are cooled rather unequally. To avoid this effect, annealing at 700°C followed by cooling in furnace was added. In spite of this measure that could lead to the homogeneity of properties, their scatter as well as the occurrence of brittleness were still observed. To solve these technological problems

experimental works were focused on the analysis of forgings without defects, damaged forgings and heat-treatment after forging.

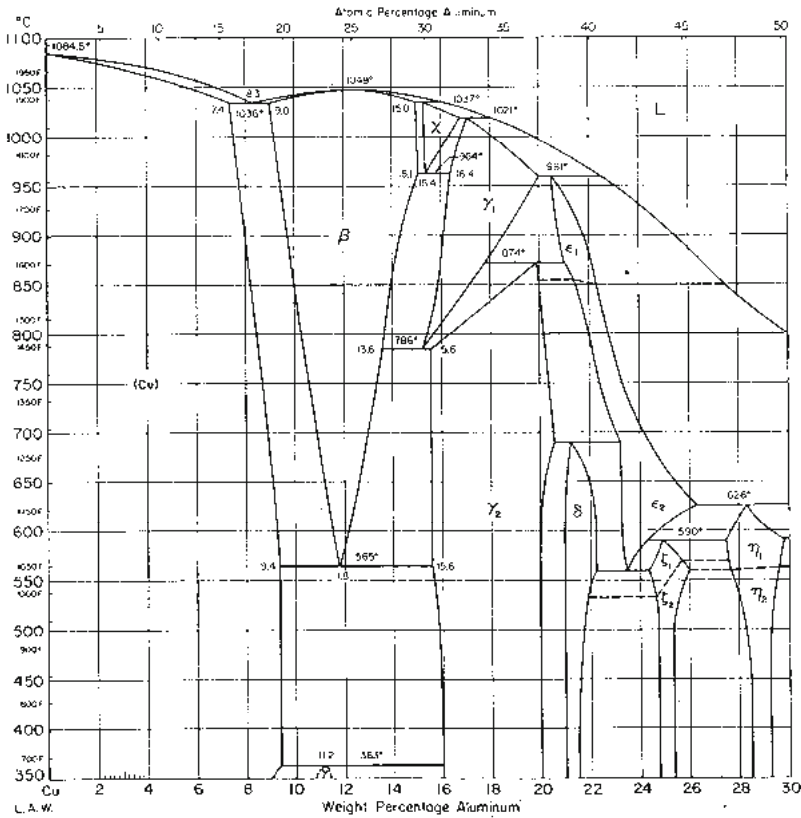


Figure 2 Part of Cu-Al equilibrium binary diagram



Figure 3 Damage of forgings occurring during punching holes and caused by the brittleness of material

2.3 Experimental results and their discussion

At first, chemical analysis of intact and damaged forgings was carried out. It followed metallographic analysis of three forgings (A, B, C) with different Al contents. Forgings A and B were suitable for the following processing while forging C was

damaged during the punching holes. All forgings were after forging annealed at 700°C and then cooled in furnace. Chemical compositions of forgings investigated as well as the composition according to ČSN 42 3145 Standard is given in Table 1, hardness results are presented in Table 2. Microstructures of B and C forgings in unetched state are shown in Fig. 4 and 5, those ones after etching in Fig. 6 and 7. Microstructures of A and B forgings are the same.

Tabel 1 Chemical composition of ČSN 42 3145 (CuAl9Fe3) alloy and some forgings

Alloy	Zn	Al	Mn	Ni	Fe	Sn	Pb	Si	Cu
ČSN 42 3145		8.7			2.0				Rem.
	1,0	10.7	0.50	1.0	4.0	0.20	0.10	0.20	
A	0,36	8.55	0.26	0.64	2.59	0.088	0.031	0.05	Rem.
B	0,46	9.04	0.10	.21	2.79	0.14	0.055	0.05	Rem.
C	0,17	10.10	0.22	0.27	2.52	0.12	0.030	0.05	Rem.

Tabel 2 Hardness HV 30 of some forgings

Hardness / Forging	A	B	C
HV30	166	169	217

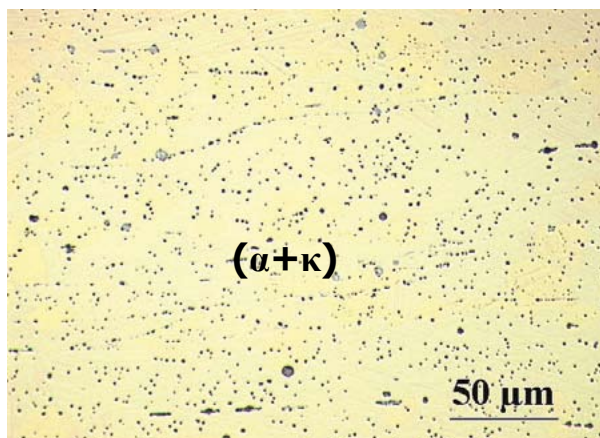


Figure 4 Microstructure of the forging B, unetched

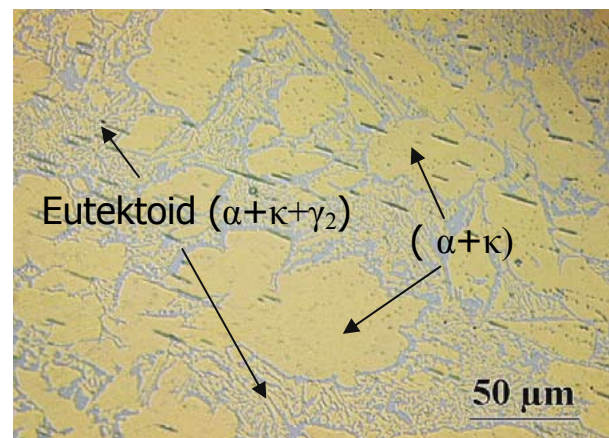


Figure 5 Microstructure of the forging C, unetched

In compliance with the equilibrium diagram (Fig. 2) we found that the microstructure of forgings with Al contents lower than 9.4 % after cooling from 700°C in furnace was formed by a phase containing fine particles of ferrous κ phase. The microstructure of forging containing 10.1 % Al consisted of (α+κ) phases and (α+κ+γ₂) eutectoid. The occurrence of hard and brittle grey-blue γ₂ phase in forging C is connected with the increase of hardness and brittleness. It follows that the additionally applied annealing is not effective in the case of material containing more than 9.4 % Al and in the case of materials with less than 9.4 % Al is substantially needless.

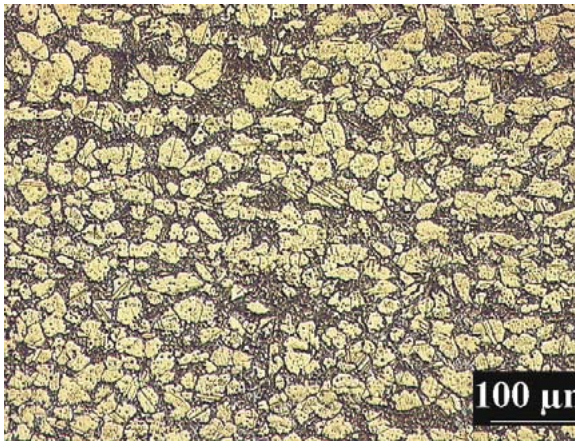


Figure 6 Microstructure of the forging C, etched

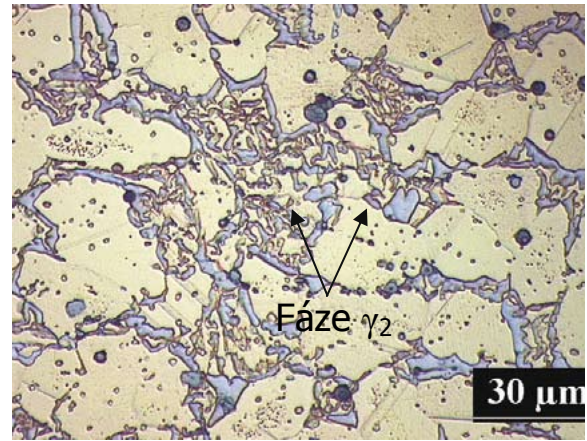


Figure 7 Microstructure of the forging C, etched

To obtain sufficient plasticity, it was necessary to propose another heat-treatment which would minimize the contents of γ_2 phase in the case of higher amount of Al in the alloy (particularly in the case, when Al contents is close to upper limit, i.e. 10.7%). Various procedures leading to the reaching sufficient plasticity (involving rapid cooling from the forging temperature followed by annealing under different conditions) were suggested and tested – regardless of Al contents in the alloy to ensure the further processing at the customer. Considering the operation conditions as well as the minimalization of energy costs, the following procedure shows to be the most appropriate: annealing after forging at 650°C followed by cooling in furnace to 570°C. Cooling to 570°C results in the structure consisting of α , κ and β phases with maximum fraction of weak α phase. This temperature is sufficiently high to prevent the eutectoid decomposition that starts at 565°C. Naturally, the decomposition can occur during the cooling and to prevent it, a sufficiently high cooling rate must be chosen to overcome safely the range between 565 and 350°C. At temperatures fewer than 350°C it is not necessary to keep a high cooling rate because the decomposition of β phase proceeds slowly and its transformation to γ_2 phase can be neglected.

To determine the optimum operation conditions of cooling from 570°C that prevent massive formation of γ_2 phase during the eutectoid decomposition, three modes of cooling conditions were carried out. The procedure of heat-treatment was as follows:

650 °C/1 h, furnace cooling to 570 °C

- out of furnace and cooling in air (I)
- cooling in furnace (1.5 h) to 350 °C (II)
- cooling in furnace (3 h) to 200 °C (III)

Forgings containing 7.9, 9.2 and 10.0% Al which were annealed after forging at 700°C and then slowly cooled in furnace were tested. The results of hardness measurements are given in Table 3.

The following conclusions can be drawn:

1) The decisive effect of Al on mechanical properties was confirmed. At the lowest Al contents, no annealing procedure has important effect on final hardness. The effect of cooling rate on hardness changes is the most apparent at the highest Al contents.

2) In the case of material containing less than 9.4% Al, the heat treatment of forgings is not necessary. The forgings can be cooled in air after processing.

3) Temperature 650°C is sufficiently high for obtaining the γ_2 phase free structure before the cooling in furnace to 570°C.

4) Slower cooling from 570°C to 200°C leads to apparent increase in the final hardness. In materials with higher Al contents (up to 10.7%), the above mentioned cooling can cause the increase of γ_2 phase fraction and, consequently, the increase of hardness (HV30 over 200) and brittleness as well. In spite of fact that the specimens with the highest contents of Al were not at our disposal, it seems to be necessary to keep the cooling rate from 570°C in this case higher than it was applied in type C treatment.

Tabel 3 Hardness of the original state and after heat treatment

Al	7,9%		9,2%		10,0%	
	Hardness HV30	HRB	Hardness HV30	HRB	Hardness HV30	HRB
Original state	155	80,3	177	87,2	247	97,0
Mode I	155	81,6	159	86,5	168	86,3
Original state	140	75,7	184	90,5	232	94,9
Mode II	141	74,3	173	88,3	179	88,4
Original state	147	78,4	194	90,7	232	94,5
Mode III	145	79,0	177	88,2	188	89,6

3. Conclusions

Experimental results show that the following technological measures should be accepted for obtaining required properties of CuAl9Fe3 forgings:

1) It is necessary to prevent massive formation of brittle γ_2 phase originating during eutectoid decomposition at 565°C. The decisive role is attributed to Al contents in the alloy.

2) In the case of material with Al contents lower than 9.4 %, no heat-treatment is required and the forgings can be freely cooled in air without any demands on the cooling rate.

3) Materials in which Al contents is higher than 9.4% require after forging the annealing at 650 °C for 1,5 h followed by cooling in furnace to 570°C, the cooling rate being lower than 70 °C/h. It is inadmissible to go under temperature 565°C.

4) After taking out from furnace to air at 570°C, cooling rate higher than 150°C/h is necessary to apply.

Acknowledgements

The financial support of the Ministry of Industry and Trade of the Czech Republic under project No. FI-IM5/095 is gratefully acknowledged.

¹ Ing. Vladivoj Očenášek, CSc., SVÚM a.s., Podnikatelská 565, 190 11 Praha 9, Czech Republic, Tel.: +420 608 534 619, e-mail: ocenasek@svum.cz

² Ing. Vlastimil Karas, KOVOLIT, a.s., Nádražní 344, 664 42 Modřice, Czech Republic, Tel.: +420 606 740 718, e-mail: vlastimil.karas@kovolit.cz

INFLUENCE OF HEAT TREATMENT ON STRUCTURE AND PROPERTIES OF BRASS AFTER DRECE PROCESSING

Stanislav Rusz¹, Lubomír Čížek¹, Jan Kedroň¹, Stanislav Tylšar¹, Zbyhněv Žmija²

Abstract

Contribution concerned the whole production of UFG materials, using forming process DRECE in brass. The heat treatment on the part of sheet was applied after DRECE processing. For orientation information, whether grain was refined preliminary metallographic analysis was made. Mechanical properties of studied samples by Vickers hardness method were tested.

Keywords: DRECE machinery, hardness, structure

1. Introduction

This research concerned the whole production of UFG materials, using Severe Plastic Deformation (SPD). Use of these materials is very versatile – either directly as semi-products for subsequent further processing with lower number of operations (created structure is preserved in final products) or for production of final products from semi-products.

News technologies, which use high deformation for obtaining of fine-grained structure, comprise namely the following authors [1-3]. Technologies of severe plastic deformation can be defined as processes, which create in material high degree of deformation in order to achieve grain refinement. These new technologies for production of semi-finished products with ultra-fine grained structure differ from conventional technologies. While in classical technologies change cross-section of the processed material, the cross-section of material processes by SPD remains unchanged. Several types of SPD technologies serving for production of UFG metals was developed already at the beginning of the nineties.

2. DRECE Machinery

Forming process DRECE is an extrusion technology with limited cross-sectional reduction to achieve high degree of deformation of suitable selected material. Equipment DRECE is based on process CONFORM, modifying for sheet forming. A prototype of this equipment has been put into use from the end of year 2008 at workshop of VSB-Technical University of Ostrava, Faculty of Mechanical Engineering, Department of Mechanical Technology. Prototype of the equipment is shown at Figure 1.



Figure 1 DRECE machinery general view

3. Experimental methods and material

Experiments with use of formed structural material bras were made on the DRECE machines in order to achieve grain refinement in the strip of sheet with dimensions 58 x 2 x 1000 mm [4].

Altogether 6 passes were made through the DRECE tool. The heat treatment (450°C/15min/air) on the part of sheet was applied after DRECE processing. The extruded samples of bras after all passes were then cut from sheets into individual series for manufacture of individual testing specimens for metallographic evaluation and mechanical tests on the surface of sheets marked by symbols MoX, (number of pass X = 1-6) for samples without heat treatment and MoHTX for samples with heat treatment. Hardness of initial state is signed MoI.

Mechanical properties of studied samples by Vickers hardness method were tested. Results of these tests for samples without heat treatment are showed in Table 1 and for samples with heat treatment in Table 2.

Table 1 Average values of hardness of bras on the samples without heat treatment

Sample	Hardness HV5
MoI	93
Mo2	127
Mo4	165
Mo6	160

Table 2 Average values of hardness of bras on the samples with heat treatment

Sample	Hardness HV5
MoHT2	327
MoHT4	304
MoHT6	324

For orientation information, whether grain was refined preliminary metallographic analysis was made on light microscope NEOPHOT 2. After usual metallographic preparation the samples were chemically etched. Results of selected micrograph are shown in Figure 2.

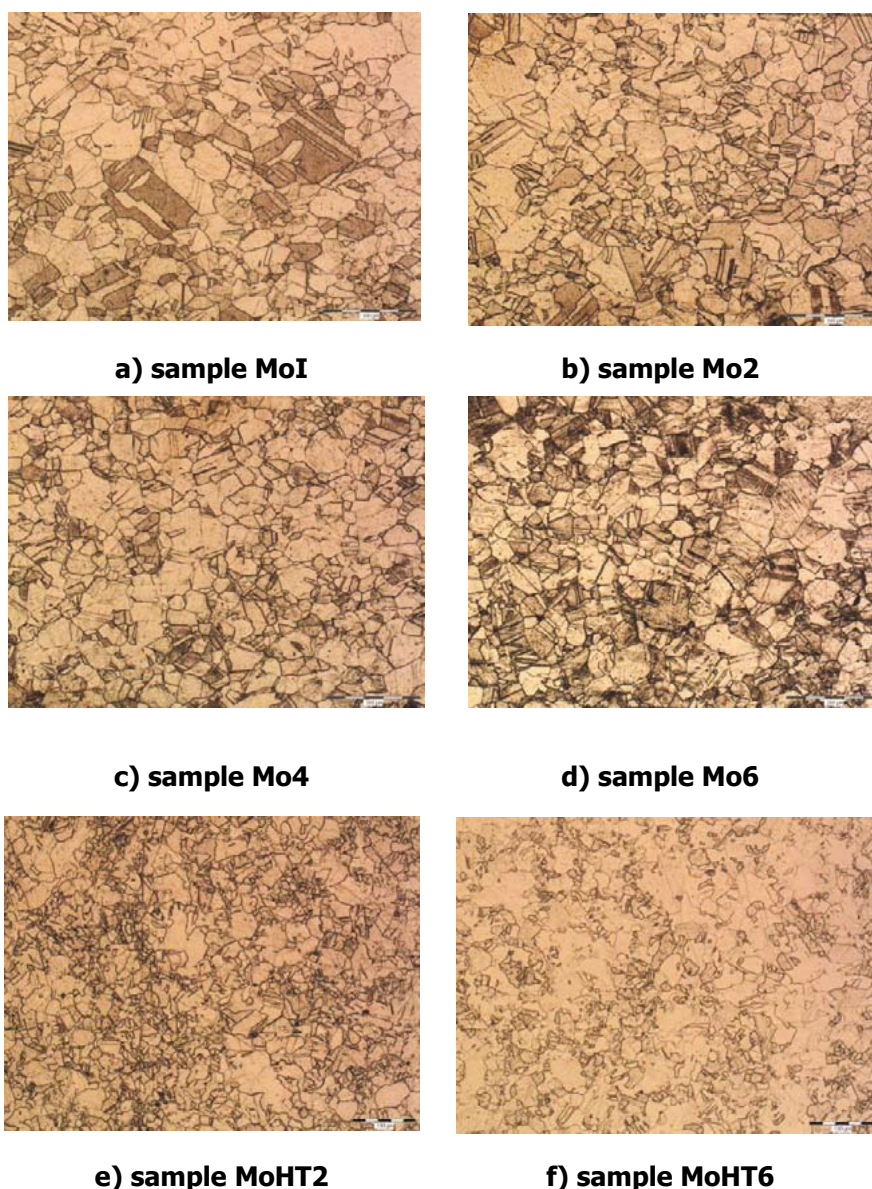


Figure 2 Microstructure of the bras samples

4. Discussion of results

Average values of hardness in Table 1 from five measurements were calculated. As it is seen from Table 1 for samples with heat treatment, these values rapidly increase from 1st to 4th passes. After 4 pass the value of hardness stay nearly the same [4].

In the case of samples after heat treatment hardness strongly increase at all passes on the practically the same values in 300-327 which is much higher than in the case of samples without heat treatment.

Microstructures of bras samples are shown on the Figures 2a-2f. Figure 2a shows microstructure of initial state sample of bras. This microstructure consists from grains in agreement with fact that material was formed before DRECE machining.

The microstructures samples without heat treatment after passes through DRECE tool are shown in Figures 2b-2d. As it is seen from these micrographs refining of grains after each pass was only small. The microstructures samples with heat treatment after passes through DRECE tool are shown in Figures 2e-2f. As it is seen

from these micrographs refining of grains is much bigger than in the case of samples without heat treatment.

5. Summary

It has been designed as prototype equipment for production of UFG structure in strip of sheet made of non-ferrous metals with subsequent possibility of deformation also of steel sheets with thickness 2 mm. This process involves primarily creation of sufficient number of shear systems with different orientation in crystallographic lattice. Creation of UFG structure in strip of sheet is closely connected to the design of suitable geometry of forming tool, appropriately dimensioned power unit and control system enabling setting of various values of peripheral velocities. From the viewpoint of forming parameters higher number of passes will bring considerable strengthening of the formed material.

According to the degree of the obtained results of extrusion of the sheet made of brass it is possible to state that the equipment is fully functional.

The equipment DRECE is at the stage of verification and future works will verify influence of technological parameters on increase of efficiency of SPD process for obtaining of UFG structure in non-ferrous metals.

From the viewpoint of forming parameters higher number of passes will bring considerable grain refining and strengthening of the formed material.

Heat treatment applied after passes through DRECE tool significantly contributes to intensifying this procedure.

Acknowledgements

The work was financed by aim of project MPO No. 2A-1TP1/124

References

- [1] Gutkin, M. Yu., Ovidko, I. A., Pande, C. S.: Theoretical models of plastic deformation processes in nanocrystalline materials, *Reviews on Advanced Materials Science*, September 2001, vol. 2, pp. 80–102
- [2] Kobayashi, M. at all: Research and Development of Superplastic Materials „Recent Progresses and Future Prospects“, In: *Metallurgical Transactions 18A*, 1987, pp. 685–695
- [3] Inwahashi, Y., Wang, J., Horita, M., Nemoto, Z., Langdon, T. G.: Principle of equal-channel angular pressing for processing of ultra-fine grained materials, *Scripta Materialia*, vol.35, 1995, pp.143–147
- [4] Ruzs, S.: Progress report of the project MPO No. 2A-1TP1/124 for the year 2009, pp. 1–38

¹ Prof. Stanislav Ruzs, doc. Lubomír Čížek, Ing. Jan Kedroň, Ing. Stanislav Tylšar, VŠB – TU Ostrava, Fakulta strojní, 17 listopadu 15, 708 33 Ostrava – Poruba, Czech Republic, Tel.: +420 597 323 315, e-mail: stanislav.ruzs@vsb.cz

² Ing. Zbyhňev Žmija, Vývoj, projekce, konstrukce, výroba – strojů, Beskydská 722, 739 61 Třinec, Czech Republic, Tel.: +420 558 958 246, e-mail: zbyhnev.zmija@gmail.com

FORMING TECHNOLOGIES IN AUTOMOTIVE INDUSTRY BY APPLYING LIGHT WEIGHT MATERIALS

Frank Schieck¹, Alexander Paul², Marco Pröhl³

Abstract

The use of new materials and high strength steel is applied to the car body and structure parts based on the debate around climate changes and the demand to lower fuel consumption. The Fraunhofer Institute for Machine Tools and Forming Technology has been developing new forming technologies for applying sheet metal and tubes for many years. Hydroforming and press-hardening offer to shape new geometries at room temperature or elevated temperature.

Keywords: hydroforming, hot forming, hot metal gasforming, tempered, press hardening, elevated temperatures, steel, magnesium, profiles, tubes, lightweight, strength

1. Introduction

The automotive industry today is constantly changing and is characterized by a sustained process of development. In particular, increased demands in terms of safety and comfort have led to a considerable increase in vehicle weights over the past few years. Further essential requirements in state-of-the-art car construction are vehicles' environmental protection and economic efficiency, which reflects a redefinition of the targets of development for current and future vehicle generations where driving down vehicle resource consumption and resource- and energy-efficient production are the focal points of the automobile industry's efforts.

One of the foremost challenges that the vehicle manufacturers will be confronted with in coming years will be a substantial reduction in fuel consumption. Here, there is not only a potential for devising highly efficient and environmentally friendly drives, but also for reducing the vehicle weight. German car manufacturers estimate that it will be necessary to drive down vehicle weight by as much as 30% in coming years without restricting the high level of convenience and safety standards [1].

This puts the idea of lightweight engineering into focus that, when taken overall, has become a synonym for a revolutionary industrial development [2, 3]. The consistent implementation of lightweight engineering concepts in vehicle structure is seen as an important contributory factor to achieving the targeted weight savings without affecting the function, safety and service life of the structure. That makes lightweight material construction one of the most essential strategies for driving down weight along with the methods of conditional, form or structural lightweight engineering [4, 5, 6, 7]. It is not the absolute strength parameters that are used for analyzing lightweight material engineering, but the characteristic figures with

reference to the density of the material such as E-module, the apparent yielding point $R_{p0,2}$ or tensile strength R_m [8, 9].

Lightweight vehicle engineering is not only determined by aluminum and magnesium alloys, but also by super high strength steel materials. In addition to sheet metal-based components, an increasing trend for closed, weight and functional optimized profiles for structural applications has been identified. Due to the burgeoning complexity of components and the fact that the forming characteristics of metallic lightweight materials are frequently limited at room temperature, conventional forming processes such as hydroforming are increasingly running up against feasibility limits.

One approach to meeting these challenges is applying temperature as an active process parameter during the forming operation. Utilizing higher forming temperatures provides an opportunity to measurably boost the ductility of the material and therefore the forming properties in connection with it while allowing an unmistakable reduction in the yield stress and therefore the forming forces or pressures needed. Below, magnesium wrought alloys and high-strength steels will be used to demonstrate solutions and potentials for implementing tempered forming processes based on active media (T-IHU).

2. TeMaK – Series production components made of magnesium wrought alloys

Machining magnesium wrought alloys calls for some changed production routines over other material (such as steel and aluminum alloys) which is why it makes higher requirements of the thermal regime in connection with the forming processes. Therefore, in the TeMaK project the fundamentals for the utilization of magnesium wrought alloys in a series production were outlined. During this project a passenger car door on a scale of 1:1 entirely out of magnesium wrought alloys AZ 61 A was manufactured to demonstrate the technical feasibility (Figure 1).



Figure 1 The inside component of a passenger car door with a jointed frame made of a magnesium wrought alloy

The structure of this demonstrator includes the load-bearing structural frame with jointed hinge reinforcements, the inside component of the door and the skin. The load-bearing structural frame consists of two magnesium profile segments that are jointed by welding. A complex bent magnesium pipe is used for the first segment

while the second segment is a magnesium profile formed by hydroforming and simultaneously jointed with the hinge reinforcements. The complete structural frame is also integrated into the inside component of the door by welding. Finally, the skin is jointed with the subassembly by folding. In the following section the focus will be on the tempered forming and joining of the structural frames by hydroforming.

In two experimental series the hydroforming connection of the magnesium profile with the hinge reinforcement was studied. Therefore, the extent to which the magnesium profile can be formed in and around the hinge reinforcement by the T-IHU process was measured. In preliminary studies, the circumference could be extended by as much as 75% without preforming operations under ideal geometric circumstances. The extensions in circumference that can be achieved without component part failure with preforming operations such as forming a circular pipe to cuboid form dropped to 25%. The reasons for this are seen in the impeded axial material feed due to the preforming geometry, the material distribution and in the restricted material flow in the forming zone.

Furthermore, scientists at the Fraunhofer IWU studied whether the form closure of the magnesium profile and hinge reinforcement can absorb sufficiently high forces without moving the hinge reinforcement on the magnesium profile. Therefore, forming experiments with various means of feeding, varying calibrating pressures and variably inclined pressure build-up curves were analyzed. Magnesium profiles were heated up in two stages for the forming process: in the first step by using 30 seconds of inductive heating to 300°C and then 30 seconds of maintaining this temperature at a lower performance level. The resulting component part geometry and the joining area were completely formed and correspondingly fully jointed. Figure 2 shows such a component part.



Figure 2 Hydroformed jointed structural frame component with a hinge reinforcement (forming temperature = 300°C, forming pressure = 35 MPa)

It was additionally analyzed whether and to what extent there was local thinning in the material in the area of the stamping at the form closure on the magnesium profile. The profile laid itself well onto the hinge reinforcement in the forming operation during the experiment without bursters or local material thinning. The maximum thinning of the experimental components was 19%, which means that it may be assessed as non-critical.

3. Press hardening

High strength and super high strength steels offer lightweight engineering potential along with lightweight construction via classical lightweight metals such as aluminum and magnesium. There, adjusting mechanical properties during the forming process is of particular interest. Combining hot forming with adjusting properties in one forming stage is known as press hardening and has already been used industrially in sheet-metal forming [10]. Another boost in the lightweight engineering factor was achieved by transferring this technology to closed profiles. Unfortunately, liquid active media such as thermal oil cannot be used for forming because temperatures ranging from 800° to 1,000°C depending upon the material are needed for hardening. This is the reason why gaseous pressure media are used for forming with press hardening steel materials. Figure 3 shows the scheme of such a gas forming device.

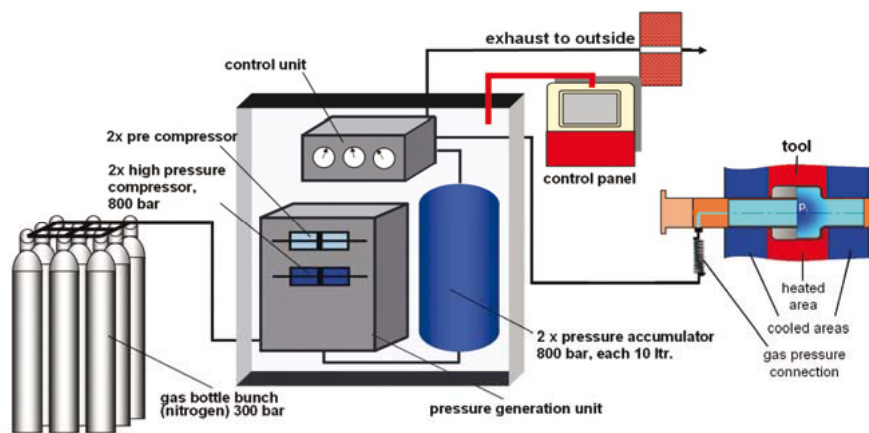


Figure 3 Scheme of a gas forming device

There is a trend towards using more super high strength materials which is why the Fraunhofer Institute for Machine Tools and Forming Technology is studying materials at a high level of strength and sufficiently high elongation at rupture for their applicability in press hardening processes based on active media. The first step was the press hardening of the LH800® air hardening steel (Figure 4) from the Salzgitter AG [11].

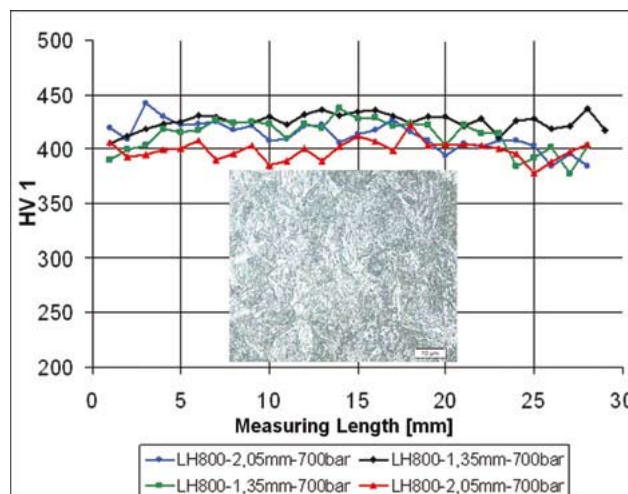


Figure 4 The microhardening distribution for IHU-press hardened LH800® and a polished section with pure martensite

The evaluation of these studies indicated engineering process limits. Not only minimal moldable radiuses were analyzed, but also the changes in hardness over the length of the part, thus determining corresponding strengths. Final strengths that are three times higher than the original material (1,200-1,900 N/mm² depending upon the material) could be documented. Furthermore, the hardness parameters were on a constantly high level over the entire distribution of the cross-section. At present, not only the LH800® air hardening steel, but also other materials such as 34MnB5 and MW1000L are studied.

Conventional press hardening can be used to manufacture component parts that have approximately the same component part properties over their entire geometry. Unfortunately, the high level of hardness makes mechanical trimming and joining of single press-hardened parts into subassemblies much harder. Furthermore, there is a need for component parts with strength properties differing from one area to another to pass on loads and absorb impact energy. This is the reason why the Fraunhofer IWU is presently studying various technologies to achieve these tailored properties on the component part. The range of feasible solutions spans from partial component part heating to various cooling rates per component part section.

4. Summary

Altogether, it can be stated that temperature-supported forming operations based on active media allow a considerable shift in the limits of hydroforming. This is primarily the case with the typically lightweight engineering materials where much greater complexity can be built in component part geometries with enhanced component part properties. In particular, magnesium wrought alloys that can only be insufficiently formed at room temperature profit substantially from the boost in forming temperatures. Potentially extending circumferences by 75% and integrated forming and joining processes offer a major potential. This means that the basic development for forming and dividing structures made of magnesium have been achieved and successfully demonstrated by using the example of the convertible door demonstrator. In other words, using this material in new applications in series production is coming within our grasp.

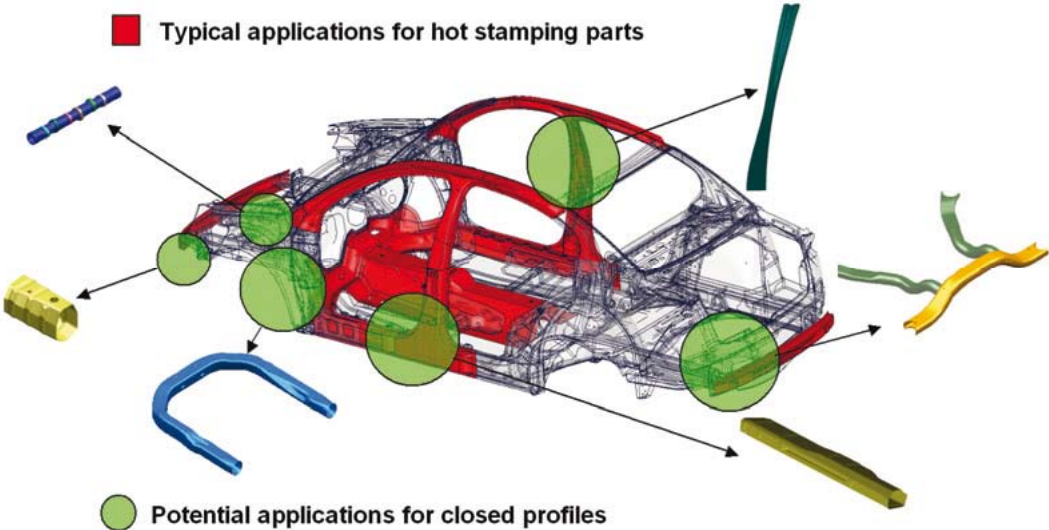


Figure 5 Potential applications for press-hardened profiles

Furthermore, Fraunhofer IWU was able to use various demonstrators to document the process capability of an integrated press hardening process in the forming process based on active media while laying the fundamentals for the optimization and further development of this combination of techniques. The combination of gas forming and press hardening techniques makes it possible to combine the excellent strength properties of press-hardened component parts with the advantages of closed complex profile components. Figure 5 shows some of the possible applications for flangeless press-hardened profile components in the car body structure. The Fraunhofer Institute for Machine Tools and Forming Technology is planning on continuing its work to transfer this technique to large-format structural components such as a flangeless B-pillar with tailored properties.

References

- [1] BMBF-Workshop: Werkstoff- und produktionstechnische Potenziale für sparsame, umweltverträgliche und wettbewerbsfähige Kraftfahrzeugkonzepte. Bonn 31.01./01.02.1997
- [2] Waschke, T.: Entwicklungen im Umfeld des Automobils, Gesellschaftliche Entwicklungen. Plenarvortrag zum BMBF-Workshop „Werkstoff- und produktionstechnische Potenziale für sparsame, umweltverträgliche und wettbewerbsfähige Kraftfahrzeugkonzepte“, 31.01./01.02.1997.
- [3] Neugebauer, R.; Bräunlich, H.: Lightweight Construction by Innovative Forming Technologies. Proceedings of the 6th International Conference on Technology of Plasticity “Advanced Technology of Plasticity 1999”, p. 1119-1128, Nuremberg 29.-24.09.1999.
- [4] Klein, B. : Leichtbau-Konstruktion, Berechnungsgrundlagen und Gestaltung. Friedr. Vieweg & Sohn Verlagsgesellschaft mbH, Braunschweig/Wiesbaden, 1994.
- [5] Schmidt, W.; Puri, W.: Systematische Entwicklung gewichtsoptimierter Bauteile. Tagungsband zum 11. Symposium „Design for X“, S. 37-40, Schnaittach, 12./13.10.2000.
- [6] Geiger, M.; Hofmann, A.: Neue Entwicklungen in der Aluminiumblechumformung, Erlangen. Das Umformen von Aluminium im Automobilbau. Bad Nauheim: Praxis Forum, 1999, S. 111-131.
- [7] Hoffmann, H.; Toussaint, A.: Strategies and Future Developments in the Manufacturing Process of Lightweight Car Bodies. Advanced Technology of Plasticity, Bd. II, S. 1129-1140, Springer Verlag Berlin 1999.
- [8] Drewes, E.-J.; Wagner, S.; Welsh, F.: Karosseriegestaltung unter Berücksichtigung moderner Stahlwerkstoffe und neuer Fertigungsverfahren. FTK'97 Innovation durch Technik und Organisation, S. 96-106, Springer Verlag Berlin 1999.
- [9] Novotny, S.: Innenhochdruck-Umformen von Blechen aus Aluminium- und Magnesiumlegierungen bei erhöhter Temperatur. Dissertation, Technische Fakultät der Friedrich-Alexander-Universität Erlangen Nürnberg.
- [10] Kuhn, D.: Kirchhoff investiert in Warmumformlinie – auch in wirtschaftlich schwierigen Zeiten, Blechnet (2010), Nr. 4.
- [11] Neugebauer, R.; Schieck, F.; Paul, A.: Presshärten von Hohlprofilen mittels Innenhochdruck-Umformung, In: Blechnet (2010), Nr. 2, S. 34-35.

¹ Dipl.-Ing. Frank Schieck, Fraunhofer Institut für Werkzeugmaschinen und Umformtechnik IWU, Reichenhainer Str. 88, 09126 Chemnitz, Germany. Tel.: +49 (0)371 5397 1202, e-mail: frank.schieck@iwu.fraunhofer.de

² Dipl.-Wirt.-Ing. Alexander Paul, Fraunhofer Institut für Werkzeugmaschinen und Umformtechnik IWU, Reichenhainer Str. 88, 09126 Chemnitz, Germany. Tel.: +49 (0)371 5397 1344, e-mail: alexander.paul@iwu.fraunhofer.de

³ Dipl.-Wirt.-Ing. Marco Pröhl, Fraunhofer Institut für Werkzeugmaschinen und Umformtechnik IWU, Reichenhainer Str. 88, 09126 Chemnitz, Germany. Tel.: +49 (0)371 5397 1180, e-mail: marco.proehl@iwu.fraunhofer.de

SOLUTION OF MODERN PAIR OF GUIDE AND VALVE OF PISTON ENGINES

Břetislav Skrbek¹, Vladimír Nosek¹, Martin Kysel¹, Peter Sláma²

Abstract

The introduction to questions – guide of valve stem of combustion piston engines; Stribeck curve of $\mu = \mu((\eta \cdot v)/p)$ dependence; specific conditions of sliding movement of valve stem – valve guide; RVS technology method principle; anticorrosion protection of valve stem by chromium layer with thickness about 15 μm . Stem materials and understanding of Cr layer creation as function of their properties. Valve guide is pressed in undercooled state into heads of cylinders and in the assemble is drilled into final positions with seats of valves for precious valve guides. Valve guides must be well machinable. History of cast iron development for valve guide regarding engine development. CuAl bronzes and special Ni alloys for bio and stechio.

Keywords: valve guide, sliding pair, material

1. Introduction

The valves of piston combustion engines perfect limits intake period, combustion of flammable mixture and exhaust of combustion gas. The output power stability and ecology of engine operation depends on correct valve guide. The solution of reliable valve – guide pair is topical for both design and material engineering of development of classic but especially alternative fuel engines. The developed materials must ensure guaranteed operation durability of liquid friction with minimum adhesion wear at worsening both temperature and corrosion conditions.

2. Stribeck curve

The **Stribeck curve** of $\mu = \mu((\eta \cdot v)/p)$ dependence and course of oil greasing layer thickness is illustrated in Figure 1. The lubrication is insufficient for very low velocities where: v [m.s⁻¹] – friction velocity, μ [-] – friction coefficient, η [Pa.s] – dynamic viscosity, p [Pa] – pressure. The scheme describes 3 zones (Figure 1.4). The dry friction occurs in zone I, the friction coefficient is greater then 0,1. The limiting friction occurs in zone II, where the friction coefficient is between 0,1 and 0,005. The zone III is zone of liquid friction with friction coefficient lower then 0,005. The thickness of lubrication layer for each zone is marked as h_I , h_{II} and h_{III} . The friction in rotary sliding bearings begins by zone I at start only. The displacement sliding motion in guide of valve proceeds through adverse zone of adhesive friction I at each revolution of camshaft of engine distribution.

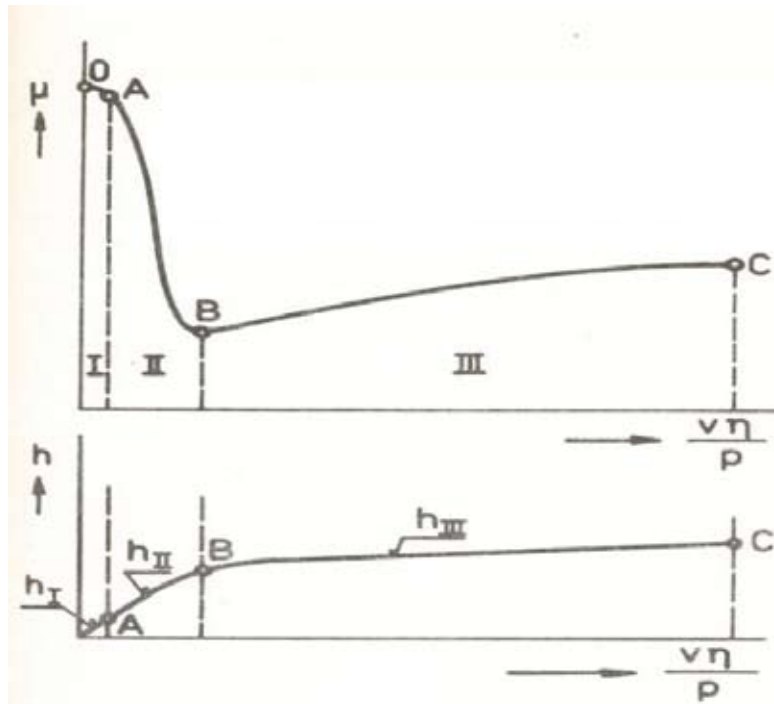


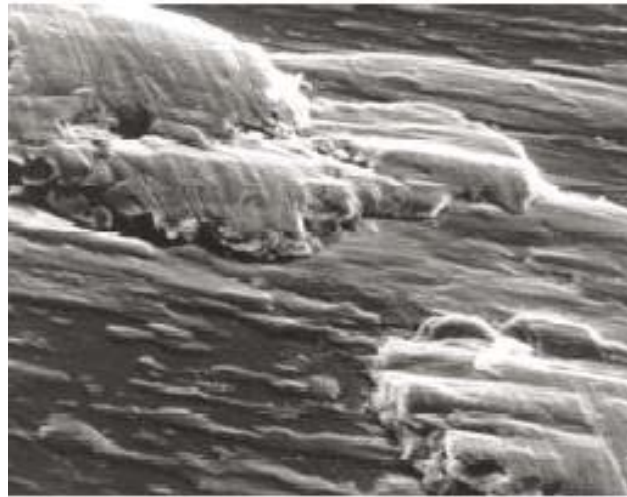
Figure 1 Stribeck curve [3]

3. Title Factors of adhesion wear [2]

The surface contact between two parts occurs on big amounts of contact facets. Their creation is accompanied by both plastic and elastic deformation of tips of particular asperities. The microjoints are created on uncovered contact facets under influence of adhesion forces. The extraction and particles creation is caused by adhesion forces. The joints failure is affected by rapid local temperature enhancement. The diffusion is enhanced by it and it can occur firm connection between broken away particle and another material surface (Figures 2 and 3). The precondition for transfer blocking gives sliding pair from „unweldable“ materials, thermally conductive materials, failure of barrier layers from oxidation or another chemical reaction. E.g. $\alpha\text{-Fe}_2\text{O}_3$ coating of steels is favorable and it acts as protective layer and lubricant. The chemical reactions can enhance wear as well. The hard metal oxides feature abrasion.

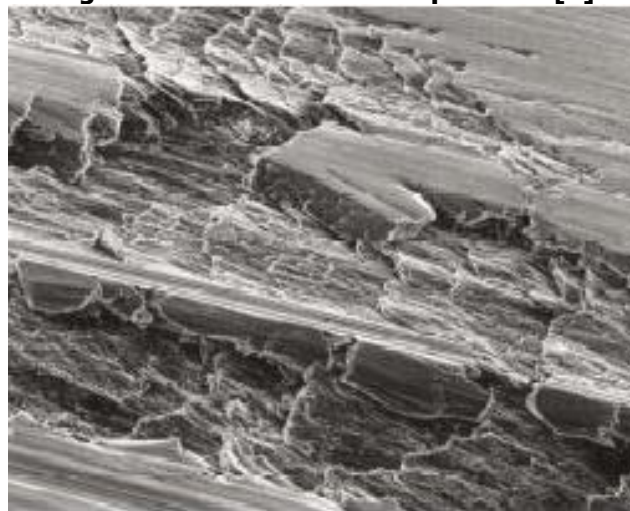
The operation factors of guide – valve pair durability:

- Too low or too large clearance between valve guide and stem.
- Insufficient lubrication.
- Bad sealing (dirtiness infiltration)
- Big oil amount input because of big clearance and subsequent seizing (functionless wiper blade – carbonization).



10 μm

Figure 2 Firm connection of particles [5]



100 μm

Figure 3 Particles extraction from material [5]

3.1. Decreasing of friction effect and wear by RVS technology

RVS method principle RVS technology is based on atomic exchange reaction between basic material and RVS component means. This all is caused by heat, friction and kinetic energy is originated by it. The so called ferrosilicium (metalloceramic) surface structure on surface of part is originated [6]. This FeSi metalloceramics lattice is greater than original surface. The crystals are lifted over the worn surface and substitute it [7]. The friction material must be on basis of iron because the RVS components react only with this surface. The RVS means are dispersion multicomponent mixtures of additives, catalysts and minerals (serpentinite, nephrite and shungite). The lubricants and oils are used as carrying medium. The main benefits are zero change of oil viscosity (very low concentration) and ecology compatibility [6].

Very high temperatures about 900 – 1400 °C are originated in sites of contact. So high temperatures support exchange reactions between basic material and RVS mixture. The creation of new surface layers with thickness from several tenths upto

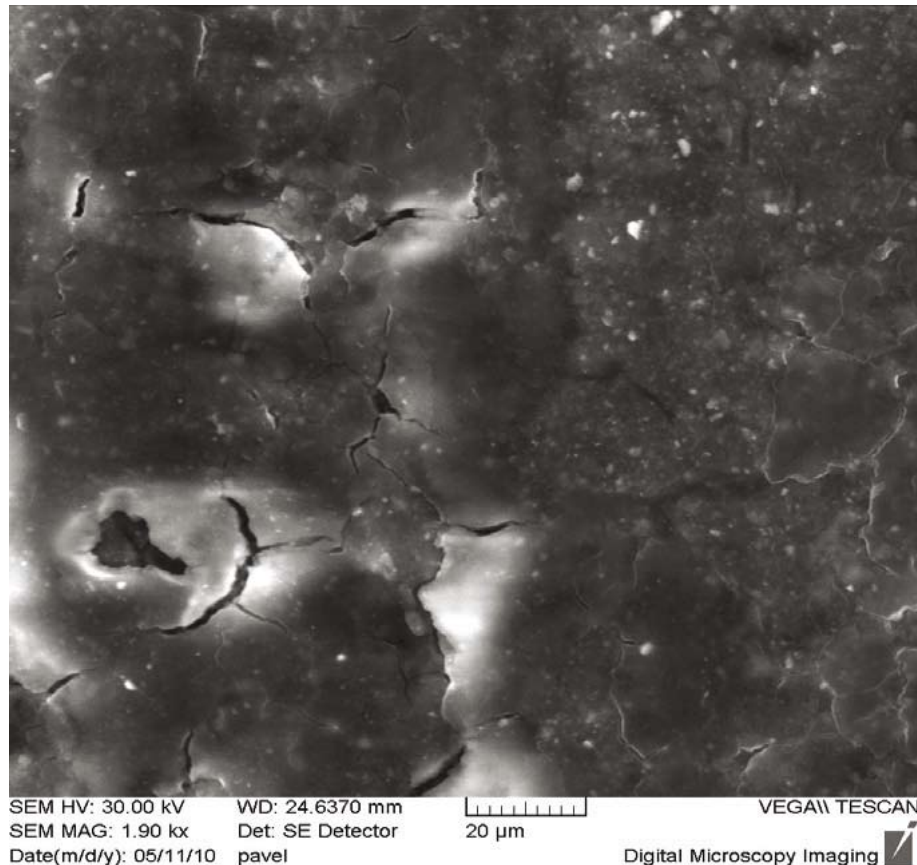
tens of micrometers occurs by it. The increasing metalloceramic (ferrosilicium) structure has much lower roughness than the original layer. Very considerable sink of friction and wear occurs by it. Hardness of this layer is 63 – 70 HRC (mostly exceeds hardness of original surface on which is the RVS method applied.) Chemical reaction is automatically stopped as soon as the lowering of friction coefficient between friction pair occurs because thermal energy supporting layer creation reaction sinks to minimum. The ferrosilicium layer is only hardly separable from original substrate. It is classified as modified layer of material (it is not coating). The protection against wear is 5 – 6 times greater than at application of custom lubricants. The friction coefficient is very low ($f = 0,003$).

4. The stem of valve

The sliding lengths of valve stems in objective region of engines are chromium plated. The weak guide can be used if the stem surface has low roughness. This limiting value for chromium valves is $0,04 \mu\text{m Ra}$, for other ones $0,06 \mu\text{m Ra}$ [5]. The chromium layer has positive effect on sliding properties in the guide and resistance against corrosion and wear [8]. The end of stem must resist against great contact loads from rocking arm. For this reason it is hardened by induction, surface and bulk hardening [1]. The valve material resists against wear under heat, it is great at dimensional stability, corrosion resistance, strength and fracture resistance [4]. EN 10090 (42 0944) standard describes usability of steels and alloys for combustion engine valves. The manufacturing of exhaust valves is common in performance which is named as trimetallic = Co overlay + head of austenite steel or Ni alloy + resistance or friction overlaid stem from martensite chromium steel with hardened shank intended for contact with rocking arm [4]. The stem is from hardened chromium steel [1]. In Czechia is applied martensite steel 17 115 . **Hard chromium layer:** Chromium generally resists against chemicals, high temperatures, it has an extraordinary hardness and great wear resistance [8]. Hard chromium plating belongs to electroplating. These chromium coatings are electrodeposited. The chromium is deposited from chromic acid by sequential reduction or is deposited from chromic acid directly. Chromium deposition from chromium plating bath is given by valency. The coating with thickness from $1 \mu\text{m}$ up to several mm can be deposited at using hard chromium plating [9]. Excellent anticorrosion protection for valves is ensured by chromium layer with thickness about $15 \mu\text{m}$.

The electroplating of these hard chromium coatings cause high hardness (from 800 to 1200 HV) [9]. The chromium, in this way deposited, is a mixture of allotropic structures, b.c.c. and h.c.p. The lattice deformation conditioning hardness is caused by seals of chromium oxygen compounds especially. The chromium layers hardness is given by chromic oxide content. The content of this compound in chromium layer is about 1%. The hydrogen takes a part at deformation only partly. The forms of chromium differ ones from another by both hydrogen content and crystalline form. The crystallization effects chromium layer hardness. The hardness grows at first with increasing current density and temperature to maximum and it sinks after it. This action is accompanied by increasing grain coarsening, the mutual cohesion sinks by it. The hardness can be effected by electrolyte composition [10]. **Optimum hardness of stable coatings is about 860 HV.** Coatings with higher hardness are unstable.

Excellent friction values can be obtained at application of pair of hard chromium with pearlite cast iron, composite metal or leaded bronze. Good values can be achieved for soft steel or hard steel with low roughness and satisfactory lubricating. The bad results are shown at friction of chromium against chromium or light alloys or phosphor bronze [10].



Obr.4. Cr surface worn by operation

5. Guide of valve

The guide of valve leads off 25 % of heat, which is created by engine [8]. ONA 30 2207 standard (after entering into EU invalid) specifies guide requirements for common piston engines. The matrix must be pearlite (maximum 10% of free ferrite) for cast iron guides. The Guide of valve is pressed overcooled into heads of cylinders and it is drilled into final positions with seats of valves for perfect guide of valves in the set with head. Valve guides must be well machinable for this reason.

5.1. Development of guide material in time

The guide development has its own history. The guides were from unalloyed cast iron with uniform flake graphite and pearlite matrix (quality ČSN 422425; casting ČSN 01 4470.4; hardness from 190 to 240 HB). The cast iron with flake graphite has damping ability and with it vibration level lowering. The structure of real castings was inhomogeneous; the matrix is ferrite with pearlite cell boundaries up to depth 1,5mm. It is pearlite from 1,5mm to 5mm (70 - 85%), which is best quality. The overcooled graphite with 90% of ferrite bordered by pearlite (40 - 60%) occurs from

5mm up to center of guide. The critical parameter was durability in this time, no reliable operation at warm. The pearlite matrix should be ensured by copper alloying. The isothermal hardening in salt bath 350 °C warm of guide workpieces was more efficient. The bainite (ausferit) excels with high wear resistance, strength and hardness (260-300 HB) at satisfactory final machinability [11]. Is there opportunity to harden castings from cheaper cast iron of quality 42 2415. This cast iron is applicable up to isothermal hardening temperature, its properties are change (350 – 400°C).

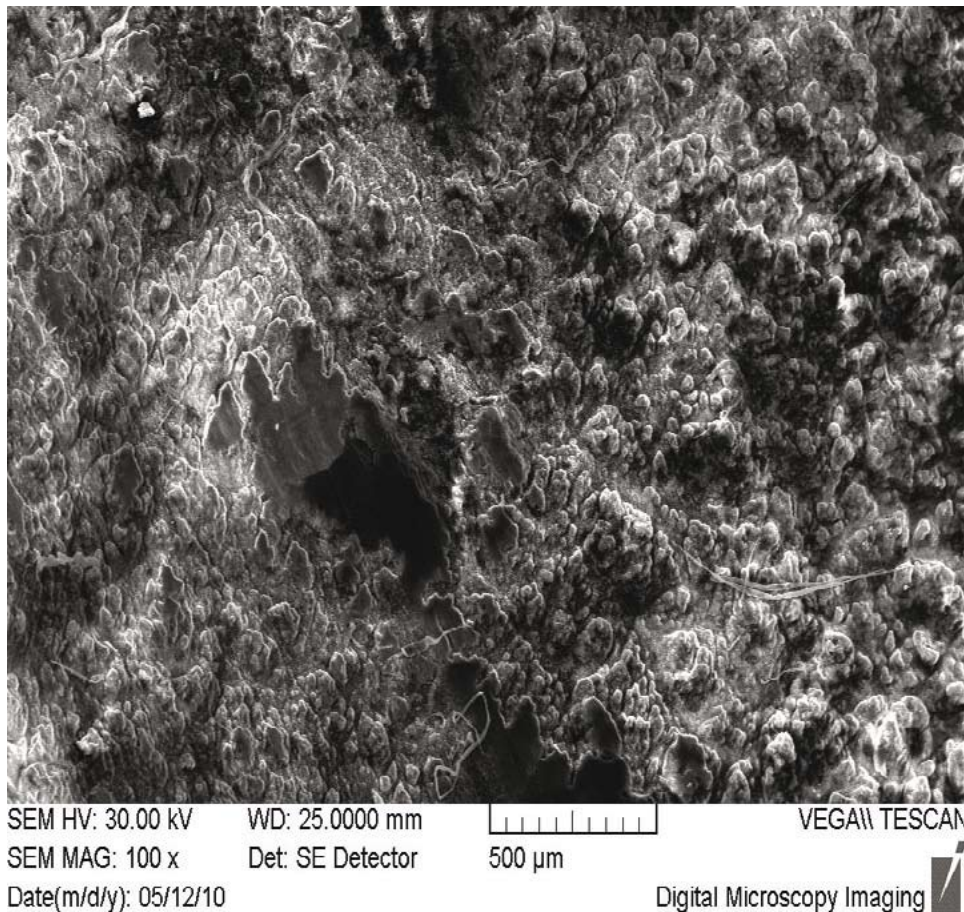


Figure 5 Cast iron valve guide surface worn by operation

The maximum durability for cast iron is ensured by guide with composition: C 3,2 – 3,5; Si 1,8 – 2,2; Mn 0,6 – 0,8; P 0,65 – 0,9; S max 0,12; Cr max 0,2 [%]. This alloy resists up to 600 °C, but the result of composition is difficult machinability. The use of alternative fuels (e.g, biogas) leads to considerable high-temperature corrosion loading of parts adjacent to combustion space. The cast iron guides do not meet the demands (Figure 6b). CuAlFe special alloys were developed for these applications.



a)



b)



c)

Figure 6 Section through cast iron guide of valve. a) quality sliding area, b) worn by adhesion and hot corrosion, c) valve with chromium plated stem

Analysis of special alloy CuAlFe, results in weight percentage:

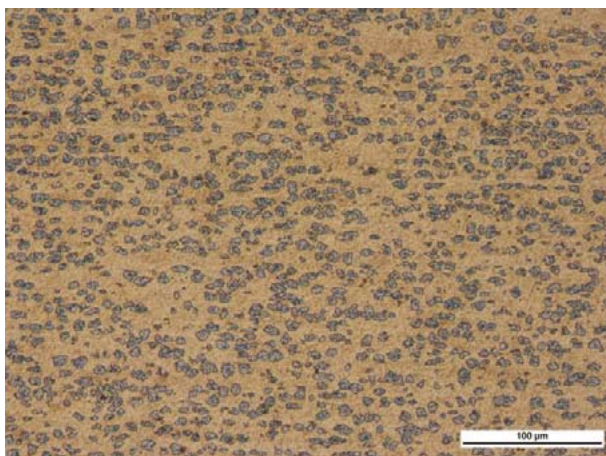
Fe	Mn	Al	Ni	Cu rest
3,80	1,15	14,33	0,0	

Measurement method: AAS. The structure (Fig. 7) is not similar to classical Al bronzes (Figure 8). The structure contains a larger amount of hard phases γ_2 , the measured hardness is 315 HV10. The hardness and strength of these Cu alloys can be modified by precipitation strengthening and other procedures of heat treatment [10]. The hardness about 300 HV can be recommended for sliding applications.

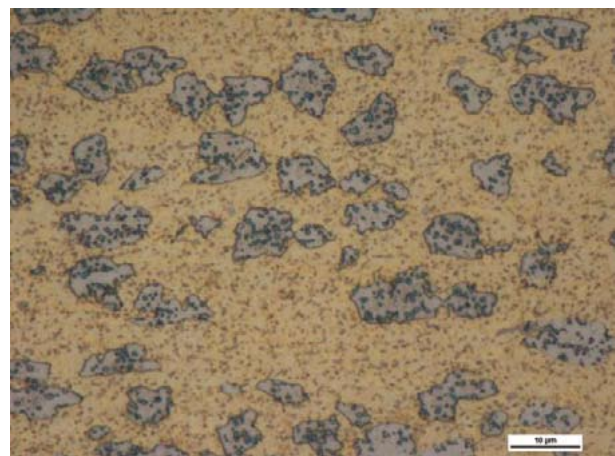
The engines with highest thermal loading (e.g. gas engines in the „stechio“ regime of combustion) exploit developed „exotic“ alloys on basis Ni Ag and other metals or cheaper e.g. Ni Cr13Mo2Bi5Sn4Fe2. Their metallurgy and heat treatment is not simple and they are legal protected. The diagnostics of in this contribution described alloys is developed with subvention of research plan MSM4674788501.

References

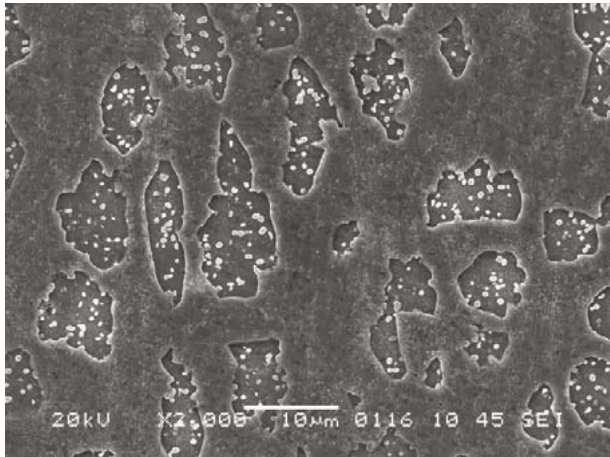
- [1] Kolektiv autorů: *Provozní degradace austenitických ventilových ocelí : sborník semináře se zahraniční účastí : 9. října 2006, Liberec*. Vyd. 1. Liberec : Technická univerzita v Liberci, 2006. 111 s. ISBN 8073721139.
- [2] Vocel, M.; Dufek, V. et al.: *Tření a opotřebenění strojních součástí*. Vyd. 1. Praha: SNTL, 1976. 374 s.
- [3] Boháček, F. et al.: *Části a mechanismy strojů II : Hřídele, tribologie, ložiska*. Brno: VUT, 1983. 214 s.
- [4] Skrbek, B.: *Materiály pro konstrukční aplikace*. Vyd. 1. Liberec : Technická univerzita, 2003. 60 s. ISBN 8070836636.
- [5] Výměna ventilů, vodítek a vložek sedel ventilů. In *Návod pro instalaci*. [s.l.] : [s.n.], [2009] [cit. 2010-03-04]. Dostupné z WWW: <http://www.cesomot.cz/doc_cz/AE_pokyny_pro_vymenu_ventilu_voditek_a_vlozek_sedel_ventilu.pdf>
- [6] Povrchové úpravy a renovace technologiemi RVS. *Technologie pro povrchové úpravy* [online]. 2005, 4, [cit. 2010-03-05]. Dostupný z WWW: <<http://www.mmspektrum.com/clanek/povrchove-upravy-a-renovace-technologie-mi-rvs>>.
- [7] *RVS SPEED* [online]. 2009 [cit. 2010-03-06]. Dostupné z WWW: <<http://www.rvspeed.cz/rvs-technology/>>
- [8] Komponenty ventilového rozvodu. In *Úplný výrobní program ventilových rozvodů pro trh náhradních dílů*. [s.l.] : [s.n.], [2009] [cit. 2010-03-15]. Dostupné z WWW: <http://www.cesomot.cz/doc_cz/AE-vyrobní-program-ventilových-rozvodu.pdf>.
- [9] Bartl, D. O.; Mudroch, O.: *Technologie chemických a elektrochemických povrchových úprav*. Praha : SNTL, 1957.
- [10] Sláma P., Podaný P., Macháčková, K., Světlá, M., Macháček, J.: *Struktura a vlastnosti lisovaných tyčí ze CuAl10Ni5Fe4*. Konference METAL2010, Rožnov pod Radhoštěm.
- [11] Beneš, L., Kaloč, R. *Tribological aspects of the railway wheel – rail contact*. In. Sci. Papers of the university Pardubice, Series B, The Jan Perner Transport Faculty, 12 (2006) str.21-26



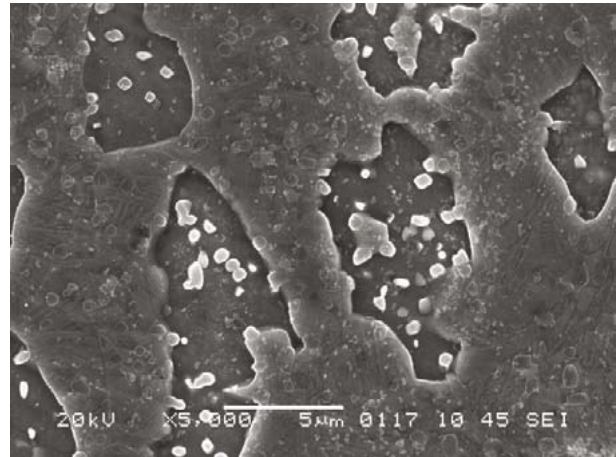
a) 200x



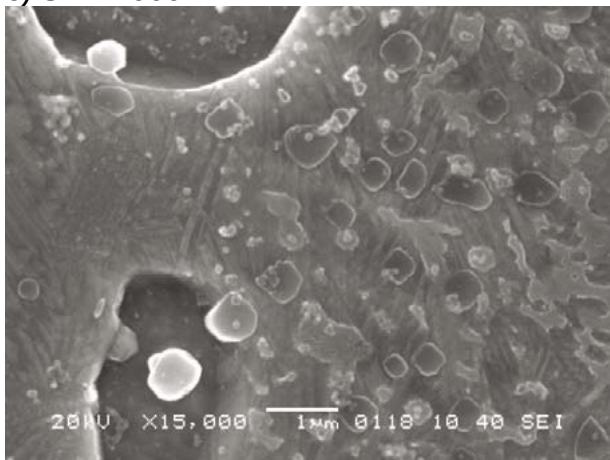
b) 1000x



c) SEM 2000x



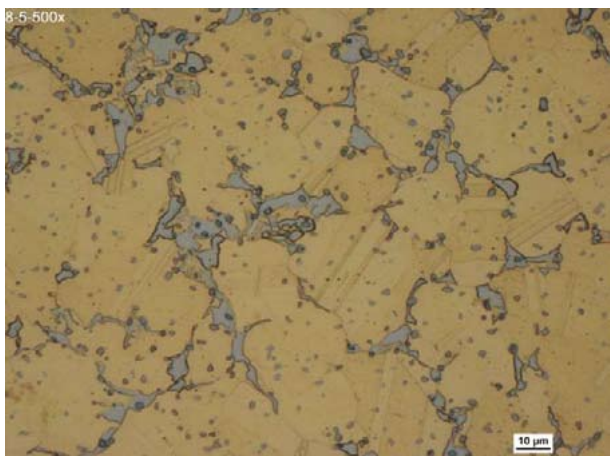
d) SEM 5000x



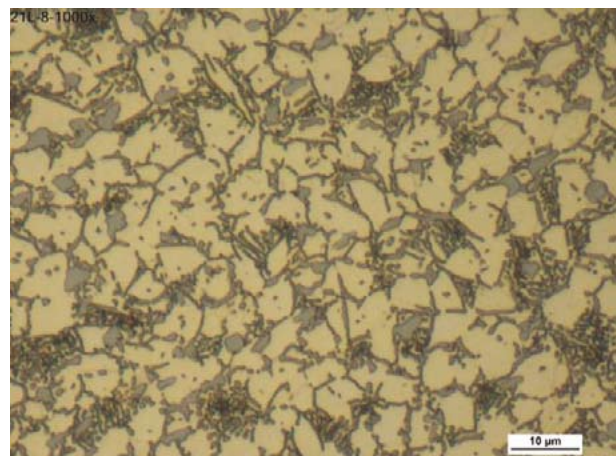
e) SEM 15000x

Figure 7 Structure of special CuAlFe alloy

For a comparison of the structure 2 Al alloys bronzes. Hardness alloy CuAl10Fe3Mn1,5 after quenching is approx. 200 HV10, hardness alloy CuAl10Ni5Fe4 after quenching is up to 300 HV10. After annealing the hardness is lower.



a) 500x CuAl10Fe3Mn1,5
Annealed 850°C, slow cooled



b) 1000x CuAl10Ni5Fe4
Annealed 800°C, slow cooled

Figure 8 Structure of Al bronze

-
- ¹ Doc. Ing. Břetislav Skrbek, CSc., TU v Liberci, Czech Republic, e-mail: bretislav.skrbek@tul.cz
Ing. Vladimír Nosek, TU v Liberci, Czech Republic, e-mail: Vladimir.nosek@tul.cz
Bc. Martin Kysel, TU v Liberci, Czech Republic, e-mail: kysel.martin@gmail.cz
- ² RNDr. Peter Sláma, COMTES FHT a.s., Průmyslová 995, 334 41 Dobřany, Czech Republic,
Tel.: +420 377 197 344, e-mail: peter.slama@comtesfht.cz

STRUCTURE DEGRADATION OF NI BASE SINGLE CRYSTAL ALLOY UNDER CREEP CONDITION

Jozef Zrník¹, Pavel Strunz², Maurice Maldiny³, Alfred Wiedenmann⁴

Abstract

The creep degraded nickel base single crystal superalloy CMSX-4 of two axial orientations [001] and [111] was investigated with aim to assess the structure degradation. Constant load creep tests were conducted in the stress/temperature ranges of 250 – 780 MPa / 750 – 950°C resulting in rupture time variation from 50 to 4000 hours. A combination of scanning electron microscopy (SEM) and non-destructive small-angle neutron scattering method (SANS) was used to investigate the directional coarsening (rafting) of the gamma prime (γ') precipitates in relation to the stress and temperature applied as well as to the initial crystallographic orientation of the specimens. The SANS results are discussed in terms of the correlation with the raft development, the axial orientation of specimen, the creep parameters and the mechanical properties.

Keywords: SX Ni base superalloy, creep, structure, small angle neutron scattering

1. Introduction

Nickel base superalloys are widely used for heavy duty gas turbine buckets, where stability of microstructure is an important factor determining mechanical properties under service conditions. The basic microstructure of single crystal (SX) nickel base superalloys contains two phases – the gamma (γ) matrix, which is hardened by precipitates of γ' phase. The drawback of SC superalloys is their metallurgical instability at high temperatures. The changes in their morphological characteristics are most sensitively reflected in their deformation behaviour and result usually in an acceleration of degradation process [1, 2]. In these alloys, the morphological evolution of the γ' precipitates at high temperatures may be considerably altered by the application of a (uniaxial) external stress [3]. Under high temperature creep conditions, the γ/γ' microstructure first becomes rafted, then slowly coarsens and becomes irregular [4, 5]. This phenomenon, known as directional coarsening or “rafting”, corresponds to a breaking of the overall cubic symmetry of the γ' precipitate shape and results in the formation of large platelets perpendicular to the stress direction. The extent of degradation in the microstructure reduces then the mechanical properties of SC superalloys and depends on the exposure temperature, time of exposure and to a lesser extent on the applied stress. The mechanical parameters of single-crystal superalloys also seem to depend on the load axis orientation with respect to the crystallographic directions.

To check the response of the structural parameters especially to the applied load at elevated temperatures, both destructive and non-destructive testing can be used. Small-angle neutron scattering (SANS) [6, 7] proved to be an effective non-destructive tool for the assessment of the microstructure of alloys. The effect of rafting on the neutron scattering pattern has been demonstrated in earlier studies which employed this bulk-sensitive technique [8, 9]. To assess the morphological changes responsible for or connected with the orientation dependence of mechanical parameters, SANS can be used together with the local information obtained by SEM.

The aim of this study was to assess the morphological changes of γ' precipitates corresponding to the observed of mechanical properties on mutual crystallographic and load direction orientation in crept single crystal superalloy CMSX-4.

2. Experimental

2.1 Microstructure

The CMSX-4 SX was experimental material, which has outstanding combination of the high temperature strength and corrosion resistance. The composition of the alloy in mass % is as follows: 9.7Co, 6.5Cr, 0.6Mo, 6.4W, 5.7Al, 1Ti, 0.1Hf, 6.5Ta, 3Re, the balance is being nickel. The alloy was provided in the form of cylindrical bars with growth direction of [001] and [111]. All the bars used in this experiment had the above mentioned crystallographic direction oriented within 10° around the longitudinal axis of the bar for both growth directions. The standard heat treatment was applied to optimize structural parameters of γ' including the size, morphology and volume fraction [10].

The microstructure of the heat treated SX specimens and creep exposed specimens was then examined by the scanning electron microscopy (SEM). Samples for observation were metallographically prepared and etched. SEM observations of the creep exposed specimens were performed on section cut parallel to the crystallographic direction (specimen axis) of [001] or [111].

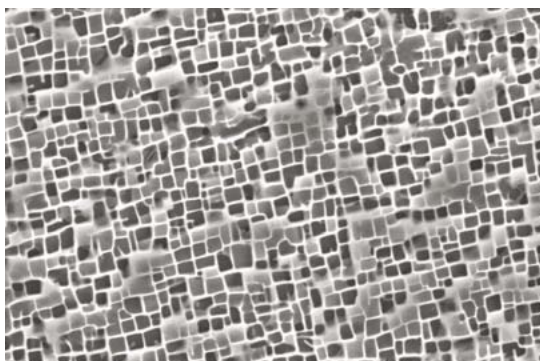


Figure 1 SEM micrograph of CMSX4 after standard heat treatment

2.2 Creep testing

The specimens for the creep rupture tests (gauge length of 60 mm, diameter of 6 mm) for both orientations were machined from the heat treated SC bars. The constant load creep tests were performed until rupture. The creep test conditions are stated in Table 1. One sample for each particular creep condition was tested.

2.3 SANS measurement

CMSX4 alloy microstructure was investigated by SANS after various loadings (temperature, stress) and at two orientations of the load axis mentioned above. An Euler cradle (for adjustment of ω , χ and ψ angles) was used to set the samples to several special orientations. An Euler cradle (for adjustment of ω , χ ψ angles) was used to set the samples to several

Table 1 Experimental creep conditions and results

Sample	Load axis	Temp. (°C)	Nominal stress (MPa)	Time to rupture (h)	Creep strain to rupture	Morphology determined by SANS and SEM
C397h	[001]	---	---	---	---	---
C397	[001]	750	780	1000	15	no rafting
D431	[001]	900	500	100	21	partial rafting
E430	[001]	900	300	2000	27	rafted
E415	[001]	950	250	500	30	rafted
B398h	[111]	---	---	---	---	---
B398	[111]	750	780	500	22	no rafting
C404	[111]	900	500	50	22	partial rafting
E451	[111]	900	300	4000	20	rafted
A396	[111]	950	250	2000	20	rafted

and the neutron wavelength $\lambda=7.5 \text{ \AA}$ (in order to avoid a multiple Bragg scattering at certain sample orientations). The covered range of the scattering vector magnitude $Q = |\mathbf{Q}|$ was approximately $3 \times 10^{-3} \text{ \AA}^{-1}$ to 0.02 \AA^{-1} , where the magnitude $Q = |\mathbf{Q}| = |\mathbf{k}-\mathbf{k}_0|$ (\mathbf{k}_0 and \mathbf{k} being the wave vectors of the incident and scattered neutrons, respectively, and $|\mathbf{k}| = |\mathbf{k}_0| = 2\pi/\lambda$).

3. Results

3.1 Mechanical tests.

The specimens of the single crystal superalloy CMSX-4 were subjected to various tensile creep stresses at different temperatures and they showed a different deformation behaviour with regard to the strain to rupture and the lifetime for two load-axis orientations of [001] and [111]. The creep data for different strain and testing temperature are presented in Table 1. As shown in Fig.2, the time to rupture is significantly larger for [100] load axis for the low temperatures and high stresses. On the other hand, the time to rupture is much larger for the [111] exposure when the sample undergoes deformation at a relatively high temperature and low stress.

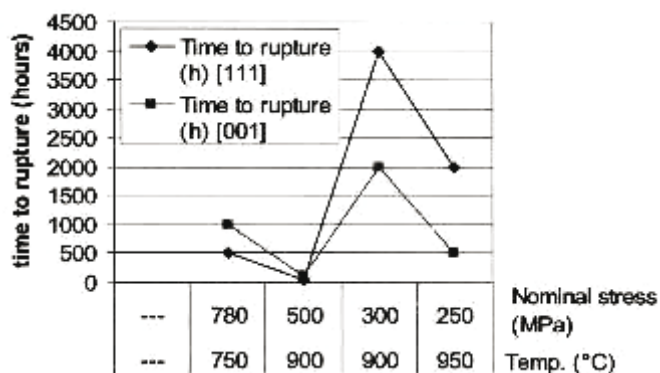


Figure 2 The time to rupture dependencies for the different stresses and temperatures.

3.2 Creep microstructure characteristics

The microstructure of SC superalloy after standard heat treatment, which is composed of γ matrix and γ' phase, is documented in Fig. 1. The cuboidal precipitates are arranged uniformly through the γ matrix. The average edge length of the cuboidal γ' precipitate is about $0.5 \mu\text{m}$. The volume fraction of γ' is over 65%. The SEM micrographs of the crept specimens for the various creep conditions (stated in Table 1) are presented in Fig. 3a for the [001] axis orientation and in Fig. 3b for the [111] axis orientation.

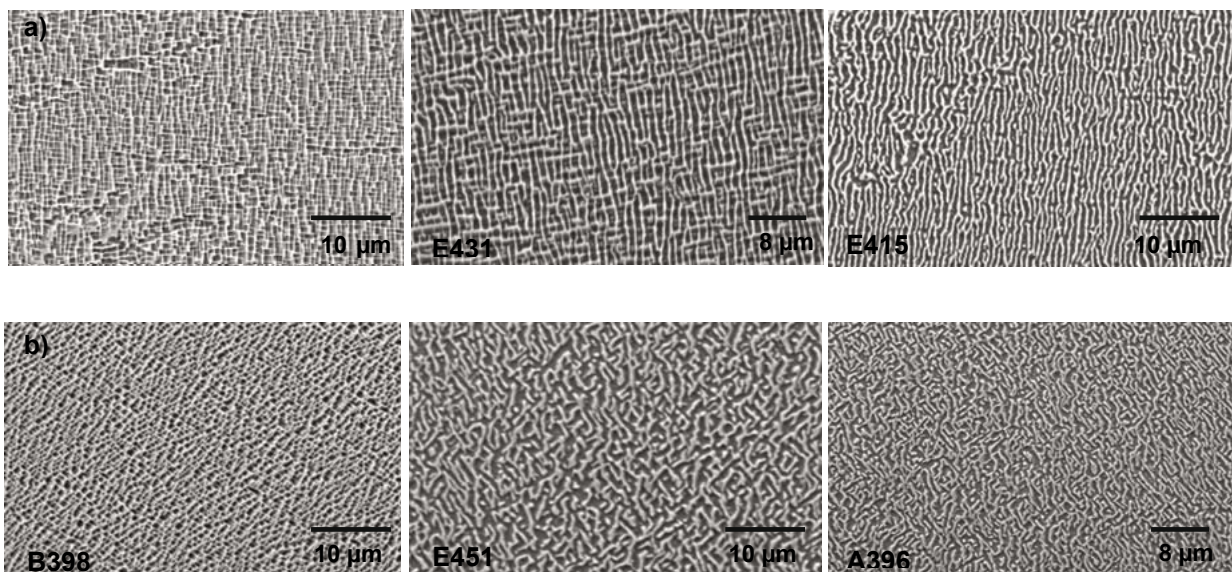


Figure 3 The SEM micrographs demonstrating the change of the γ' morphology during the creep exposure for SC specimens with axis orientation of: a) [001] and b) [111].

Generally, for both load-axis orientations, the crept specimens exposed at the lower temperature of 750°C and at higher stress showed no rafting. The specimens exposed at the higher temperature of 900°C and medium stress of 500 MPa showed partial rafting. The other specimens exposed at 900°C/300 MPa as well as at 950°C/250 MPa are fully rafted. A quantitative comparison of [111] and [001] creep exposed specimens, considering the start of raft formation, shows no striking differences, although variations in γ' morphology were observed, as shown in Fig. 3.

3.3 SANS results

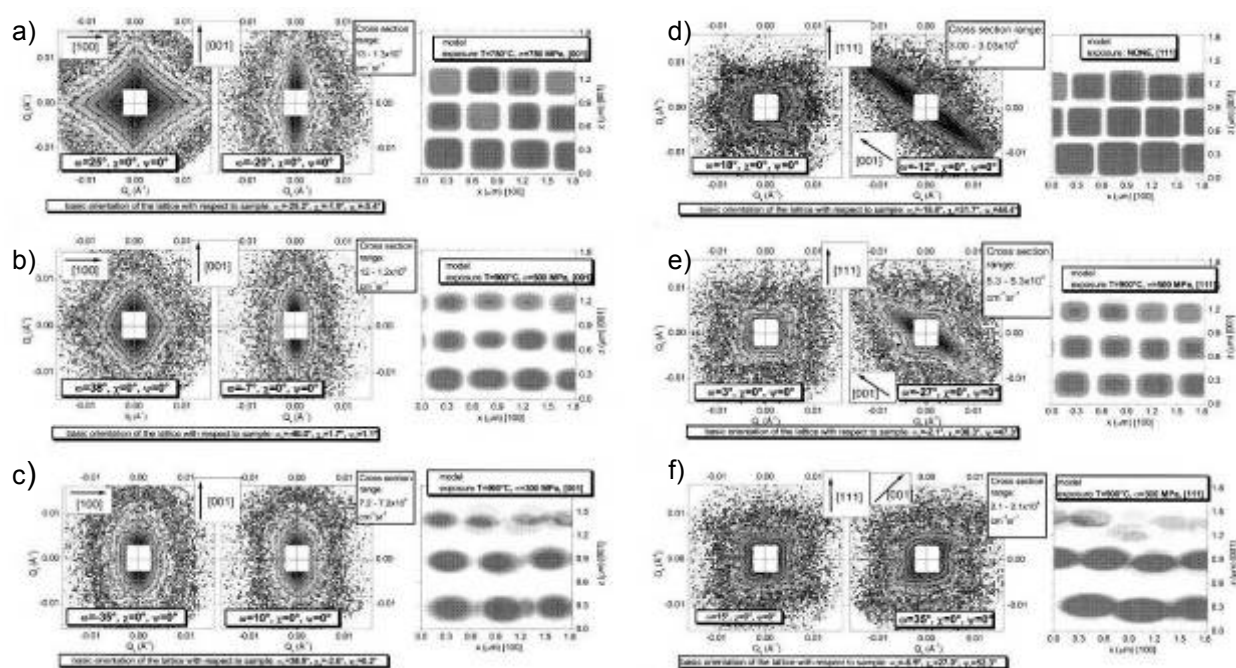


Figure 4 The selected 2D SANS patterns and the optimum models for the load axes [001] and [111]. Exposure a) $T=750^{\circ}\text{C}$, $\sigma=780$ MPa, b) $T=900^{\circ}\text{C}$, $\sigma=500$ MPa, c) $T=900^{\circ}\text{C}$, $\sigma=300$ MPa, d) none, e) $T=900^{\circ}\text{C}$, $\sigma=500$ MPa, f) $T=900^{\circ}\text{C}$, $\sigma=300$ MPa

The measured and fitted 2D data are displayed in Fig. 4 for the selected specimens and orientations. Each specimen was then measured in 9 orientations, including those with low-index crystallographic directions parallel to the incoming beam as well as those without this special relation. The 2D anisotropic data were fitted at once in order to take into account the strong anisotropy of a 3D cross section in the reciprocal space, corresponding to the cuboidal and/or rafted shape of the precipitates. The precise orientation of the crystal lattice with respect to the sample axis and edges (ω_0 , χ_0 and ψ_0 angles) was also determined by the fit. Two selected (out of nine) orientations are plotted in Fig. 4 for the selected samples.

4. Evaluation

4.1 Modelling

The measurements were evaluated by the NOC program for anisotropic SANS data treatment [11]. The analysis procedure is based on the numerical simulation of a scattering profile generated from a three-dimensional (3D) microstructural model of a particle system. The calculated profile is matched with the experimental curve by a weighted least square method in order to find the microstructural parameters which can be in principle extracted from the measured data.

In agreement with the direct-imaging technique (SEM) and with the symmetry of the SANS data at various sample orientations, ordered cuboidal or rafted particles were used as a model for the non-exposed and all the variously exposed samples. The shape of one individual particle can be varied in a simple way using only one shape parameter β [11] which is 0 for a cube or block having sharp edges and becomes > 0 for a cuboidal particle. In the case when $\beta = 1$, the particle has a spherical or ellipsoidal shape. These particles compose an array resembling γ' precipitates in a superalloy using the mean distance and its variance as well as the mean size and its variance. Additionally, an orientational distribution of the 3D modelled cross section is included, which in fact represents an orientational distribution of normals to the γ - γ' interface. This distribution is characterized by its full width in half maximum (FWHM).

4.2 Fitting

In the present case, where the precipitates in CMSX-4 after standard heat treatment are large, the measured scattering curves do not contain information on the size and distance. Therefore, the mean distance was fixed at a reasonable value. The precipitate sizes in [100] and in [001] directions could be fixed in a similar way. However, as they indirectly determine the amount of interface perpendicular to [100] and the amount of interface perpendicular to [001] (see the models in Fig. 4) and thus also the degree of the rafting, it was left free. A certain variation of the size and distance of the modelled particles, which can be observed in Fig. 4, was allowed using non-zero variances of the size and distance distributions in the preliminary fit. The size and distance variation was performed basically only in order to correspond better with variations visible in the SEM micrographs.

Because the measurement was performed at nine various orientations, the representation of the 3D cross section is sufficient to refine the orientation angles ω_0 , χ_0 and ψ_0 together with fitting of the microstructural parameters. The parameters which can be determined are: morphology (cuboids or rafted precipitates; their

particular shape defined by β , interface orientation distribution FWHM and specific interface between γ and γ' .

The sections through 3D real-space models representing the precipitates, which match best the measured data for the selected samples, are depicted in Fig. 4. It should be pointed out that three equivalent subsets of rafts, perpendicular to the crystallographic directions [100], [010] and [001], are in fact modeled in the case of the [111] deformed samples (Fig. 4 d,e,f). However, the significantly good correspondence of all the modeled SANS curves with those measured indicates that the model describes the important characteristics of the γ' precipitate microstructure as well as their trends rather well.

5. Discussion

5.1 Creep exposed microstructure evaluation

The shape parameter equals approximately 0,27 for the unexposed sample (i.e. cuboidal shape). The shape evolves towards oblate ellipsoid ($\beta = 1$) for the most loaded samples (900°C/300 MPa and 950°C/250 MPa). It should be noted, however, that even the lowest temperature exposure (750°C/780 MPa) leads to the change of cuboidal shape of precipitates ($\beta = 0,4$) and probably also to a small elongation (<10%) of precipitates in [100] and [010] directions with respect to [001].

Among the samples with the load axis [001], the sample exposed at 750°C with 780 MPa (time to rupture 1000h) showed practically no rafting indication (as the scattering pattern has nearly fourfold symmetry when both [100] and [001] are perpendicular to the beam), except the small elongation mentioned above. The sample exposed at 900°C with 500MPa (100h) clearly showed partial rafting. It can be deduced that the diffusion effects do not last long enough to form rafts for the samples exposed at lower temperatures and higher stresses. The other two samples exposed at 900°C with 300MPa (2000h) and at 950°C (250MPa, 500h) exhibited a full rafting (practically no dependence of the SANS pattern on the rotation around the load axis). The rafting thus occurs only above a temperature threshold which is between 750 and 900°C.

The estimation of the precipitates morphology for samples with load axis [111] is more difficult as the raft microstructure is more complex. It can be deduced that there is no raft formation with interfaces perpendicular to the stress axis (i.e. to [111]). The coarsening occurs uniformly in all three planes (100), (010) and (001). Due to this equivalence (unlike the samples stressed along [001]), there is no change in the general character of the SANS pattern: streaks do not disappear fully in certain crystallographic directions during the rafting process, they are only more smeared for the more exposed samples. By combining SANS and SEM, similar morphology to the [001] exposed samples can be deduced (except that the morphology is equivalent for all three directions [100], [010] and [001] in the case of [111] deformation whereas it was uniaxial in the case of the samples exposed along [001]).

5.2 Specific surface of γ'

This parameter can be obtained by fit of the specific area of the interface between γ and γ' . In order to obtain its evolution in an absolute scale, a qualified estimation of the scattering contrast has to be carried out. It can be obtained by using an

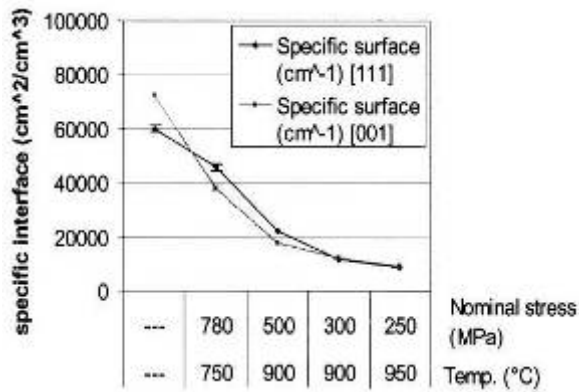


Figure 7 The dependence of the interfacial area between γ and γ' on exposure

estimation of the average precipitate size in a non-exposed condition ($0.5\mu\text{m}$) and γ' volume fraction estimation (65%) from SEM. Using this scattering contrast estimation, the evolution of the specific interfacial area in absolute magnitude can be plotted as showed in Fig 5. It can be seen when comparing the non-exposed sample with the one loaded at $750^\circ\text{C}/780$ MPa that even without rafting occurrence there is a change of the interfacial area. As no rafting occurred here, the specific interface decrease is here caused by disappearance of small precipitates from

the distribution. Further decrease of the specific surface (temperatures 900 and 950°C) is caused by coarsening of the precipitates due to rafting, which removes some interfaces and thus lowers the specific area. The growth of the precipitates is the second cause of the strong decrease of the interfacial area.

CONCLUSIONS

There is no significant observable morphological difference at low temperatures and high stresses between samples loaded along [001] and [111] axes (initial and $750^\circ\text{C}/780$ MPa as well as $900^\circ\text{C}/500$ MPa loaded samples). There is either no or only partial rafting in these samples. Nevertheless, among these samples, the [001] exposed ones exhibit higher time to rupture than [111] ones. It is likely that the dislocations pass through the samples loaded along [111] more easily. This is understandable as three equivalent slip plane systems are favorably oriented in this case. SANS showed that there is no or only a very small impact of this fact on the γ' morphology.

On the other hand, as soon as full rafting occurs ($900^\circ\text{C}/300$ MPa and $950^\circ\text{C}/250$ MPa loaded samples), the more favorable (from the point of view of the time to rupture) are, in turn, the [111] samples. Here, the microstructural difference between [001] and [111] samples are evident:

a) The rafts are formed equivalently perpendicular to crystallographic directions [100], [010] and [001] in the case of [111] deformed samples (a "zigzag" form) whereas the rafts are exclusively perpendicular to [001] in the case of [001] deformed samples;

b) Orientation distribution of the interfaces between γ and γ' is much larger for [111] samples.

Most probably, both effects help to hinder the movement of dislocations and/or crack propagation and are thus responsible for the more stable microstructure of the [111] loaded samples in the cases where rafting occurs. However, it is difficult to assess which of these two features is dominant.

Acknowledgements

The authors would like to thank BENSC (HMI Berlin) for providing the beamtime. Author (P. Strunz) acknowledges the support by MSM2672244501 project. J. Zrník acknowledges the support of the Ministry of Education of the Slovak Republic (COST 538 Action project).

References

- [1] J. W. Brooks, P.J. Bridges: *Superalloys 1988*, Publication of TMS, (1988), p. 31
- [2] J. F. Radawich: *Superalloys 718, 625, 706 and derivatives*, TMS publication, USA, 1994, p. 635
- [3] J. C. Chang, S. M. Allen: *J. Mater. Res.* 6, 1999, p. 1843
- [4] T. M. Pollock, A.S. Argon: *Acta Metall. Mater.* 42, 1994, p. 1895
- [5] A. Epishin, T. Link, P.D. Portela, U. Brückner: *Acta mater.*, 48, 2000, p. 4169
- [6] O. Paris, M. Fähmann, E. Fähmann, T. M. Pollock, P. Fratzl: *Acta mater.*, 45, 1997, 3, p. 1097
- [7] G. Kostorz, in: *Neutron Scattering (Treatise on materials science and technology)*, ed. by Kostorz G, Academic Press, New York, 1979. p. 227-289.
- [8] P. Strunz, J. Zrník, R. Gilles, A. Wiedenmann: *Physica B* 276-278, 2000, p. 890
- [9] P. Strunz, J. Šaroun, P. Mikula, P. Lukáš, F. Eichhorn: *J. Appl. Cryst.* 30, 1997, p. 844
- [10] Keiderling, U. & Wiedenmann, A.: *Physica B* 213-214, 1995. p. 895
- [11] P. Strunz, R. Gilles, D. Mukherji and A. Wiedenmann: *J. Appl. Cryst.* 36, 2003, p. 854

¹ prof. Ing. Jozef Zrník, CSc., COMTES FHT a.s. Průmyslová 995, 334 41 Dobřany, Czech Republic
Tel.: +420 377 197 342, e-mail: jzrník@comtesfht.cz

² Dr. Pavel Strunz, Research Centre Řež, 25068 Řež near Prague, Czech Republic
Tel.: +420 2 66 17 2034, e-mail: strunz@ujf.cas.cz

³ Dr. Maurice Maldini, CNR-IENI, Via Cozzi 53, 20125 Milano, Italy
Tel.: +39(0)266173330, e-mail: maldini@ieni.cnr.it

⁴ Dr. Alfred Wiedenmann, HMI Berlin, Glienickestrasse 100, D-14109 Berlin, Germany,
e-mail: wiedenmann@hmi.de

CONDITIONS FOR FORMATION OF BORON OXIDE AND NITRIDE IN BORON-ALLOYED STEELS

Zdeněk Adolf¹, Jiří Bažan², Ladislav Socha³

Abstract

The higher value of the product of boron and oxygen concentrations, or of boron and nitrogen concentrations than the value corresponding to the balance for the given temperature is thermo-dynamic criterion of nucleation of the new phase (B_2O_3 or BN). It followed from calculations that theoretical temperature of the beginning of B_2O_3 oxide nucleation is higher than temperature of the beginning of BN nitride nucleation. During solidification and cooling down of steel boron oxide will be formed preferentially before boron nitride. The work was prepared at solution of the projects FR-TI1/477 and FR-TI1/222 under financial support of the Ministry of Industry and Trade (MPO ČR).

Keywords: boron in steel, nucleation, non-metallic inclusions

1. Introduction

The paper presents a thermodynamic analysis of probability of formation of boron oxide and nitride in boron- and nitrogen-microalloyed stainless steels. Steels are designated for castings or forgings for manufacture of turbine blades, pivots for equipment of hydraulic power plants or structural elements with increased strength. Targeted chemical composition is given in table 1.

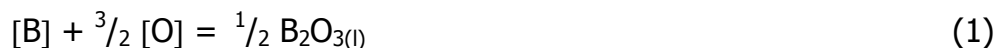
Table 1 Targeted chemical composition of steel

Element. (% wt.)							
C	0.04	S	0.001	V	0.05	Nb	0.017
Mn	1.57	Cr	17.5	W	0.02	B	0.004
Si	0.6	Ni	10.5	Al	0.050	N	0.0126
P	0.020	Mo	0.07	Ti	0.40		

The objective of this work is to determine, at which temperatures B_2O_3 oxide or BN nitride is being formed during cooling and solidification of steel. Formation of new phase (inclusion) is related to content of boron, nitrogen and oxygen in steel.

2. Thermodynamic balance

Temperature dependencies of Gibbs energy for formation of B_2O_3 and BN were derived from table data [1] and [2] with use of the equations:





$$\Delta G_1^0 = -411\,990 + 143,585 T \quad (3)$$

$$\Delta G_2^0 = -277\,737 + 97,95 T \quad (4)$$

Due to the fact that melting temperature of B_2O_3 is $450\text{ }^\circ\text{C}$ [2], this oxide is at temperatures of steel solidification in liquid state.

It is possible to derive from the equations (3) and (4) the following relations for temperature dependencies of equilibrium constants:

$$\log K_1 = \frac{21\,517}{T} - 7,50 \quad (5)$$

$$\log K_2 = \frac{21\,894}{T} - 5,116 \quad (6)$$

The following is valid for equilibrium constants of the reactions (1) and (2):

$$K_1 = \frac{a_{B_2O_3}^{1/2}}{(a_{[B]} \cdot a_{[O]}^{3/2})_{equilibrium}} \quad (7)$$

$$K_2 = \frac{a_{BN}}{(a_{[B]} \cdot a_{[N]})_{equilibrium}} \quad (8)$$

Assuming that clean boron oxide and boron nitride are formed, it is possible to consider their activities to be equal to one. It is similarly possible to assume unequivocally that solutions of boron, oxygen and nitrogen in steel are diluted, and that activities of these elements are equal to mass percentage. It is then possible to adjust the equations (7) and (8) to these forms:

$$([B] \cdot [O]^{3/2})_{equilibrium} = \frac{1}{K_1} \quad (9)$$

$$([B] \cdot [N])_{equilibrium} = \frac{1}{K_2} \quad (10)$$

Due to the fact the equilibrium constants K_1 and K_2 are function of temperature only in accordance with the equations (5) and (6), equilibrium products of concentrations of boron with oxygen and boron with nitrogen depend only on temperature (see the equations (11) and (12)) and it is also possible to calculate them from temperature dependencies.

$$\log ([B] \cdot [O]^{3/2})_{equilibrium} = -\frac{21517}{T} + 7,50 \quad (11)$$

$$\log ([B] \cdot [N])_{equilibrium} = -\frac{11894}{T} + 5,116 \quad (12)$$

It is subsequently possible to affirm logically, that formation of boron trioxide or boron oxide at the temperature T is conditioned by higher value of the real product of boron and oxygen concentration, or boron and nitrogen concentration that it would correspond to the equilibrium.

$$([B] \cdot [O]^{3/2})_{real} \geq ([B] \cdot [O]^{3/2})_{equilibrium} \quad (13)$$

$$([B] \cdot [N])_{real} \geq ([B] \cdot [N])_{equilibrium} \quad (14)$$

It follows from the equations (11) and (12) that with decreasing temperature the value of equilibrium products (13) and (14) also decreases and therefore probability

of formation of the inclusions B_2O_3 and BN increases, since real products (13) and (14) remain constant.

3. Discussion of results

The derived relationships were applied to the steel microalloyed by boron and nitrogen of the required chemical composition – see table 1.

Theoretical dependencies of the temperatures of the beginning of formation of B_2O_3 or BN on the content of oxygen and nitrogen are given in figures 1 and 2.

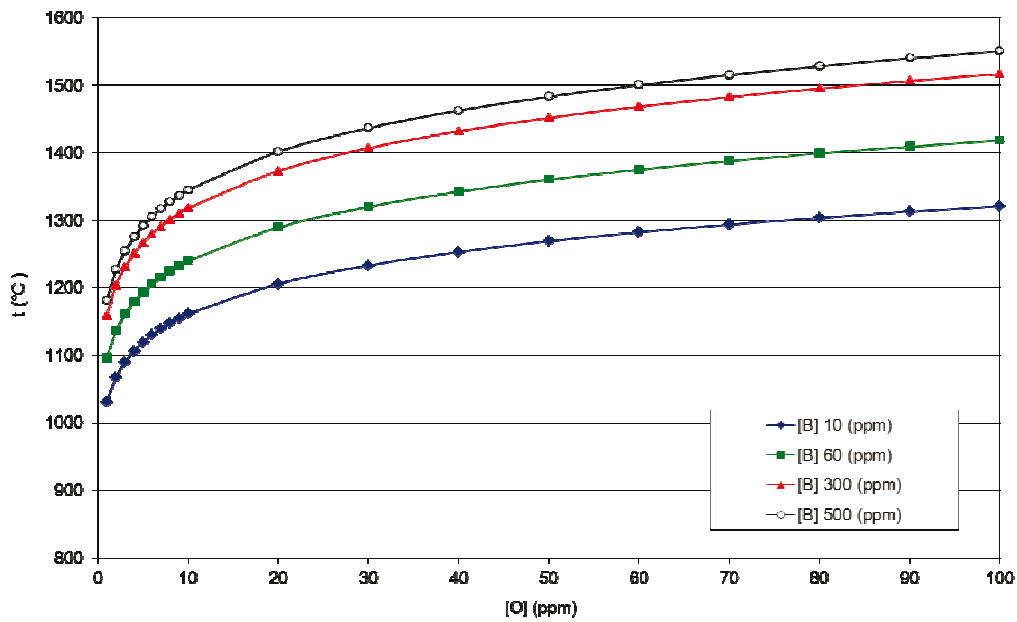
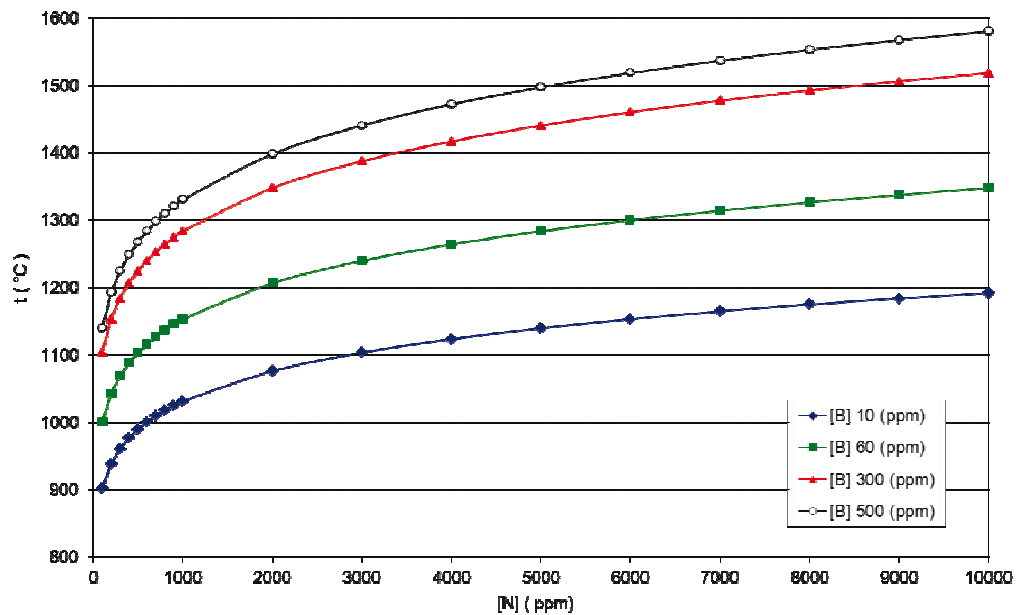


Figure 1 Dependence of the temperature of the beginning of formation of B_2O_3 on the content of oxygen in



steel

Figure 2 Dependence of the temperature of the beginning of formation of BN on the content of oxygen in steel

These dependencies were calculated from the equations (5) and (6), adjusted for 0.001 %mass, 0.006 %mass, 0.03 %mass and 0.05 %mass of boron.

It follows from Fig. 2 that for example theoretical temperature of the beginning of nucleation of the BN nitride is for the nitrogen content of 100 ppm in the interval 903°C, 1001°C, 1104°C and 1040 °C, or for 200 ppm of nitrogen in the interval 939°C, 10043°C, 1154°C and 1193°C. Theoretical temperature of the beginning of nucleation of the oxide B₂O₃ is for the achieved oxygen contents (10 ppm) higher, namely 1161°C, 1240°C, 1318°C and 1345°C, for 20 ppm of oxygen it is 1206°C, 1290°C, 1373°C and 1402°C. It follows therefore that boron oxide will be formed preferentially before boron nitride during cooling of steel.

For the steels with the above mentioned boron contents equilibrium temperatures and equilibrium nitrogen contents corresponding to 10 - 100 ppm of oxygen in steel are shown in Fig. 3. It is evident from the figure that B₂O₃ oxides can be formed only at higher contents of oxygen than it would correspond to an equilibrium (right to the curve). Similarly boron nitrides can be formed only at higher nitrogen contents that it would correspond to an equilibrium (above the curve), since inequalities (13) and (14) are fulfilled.

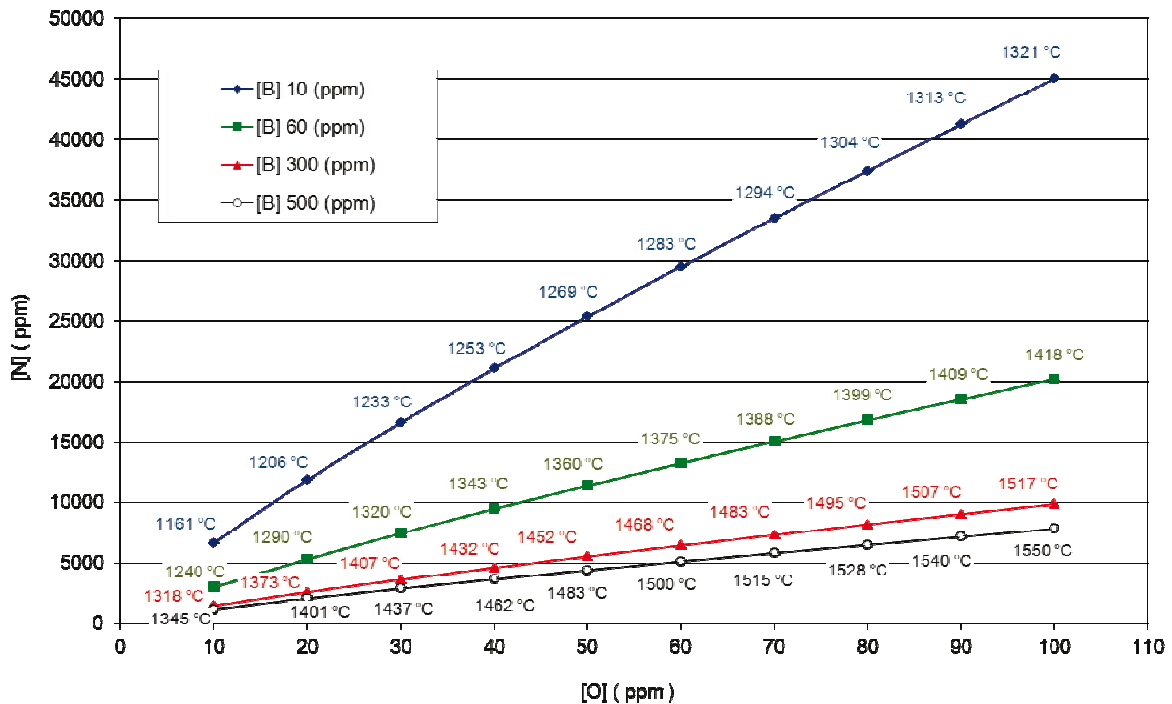


Figure 3 Equilibrium temperatures and equilibrium contents of nitrogen corresponding to the oxygen content in steel of 10 to 100 ppm

4. Conclusions

The paper deals with thermodynamic balance of probability of formation of oxide B₂O₃ and nitride BN in boron-microalloyed steels. The balance has proved that boron oxide is more stable than boron nitride and therefore at cooling of steels it is formed preferentially.

References

- [1] FRUEHAN, J. et al. *The Making Shaping and Trating of Steel*. Pittsburgh 1998, 767 pp., ISBN 0-930767-02-0
- [2] LEITNER, J. *Databáze termodynamických údajů pro příměsi v taveninách na bázi železa*. [Database of thermodynamic data for admixtures in iron based melts]. VŠCHT Praha, 2002, 23 pp.

¹ Prof. Ing. Zdeněk Adolf, CSc., VŠB-Technical University of Ostrava, Department of Metallurgy, 17. listopadu 15/2172, 708 33 Ostrava-Poruba, Czech Republic, Tel.: +420 59 732 5135, e-mail: zdenek.adolf@vsb.cz

² Prof. Ing. Jiří Bažan, CSc., VŠB-Technical University of Ostrava, Department of Metallurgy, 17. listopadu 15/2172, 708 33 Ostrava-Poruba, Czech Republic, Tel.: +420 59 732 5231, e-mail: jiri.bazan@vsb.cz

³ Ing. Ladislav Socha, Ph.D., VŠB-Technical University of Ostrava, Department of Metallurgy, 17. listopadu 15/2172, 708 33 Ostrava-Poruba, Czech Republic, Tel.: +420 59 732 3534, email: ladislav.socha@vsb.cz

ASTM A694 F60 HEAT TREATMENT AND MECHANICAL PROPERTIES

Martin Balcar¹, Jaroslav Novák², Libor Sochor³, Pavel Fila⁴, Ludvík Martínek⁵

Abstract

Production of heavy steel forgings of microalloy steels seeks possibilities to take advantages associated with the benefit of application of microalloying elements and thermomechanical treatment at the level of mechanical properties attained, known from production of sheets, strips and tubes.

The paper documents the influence of quenching temperature on values of mechanical properties and structure of F60 steel according to ASTM A694.

Verification of quenching temperature influence contributes to optimization and determination of a complex method of microalloy steel heat treatment. Steel structure and mechanical properties after the quenching constitute initial as well as basic criterion to achieve requested mechanical properties at properly chosen tempering temperature.

The paper has been solved within the EUREKA programme of the OE 08009 E!4092 MICROST project. The project was implemented based on government resources with financial support of the Ministry of Education, Youth and Sport of the Czech Republic

Keywords: A694 F605, HSLA steel, quenching and tempering

1. Introduction

As the requirements for structural steel properties are growing, the development of use of microalloying elements even in the field of production of forgings and castings takes place.

Production of heavy steel forgings of microalloy steels does not allow to immediately take advantages associated with the benefit of application of microalloying elements and thermomechanical treatment known from production of sheets, strips and tubes. In the case of production of steel forgings, the forming and heat treatment process mainly features different forming and heat treatment conditions compared to thin-walled products (sheets, strips, tubes).

Development and verification of F60 steel production and treatment technology according to ASTM A694 under ŽDAS, a. s. conditions constitute a number of technological changes and introduction of new process elements in the field of steel making and subsequent thermomechanical treatment. Verification of quenching temperature influence on properties and structure of F60 forged steel contributes to optimization of complex HSLA steel making technology at ŽDAS, a. s.

2. Experimental Material

Verification of quenching temperature influence on structure and mechanical properties of modified F60 steel according to ASTM A694 made by EOP/LF/VD technology was carried out on forged piece samples with dimensions (100x100x150)mm. Basic chemical composition of the steel is shown in Table 1.

Table 1 Basic chemical composition HSLA steel F60 (wt. %)

C	Mn	Si	P	S	Cr	Ni	Mo	V	Al	Nb	N
0.10	1.08	0.33	0.003	0.001	0.16	0.77	0.27	0.04	0.027	0.034	0.0037

Modified F60 steel according to ASTM A694 is typical low carbon steel with addition of alloying elements, manganese, silicon, nickel and molybdenum. Moreover, the steel is microalloyed by vanadium, aluminium and niobium. Concentration of other elements is at the level like residual elements and the rest is iron.

After the forming process, the forgings were "anti-flake" annealed up to a temperature of 650°C for a period of 10 hours and subsequently normalized at a temperature of 930°C with air cooling.

3. Laboratory Heat Treatment

The heat treatment itself was carried out on forged steel samples under laboratory conditions. Verification of influence of austenitization – quenching temperature (T_A) on the structure and mechanical properties was proposed for the temperature range (880 to 940)°C with subsequent water quenching and tempering $T_p = 620$ °C with air cooling. Sample marking and heat treatment carried out are as follows:

sample L1 : $T_A = 880$ °C/6 hours/water +	$T_p = 620$ °C/8 hours/Air
sample L2 : $T_A = 890$ °C/6 hours/water +	$T_p = 620$ °C/8 hours/Air
sample L3 : $T_A = 900$ °C/6 hours/water +	$T_p = 620$ °C/8 hours/Air
sample L4 : $T_A = 910$ °C/6 hours/water +	$T_p = 620$ °C/8 hours/Air
sample L5 : $T_A = 920$ °C/6 hours/water +	$T_p = 620$ °C/8 hours/Air
sample L6 : $T_A = 930$ °C/6 hours/water +	$T_p = 620$ °C/8 hours/Air
sample L7 : $T_A = 940$ °C/6 hours/water +	$T_p = 620$ °C/8 hours/Air



Picture 1 Forging - (100 x 100 x 150)mm

4. Mechanical Properties of HSLA Steel ASTM A694 F60

The samples to determine attained parameters of mechanical properties and to evaluate the structure were taken from central zones of the forgings. Evaluation of mechanical properties was carried out in longitudinal direction.

Table 2 shows the requested level and attained values of mechanical properties of individual F60 steel samples.

Table 2 Mechanical properties HSLA steel F60 - according temperature of austenitization

	T _A	R _e	R _m	A ₅	Z	KV ₋₄₆ ⁰ C			AVG KV ₋₄₆ ⁰ C
		/MPa/	/MPa/	/%/	/%/	/J/			/J/
Requir.		415 – 565	520 – 760	min. 20	min. 35	ø KV min. 63			ø KV min. 63
L1	880°C	548	639	21,6	76,0	299	300	217	272
L2	890°C	550	653	22,2	75,0	255	229	286	257
L3	900°C	561	653	21,8	75,0	213	217	218	216
L4	910°C	573	667	22,2	75,0	101	214	89	135
L5	920°C	576	662	23,0	76,0	189	137	27	118
L6	930°C	576	672	22,8	74,0	124	204	238	189
L7	940°C	576	671	22,4	75,0	86	153	31	90

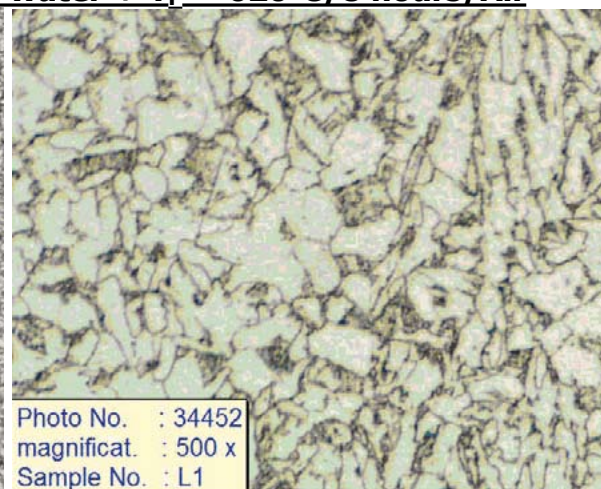
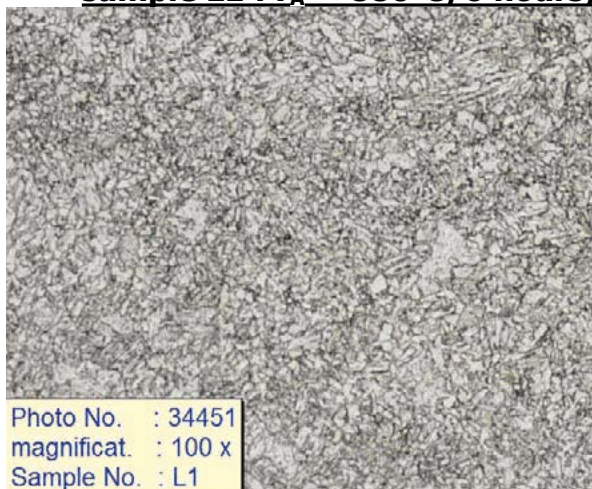
Austenitization temperature influence on change in mechanical properties of forged, quenched and tempered F60 steel is visible from Table 2. It is obvious that steel strength increase accompanied by significant toughness drop takes place as the austenitization temperature is increasing.

5. Microstructure of Samples of HSLA Steel ASTM A694 F60

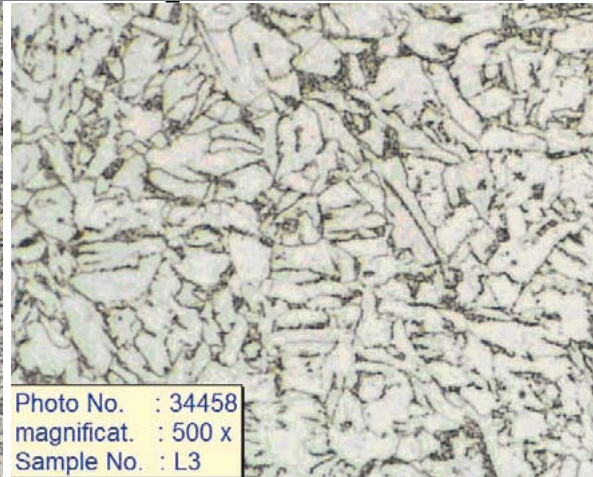
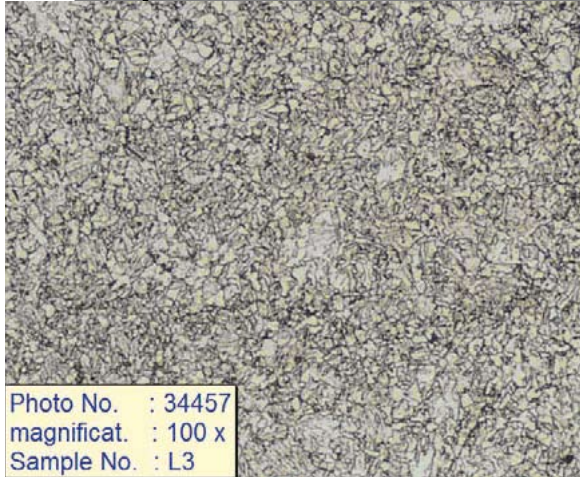
Similarly as in the case of mechanical properties evaluation, steel structure evaluation was carried out in the given point of the sample.

Steel structure for concrete heat treatment states (T_A = 880, 900, 920, 940°C) is shown below:

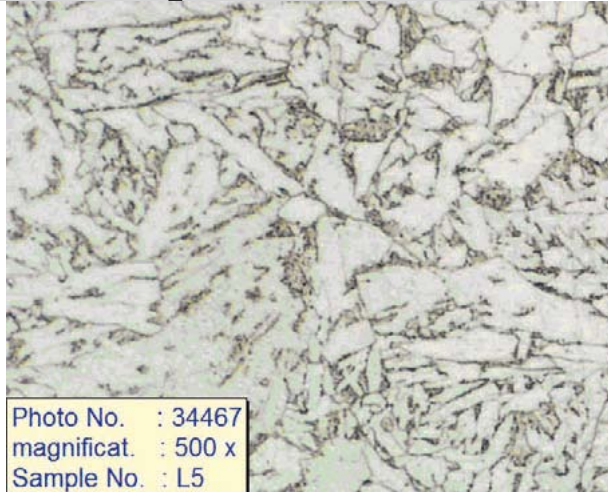
sample L1 : T_A = 880°C/6 hours/water + T_P = 620°C/8 hours/Air



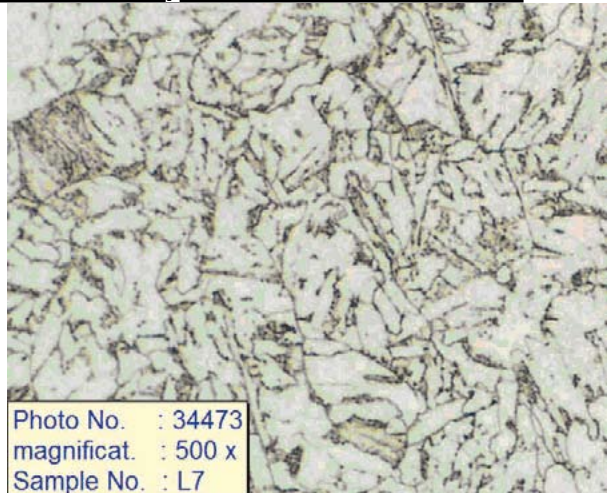
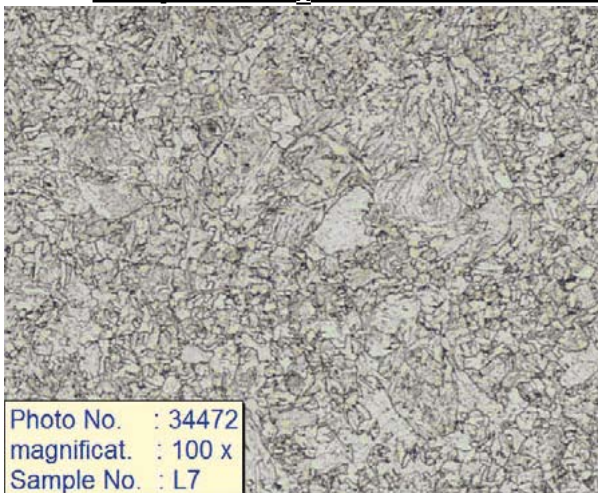
sample L3: $T_A = 900^\circ\text{C}/6 \text{ hours}/\text{water} + T_P = 620^\circ\text{C}/8 \text{ hours}/\text{Air}$



sample L5: $T_A = 920^\circ\text{C}/6 \text{ hours}/\text{water} + T_P = 620^\circ\text{C}/8 \text{ hours}/\text{Air}$



sample L7: $T_A = 940^\circ\text{C}/6 \text{ hours}/\text{water} + T_P = 620^\circ\text{C}/8 \text{ hours}/\text{Air}$



After the quenching and tempering, the microstructure of all samples – forgings is practically the same. **Ferrite, bainite, granular pearlite and sorbite occur.** It is evident from a series of snaps magnified 500 times, where the secondary grain can be compared better, that the secondary grain does not change notably as the quenching temperature is increasing.

Above mentioned fact is confirmed by results of evaluation of austenitic grain size by means oxidation method according to ASTM E 112 – 97 with using the LECO IA32 image analysis. Results of austenitic grain size measurement are shown in Table 3.

Table 3 Austenitic grain size - HSLA steel F60 - ASTM E 112 – LECO IA32

	T_A	Austenitic grain size (μm)
L1	880°C	11,3 ± 0,4
L2	890°C	11,2 ± 0,4
L3	900°C	10,7 ± 0,3
L4	910°C	11,3 ± 0,5
L5	920°C	11,4 ± 0,2
L6	930°C	9,4 ± 0,6
L7	940°C	10,3 ± 0,4

From the results shown in Table 3, it is not possible to observe direct influence of quenching temperature on austenitic grain size change. All the samples show a very fine structure.

6. Conclusions

From results of experimental work attained follows direct influence of quenching temperature on mechanical properties of ASTM A694 F60 steel.

Was observed growth in strength values and drop in impact value as the temperature of quenching was increasing. The most favourable results of mechanical properties were attained with quenching temperatures 880oC, 890oC and 900oC.

Steel microstructure after the quenching and tempering is comparable for all the samples. Ferrite, bainite, granular pearlite and sorbite occur. Evaluation of austenitic grain size by oxidation method according to ASTM E 112-97 confirmed the grain size uniformity, when comparing all experimental samples, without provable influence of quenching temperature.

Further optimization of steel mechanization properties and structure can be awaited after the verification of influence of the tempering temperature. Subsequently, it will be possible to determine a complex optimized heat treatment process for HSLA steel ASTM A694 F60.

The paper has been solved within the EUREKA programme of the OE 08009 E!4092 MICROST project. The project was implemented based on government resources with financial support of the Ministry of Education, Youth and Sport of the Czech Republic

¹ Ing. Martin Balcar, ŽĎAS, a.s., Strojírenská 6, 591 71 Žďár nad Sázavou, Czech Republic, Tel.: +420 566 64 2136, e-mail: martin.balcar@zdas.cz

² Ing. Jaroslav Novák, ŽĎAS, a.s., Strojírenská 6, 591 71 Žďár nad Sázavou, Czech Republic

³ Ing. Libor Sochor, ŽĎAS, a.s., Strojírenská 6, 591 71 Žďár nad Sázavou, Czech Republic

⁴ Ing. Pavel Fila, ŽĎAS, a.s., Strojírenská 6, 591 71 Žďár nad Sázavou, Czech Republic

⁵ Ing. Ludvík Martínek, Ph.D., ŽĎAS, a.s., Strojírenská 6, 591 71 Žďár nad Sázavou, Czech Republic

STRUCTURE AND PROPERTIES OF ULTRA-FINE GRAIN TITANIUM USED FOR SPECIAL APPLICATIONS

Miroslav Greger¹, Ladislav Kander², Václav Mašek³, Petra Kočíšćáková⁴

Abstract

The main goal of the presented paper was to describe deformation behaviour of the titanium during one of the process of ECAP method. Design of experiments rested in extrusion at temperature in range from room temperature up to 280°C. Among used methods for determination of intended aims were tensile tests, small punch tests-test method used for evaluation of material properties flat disc penetrated by puncher, TEM, SEM. Mechanical properties were evaluated using standard tensile tests as well as very potent method - small punch tests.

Keywords: Titanium, structure, properties

1. Introduction

For these reasons commercially pure (CP) titanium, still remains to be a preferred material for dental applications. Development trend in case of this material is oriented on preservation of low value of the modulus of elasticity and on increase of mechanical properties, especially strength. According to the Hall-Petch relation it is possible to increase considerably strength properties of metals by grain refinement. That's why it is appropriate to use for dental implants rather fine-grained Ti instead of coarse-grained Ti. Use of nano-materials concerns numerous fields including medicine. Bulk nano-structural metallic materials are used for dental applications. These are materials with the grain size smaller than approx. 100 to 300 nm. High-purity titanium is used for dental implants. Chemical composition of CP Ti for dental implants must be within the following interval.

2. Structure and properties of titanium

The average grain size of the as-received CP titanium according to ASTM standard is No. 4. Tensile specimens with circular cross section 3 mm in diameter and with a gage length 25 mm were machined with the tensile axis oriented parallel to the final rolling direction. Tensile tests were performed on servohydraulic testing machine MTS 100 kN at constant stroke control movement 0,5 mm/min [1].

The titanium samples were deformed at room temperature with different initial strain rates. Microstructure in initial state is shown in Fig. 1, microstructure in the state after cold rolling is shown in Fig. 2.

True stress-true strain curves in initial state as well as after 6 passes ECAP are shown in Fig.3.

Specimens were sectioned along the gauge and grip parts of the deformed sample. The samples were then polished etched using 10 % HF, 10 % HNO₃ and 80 % H₂O for 20 second. Chemical analysis and mechanical properties (CP) titanium are given in the Table 1-2.

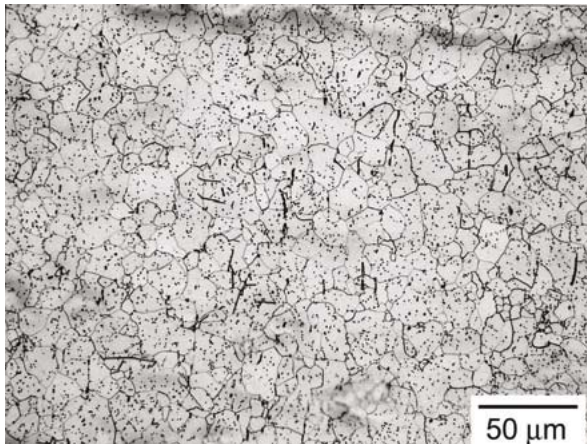


Figure 1 Initial microstructure of titanium

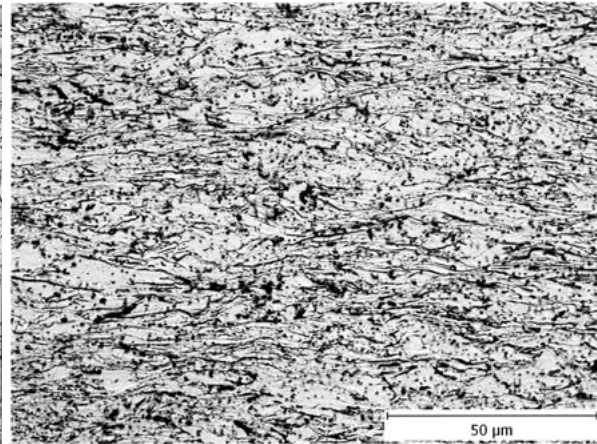


Figure 2 Microstructure of titanium after cold rolling

Table 1 Chemical analysis titanium [wg.%]

N	O	C	Fe	Al	Cr	Ti
0.004	0.068	0.008	0.03	0.01	0.01	Rest.

Table 2 Tensile properties of titanium after annealing :649 C°/1 hour

R _m [MPa]	R _{p0,2} [MPa]	A [%]	Z [%]
375	230	51	71

3. Manufacture of ultra-fine grain titanium

The main objective of experiments was manufacture of ultra-fine grain Titanium, description and optimisation of its properties from the viewpoint of their biocompatibility, resistance to corrosion, strength and other mechanical properties from the viewpoint of its application in dental implants. Chemical purity of semi products for titanium was ensured by technology of melting in vacuum and by zonal remelting. The obtained semi-product was under defined parameters of forming processed by the Equal Channel Angular Pressing (ECAP) technology. The output was ultra-fine grain titanium with strength about 1050 -1100 MPa [2, 3]. The obtained ultra-fine grain titanium will be further processed by technology (of rotation forging) and drawing to the shape suitable for dental implants.

4. Results and discussion

Samples from individual heats were processed by the ECAP. The samples for mechanical tests and for micro-structural analyses were prepared from individual variants of processing. Evaluation of mechanical properties was carried out by

standard tensile test as well as small punch test. On the basis of the results of standard tensile tests (Fig. 3), particularly the obtained strength values, several variants were chosen for more detailed investigation of developments occurring in the structure at application of the ECAP and subsequent drawing after heat treatment [4]. Structure of ultra-fine grain titanium after application of the ECAP process is shown in the Fig. 4. The structure was analysed apart from light microscopy also by the X-ray diffraction.

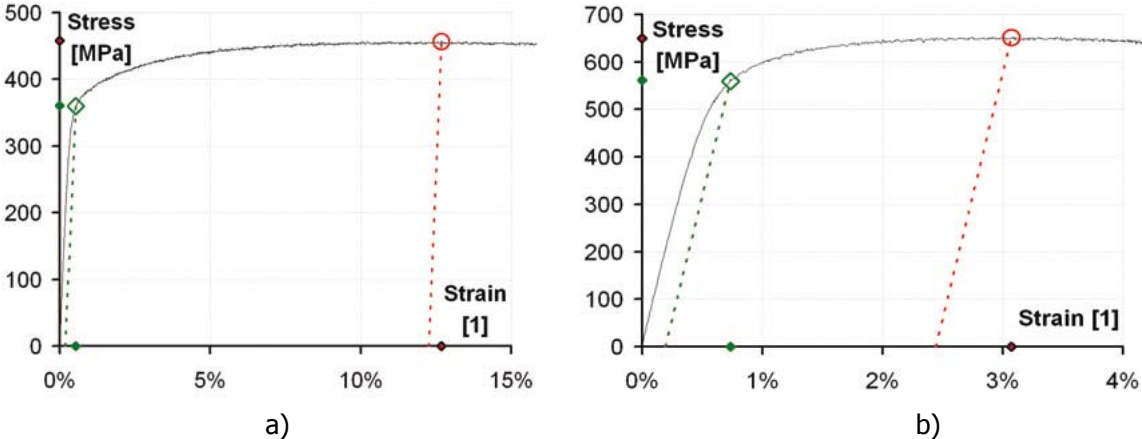


Figure 3 Stress – strain curve titanium: a) initial sample, b) after 6 passes ECAP

From samples after ECAP were also manufactured specimens for small punch tests (8 mm in diameter, 0,5 mm in thickness) to evaluate new correlation between standard tensile tests and small punch tests for titanium. Small punch tests were carried out in Material & Metallurgical Research, Ltd. according to accredited procedure at stroke rate 0,2 mm/min [1]. New correlation was build and verified summarises effect of number of passes on mechanical properties of titanium after passes ECAP from 2 to 9. Results were correlated with tensile test results and are presented in Fig. 5 for tensile strength of titanium. In the Figure 5 is also presented correlations for structural steels (dashed line), that have been developed for last 12 years. From figure is clearly seen, that origin correlation for structural steel can not be used for evaluation of mechanical properties of titanium by small punch test, slope of new developed correlation changed significantly probably due to friction coefficient effect or lattice effect. Work is still continuing to evaluate reason of this effect as well as to get a more results for titanium and Ti alloys.

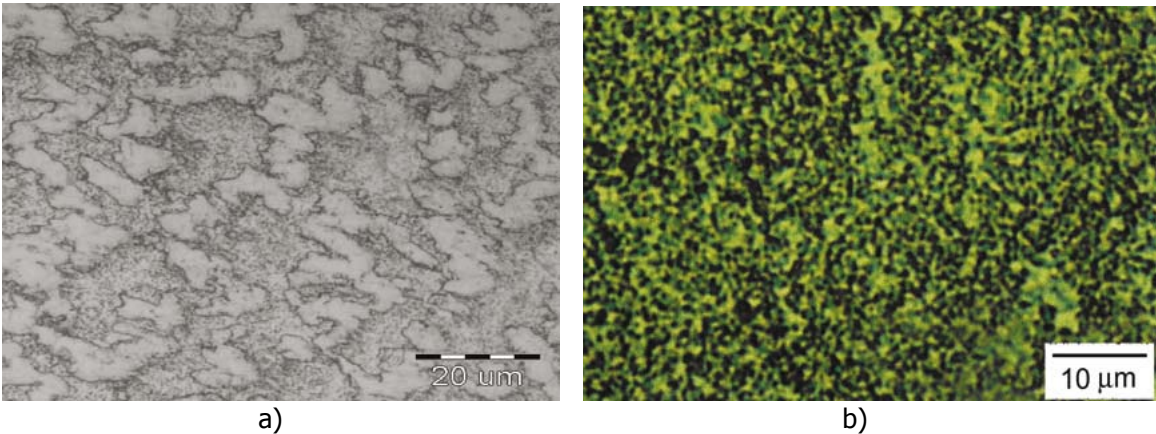


Figure 4 Microstructure of titanium after ECAP: a) 4 passes, b) 12 passes

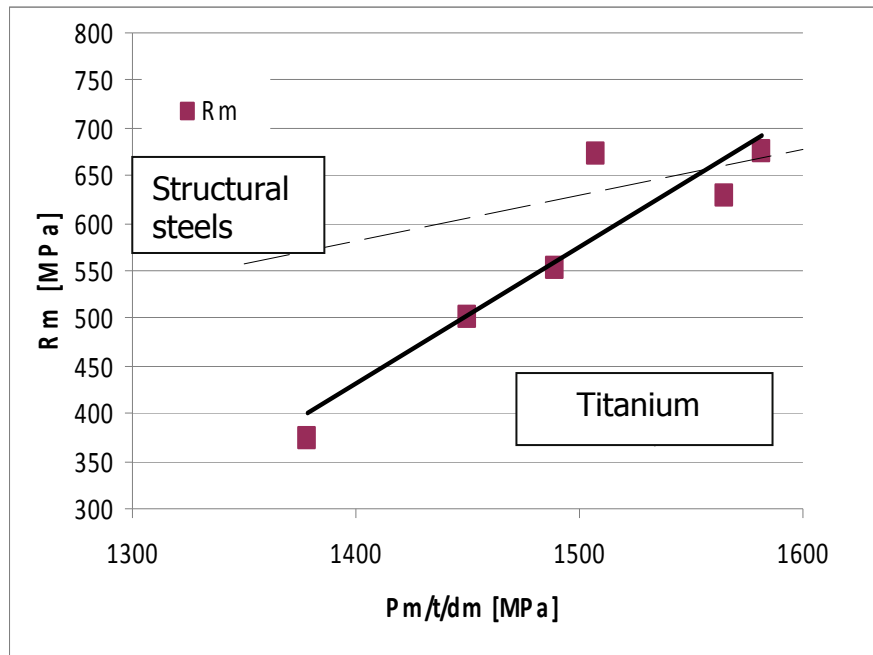


Figure 5 Correlation of tensile strength evaluated by tensile test and small punch test for titanium – comparison with structural steels correlation

4.1 SEM a TEM analyse of fracture surfaces

For detailed investigation of the samples after tensile test SEM JEOL JSM 6490L was used. Details of fracture areas at selected grains size (2 and 8 passes) are shown in Fig. 6. The evolution of damage and final fracture in ultra-fine grains titanium is only beginning to be understood. The absence of substantial macroscopic tensile ductility in ultra-fine grains titanium together with the observation of dimpled rupture on fracture surfaces leads to the hypothesis that deformation is localised. Fracture surfaces resulting from tensile tests have frequently shown dimpled rupture in microcrystalline titanium.

Further, it has been shown that the dimple size is significantly larger than the average grain size; in addition (Fig. 6), a pair of mating fracture surfaces was shown that clearly illustrated the presence of significant stretching of the ligaments between the dimples that was taken to be indicative of appreciable local plasticity. An example of a fracture surface obtained from a tensile specimen of ultra-fine grained titanium with a grain size of around 250 – 300 nm is shown Fig. 6a. It reveals dimpled rupture with the dimple depth (3-4 μm) being an order of magnitude larger than the grain size. Furthermore, the dimple size is uniform and extends across most of the specimen cross-section. When the grain size is reduced to 0,1 μm or less as in the case of titanium after 8 passes ECAP [5].

After 8 passes structure was formed by fine grains. Refinement of the structure was produced by mechanism of recrystallization of deformed matrix. Even after 8 passes grain size was not uniform, in structure was observed fine grains as well as areas with texture. Comparison of substructure of titanium in initial state and after 8 passes can be seen in the Fig. 7,8.

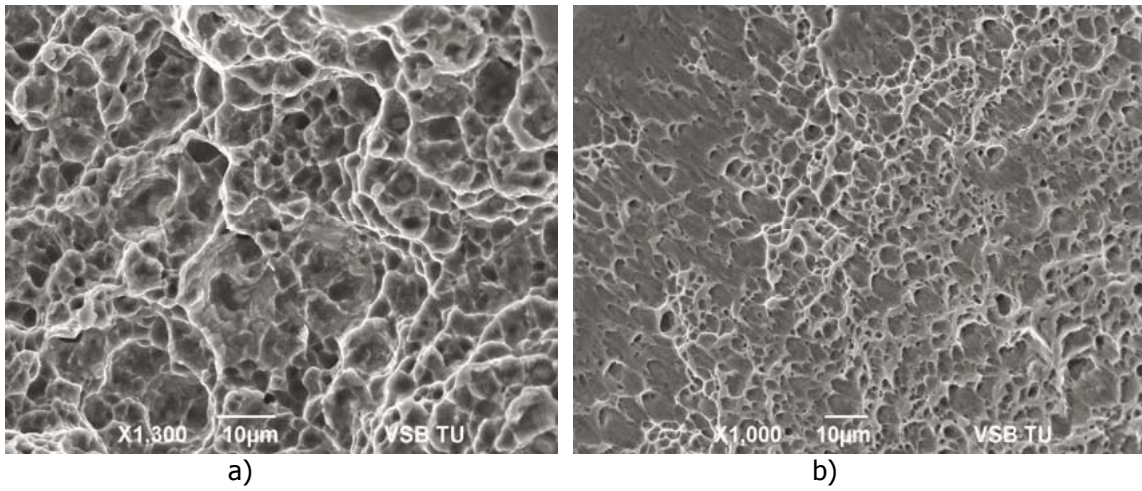


Figure 6 Fracture area of the sample after ECAP: a) 2 passes, b) 8 passes



Figure 7 Substructure of titanium Grade 1 in the initial state (X 10 000)



Figure 8 Substructure of the sample after 8 ECAP passes

5. Conclusions

Technology of manufacture of ultra-fine grain titanium was proposed and experimentally verified. Grain refinement in input materials was obtained using the equal channel angular pressing process. In conformity with the Hall-Petch, relation the strength properties of commercially pure titanium increased significantly as a result of grain refinement. The obtained mechanical properties correspond with the declared requirements. Ultra-fine grain has higher specific strength properties than ordinary titanium. To evaluate mechanical properties of Ti standards tensile tests were carried out as well as very potential method (small punch test) were used. New correlation has been found for titanium that differs significantly from correlation using for steels.

Based on the experimental results can be seen that small punch test method can be used for evaluation of mechanical properties of titanium especially in the case, when small amount of experimental materials is expected.

Further work is necessary to get more data for new developed correlation on titanium and Ti alloys.

Acknowledgements

The authors are grateful to the Grand Agency of the Czech Republic, project No. 106/09/1598 and the Czech Ministry of Education, project No. VS MSM 619 891 0013 and No. VS MSM 258 708 0701.

References

- [1] Kander, L., Mikuláš, D.: Evaluation of mechanical properties of composite coatings using small punch test method. *Hutnické listy*. 2010, vol..63, pp. 110-114.
- [2] Valiev, R. Z., et al.: Nanostructured titanium for biomedical applications: New developments and challenges for commercialization. *Nanotechnologies in Russia*. 2008, vol.3, pp. 593-601.
- [3] Zhu, Y. T., Lowe, T.C., Valiev, R. Z., Stolyarov, V. V., Latysch, V. V., Raab, G. J.: *United States Patent* no. US 6,399,215 B1, (2002).
- [4] Greger, M., Kursá, M., Drápala, J.: Formation of ultra fine grained structure and mechanical properties by ECAP deformation, *Rare Metals*. 2009, vol. 28, no. 1, p. 770-773.
- [5] Greger, M., Kander, L.: Mechanical Properties of Titanium after Severe Plastic Deformation, *Hutnické listy*. 2009, vol. 62, no. 4, p 50- 55.

¹ Doc.Ing. Miroslav Greger, CSc., VŠB -Technical University Ostrava, 17. listopadu 15, 708 33 Ostrava-Poruba, Czech Republic. Tel.: +420 596 994 434, e-mail: miroslav.greger@vsb.cz

² Ing.Ladislav Kander, Ph.D., Material & Metallurgical Research Ltd, Pohraniční 31, 706 02 Ostrava-Vítkovice, Czech Republic. Tel.: +420 724 513 089, e-mail: ladislav.kander@mmvyzkum.cz

³ Ing. Václav Mašek, ŠKODA TRANSPORTION a.s. Tylova 57, 301 28 Plzeň, Czech Republic. Tel.: +420 605518 129, e-mail: TRADE25@seznam.cz.

⁴ Ing. Petra Kočíšáková, Ph.D., VŠB -Technical University Ostrava, 17. listopadu 15, 708 33 Ostrava-Poruba, Czech Republic. Tel.: +420 596 993 1234 , e-mail: petra.kociscakova@vsb.cz.

STRUCTURAL MATERIALS AND FLUORIDE SALTS FOR HIGH TEMPERATURE APPLICATIONS

Pavel Hosnedl¹, Zbyšek Nový², Pavel Konopík³, Jan Džugan⁴, Filip Tikal⁵

Abstract

There has been a special Ni base alloy MONICR for high temperature applications in fluoride salt environments developed in the framework of the complex R&D program for the Molten Salt Reactor (MSR) – SPHINX concept development in the Czech Republic. Selected results of MONICR alloy tests and results of semi products fabrication from this alloy are discussed in the paper. The results of the structural materials tests are applied on semi-products and for the design of the testing devices as the autoclave in loop arrangement for high temperature fluoride salts applications.

Keywords: structural material, fluoride salts, tests

1. Introduction

The direction of material research within national consortium SPHINX project [1] is oriented to several basic segments – research-development work on experimental heats of the new MONICR type range, tests of properties of the MONICR range construction material and third, development and implementation of experimental equipment [1,2,3].

The MONICR-range material is nickel-based alloy developed in SKODA JS plc and in Research Centre - COMTES FHT Inc. The major intended specific use of the alloy material is in nuclear power industry and chemical industry for high-temperature applications with fluoride salts.

The alloy has been developed for the vessels of the Transmutor reactor with the primary circuit containing fuel in the form of molten fluoride salts and for the secondary circuit, where as the heat-transfer medium fluoride salt was also chosen. In general the alloy has wider application in nuclear power industry.

In such extremely aggressive environment the alloy shows very high resistance against corrosion, flow consistency and excellent toughness.

2. R&D work on experimental heats

The direction of material research within national consortium SPHINX project [1] is oriented to several basic segments – R&D work on experimental heats of the new MONICR type range, tests of properties of the MONICR range construction material and third, development and implementation of experimental equipment [1,2,3].

The MONICR-range material is nickel-based alloy developed in SKODA JS plc and in Research Centre - COMTES FHT Inc. The major intended specific use of the alloy

material is in nuclear power industry and chemical industry for high-temp. applications with fluoride salts.

The alloy has been developed for the vessels of the Transmutor reactor with the primary circuit containing fuel in the form of molten fluoride salts and for the secondary circuit, where as the heat-transfer medium fluoride salt was also chosen. In general the alloy has wider application in nuclear power industry. In such extremely aggressive environment the alloy shows very high resistance against corrosion, flow consistency and excellent toughness. Within the frame of development work on transmutation technologies two parallel directions of the MONICR material research and development were determined: The first direction focuses on stabilization of the alloy properties within the entire spectrum of semi-products and on further development of the originally developed construction material applying new metallurgy and technological procedures aiming to homogenize the final material microstructure that has essential influence on material properties and may secondary influence material corrosion properties during simulation of Transmutor operating conditions for given values of operating temperature of up to 710°C. The second direction is based on the development results of the basic range of MONICR alloying (A) and on application of state-of-the-art metallurgical, technological, test and evaluation methods. The aim of this development range is to increase the manufacture properties of the original MONICR alloy by combination of new chemical composition variants and by using modern procedures of material property simulation and testing on newly designed specific testing stands. It is commonly known that grain size is one of the most important characteristic features significantly affecting mechanical properties; grain size may fundamentally influence the strength, creep strength, creep rate, fatigue failure, crack initiation, crack growth rate and spread, initiation and rate of corrosion. On the other hand the homogeneous fine-grained structure under consideration shows higher values of low-cycle fatigue life and yield strength. Therefore, in order to achieve such a condition of the required alloy microstructure and properties, thermo-mechanical treatment is used. The treatment above may be applied as one of the ways to modify the structure under development and to improve mechanical properties of the experimental alloy. Nevertheless forming of nickel alloy is very often problematic due to high forming resistance and insufficient knowledge of optimal forming conditions. Therefore detailed investigation of formability is necessary. In order to define precise forming parameters, including heat-up temperature and reduction level, it is necessary to perform detailed formability research.

Numerical simulation of forming enables on-line visualization of conditions at all parts of the semi-product formed. High price of the alloy and very strict requirements for quality and reliability of the material requires simulation of forming technologies and careful analysis of the results. Prior to the numeric simulation the results of formability tests and re-crystallization schemata were also analyzed in order to obtain forming parameter data. On the model alloy samples, used for simulation of forming, creep tests with a number of additional tests were carried out.

On the basis of previous research work, experiments and technology verification we designed a new MONICR (A) type range. With the new MONICR (A) type range the content of exogenous and endogenous inclusions has been minimized and the entire manufacture and treatment of the alloy is subject to the strictest nuclear requirements for construction materials. Compared to the original basic MONICR

alloy, during the development of the new type range most modern approaches were designed and implemented both during basic industry and processing of semi-products. The actual tests and test evaluation are carried out on absolutely unique equipment available only abroad. We cooperate closely with such workstations. Research work results are processed in a research report [1-3].

The program continues in the form of verification experiments aiming to review enhanced application possibilities of the MONICR material (cooperation with national and other foreign institutions). Successful mastering of research and development of the new MONICR-type range shall result in the second phase of licensing of the material.

2.1 Small Punch Tests (SPT)

Newly we included the research program of testing and simulation of MONICR-type range alloy properties by means of the Small Punch Test versus PC Simulation method. Evaluation of material characteristics for the tensile test based on the test on mini-sized samples – Small Punch Test – is carried out in two basic steps.

The first step includes performance a small punch test on a testing load machine at determined parameters and evaluation of results for the purpose of data preparation for FEM simulation.

The second step is concerned with solution of the inverse task by the use of the FEM program of DEFORM – calculation of the tensile diagram of the material examined based on the data measured by the Small Punch Test method.

Based on the first tests we may already state there is good correlation between the tests and PC simulation. Manufacture of small-diameter seamless tubes by means of standard methods seems quite problematic, the attention drawn to mastering of this part is extraordinary and it is the „Small Punch Tests versus PC Simulation“ research that looks very promising due to good correlation. Performance of small punch tests and subsequent simulation is presented in Figures 1 to 6.



**Fig. 1. Detail of a test fixture for a SPT
D=8mm, H=0,5mm**

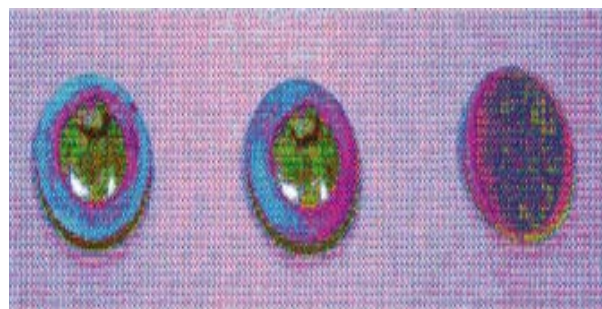


Fig. 2. Test samples for a SPT

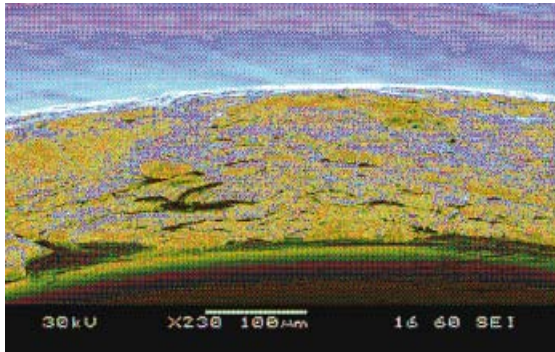


Fig. 3. Fracture edge after the SPT; REM, 230x

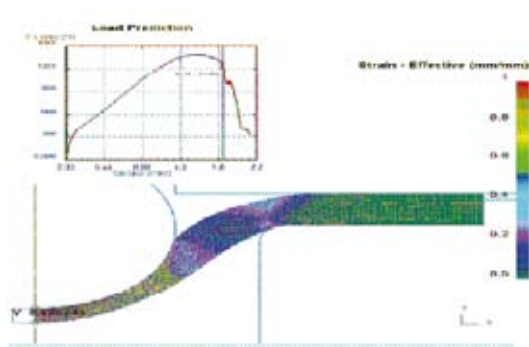


Fig. 4. FEM analysis of the SPT (before occurrence of a crack)

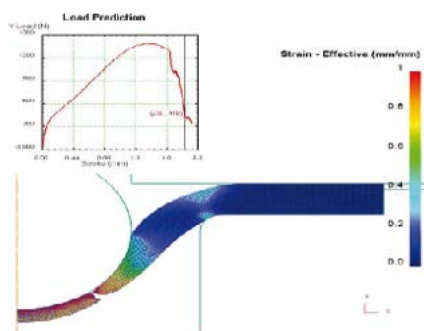


Fig. 5 FEM analysis of the SPT distribution and force

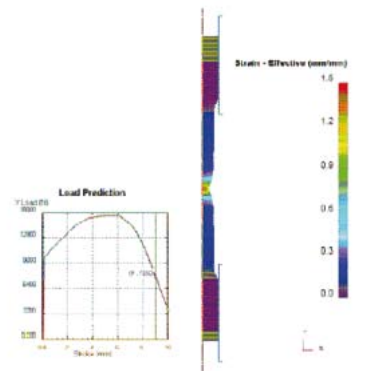


Fig. 6 FEM analysis of the SPT def.

3. Development and Implementation of Experimental Equipment

Results of the research, technology transfer and semi-products treatment technologies were proved during manufacture of experimental equipment of the MONICR alloy, where all technological procedures – starting with forming, cold plate centering, tube extrusion, heat treatment application, etc. up to electron beam welding and welding with additional materials – were verified.

The best proof of direct applicability of the designed and tested procedures of the designed and tested technologies are the products of the MONICR construction material – e.g. an experimental ampoule for corrosion tests and an autoclave of the same material. The manufacture of small-diameter seamless tubes seems

problematic; extreme attention is drawn to mastering of this part – see Small Punch Tests (SPT).

For its own independent research activities in the field of applied non-nuclear experimental verification tests of the new type range of the MONICR construction material has designed, manufactured and complex tested the above mentioned AUTOCLAVE system in a loop arrangement (Figs. 7 to 10).

For the purpose of its safe operation the former chemical and corrosion laboratory was reconstructed. Functionality of all systems has been tested and documented by means of an inspector's report. The following photos are presented

in chronological sequence and at the same time these photos demonstrate the function and assembly of the entire autoclave system including the measurement and evaluation system.

The equipment is in full operation – for instance successful short-term tests at the temperature of LiF-NaF-ZrF₄ fluoride salt of 900°C and a 72-hour trial operation with the same fluoride salt at the temperature of 800°C have been carried out. Due to the limited extent of this chapter other related work has not been included in this entry. The licensing process of the autoclave system in the loop arrangement has been initiated. [4]

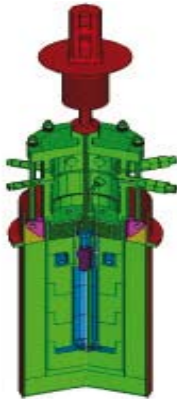


Fig.7 3D autoclave vessel

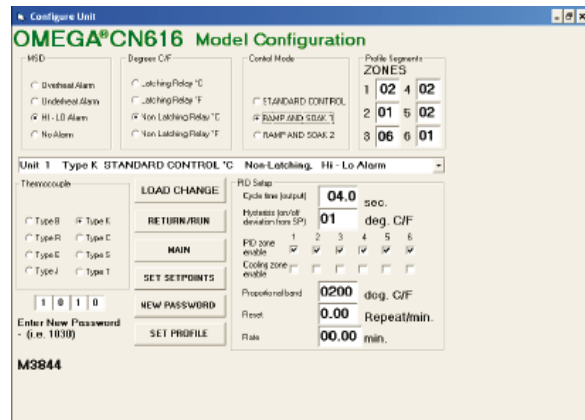


Fig. 8 Control panel of the OMEGA CN616 program



Fig. 9 First version of the AUTOCLAVE System



Fig. 10 Final version of the AUTOCLAVE system in the loop arrangement

4. Corrosion of Materials in Molten Salts and Redox potential

Within the monitoring of MONICR alloy corrosion properties, an independent reference laboratory of the Kurtchatov Institute in Moscow performed corrosion experiments in MONICR alloy ampoules in molten fluoride salts (LiF-NaF). In order to assure corrosion experiment results reproducibility, LiF and NaF were first cleaned

from admixtures. The first cleaning of granulated mixture LiF-NaF was performed at a temperature of 700°C. The second cleaning of molten salt mixture is by vacuum sublimation method and drying in a MONICR alloy ampoule with homogeneous filling of the ampoule with salt mixture. The sketch of equipment for the research of physical-chemical properties of MONICR alloy samples is shown in Fig. 11. The sketch of a chemical reactor for corrosion tests is shown in Fig. 12.

The corrosion characteristics analysis was performed in the scope of above-design temperatures ranging from 720°C to 780°C for the period of 550 hours. Based on the measurements the Kurtchatov Institute experts made the following conclusions:

1. The total loss of salt mixture mass caused by evaporation and condensation of vapours was lower than 1%
2. Geometric shape and sizes of cylindrical samples did not change
3. Change of samples mass after experiments was less than 0.001 g which corresponds to the accuracy of weight analysis
4. Corrosion rate of both annealed and non-annealed samples was less than 4.3×10^{-5} g/day (mean value)
5. Preliminary annealing of samples in vacuum ($p < 10^{-3}$ mmHg) at a temperature of 850°C does not practically have any effect on corrosion rate and the results are within weighing errors
6. After the exposition the colour of samples changes from light silver to grey (dim), which is caused by surface film formation on the sample.

Electric current flow dependence characteristics (volt-amperes curves) in a vessel at a constant rate of electrical potential increase between a working (basic) electrode and a reference electrode are diagrammatised in Fig. 13. Before the beginning of measurements, method sensitivity tests were carried out using a probe holder REDOX potential of salt with a MONICR alloy sample was practically constant for the period of 100 hours, i.e. during the measurements and salt sampling. Its value changed from 1,28 to 1,31 V. It led to the conclusion that the rate of corrosion products accumulation was negligible small and did not have any impact on the change of MONICR alloy corrosion properties. It results from the analysis of experimental values that weight volumes of Ni and Cr in molten salt were lower than 0,001%, which corresponds to sensitivity limit of atom-emission spectrometer with induction-bound plasma. Corresponding to it is that the weight of corrosion products (Ni, Cr and Fe) in molten salt is lower than 0,0005 to 0,001 g. The result corresponds to the corrosion properties measurements.

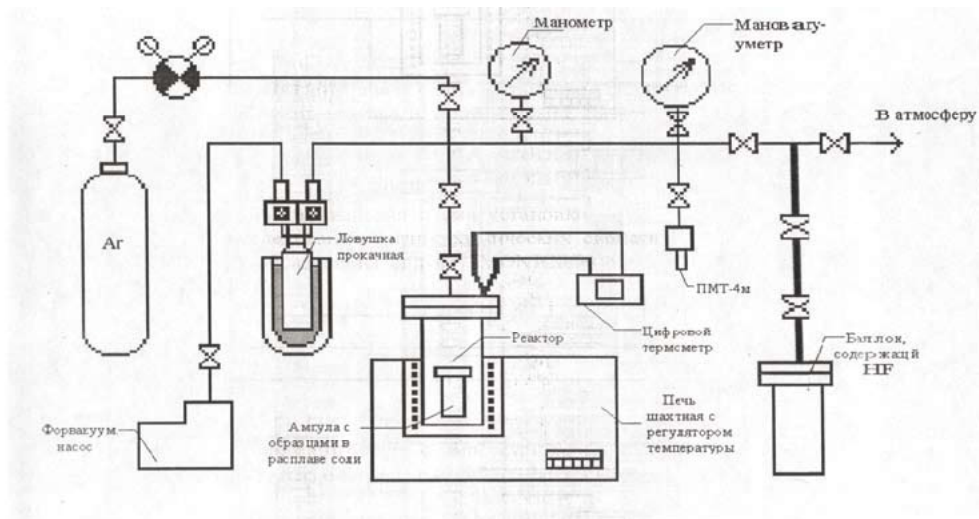


Fig. 11 Kurchatov research equipment for physical – chemical testing of MONICR

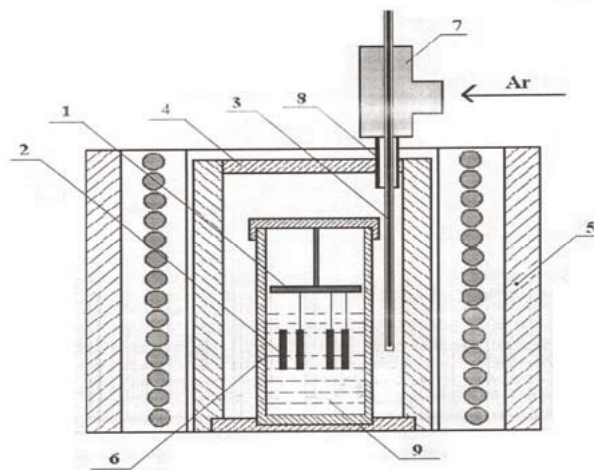


Fig. 12 Chemical reactor for corrosion testing

Specimen	Type of specimen	$R_{p0.2}$, MPa	R_{B7} , MPa	A_{m7} , %	A_{57} , %
5		323	480	32,9	48,9
13	Surveillance spec.	515	902	35,6	38,6
17	Post- corr. tests	478	884	36,5	48,5
18	Post- corr. test	499	894	34,9	44,3

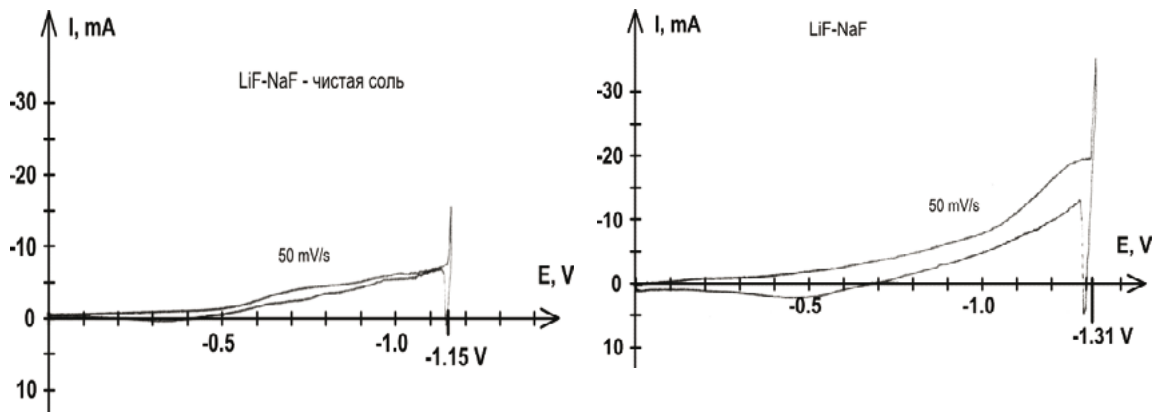


Fig.13 Corrosion testing curves of MONICR with REDOX potential measurement

4.1 Corrosion experiments results:

- a) There is practically no difference between the results from measurements of tensile tests material properties (plastic and strength properties) after corrosion tests (550 hours) and comparative (surveillance) specimens.
- b) The measurement of REDOX potential indicates low corrosion activity of fluoride salt melt and a high degree of salt purity which is substantial for the analysis of MONICR material samples corrosion parameters.
- c) The applied two-stage method of salt purification allows preparing high-purity fluoride salts for the testing of MONICR samples (1000 to 2000 hours) under neutron and γ quanta irradiation in the reactor.
- d) The measurement of REDOX potential with checking of the molten salt purity degree allows checking the corrosion process kinetics.
- e) During the meeting in Moscow where the corrosion experiments results were handed over to us, we were advised by Prof. Prusakov's colleagues and he himself confirmed that the MONICR material corrosion tests results were minimally as good as the results of previously performed Hastelloy N material tests.

Experiments in the Kurtchatov Institute are going on by irradiation experiments in the reactor IR 8 with MONICR material and salt mixture LiF (59,5 mol%)-NaF (40 mol %)-UF₄ (0,5 mol%).

5. Conclusions

The results of the test for determination of recrystallization conditions of the new MONICR type range and their transfer into the manufacture technology of semi products are considered extremely important. Forward-looking the direction of Small Punch Tests and PC simulation applications is considered quite promising. Correctness of the successive steps in the experimental equipment development and trends in further improvement and development of experimental equipment have been verified by means of real-life tests of the autoclave.

The MONICR type range and the autoclave system in the loop arrangement are subject to a licensing procedure. The experimental studies on corrosion phenomena in metallic materials exposed to fluoride salt melts should continue in the future because there are still many opened questions to be answered before the industrial

application of the candidate materials can be acceptable. Other interesting results have not been included due to the limited extent of the paper.

References

- [1] Hron M., Matal O., Hosnedl P., at all. SPHINX reports, 2006-2009, Prague
- [2] Hosnedl P. R&D Structural material new type of the MONICR SKODA Alloy, Research report, AE 12110/Dok C, Plzen 2006
- [3] Hosnedl P. Development of the experimental devices for the corrosion tests in the fluoride salts, Research report, AE 12112/Dok C, Plzen 2006,
- [4] Prusakov, KI Moscow, Ampoules corrosion experiments of the MONICR alloy in molten fluoride salts
- [5] Hosnedl P., Cabet C., Delpeche M., Koning R., at all....MOST Project – 5FW Programme
- [6] Hosnedl P., Cabet C., Delpeche S., Koning R., Ignatiev at all....ALISIA Project – 6FW Programme EC

¹ Ing. Pavel Hosnedl, COMTES FHT a.s., Průmyslová 955, 334 41 Dobřany, Czech Republic, Tel.: +420 377 197 346, e-mail: pavel.hosnedl@comtesfht.cz

² Dr. Ing. Zbyšek Nový, COMTES FHT a.s., Průmyslová 955, 334 41 Dobřany, Czech Republic, Tel.: +420 377 197 301, e-mail: zbysek.novy@comtesfht.cz

³ Ing. Pavel Konopík, COMTES FHT a.s., Průmyslová 955, 334 41 Dobřany, Czech Republic, Tel.: +420 377 197 352, e-mail: pavel.konopik@comtesfht.cz

⁴ Ing. Jan Džugan, Ph.D., COMTES FHT a.s., Průmyslová 955, 334 41 Dobřany, Czech Republic, Tel.: +420 377 197 350, e-mail: jan.dzugan@comtesfht.cz

⁵ Ing. Filip Tikal, Ph.D., COMTES FHT a.s., Průmyslová 955, 334 41 Dobřany, Czech Republic, Tel.: +420 377 197 323, e-mail: filip.tikal@comtesfht.cz

OPEN-DIE FORGING OF DUPLEX STEELS

Petr Martínek¹, Pavel Podaný², Ivana Poláková³

Abstract

This paper covers the production of and problems related to open die forging of nitrogen-alloyed duplex steels. The first part of the study is devoted to numerical simulation of ingot forging and to the measurement of strength values. The second part describes a metallographic analysis of the cast state of duplex steels and the influence of the cooling rate on precipitation of secondary phases after open die forging.

Keywords: Duplex stainless steels, sigma phase, delta ferrite

1. Introduction

The history of duplex or two-phase austenite-ferrite stainless steels is almost as long as that of stainless steels but the interest of the industry in this group of steels has been increasing recently [1]. This mainly applies to applications where austenitic steels do not provide a guarantee of fault-free and safe operation, particularly in environments where stress-corrosion cracking may occur. The ferrite/austenite ratio is mainly governed by the content of ferrite formers and ranges from 30 to 50 %. It also depends on heat treatment. Austenite-ferrite steels normally contain 0.02 % C and 0.25 % N and various levels of Cr, Ni and Mo but there are a number of variants of these steels with different alloying element levels [2]. Duplex stainless steels are used in numerous applications in chemical, petrochemical, paper and power industry thanks to their attractive combination of good mechanical properties and high corrosion resistance. Their resistance to uniform corrosion is similar to that of austenitic steels. However, the strength is much higher, in part due to about 0.15% nitrogen addition. Austenite-ferrite steels have good resistance to stress-corrosion cracking in environments containing higher concentration of chlorides. However, problems occur in environments where atomic hydrogen forms [2].

Treatment involving high temperatures, such as forging, extrusion or rolling is critical for duplex steels due to formation of precipitates of deleterious phases - namely the sigma phase [3]. Sigma phase is one of very common intermediate phases, being hard brittle, non-magnetic and stable. Precipitation of the sigma phase in steel increases the brittleness, hardness, ultimate and yield strengths whereas the elongation and reduction of area in ambient temperature tensile test decrease – with growing proportion of sigma phase. Changes in mechanical properties can be detected even if the precipitation of the sigma phase cannot yet be confirmed by metallographic or X-ray techniques. Sigma phase precipitates first at points of contact between grains, then at grain interfaces and upon longer time at higher temperatures on non-coherent grain boundaries and inclusions within grains.

2. Compression Test and Numerical Simulation of Forging

Formability of duplex steels at high temperatures depends on the initial microstructure which is characterized by volume fractions of phases, sizes and shapes of grains, chemical composition, strain rate and various strengthening mechanisms in ferrite and austenite.

Most manufacturers recommend the top hot forming temperature to be between 1,100 °C and 1,150 °C. After hot forming, solution annealing followed by rapid cooling should be performed to restore the mechanical properties and corrosion resistance and to dissolve any intermetallic precipitates. For the duplex steel S31803, the experimental material used (tab. 1) the recommended forming temperatures are between 950 and 1,150 °C.

Table 1 Chemical composition of experimental material

Element	C	Mn	Si	P	S	Cr	Ni	Mo	Ti	N
Sample	0.03	1.41	0.28	0.02	0.007	22.30	5.60	3.25	0.005	0.178

Compression test was used to obtain initial data for simulation of forming processes. 3 different strain rates were used: 0.3, 3 a 30 [s^{-1}] between the temperatures of 800 °C and 1,200 °C.

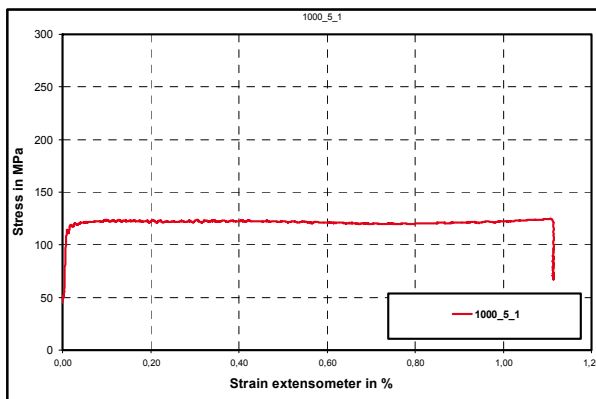


Fig. 1. Results of compression test, strain rate of 0.3 s^{-1} , temperature of 1,000 °C

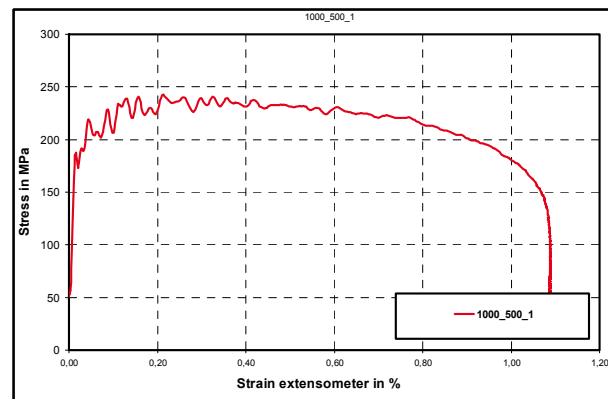


Fig. 2. Results of compression test, strain rate of 30 s^{-1} , temperature of 1,000 °C

The simulation software DEFORM 3D Multiple Operations was used for simulating open die forging of 8K3,4 ingot. The final forging is a \varnothing 370 mm bar. Forging of an ingot consists of several operations:

- Upsetting to reach the \varnothing 820 mm
- Forging into a 600 mm quadrilateral section
- Forging into a 425 mm quadrilateral section
- Forging into a 390 mm octagon section
- Forging to \varnothing 370 mm

Prior to each operation, the ingot was heated in a furnace to the forging temperature of 1,150 °C. Once heated, the ingot was removed from the furnace and transferred to the press for forging. Transport and handling time was about 3 minutes. The amount of reduction was about 20 mm per area (40 mm per dimension). The swages were 380 mm-wide flat blocks. For the last operation, the

flat lower swage was replaced with a wedge-shaped swage with an angle of 110° and an identical width of 380 mm. Swage displacement was the same in all cases: 285 mm, i.e. $\frac{3}{4}$ of the swage width. The workpiece was rotated 90° in each pass and the reductions were identical. The first reduction in each pass was applied on the end by the manipulator jaw.

The purpose of the simulation was to analyse and optimise the manufacturing process with regard to quality of the final product. The computation yields information on the material flow, strain and possible defects forming during the entire process.

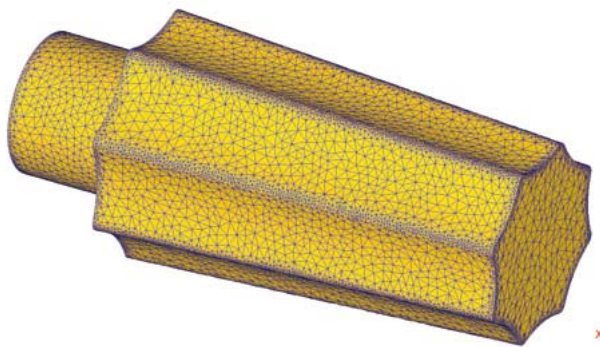


Fig. 3. Model of the ingot 8K3,4

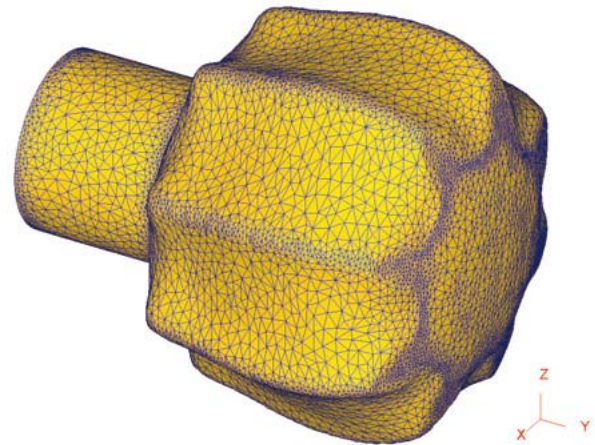


Fig. 4. Forging shape after upsetting

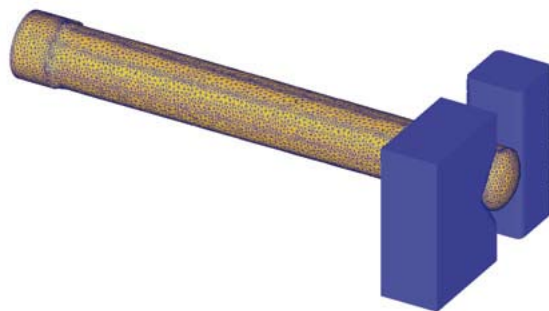


Fig. 5. Shape of the workpiece at the end of forging process

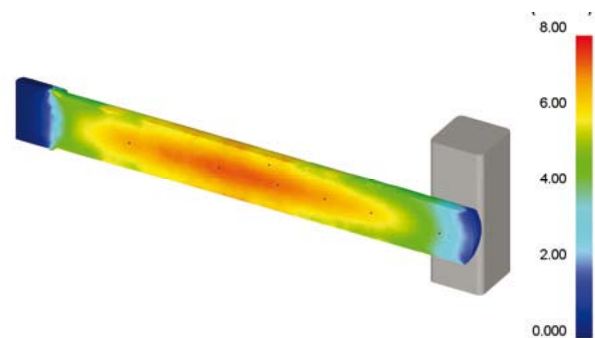


Fig. 6. Strain in the ingot at the end of the forging process

3. Metallographic Examination

Microstructure of specimens was revealed by etching in Beraha II with additional Potassium metabisulfite ($K_2S_2O_5$) and photographed using the light microscope NIKON EPIPHOT 200. Quantitative image analysis of the microstructure was performed using the software NIS Elements 3.1. Detailed observation was carried out in the SEM JOEL JSM 6380 and local chemical composition was measured by EDX method in INCA sight analyser.

The first metallographic observation involved the as-cast state of the ingot. Three specimens were obtained and marked A, B and C according to the following chart (Fig. 7). Area fraction of phases was evaluated first for all three specimens (Fig. 8). There are equal proportions of ferrite (50 %) and austenite (50 %) in the centre of

the ingot. Near the surface of the ingot,

the ratio of phases changes towards less ferrite (45 %) and more austenite (55 %). The difference between the phase ratios near the surface and in the centre of the ingot is close to the measurement error. Despite, a clear trend of phase ratio vs. location in the ingot can be observed. This may be due to different solidification conditions during crystallization.

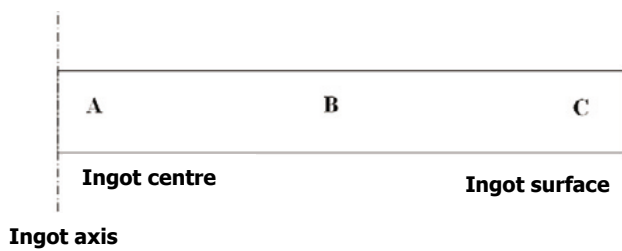


Fig. 7. Schematic of taking samples

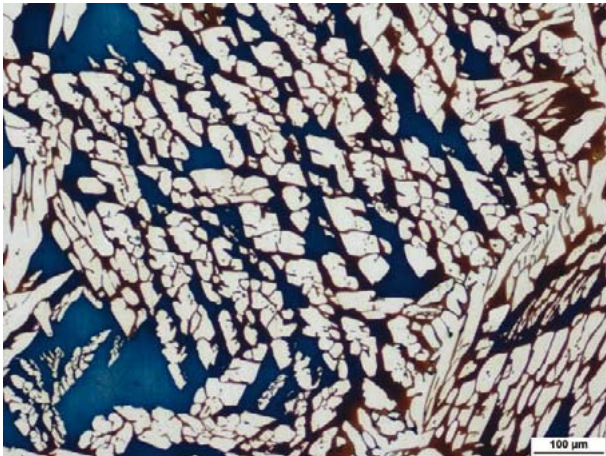


Fig. 8. As-cast state of duplex steel, 100x



Fig. 9. Sigma phase along grain boundaries, 1000x

Microstructure contains particles of secondary phases (Fig. 9) which precipitated non-uniformly. The specimen contains areas where the particles are scarce and other regions where the austenite-ferrite interface is delineated with them (Fig. 10, 11)

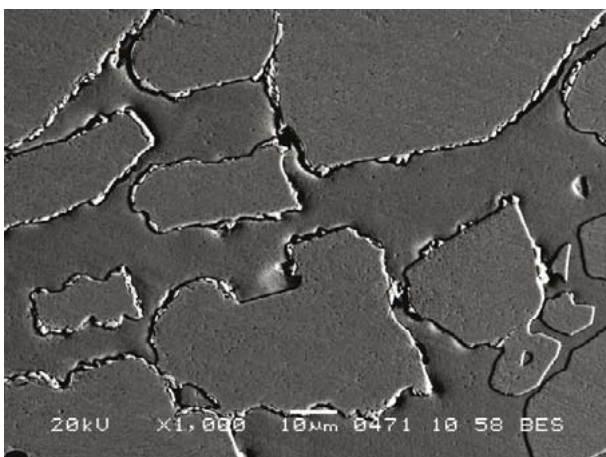


Fig. 10. Sigma phase along grain boundaries, 1000x

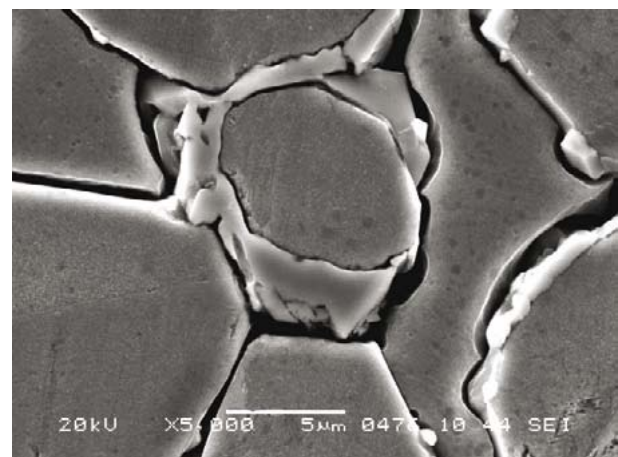


Fig. 11. Sigma phase along grain boundaries, 5000x

After measuring chemical composition by EDX it was found that they are probably the sigma phase. Due to non-uniform distribution of precipitates, attempts to measure their amount and determine their precise distribution throughout the ingot would be probably unsuccessful. However, one can assume there will be greater amount of secondary phases in the middle of the ingot than near its surface. The

amount of precipitated sigma phase is directly proportional to the amount of ferrite (greater proportion in the centre of the ingot). Thermal conditions during solidification are more favourable for precipitation of secondary phases in the centre of the ingot than near the surface.

The influence of cooling after final deformation on precipitation of the sigma phase was explored as well. Marking of specimens and forming conditions are shown in tab. 2.

Table 2 Marking of specimens and forming conditions

Sample	Hold at forming temperature	Forming between 1,200°C and 900°C / cooling
1	10 hours	Water quenching after final deformation
3	10 hours	Air cooling after final deformation
5	7 hours	Water quenching after final deformation
7	7 hours	Air cooling after final deformation

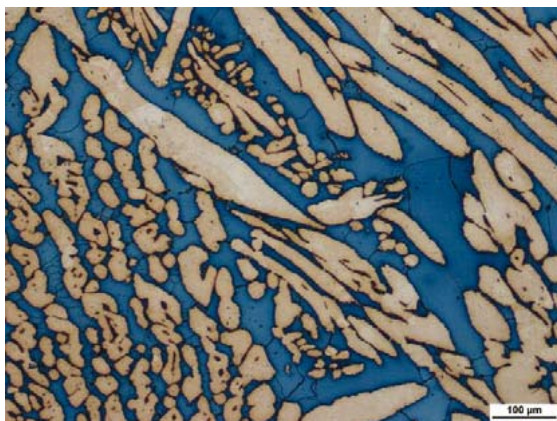


Fig. 12. Specimen 1, 100x

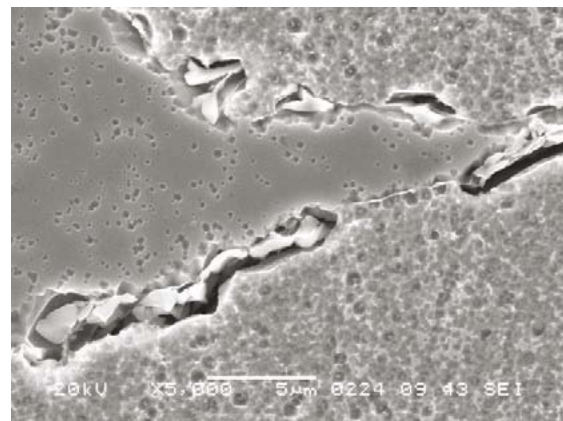


Fig. 13. Specimen 3, 5000x

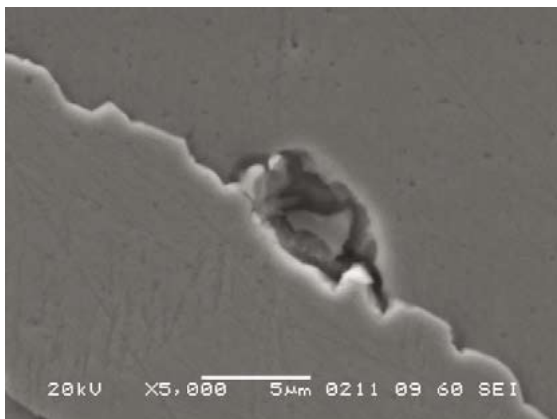


Fig. 14. Specimen 5, 5000x

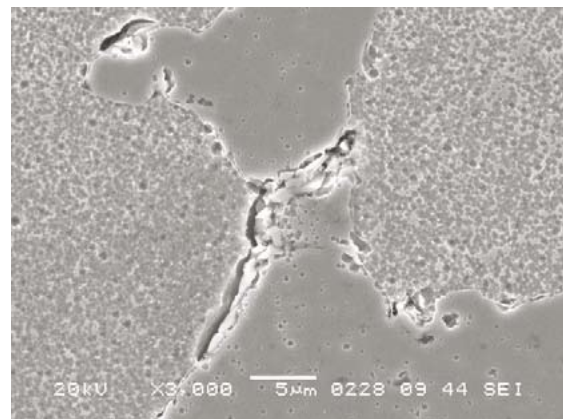


Fig. 15. Specimen 7, 3000x

Material of the specimen 1 became fully homogenized during the 10-hour hold at the forging temperature. All secondary phases dissolved. Water quenching did not allow precipitation of new phases which is why the microstructure contains neither particles nor heterogeneous locations.

Specimen 5 contains small isolated particles on the grain boundaries.

During air cooling from the forging temperature, new phases precipitated in specimens 3 and 7. This is why quantification of sigma phase was attempted.

Specimens were etched in an etchant which reveals the sigma phase and allows thresholding for its identification. Electrolytic etching with 20% sodium hydroxide (NaOH) at 3 V voltage for 10 s was used. The etchant colours the sigma phase orange, whereas ferrite becomes brown and austenite remains light (Fig. 16, 17). Area fraction measurement for the sigma phase was only performed on specimens 3 and 7. In specimen 1, sigma phase was not present. In specimen 5, the amount of sigma phase was too small for the area fraction to be measured.

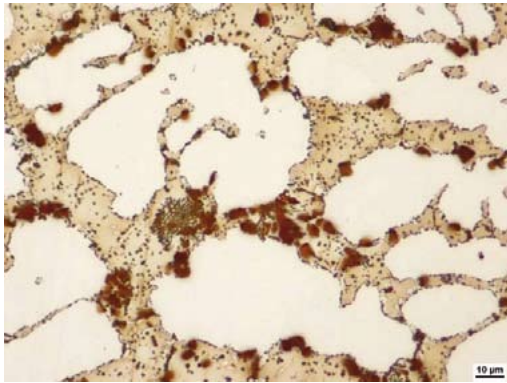


Fig. 16. Specimen 3 - sigma phase, 500x

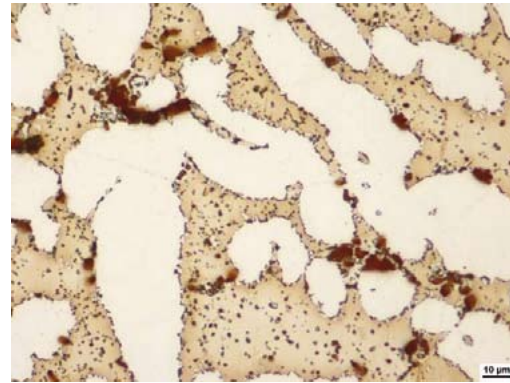


Fig. 17. Specimen 7 - sigma phase, 500x

The area or volume fraction for specimen 3 was 1.8 %. For specimen 7 this was 0.9 %. Precipitation was more intensive in the specimen with longer hold at the forging temperature (10 hours). The amount of sigma phase is greater in specimen 3 than in specimen 7.

4. Conclusions

Tensile testing was carried out to obtain initial data for numerical simulation of open-die forging. The state of the workpiece during forging was simulated on the cross-section along its axis to allow evaluation of temperature, strain and stress. The graphs show changes in temperature and strain at selected points along the axis and at one point 5 mm below the surface for comparison. Information on the material flow can be obtained by tracing positions of the selected points in the entire process.

Metallographic observation revealed that sigma phase is present in the material after ingot casting. After 10-hour hold at the forging temperature and water quenching, the material is homogenized and all secondary phases are dissolved. During air cooling, sigma phase precipitates again. More intensive precipitation takes place in the workpiece upon 10-hour hold at the forging temperature than in that upon 7-hour hold.

References

- [1] M. Liljas, "80 years with duplex steels: a history review and prospects for the future", 6th European Stainless Steel Conference Science and Market, ISBN 91-974131-9-4, Helsinki, Finland, June 10-13.2008.
- [2] M. Sosnová, P. Martínek, P. Podaný, M. Balcar: Special steels alloyed by nitrogen for power and chemical industry
- [3] Euro Inox. Stainless steels. Properties. www.euro-inox.org

¹ Ing. Petr Martínek, COMTES FHT a.s., Průmyslová 955, 334 41 Dobřany, Czech Republic
Tel.: +420 377 197 344, e-mail: petr.martinek@comtesfht.cz

² Ing. Pavel Podaný, COMTES FHT a.s., Průmyslová 955, 334 41 Dobřany, Czech Republic
Tel.: +420 377 197 340, e-mail: pavel.podany@comtesfht.cz

³ Ing. Ivana Poláková, COMTES FHT a.s., Průmyslová 955, 334 41 Dobřany, Czech Republic
Tel.: +420 377 197 321, e-mail: ivana.polakova@comtesfht.cz

RECRYSTALLIZATION OF NICKEL SUPERALLOYS

Zbyšek Nový¹, Petr Motyčka², Pavel Podaný³, Jaromír Dlouhý⁴

Abstract

The paper deals with monitoring conditions of recrystallization in MoNiCr nickel superalloy. The alloy is determined for modern conceptions of nuclear reactors in which molten fluoride salts are used in the primary and/or secondary circuit as coolants. It represents a material alternative with high corrosion resistance in the area of fluoride salts and it has very good creep properties in the temperature range of 650 – 750 °C as well.

The manufacture of vessels and fittings from MoNiCr alloy requires managing the technology of forming of this high-alloyed material. The key moment seems to be forming of cast state of the material to the state of cast recrystallized microstructure with a homogenous fine grain. A kind of stress condition is besides temperature very important at hot forming. Nickel alloys are able to accept a significantly higher deformation level if compression stress prevails. Forming with compression state of stress increases probability that material will without failure reach such a level of deformation which causes recovery and recrystallization processes. Preceding cold deformation essentially accelerates the recrystallization process of a deformed cast structure.

Keywords: Nickel alloys, recrystallization, thermo-mechanical treatment

1. Introduction

Current nuclear power engineering is mostly represented by light-water nuclear reactor which use low-enriched uranium in the form of uranium dioxide as their fuel. However the current use of a uranium raw material is low, in most cases it ranges between 3 and 5%. The limited number of reactors use mixed uranium-plutonium fuel which increases the primary use of the uranium raw material.

The research of fourth type reactors system deals with the way how to prevent from non-economical uranium exhaustion.

- Improving nuclear reactors safety
- Increase in nuclear reactors energy efficiency
- Closure of nuclear reactors fuel cycle
- Partial changeover to thorium-uranium fuel cycle
- Reducing spent fuel radioactivity level
- Disposal with spent fuel

Increase in nuclear power plants energy efficiency is possible by increasing the output coolant temperature in the reactor. It can be reached if a different coolant from water is used. Sodium, lead, gases, supercritical water and other media are under consideration.

One of the conceptions for the fourth generation reactors is a molten salt reactor where molten fluoride salts medium is considered in the primary and also in the secondary circuit.

Main advantages of this reactor type is high efficiency, high level of nuclear fuel use, low radioactivity of spent fuel, usability of thorium-uranium cycle. The main disadvantage is the complexity of economy with fluoride salts and the fact that at present there is not available any suitable material for vessels and fittings in which molten fluoride salts will flow at temperatures 700°C-800° C. These materials must have extreme corrosive and creep resistance. It is nevertheless necessary to make moulded plates and pipes which must be bent and hermetically joined together – they must be welded to the shape of final fittings. Forming of semifinished products from cast ingot is one of the technologically most complicated operations during vessels and fittings manufacture.

At present the most probable alternative for materials of fittings with fluoride salts seems to be superalloys on the nickel base. Experimental programmes use pure nickel, alloys of Hastelloy, Inconel types and others. Another technically actual option is the use of a material on the carbon base – graphite or carbon composites.

For many years COMTES FHT a.s. company has been participating in research consortia that deal with the research of reactors in which the use of molten fluoride salts as medium for the primary or secondary circuit (or circuits) is considered.

2. Experimental programme

An experimental programme is made on MoNiCr alloy of which chemical composition is stated in the Table 1.

A critical phase of nickel superalloys forming seems to be disruption of ingot cast microstructure and starting recrystallization processes in the cast structure. On that ground in COMTES FHT a.s. there was realized the experimental programme which was focused on recrystallization of cast microstructure of MoNiCr nickel alloy. This alloy was developed in COMTES FHT a.s. company for manufacture of experimental loops. The experimental programme can be divided into four stages:

1. Measurement and evaluation of strain deformation characteristics of MoNiCr alloy in the area of forming temperatures.
2. Evaluation of strain-deformation characteristics with preceding hot deformation with alternating sense of strain.
3. Evaluation of the influence of hot deformation parameters on the behaviour of recrystallization processes.
4. Evaluation of the influence of cold deformation parameters on the behaviour of recrystallization processes.

Table 1 Chemical composition of the Ni superalloy written in this paper.

Element	Ni	Cr	Mo	Ti	Fe	Mn	Nb	Al	W
%	base	6,8	15,8	0,03	2,3	0,04	0,01	0,26	0,06

Ad 1/ From cast ingot of MoNiCr alloy specimens represented in Fig. 1 were taken. These specimens were tested on the simulator of heat deformation cycles, Fig. 2. By resistance heating there was heated the body of a specimen to the controlled temperature and consequently loaded fluently by growing tensile force. By this way stress-strain characteristics were gained and evaluated – the deformation in the interval of forming temperatures – from 1000 °C to 1250 °C.

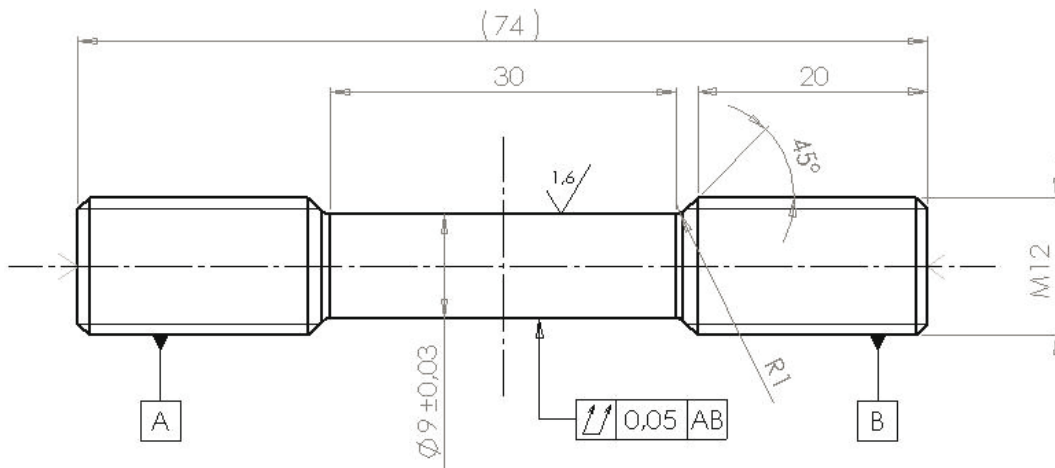


Fig. 1 Shape and dimensions of the specimen for tests and simulations.

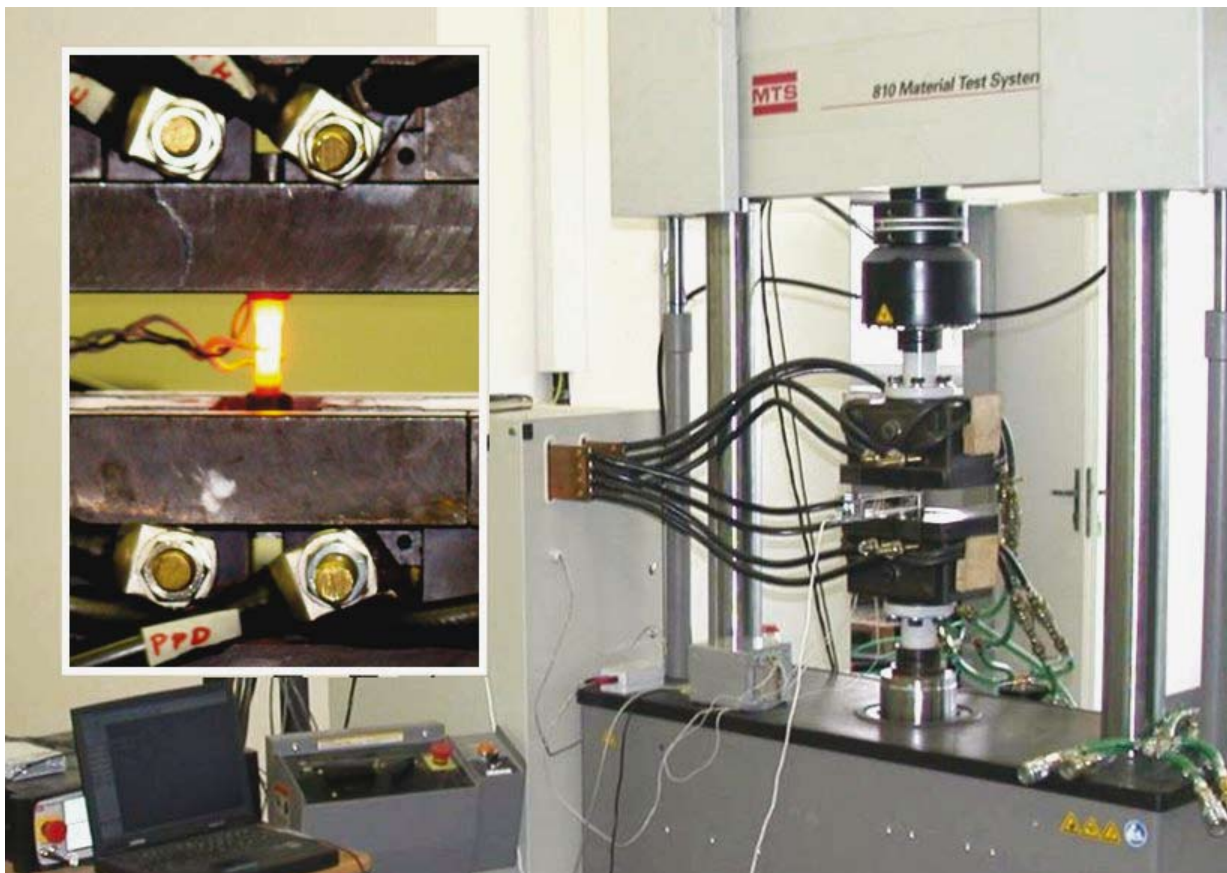


Fig. 2 Servo-hydraulic mechanical testing system MTS complemented by resistance heating was used for mechanical testing and simulation of thermo-mechanical processing of nickel alloy samples.

Ad 2/ Consequently the experiment was repeated when cyclic deformation preceded the tensile test – Fig. 3. The size of each partial tensile and strain deformation was the same. Cyclic deformations were performed at 1200°C in all cases.

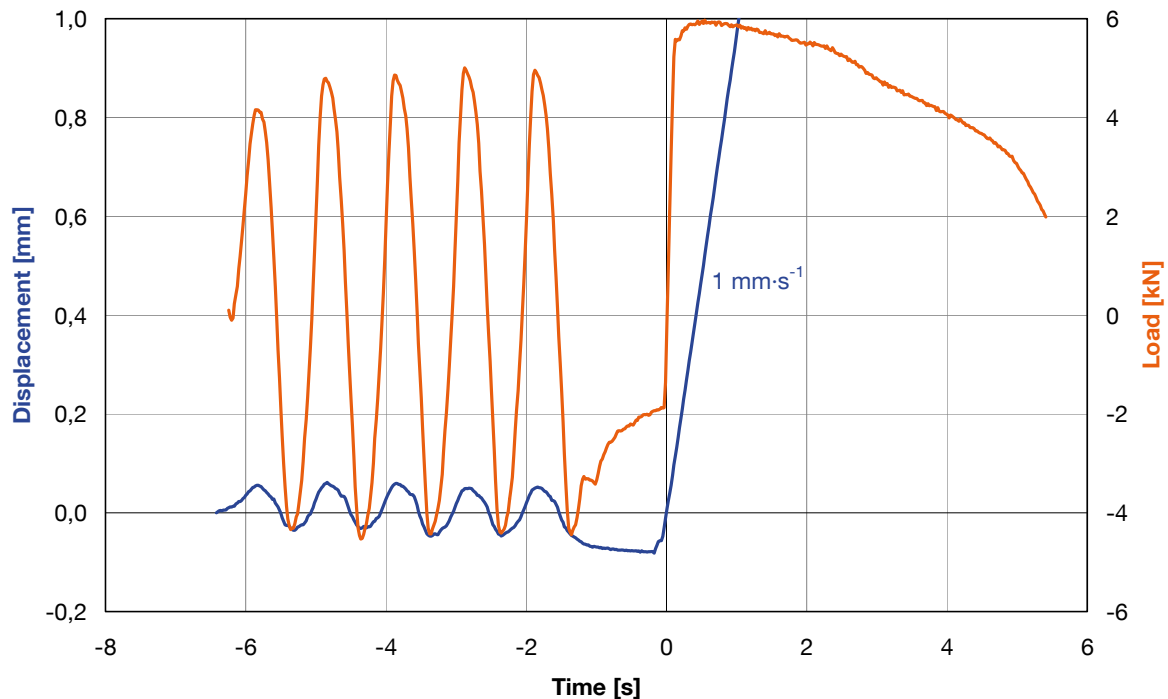


Fig. 3 Example of cyclic heat deformation prior to heat-tensile test (1200°C).

Ad 3/ Specimens in cast state of geometry the same as in Fig. 1 were tested on the simulator by next series of forming. There was in turns applied compression and tensile stress at the temperature of 1200°C, after the deformation there followed cooling on the air. Each partial compressive deformation was bigger than the preceding tensile deformation. Total logarithmic degree of deformation was graduated on single specimens approximately from 0.5 to 2.5. The processing is shown in Fig. 5a. On the specimens a metallographic analysis including quantitative evaluation of recrystallized grain was then done.

Ad 4/ Specimens in the cast state were again treated on the simulator of heat deformation cycles. To the high-temperature forming there preceded a cold deformation which was realized again on the physical simulator. Table 2 shows the overview of performed ways of treatment. On the specimens a metallographic analysis including the evaluation of recrystallized grain was performed.

Table 2 Overview of samples processed by cyclic cold deformation and subsequent cyclic hot deformation.

Size of the embedded deformation		Deformation at 1200°C		
		0.3	0.7	1.1
	0.00	C0-H0.3	C0-H0.3	C0-H0.3

Deformation at room temperature	0.05	C0.05-H0.3	C0.05-H0.7	C0.05-H1.1
	0.25	C0.25-H0.3	C0.25-H0.7	C0.25-H1.1

CD ...cold deformation **HD** ...hot deformation

3. Results

In Fig. 4 there can be seen records of tension curves – deformation made on the specimens from cast MoNiCr material in the temperature range of 1050° – 1250 °C. Ductility up to the breaking limit of Ag is very low at this cast material, it concerns units of percent at all measured temperatures. The maximum strength is very high in comparison to alloyed steels. Material ductility does not grow even at cyclic hot deformation preceded. The material gets damaged earlier than the embedded deformation reaches the value sufficient for massive development of recrystallization.

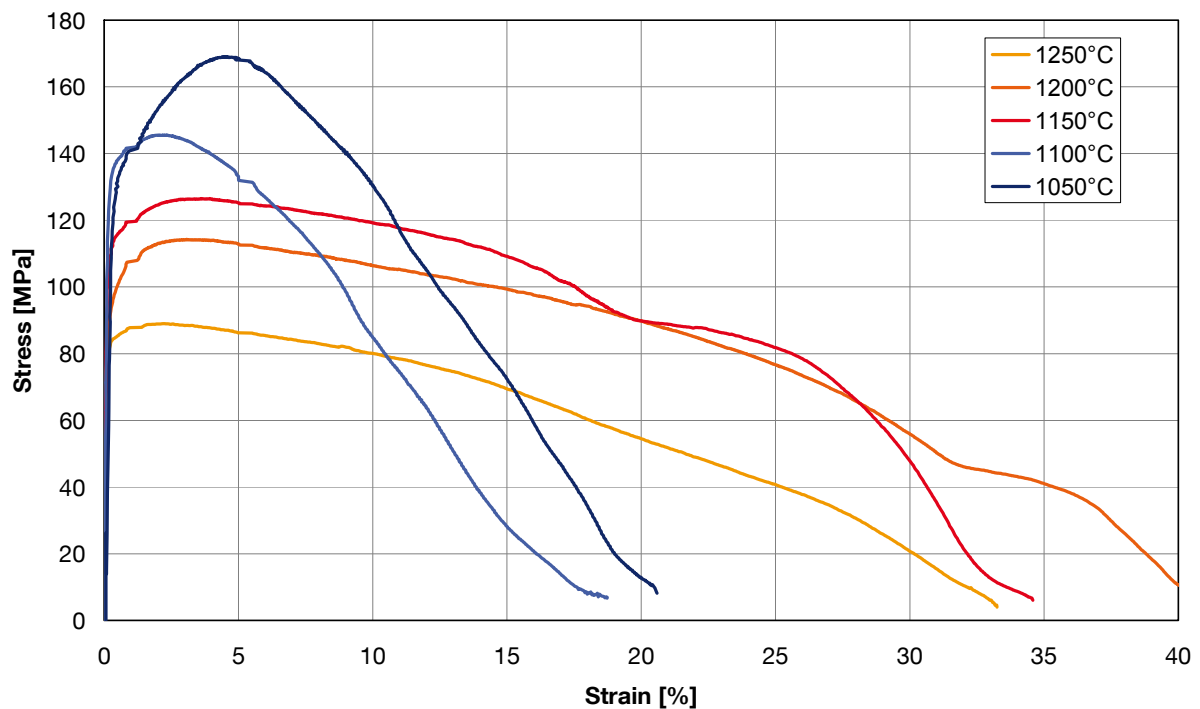


Fig. 4 The results of tensile tests on samples heated by resistance heating.

The prevalence of compression stress during cyclic deformation was more favourable for recrystallization progress.

Fig. 5b – 5f depict treatment of specimens at high forming temperatures and their final microstructure. It is evident that gradual increasing of embedded deformation leads to the increase in recrystallized grain share. The recrystallization extent however grows very slowly, the cast structure is stable. At lower deformation stages recrystallization behaviour is evident only on the borders of casting grains, at higher levels it passes into grains bodies. Neither at the highest level of the embedded deformation recrystallization is homogenous in the whole body of a treated specimen.

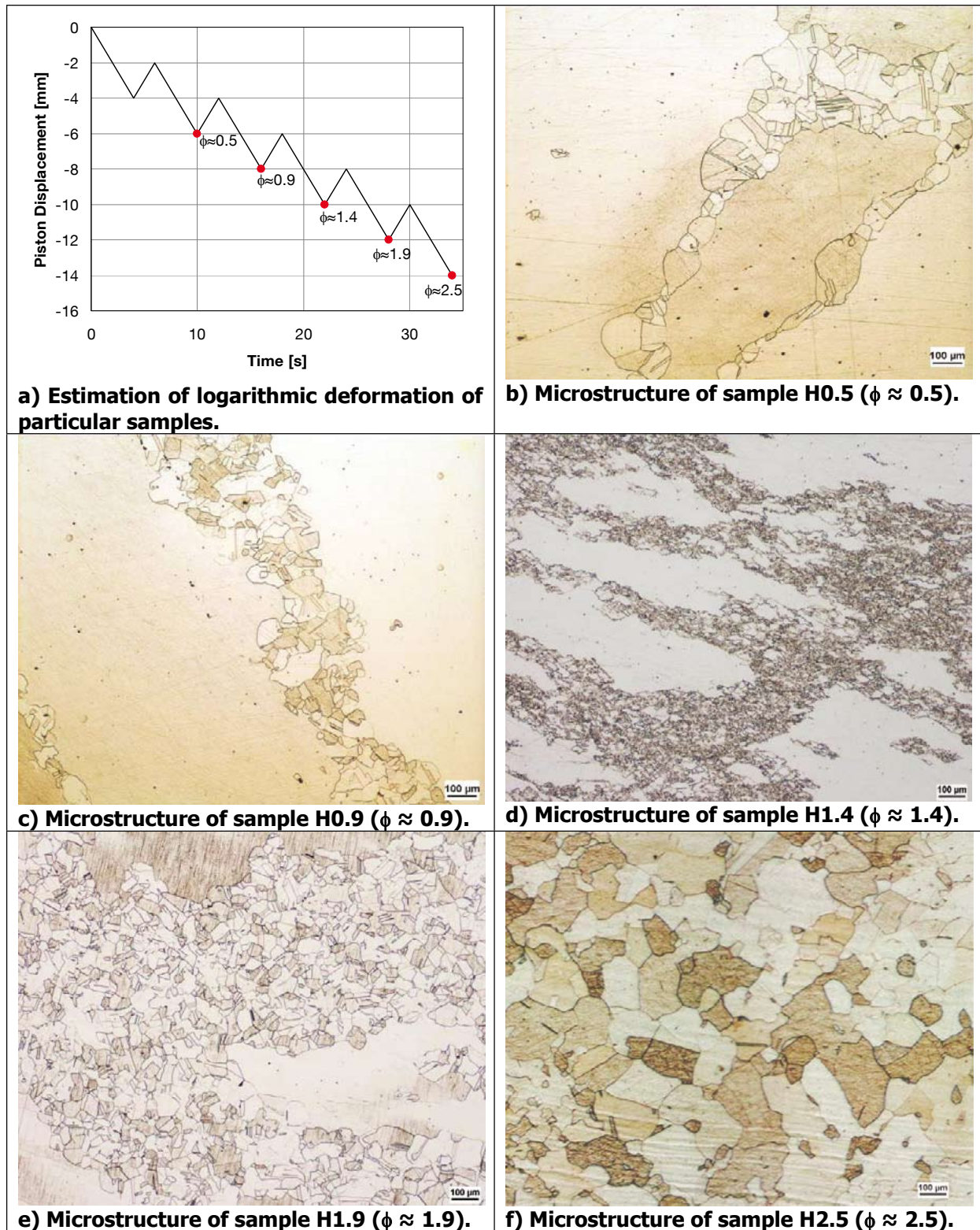


Fig. 5 The processing of samples H0.5, H0.9, H1.4, H1.9, H2.5. Red points at graph a) represents ends of regimes of individual samples. Estimate of the total strain as the sum of the absolute values of the logarithmic deformation computed in accordance with changes in body length of the sample. Uniform deformation on the „effective“ length of 21.5 mm was considered.



Fig. 6 Preferential recrystallization of the Ni superalloy at grain boundaries and surface after cyclic hot forming.

It is evident that besides grain borders recrystallization happens easier also on the specimen surface where it makes a very homogenous belt of fine grains (see Fig. 6). Inhomogeneity is caused partly by the stability of casting structure, partly by uneven distribution of deformation in the treated specimen. Fig. 7 show numerical modelling of graduation of embedded deformation to the specimen. In Fig. 5 there is in a well arranged way demonstrated the process of recrystallization at increasing embedded deformation level. Surface areas of all specimens were evidently recrystallized due to the accumulation of preceding cold deformation owing to specimen body machining.

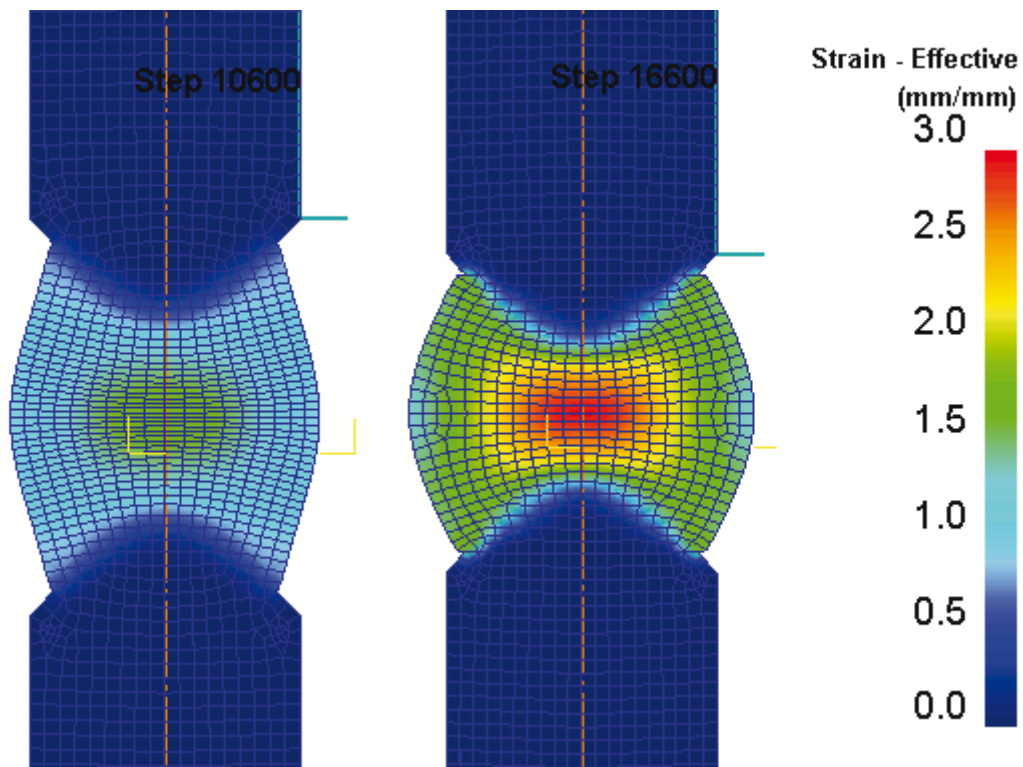


Fig. 7 Distribution of effective strain according to computer simulation (DEFORM) corresponding to phases $\Phi=1.4$ and $\Phi=2.5$ in the Fig. 5a.

Fig. 8 to **Fig. 13** illustrate microstructures of specimens by which the cold deformation preceded hot forming. It was testified that cold deformation significantly supports process of dynamic and postdynamic recrystallization at hot forming. Speeding of the recrystallization process is obvious already at preceding of a relatively small plastic deformation.



Fig. 8 Sample C0-H0.3.



Fig. 9 Sample C0-H1.1.



Fig. 10 Sample C0.05-H0.3.



Fig. 11 Sample C0.05-H1.1.

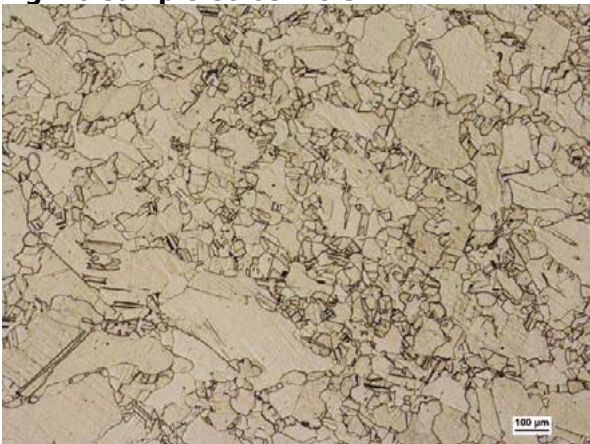


Fig. 12 Sample C0.25-H0.3.

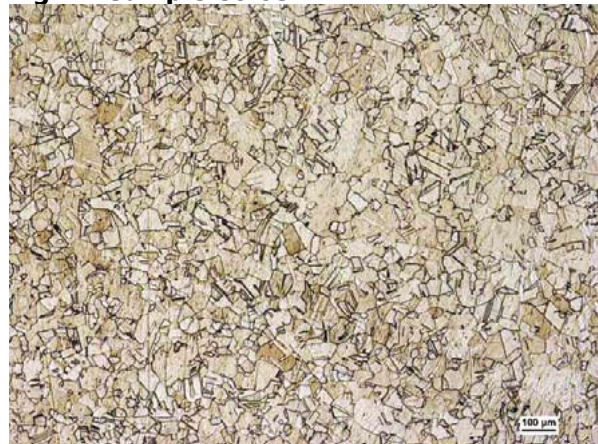


Fig. 13 Sample C0.25-H1.1.

Diagram in Fig. 14 comprehensively represents the influence of size of cold and hot deformation on the share of a recrystallized structure. It is interesting that already cold deformation $\square = 0.05$ essentially influences the behaviour of dynamic and postdynamic recrystallization and final share of the recrystallized structure.

In comparison to the state when the material was not cold deformed, the share of recrystallized structure grew by 20 – 30%. Cold deformation $\Phi_c = 0.25$ enhances the share of recrystallized microstructure by 40 – 50%.

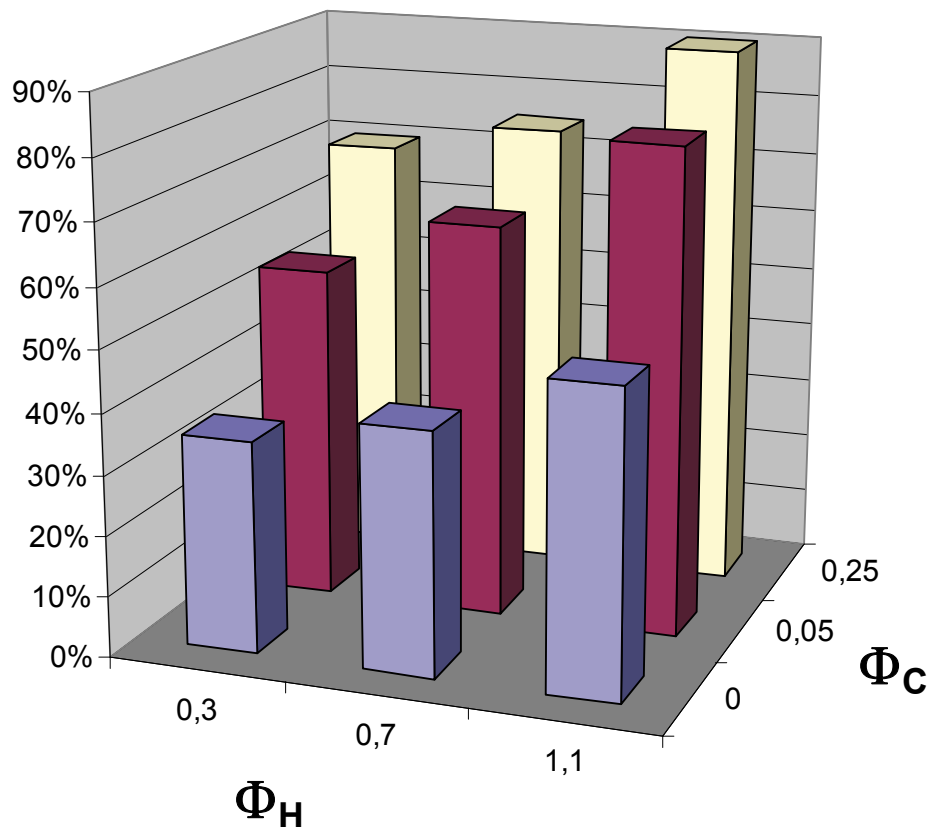


Fig. 14 The share of recrystallized structure dependence on amount of cold (Φ_c) and hot (Φ_H) deformation.

5. Conclusion

The following facts were found out during the research of MoNiCr alloy recrystallization behaviour:

- At hot forming of cast structure the recrystallization process requires a high deformation level for its start-up. The structure has to be deformed approximately by level $\Phi = 2.5$ that the recrystallization occurs in the whole grains volume.
- The start of the recrystallization process is significantly accelerated by preceded cold forming. At cold deformation $\Phi = 0.25$ which was followed by hot deformation $\Phi = 1.1$ the structure was perfectly recrystallized.
- Warm strength of the monitored alloy is very high. Even at 1200°C it significantly exceeds 100 MPa. Ductility to the maximum stress is very low.

After reaching the maximum stress the material is further deformed but first cracks start to arise. When the deformation continues a neck is not formed.

Acknowledgements

The paper was realized due to the support of project "1M06032 Research Centre of Forming Technologies" supported by Ministry of Education, Youth and Sports of Czech Republic

References

- [1] Donachie M. J., Donachie S. J. *Superalloys, A Technical Guide*, The Materials Information Society, Materials Park, OH 44073-0002, 2002, ISBN 0-87170-749-7.
- [2] Tu W. J., Pollock T. M. Deformation and Strain Storage Mechanisms during High-Temperature Compression of a Powder Metallurgy Nickel-Base Superalloy, *Metallurgical and Materials Transactions A*, p. 2002-2009, Vol. 41A, 2010.
- [3] Monajati H., Jahazi M., Yue S., Taheri A. K. Deformation Characteristics of Isothermally Forged UDIMET 720 Nickel-Base Superalloy, *Metallurgical and Materials Transactions A*, p. 895-905, Vol. 36A, 2005.
- [4] Jones R. M. F., Jackman L. A. The Structural Evolution of Superalloy Ingots during Hot Working, *JOM*, p. 27-31, Vol. 51 (1), 1999.

¹ Dr. Ing. Zbyšek Nový, COMTES FHT a.s., Průmyslová 995, 334 41 Dobřany, Czech Republic, Tel.: +420 377 197 301, e-mail: zbysek.novy@comtesfht.cz

² Ing. Petr Motyčka, COMTES FHT a.s., Průmyslová 995, 334 41 Dobřany, Czech Republic, Tel.: +420 377 197 351, e-mail: petr.motycka@comtesfht.cz

³ Ing. Pavel Podaný, COMTES FHT a.s., Průmyslová 995, 334 41 Dobřany, Czech Republic, Tel.: +420 377 197 340, e-mail: pavel.podany@comtesfht.cz

⁴ Ing. Jaromír Dlouhý, COMTES FHT a.s., Průmyslová 995, 334 41 Dobřany, Czech Republic, Tel.: +420 377 197 341, e-mail: jaromir.dlouhy@comtesfht.cz

SELECTED MODERN OPERATIONS AND RESEARCH SUBJECT MATTERS IN MATERIALS FORMING

Kliber J.¹

Abstract

High pressure torsion processing. Forging a steel gear wheel. Viscous pressure forming. Hybrid neural-GA model to predict and minimise flatness value of hot rolled strips. Superplastic properties of Pb-62%Sn eutectic alloy upon equal channel angular pressing. Three dimensional thermo-mechanical simulation of tube forming process in Diescher's mill. Cross wedge rolling. Progress in shell hydroforming. Ring rolling. Fabrication of metal matrix composites by metal injection molding.

Keywords: New forming technologies

HIGH PRESSURE TORSION PROCESSING

Cyclic plastic deformation introduced by forging with a rotating lower anvil leads to materials with grain size between 20 and 200 nm, depending on various factors. This severe plastic deformation process known as High Pressure Torsion (HPT) can be used for forming nanopowders in order to refine their microstructure. Mechanical properties of such products are given by the amount of plastic deformation, i.e. by the total amount of strain [1]. Understanding this relationship and the impact of repetitive deformation is crucial. It is not only the individual deformation cycles but the plasticity limit as well that play a role in this process. Software simulation is used for modelling laboratory or plant processing prior to its actual application. Figure 1. outlines the principles of the HTP process. The workpiece is held and compressed between the upper and lower anvils. The lower anvil rotates, thereby exerting shear forces through friction between its surface and the material. Development of the software model was based on dislocation structures.

$$\tau^r_c = \alpha G b \sqrt{\rho_c} \left(\frac{\dot{\gamma}^r_c}{\dot{\gamma}_0} \right)^{\frac{1}{m}} \quad (1)$$

$$\tau^r_w = \alpha G b \sqrt{\rho_w} \left(\frac{\dot{\gamma}^r_w}{\dot{\gamma}_0} \right)^{\frac{1}{m}} \quad (2)$$

It comprised the classical equation (1) and the equation (2), where $\dot{\gamma}_c^r$ and $\dot{\gamma}_w^r$ denote the shear strain rate in the centre of the cell and near its boundary, respectively, G is the shear modulus of elasticity, b denotes the Burgers vector, $\dot{\gamma}_0$ is

the initial reference shear strain rate, $1/m$ denotes the strain rate coefficient and α is normally 0.25. The above equations are useful for determining the dislocation density and understanding how the hardening of material depends on the imparted strain.

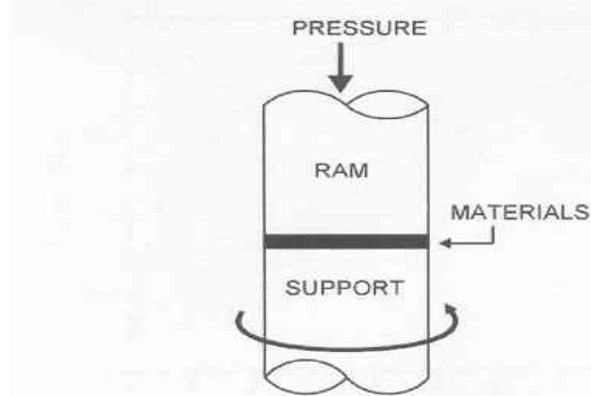


Figure 1 Schematic diagram of high pressure torsion processing [1] [Yoon]

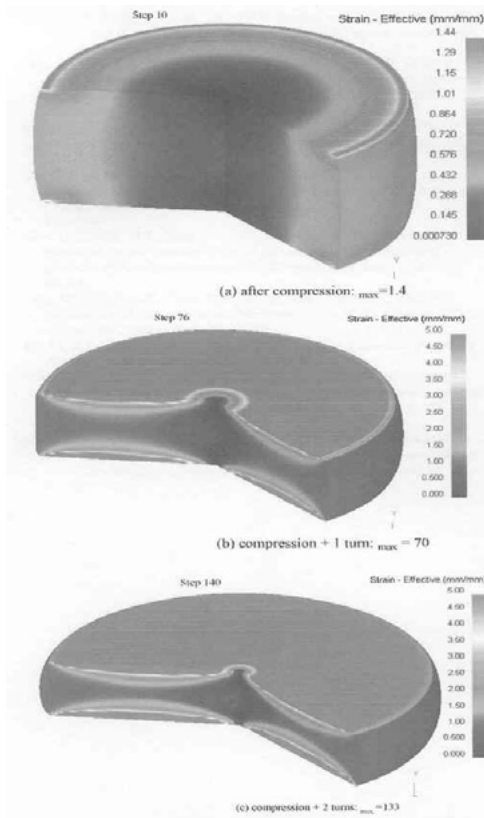


Figure 2 Deformed geometries with effective strain contour after compression [1] [Yoon]

FORGING A STEEL GEAR WHEEL

This is the KOBO method using a rotating and tilting upper anvil [2]. Conventional forming typically requires heating of the workpiece to about 1 100 °C, which is accompanied by grain growth and surface oxidation. This applies to processes with lower forming temperatures as well. (In such case, stresses and forces required for forming are higher.) The KOBO technique was tested at temperatures between 600

The actual simulations were carried out using the DEFORM software. The experimental material was polycrystalline copper. Its hardening equation had the form of a power function up to about 450 MPa (peak strain) at true strain of about 5. Computer simulation was also used to determine the diameter and height of the workpiece, which were 20 and 10 millimetres, respectively. Figure 2. shows its results: section a) is a classical upsetting process, section b) refers to upsetting with a single revolution and section c) displays results of upsetting with two revolutions.

Upon simple upsetting without torsion, the microstructure in the centre of specimen was less distorted than subsurface layers. With increasing number of revolutions, the amount of strain introduced into subsurface layers under the anvil increased. The main finding of this study is that the strain variance in the axial direction is much more pronounced than the strain variance in the radial direction.

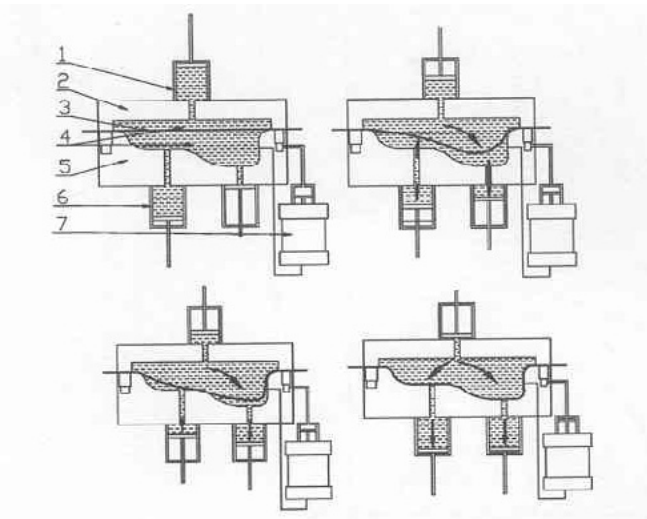
and 950 °C with an actual forged piece of medium-carbon steel (0.45% C). Experimental conditions included a vertical velocity of the anvil of 5 mm/s, the anvil tilt angle of $\pm 4^\circ$ and a frequency of 3 Hz. The total forging time was no more than 15 seconds.

The results suggest that

- comparable values of stress and applied forces can be achieved by the KOBO technique at lower temperatures,
- the technique improves the filling of the die cavity,
- the resulting microstructure and mechanical properties are comparable to those of forgings produced by conventional forging.

VISCOUS PRESSURE FORMING

This technique begins to be used mainly in pressing. Viscous Pressure Forming (VPF) differs from classical pressing in that it uses a semi-solid viscous material as a pressure medium.



The viscous medium can be applied on one or both sides of the sheet in order to improve its formability. The method is intended for processing of high-strength, difficult-to-form materials and for producing 3D features. It was first used in 1992 and developed and improved subsequently. In the process, the viscous medium forces the material to fill the die cavity. A schematic drawing is shown in Figure 3

Figure 3 Schematic diagram of VPF. (1) medium injection cylinder; (2) upper die; (3) blank sheet; (4) viscous medium; (5) die; (6) medium outlet cylinder; (7) blank holder cylinder [4] [Roades]

The technique is typical with very low strain rates of about 10^{-1} to 10^{-4} s⁻¹. The viscous medium exerts both normal pressure and shear stress, which makes the VPF different from conventional pressing, see Figure 4, as shown by a different stress-strain curve.

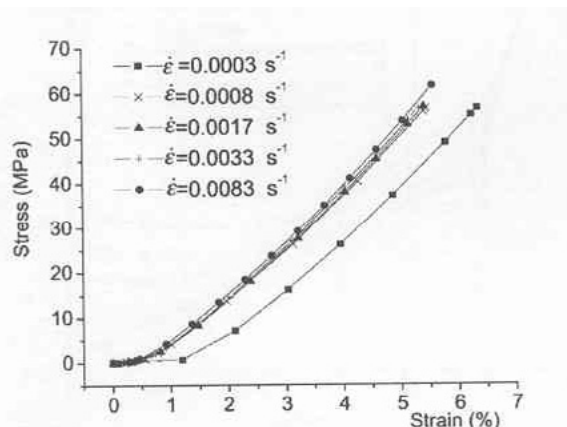


Figure 4 Relationship curves between the stress and strain of the viscous medium

HYBRID NEURAL–GA MODEL TO PREDICT AND MINIMISE FLATNESS VALUE OF HOT ROLLED STRIPS

Solving this problem is extremely difficult, as the resulting flatness of hot-rolled strip depends on a number of both deterministic and random variables [5]. The flatness of the strip is given by changes in its thickness in longitudinal and transverse directions, as expressed by equations (3) and (4) [6].

$$\text{Steepness}(\%) = (H/L) \times 100 \quad (3)$$

$$\text{Flatness index} = (\Delta L/L) \times 10^5 = (\pi H/2L) \times 10^5 \quad (4)$$

The rolling process is rather non-uniform. One could even say that the resulting strip flatness is independent from certain input parameters. Conventional control methods for rolling mills require complex mathematical patterns, which are often difficult to apply on-line. A neural network combined with a genetic algorithm is therefore a novel approach aimed at minimization of flatness indices. The experiment was carried out in the second rolling line of a continuous mill with 6 four-high stands and at the forming temperature between 870 and 900 °C. These stands were equipped with the CVC technology with an axial movement of working rolls of ± 150 mm. The total of 18 variable parameters were used for controlling the process, such as: average flatness, entry thickness at individual stands 1..n, entry and exit temperatures, exit speed, strip width and others.

Neural analysis is rather well known, and therefore only the principles of the genetic algorithm will be explained here. Genetic optimisation analysis is based on the natural selection process. The algorithm is applied to a data set termed population. While the experiment gradually produces a new population, genetic criteria are applied until the optimum result is reached.

The practical effects were tested in a process with the final thickness of 1.82 to 2.22 mm. The hybrid model showed marked improvement in flatness parameters, see equations (1) and (2).

SUPERPLASTIC PROPERTIES OF PB-62%SN EUTECTIC ALLOY UPON EQUAL CHANNEL ANGULAR PRESSING

The group of materials processed by the ECAP techniques is expanding gradually. They range from simple copper alloys to difficult-to-form magnesium alloys [7]. This process takes place at rates of about 10^{-3} s^{-1} . If the input material grain size is about 14 μm , the process involves superplastic deformation. In this experiment, 1, 4, 8 and 16 passes through the angular channel were used at the room temperature. The resulting grain size decreased to 8 μm and the elongation was between 2 000 and 3 000 %. This alloy possesses rather low strength of 5 – 20 MPa. In accordance with the theory, the strain rate has significant impact on its behaviour, see Figure 5a. Additional tests have shown that with the strain rate of 10^{-4} s^{-1} , even higher elongation values can be achieved. Peak stress values have not been changing significantly with increasing number of passes, unlike the strain values, at which peak stress occurs, Figure. 5b.

CROSS WEDGE ROLLING

This new wedge rolling method uses one wedge plate and two shaped rolls. It is termed Wedge-Rolls Rolling (WRR) [9]. As a modern forming method it is used for making stepped shafts, connecting rods and shanks. However, it can be used for shaping billets into non-symmetric formed products as well. Its benefits include high productivity, material utilization good to excellent mechanical properties of products, simple automation and environmentally favourable low energy consumption. There are a number of alternatives of the Cross-Wedge Rolling (CWR) method, shown in Figure 8. The effects of deformation steps within the material were explored in greater detail with the aid of the MCS. Superform 2004 software. One of the results is shown in Figure 9. With increasing angle β , which is the angle of the apex of the wedge, the maximum strain value decreases. Computer simulation allows to optimise the remaining geometric parameters of the wedge as well. This leads to optimisation of the strain introduced and of the final dimensions of the formed piece.

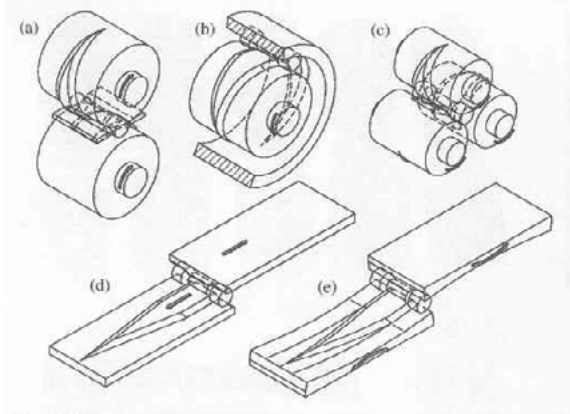


Figure 8 Methods of cross-wedge rolling in configurations: (a) two wedges, (b) wedge concave segment, (c) two flat wedges, (d) two concave wedges [9] [Pater]

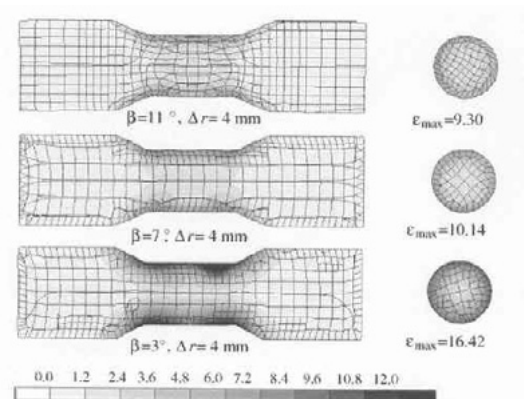


Figure 9 Calculated strains distribution in parts by means of WRR at: $d_0 = 25$ mm. [9] [Pater]

PROGRESS IN SHELL HYDROFORMING

This method has been known for about 20 years but was mostly presented to the public through works of art such as the one in Figure 10 which is a steel football produced by this method [10]. The method is also known as Integral Hydro-Bulge Forming (IHBF). The complexity of its products has been developing: from single-layer to double-layer parts, from conventional pressure levels to high-pressure applications, from spherical to ellipsoid and cylindrical structures and from single-thickness walls to products with variable wall thickness. At present, one of the largest products made by this process is a spherical tank with the radius of 9 400 mm and a thickness of 24 mm. This technique does not require the use of dies. The process is based on forcing a liquid into a product with a predefined shape. The volume of the liquid increases with continuing deformation. Compared to traditional manufacturing of similar products, the hydrobulging method brings advantages in flexibility of production, being suitable for single pieces or large series, in markedly shorter lead-

time, and lower equipment cost. Large plastic deformation reduces residual stresses in the vicinity of welded joints.



Figure 10 Hydrobulged steel football of 4000 mm diameter [10] [Wang Z.R.]

RING ROLLING

Rail wheels have been produced by axial-radial rolling since 1842. Over the time, efforts have been made to develop the technology further. Unlike simple forming processes, which had been modelled on computers, a number of times, the axial-radial rolling (with the main roll, two forming rolls and conical axial rolls) is very complicated to simulate [11]. This process is now being examined by means of virtual reality methods involving dynamic changes in the course of programming, the so-called LS.Dyna, which can capture changes in geometric nonlinearity, material nonlinearity and contact nonlinearity. In essence, this involves finding dynamic equilibrium conditions, whereupon the process diagram can be used for calculating the state at time t and setting parameters for the time $t+1$. ANSYS software has been used for this purpose. One of results of this modelling process is shown in Figure 11. The diameter of the wheel processed by actual rolling is 500 mm.

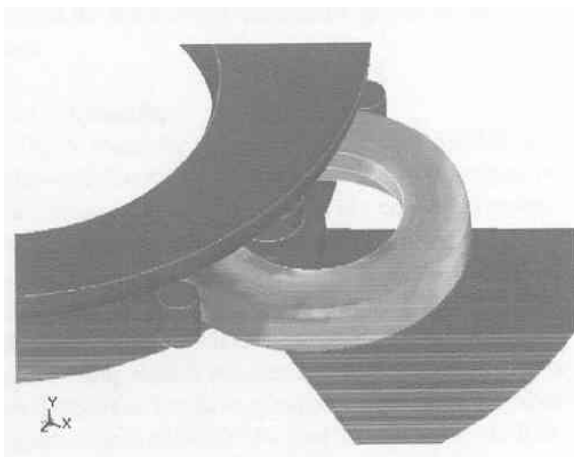


Figure 11 Cut picture of the ring rolls at the final state. [11] [Wang Z.W.]

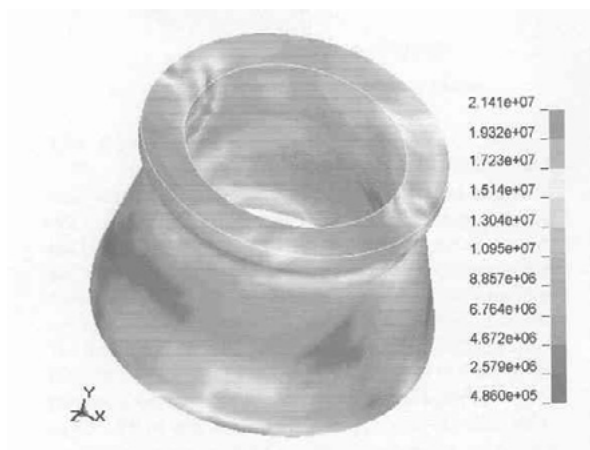


Figure 12 Stress contour of the ring at the final state [11] [Wang Z.W.]

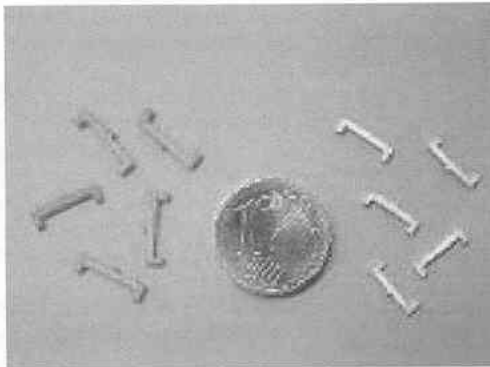
Rolling takes place at the temperature of 1 050 °C. During the 30 s cycle of production, the temperature drops by 50 °C. Simulation of another product (from Ti6Al4V) was conducted with the forming temperature of 950 °C. The stress curve at

finish-rolling has been recorded see Figure 12. Areas with higher stresses also exhibit high strains. This computer-based method allows the manufacturer to prevent various defects in the actual product.

FABRICATION OF METAL MATRIX COMPOSITES BY METAL INJECTION MOLDING

This is a fairly recent technology for manufacturing complex near-net shape products. It has a number of variants focused on making materials with very demanding chemical composition. These include the following: production of tungsten and molybdenum which, thanks to their high temperature resistance, have ever increasing importance for high-temperature applications in electronics, aviation industry, telecommunications, medicine and defence [12].

They also include new tungsten-copper alloys with excellent thermal properties (high microwave absorption capacity). This tungsten alloy with 25% copper is a product of powder metallurgy with 95% theoretical density upon homogenizing. Other alloys of this type include W-Ni-Fe alloys. Titanium receives attention in regard to its compatibility, high chemical stability and excellent properties, which applies to Ti6Al4V and other materials as well. Intermetallic compounds, such as Ni₃Al, have suitable chemical composition for the injection molding process. Metals are processed by the MIM method (Metal Injection Molding). Even steel can be processed by this technique, although conventional forming is much more cost effective. The study



was carried out using the 316L steel with TiC or TiN powders. The resulting composite showed excellent hardness-related properties. Unlike conventionally produced steels, this material can meet requirements for very accurate carbon level. Its relative density is between 90 and 99 % of density of steel. The technique can be used for making bimetallic structures where a metallic substrate is coated with steel or another heavy metal cladding.

Figure 13 MicroMIMed encoder composited by a non-magnetic steel (316L) , interface area about 850 μm x 850 μm [12] [Ye] (Courtesy of Philipp Imgrud, IFAM, Germany)

Its relative density is between 90 and 99 % of density of steel. The technique can be used for making bimetallic structures where a metallic substrate is coated with steel or another heavy metal cladding. The workpiece used as substrate is made by a forging process and transferred to another device where the bimetallic coating is deposited. The most recent orientation of this method is production of very minute components: the microsystem technology (μMIM) for manufacturing nano and millimetre-sized parts. Micro Metal Injection Molding (μMIM) offers dramatic reduction in mass production costs and production of geometrically complex parts to tight tolerances. Certain small components of mobile phones are manufactured in the amount of 100 million a year [13]. Figure 13 shown an example product. In this case the μMIM processes not only homogeneous materials but also WC-Co or other

composites. This is still an emerging field requiring pure powder materials with uniform grain size.

This investigation was conducted with the support of GRANT AGENCY of CZECH REPUBLIC under the project 106/07/0631. Additional support was performed on an instrument developed under the MSM 6198910015 research plan and CZ.1.05/2.1.00/01.0040.

References

- [1] S. Ch. Yoon, Z. Horita, H. S. Kim, Finite element analysis of plastic deformation behavior during high pressure torsion processing, *Journal of Materials Processing Technology*, 201 (2008) 32-36.
- [2] W. Bochniak, A. Korbel, R. Szyndler, R. Hanarz, F. Stalony-Dobrzański, L. Błaz, P. Snarski, New forging method of bevel gears from structural steel, *Journal of Materials Processing Technology*, 173 (2006) 75-83.
- [3] Z. J. Wang, J. G. Liu, X. Y. Wang, Z. Y. Hu, B. Guo, Viscous pressure forming (VPF): state - of - the - art and future trends, *Journal of Materials Processing Technology*, 151 (2004) 80-87.
- [4] M.L.Roades, L.J.Roades, Method and apparatus for die forming sheet material, US Patent 5 085 068 (1992).
- [5] S. John, S. Sikdar, P. K. Swamy, S. Das, B. Maity, Hybrid neural-GA model to predict and minimise flatness value of hot rolled strips, *Journal of Materials Processing Technology*, 195 (2008) 314-320.
- [6] S.R.Schwarz, R.F.Trenty, D.F. Ellerbrock, Terms and definitions on geometrical attributes/profile flatness and surface. In Proc. of Seminar on Cold Strip Mill Profile, Flatness and Surface, Pittsburgh, PA, February, 25-26, p.III-49, 1992.
- [7] S. Lee, Superplastic properties of Pb-62%Sn eutectic alloy after equal channel angular pressing (ECAP), *Journal of Materials Processing Technology*, 201 (2008) 441-444.
- [8] Z. Pater, J. Kazanecki, J. Bartnicki, Three dimensional thermo-mechanical simulation of the tube forming process in Diescher's mill, *Journal of Materials Processing Technology*, 177 (2006) 167-170.
- [9] Z. Pater, A. Gontarz, W. Weroński, Cross-wedge rolling by means of one flat wedge and two shaped rolls, *Journal of Materials Processing Technology*, 177 (2006) 550-554.
- [10] Z. R. Wang, G. Liu, S. J. Yuan, B. G. Teng, Z. B. He, Progress in shell hydroforming, *Journal of Materials Processing Technology*, 167 (2005) 230-236.
- [11] Z. W. Wang, S. Q. Zeng, X. H. Yang, C. Cheng, The key technology and realization of virtual ring rolling, *Journal of Materials Processing Technology*, 182 (2007) 374-381.
- [12] H. Ye, X. Y. Liu, H. Hong, Fabrication of metal matrix composites by metal injection molding-A review, *Journal of Materials Processing Technology*, 200 (2008) 12-24.
- [13] J.L.Johnson, R.M.German, PIM Materials, *Advanced Material Processing*, 161 (4) 35-39.

¹ prof. Ing. Kliber Jiří, VŠB TU Ostrava, 17.listopadu 15/2172, 708 33 Ostrava-Poruba, Czech Republic, Tel.: +420 596 994 463, e-mail:jiri.kliber@vsb.cz

STEEL AND WHAT WE STILL DO NOT KNOW ABOUT IT

Bohuslav Mašek¹

Abstract

New processing strategies have allowed steel to compete better with other materials and the possibilities of its applications have been extended. This has been enabled particularly due to modifications to the microstructure of steel, resulting in a variety of interesting properties and combinations of properties. From the many possible advanced steel grades this article looks at the results of co-operative research projects between COMTES FHT Company and Research Centre of Forming Technology at University of West Bohemia.

Keywords: TRIP steel, Q-P process, thixoforming

1. Introduction

As steel has been optimized for centuries, its innovative improvement now has to reach into the area of partially metastable structures. Suitable structure design can then result in an interesting combination of properties. One of the key features of mechanical properties is strength-ductility balance. New possibilities for precisely controlling structure during processing enable us to obtain both high strength and high ductility. This not only guarantees good processing-ability of steel, but it also allows for the enhancement of safety aspects of constructions. This trend represents a fundamental step towards a safer society, which is one of the primary objectives of recent developments in human society.

2. TRIP Steels in New Applications

One way of increasing the efficiency of part production is the application of cheaper low alloyed steels in innovative technologies, which enable the production of complicated shapes. Materials suitable for this purpose include TRIP steels.

TRIP steels possess a multiphase microstructure, consisting of ferrite, bainite and retained austenite. These steels have an excellent combination of high ductility and good strength [1]. TRIP steels have been used mostly in the auto-body industry to produce thin sheet parts for car bodies. The potential of these steels has not yet been exploited in the area of bulk applications. This research presents a possible application of these steels in unconventional production of hollow semi-products with rotational symmetry by forming. Demonstrational stepped thin-walled semi-products with diameters of 37-40mm and wall thickness around 4 mm were produced with the help of a technological chain containing warm rotary spin extrusion, intercritical annealing and cold flow forming.

Two types of TRIP C-Mn-Si and C-Mn-Si-Nb steels were used in the development of the new technological chain. C-Mn-Si steel's chemical composition is typical for TRIP steels, necessary for ensuring a suitable microstructure. The second steel is further micro-alloyed with niobium, which slightly increases its strength.

In the first step warm rotary spin extrusion was used to create hollow semi-products. Rotary spin extrusion is designed for efficient, flexible and wasteless production of hollow products from bar materials. Different inner profiles can be produced using shaped punches [2, 3].

The forming process is based on the axial pressing of a punch against the machined part with synchronous application of three unpowered forming rollers. The rollers prevent free flow of material in a radial direction. This means that the material moves against the punch, thus forming a hollow product. This technological step sees intense deformation of the ferritic-pearlitic microstructure. Pearlitic areas were regularly distributed and very fine.

An intercritical annealing process was performed for further modification of the structure before final cold forming. On the basis of the previous results, semi-hollow products were processed using the same heat treatment strategy with 15 minutes austenitization hold at 810°C and subsequent bainitic transformation in salt bath at 420°C for 8 minutes. The semi-products were finally cooled in air to room temperature. The microstructure of C-Mn-Si steel after annealing was made of retained austenite islands dispersed in a bainite and ferrite matrix. Mechanical properties reached a ductility of $A_{5mm} = 30\%$ and tensile strength up to nearly 1000 MPa.

Because of the material's high plasticity it was possible to carry out cold rolling to the final shape. Incremental reduction rolling was used for this technological step.

The aim of this step was not only to achieve the desired final shape but also to create a structure with excellent properties. Semi-products were reduction cold rolled to produce hollow semi-products with ca. 4mm walls.

Reduction passes with 6 % deformation were applied. Two steps were formed. The first reduction was from 50 mm to 42 mm diameter the second one was to 37 mm (Figure 1). Samples for metallographic analyses were taken from both areas. The resulting microstructures were formed of a ferrite matrix with fine islands of M-A constituent. Mechanical properties were measured using mini-samples for tensile testing. After the reduction the strength of TRIP Steel was ca. 900 - 950 MPa with 20 % ductility.



Figure 1 An example of a hollow semi product from TRIP steel C-Mn-Si-Nb

3. Incrementally formed Advanced High Strength Low-Alloyed Steels

Modern advanced high strength steels processed using thermomechanical treatments can attain substantially better properties when compared to conventional treatments. This can be seen in new possibilities of thermomechanical treatment for C-Si-Cr steels. Very high strength can be reached using conventional treatments, but ductility drops down to lower values. The aim of this experiment was to design an unconventional thermomechanical treatment procedure in order to reach yield strength of up to 2000 MPa with ductility over 10%.

One of the goals when developing new kinds of steels is their economical efficiency, where the properties of such steels are mostly achieved not by adding high amounts of alloying elements, but by using special procedures of heat treatment or, in particular, thermomechanical treatment.

Generally three new processing strategies have been developed in recent years: the TRIP-effect, which was presented in the previous part of this article, long-time low-temperature annealing and the quenching and partitioning (Q-P) process. The first two methods employ a combination of bainite, ferrite and retained austenite to obtain good mechanical properties. Carbide precipitation is suppressed and carbon is used for the chemical stabilization of retained austenite during this treatment. In the case of the third treatment, the Q-P process, a martensitic structure is achieved in place of bainitic ferrite (Figure 2). This structure enables higher strength values than in the two previous cases.

The properties of the resulting structures are influenced not only by the fraction of individual phases, but especially by their morphology and distribution. While designing new procedures it is necessary to optimize individual processing parameters, in particular the austenitization temperature, cooling rate, and both the temperature and time period of the isothermal holding time for retained austenite stabilization. When using thermo-mechanical treatment other parameters accrue, such as the deformation rate and its temperature interval.

When optimizing the Q-P process it is necessary to determine the influence of individual parameters to obtain a sufficient quantity of retained austenite, thus ensuring excellent mechanical properties. A deformation within the cooling phase is performed in order to refine the structure. Finding a suitable temperature interval for the deformation represents another optimization parameter.

The procedure of the Q-P process is used on experimental low-alloy C-Si-Cr steel. Silicon is one of the main alloying elements of this steel. It suppresses carbide formation throughout the martensite transformation. Another component is manganese, which stabilizes the austenite and reduces pearlite transformation. Another alloying element is chromium which serves as a solid solution hardener.

The proposed treatment entails heating to 900°C with a holding time of 100 s followed by a twenty step anisothermal incremental deformation within a temperature interval from 900 to 820°C (Figure 3).

After multiple deformations in the temperature range 900-820°C the sample is cooled to 200°C, which is just 20°C over the M_f temperature. After cooling, the sample is heated immediately up to 250°C, and held for 600 s. Small ferritic grains were detected in the incurred martensitic structure. X-ray diffraction analysis found

that the retained austenite fraction significantly increased to 15%. Tensile strength reached 2090 MPa and the ductility ca. $A_{5mm} = 12\%$.

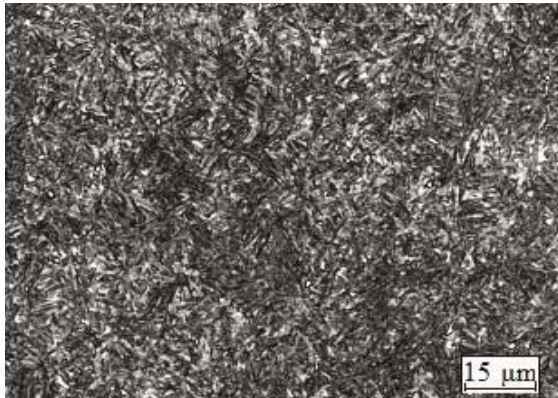


Figure 2 Typical microstructure obtained by Q-P treatment

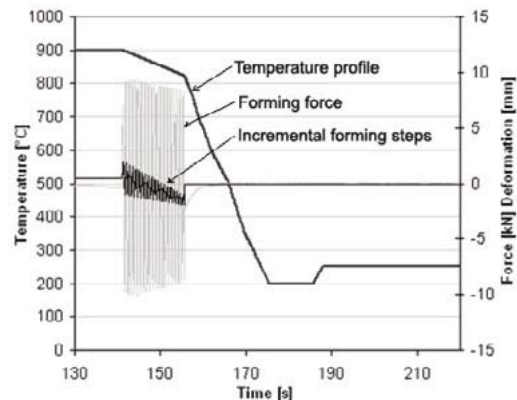


Figure 3 Incremental forming technology with integrated Q-P treatment

4. Special Metastable Microstructures of Steels Obtained from Semi-solid State

It is possible to obtain new unconventional structures with specific mechanical and physical properties not only by the development of new types of materials but also by treatment of conventional materials using unconventional innovative technological procedures. One of these technologies is forming in a semi-solid state involving rapid solidification of miniature components from steels (Thixoforming). The structure of originally ledeburite steel can consist of 95 % of metastable austenite after the treatment. Metastable austenite is located particularly in globular and polygonal grains while the remaining interspace is filled by a lamellar network.

Thixoforming as an unconventional forming technology has been known since the 1970s. Many working groups around the world have been dealing with the research and following industrial exploitation of low-melted alloys forming in semi-solid state [4]. The following results were achieved using materials with high melting temperature, specifically on steels. With these steels it is possible not only to simplify the technological procedure of component production and minimize chip machining but also to obtain products with complex shapes, unconventional structures and physical properties.

Because of the high temperature of semi-solid treatment of steel, intensive deformation, rapid solidification and cooling under high pressure, considerable structural changes occur during minithixoforming which cannot be attained by conventional material treatment. Characteristic dimensions of products that can be achieved are lengths of ca. 20 mm and thicknesses of several millimetres.

The final microstructure after forming in semi-solid state is in contrast to as-cast dendritic microstructure characterised by globular and polyhedral grains surrounded by a fine lamellar eutectic net. The structure of steels with proper alloying consists of metastable austenite which cannot be developed in conditions of conventional cooling or quenching [5]. These structures are attractive particularly because of their mechanical and physical properties. The thermal and mechanical stability of the

structures depends on the chemical and energetic state of the exploited material. The degree of stability under different conditions of thermal and mechanical loading will predetermine their possible practical application.

In experimental forming in the semi-solid state, a die cavity with various shapes of elongated groove was chosen. The process parameters were successively optimized. To fill the die cavity completely, it is necessary to heat the material at least to a temperature of 1290°C. At this temperature the fraction of liquid phase in the material is ca. 40 %. After optimizing the process, complex-shaped semi products were obtained.

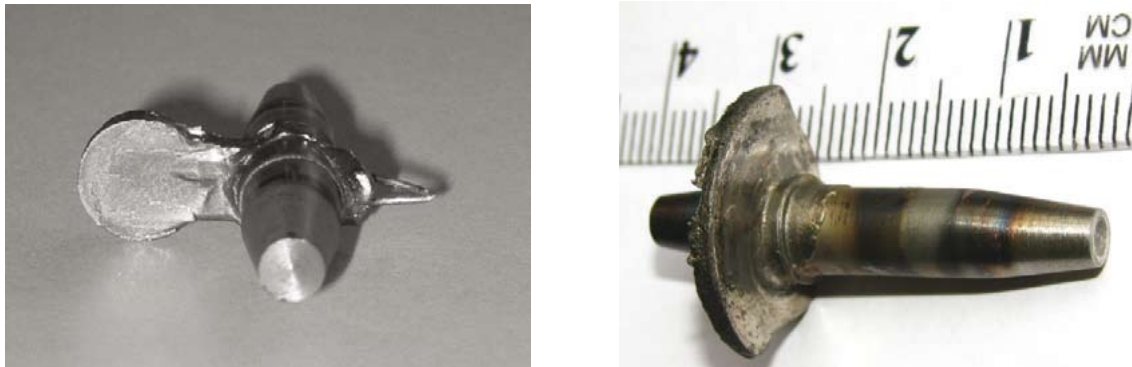


Figure 4 Two examples of semi-products obtained by minithixofforming

Material treatment	Percentage of metastable austenite	HV 10
Steel X210Cr12 in annealed state	-	203
After thixofforming	96%	332
200°C/1h	95%	375
350°C/1h	95%	461
500°C/1h	89%	443
550°C/1h	5%	757
600°C/1 h	1%	597
-196°C/1h	89%	366
Cold deformation	85%	421

Table 1 Heat treatment with the final fraction of single phases

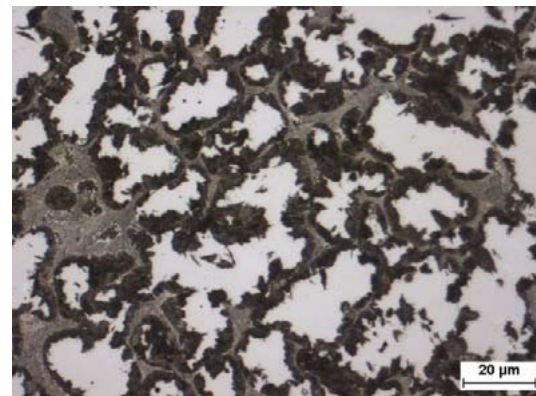


Figure 5 Structure of steel in product after minithixofforming annealed at 500°C for one hour

To evaluate the stability of metastable austenite, experimental samples were subjected to thermal and mechanical loading (Tab. 1). Thermal stability tests showed a high stability of austenite up to 500 °C. During heating at temperatures above 500 °C and subsequent cooling to room temperature, metastable austenite decomposed and a special structure occurred which possessed high hardness of 757HV in contrast to the initial state after thixofforming with a hardness of 332 HV 10. After thermal expositions above 500 °C, the final microstructure depends strongly on the level of the heating temperature. After expositions at about 550 °C the microstructure consists of martensite matrix, troostite formed along the original austenite grain boundaries and carbides network. An increase of exposition

temperature to 600 C resulted in the intensive diffusion process of austenite decomposition. Martensite transformation temperature was reached during expositions in the range of cryogenic temperatures and therefore martensite needles appeared in austenite.

5. Conclusion

Steel has served humanity for several thousand years as a structural material and recent development suggests that it is going to be one of the key materials for the future. It still cannot be easily replaced in many constructions due to its E modulus. Many available microstructural variations can furthermore result in a wide range of mechanical and physical properties at usually convenient economical conditions. Another big advantage of this material is its full and unrestricted recyclability without a loss of quality or properties.

Acknowledgements

This paper includes results created within the project 1M06032 Research Centre of Forming Technology and within the project 106/09/1968 Development of New Grades of High-Strength Low-Alloyed Steels with Improved Elongation Values.

References

- [1] Bleck, W. Using the TRIP effect – the dawn of a promising group of cold formable steels. International Conference on TRIP – Aided High Strength Ferrous Alloys. Bad Harzburg: GRIPS, 2002, p. 13-24.
- [2] Neugebauer, R.; Weidlich, D.; Thomas, V. Neues modulares Maschinenkonzept zum Bohrungsdrücken. Umformtechnik; 1997, 3, p. 46-48.
- [3] Neugebauer, R.; Weidlich, D.; Thomas, V. Experimentalanlage zum Bohrungsdrücken, BDM2000 - Prototyp einer neuen Maschinengeneration. Umformtechnik, 1999, 1, p. 24-25.
- [4] Püttgen, W.; Bleck, W.; Hirt, G.; Shimara, H. Thixoforming of Steels – A Status Report, Advanced Engineering Materials, 9, No. 4 (2007), p. 231-245.
- [5] Ceuard. P.; Sourmail, T. Thixoforming of Steel: A state of the Art from an Industrial Point of View. The 10th International Conference on Semi-Solid Processing of Alloys and Components, HIRT G. (Ed.), p. 25–35, ISBN 3-908451-59-0, Aachen, 2008, Trans Tech Publications LTD, Zuerich.

¹ Prof. Dr. Ing. Bohuslav Mašek, The Research Centre of Forming Technology, University of West Bohemia in Pilsen, Univerzitní 8, 306 14 Pilsen, Czech Republic. Tel.: +420 377 63 8050, e-mail: masekb@kmm.zcu.cz

MINI-THIXOFORMING TOOL STEEL X210Cr12

David Aisman¹, Hana Jirkova², Bohuslav Masek³

Abstract

Mini-thixoforming is a technology used for forming material in a semi-liquid or semi-solid state. A die was designed for this technology and practical testing was carried out using a range of forming strengths and temperatures. The shape of the hollow was varied to find out fluidity. Steel workpieces of various shapes several millimetres in size were created using this technology. X210Cr12 steel was selected for thixoforming as its alloying gives it a wide temperature interval between solid and liquid states.

Key words: semi-solid state, thixoforming, X210Cr12

1. Introduction

The first experiments with forming metals in a semi-solid state date back to 1972. Alloys of tin and lead were used at temperatures between solid and liquid. The resulting structures were so unusual that they immediately became the centre of attention for many research teams who started to investigate the hidden potential of this technique. Since then thixoforming is generally referred to 'semi solid metal forming' (SSM). Thixoforming combines the advantages of casting and forming and allows the manufacture of complex shaped components (Fig. 1).

The essence of the process is the formation of a semi-product which, after heating to melting temperature, is partially in a liquid form and partially in a solid form. The proportion of the melt is usually between 40 – 60%. The semi-product then exhibits thixotropic behaviour, which means it has high viscosity which rapidly falls when subjected to shear stress. When left at rest, the material re-acquires its high viscosity which asymptotically resembles its original value. This technology gives rise to very unusual structures even with conventional materials. For example, high-alloyed steels whose structure after working in a semi-solid state is composed predominantly of globular or spheroid polyhedral particles of metastable austenite enclosed in a lamellar network.

1. Mini-thixoforming

A new as yet unpublished method for manufacturing small components in the semi-solid state is 'mini-thixoforming'. Mini-thixoforming differs from conventional thixoforming in that it is necessary to develop new approaches for managing the temperature fields in the small volume of the material - this means range of volumes up to one cubic centimetre. Minimum temperature deviations must be ensured throughout the heating process to obtain even distribution of temperature

throughout the entire volume of the semi-product. Another advantage of mini-thixoforming is the very rapid solidification from the semi-liquid state after deformation. This means that unconventional structures can be obtained even with commonly used industrial materials, which have an interesting combination of not only mechanical but physical properties. These are multi-phase structures which are a result of, among other things, uneven distribution of chemical elements in the liquid and solid phases.

2 Experimental apparatus

A titanium die was designed for the mini-thixoforming process. Titanium offers a good combination of ultimate strength, ductility and has a more favourable mass than steel. It also has excellent corrosion resistance in strongly oxidising conditions. A very important requirement is that the die should be non-magnetic, as heating is carried out using resistance-induction heating.

For ease of manipulation of the tool and semi-products, the die is composed of four parts which ensure problem-free disassembly of the die and it means there is no need for lubricant. A special principle for forming is lateral compression of the heated material into the forming cavity (Fig. 1).

The temperature of the semi-product is continually monitored using a thermocouple. The thermocouple is attached to the semi-product by a corundum tube which also prevents the metal from flowing into the tensometer channel during forming.

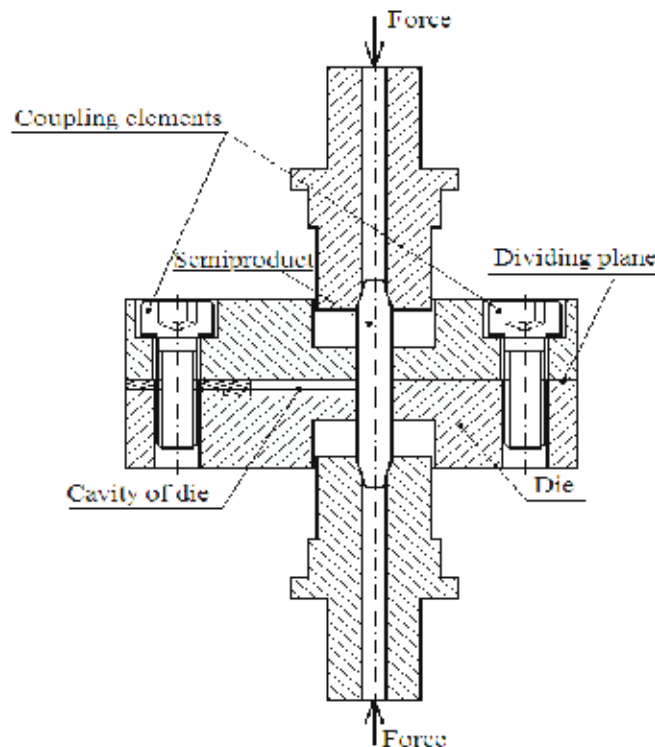


Fig. 1 Diagram showing mini-thixoforming and the principle of lateral compression

Properties of the used materials

X210Cr12 tool steel was selected for the experiment (Tab. 1). It has a wide temperature interval between the solid and liquid state which means that it is

suitable for working in a semi-solid state. This material is also characterized by the fact that it is difficult to form and machine using conventional methods because its high chromium content makes the material very hard and relatively brittle. The initial structure is formed of a ferrite matrix with globular cementite and primary chrome carbides (Fig. 2). After thixoforming, because of the high heating temperature and very rapid cooling, the structure of the semi-product was formed of polyhedral grains of austenite bordered by a fine network formed of a mixture of ledeburitic carbides and austenite (Fig. 9).

Tab. 1 Chemical composition of X210Cr12 steel

C	Cr	Mn	Si	Ni	P	S
1.8 – 2.05	11- 12.5	0.2 – 0.45	0.2 – 0.45	max 0.5	max 0.03	max 0.035

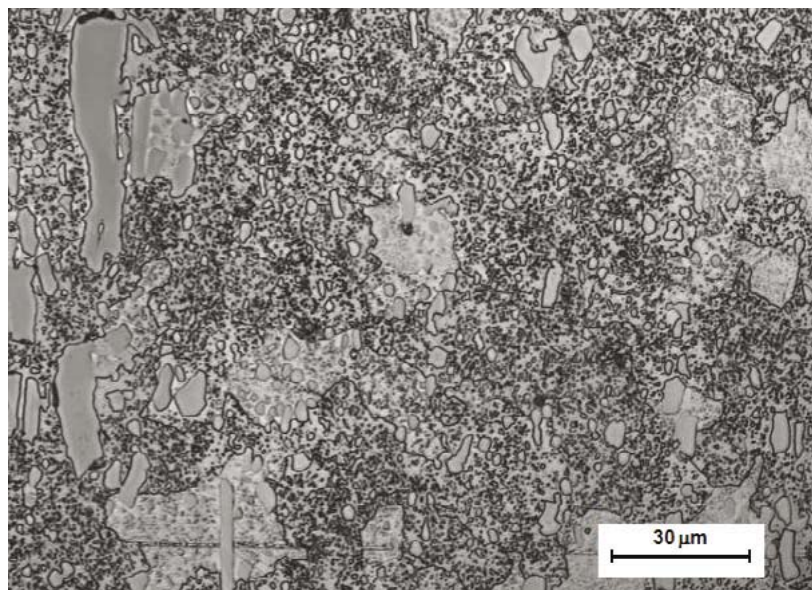


Fig. 2 Initial structure of X210Cr12 steel

2.2 Technological aspects of mini-thixoforming

The rapid solidification during thixoforming allows unconventional structures to be obtained even using conventional materials. From a technological point of view however, it is best that the material is kept at the highest possible temperature throughout the deformation process so as to achieve the required filling of the cavity. Due to the need of high temperature there is a risk of overheating the die resulting in slow cooling of the material. This means that it is essential to accelerate the whole thixoforming process to avoid this undesired effect.

A simple flat cavity (width 5 mm, length 15 mm and thickness 3 mm) was designed for the first experiment. After optimizing the parameters, we were able to completely fill the cavity (Fig. 3). Next the cross section of the cavity inlet was reduced in size and lengthened. The thickness of the cavity was reduced to 1.5 mm and extended to 20 mm, maintaining a width of 5 mm. Even at this thickness, the cavity was filled, despite the reduction in the surface quality being in the final third which may have been caused by the limited volume of melted metal (Fig. 3).

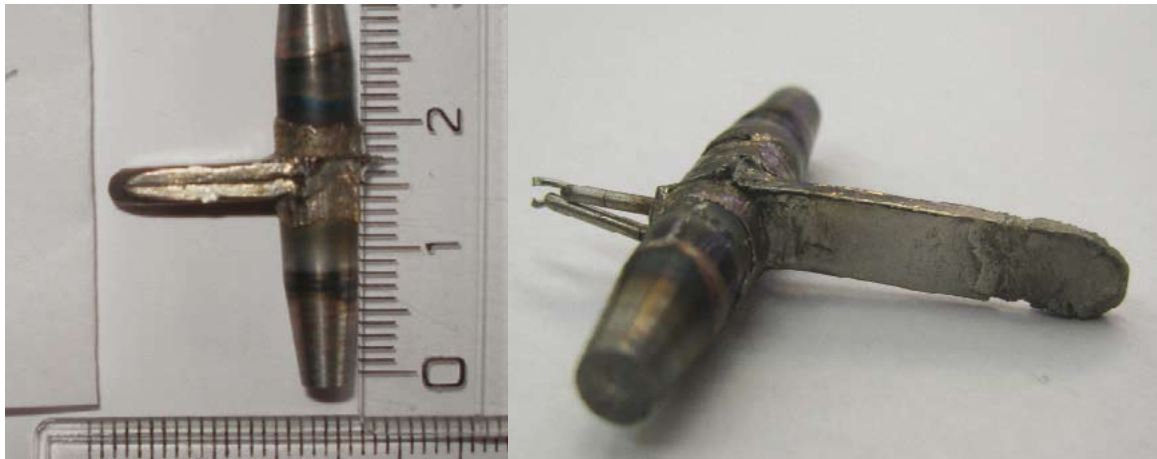


Fig. 3 Left: Demonstrator with short, perfectly filled cavity; Right: Example of imperfectly filled flat cavity

After the experiments with straight cavities, variously shaped demonstrators were designed to test the ability of filling the cavity through a tapered inlet opening. The modular construction of the die not only allowed changes to the shape of the cavity but also the lining of the die and changes not only the shape but also the inlet opening. It was shown that, given enough volume of melted material, it is possible to perfectly fill the cavity (Fig 4). The cross section of the inlet opening was 5x3, 3x3 and 3x1.5 mm.

Further experiments were designed with a view to the miniaturization of the resulting product. The input with cross section 2.5 mm x 2 mm conically tapering to 1.5 mm x 2 mm was filled practically with no remaining unfilled space (Fig. 5), and further reduction to 0.8 mm x 5 mm resulted in only slight leakage up to 6 mm.



Fig. 4 Completely filled cavities with tapered inlet opening



Fig. 5 Conically tapered straight cavity

3. Metallographic analysis of the semi-products

Metallographic analysis showed that the structure after thixoforming is composed of polyhedral grains of austenite surrounded by a fine carbide mesh (Fig. 6). This structure is evenly distributed throughout the burr, only at the edges usually originated dendritic segregation structures. These layers are not always the same thickness and in few cases they did not arise. The original expectation that the thickness of the dendritic layer is proportional to the dimensions of the product was not confirmed.

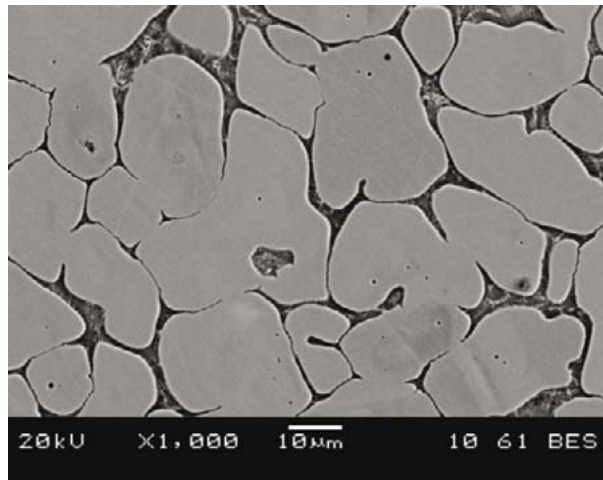


Fig. 6 Structure of X210Cr12 steel after thixoforming

4. Conclusions

The experiments showed that forming X210Cr12 steel in the semi-solid state can be used to manufacture even very small components of various shapes. Thixoforming was carried out in a die cavity and the shapes of the resulting demonstrators varied. From the results it is clear that the ability of the material to fill the entire volume of the die cavity is excellent in case there is enough metal melt and adequate inlet opening thickness provided. At thicknesses less than 1 mm the fluidity of the metal using this technology is significantly lower.

Acknowledgements

This paper includes results created within the project 1M06032 Research Centre of Forming Technology.

¹ Ing. David Aišman, Západočeská univerzita, Výzkumné centrum tvářecích technologií,
e-mail: daisman@vctt.zcu.cz

² Dr. Ing. Hana Jirková Ph.D., Západočeská univerzita, Výzkumné centrum tvářecích technologií,
e-mail: hstankov@vctt.zcu.cz

³ prof. Dr. Bohuslav Mašek, Západočeská univerzita, Výzkumné centrum tvářecích technologií,
e-mail: masekb@vctt.zcu.cz

INFLUENCE OF CARBIDES SPHEROIDISATION ON MECHANICAL PROPERTIES IN MEDIUM CARBON STEEL

Daniela Hauserová¹, Jaromír Dlouhý², Zbyšek Nový³, Jozef Zrník⁴

Abstract

The goal of research into rapid carbide spheroidisation process is to significantly cut down the duration of selected heat treatment processes. The combination of a suitable pre-heating temperature and an appropriate amount of strain leads to transformation of initial ferrite-pearlite microstructure with lamellar pearlite into desired ferrite matrix with spheroidised carbides.

Keywords: accelerated spheroidisation, deformation, grain refinement

1. Introduction

Current processes leading to carbide spheroidization rely on diffusion of carbon in a workpiece heated to a temperature close to or slightly below critical temperature A_{c1} . Diffusion-based processes of this type are usually long-term and time-consuming. The holding times of up to tens of hours make this type of annealing one of the most expensive heat treatment processes ever. During annealing, softening processes are under way in the microstructure and, in some cases, recovery and recrystallization take place as well. Naturally, the morphology of carbides changes as well. The strength and hardness of the steel workpiece decline, while its ductility increases and its plastic deformation capability is recovered. The newly-designed and patented thermomechanical process brings several-fold reduction in the processing time and results in considerable cost savings.

The paper presents evidences on the influence of plastic deformation introduction on the carbide spheroidization process. Significant acceleration of the process relates to steel heating at a temperature a bit under the transformation temperature A_{c1} and to introducing plastic strain into the material (Zhang S. L., 2006).

2. Experimental

The experimental programme was performed using structural carbon steel C45 with the chemical composition listed in tab. 1. The initial microstructure consisted of ferrite and lamellar pearlite with pronounced banding along the axis of the bar stock. Hardness of the as-received material was 180 HV, proof stress $R_{p0,2}=378$ MPa, ultimate tensile strength $R_m=673$ MPa, elongation $A=29$ % and impact toughness $KCV=42$ J/cm².

Table 1 Chemical composition of C45 steel [wt. %]

C	Si	Mn	S	P	Cr	Ni	Cu	Mo	Ti	V	W
0.42	0.24	0.69	0.019	0.016	0.12	0.16	0.12	0.02	0.002	0.004	0.01

2.1. Treatment Schedules

Conventional Soft Annealing – the HT schedule

For the purpose of comparison with the newly-designed thermomechanical process, conventional soft annealing was carried out. This heat treatment consisted in 12-hour hold at 710°C and slow furnace cooling for 30 hours (HT specimen).

Thermomechanical Treatment – TMT 1 schedule

The stock with the diameter of 50 mm and the length of 70 mm was heat treated in an air furnace and then formed to various reduction levels between flat swages of a hydraulic press with the ram speed of 25 mm per second. The processing schedule included heating of the workpiece through ought thickness to a temperature slightly below Ac1, one-hour hold and subsequent plastic deformation in two perpendicular directions in a press. After forming, the workpiece was left to cool in air. The soaking temperature was 710°C and the total effective strain $\bar{\varepsilon}$ was calculated by numerical simulation as 4 in the specimen centre (the TMT1 schedule).

Thermomechanical Treatment – TMT 2 (TMT1 shedule + water cooling)

The TMT2 schedule was carried out to investigate whether there was austenite present in structure during the TMT process. The schedule consisted of heating to 710°C and forming in a press (as in the TMT1 schedule). The sample was put in a water immediately after the plastic deformation.

Thermomechanical Treatment – TMT 3 (TMT1 shedule + post-treatment)

The TMT3 post-treatment schedule was designed to investigate the effect of the hold after plastic deformation on the microstructure. The schedule consisted of heating to 710°C and forming in a press (as in the TMT1 schedule) and subsequent hold at 710°C. The treated specimen cooled then in air.

The specimens were processed in an atmosphere furnace and plastically deformed between flat swages of a hydraulic press. Metallographic structure observation was performed on longitudinal sections of all specimens in order to examine and to compare microstructures throughout the specimen cross-section. The microstructure was observed using light and scanning electron microscopes. Vickers HV30 hardness was measured on specimens. Specimens with the gauge length of 20 mm and a diameter of 4 mm were used for tensile testing. Charpy impact test was carried out using miniature specimens with the dimensions of 3×4×27 mm with a 1 mm-deep V-notch.

2.2. Numerical Simulation

Numerical simulation of the thermomechanical treatment was carried out using the software DEFORM to monitor the distribution of strain and temperature throughout the specimen. Effective strain magnitude and a temperature increase due to plastic deformation primarily in the centre of the specimen (point P1) but also halfway between the centre and the surface (point P2) were monitored (Tab. 2).

Effective strain was calculated by numerical simulation according to the equation (1).

$$\bar{\varepsilon} = \frac{\sqrt{2}}{3} \sqrt{(\varepsilon_1 - \varepsilon_2)^2 + (\varepsilon_2 - \varepsilon_3)^2 + (\varepsilon_3 - \varepsilon_1)^2} \quad (1),$$

where ε_1 , ε_2 and ε_3 are principal strains and $\bar{\varepsilon}$ is the effective strains.

Table 2 Numerical modelling of the thermomechanical treatment (TMT1) schedule

Schedule	Soaking temp. [°C]	Values upon first deformation		Values upon second deformation	
		$\bar{\varepsilon}$ []	T [°C]	$\bar{\varepsilon}$ []	T [°C]
TMT1 at point P1	710	2.9	770	3.9	741
TMT1 at point P2	710	1.5	746	2.5	751

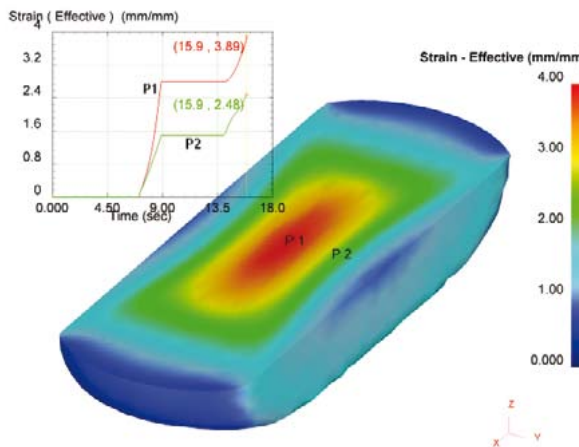


Figure 1 Distribution of effective strain after second compression of the TMT1 specimen.

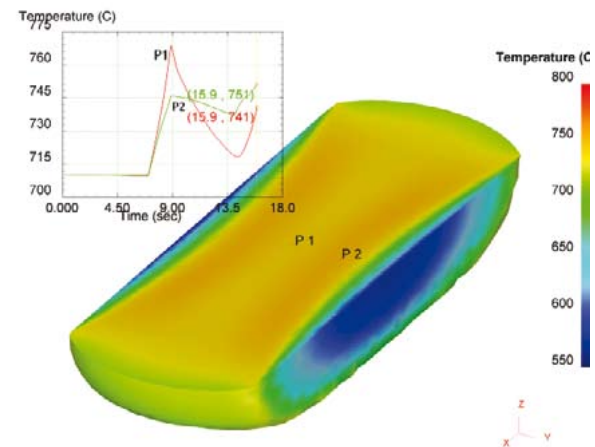


Figure 2 Temperature field after second compression of the TMT1 specimen.

3. Results and Discussion

The experimental programme was carried out using C45 steel with lamellar pearlite in the as-received state upon rolling (Fig. 3). With this cementite morphology, the transformation to globular form is relatively difficult, as evidenced by the reference sample. It was annealed for 12 hours at 710°C and furnace cooled for 30 hours. Cementite lamellae only broke down partially throughout the specimen (Fig. 4).

The hardness of conventionally annealed specimen decreased from the as-received state (180 HV30) to 148 HV30. Other mechanical properties are listed in tab. 3. The ultimate strength decreased to 541 MPa and elongation increased to 33 %. Impact toughness value increased to 45 J/cm².

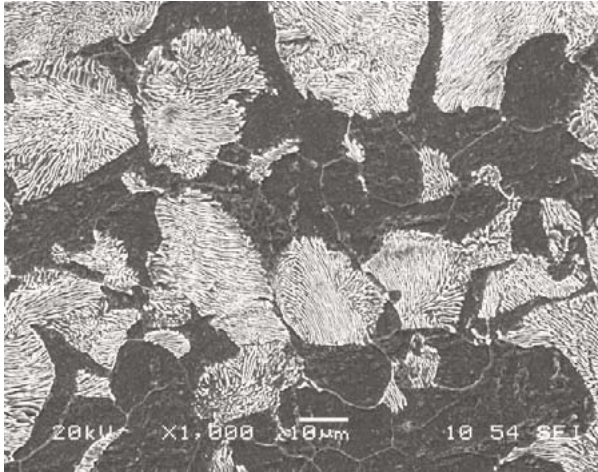


Figure 3 Initial state: pearlite-ferrite microstructure with lamellar pearlite prevailing



Figure 4 The HT schedule: 710°C/12 hours, furnace cooling/30 hours. Partially spheroidized microstructure

Table 3 Mechanical properties for individual schedules

Notation	Schedule	HV 30	R _{p0,2} [MPa]	R _m [MPa]	A [%]	KCV [J/cm ²]
Initial state	Upon hot rolling	180	378	673	29	42
HT	710°C/12 hours, furnace cooling/30 hours	148	298	541	33	45
TMT1	710°C/1 hour, deformation, air cooling	176	482	611	24	51
TMT3 P1 point	710°C/1 hour, deformation, 710°C/1hod, air cooling	145	385	539	30	55
TMT3 P2 point	710°C/1 hour, deformation, 710°C/1hod, air cooling	150	418	552	33	62

Microstructures of thermomechanically treated specimens contain completely spheroidized cementite. The microstructure of the TMT1 specimen which was cooled in still air after plastic deformation is highly non-uniform due to non-uniform distribution of plastic strain (Fig. 1). In the centre of the specimen, where the amount of strain was largest, short-range diffusion of carbon accelerated within short time, leading to complete spheroidization of carbides and refinement of ferritic grain. In ferrite regions, the grain size was between 5 and 10µm. In areas with high density of carbide particles, the ferrite grain size was about 2µm. Ferrite grain size in the as- received state was about 20µm (Fig. 3).

Rapid carbide spheroidization and ferrite grain refinement therefore operated concurrently (ASR – Accelerated Spheroidization and Refinement). The microstructure between the centre and the surface of the specimen changed slowly. With increasing distance from the specimen centre, the amount of strain introduced decreased and resulted in less effective carbide spheroidization. Near the specimen surface where the introduced strain was the smallest, lamellar pearlite morphology prevails and ferrite is only partially recrystallized. Mechanical properties of TMT1 specimens measured in its centre are listed in tab. 2. The hardness reached

176 HV30, the proof stress was 482 MPa, ultimate strength 611 MPa and elongation was 24 %. Impact toughness increased to 9 J/cm² more than in the as-received state, i.e. to 51 J/cm².

In the centre of the thermomechanically treated specimens occurred redistribution of carbon from pearlitic to ferritic regions. This homogenization of carbon content is facilitated by austenitization of structure in the middle of the specimen during plastic deformation (which causes increase of temperature over the critical temperature). To prove austenitization, the TMT2 schedule was carried out. TMT2 schedule consisted of the same thermomechanical treatment like schedule TMT1, but the sample was put in water immediately after plastic deformation.

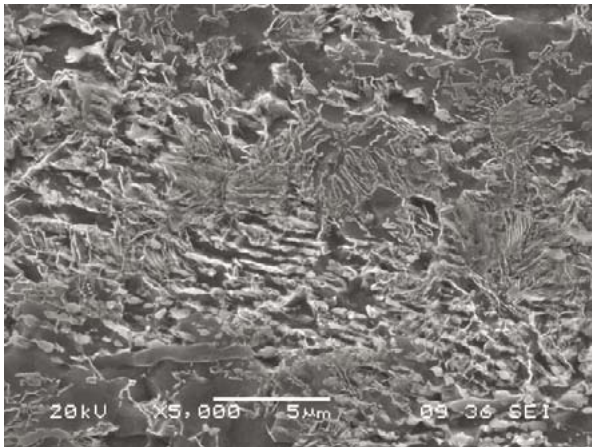


Figure 5 P1 point of the TMT2 specimen: 710°C/1 hour, deformation, water cooling; pearlitic region.

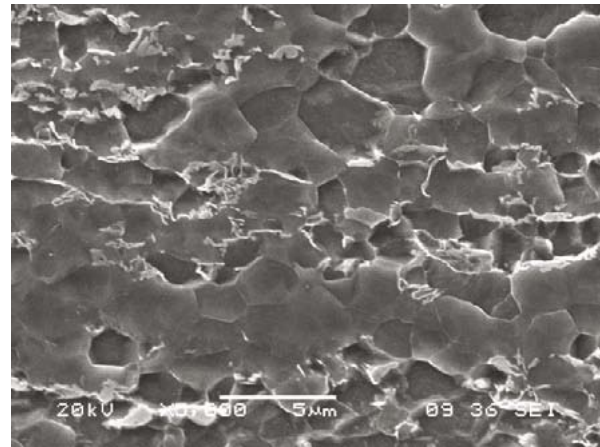


Figure 6 P1 point of the TMT2 specimen: 710°C/1 hour, deformation, water cooling; ferritic region.

There was present both original and new pearlite together with ferrite in the centre of the specimen TMT2. Pearlitic regions contains significant amount of finer lamellas beside original partially spheroidised pearlitic lamellas. These fine lamellas originate from austenite decomposition during water cooling of the sample (Fig. 5). Sparse fine lamellas are also present in originally ferritic regions and shows diffusion of carbon to the ferrite (Fig. 6). This fine pearlite occurred only in the centre of the TMT2 specimen, in outer regions towards the surface was the microstructure the same, as in TMT1 specimen. It shows that austenitization took place probably only in the centre of the sample, where sufficient degree of deformation caused increase of temperature over A_{c1} .

TMT3 specimen, which was mechanically worked in the same fashion as the TMT1 one, was placed in a furnace for 1 hour at 710°C immediately after the deformation. After one-hour hold and subsequent air cooling, carbides were spheroidized in an almost entire volume of the specimen (Fig. 7, 9). This is apparent in comparison with the TMT1 schedule (Fig. 8). During the hold, ferrite grain became coarser, matching the as-received grain size (20 to 30 µm). In pearlite regions globular cementite particles prevented grain growth, by which the grain size of 2 to 3µm was retained (Fig. 10). It is only near the surface of the specimen TMT3 where minor proportion of preserved lamellae can be found (Fig. 11).

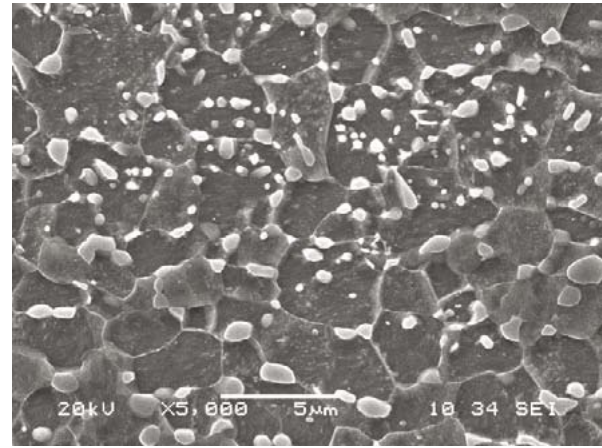
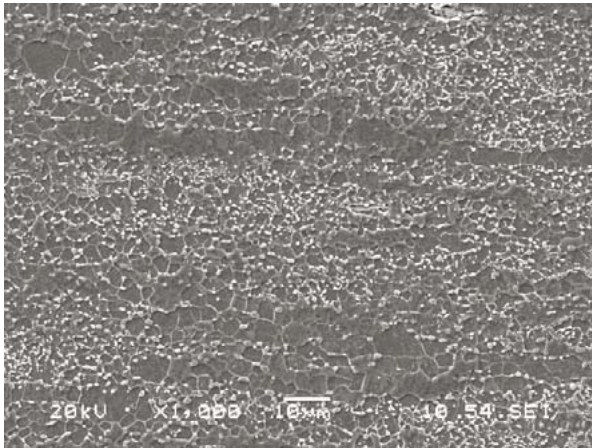


Figure 7 P1 point of the TMT3 specimen: 710°C/1 hour, deformation, 710°C/1 hour, air cooling.

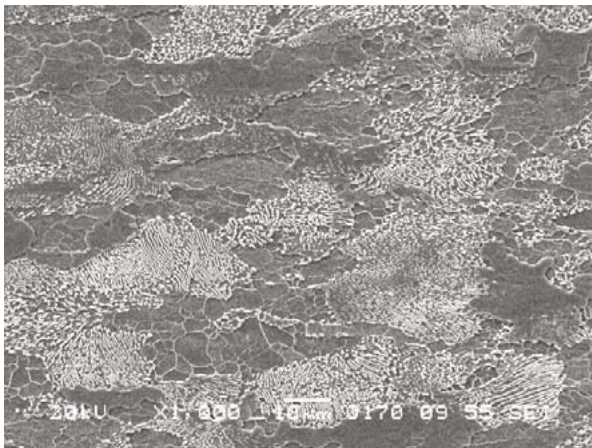


Figure 8 P2 point of the TMT1 specimen: 710°C/1 hour, deformation, air cooling; Partially spheroidized carbides between the centre and the surface of the specimen

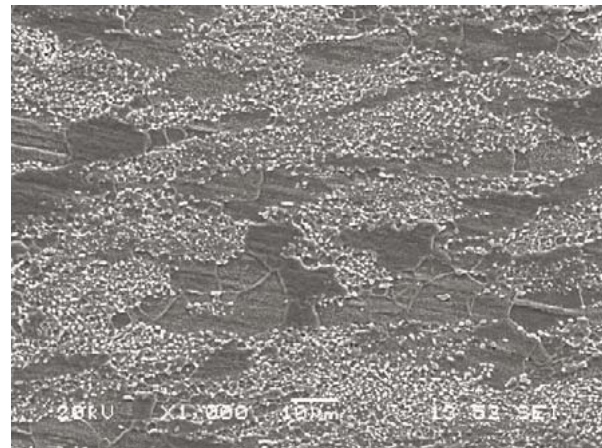


Figure 9 P2 point of the TMT3 specimen: 710°C/1 hour, deformation, 710°C/1hour, air cooling; High degree of carbide spheroidization between the centre and the surface of the specimen

Mechanical properties of specimen TMT3 are listed in tab. 2. Hardness in the centre (point P1) decreased (in comparison with the TMT1 specimen which had no hold) by 30HV, proof stress decreased to 385 MPa, strength to 539 MPa, elongation increased by 6 % to 30 % and impact toughness rose to 55 J/cm². At point P2, i.e. halfway between the centre and the surface of the specimen, Vickers hardness was 150HV, proof stress equalled 418 MPa, the strength was 552 MPa, elongation 33% and notch toughness increased to 62 J/cm². **Thanks to the hold at temperature, mechanical properties have almost uniform values throughout the specimen.**

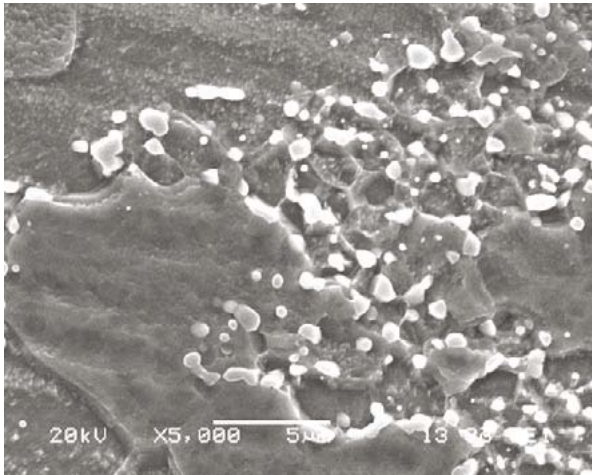


Fig. 10 P2 point of the TMT3 specimen: 710°C/1 hour, deformation, 710°C/1hod, air cooling; Spheroidized carbides, coarsened ferrite grain in ferrite regions, constant ferrite grain size in regions with high density of carbides

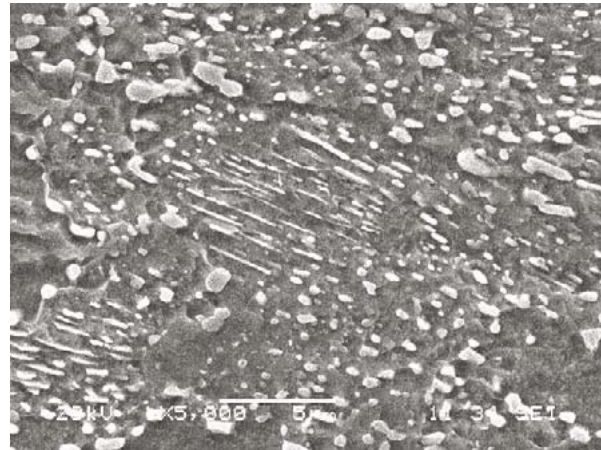


Fig. 11 The surface of TMT3 specimen: 710°C/1 hour, deformation, 710°C/1hod, air cooling; Spheroidized microstructure with a small proportion of lamellar cementite

The plastic deformation caused a temperature increase in the centre of the specimen from 710°C to about 770°C (1st deformation), 746°C (2nd deformation). This conditions initiates dynamic recrystallization.

TMT1 specimen shows that for the complete spheroidization to take place during the plastic deformation stage, large strains are required (and possibly higher temperatures), which were only reached in the centre of the specimen. In the TMT3 specimen is it apparent that mechanism supporting spheroidization is still operating during subsequent one-hour hold at a temperature just below A_{c1} . During this hold, the grain in ferrite regions coarsens, whereas in the area with high carbide density cementite particle pin the migrating grain boundaries and keep ferrite grains small (Fig. 10). This is why cementite particles are present on the grain boundaries.

Initial state of material – as rolled ferrite–pearlite steel does not store significant amount of free energy. Soft annealing process is long, because the difference between the free energy of lamellae and spheroidized pearlite (driving force for speheidisation) is small. The free energy of the pearlite system is considerably influenced by the interfacial energy of the ferrite/cementite interface. Large surface of cementitic lamellae is sensitive to became high energy locality. The interfacial energy is considerably raised by plastic deformation – it increases the energy difference between lamellar and spheroidized microstructure.

Carbon diffusion along ferrite/cementite interface is facilitated by increased interfacial energy. Carbon diffusion in ferrite and cementite is further enhanced by high density of lattice defects (causing higher solubility of carbon in ferrite - Shin D. H., 2000). Enhanced diffusion supports fast spheroidisation. Austenitization isn't the necessary condition for the fast spheroidisation, globular carbides arises both in transformed and nontransformed regions.

Very small ferrite grains are stabilised in regions with high density of spheroidised carbides, if the recrystallization of ferrite occurred. This phenomena is called Accelerated Spheroidization and Refinement (ASR). Spheroidisation of carbides is accelerated by introducing of the plastic deformation at a suitable temperature, but whole process of fast carbide spheroidisation is maintained active during consequent hold at temperature slightly below critical temperature A_1 .

3. Conclusions

A thermomechanical treatment process has been designed, which leads to carbide spheroidization over a very short time thanks to plastic deformation. Recrystallization takes place concurrently with carbide spheroidization and at least markedly changes the grain size (ASR – Accelerated Spheroidization and Refinement). It was found that the deformation facilitated carbide spheroidization even during subsequent hold close to the transformation temperature A_1 . The critical factors affecting the degree of spheroidization and recrystallisation include the magnitude of plastic strain introduced and the thermal schedule. Future research involve optimisation of thermomechanical treatment parameters. Its purpose will be to achieve suitable properties within minimum time period or to control individual properties by appropriate selection of thermomechanical treatment parameters.

Acknowledgements

This paper includes results achieved within the project GACR P107/10/2272: Accelerated Carbide Spheroidisation and Grain Refinement in Steels.

References

- [1] Zhang S. L., Sun. X. J., & Dong H., Effect of deformation on the evolution of spheroidization for the ultra high carbon steel. *Materials Science and Engineering*, 2006, Vol. 432, No. 1- 2, 324-332, ISSN 0921-5093.
- [2] Shin D. H., Kim B. C., Park K., Choo W.Y., Microstructural changes in equal channel angular pressed low carbon steel by static annealing, *Acta materialia*, 2000, Vol. 48, pp. 3245-3252.

¹ Ing. Daniela Hauserová, COMTES FHT a.s., Průmyslová 955, 334 41 Dobřany, Czech Republic, Tel.: +420 377 197 333, e-mail: daniela.hauserova@comtesfht.cz

² Ing. Jaromír Dlouhý, COMTES FHT a.s., Průmyslová 955, 334 41 Dobřany, Czech Republic, Tel.: +420 377 197 341, e-mail: jaromir.dlouhy@comtesfht.cz

³ Dr. Ing. Zbyšek Nový, COMTES FHT a.s., Průmyslová 955, 334 41 Dobřany, Czech Republic, Tel.: +420 377 197 301, e-mail: zbysek.novy@comtesfht.cz

⁴ prof. Ing. Jozef Zrník, CSc., COMTES FHT a.s., Průmyslová 955, 334 41 Dobřany, Czech Republic, Tel.: +420 377 197 342, e-mail: jozef.zrnik@comtesfht.cz

SUBSTRUCTURE OF DEEP CRYOGENICALLY TREATED HS6-5-2 HIGH SPEED STEEL

Jerzy Jeleńkowski¹, Aleksander Ciski², Tomasz Babul³

Abstract

Research of HS6-5-2 high speed steel heat treated for secondary hardness, processed in a conventional mode or in a mode with use of deep cryogenic treatment (DCT), results that DCT reduces martensite grain size and causes an increase of quantity of sites for nucleation of clusters, which act as a nuclei of B1 type carbides. Clusters and lamellar forms of this phase are present in the microstructure of steel after conventional mode of heat treatment.

Keywords: high speed steel, deep cryogenic treatment, carbides

1. Introduction

Since the 50's of last century there was a opinion [1-5] that the transformation of cementite to the special carbides proceeds by an "in situ" mechanism, i.e. by the formation of a new nucleus in a site of dissolved, more unstable carbide. The theory of special carbides forming by "in situ" mechanism assumed an existence of three stages: 1) cementite precipitates from the martensite, in cementite the concentration of iron and carbon atoms is close to the concentration in solid solution, 2) when the chromium content in cementite reaches a critical concentration, Cr atoms are segregated between the steel matrix and the nascent carbide phase, 3) a lattice of cementite is rebuilt "in situ" to the special carbide [1]. According to [6] cementite may dissolve in solid solution and after that the carbon atoms are involved in the precipitation from solid solution ("ab initio") of a special carbide in sites where previously there were particles of cementite. In the process of growth, the carbides take shape of needles, plates or rods [7].

In [8] for the first time the possibility of nucleation of Cr₇C₃ carbide by spinodal mechanism was maintained. Nowadays, the formation of special carbides is considered as consisting of two stages: 1) formation of clusters – zones consisting of carbide forming elements and carbon; and 2) the rebuilding of these areas into a special carbide. The first step is a spinodal decomposition and this mechanism underlies the observed structural phenomena. The formation of clusters occurs simultaneously in the whole volume, wherein the density of clusters is almost an order of magnitude higher than the dislocation density. With the increase of tempering temperature and time, grow only clusters not connected with defects of the crystalline structure of the matrix, thus these located on planes {100}_α. Clusters transform into the lamellar forms, probably by the dissolution of smaller ones, that is the globules at dislocations, i.e. in small areas that do not allow getting a more

stable shape needed for further growth. Also a random orientation of the dislocations doesn't allow clusters taking the preferred direction of growth.

In the early 70's it was known that the formation of Mo_2C and VC carbides is always through the GP (Guinier-Preston) zones, and therefore they are always coherent with the matrix [9,10]. In the stage of the existence of mixed zones – globules, tetragonal deformation of the lattice of Fe_α (BCC) matrix occurs, and when the degree of tetragonality (c/a) reaches 1.41 (which corresponds to the FCC lattice) carbide of the B1 structure is formed. The formation of the carbide phase, even if its final structure will be different, takes place simultaneously in the whole volume, both at dislocations, as well as at boundaries of martensite laths. B1 carbides are phases with a very wide area of homogeneity, depletion of carbon and elevated concentration of vacancies. For example, in the VC_y carbide ($0,66 < y < 0,88$), with a decrease of carbon concentration, there is ability for substantial arrangement. It was stated [8,11,12,13] that with the increase in arrangement, B1 crystal structure is achieved, in which the volume of elementary cell increases 8 times, as compared with the baseline one. The cell contains 32 vanadium atoms and 32 ion nodes, occupied by the carbon and vacancies. This is the reason why the VC may have a regular (B1), rhombic or rhombohedral lattice structure, and may contain up to 50 % of W and Mo, and up to 25 % of Cr.

Important role in the formation of special carbides play vacancies [14]. Vacancies are causing that at temperature below 250°C the least stable carbides are formed, for example $\varepsilon - \text{Fe}_3\text{C}$, but the precipitation of a coherent carbide $\alpha' - \text{Fe}_{16}\text{C}_2$ at temperature lower than 100°C is also possible, when the substitutional elements are still not mobile. In high speed steels, in addition to mentioned carbides, B1 carbides and η -carbides with a regular structure consisting of 96 metallic atoms (Fe atoms and the metals of group V and VI) and 16 carbon atoms can be formed [15].

The literature information states that deep cryogenic treatment causes increase in hardness, toughness and wear resistance [16-18]. During tempering the highly alloyed retained austenite with carbide precipitations transforms into secondary martensite [19].

The purpose of this study was, using advanced methods of structural researches, revealing the changes in substructure of HS6-5-2 high speed steel made with DCT, in comparison with conventional heat treatment for secondary hardness.

2. Material and experimental procedure

Research was conducted on HS6-5-2 high-speed steel. Chemical composition of samples was analysed with aid of Analytical Spectrometer Foundry Master 01D0058. The results of measurements are given in Table 1.

Table 1 Chemical composition of samples

	Chemical composition, weight %							
	<i>C</i>	<i>Si</i>	<i>Mn</i>	<i>Cr</i>	<i>Mo</i>	<i>V</i>	<i>W</i>	<i>Co</i>
Typical composition	0,82÷0,92	≤0,5	≤0,4	3,5÷4,5	4,5÷5,5	1,7÷2,1	6,0-7,0	≤0,5
Actual composition	0,83	0,31	0,26	4,25	4,2	1,78	6,08	0,34

Samples used for testing by light microscopy and X-Ray phase analysis were cylindrical in shape, with a thickness of 5 mm and diameter of 10 mm. For SEM-TEM investigations a foils cut from the rode samples (diameter of 3 mm) were used. The

same rods were used for preparation of disc samples (diameter of 3 mm) used in calorimetric studies. DSC samples were cut using electric spark method and had mass of 10 mg.

All samples were tested in three modes of heat treatment. Treatment modes and obtained values of hardness are summarized in Table 2.

Table 2 Routes of heat treatment and obtained hardness of samples

Mode	Route of heat treatment	Hardness
A	Austenitizing (1200°C) + Quenching + Tempering (550°C, 2 h)	936 HV1
B	Austenitizing (1200°C) + Quenching + DCT (-180°C, 24 h)	863 HV1
C	Austenitizing (1200°C) + Quenching + DCT (-180°C, 24 h) + Tempering (550°C, 2 h)	902 HV1

The phase composition was analysed by means of the Bruker AXS D8 Discover 2 X-Ray diffractometer. Transmission electron microscopy and scanning electron microscopy analyses were conducted with aid of scanning-transmission electron microscope HITACHI HD2700 (resolving power of 0.14 nm), equipped with an energy-dispersive X-Ray spectrometer (EDS), allowing spectral analysis of chemical composition in areas with a diameter of 0.5 mm. Elemental mapping was also performed. Studies of thermal stability in the range of temperatures from -196 °C to 400 °C were performed using differential scanning calorimetry (DSC), with aid of the Parkin Elmer calorimeter. The samples were cooled down and heated up at a rate of 10 °C/min.

3. Results of tests

3.1 X-Ray Diffraction (XRD)

In the examined samples, regardless of the applied heat treatment, presence of Fe_α (martensite, ferrite), Fe_γ (austenite), M_6C (Fe_3W_3C or Fe_4W_2C), VC was identified. There was no splitting of the $(110)_\alpha$ line, typically observed for martensite in carbon steels.

The relatively lowest intensity of diffraction lines from the phase components, except for Fe_γ and M_6C , was observed in the mode of heat treatment B, while the highest was observed, except for Fe_γ , in the mode C.

Qualitative analysis of the diffraction line positions of the Fe_α lattice versus $\sin 2\theta$, of steel heat treated in modes A, B and C, showed the following sequence of (d_{hkl}) values: $d_{Bhkl} < d_{Chkl} < d_{Ahkl}$. These values, in relation to the dimensions of the interplanar distances, correspond to the same relationships between the dimensions of lattice parameters of martensite. This means that the parameter of Fe_α unit cell is the highest after the heat treatment for secondary hardness without deep cryogenic treatment (mode A), and the lowest after the DCT and heating up to room temperature (mode B).

3.2 SEM/TEM observations

Imaging of the structure using TEM/SEM showed that in each one of the heat treatment modes, martensite has the lamellar-lenticular structure, internally twinned, with the fairly evenly distributed dislocations. Morphology of martensite of steel tempered for secondary hardness is characterized by a partial disappearance of twins and midribs. However, there remain the same quantity and size of primary carbides

and primary austenite grains with size of 8–10 μm , which corresponds to the grain size number 10-11 on the 1910-1911 ASTM scale (Fig. 1-3). Carbides of the spherical shape and a diameter of about 1 μm are generally located within the martensite grains, whereas these oval-shaped with a diameter of about two times higher, at the grain boundaries. There are also differences in the size of martensite plates. In the mode A samples plates have length of about 1-2 μm and width of about 0.3–0.4 μm , while in deep cryogenically treated samples (modes B and C) these dimensions are an order of magnitude shorter and thinner (Fig. 4).

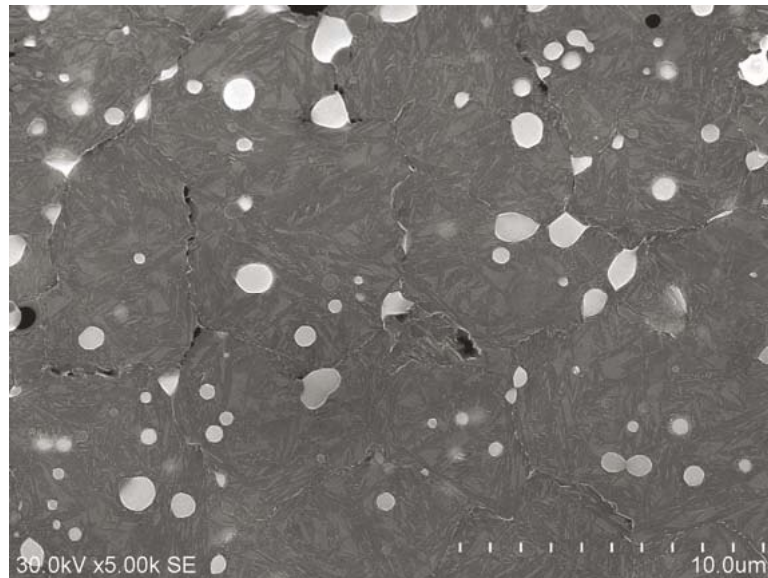


Figure 1 SEM micrograph of sample heat treated in mode A

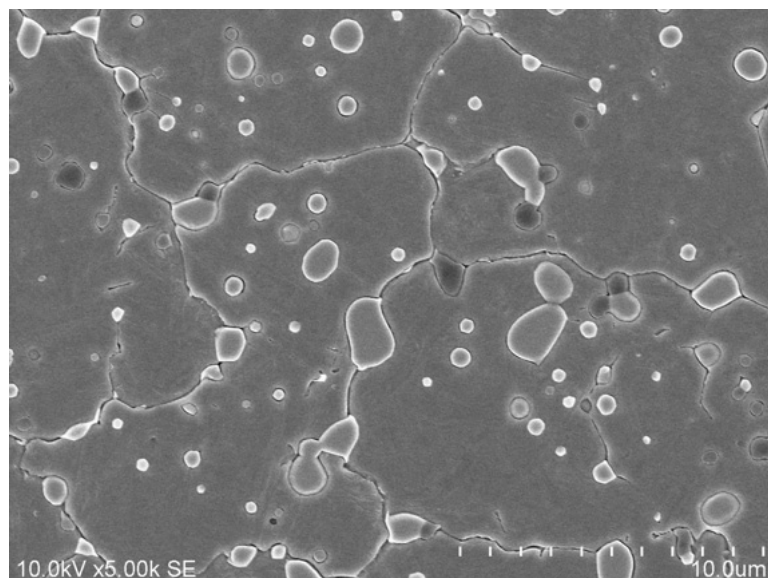


Figure 2 SEM micrograph of sample heat treated in mode B

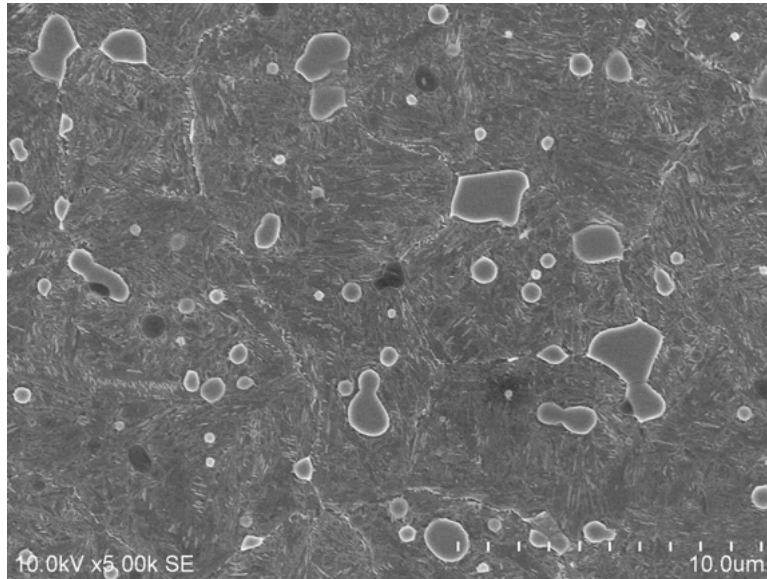


Figure 3 SEM micrograph of sample heat treated in mode C

In the matrix of samples heat treated in mode A, there are present clusters-globules with a diameter of 10–15 nm located at dislocations, and plates situated at the grain boundaries and within the martensite twins, with a thickness of about 10–15 nm and length up to about 100 nm. In mode B, globules and plates have clearly defined contours. Globules are also likely at dislocations in austenite. Local configuration of some plates resembles morphology of the tweed-like structure, i.e. the morphology of precipitations formed by the spinodal decomposition. In mode C, in addition to a considerable refinement of the martensite and sharp contours of phases, the morphology of martensite seems to be similar to that observed in mode A (Fig. 4-6).

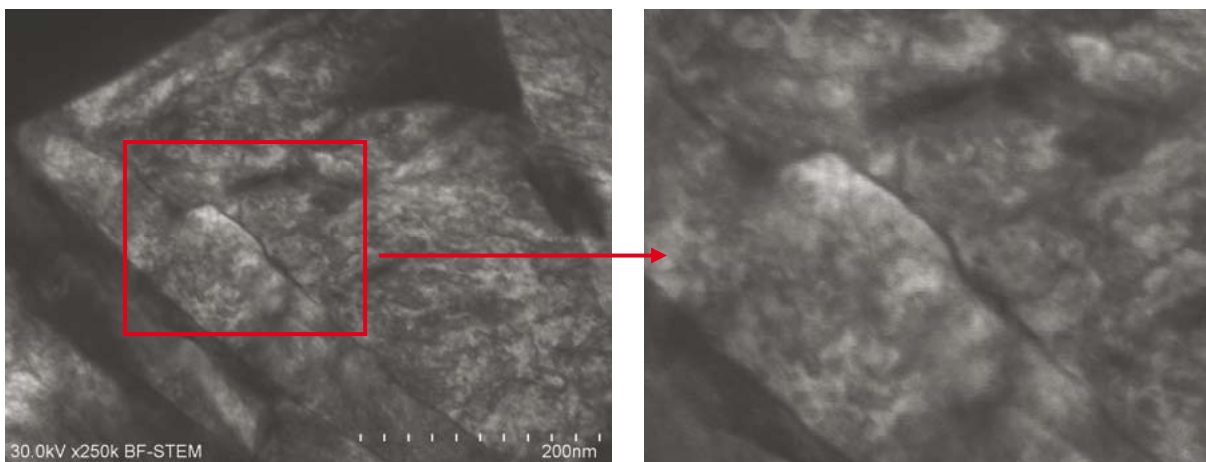


Figure 4 TEM micrographs of samples heat treated in mode A

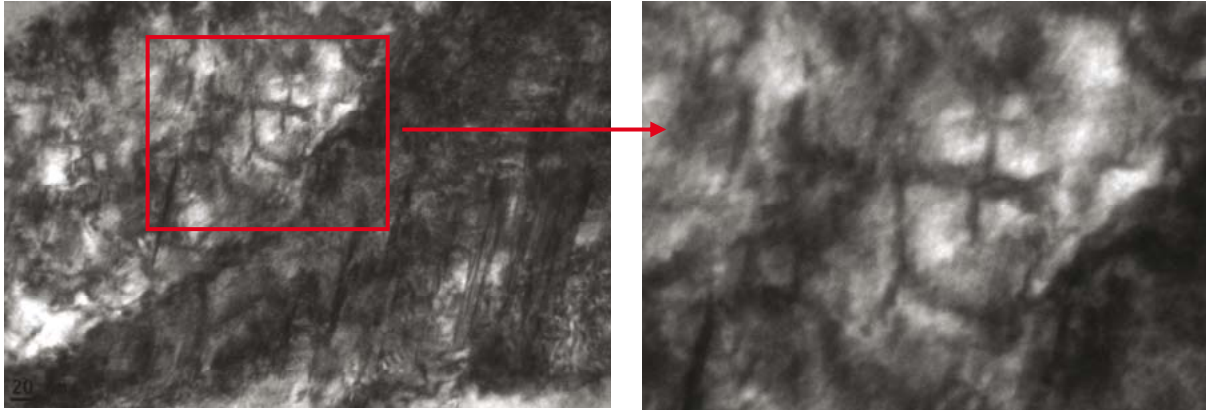


Figure 5 TEM micrographs of samples heat treated in mode B

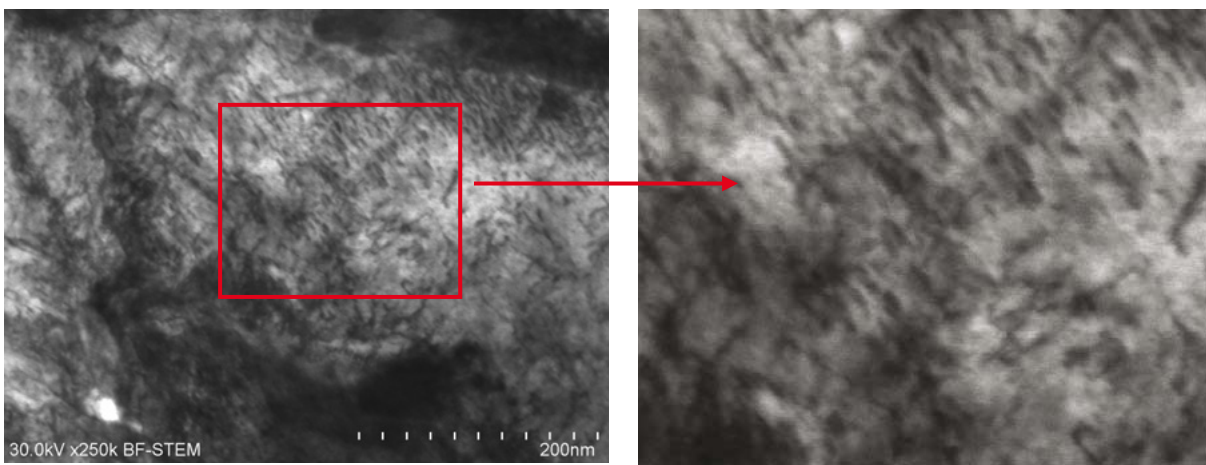


Figure 6 TEM micrographs of samples heat treated in mode C

3.3 TEM diffraction

When comparing the samples heat treated in mode C with these from the mode A, increased intensity of the reflections from the carbides was noted. From the reflections of the matrix the streaks in the $\langle 110 \rangle_{\alpha}$ direction are formed and linked along the $\langle 100 \rangle_{\alpha}$ direction, there is also a diffuse scattering around them (Fig. 7,9). This demonstrates the dissolution of some precipitations, what is also confirmed by the increase of the lattice parameter of the matrix.

When comparing samples from mode B and C, it can be concluded that already when heating up from cryogenic treatment temperature to room temperature, and then at the time of tempering, the evolution of clusters from globules at dislocations to the plate precipitations on planes $\{100\}_{\alpha}$ occurs (Fig. 8,9).

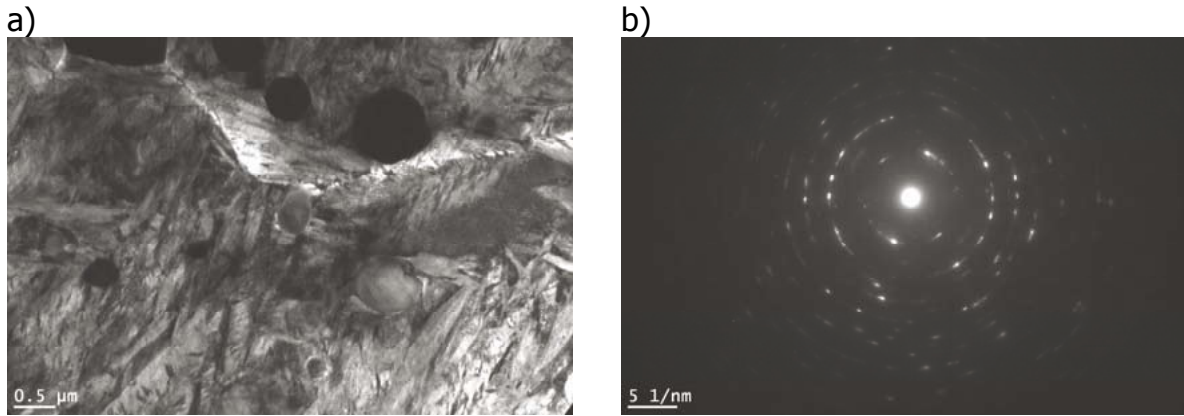


Figure 7 TEM micrograph (a) and diffraction pattern (b) of sample heat treated in mode A

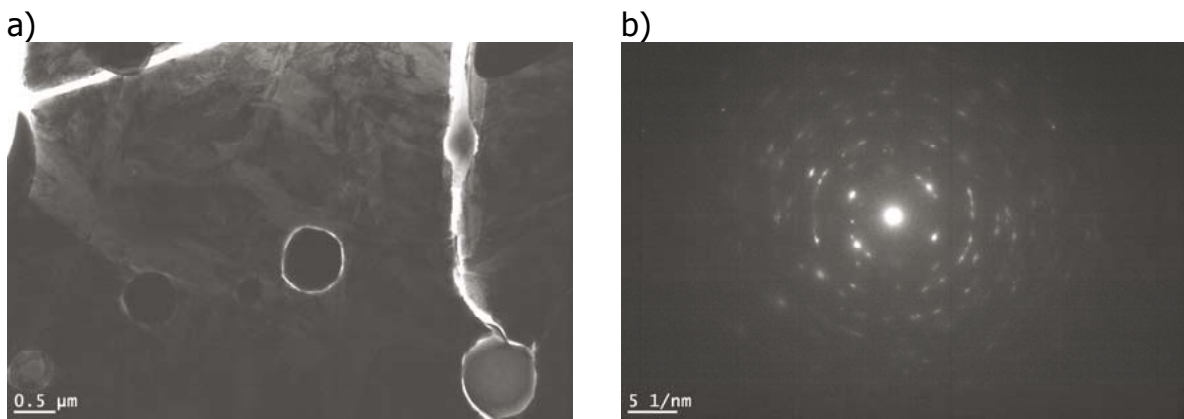


Figure 8 TEM micrograph (a) and diffraction pattern (b) of sample heat treated in mode B

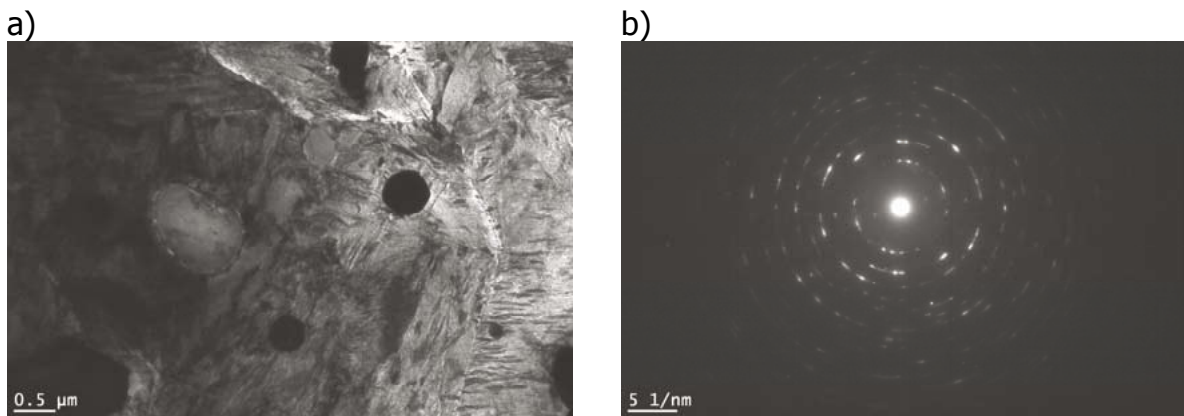


Figure 9 TEM micrograph (a) and diffraction pattern (b) of sample heat treated in mode C

3.4 Energy Dispersive X-ray Spectroscopy (EDS)

For comparative qualitative analysis of the chemical composition of carbide phases energy the dispersive X-ray spectroscopy and elemental mapping were used. Places of measurements are shown on Figure 10, while obtained results are presented in Table 3.

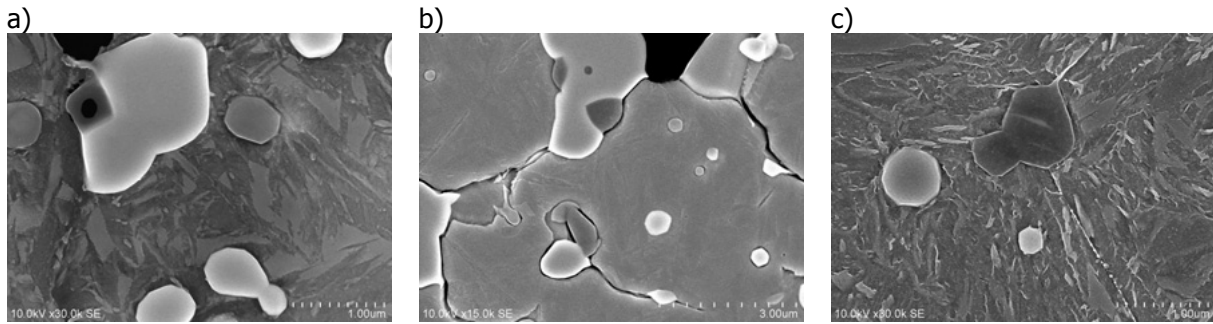


Figure 10 Places of measurements of chemical composition of samples heat treated in mode A (a), B (b) and C (c)

Table 3 Chemical composition, weight %

Mode	C	V	Cr	Fe	Mo	W
A	10.52	4.74	3.51	60.53	5.41	11.07
B	4.93	2.38	3.10	74.71	5.16	9.72
C	5.98	6.13	3.78	71.37	4.45	8.28

As can be seen from Table 3, in modes A and C, spheroidal VC carbides present in the matrix, with size smaller than 1 μm contain also molybdenum, tungsten and chromium. In two to three times larger oval M_6C carbides, located mainly at the grain boundaries, in addition to tungsten content, the molybdenum and small amount of chrome is present. In comparison with the sample after DCT and tempering (mode B) there is lower content of V, Cr and Mo. The content of tungsten is also lower than after standard heat treatment.

In samples heat treated in mode B the massive carbides at grain boundaries contain a considerable amount of tungsten and molybdenum, but no vanadium. In dispersive carbides there is the highest percentage of vanadium. Chromium is evenly distributed in the matrix. In comparison with mode A there is a higher amount of vanadium, lesser amount of tungsten and molybdenum and comparatively low amount of chromium.

In mode C, in large carbides there is a high amount of W and Mo; and low amount of V and Fe. The microstructure consist of more very fine carbides in the matrix, in a form of very evenly distributed plates.

3.5 Differential Scanning Calorimetry (DSC)

As it was mentioned at the outset, all samples were subjected to the identical thermal cycle: cooling down from the room temperature to LN_2 temperature, soaking for 5 minutes at cryogenic temperature, heating up to 400°C and cooling down back to the room temperature. The samples were cooled down and heated up at a rate of $10^\circ\text{C}/\text{min}$. Exemplary calorimetric measurements are shown on Figure 11, while the results of the analysis are summarized in Table 4.

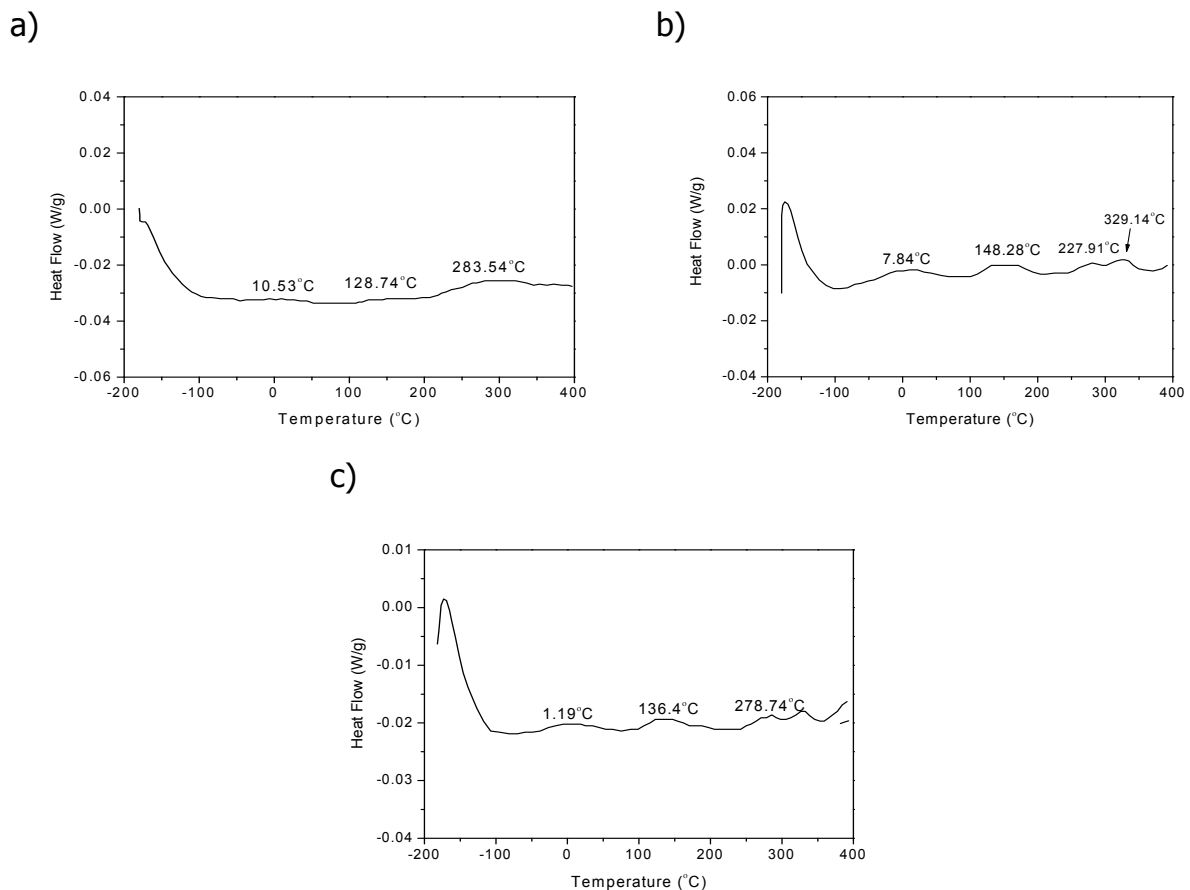


Figure 11 DSC thermograms of samples heat treated in mode A (a), B (b) and C (c)

As it is apparent from the thermograms and the data contained in Table 4, the samples heat treated for secondary hardness (modes A and C), reveal appearance of 3 peaks. The third peak in mode A shows an order of magnitude greater amount of generated heat, in comparison with mode C. In steel sample heat treated in mode B, also the fourth peak was observed, wherein the first three peaks, as compared to the mode A and C, almost didn't change their position on the axis of temperature. The first two low-temperature peaks were energetically richer.

The temperature range at which the exothermic thermal effects were recorded indicates that these effects are in the area of diffusion of interstitial atoms. This indicates a stage of unstable carbide dissolution and diffusion of interstitial atoms, probably carbon, into the clusters of carbide forming elements. Thermal effect related to the first, the lowest temperature peak, reveals the zonal stage of forming of clusters. Second peak may be dominated by the change of shape of clusters from globular to disc, what is distinctly illustrated by two first peaks of samples heat treated in mode B.

Thermal effects recorded at a temperature above 250 °C are probably associated with the precipitation of metastable B1 phase and the other phases remaining until reaching of the temperature of secondary hardness effect. It should be noted that the conditions of heat treatment for secondary hardness of the samples in the modes of A and C didn't complete the process of nucleation and growth of special carbides.

Table 4 Results of calorimetric examinations (DSC)

Mode	Temperature	Heat flow
	°C	J/g
A	10,5 (-27,3)	0,29
	128,7 (100,8)	0,64
	283,5 (212,4)	2,10
B	7,8 (-70,5)	1,79
	148,3 (102,2)	1,45
	277,9 (256,4)	0,23
	329,1 (306,4)	0,52
C	1,2 (-98,3)	0,65
	136,4 (100,0)	0,43
	278,7 (258,6)	0,13

In the brackets are given the temperatures of a beginning of the exothermic effect during heating up from the temperature of -196 °C to 400 °C. During cooling down of the samples from the room temperature to -196 °C, thermal effects were not observed.

4. Summary and discussion

Imaging of the structure using TEM showed that the martensite obtained after quenching, deep cryogenic treatment and heating up to the ambient temperature, has a lamellar-lenticular structure, internally twinned, with very high density of dislocations. At dislocations, inside martensite plates and at the grain boundaries there are present globular shaped clusters with the size of a few nanometers. In martensite twins the clusters, or already formed B1 carbides plates, are arranged on $\{100\}_\alpha$ planes.

Morphology of martensite of steel tempered for secondary hardness is characterized by a disappearance of twins and midribs. The size of primary austenite grains and size of carbide precipitations remain unchanged. There are differences in the dimensions of the martensite plates. In deep cryogenically treated samples dimensions of the plates are almost an order of magnitude shorter and thinner.

The structure of HS6-5-2 steel, regardless of the applied heat treatment, consists of primary carbides, $M_6C(Fe_3W_3C; Fe_4W_2C)$ containing Mo, V and Cr, and highly refined VC vanadium carbides, containing W, Mo and Cr. Qualitative assessment (elemental mapping) of the concentration of atoms of alloying elements in carbides indicates that this concentration (with the exception of tungsten) is higher after the deep cryogenic treatment.

In the clusters and surrounding matrix, there is a high stress state deforming the lattice structures, thus revealing the contours of the globules. The carbide lattice type is imposed by the steel matrix to minimize stresses. Coherent with the matrix crystal B1 structure decreases the carbide phase volume changes in comparison with the matrix by over a dozen percent and reduces the stress state in the carbide and matrix.

Qualitative analysis of changes of the matrix lattice parameter of quenched and deep cryogenically treated steel, showed the lowest value among the other tested modes of treatment. When comparing stage C to B it can be concluded that during tempering occurs the evolution of clusters from globular shapes located at dislocations to the plate precipitations on close-packed lattice planes. This process in the modes of treatment A and C was not completed. Probably at the stage of treatment B, the shape and chaotic arrangement of globules in the Fe_α matrix doesn't favour their rapid growth.

TEM images analyses of samples heat treated in mode B, with diffraction patterns and indexing of additional reflections, confirm that carbides precipitating during heating up from cryogenic temperature to room temperature have structure of B1 type. The stage of carbides growth is indicated by blurred and thickened streaks oriented in the $\langle 110 \rangle_{\alpha}$ direction. The TEM images of samples heat treated in mode C, as distinguished from the mode B, show almost identical plates parallel to $\{100\}_{\alpha}$.

In the C mode samples, the lattice parameter increases relatively. Also the increase of intensity of reflections from all of the steel phase components is observed. From the reflections of the matrix the streaks in the $\langle 110 \rangle_{\alpha}$ direction are formed and linked along the $\langle 100 \rangle_{\alpha}$ direction, there is also a diffuse scattering around them. In conclusion, the process of carbide dissolution is observed.

The nature of the calorimetric curve is consistent with the precipitation sequence. The first two thermal effects are probably connected with the creation of zones. The highest exothermic effect at 270-320 °C is associated with the precipitation of a more stable phase B1, remaining until the range of the secondary hardness effect.

5. Conclusions

Deep cryogenic treatment does not alter the amount and distribution of micron-sized special carbides, whereas it refines the substructure of martensite laths and plates. The rate of reduction of size is about ten times (about one order of magnitude).

In the quenched and deep cryogenically treated steel, after heating it up to room temperature, at dislocations in martensite and austenite there are present globular clusters with the size of a few nanometers, while at the boundaries of transformation twins and inside of the twins there are plates or discs located on $\{100\}_{\alpha}$ planes. As it was stated during electron diffraction in TEM investigations, they are probably carbides with a B1 lattice structure.

During the calorimetric investigations the certain amount of heat was released as a result of the thermal recovery process. Higher density of vacancies, higher internal work-hardening and stress relaxation propensity result in stability of B1 or carbides formed from B1.

During tempering the evolution of clusters-globules occurs, from the shape of the globules at dislocations to plate precipitations at close-packed lattice planes. Used in the studies times and temperatures of the processes, with or without DCT, didn't lead to the completing of evolution of clusters to a special carbides.

Acknowledgements

The presented investigations were conducted within the framework of Eureka-Eurostars Project E!4261 – TECTECH, titled "Novel methods of heat treatment and thermo-chemical treatment of tools and machine parts".

References

- [1] Kuo K.: J. Iron Steel Inst., 181, 1955, 128–134
- [2] Goldschmidt J.: Iron Steel Inst., 170, 1952 189–205
- [3] Kelly A., Nicholson R. B.: Precipitation Hardening Progress in Materials Science, Pergamon Press, N.Y. 1963
- [4] Hudremont E.: Handbuch der Sonderstahlkunde, 1956, Springer – Verlag Berlin, Zweiter Band, wyd ros. 1960

- [5] Sato T., Nisidzawa T.: „Nixon Kindzoky Hakkaisi” 1957, t. 21, n 11, 662–665, cyt. za poz. 14
- [6] Mukherill T., Stumph W. E., Sellars C. M., Tegart W. J.: J. Iron Steel Inst. 1969, v. 207, n, 5, 621–631
- [7] Kuo K. J.: J. Iron and Steel Inst. 1956, v. 170, n. 11 258–268
- [8] Inoue A., Arakawa S., Masumoto T.: Trans. Japan Inst. Metals, 1978, v. 19, n. 1, 11–17
- [9] Guinier A.: Solid State Physics, Academic Press, v. 9, 1959
- [10] Davis D. M., Raplh B.: J. Iron Steel Institute, 1972, v. 210, n 4, 262–264
- [11] Collongues: La non-stoechiometrie. Masson et Cle, Editeurs, Paris, 1971, s. 206/207, wydanie ros. “Mir” Moskwa z 1974
- [12] Chaczaturjan A. G., Teoria fazowych prewraszczenii i struktura twjordych rastworov, M. Nauka, 1974
- [13] Kurdjumov G. W., Utievski L. M., Entin R. I.: Prewraszczenia v zelezie i stali, M. Nauka 1977
- [14] Ustanovszczikov Ju. I.: Vtoricznoje tverenije konstrukcyjnych legirovannyh stalej, M. Metałurgia 1982.
- [15] Łaszko F. N., Zasławskaja L. W., Kozłova M. M.: Fizko-chimiczeskij analiz stalej i spławow, Izd, metałurgia, 1978
- [16] Collins, D.N.: Cryogenic treatment of tool steels. Advanced Materials and Processes, ASM International 1998, 12, 23–29
- [17] Meng F., Tagashira K., Azuma R., Sohma H.: Role of Eta-carbide Precipitations in the Wear Resistance Improvement of Fe-12Cr-Mo-V-1,4C Tool Steel by Cryogenic Treatment. ISIJ International Vol 34 (1994), No 2, pp. 205-210
- [18] Yun D., Xiaoping L., Hongshen X.: Deep-cryogenic treatment of high speed steel and its mechanism. Heat Treatment of Metals, 1988, 3, 55–59
- [19] Cajner F., Leskovsek V., Landek D., Cajner H.: Effect of Deep-Cryogenic Treatment on High Speed Steel Properties, Materials end Manufacturing Processes, 24: 743–746, 2009

¹ Prof. Jerzy Jeleńkowski, Ph.D. D.Sc., Institute of Precision Mechanics, Duchnicka 3, 01-796 Warsaw, Poland, Tel.: +48 22 56 02 661, e-mail: jjele@imp.edu.pl

² Aleksander Ciski, M.Sc. Eng., Institute of Precision Mechanics, Duchnicka 3, 01-796 Warsaw, Poland, Tel.: +4822 56 02 942, e-mail: ciski@imp.edu.pl

³ Tomasz Babul, Ph.D. Eng., Institute of Precision Mechanics, Duchnicka 3, 01-796 Warsaw, Poland, Tel.: +48 22 56 02 805, e-mail: tomasz@imp.edu.pl

SOLIDIFICATION MICROSTRUCTURES IN THE POWDER PARTICLES OF HYPEREUTECTIC IRON BASED ALLOY

Martin Kusý¹, Mária Behúlová², Peter Grgáč³

Abstract

In the atomisation, very different undercoolings and consequently a variety of microstructures can develop in the quasi-spherical particles with the same diameter. Five main types of solidification microstructures were identified in the particles of rapidly solidified powder from the Ch3F12 hypereutectic iron based alloy. Based on the mathematical model, the reasons for the development of various types of solidification microstructures are discussed.

Keywords: tool steel of ledeburite type, undercooling, rapid solidification

1. Introduction

The basic principles and effects of rapid solidification processing of melts have been successfully exploited in several progressive technologies of production and treatment of materials. High cooling rates of the melt enable to attain large melt undercoolings below the equilibrium liquidus temperature [1-2] leading to the nucleation and rapid nonequilibrium solidification of phases and morphological variants of primary microstructures which are impossible to obtain by conventional metallurgical technologies. Generally, the increase of initial melt undercooling results in the enhancement of homogeneity of solid phase, microstructure refinement, to the formation of metastable crystalline and quasi-crystalline phases, and also metallic glasses [3-5]. The development of final solidification microstructures is determined particularly by thermodynamic and thermokinetic conditions of rapid cooling, nucleation and solidification of melt [5-7].

Tool steels of ledeburite type form a group of alloys produced by powder metallurgy using the gas atomization of melt followed by consolidation of rapidly solidified (RS) particles. They are characteristic by the high wear resistance resulting from the carbide phases of solidification origin present in their microstructure. Size, morphology and distribution of carbides have a crucial influence on their technological and utility properties [8].

In the paper, the solidification microstructures developed in hypereutectic Fe–Cr–V alloy prepared by the nitrogen gas atomisation are presented and analysed. Based on the thermo-kinetic newtonian model of rapid solidification of spherical droplets, the thermo-physical conditions responsible for the development of morphologically different types of carbide phases in the single rapidly solidified powder particle are predicted and discussed.

2. Experimental material and methods

RS powder from Ch3F12 hypereutectic iron based alloy with the chemical composition of 3% C–3% Cr–12% V (wt.%) was prepared by the nitrogen gas atomization. Globular powder particles were screened into the thirteen standard size fractions ranging from less than 40 μm up to 250–400 μm .

For microstructural analysis, RS powder particles were bounded by electrolytically deposited nickel, metallographically prepared using standard methods and NITAL etched. Methods and experimental techniques of light microscopy (LM), scanning electron microscopy (SEM), transmission electron microscopy (TEM), Mössbauer spectrometry and X-ray diffraction analysis were applied. The analysis of minimum 200 particles from each size fraction was accomplished to evaluate the relative proportion of the main types of solidification microstructures in the analysed powder.

3. Results and discussion

Based on Mössbauer spectra of RS powder obtained in transmission geometry (Fig. 1a) and X-ray diffraction analysis (Fig. 1b), the main constituent of the rapidly solidified powder was found to be the metastable austenite [9-10]. Magnetic α -phase was identified as a minor constituent. The presence of vanadium rich carbide phases of M_4C_3 and chromium rich carbide phases M_7C_3 types was detected by X-ray analysis and selection area diffraction by TEM on single-stage carbon replicas [11-12].

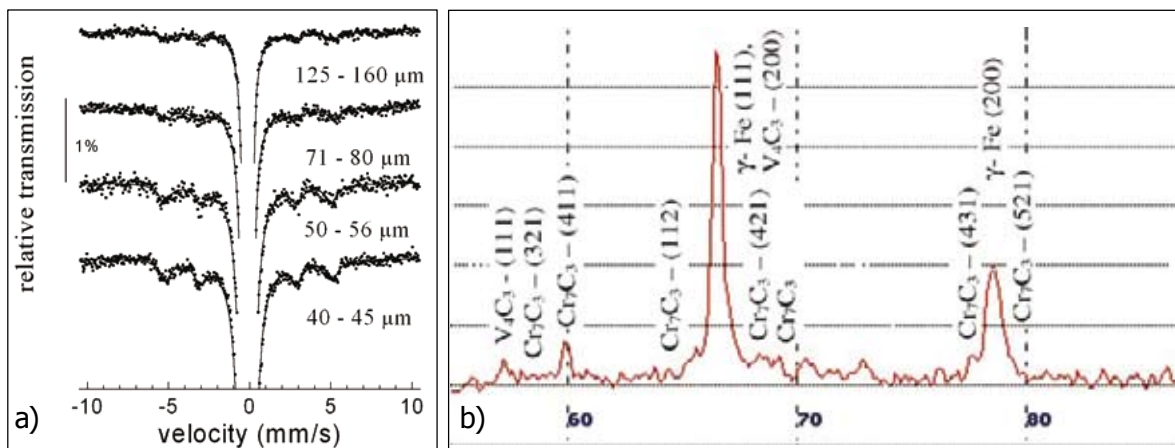


Fig. 1 Phase identification a) Mössbauer spectra of RS powder particles from chosen standard size fractions and b) X-ray diffraction pattern of RS powder in the base state

Based on the morphological analysis of primary microstructures, five main types of solidification microstructures were identified in the RS powder particles:

1. microstructure with the disperse globular carbides (Fig. 2a) – is defined as a structure with globular and quasi-globular carbide particles evenly dispersed in the matrix.
2. microstructure with star-like carbides (Fig. 2b) – is characteristic by the presence of isolated carbides with the morphologically variable multi-arm star-like formations.
3. microstructure with the primary carbides in the centres of eutectic colonies (Fig. 2c) – this structure contains star-like carbides surrounded by lamellar eutectic whereby the primary carbide phase intergrowths continually to the carbide skeleton of eutectic colony.

4. microstructure with eutectic colonies without primary carbides (Fig. 2d) – colony with the characteristic features of sectorial growth of lamellar carbides, in the center of eutectic colony the primary carbide was not developed.
5. microstructure with eutectic spherulites (Fig. 2e) – microstructure without primary carbides is characteristic by a very fine lamellar morphology of eutectic formations with quasi-spherical shape.

The map of solidification microstructure population (Fig. 2f) shows the percentage representation of single types of solidification microstructures in standard size fractions. Microstructures with globular and star-like carbides were found over the entire range of granulometric fractions. The microstructure with primary carbides in the centres of eutectic colonies and eutectic colonies without primary carbides were observed only in the RS particles less than 125 μm in diameter. Eutectic spherulites were identified in the particles with diameter smaller than 71 μm .

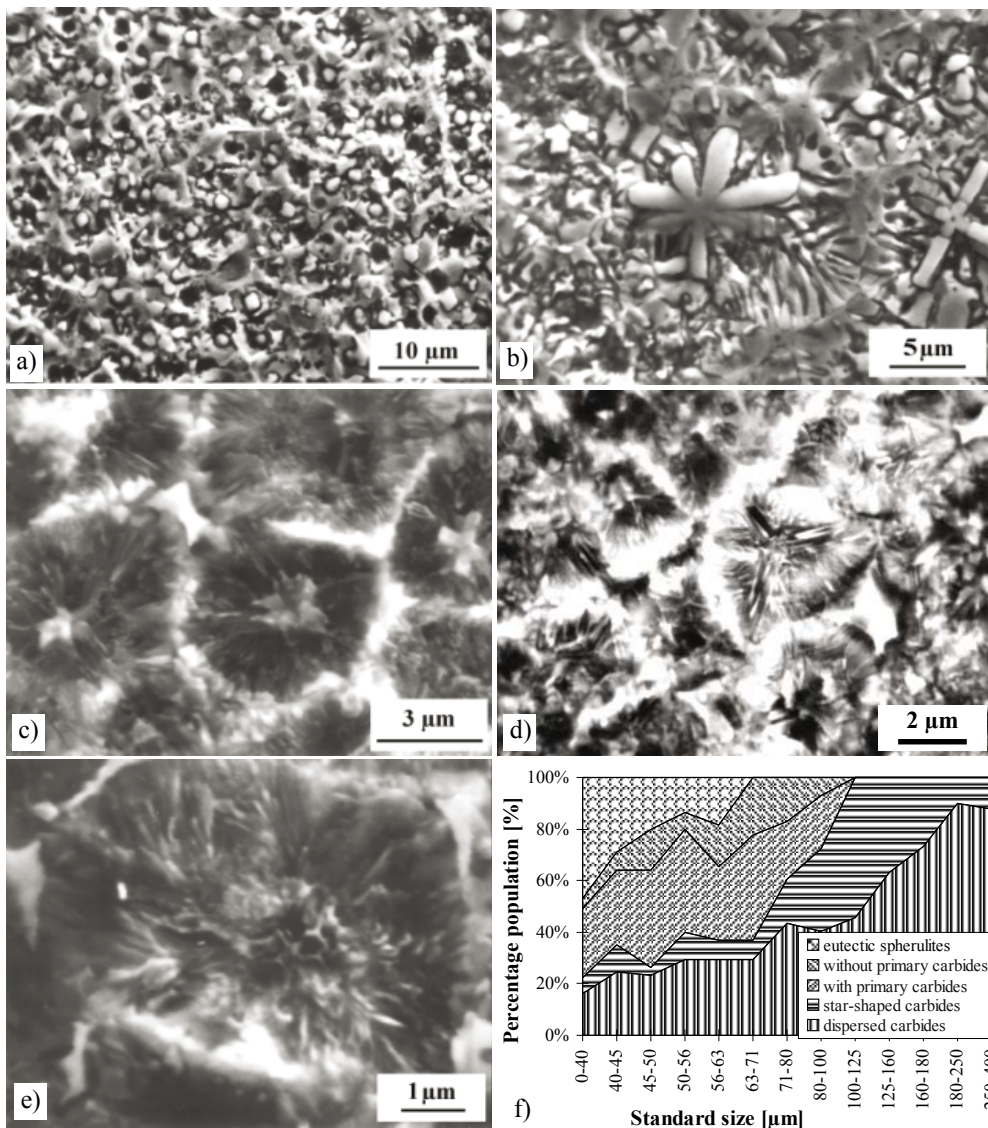


Fig. 2 Morphological variants of solidification microstructures observed in hypereutectic Ch3F12 alloy a) microstructure with the dispersed globular carbides, b) microstructure with the star-like primary carbides, c) microstructure with the primary carbides in the centers of eutectic colonies, d) microstructure with eutectic colonies without primary carbides, e) microstructure with eutectic spherulites refined and f) their percentage population in investigated granulometric fractions

Generally, the cooling and solidification of particles in atomization process proceeds in several stages: rapid cooling of molten particle by atomizing gas, nucleation, rapid crystal growth during recalescence connected with fast temperature increase due to the latent heat released (quasi-adiabatic phase of solidification), quasi-isothermal period of structure development in the semi-solidified particle at approximately constant temperature and finally, the cooling of solidified particle.

The nucleation temperature (the initial melt undercooling below the equilibrium liquidus temperature achieved before nucleation) depends mainly on the intensity of cooling and the melt purity. As the smaller particles are quenched more intensive, the larger initial undercoolings can attain supposing that particle solidification starts by homogeneous nucleation [12-13]. However, the heterogeneous nucleation with not so high initial undercooling is more probable. The level of initial undercooling consequently influences the recalescence phase through the velocity of the solid-liquid phase interface and the rate of latent heat released during solidification. The intensity of particle cooling becomes more relevant again in the phase of quasi-isothermal solidification influencing the duration of this period. According to the recalescence temperature and duration of the quasi-isothermal plateau, microstructures developed in the recalescence period of rapid solidification can be influenced or remain unaffected during quasi-isothermal period of crystallization [14].

Based on the morphological features, the microstructures identified in powder particles from Ch3F12 hypereutectic alloy were divided into two groups: microstructures morphologically non-affected and affected during post-recalescence period of solidification [9-10]. The first group consists of microstructures containing lamellar morphology of vanadium rich carbide phases of M_4C_3 type (eutectic spherulites and eutectic colonies with and without primary carbides) which does not alter during the quasi-isothermal period of solidification. The second group of microstructures is typical by the presence of "anomalous" eutectic with spherical carbide phases (microstructure with dispersed globular carbides and star-like carbides) developed presumably due to the thermally induced fragmentation and spheroidisation of carbide lamellae in the phase of quasi-isothermal solidification.

The thermo-kinetic newtonian model of cooling and rapid solidification of a spherical droplet in the gas atomization process was developed to obtain the quantitative values for the explanation and prediction of microstructure development in powder particles from the Ch3F12 tool steel and to study the influence of different cooling conditions and parameters on the thermal history of a rapidly solidified droplet [12-13]. The process of droplet solidification in the gas atomization starts likely by heterogeneous nucleation with various initial undercoolings. Fig. 3 and Fig. 4 illustrate the influence of nucleation temperature on the thermal history of droplets with diameters of 50 μm and 300 μm solidifying in the nitrogen gas atomization with the initial gas velocity of 500 $\text{m}\cdot\text{s}^{-1}$ and quantify the corresponding recalescence temperatures and durations of quasi-isothermal plateau in the dependence on the particle diameter. The supposed undercoolings correspond to the values obtained by levitation experiments in similar Fe-C-Cr-V alloy [15].

The overall duration of the cooling and solidification of the larger droplet is substantially longer (Fig. 3a,b). The decrease in the nucleation temperature results in the lower recalescence temperature and the shorter time of quasi-isothermal period of solidification. The recalescence temperatures are higher than the equilibrium solidus temperature of 1290 $^{\circ}\text{C}$ (Fig. 4a). Duration of the quasi-isothermal plateau (Fig. 4b)

ranges from about 0.2 milliseconds for the particles 50 μm in diameter nucleated at the temperature of 1100 $^{\circ}\text{C}$ to more than 60 milliseconds for the droplets with diameter of 400 μm started solidification at the temperature of 1400 $^{\circ}\text{C}$.

Based on the comparison of results of numerical simulation and microscopic analyses in the form of microstructural map (Fig. 2f), the initial undercooling below the equilibrium liquidus temperature for the development of microstructure with eutectic spherulites was estimated to be more than 280 $^{\circ}\text{C}$. The initial undercooling at the level of approximately 270 $^{\circ}\text{C}$ can be sufficient for the formation of microstructure with eutectic colonies. In the droplets with diameter larger than 100 μm , the extension of quasi-isothermal plateau together with enhancement of recalescence temperature can generate advantageous time and thermal conditions for the thermally induced fragmentation and following globularization of eutectic formations developed during the recalescence period. The minimum time necessary to break-up the finest carbide lamellae was estimated to be approximately 2 milliseconds. However, the degree of globularisation depends on the cooling conditions of solidifying particles governed the level of recalescence temperature and the duration of quasi-isothermal solidification.

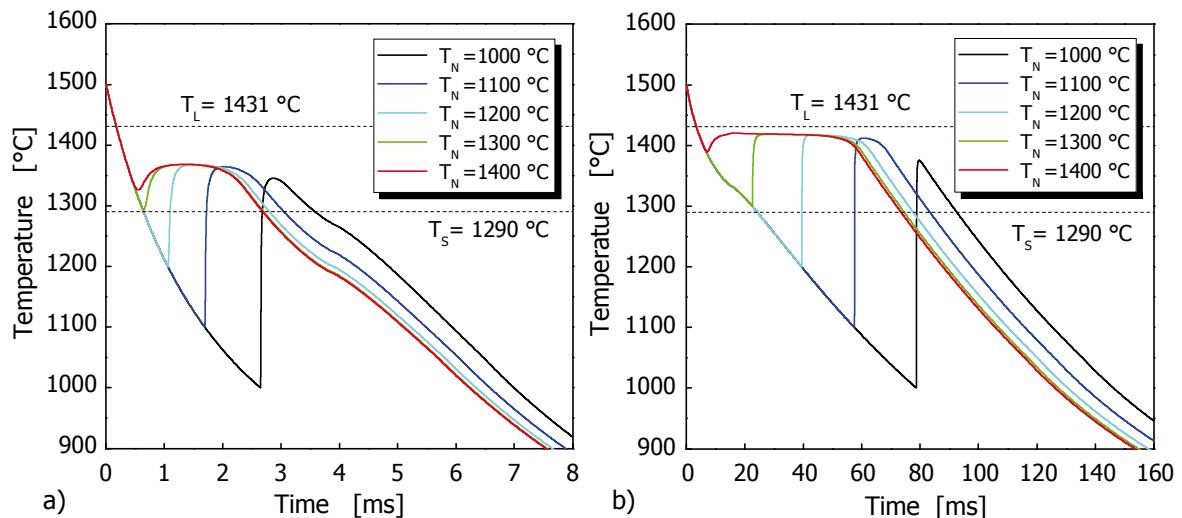


Fig. 3 The thermal history of rapidly solidifying droplets with diameter of a) 50 μm and b) 300 μm nucleated at different nucleation temperatures

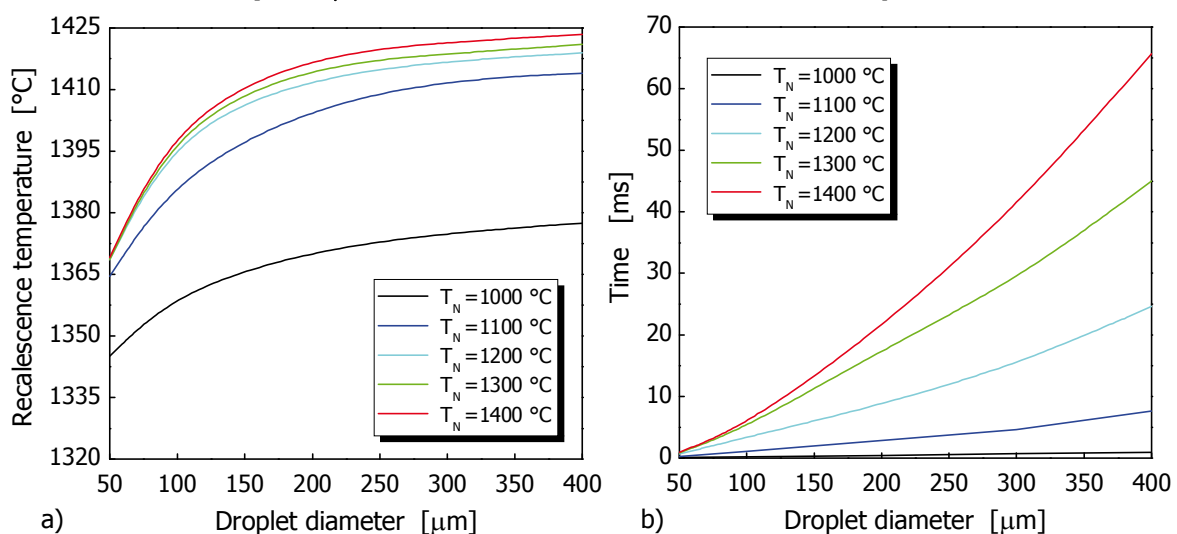


Fig. 4 Dependence of a) the recalescence temperature and b) duration of quasi-isothermal solidification on the droplet diameter for different supposed nucleation temperatures

4. CONCLUSIONS

Five main types of solidification microstructures were identified in the rapidly solidified powder particles from the CH3F12 hypereutectic alloy. Based on the morphological features of carbide phases and computed thermal history of RS particles, the microstructures were divided into two groups - microstructures morphologically non-affected during the post-recalcence period of solidification and microstructures with morphological transitions occurring during the quasi-isothermal period of solidification. The thermo-physical conditions for the development of different microstructures were predicted using the prepared thermo-kinetic mathematical model of rapid solidification of a spherical droplet in atomization process.

Acknowledgements

The research has been supported by VEGA MS and SAV of the Slovak Republic within the projects No. 1/0837/08, 1/0148/08 and the EU project ITMS 26220120014.

References

- [1] Jacobson, L. A., McKittrick, I.: Rapid solidification processing. *Mater. Sci. Eng.*, Vol. R11, No 8, 1994, p. 355.
- [2] Herlach, D., Galenko, P., Holand-Moritz, D.: *Metastable solids from undercooled melts*. Pergamon Press, Amsterdam, 2007, ISBN 978-0-08-04368-8
- [3] Herlach, D. M.: Non-equilibrium solidification of undercooled metallic melts. *Mater. Sci. Eng.*, Vol. R12, 2004, p. 177
- [4] Perepezko, J. H., Hiladad, K.: Metallic glass formation reactions and interfaces. *Mater. Sci. Eng. B*, Vol. 148, 2008, p. 171
- [5] Perepezko, J. H., Hockel, P. G., Paik, J. S.: Initial crystallization kinetics in undercooled droplets. *Termochimica Acta*, Vol. 388, 2002, p. 129
- [6] Perepezko, J. H.: Nucleation controlled phase selection during solidification. *Mater. Sci. Eng.*, Vol. A 413–414, 2005, p. 389
- [7] Clavaguera-Mora, M. T.: *et al.* Crystallisation kinetics and microstructure development in metallic systems. *Progress in Materials Science*, Vol. 47, 2002, p. 559
- [8] Grgač, P.: *High alloyed tool materials prepared by powder metallurgy of rapidly solidified particles*. Habilitation thesis. Trnava, 1991
- [9] Kusý, M.: *PhD. Thesis*. MTF STU Trnava, 2001.
- [10] Kusý, M., Grgač, P., Behúlová, M., Výrostková, A., Miglierini, M.: Morphological variants of carbides of solidification origin in the rapidly solidified powder particles of hypereutectic iron alloy. *Mater. Sci. Eng.*, Vol. A375-377, 2004, p. 599
- [11] Kusý, M.: *et al.* Solidification microstructures in the rapidly solidified powder of high alloyed V-Cr-tool steel. *J. of Mater. Process. Technology*. Vol. 157–158, 2004, p. 729
- [12] Behúlová, M.: *PhD. Thesis*. Sjf STU, Bratislava, 1995
- [13] Behúlová, M.: Influence of initial nitrogen gas velocity on the microstructure development of Ch3F12 alloy in atomization process. *Metallic materials*, Vol. 43, No. 2, 2005, p. 145.
- [14] Karma, A.: Model of grain refinement in solidification of undercooled melts. *Int. Journal of Non - Equilibrium Processing*, Vol. 11, 1998, p. 201
- [15] Grgač, P. *et al.* Influence of melt undercooling on the microstructure of levitated Cr–Mo–V tool steel. *Mater. Sci. Eng.*, Vol. A449-451, 2007, pp. 658-661

¹ Assoc. Prof. Ing. Martin Kusý, PhD., Slovak University of Technology in Bratislava, Faculty of Materials Science and Technology in Trnava, Paulinska 16, 917 24 Trnava, Slovak Republic, Tel.: +421 918 646047, e-mail: martin.kusy@stuba.sk

² Assoc. Prof. RNDr. Mária Behúlová, CSc., Tel.: +421 33 5511601 36, e-mail: maria.behulova@stuba.sk

³ Prof. Ing. Peter Grgač, CSc., Tel.: +421 905 373205, e-mail: peter.grgac@stuba.sk

***Tento článok vznikol vďaka podpore v rámci
OP Výskum a vývoj pre projekt
Centrum pre vývoj a aplikáciu
progresívnych diagnostických metód
v procesoch spracovania kovových
a nekovových materiálov, ITMS: 26220120014,
spolufinancovaný zo zdrojov
Európskeho fondu regionálneho rozvoja.***



Európska únia
Európsky fond regionálneho rozvoja



Podporujeme výskumné aktivity na Slovensku/
Projekt je spolufinancovaný zo zdrojov EÚ

INFLUENCE OF INITIAL PEARLITE MORPHOLOGY ON THE RESULTING STRUCTURE AND DISTRIBUTION OF DEFORMATION AFTER COLD FLOW FORMING PROCESS

Malina J.¹, Jirková H.², Mašek B.³

Abstract

An advanced technology enabling the manufacture of stepped hollow products which are hard to manufacture using conventional technologies, and which at the same time contributes to the effective use of the material, is flow forming process. The purpose of our research was to evaluate the influence of the initial pearlite morphology on the formability of a low-alloyed steel workpiece using this technology.

Keywords: pearlite morphology, reduction rolling, deformation

1. Introduction

A stepped hollow shaft made from low-alloyed steel 16MnCrS5 was formed by flow forming process. Tubes with various initial technologies and mechanical properties were used as workpieces. The influence of the initial morphology of pearlite in the workpieces was investigated, not only in relation to formability but also in relation to the size of the reduction and the quality of the internal and external surfaces of the resulting product. The changes in microhardness were evaluated on the finished part, which provides information about the distribution of deformation across the wall of the workpiece. Mechanical properties were measured at selected sites on the part. Finally, the correlation between structure, ultimate strength, microhardness HV 0.2 and size of reduction of the initial workpiece was evaluated. From these results it is possible to design a suitable pearlite morphology for achieving a high quality workpiece.

2. The initial state of workpiece

The material of the initial thin walled workpiece used in the experiment was 16MnCrS5 steel with chemical composition as in Table 1. The 60mm diameter workpiece with 6mm walls was reduced to the required diameters of 45mm and 40mm (Fig.1).

Table 1 Chemical composition of 16MnCrS5 steel

Element	C	Si	Mn	Cr	S	P
%	0.16	0.4	1.2	1.0	0.03	0.03

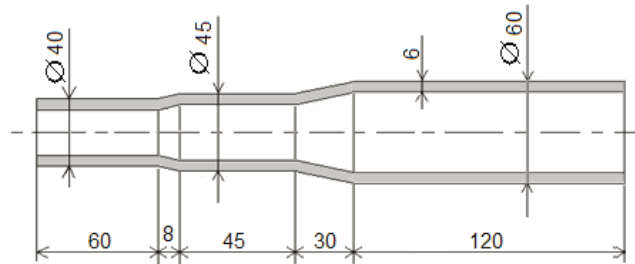


Figure 1 Diagram of the resulting form of the product after flow forming process

Reduction to the required diameter was performed on workpieces with three different pearlite morphologies. The first variant contained pearlite in a globular form (Fig. 2). This pearlite morphology should create maximum formability of the material. Microhardness was 157 HV 0.2 and ultimate strength was 472 MPa.

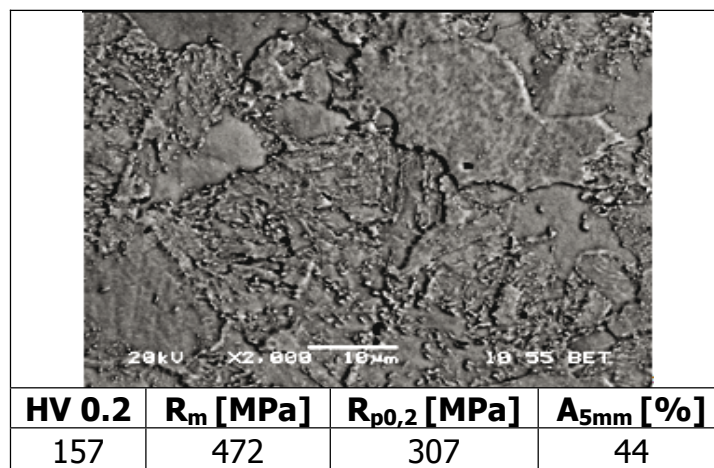


Figure 2 Detail of ferrite-pearlite structure with globular pearlite

The structure of the second variant contained a mix of lamellar and globular pearlite with a microhardness of 172 HV 0.2 and ultimate strength 508 MPa (Fig.3)

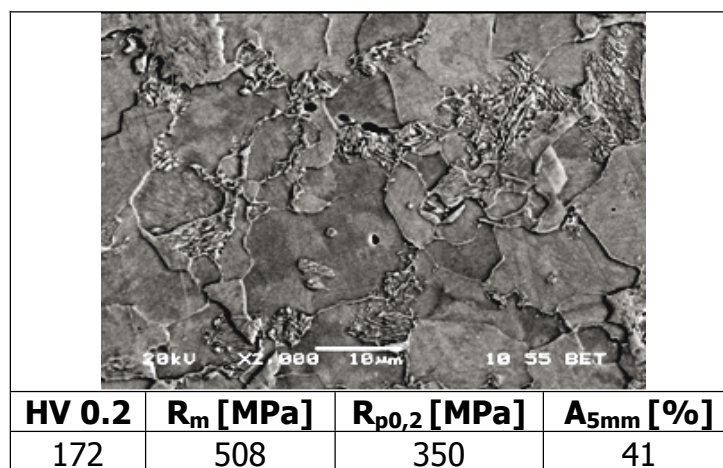


Figure 3 Ferrite-pearlite structure with mixed pearlite morphology

This structure was selected in order to achieve better formability created by the globular pearlite and greater strength from the lamellar pearlite.

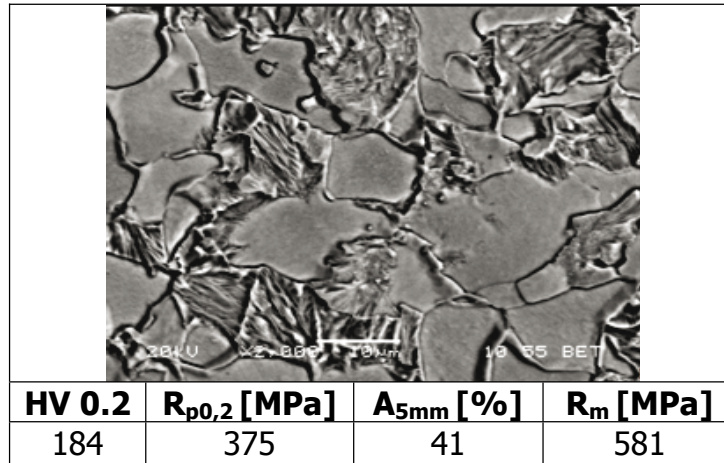


Figure 4 Detail of ferrite-pearlite structure with lamellar cementite

For the third variant, the material used contained only lamellar morphology with greater strength but lower formability. Its microhardness was 184 HV 0.2 and ultimate strength 581 MPa (Fig. 4).

3. Experiment

Flow forming was carried out at room temperature with intensive cooling especially in the deformation regions. Feed speed was 2 mm/rev, which combines effective use of machine time with the possibility of achieving the required deformation material.

3.1 Evaluation of deformation of surface layers

An area 0.25 mm from the surface was selected for comparison of structures after individual reductions and for different material states.

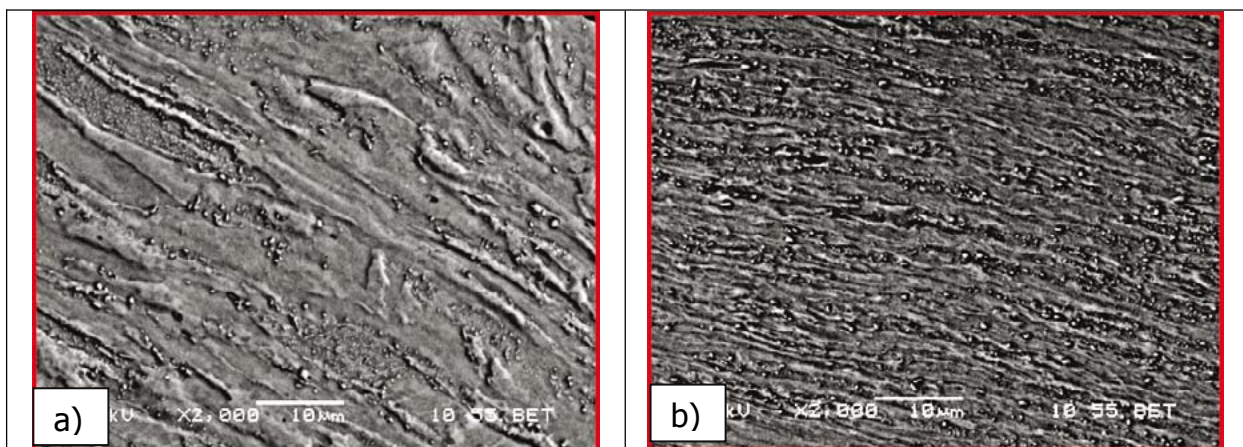


Figure 5 Globular structures in the surface layer in cross section after reductions to diameters a) 45 cm and b) 40 cm at a distance of 25 mm from the external surface of the workpiece

For the material with globular pearlite morphology with reduction to 45 mm, there is significant deformation and relatively even distribution of deformation in the structure, particularly in the surface layers (Fig. 5a). As distance increases from the

surface, deformation is not so marked. After reduction to 40 mm, the high formability of the material leads to significant deformation of the initial structure resulting in a strongly aligned ferrite structure with evenly dispersed cementite (Fig. 5b).

Table 1 Values of microhardness and mechanical testing a) after reduction to 45 mm diameter and b) after reduction to 40 mm

a)	HV 0.2	R _m [MPa]	R _{p0,2} [MPa]	A _{5mm} [%]	b)	HV 0.2	R _m [MPa]	R _{p0,2} [MPa]	A _{5mm} [%]
		202	620	618		26		210	640

After reduction to the required diameter, samples were taken from the walls parallel to the external surface. They were subjected to mini tension testing and microhardness values of HV 0.2 were also obtained (Tab. 1). From these results the expected increase in mechanical properties as the size of deformation increases is clear. Maximum hardness values in the centre of the wall were 210 HV and ultimate strength 640 MPa.

Forming of the second structural variant with a mixed lamellar-globular pearlite morphology leads to a greater concentration of deformation in the ferritic areas and less in the cementite areas. The cementite is 'stretched' in the direction of the deformation. The pearlite areas are only broken down locally and the presence of remnant lamellar cementite is apparent in the structure (Fig. 6a). Reduction to the smallest diameter leads to considerable breakdown of the lamellar pearlite, nevertheless lamellar pearlite is still observed in several areas (Fig. 6b). Finally, material is removed from the workpieces to evaluate the mechanical properties of the final product after reductions to both diameters (Tab. 2).

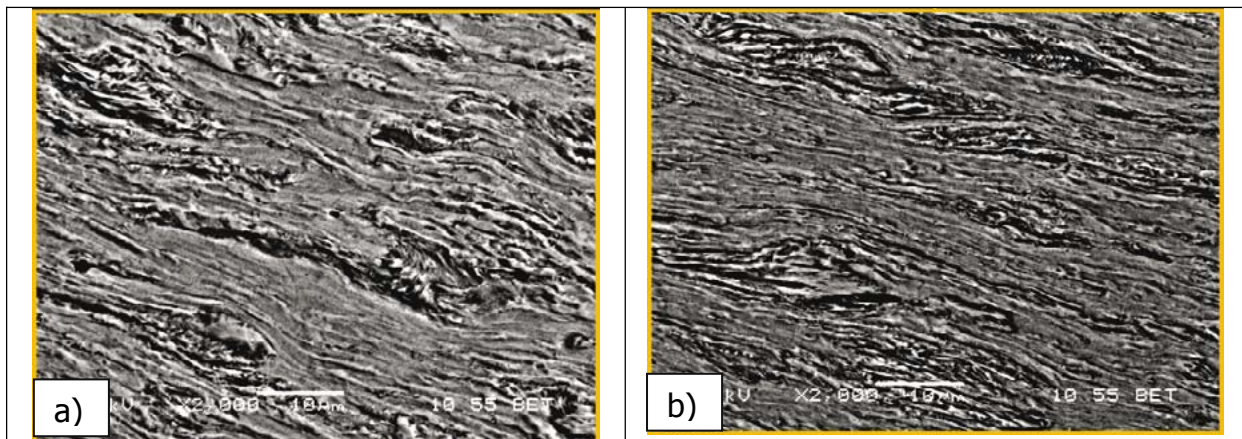


Figure 6 Originally mixed structure in surface layers in surface layers in cross section after reductions to diameters a) 45 mm and b) 40 mm at a distance of 25 mm from the external surface

Table 2 Values of microhardness and mechanical testing a) after reduction to 45 mm diameter and b) after reduction to 40 mm

a)	HV 0.2	R _m [MPa]	R _{p0,2} [MPa]	A _{5mm} [%]	b)	HV 0.2	R _m [MPa]	R _{p0,2} [MPa]	A _{5mm} [%]
		215	657	555		26		228	683

As in the first case, the larger the reduction, the higher the microhardness values. Reduction to the smallest diameter resulted in a microhardness of 228 HV 0.2 and ultimate strength of 683 MPa.

The final material variant with initial lamellar pearlite morphology exhibited the lowest formability of all three variants, and reduction to the middle diameter resulted in only minimal deformation to the structure in the surface areas (Fig. 7a). After reduction to the smallest diameter, significant deformation of the surface layers was apparent, but mostly concentrated in the ferritic areas; areas of lamellar pearlite were only minimally deformed (Fig. 7b).

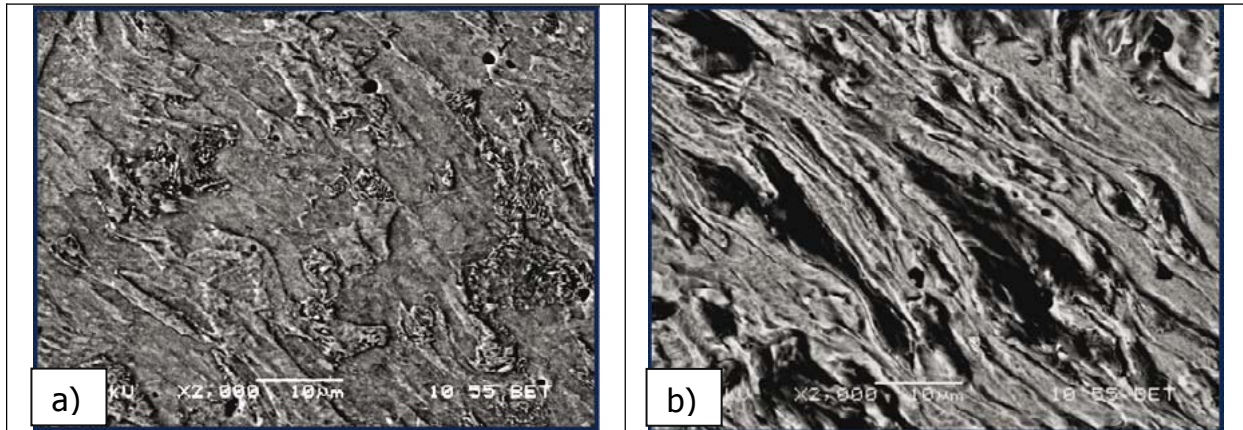


Figure 7 Originally lamellar structures in surface layers in cross section after reduction to diameters a) 45 cm and b) 40 cm at a distance of 25 mm from the external surface

Samples were taken from the centre of the walls for mechanical testing. Microhardness of HV 0.2 for this variant was the highest value of all three variants. Reduction to the smallest diameter resulted in a microhardness of 248 HV 0.2. After this reduction, the highest ultimate strength values were also obtained, 750 MPa, which is approximately 10% higher than the variant with the globular pearlite and approximately 17% more than the variant with mixed morphology (Tab. 3).

Table 3 Values of microhardness and mechanical testing a) after reduction to 45 mm diameter and b) after reduction to 40 mm diameter

a)	HV 0.2	R _m [MPa]	R _{p0,2} [MPa]	A _{5mm} [%]	b)	HV 0.2	R _m [MPa]	R _{p0,2} [MPa]	A _{5mm} [%]
	238	740	716	26		248	750	736	26

3.2 Comparison of values of microhardness and ultimate strength Srovnávací vyhodnocení mikrotvrlosti a mezí pevnosti

The results of mechanical testing for all variants were compared to find any relationships between microhardness, size of reduction, structure and ultimate strength. Using regression analysis (least squares method) on the results, a coefficient for the relation between the ultimate strength and microhardness HV 0.2 was established. The value of this coefficient is 3.08, standard deviation ± 0.08 and it enables ultimate strength values to be determined in the centre of walls for products with a microhardness of HV 0.2. A graph was also plotted for determining

the value of ultimate strength on the basis of the microhardness of the initial workpiece (Fig. 7). It is clear that pearlite morphology has a significant effect on this coefficient.

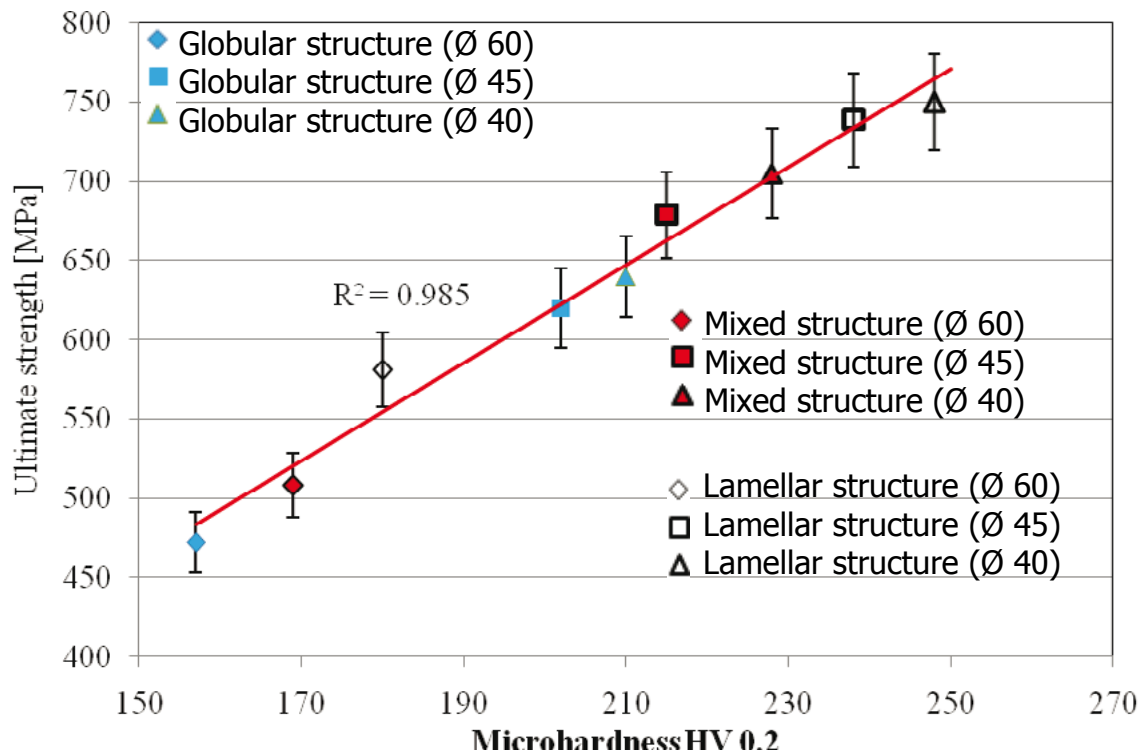


Figure 7 Graph to determine relationship between strength and microhardness HV 0.2 with reliability value R^2 0.985

4. Conclusion

Evaluation of the results obtained from the workpieces with all three pearlite morphologies (globular, mixed and lamellar) and reduced using flow forming process, shows that 16MnCrS5 is formable using the selected technology in all three material states.

The coefficient expressing the relationship between microhardness and ultimate strength enables relatively accurate prediction of the mechanical properties of a final product on the basis of the microhardness of the initial workpiece, and also in relation to the size of the reduction.

Acknowledgements

This paper includes results created within the project 1M06032 Research Centre of Forming Technology and within the project P107/10/2272 Accelerated Carbide Spheroidization and Grain Refinement in Steels. The projects are subsidised from specific resources of the state budget for research and development.

¹ Ing. Jiří Malina, Západočeská univerzita, Výzkumné centrum tvářecích technologií, mail: mali@centrum.cz

² Dr. Ing. Hana Jirková Ph.D., Západočeská univerzita, Výzkumné centrum tvářecích technologií, mail: hstankov@vctt.zcu.cz

³ prof. Dr. Bohuslav Mašek, Západočeská univerzita, Výzkumné centrum tvářecích technologií, mail: masekb@vctt.zcu.cz

UNCONVENTIONAL THERMOMECHANICAL TREATMENT OF ADVANCED HIGH STRENGTH LOW-ALLOYED STEEL

Bohuslav Mašek¹, Hana Jirková², Danuše Klauberová³, Martin Petrevec⁴,
Přemysl Beran⁵

Abstract

Modern advanced high strength steels processed in unconventional ways of heat or thermomechanical treatment can reach substantially better properties compared to conventional treatments. This paper presents new possibilities of thermomechanical treatment for the 42SiCr steel. Through the conventional treatment very high strength can be reached, but the ductility drops down to lower values. The aim of this experiment was to design and test an unconventional thermomechanical treatment procedure in order to reach the yield strength to 2000 MPa with ductility over 10%. For this purpose, the Q-P process (quenching and partitioning process) was modified and optimized in several steps. The stability of retained austenite was determined by means of neutron diffraction under cold deformation. The influence of the technological process parameters on the structure development was documented via metallography and the resulting mechanical properties were measured by means of tensile test.

Keywords: *unconventional thermomechanical treatment, Q-P process, low-alloyed steel*

1. Introduction

One of the goals when developing new kinds of steels is their economical efficiency, whereas the properties of such steels are mostly achieved not by adding high amounts of alloying elements, but using special procedures of heat treatment or thermomechanical treatment. Three new processing strategies have been developed in recent years: the TRIP-effect, long-time low-temperature annealing and the quenching and partitioning (Q&P) process. The first two methods employ the combination of bainitic ferrite and retained austenite to obtain good mechanical properties. Carbide precipitation is suppressed and carbon is used for the chemical stabilization of retained austenite during this treatment. In the case of the third treatment, the Q-P process, martensitic structure is achieved in place of bainitic ferrite. This structure enables higher strength values than in the two previous cases. The properties of the resulting structures are influenced not only by the fraction of individual phases, but especially by their morphology and distribution. While designing new procedures it is necessary to optimize individual processing parameters, in particular the austenitization temperature, cooling rate, and both the temperature and time period of the isothermal holding time for retained austenite

stabilization. When using thermomechanical treatment other parameters accrue, such as the deformation rate and its temperature interval.

The optimization of the whole technological process on real technology is generally highly time consuming and expensive due to the number of experiments which need to be carried out using the trial & error method. To considerably increase the efficiency and acceleration of the optimization process, physical, material-technological modelling can be used. This method, which has been used for the research mentioned below, enables the optimization of relevant parameters of the real process on small amounts of material.

2. Q-P Process

The Q-P process represents a new type of heat treatment for low-alloy steels. The treatment is composed of quick quenching to a temperature between M_s and M_f , low-temperature tempering and cooling to room temperature. Unlike quenching and tempering, there is no transformation of supersaturated tetragonal martensite to cubic martensite with simultaneous formation of ferrous carbides during the low-temperature tempering. Carbon diffusing from the supersaturated martensite stabilizes the non-transformed austenite which remains stable even when cooled down to ambient temperature. In this case, the creation of carbides is suppressed by choosing a suitable alloying strategy and heat treatment conditions. [1, 2]

The resulting structure is composed of martensite and stabilized foil retained austenite (Fig. 1). The amount of retained austenite depends on several parameters. It is the question of the lowest supercooling temperature during quenching, low-temperature tempering temperature, holding time at this temperature and chemical composition of the material.

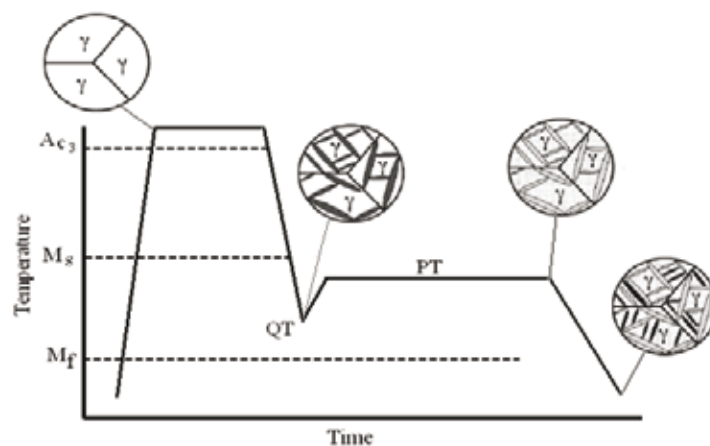


Figure 1 Diagram of Q&P process showing microstructures [1]

3. Thermomechanical treatment

When optimizing the Q-P process it is necessary to determine the influence of individual parameters to obtain a sufficient quantity of retained austenite, thus ensuring excellent mechanical properties. A deformation within the cooling phase is performed in order to refine the structure. Finding a suitable temperature interval for the deformation represents another optimization parameter.

3.1. Thermomechanical simulator

The material-technological modelling utilizing a thermomechanical simulator is used for the optimization process.

A high-speed simulator enabling precise operating of the temperature and deformation course mode has been developed at the Research Centre of Forming Technology (FORTECH). A unique control system enables rapid changes to temperature and deformation parameters, thus very accurately simulating real process conditions. For steels, temperature gradients of over 100°C/s during the heating process and 250°C/s during cooling can be achieved. A speed of 3 m/s can be reached by the deformation component. Apart from the in-built sensor array of the simulator, there are other external monitoring devices available which can be connected to the control and monitoring system of the simulator.

3.2. Model treatment

The model procedure of the Q-P process is used on experimental low-alloy steel designated 42SiCr. Silicon is one of the main alloying elements of this steel. It suppresses carbide formation throughout the martensite transformation. Another component is manganese, which stabilizes the austenite and reduces pearlite transformation [3]. Another alloying element is chromium which serves as a solid solution hardener.

The proposed model treatment entailed heating to 900°C with a holding time of 100 s followed by a twenty step anisothermal deformation within a temperature interval from 900 to 820°C. After deformation, several cooling strategies were carried out to determine their influence on the structure development, especially on the stabilization of retained austenite (RA). The RA fraction was determined using X-ray diffraction analysis, while neutron diffraction analysis was used to compare the results. The latter method enabled the deformation stability of RA to be determined in-situ.

In the experiment, the influence of the supercooling temperature between M_s and M_f and of the temperature of the holding time when carbon is isothermally redistributed was found.

In the first case the sample was cooled to 250°C. It was held for 600 s at this holding time (Tab. 1). This temperature lies 55°C below M_s . The resulting material structure was martensitic with hardness 604 HV10 (Fig. 2).

To determine the influence of the isothermal holding time the temperature was increased to 300°C in the next strategy (Tab. 1). The experiment resulted in martensitic structure with visible RA areas with hardness 602 HV10 (Fig. 3). X-ray diffraction analysis determined the RA fraction to be 10%.

The influence of overcooling near the M_f temperature was examined in the next step to further support the stabilization of RA during cooling.

Table 1 Table of proposed thermomechanical treatment with Q-P process

Mode	RA fraction [%]	HV 10	R_m [MPa]	A_{5mm} [%]
900°C/100 s – 250°C/600s	-	604	-	-
900°C/100 s – 300°C/600s	10	602	-	-

900°C/100 s – 200°C – 250°C/600s	15	546	2073	10
900°C/100s – 200°C/10s–250°C/600s	16.5	546	2087	13
900°C/100s – water cooling to ambient temperature – 250°C/600s	4.5	558	-	-

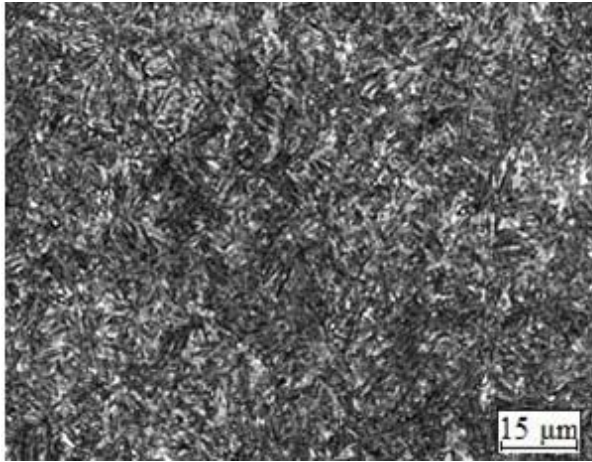


Figure 2 Isothermal holding time 250°C/600s

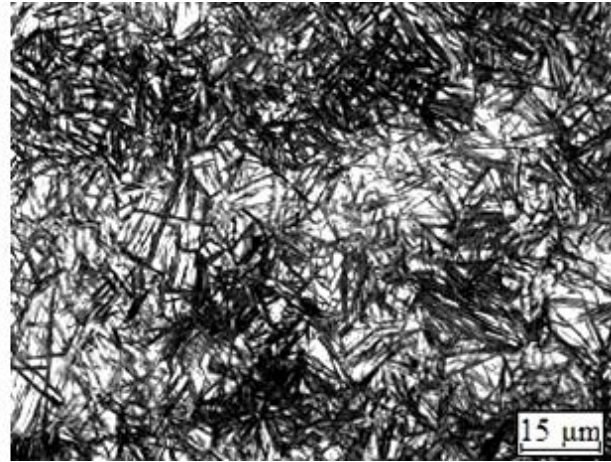


Figure 3 Isothermal holding time 300°C/600s

After multiple deformations in the temperature range 900-820°C the sample was cooled to 200°C, which is just 20°C over the M_f temperature. After cooling, the sample was heated immediately up to 250°C, and held for 600 s (Tab. 1). Small ferritic grains were detected in the incurred martensitic structure (Fig. 4). X-ray diffraction analysis found that the retained austenite fraction significantly increased to 15%. Carbon diffusion from supersaturated martensite to austenite during the isothermal holding time probably caused reduction of hardness, as the measured hardness yielded just 546 HV10, which is 50HV less than in the case without overcooling at the same isothermal holding time. After this treatment, mechanical

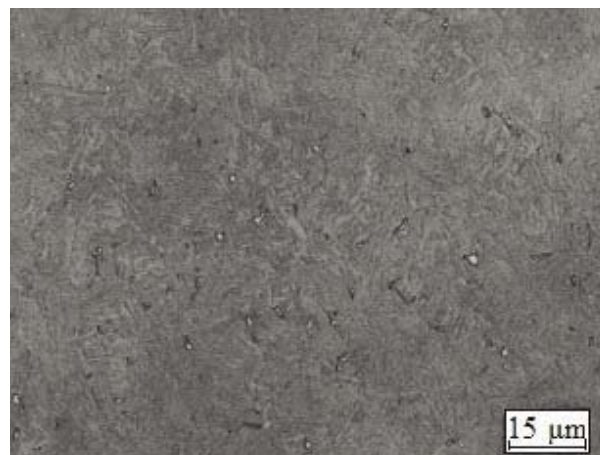


Figure 4 Overcooling to 200°C, isothermal holding time at 250°C/600s

properties were examined by tensile testing. The tensile strength reached 2073 MPa with ductility about $A_{5mm} = 10\%$.

In the next step it was necessary to determine if the holding time at the overcooling temperature before isothermal holding causes another increase in

the RA fraction (Tab. 1, Fig. 5, Fig. 6). Therefore the sample was held for 10 s after overcooling at 200°C. After this holding time, the sample was heated to 250°C. A 600 s isothermal holding time at this temperature followed. In comparison with the previous mode without the 200°C delay, another slight increase in the RA fraction to 16.5% occurred. The hardness of the structure remained unchanged. No significant changes to the mechanical properties were observed. Tensile strength yielded 2087MPa and ductility about $A_{5mm}=13\%$.

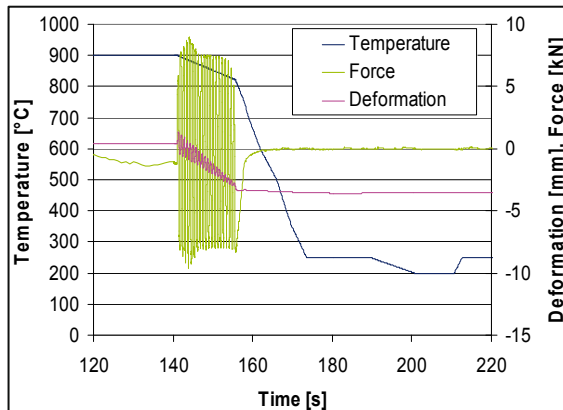


Figure 5 TMT with twenty step incremental deformation

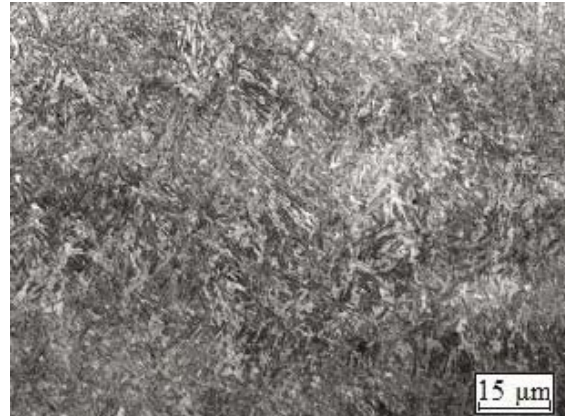


Figure 6 Overcooling to 200°C, delay 10 s, isothermal holding time 250°C/600 s

To compare, another structure development and RA fraction were experimentally verified on a sample rapidly cooled in water to ambient temperature with subsequent tempering at 250°C (Tab. 1). Mainly martensitic structure with hardness 558 HV10 was observed on a confocal scanning laser microscope. X-ray diffraction analysis revealed that ca. 4.5% RA was stabilized within the structure.

3.3. Neutron diffraction with tension load

To study the stability and the proportion of residual austenite during cold deformation, which have a large influence on the mechanical properties of obtained structures was used the *in-situ* neutron diffraction analysis with tensile load. For this experiment were prepared samples with thermal scheme in which were achieved the best mechanical properties and the highest portion of retained austenite. It was the regime of 10 s holding time supercooling to 200°C and subsequent heating to 250°C with delay of 600 s.

The diffraction patterns were collected on the neutron powder diffractometer MEREDIT, which was equipped for this purpose with deformation rig. Course of the tensile load was controlled in the elastic region of deformation by the force applied to the sample. In the plastic deformation region it was the strain control regime with the help of the extensometer MTS with the base of 3 mm. Neutron diffraction patterns of the deformation zone of the sample ($4 \times 6 \text{ mm}^2$) were collected in the range $10\text{-}110^\circ 2\theta$ with the step of 0.1° and delay of 200 sec in each step. Amount of the retained austenite in the virgin sample obtained from the neutron and X-ray diffraction are in the good agreement.

Evolution of the retained austenite content as a function of the total deformation is shown in the Fig. 7. In the elastic region there was a small decrease of RA content

which continue also at the beginning of the plastic region of the deformation up to 0.75% of total sample deformation. Then followed by sharp decrease of RA content from 13.5% to 9%. With further deformation the RA content dwindled to around 6%. The rupture of the sample carried out with total deformation of 8%.

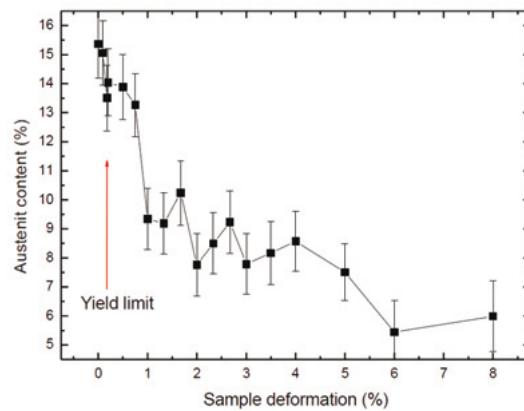


Figure 7 Evolution of the residual austenite content as a function of the total deformation.

4. Conclusion

In the course of the experimental programme three different cooling strategies were examined for the Q-P process. All three strategies resulted in martensitic structure with various RA fractions from 4.5 to 16.5%. It was found that the overcooling temperature between M_s and M_f temperatures plays a significant role on the stabilization of RA in the structure, and that a further increase in RA can be achieved by using suitably chosen parameters for the overcooling before heating to the temperature of the holding time, where carbon is being isothermally redistributed.

Structures with the highest RA fraction reached a tensile strength over 2000 MPa with a ductility of 10%.

Neutron diffraction in-situ method during the tensile test showed that there was just a slight decrease in the RA fraction at the beginning. In the deformation range from 0.75 to 1% an intensive decrease from about 13% to 9% was observed. Further deformation caused only a slight decrease in the RA content. Even at 8% deformation, 6% of stable RA still remained in the structure.

Acknowledgements

This paper includes results created within the project 1M06032 Research Centre of Forming Technology and within the project 106/09/1968 Development of New Grades of High-Strength Low-Alloyed Steels with Improved Elongation Values. The projects are subsidised from specific resources of the state budget for research and development.

References

- [1] Edmonds, D.V. et al.: *Materials Science and Engineering A* 438–440 (2006) 25–34, Quenching and partitioning martensite – A novel steel heat treatment
- [2] Gerdemann, F.L.H.: *Microstructure and hardness of 9260 steel heat-treated by the quenching and partitioning process*, Aachen University of Technology, Germany, 2004
- [3] Kraus, V.: *Tepelné zpracování a slinování*, Západočeská Univerzita v Plzni, Plzeň, 2000

¹ Prof. Dr. Ing. Mašek Bohuslav, Západočeská univerzita Plzeň, Fakulta strojní, FORTECH,
e-mail: masekb@kmm.zcu.cz

² Dr. Ing. Hana Jirková, Západočeská univerzita Plzeň, Fakulta strojní, FORTECH, Czech Republic,
e-mail: h.jirkova@email.cz

³ Ing. Danuše Klauberová, Západočeská univerzita Plzeň, Fakulta strojní, FORTECH, Czech Republic,
e-mail: d.klauberova@seznam.cz

⁴ Ph.D. Ing. Martin Petretec, Academy of Sciences of the Czech Republic, Czech Republic,
e-mail: petretec@ipm.cz

⁵ Dr. Ing. Přemysl Beran, Nuclear Physics Institute of the Academy of Sciences of the Czech Republic,
Czech Republic, e-mail: pberan@ujf.cas.cz.

LASER WELDING OF HIGH STRENGTH STEELS

Stanislav Němeček¹, Tomáš Mužík¹, Miroslav Urbánek², Zbyšek Nový²

Abstract

Results comparing properties of laser welds with welds achieved by arc methods on high strength low alloyed steels - multiphase TRIP700 steel, martensitic grade DOCOL1200M steel or military steel P2 are introduced. Laser joints retain the properties of the original material without any major degradation. The fracture behaviour is quite different – MIG and TIG weld cracks propagate at the heat affected zone. Laser welded sheets cracks at basic material, approx. 20 mm from the joint.

Keywords: laser welding, high strength steels, properties

1. Introduction

Recently, a number of new high-strength materials have been developed. It has been reported that up to 70% of modern alloys have been designed in the recent decade. Automotive industry offers an illustrative example where the proportion of high strength steels (HSS) grows at the expense of mild steels. In most of these steels, the chemical composition has been simplified (low-alloyed, low-carbon steels) and the heat and thermomechanical treatment procedures have been optimised. Hence, these changes are related to changes in microstructure: grain refinement, proper phase composition, etc. However, a number of properties achieved in such fashion are then degraded by subsequent treatment. One typical example might be welding where the effects of heat can reduce the values of the material's properties by more than 30% of original values. In the heat affected zone (HAZ), grain growth and changes in phase composition take place; and most cracks propagate along this zone's boundary. This is the reason why new processes must be sought for new materials.

A development with a similar pace can be seen in power lasers. The prices and running costs keep decreasing, whereas the electrical energy efficiency and quality of the beam increase. Power lasers are therefore used for not only cutting and welding mass products but also in ordinary engineering practice in small and medium batch production for surface hardening or deposition of films.

The paper brings a comparison between the results of arc and laser welding of high-strength and fine-grained steels in terms of deterioration of mechanical properties, microstructure changes and fracture behaviour.

2. Materials and laser technology

Except the TRIP steel specimens, all samples were welded using Laserline diode laser with the maximum power of 3.6 kW. The beam diameter was 1.2 mm and the focal distance was 200 mm. The power of the laser and the velocity of the linear movement of the beam were selected according to the thickness and type of the welded material. Argon was used as the protective gas. Automatic movement of the beam is provided by KUKA robot manipulator with the reach of 1.2 m diameter. In all cases these were butt welds which are suitable for mechanical properties testing.

2.1 Multiphase TRIP Steels

Multiphase steels were represented by a TRIP steel containing 0.2% C, 1.5% Mn and 1.5% Si. A tube with 1 mm wall thickness was TIG arc-welded using a filler material with the composition of 0.1C-1.7Mn-1Si (OK AUTROD 12.58), the specimen was marked as TRIP TIG. Another weld was created using TRUDISC disc laser with the power of 2 kW with no filler material, marked as TRIP D. The third weld was made using Rofin DS015HQ disc laser with the following welding parameters: focal distance of 200 mm, beam diameter 0.15 mm, welding speed 5 m/min, specimen TRIP R.

2.2 P2

The impact of one-side and two-side welding on changes in mechanical properties was examined in this high-strength material. The composition of the material corresponds to the C and Mn levels with the reported values of YS and UTS. The sheet with 6 mm thickness was welded through thickness from one side, making the specimen P2-1. The specimen P2-2 had double welds, shown in Fig. 1. The steel is used in military applications for production of fighting vehicles and bullet-proof containers.

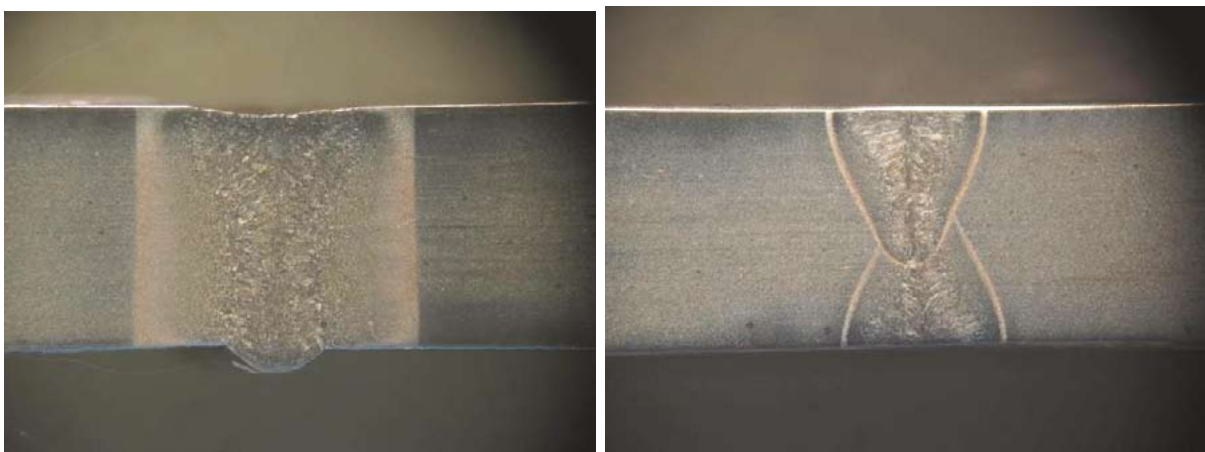


Figure 1

2.3 UHSS Martensitic Steel DOCOL 1200

The material DOCOL 1200M with martensitic microstructure is a low-carbon manganese-alloyed steel (0.11%C; 1.7%Mn) with reported values of YS = 950 MPa

and UTS = 1,200-1,400 MPa. Thanks to low levels of alloying elements and carbon, it shows good weldability. The wall thickness of the workpiece was 1 mm. Typical applications for Docol M are door beams, bumper reinforcements, cutting tools, clutch discs, seats, etc.

For laser welding of DOCOL material a laser with the power of 3.5 kW and beam velocity of 4.4m/min was used. The MAG welds (I = 58 A, U = 18.4 V, gas 15 l/min, Ar 82%+CO₂ 18%, wire dia. 0.8; 2.5 m/min) were denoted as Docol MAG. Welding parameters for the specimen Docol TIG were as follows: welding current of 53 A DC, Kemppi maston Tig equipment, MLS 3000 AC DC with the filler wire gl 113.

3. Results and Discussion

3.1 TRIP Steels Welds

Macrographs of welds are shown in figures 2 and 3. TIG welding results in a weld with the width of 5 mm. The width of the HAZ is almost identical. Test bars fractured in all cases at the interface between the HAZ and the parent metal, Fig. 2. On the other hand, the width of laser welds is no more than 0.4 mm in both cases and the HAZ width is about 150 μ m. The TRIP D weld TRIP R is wider at the top than the TRIP R weld, which can be attributed to the quality of the laser beam optical system. In case of both welds, however, the fracture occurred outside the weld and the HAZ, in the distance of about 10 mm. The tube material's strength was 885 MPa and its elongation was 21%. As the table of mechanical properties (Table 1) shows, the strength after arc welding declined slightly but the elongation dropped markedly. Laser welds even exhibit higher strength (which can perhaps only be explained by the presence of martensite in the weld) with twice lower elongation.

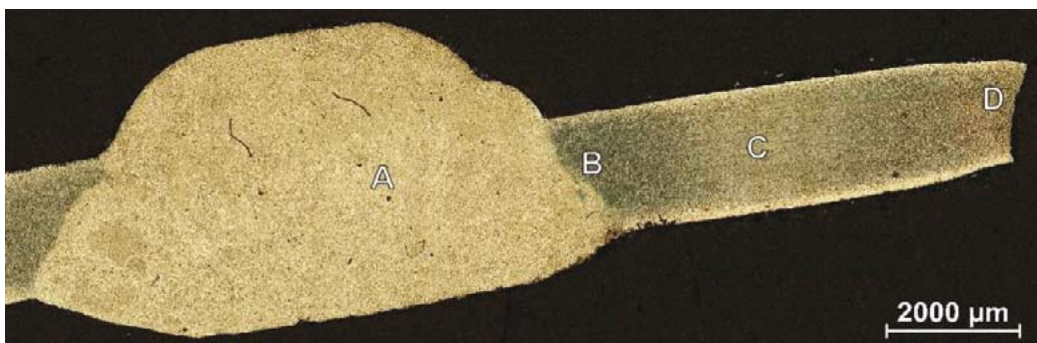


Figure 2 TRIP T weld

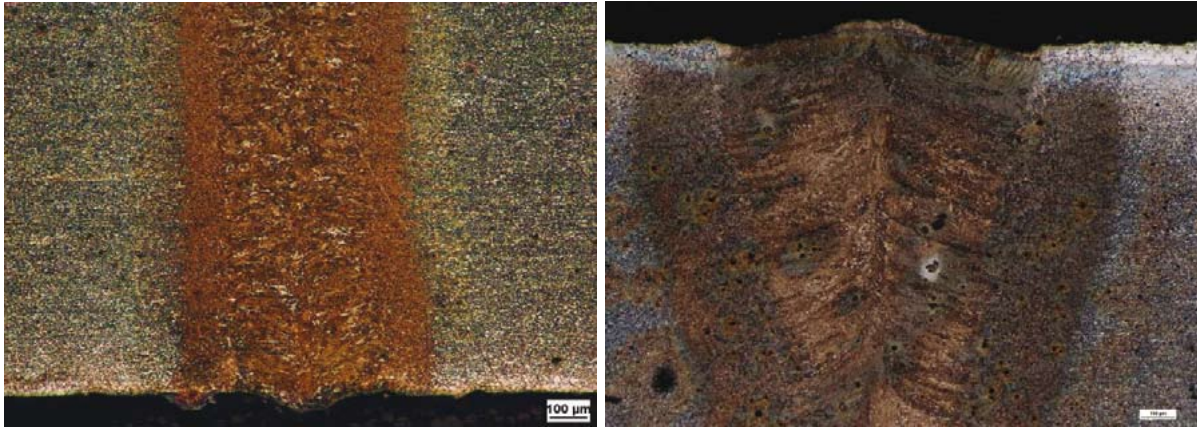


Figure 3 TRIP R weld

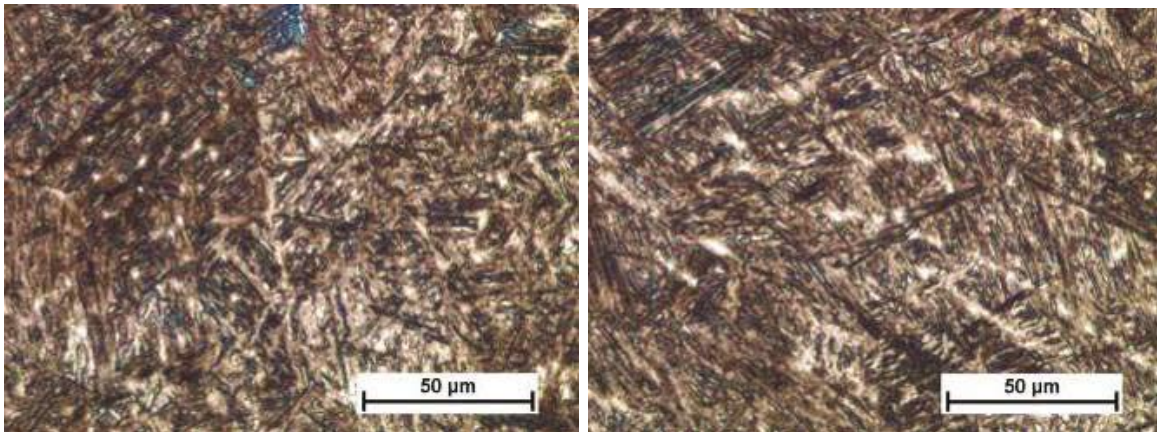
TRIP D weld

Table 1

	YS [MPa]	UTS [MPa]	A [%]
TRIP T	467	847.7	6.5
TRIP R	490	950	11.6
TRIP D	488	998	10.7

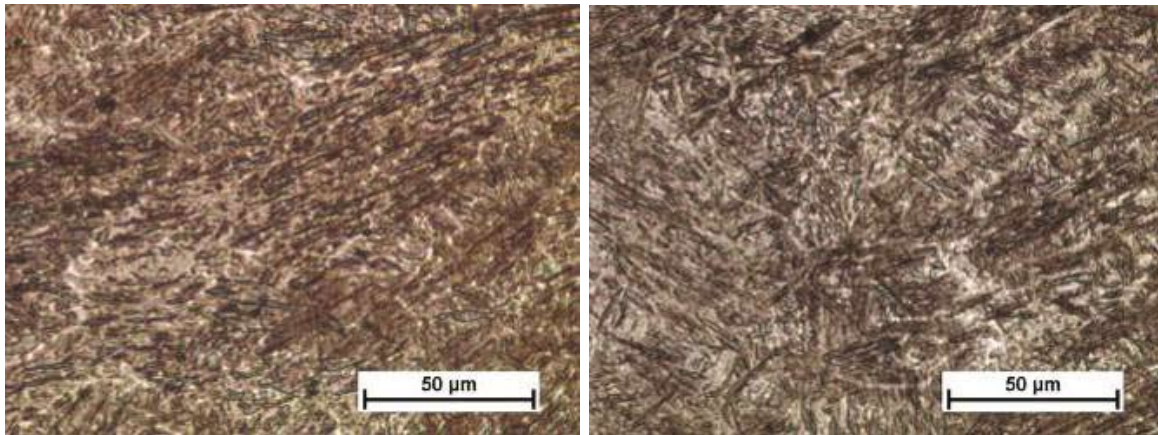
3.2 P2 Steels Welds

Appropriate butt welds were made for comparing the behaviour of one-side and double welds in high-strength steels (Fig.1). For welding through thickness from one side the beam velocity is lower. This results in greater amount of introduced heat and wider heat affected zone than in welding both sides. The weld and HAZ microstructures are finer (Fig. 4). Its impact on resulting mechanical properties is significant, see Table 2. In the double weld, the yield strength is higher by 200 MPa and the strength is even 250 MPa higher. The elongation is practically twice as high.



Specimen P2-1, weld

HAZ



Specimen P2-2, weld

HAZ

Figure 4

Table 1 Mechanical properties measured in a tensile test

	YS [MPa]	UTS[MPa]	A [%]
P2-1	1225.6	1310.1	1.8
P2-2	1419.0	1549.1	3.3

3.3 DOCOL 1200M Welds

Preparation of a new engineering design for seats with high-strength materials involved welding tests of frame prototypes. Conventional arc welding caused problems due to deterioration of properties, distortion of the welded part and insufficient productivity. For this reason, laser welding was used as an alternative process. With the current optical system, the weld width was 1.2 mm and the width of the HAZ was 0.2 mm, Fig. 5. TIG welding is known for large amount of heat introduced into the joint. This is evidenced by poor mechanical properties listed in Tab. 3, showing a drop to almost half of the original values. MAG welding is slightly more favourable, resulting in somewhat higher strength. However, the values of properties still decline significantly. Upon laser welding, strength shows only minor decrease, up to 10% of the initial value. It has been clearly shown that the heat introduced by welding is a key factor affecting the resulting properties of the joint in UHSS steels.



Figure 5 Weld micrograph

Table 3 Mechanical properties of welds in DOCOL

	YS [MPa]	UTS [MPa]	A [%]
Docol TIG	539.0	718.9	4.4
Docol MAG	610.1	732.53	3.3
Docol laser	1036.88	1080.20	0.80

Acknowledgements

The results presented here were not obtained using any project funding or subsidies from taxpayers' money. It is thus the staff of the laser department of MATEX PM Company who deserves the thanks for their activity and efforts in producing excellent results and making commercial applications of the research possible.

¹ Doc. Ing. Stanislav Němeček, Ph.D., MATEX PM s.r.o., Rokycanská 58, 312 00 Plzeň, Czech Republic, Tel.: +420 737 424 542, e-mail: nemecek@matexpm.com

¹ Ing. Tomáš Mužík, MATEX PM s.r.o., Rokycanská 58, 312 00 Plzeň, Czech Republic, Tel.: +420 603 335 954, e-mail: muzik@matexpm.com

² Ing. Miroslav Urbánek, COMTES FHT a.s., Průmyslová 955, 334 41 Dobřany, Czech Republic, Tel.: +420 377 197 322, e-mail: miroslav.urbanek@comtesfht.cz

² Dr. Ing. Zbyšek Nový COMTES FHT a.s., Průmyslová 955, 334 41 Dobřany, Czech Republic, Tel.: +420 377 197 301, e-mail: zbysek.novy@comtesfht.cz

TREATMENT OF ULTRA FINE-GRAINED STEELS USING THE STRAD METHOD

Olszar M.¹, Olszar M.², Koňářík P.³, Hermann R.⁴

Abstract

The purpose of this process is to achieve grain refinement through shearing transformation and plastic deformation after recrystallization resulting in ultra fine-grained (UFG) steels which feature higher tensile strength combined with good formability. The structure is composed of tempered martensite, ferritical grain with size of several micrometers, or hundreds of nanometers and ultra fine-grained cementite. The STRAD method can easily be used as continuous process in production.

Keywords: ultra fine-grained steel, shearing transformation, recrystallization

1. Introduction

Deformation refinement, nucleation and growth of grains during heat treatment are the essential steps in the STRAD technology. The process is shaped particularly by chemical composition, optimum temperatures and heat treatment duration depending on grain size and growth rate linked to the deformation level. The technology is fit for steels which have undergone peritectic reaction.

To ensure an effective processing all the above mentioned process parameters must be harmonized taking into account their interactions.

To accomplish a successful process the following three issues must be handled:

- diffusion-free shearing transformation,
- plastic deformation,
- recrystallization.

2. Diffusion-free shearing transformation

The transformation depends particularly on: austenitization temperature/time and cooling rate/method.

2.1 Austenitization temperature and time

The standard general rules must be applied so that the grain size growth is minimized during heating.

2.2 Cooling rate and method

In this case the procedure is more difficult. Because typically steels with carbon content below 0.2 % are processed the M_s temperature is about 500 °C – see **Fig. 1**

[4]. For that reason acicular tempered martensite is always formed. If the initial structures of the STRAD process are to be modified the hardening condition must be studied.

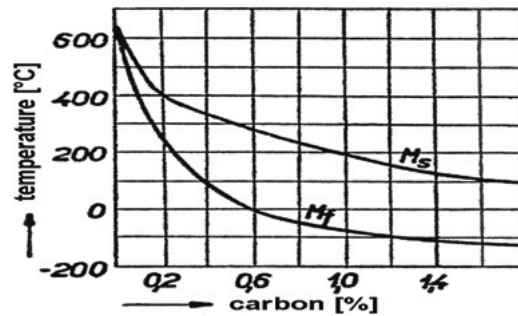


Fig. 1 – Effect of carbon on M_s and M_f positions at martensitic transformation

3. Plastic deformation

If applying the STRAD method the following must be handled:

- deformation level before shearing transformation,
- deformation level before recrystallization.

3.1 Deformation level before shearing transformation

This deformation affects particularly the grain size after transformation and values of parameters influencing the transformation including initial conditions for the following processes. The basic criterion is the position in plastic deformation process in terms of whether the texture in the formed material is generated or not with respect to the grain size.

3.2 Deformation level before recrystallization

In this case the maximum plastic deformation and forming method to which the tempered material can be subjected and what will be the impact on the basic recrystallization parameters must be known. The initial approximation and determination of general rules can be based on **Fig. 2** [1] although this diagram provides information only for grain size over 10 μm and recrystallization temperature over 500 $^{\circ}\text{C}$. The above indicates for grain size below 10 μm the classic recrystallization technology cannot be applied and about 500 $^{\circ}\text{C}$ recrystallization temperature should be selected at optimum heating time.

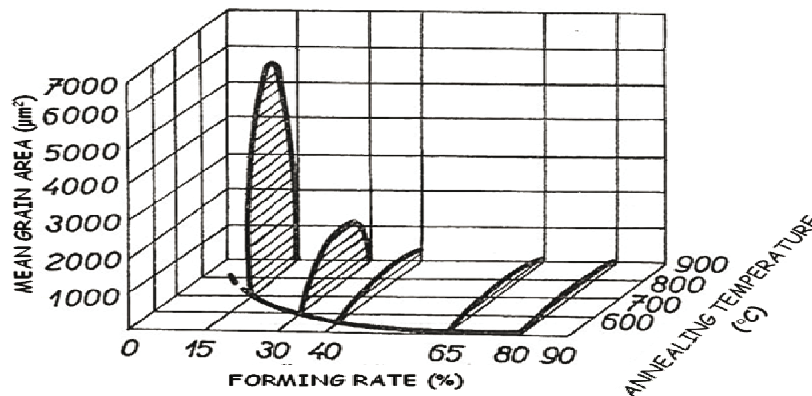


Fig. 2 – Mild steel recrystallization diagram

4. Recrystallization

Recrystallization is the key process of the STRAD method. It must be controlled so that its duration is as short as possible. The following dependencies must be known to be able to accomplish successful recrystallization:

4.1 Dependence of recrystallization temperature on carbon content

The mathematical relation between recrystallization temperature and carbon content of steel can be determined using **Fig. 3** [2]. If line Ac_{cm} is extended it intersects the temperature axis at 406 °C for pure iron. Since the line extension is located below Ac_1 it represents 100 % probability of ferrite nucleation. The line therefore determines the initial depending on carbon content. Because the line intersects also the point of 731 °C temperature at 0.8 % carbon content the mathematical expression is as follows:

$$T_R = 406.25 [\% C] + 406, \quad (1)$$

where T_R – initial recrystallization temperature and
 $[\% C]$ – carbon content in mass %.

For carbon content higher than 0.2 % the curve replacement by line can be considered but for low-carbon steel the calculated values correspond to actual recrystallization temperatures. In production practice the recrystallization is not used to restore the material formability after cold forming of steel with carbon content higher than 0.25 % when patenting is applied.

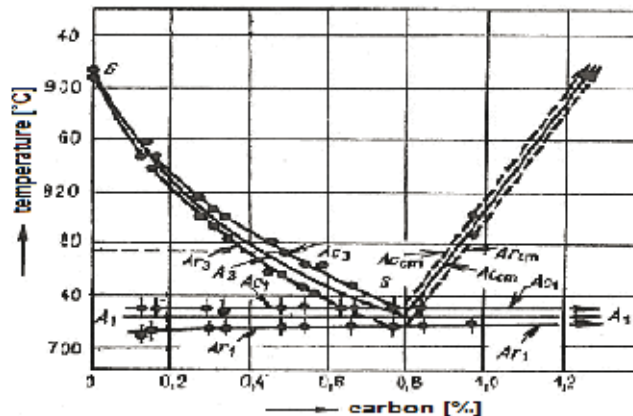


Fig. 3 – Pure iron-carbon alloy transformation points

In [1] it is stated the activation energy of grain generation declines as the temperature decreases so the rate of generation of new recrystallized grains increases.

4.2 Dependence of recrystallization time on temperature

For the ultra fine-grained structure the recrystallization start time is important. It can be determined from **Fig. 4** [3] provided the dependence of recrystallization start time at different annealing temperatures for pure iron is similar to that for steel with up to 0.2 % carbon content. The extension of line 1 intersects axis $\ln t$ at 0 value, i.e. $\ln t = 0$ for $T = 1,000$ °K; the dependence can be described by general equation

of line $\ln t = K * \frac{10^4}{T} - 10K$, where K – gradient of line, $\ln t$ – natural logarithm of recrystallization start time, T – temperature [°K]. If introducing the values from the diagram the following is the result:

$$\ln t = 2,7 * \frac{10^4}{T} - 27 \quad (2)$$

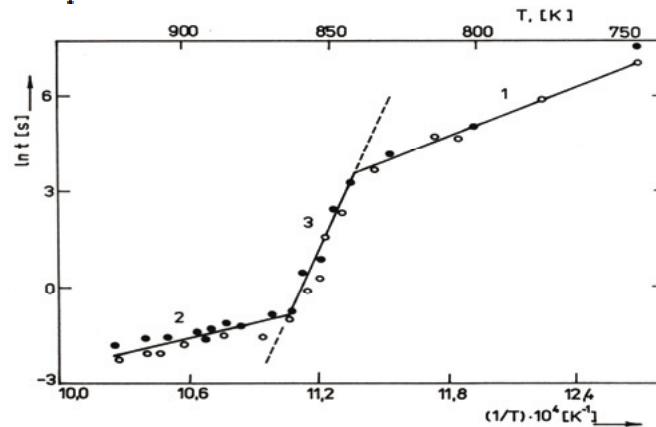


Fig. 4 – Recrystallization time start at various annealing temperatures for pure iron

4.3 Dependence of recrystallization temperature on deformation level

It is generally known that the higher the forming rate the higher the number of areas fit for the inception of nuclei which means a higher number of nuclei and finer crystals are found after recrystallization. However, the final post-recrystallization grain size depends predominantly on grain size of the original structure (the finer the better) and forming method. At the same tensile or pressure forming the recrystallized structure after pressure forming is coarser than after tensile forming. The basic dependence of recrystallization temperature on deformation rate for iron is shown on **Fig. 5** [1] which indicates that the more intense metal forming the higher increase of the internal energy of the metal and the lower the temperature at which the recrystallization starts. The figure also indicates the effect of a deformation exceeding 70 % on the recrystallization temperature is negligible. The recrystallization temperature depending on deformation level can be calculated using the following empirical formula:

$$T_R = \frac{731}{\epsilon^{0,181}}, \quad (3)$$

where: T_R – recrystallization temperature and ϵ – cross sectional deformation (area reduction).

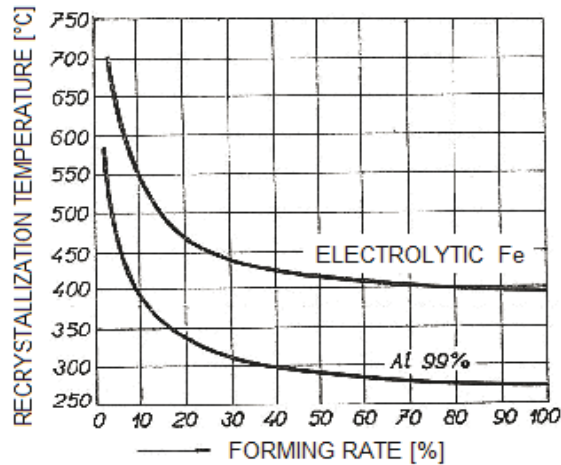


Fig. 5 - Cold forming effect on temperature necessary to recrystallization start after 1 h annealing

5. Experimental part

The input material is wire rod of 20 mm diameter made of QSt-36-3 steel of the chemical composition specified in **Table 1**.

Table 1 – Chemical composition of QSt-36-3 steel

Mass %							
C	Mn	Si	P	S	Cu	Cr	Ni
0.085	0.35	0.057	0.013	0.009	0.04	0.05	0.02

The wire was drawn using four dies to 12.5 mm diameter with 60.9 % total reduction. The wire sample was then hardened in water with 870 °C temperature and again drawn using four dies to remove scales to 7.8 mm diameter with 61 % total reduction. After that the sample was subjected to recrystallization annealing at 530 °C temperature in laboratory furnace for 12 minutes. The descaled sample was again drawn using four dies to 5.5 mm diameter with 50.3 % total reduction. The sample processed this way using the STRAD method was subjected to tensile tests and metallographic examinations. The tensile test results are provided in **Table 2**.

Table 2 – Final mechanical properties of QSt-36-3 steel after the STRAD process

Test No.	R _{p0.2} (MPa)	R _m (MPa)	A (%)	Z (%)
1	903	907	10.4	59.4
2	879	934	14.4	67.9
3	777	889	13.6	64.0
4	856	904	10.4	59.7

The metallographic examination showed the grain size as illustrated by **see Fig. 6** indicating the value of 790 nm was achieved.

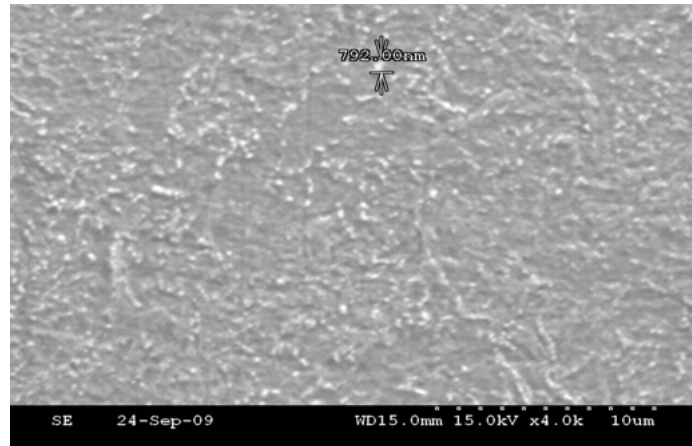


Fig. 6 – 5.5 mm diameter – 0.00079 mm

6. Conclusions

The experimental verification of the STRAD process showed the described method can be applied to improve the qualitative properties of steel and can be classified as an SPD method. The specified mechanical properties prove the wire with 0.085 % carbon content processed this way corresponds to patented wire with 0.42 % carbon content. The described method can be further developed using induction heating significantly reducing the heat treatment times which will enable additional improvement of qualitative properties of steel and make it possible to perform the processing as continuous process. If magnetic and electrical field is used in the processing then the STRAD method forms a basis for development of research of steel with hyperstructure, so-called structured carbon steel and enables theoretical research of graphen steel where cementite is replaced by graphen.

References

- [1] Jeníček, L., Ryš, P.: *Nauka o materiálu I/2, Nauka o kovech, 2. svazek vlastnosti kovů*. Academia, Prague, 1968
- [2] Jech, J.: *Tepelné zpracování oceli*. SNTL, Prague 1983
- [3] Sedláček, V. et al.: *Zotavení a rekrytalizace*. Academia, Prague, 1985
- [4] Píšek, F., Jeníček, L., Ryš, P., Cenek, M., Mazanec, K., Hribek, A. *Nauka o materiálu I/4, Nauka o kovech 4. svazek, železo a jeho slitiny*. Academia, Prague, 1975

¹ Ing. Miroslav Olszar, TŘINECKÉ ŽELEZÁRNY, a. s., Průmyslová 1000, 739 70 Třinec, Czech Republic. Tel.: +420 558 53 54 21, e-mail: miroslav.olszar@trz.cz

² Ing. Martin Olszar, TŘINECKÉ ŽELEZÁRNY, a. s., Průmyslová 1000, 739 70 Třinec, Czech Republic. Tel.: +420 558 53 32 88, e-mail: martin.olszar@trz.cz

³ Ing. Petr Koňářík, TŘINECKÉ ŽELEZÁRNY, a. s., Průmyslová 1000, 739 70 Třinec, Czech Republic. Tel.: +420 558 53 32 88, e-mail: petr.konarik@trz.cz

⁴ Ing. Radek Hermann, TŘINECKÉ ŽELEZÁRNY, a. s., Průmyslová 1000, 739 70 Třinec, Czech Republic. Tel.: +420 558 53 59 03, e-mail: radek.hermann@trz.cz

DEVELOPMENT OF NEW TOOL STEELS FOR FORGING DIES

Pavel Šuchmann¹, Jiří Krejčík², Pavel Fila³, Ladislav Jelen⁴, Eduard Psík⁵,

Abstract

New alloying concepts of steels for forging dies based on the 1.2343 steel have been introduced. By increasing the carbon content, and in some cases increasing the tungsten level and adding niobium, using a sufficient metallurgical procedure and subsequent special process for ingot forging, the hardness, toughness and wear resistance of the steel have been enhanced significantly as well as the lifetime of dies made from the improved steels.

Keywords: tool steel, forging die, lifetime

1. Introduction

Manufacturers of small closed-die forgings have been for a long time greatly interested in affordable tool steels with a good strength-toughness ratio and with a precisely specified metallurgical processing procedure. Such steels are fit for rather versatile applications involving most types of forging dies. The steel 1.2343 which is one of the most widely used materials in forging plants across Europe is a typical representative of such tool material. However, it is often difficult to find such a supplier of this steel on the Czech market which guarantees the required chemical composition and homogeneous microstructure with very low inclusion content, uniform carbide distribution and other parameters which are decisive for end-use properties of forging dies.

In recent years, companies ŽDAS a.s. and Vítkovice – výzkum a vývoj – technické aplikace a.s. in cooperation with Kovárna VIVA Zlín spol. s r. o. and research institutes SVÚM a.s. and COMTES FHT a.s. have been working intensively on optimizing the production of steel 1.2343 with the aim of achieving best possible properties while keeping competitive price. Besides the development of metallurgical processing of this steel, several chemical composition variants have been proposed for making dies with high hardness and wear-resistance requirements.

2. Manufacturing of experimental materials

2.1 Quality requirements

On the basis of long-term requirements of tool steel buyers, the following fundamental quality specifications for tool steel forgings have been identified:

- sulphur level of no more than 0.005 wt.%, very low content of phosphorus and other undesirable residual elements
- non-metallic inclusion content (according to ASTM E45-97) should not exceed values listed in tab. 1
- prior austenite grain size of $G = 8$ or finer (according to ASTM E 112)

Table 1 Highest acceptable amount of non-metallic inclusions

INCLUSIONS		
TYPE	FINE	COARSE
A (sulphides)	1.0	0.5
B (aluminates)	1.5	1.0
C (silicates)	1.0	1.0
D (globular oxides)	2.0	1.0

In addition to these fundamental criteria, microsegregation, carbide distribution and other standard microstructure parameters were evaluated according to NADCA 207.

2.2 Method of production

Experimental ingots were processed in vacuum (VD process). One of the ingots was arc-remelted in VAR equipment prior to forging. The above quality specifications have also been met by the material produced by the VD process without remelting. As expected, the vacuum remelting improved the quality parameters (resulting in zero inclusion content). However, due to high cost of this process and unavailability of the VAR equipment in the ŽDAS company, remelted ingots ceased to be used.

In order to achieve optimum amount of forging reduction, all the above materials were deformed along three axes (involving both drawing out and upsetting) with the forging reduction of at least 4.

3. Modification of the chemical composition of 1.2343 steel

With regard to special parameters of the trial die used for tool steel testing (see section 5), several chemical composition variants have been proposed (tab. 2), leading primarily to higher hardness and wear resistance. In the variant no. 1 of the 1.2343 chemical composition, an addition of niobium was used. Niobium's ability to form carbides is often used both in structural [1] and tool steels [2], [3]. In the variant no. 2, carbon and vanadium levels have been increased in addition to alloying with niobium. The purpose was to increase hardness and hardenability of the material. The variant 3 included higher carbon content and additions of tungsten and vanadium in comparison with the 1.2343 standard composition.

Table 2 Chemical composition of tool steels investigated

Material	Chemical composition (wt. %)							
	C	Si	Cr	Mn	Mo	V	Nb	W
1.2343 - standard	0.37	1.0	5.00	0.4	1.20	0.45	0.00	0.00
Variant 1 (Nb)	0.39	1.0	4.95	0.4	1.16	0.42	0.18	0.00
Variant 2 (Nb, C, V)	0.54	1.0	4.95	0.4	1.15	0.62	0.18	0.00
Variant 3 (W, V, C)	0.49	1.0	4.90	0.4	1.17	1.60	0.00	1.63

4. Analysis of properties of experimental material

Specimens taken from experimental melts were heat treated to hardnesses of 53 HRC (all specimens) and 55 and 57 HRC (only those with modified chemical compositions). Subsequently, impact toughness tests were carried out for longitudinal and transverse directions (relative to the axis of the bar forged from the initial ingot) and abrasive wear resistance tests.

Their results are listed in tab. 3, showing that modifying the chemical composition significantly improved the material's hardenability (hardness above 53 HRC is not achievable in the conventional 1.2343 steel) and wear resistance. However, all modified variants have been found to have lower impact toughness, in particular in the direction perpendicular to the axis of the forged workpiece. In order to eliminate this, the ingot forging process will be optimized further.

Table 3 Mechanical properties of specimens made from experimental alloys (tests at room temperature)

Steel type	Hardness HRC	Impact toughness KCU [J/cm ²]		Resistance to wear Ψ
		II	⊥	
1.2343 - standard	53	23	20	1.69
Variant 1 (Nb)	53	23	16	1.83
	55	16	11	1.93
	57	12	7	2.06
	53	20	15	1.85
Variant 2 (Nb, C, V)	55	15	11	1.95
	57	11	7	2.08
	53	21	15	1.82
Variant 3 (W, C)	55	15	10	1.89
	57	11	6	2.0

In addition to mechanical tests, an evaluation of microstructure according to specification described in 2.1 was carried out. All experimental materials satisfied all testing criteria. Minute inclusion content was achieved. The prior austenite grain size in all tested specimens was between G 8 and 10. An example of microstructure of standard 1.2343 grade produced in the ŽDAS company with visible prior austenite grain boundaries is shown in fig. 1.



Figure 1 Microstructure of a 1.2343 tool steel with visible prior austenite grain boundaries (G = 8)

Tempering curves were obtained for the variants with modified chemical compositions. They are shown in fig. 2 – fig. 4.

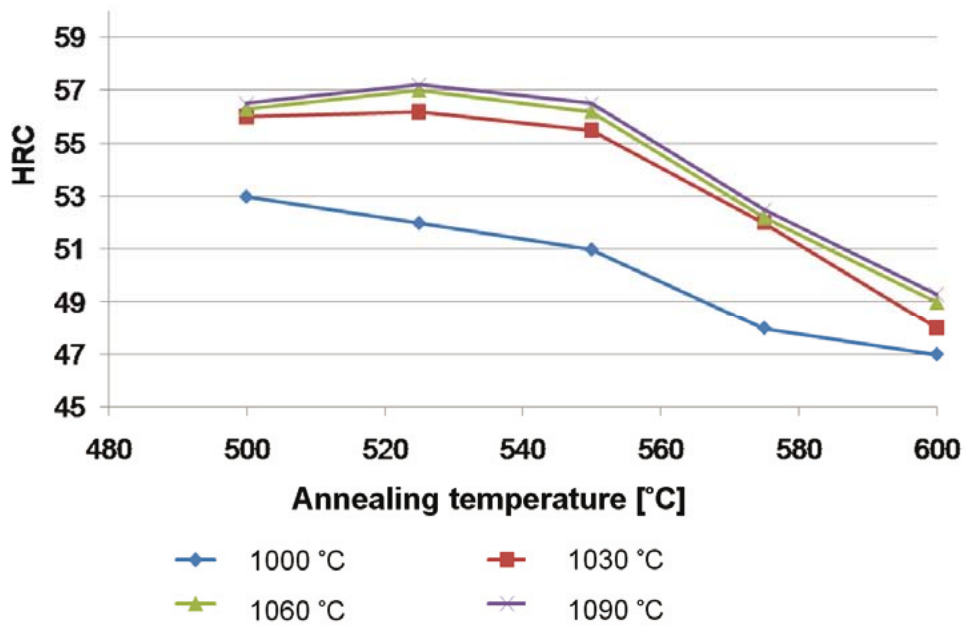


Figure 2 Annealing curves – variant 1 (Nb)

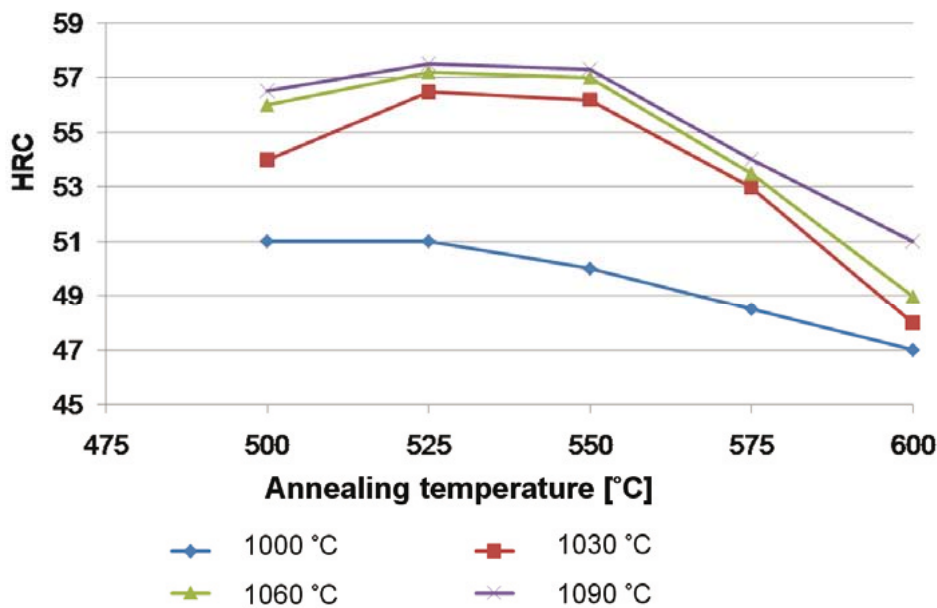


Figure 3 Annealing curves – variant 2 (Nb, C, V)

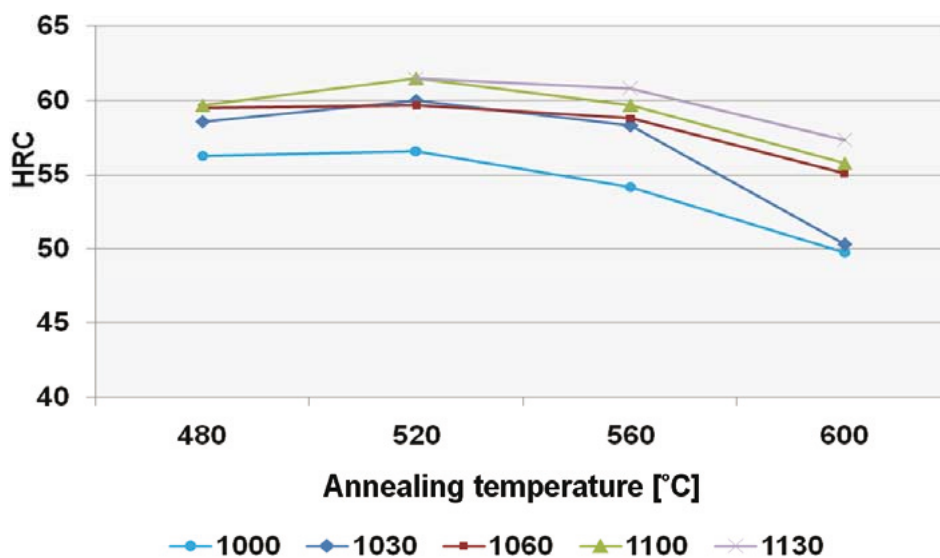


Figure 4 Annealing curves – variant 3 (W, C)

5. Testing of forging dies

The forging die shown in fig. 5 is used in Kovárna VIVA Zlín for manufacturing small forgings (with the weight of about 1 kg). With regard to production of large series (up to 100 thousand pieces yearly over several years), the die is considered a suitable candidate for testing of new tool materials. Prior to this testing initiative, the die used to be made from standard 1.2343 steel quenched and tempered to 47 HRC and its life was equal to 4,500 strokes. The nature of its wear (see fig. 5, bottom) indicates that during its service, abrasive wear and local plastic deformation rather

than cracking are the chief phenomena taking place in the die. For this reason, the die material was proposed to be treated to higher hardness.



Fig. 5 Forging die used for field tests and its worn surface

A series of tests was performed on dies from standard 1.2343 steel and from the above described modified materials conventionally treated to a hardness above 50 HRC. Forging conditions were kept stable in the course of testing. The life of dies was monitored. Results of selected tests are shown in tab. 4. They indicate that higher hardness led to a significant improvement in the die life (by about 70%) even in the variants with no modification of chemical composition. Using steel with modified chemical composition and equal hardness extended the life of the die even more. Its life was almost 100% longer than that of the initial die.

All chemical composition variants tested have proven to be beneficial in practice and can be considered usable for manufacturing forging dies.

Table 4 Results of field tests of forging dies

Die material	Relative position of workpiece axis and die parting plane	Hardness HRC	Life (no. of strokes)
1.2343	perpendicular	47	4,304
1.2343	perpendicular	53	7,080
1.2343	parallel	53	7,628
Variant 1 (Nb)	perpendicular	54	8,499
Variant 2 (Nb, C, V)	perpendicular	54	9,388
Variant 3 (W, V, C)	perpendicular	54	8,470
Variant 3 (W, V, C)	parallel	56	7,759

6. Conclusions

The above results indicate that the development of a high-quality hot work tool steel with chemical composition based on that of 1.2343 was successful. Furthermore, test pieces from steels with three different modified chemical compositions were made. The modifications led to higher hardenability and abrasive wear resistance. All investigated materials have been field-tested as forging die materials in Kovárna VIVA Zlín. Their utilization greatly extended the life of forging dies. Testing in the forging plant has also shown that in some cases the dies can be quenched and tempered to a hardness significantly higher than 50 HRC without causing in-service cracking.

With regard to favourable results of the tests, all examined variants of the steel 1.2343 can be regarded as usable hot work tool steels. Since 2009, the above variants have been protected by utility designs.

Acknowledgements

The presented results have been achieved with support of Ministry of Industry and Trade of the Czech Republic within the project TANDEM FT-TA 3/091.

References

- [1] Pereloma, E. V.; Timokhina, I. B.; Hodgson, P. D.: Transformation behaviour in thermomechanical processed C-Mn-Si steel with and without Nb, *Materials Science and Engineering A*, Vol. 273 – 275 (1999), pp. 448–452
- [2] Dobrzanski, L. A.; Zarychta, A.; Ligarski M.: High-speed steels with addition of niobium or titanium, *Journal of materials processing technology*, Vol. 63 (1997), pp. 531–541
- [3] Novak, P.; Vojtech, D.; Serak J.: Pulsed- plasma nitriding of a niobium–alloyed PM tool steel, *Materials Science and Engineering A*, Vol. 393 (2005), pp. 286–293

¹ Ing. Pavel Šuchmann, COMTES FHT a.s., Průmyslová 955, 334 41 Dobřany, Czech Republic. Tel.: +420 377 197 330, e-mail: pavel.suchmann@comtesfht.cz

² Ing. Jiří Krejčík, CSc., SVÚM a. s., Areál VÚ, Podnikatelská 565, 190 11 Praha 9-Běchovice, Czech Republic, Tel.: +420 222 726 559, e-mail: krejcik@svum.cz

³ Ing. Pavel Fila, ŽĎAS a. s., Strojírenská 6, 591 71 Žďár nad Sázavou, Czech Republic, Tel.: +420 566 642 136, e-mail: pavel.fila@zdas.cz

⁴ Ing. Ladislav Jelen, CSc., Vítkovice – výzkum a vývoj – technické aplikace a.s., Pohraniční 31, 706 02 Ostrava - Vítkovice, Czech Republic, Tel.: +420 595 952 441, e-mail: ladislav.jelen@vitkovice.cz

⁵ Ing. Eduard Psík, Kovárna VIVA Zlín, spol. s r. o., Tř. T. Bati č. p. 5266, 760 01 Zlín, Czech Republic, Tel.: +420 577051310, e-mail: eduard.psik@vivazlin.cz

ALTERNATIVE EXPLOSION-FORMED JOINT OF HIGH-STRENGTH TUBE AND SLEEVE

Miroslav Urbánek¹, Petr Nesvadba², Bohuslav Mašek³, Pavel Hronek³

Abstract

One of current advanced trends is the use of HSLA steels in frame structures. These advanced high-strength materials save the weight of the structure itself but their joining is problematic. Normally, the joints cannot be created by conventional welding, mainly due to the drop in strength in the joint. In order to retain the high strength potential of these materials, an alternative explosion-formed joint of a sleeve and a tube was designed.

Keywords: joint, explosion, forming, high-strength steel

1. Introduction

New types of low-alloyed high-strength steels show great potential for replacement of conventional structural steels in various types of structures. In this case, joints between individual components of the structure can become the most problematic locations. High-strength materials are not easily weldable. First, it is due to their chemical composition which itself, in most cases, does not guarantee good weldability. Second, their controlled microstructure completely changes due to welding and has thus different – typically worse – properties in the welded location

For these reasons, alternative techniques for making permanent joints are sought. Authors of this paper have been seeking low-cost and highly productive alternative methods of making such joints. One of such techniques meeting the required criteria is explosive bulk forming applied in the experiment. In the first step, technological ductility in expansion of the tube wall due to pressure of the explosion gas was examined. The results served for designing the second experiment in making a high-strength tube-sleeve joint with the strength above 1,000 MPa. In order to determine the load-carrying capacity and analyse the failure mode of the joint, it was tested under axial load. [4,5].

2. Explosive forming

Man has been using the effects of explosive energy for centuries, particularly in military technology. Explosives and blasting explosives in particular, offer new opportunities for use in forming and welding of metals, as they expand the potential for use of the dynamic pressure caused by the explosive not only in pressing but also in bulk forming, hole making, shearing, etc. Explosive forming has been used in past in rocket and aviation technology for forming sizable structural parts, in rail transport and many other branches of human activity. [1–3]

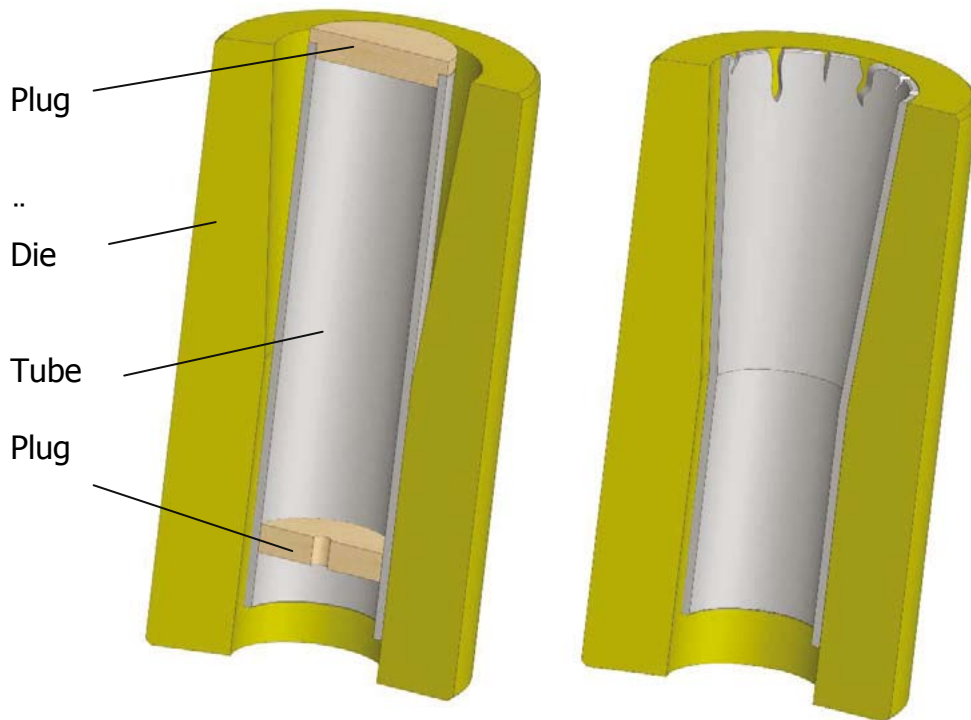


Figure 1 Schematic of the tube expansion test performed by explosion in a die, the condition before and after the explosion

SEMTEX S30 was selected for the initial bulk forming tests on tubes. Its name Semtex was formed by joining the words SEMtín (the location of the producer) + EXplosive and became the name of a range of special blasting explosives. Semtex S-type blasting explosive is a special-purpose product for explosive welding of metals, forming of metals and other applications.

In order to determine the elongation or maximum plasticity of a high-strength tube in rapid forming processes, an experiment was carried out involving forming in a die with a cylindrical cavity with a conical 4.5° end (Fig. 1). The test led to expansion of the tube to a conical shape from the initial 50 mm to the diameter of 67.3 mm. No visible cracks formed in the tube until the diameter of about 60 mm. A preliminary calculation identified the maximum useful deformation of 20%

$$A_{\max} = \frac{d_u - d_o}{d_o} = \frac{60 - 50}{50} = 0.2 \Rightarrow 20\% \quad (1)$$

For the first experiment SEMTEX S30 in the amount of 308.8 g was used. The forming medium consisted exclusively of the products of the detonation. This slightly large amount of explosive was used in order to ensure the complete deformation of the tube along the entire die length.

The findings were a basis for designing and defining the dimension of an alternative joint type and the entire explosive forming process. An electric detonator with about 0.97 g of high explosive was used. The forming medium was water within the tube closed with plugs. Forming with the aid of an explosive and water is highly efficient in energy utilization and imposes lower acoustic loads on the environment. The liquid provides rather uniform effects of pressure throughout the volume to be formed. Besides, the amount of explosive is more than one order of magnitude

lower, which reduces the cost. In this experiment, the tube with the above amount of explosive has filled the recess in the sleeve perfectly. [4,5]

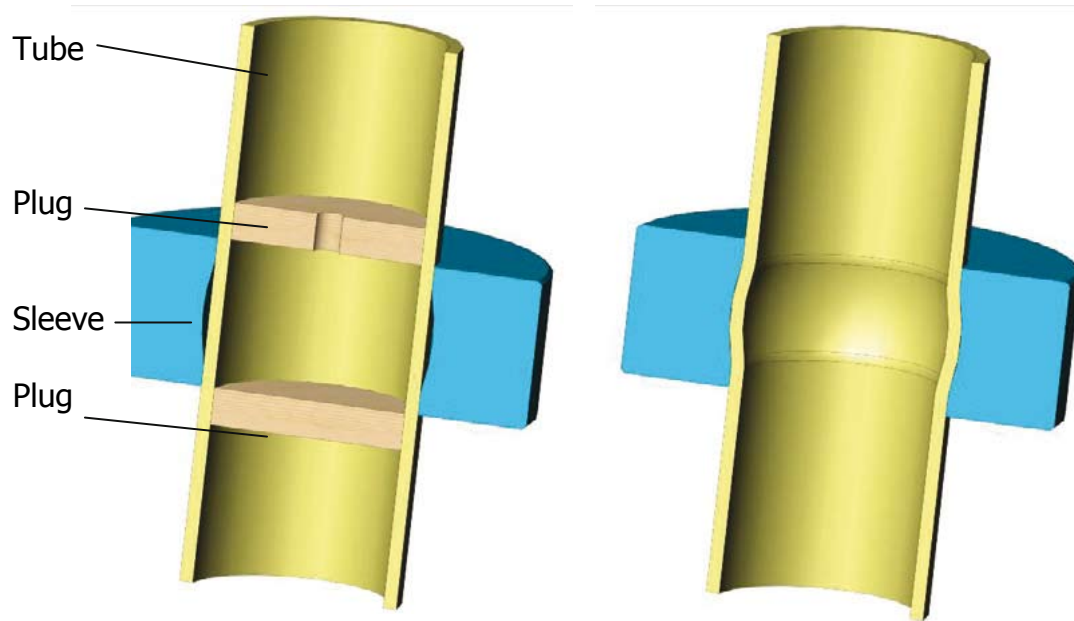


Figure 2 Schematic representation of the joining process, the condition before and after the explosion

3. Compression load-carrying capacity test

A compression load-carrying capacity test was performed on the experimentally prepared joint. The specimen with the joint was supported under the tube in order to allow the shear force to act on the entire surface of the sleeve. The load-carrying capacity of the was about 30 kN. The joint resisted the load up to 60 kN. This load did not cause a catastrophic destruction either, as stable plastic deformation occurred with the extension path of about 20 mm. The test was performed under quasi-static conditions at room temperature. The evaluated parameter was the dependence of the loading force (kN) on the cross-bar movement (mm) – Fig. 3.

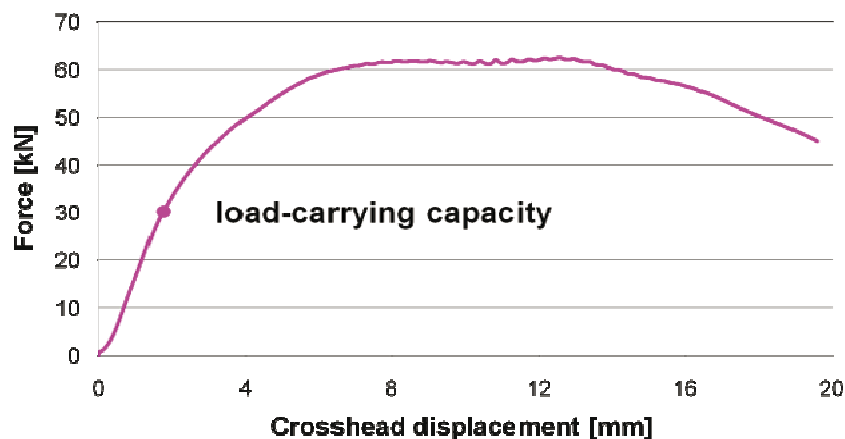


Figure 3 Behaviour of the joint under load

Explosive forming causes strengthening mainly in the impact area of the outer tube surface on the inner surface of the sleeve. This locally increases the strength of the tube and improves the load-carrying capacity of the joint. The compression load-

carrying capacity test caused a reverse forming of the bulged area into a cylindrical shape (Fig. 6). This indicates that the load-carrying capacity of the joint can be governed to a great extent by the flow stress of the tube material.

4. Metallographic Analysis

Metallographic observation and hardness profile measurement were performed after the compression load-carrying capacity test. The material of the tube consisted of fine-grained tempered martensite with uniformly dispersed fine carbides. The prior austenite grain size was about $10\mu\text{m}$.

The material of the tube was subjected to a number of deformations which caused local strengthening. The tube was formed when manufactured and, again, in the explosive forming process. Finally, it was also deformed during the load-carrying capacity test. These changes are apparent in the hardness profile. The hardness profile was measured from the bottom edge of the tube to the location of the original joint prior to destruction (Fig. 4-left). There is the first peak in the distance of 35 mm, indicating the explosive forming operation. Another peak in the distance of 20 mm represents the deformation in the mechanical testing shop.

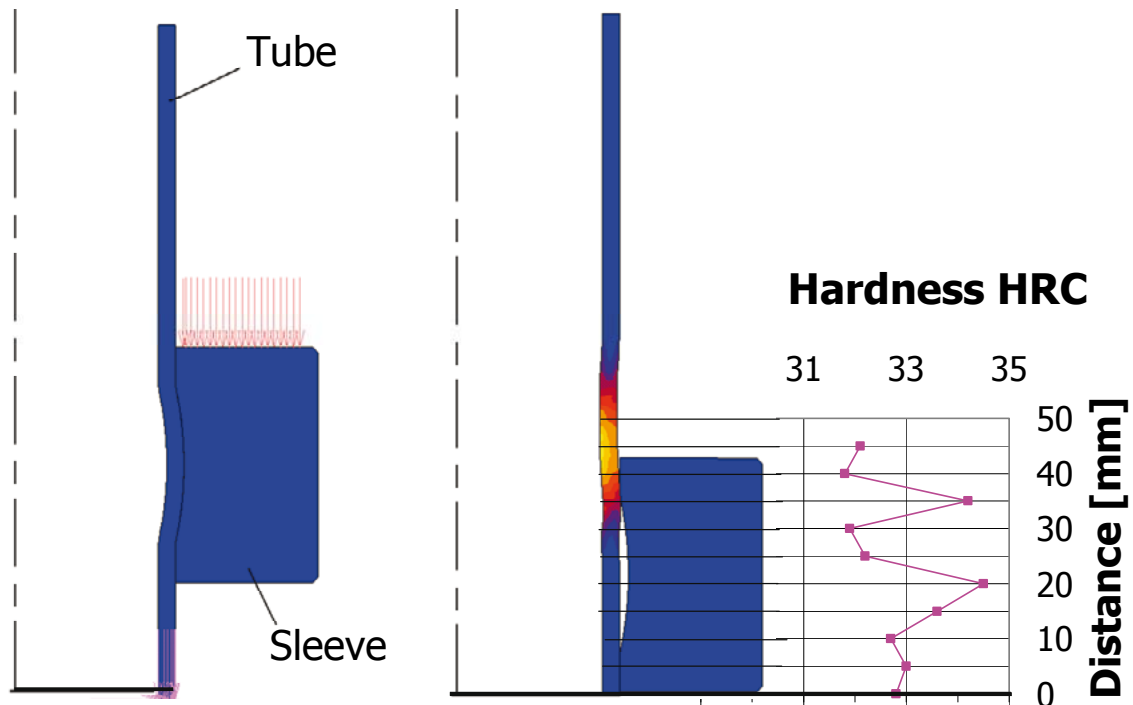


Figure 4 FEM model, Measure hardness profile

5. FEM Simulation

Assessment of the load-carrying capacity of the joint requires identification of the limit loading states which lead to progressive deformation of the material. Equally important is the analysis of the failure which, in this case, takes the form of plastic deformation. As the interaction of the components of the joint cannot be measured from outside, FEM simulation has been used.

Thanks to the axial symmetry of the joint, the problem could be solved as an axially symmetric calculation offering sufficiently fine mesh with fairly low number of elements. Difficult aspects of the problem resulted from non-linear features, such as the contact points between both components, and the elastic-plastic material of the

tube. Data characterizing the material was defined by means of a stress-strain curve for the given state of the material and the corresponding strengthening. Boundary conditions were identical to those used in testing of the joint in testing equipment.

The ramp function of the loading force acting on the joint was transmitted by the entire surface of the sleeve. The joint underwent elastic deformation under the load up to 30 kN. Further increase in the loading force led to an onset of plastic deformation – Fig. 4.

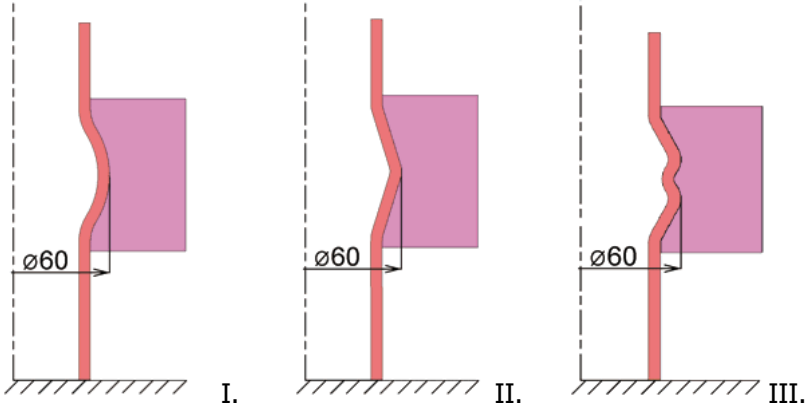


Figure 5 Three proposed alternatives of the joint geometry

On the basis of obtained results, additional three geometries of the joint were proposed. Using FEM simulation, their load analysis was performed, Fig. 6. The first one was based on the original geometry where the diameter of the bulged area was increased from 53 mm to 60 mm, Fig. 5-I. The outer diameter of 60 mm was measured as the maximum limit diameter during the previous experimental expansion of the tube in a tapered die. In another alternative, the spherical bulged region was replaced with a double-taper shape, Fig. 5-II. In the third alternative, higher strength of the joint was achieved thanks to higher yield strength of the material used. At the same time, the contact surface was made more ragged which contributed to higher load-carrying capacity of the joint, Fig. 5-III. Curves for forces required for destruction of the joint alternatives determined by FEM simulation are plotted in Fig. 6.

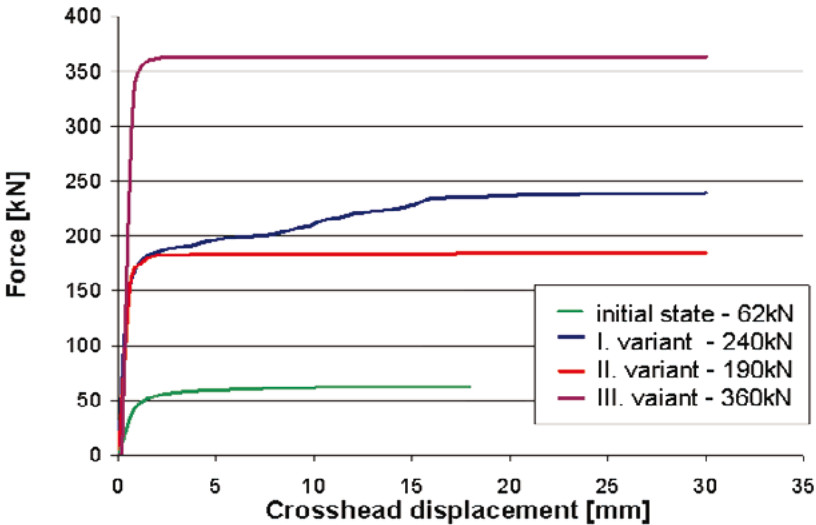


Figure 6 Load carrying capacities of optimised joints

6. Conclusion

The experiment consisted in designing and making a joint of a high-strength 50 mm diameter tube with the wall thickness of 3 mm and a sleeve. The explosive PENT in the amount of 0.97 g and water as the forming medium were used for the detonation. Forming was carried out without any tools. The load-carrying capacity of the joint was measured by means of a compression test of load-carrying capacity. The joint showed a load-bearing capacity of 30 kN but resisted the load up to 62 kN. This magnitude of load did not cause a full destruction either, as stable plastic deformation occurred with the extension of about 20 mm. The shapes of surfaces of the joint were modified with the aid of FEM analysis and the strength level will be optimized with regard to requirements on the structure.

Acknowledgements

This study was prepared with the support of the Research Centre of Forming Technology – FORTECH, 1M06032, Faculty of Mechanical Engineering of the University of West Bohemia, Czech Republic, 2010

References

- [1] Blazynski, T.Z.: Explosive welding forming and compaction. Applied science publishers London and New York, 1983, ISBN 0853341729, p. 200
- [2] Ezra, A.A.: Principles and Practice of Explosive Metalworking. Industrial Newspapers Limited, London 1973, ISBN: 0-90199405-7, p. 270
- [3] Chládek, L.; Němeček, J.; Vacek, J.: Výbuchové svařování kovů a příbuzné procesy. Red. J. Klůna, 1. vyd., Praha, SNTL – Nakladatelství technické literatury, 1971, p. 224
- [4] Pantoflíček, J.; Lébr, F.: Teorie působení výbuchu I, Výbuchové vlny. 1. vyd., Vysoká škola chemickotechnologická v Pardubicích, SNTL – Nakladatelství technické literatury, 1967, p. 88
- [5] Vacek, J.: Urychlování kovových obálek detonací trhavinových náloží. Pardubice-Semtín, VUPCH, 1998

¹ Ing. Miroslav Urbánek, COMTES FHT a.s., Průmyslová 955, 334 41 Dobřany, Czech Republic, Tel.: +420 377 197 322, e-mail: miroslav.urbanek@comtesfht.cz

² Ing. Petr Nesvadba, Explosia a.s., Výzkumné ústav průmyslové chemie, 532 17 Pardubice-Semtín, Czech Republic, Tel.: +420 466 825 793, e-mail: petr.nesvadba@explosia.cz

³ Prof. Dr. Ing. Bohuslav Mašek, FORTECH, Západočeská univerzita v Plzni, Fakulta strojní, Univerzitní 8, 306 14 Plzeň, Czech Republic, Tel.: +420 377 638 050, e-mail: masekb@vctt.zcu.cz

³ Ing. Pavel Hronek, FORTECH, Západočeská univerzita v Plzni, Fakulta strojní, Univerzitní 8, 306 14 Plzeň, Czech Republic, Tel.: +420 377 638 067, e-mail: phronek@vctt.zcu.cz

MODELLING THE PROCESS OF FORMING RAILWAY WHEELS

Michal Zemko¹, Petr Matušek², Jana Martínková¹, Mikuláš Fedorko¹,
Libor Pětváldský²

Abstract

The paper describes numerical and physical simulations of the current process of manufacturing railway wheels. The numerical simulation provides information on the material flow, strain and strain rates in the course of forming and temperature data related to the heat treatment. By physical simulation one can obtain samples with microstructures matching those of selected locations of the actual railway wheel. Combining these two techniques provides an opportunity to optimise the process in terms of both quality and energy consumption. This method was applied to the process of forming rail wheels from the steel 1.0314 at the BONATRANS GROUP a.s. plant. The paper gives results of both numerical and physical simulations and their correlations with the actual railway wheel.

Keywords: railway wheel, numerical simulation, physical simulation

1. Introduction

The process of production of railway wheels consists of a series of forming operations and subsequent heat treatment. Several alternative procedures are used for forming, the most frequent one being the combination of closed die forging and rolling in a radial rolling mill. The company BONATRANS GROUP a.s. uses the following one:

Heating the workpiece in a carousel furnace – descaling – upsetting – forming – punching – rolling – bending – 3D measurement – heat treatment

Further improvement in the process of forming railway wheels requires detailed knowledge of distribution of the key parameters - temperature and strain - throughout the wheel semiproduct across the entire forming process. The impact of changes in these parameters on the resulting microstructure and properties needs to be known as well. The present publication gives a description of the full-scale numerical simulation of processes of forming and heat treatment of railway wheels according to the current procedure used in the company BONATRANS GROUP a.s.. It also contains results of physical simulation performed in the simulator of thermal and deformation cycles. Thermal and deformation cycles applied to specimens from 1.0314 steel corresponded to actual curves for these parameters for selected locations of the railway wheel.

2. Experimental Material and Methods

A blank from 1.0314 material (Table 1) was worked under production conditions using the conventional forming and heat treatment procedures. Its microstructure was mapped in selected locations in regard to phase composition and grain size. In these locations, Vickers hardness HV30 was measured as well.

Table 1 - Chemical composition of 1.0314 steel

Element	C	Mn	Si	P max.	S max.	Cu max.	Cr max.	Ni max.
Content [vol. %]	0.42 -0.50	0.50-0.80	0.17-0.37	0.040	0.040	0.30	0.25	0.30

DEFORM software was used for computer simulation of the process of forming railway wheels. The computation was performed using data on the steel 1.0314 (according to the Czech Standard CSN 412050) which was measured by COMTES FHT a.s. The process was simulated under experimental conditions. The numerical model was calibrated using measured values of surface temperature and times related to the currently used process. Numerical simulation provided strain, strain rate and temperature vs. time curves for specified locations of the railway wheel. They were used as input for physical simulation.

Simulation of the heat treatment was based on the cycle description which had been provided. It was used for defining the thermal cycle in DEFORM software. The simulation yielded temperature vs. time curves for specified locations.

Physical simulations were carried out in the physical simulator MTS. This instrument allows to subject specimens of various sizes (up to the diameter of 12 mm) to controlled thermal and mechanical cycles. It offers simulations of both slow and rapid temperature changes (the maximum heating and cooling rate is 150°C/s). The specimen is heated by electrical resistance. Strain is introduced through alternating compressive and tensile deformation. It is possible to simulate phenomena with relatively high strain rates (up to 50 s⁻¹).

Specimens for physical simulations were manufactured from a continuously cast block supplied by BONATRANS GROUP a.s. For the purpose of taking samples, initial distance of each examined location from the edge of the cast block in radial direction was calculated by means of Point-tracking method. This guaranteed that relevant initial microstructure was used for each analysed location. Each specimen represented a particular location of the final railway wheel.

Microstructures of specimens after physical simulation were evaluated and compared with specimens from the real-world wheel where hardness was measured as well. Four locations were selected for evaluation as specified by BONATRANS GROUP a.s. Locations of the reference points on the wheel section:

- P1 point - 5 mm below the rolling contact surface
- P2 point - 35 mm below the rolling contact surface
- P3 point – the plate below the transition to the rim
- P4 point – the plate above the transition to the hub

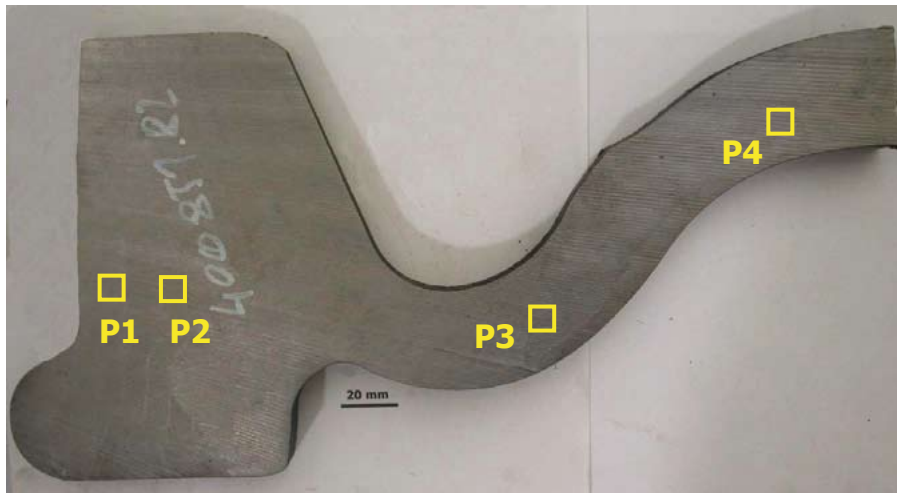


Fig. 1 Macrostructure

3. Numerical simulation

The simulation was conducted using DEFORM 2D/3D software which combines the potentials of 2D and 3D simulations. First operations could be handled as axially symmetric problems for 2D simulation, thus saving CPU time. The railway wheel production process was modelled in 2D up to the rolling operation. After the rolling simulation, the data had to be converted into a 3D model. The production process simulation was then completed in 3D.

The Point-tracking method was used to determine the temperature vs. time and strain vs. time curves for selected locations during production of the railway wheel.

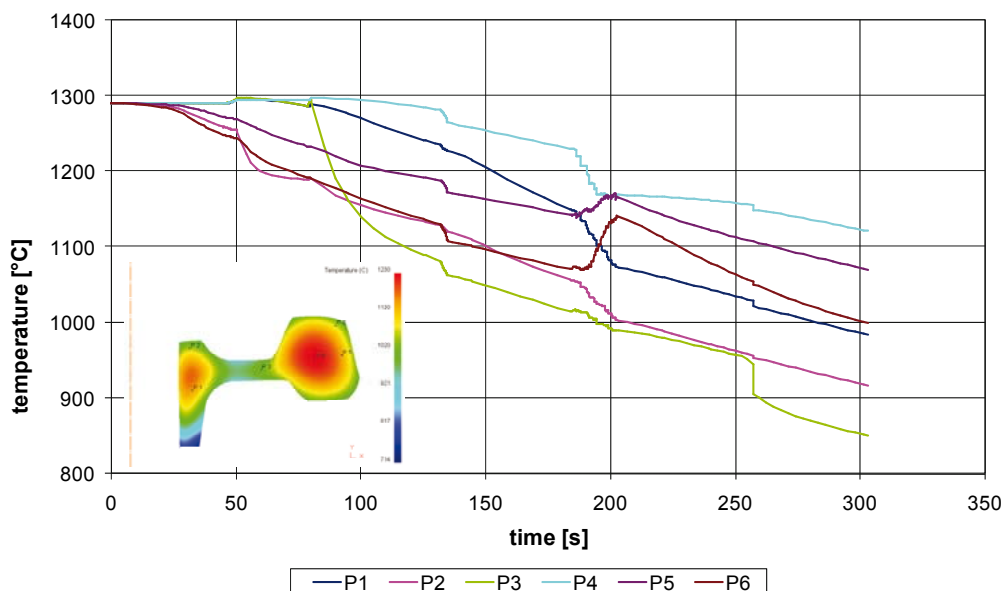


Fig. 2 – Temperature changes in selected locations during the entire forming process

Fig. 3 – Levels of strain in selected locations during the entire forming process

The thermal cycle for the DEFORM 3D module was prepared on the basis of the record provided. Temperature curves for selected points are shown in Fig. 4.

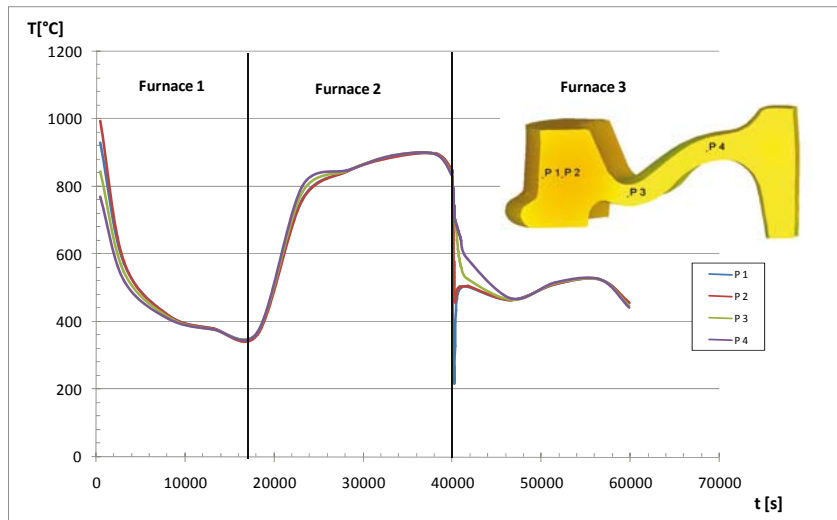


Fig. 4 Temperatures at selected points during heat treatment

4. Physical Simulation

Physical simulations were based on the numerical simulation in which the forming and heat treatment cycles were determined using DEFORM 3D.

Physical simulation cycles are shown in the following graphs for selected points. Fig. 4 displays temperature and strain during forming. Fig. 6 shows the heat treatment procedure.

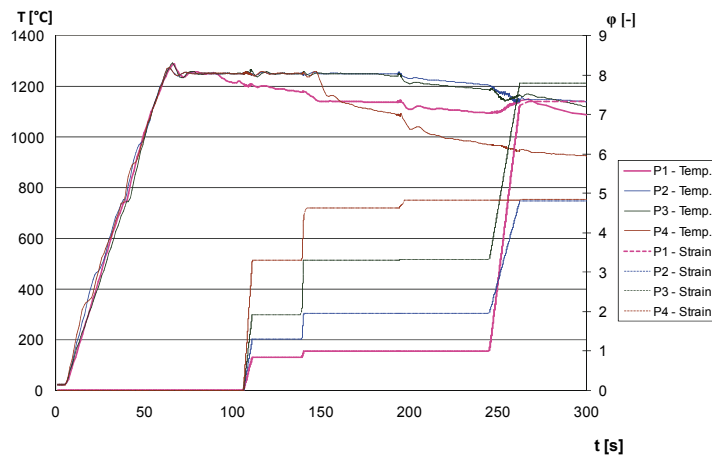


Fig. 5 Temperature and strain during forming

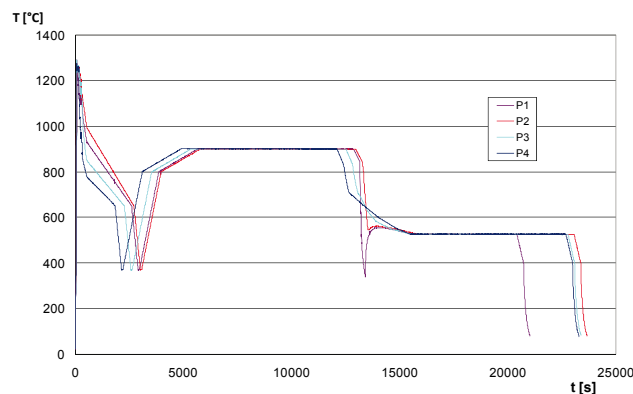


Fig. 6 Heat treatment cycle

6. Evaluation

Microstructures in the real-world part were compared with results of the simulation for all selected points. Micrographs of the actual part (AP) are shown on the left, whereas micrographs of samples from physical simulation (PS) are on the right.

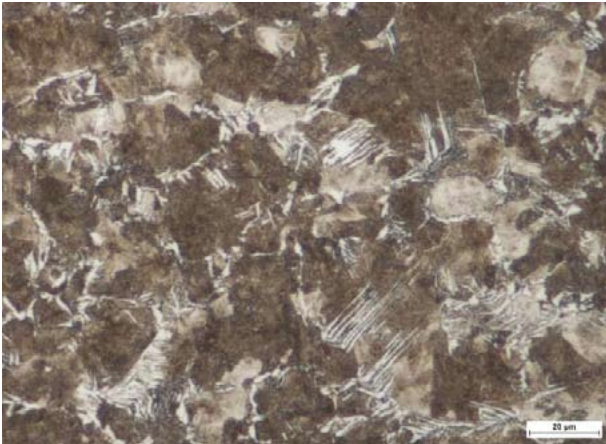


Fig. 7 Microstructure of the AP at point P1, magnification 500, hardness 266 HV30



Fig. 8 Microstructure of PS sample at point P1, magnification 500, hardness 234 HV30



Fig. 9 Microstructure of the AP at point P2, magnification 500, hardness 250 HV30

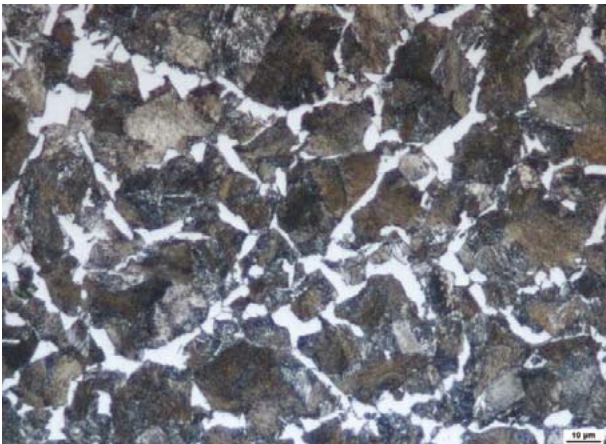


Fig. 10 Microstructure of PS sample at point P2, magnification 500, hardness 231 HV30

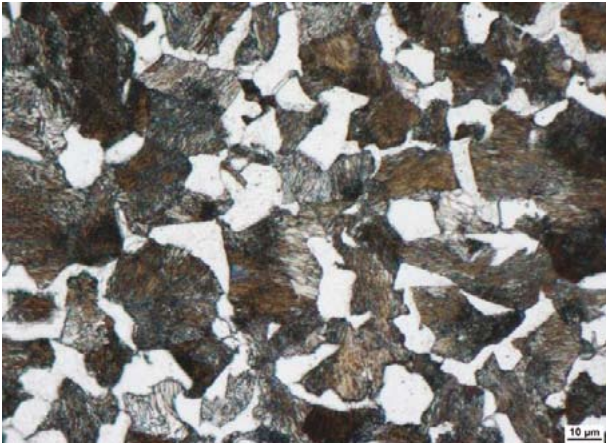
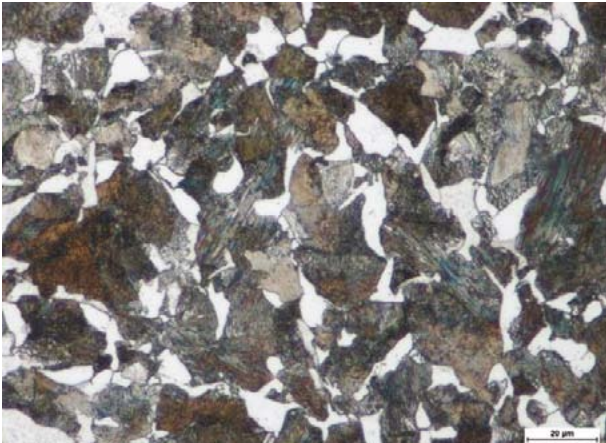


Fig. 11 Microstructure of the AP at point P3, magnification 500, hardness 209 HV30

Fig. 12 Microstructure of PS sample at point P3, magnification 500, hardness 199 HV30



Fig. 13 Microstructure of the AP at point P4, magnification 500, hardness 195 HV30

Fig. 14 Microstructure of PS sample at point P4, magnification 500, hardness 197 HV30

The microstructure consists of pearlite and ferrite. The proportion of ferrite in the microstructure at point P1 is about 5%. Some ferrite in the formed part is in the form of Widmanstätten microstructure (Fig. 7), which was not found in samples from physical simulation. The microstructure of the part has slightly finer grain which results in higher hardness.

P2 microstructures are very similar in the real-world part and in the samples, consisting of ferrite and pearlite. They contain higher fraction of ferrite (by about 10%) than those at point P1. No Widmanstätten microstructure was observed.

The microstructure at point P3 consists of pearlite and ferrite. The ferrite in the real-world material forms bands. The ferrite proportion was about 15%.

The microstructure at point P4 consists of pearlite and ferrite. The ferrite in the real-world material forms bands. The ferrite proportion was about 20%. In the microstructure of the specimen all-pearlite regions can be found (Fig. 14).

Table 2 – Hardness of the actual wheel

Measured location	Hardness HV30			Average
	Indentation 1	Indentation 2	Indentation 3	
P1	268	262	268	266
P2	244	253	252	250
P3	211	208	207	209
P4	191	198	195	195

Table 3 – Hardness of simulation samples

Measured location	Hardness HV30			Average
	Indentation 1	Indentation 2	Indentation 3	
P1	236	234	233	234
P2	231	231	230	231

P3	200	194	203	199
P4	196	200	194	197

Hardness of the real-world part was higher at all selected points than that of simulated materials. At points P1 and P2 the difference is about 20 HV, whereas hardness values at point P4 are almost identical.

5. Conclusions

Simulation software DEFORM was used for modelling and simulations of the process of forming railway wheels. Six process operations were simulated in more than 5,000 computation steps. Over 120 hours of net CPU time were required. The rolling operation was the most demanding one, requiring about 100 hours of CPU time of a high-performance multi-processor workstation.

The process was modelled according to a record obtained in production. It was compared continuously with this record. Temperatures and durations of individual simulated operations matched the real-world ones. Emphasis was laid on optimisation of the upsetting height, the impact of friction on the forming operation and the method of cooling the wheel. The 3D simulation of the rolling operation can be considered unique with regard to its low degree of simplification and, at the same time, its high precision.

Physical simulation was based on the results of numerical modelling which had been used to design the entire forming and heat treatment cycle for the railway wheel at all selected points P1 - P4. The comparison between the real-world part and simulated specimens at points P2 – P4 shows that microstructures and hardness values were almost identical. Differences were found at point P1 only. Ferrite in the microstructure of the actual wheel formed Widmanstätten microstructure in this location, whereas no such microstructure was found in corresponding simulation samples. There are also differences in hardness values. The wheel shows higher values by 32 HV30. The microstructure formed in simulation samples with initial as-cast structure matched the reference samples taken from the railway wheel in terms of hardness and microstructure characteristics and grain size. One can therefore conclude that in this study working numerical and physical models have been proposed and verified for the temperature and strain development in the rim of a railway wheel during its production process. In its utilisation one must take account of deficiencies inherent to 3D modelling of rolling and to modelling of microstructure in areas very close to the contact surface of the wheel rim.

The model was verified for a single design of the wheel and for a single material. After additional improvements to their precision, the numerical and physical models will be suitable for optimisation of the railway wheel production process.

¹ Ing. Michal Zemko, Ph.D., COMTES FHT a.s., Průmyslová 955, 334 41 Dobřany, Czech Republic, Tel.: +420 377 197 320, e-mail: michal.zemko@comtesfht.cz,

Ing. Jana Martínková, Tel: +420 377 197 341, e-mail: jana.martinkova@comtesfht.cz,

Ing. Mikuláš Fedorko, Tel: +420 377 197 321, e-mail: mikulas.fedorko@comtesfht.cz,

² Ing. Petr Matušek, BONATRANS GROUP a.s., Revoluční 1234, 735 94 Bohumín, Czech Republic, Tel: +420 597 082 626, e-mail: pmatus@bonatrans.cz,

Ing. Libor Pětvaldský, e-mail: lpetvaldsky@bonatrans.cz

SOME METALLURGICAL ASPECTS OF MAIN BATTLE TANK ARMOUR AND ANTI-ARMOUR WARHEADS

Alistair Doig¹

Abstract

The choice of steels for Main Battle Tanks (MBTs) is explained, from single plate sloped frontal armour to current multi-layered designs. The rationale for armour materials selection is discussed in terms of high strain rate sensitivity – from steels to aluminium alloy light armour vehicles (LAVs). The functioning of the 2 main types of warhead used against armour are also described. Some interesting effects of deformation at high strain rate are discussed.

Keywords: MBT armour, anti-armour warheads, properties at high strain rate

1. Introduction

Fig.1 shows the empirical log/log plot of Messrs Milne and de Marre, first graphed in ~1922 for KE projectiles. The energies to penetrate range here from 10^2 to 10^7 J.

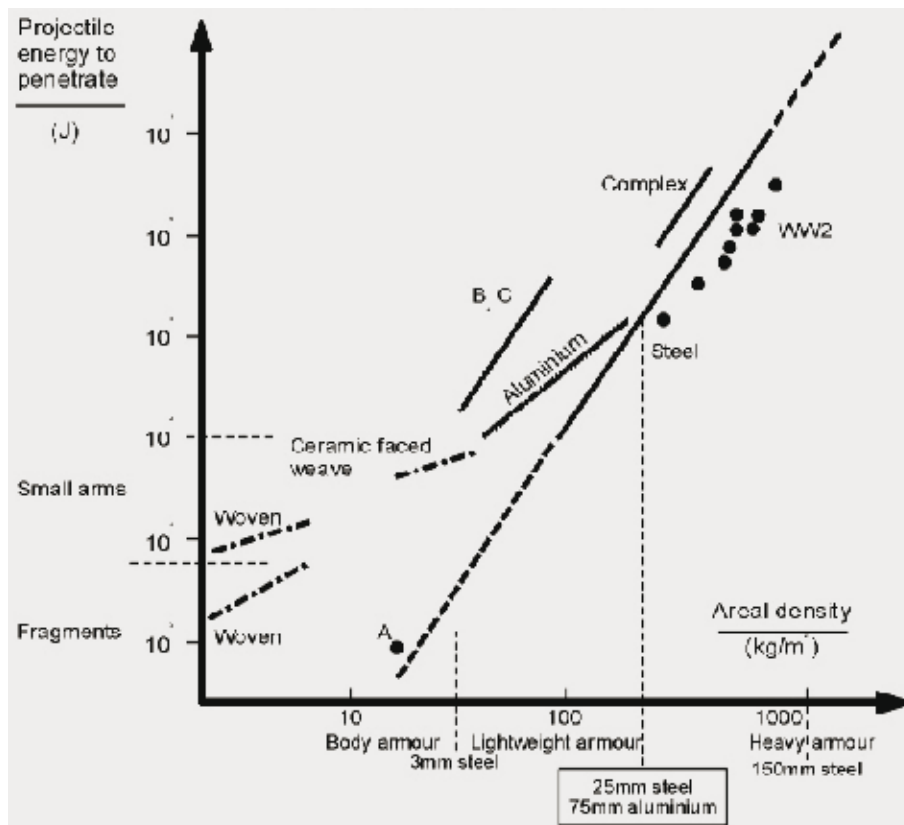


Figure 1 The Milne de Marre graph for KE penetration

They started with point 'A' the 100J arrows of Agincourt kept out by the 2mm thick 'steel' armour of the day, then added WW1 tank data. Since then WW2 tanks (and others) have been added, giving the long line for steel which is straight.

Data for aluminium alloy armours (starting with M113 APC) was added in the 1960's, also giving a straight line plot, but of lower slope. The 2 lines intersect for equiprotection at ~25mm thick steel or ~75mm thick Al. Above this point steel has the advantage over Al (requiring more energy to penetrate) and so steel armour is used for MBTs – but for thinner LAV armour Al has the advantage.

2. Steels for MBT armour

British Chieftain and early Challenger tank armours were made of single layer plates ranging from ~10mm thick for the rear panel to ~500mm thick for the frontal sloped main protection – the 'glacis plate'.



Figure 2 Challenger MBT

Plates <100mm thick were of 1.5%CrNiMo steel and plates >100 thick were of 1.5%NiCrMo steel (extra Ni for hardenability) both ordinary low alloy steels, in the water quenched and fully tempered condition to optimise impact toughness at the 300Hv (30HRC) level. Total weight is limited to 65tonnes due to railway loadings.

3. The 'heavy metal long rod' kinetic energy penetrator KE

The most efficient warhead against the front glacis plate is the so called long rod penetrator made with a 5kg 'heavy metal' core, usually tungsten alloy: W-10%NiFe.



Figure 3 120mm long rod penetrator

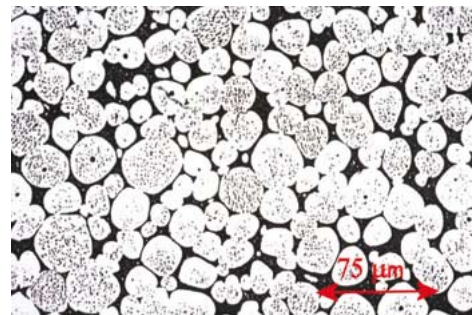


Figure 4 Long rod microstructure

Efforts continue to increase the L/D ratio (currently $\sim 20/1$) to raise the 'energy density' (J/mm^2). With a muzzle velocity of $\sim 1,700\text{m/s}$ a current long rod has the same kinetic energy as 4 carriages of a 200km/hr train (300MJ) – and that energy is concentrated on a 25mm diameter spike!

Because W has a high melting point ($\sim 3,500^\circ\text{C}$) the long rod is made by powder technology using NiFe as the binder phase. The pressed 'green' rod is liquid phase sintered at $\sim 1,500^\circ\text{C}$, when the binder melts filling in the voidage, and giving the microstructure seen in Fig.4.

4. The copper coned shaped charge penetrator

The cheaper but less lethal shaped charge warhead uses an on-board explosive charge (yellow in Fig.5) to collapse a copper cone liner.

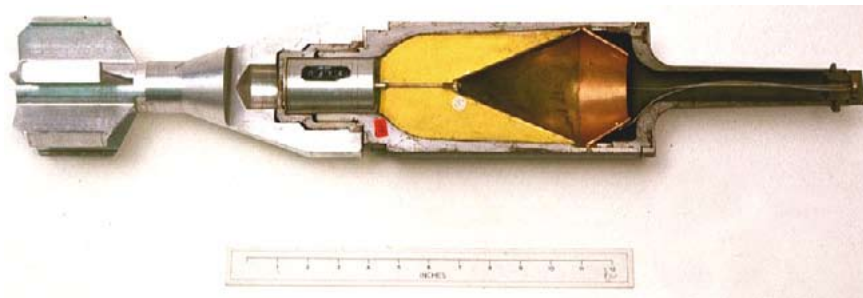


Figure 5 Cutaway of 120mm shaped charge warhead

Initiation is via a piezzo-crystal at the front of the standoff tube, and so there is no need for an on-board battery. The most common shaped charge device is the shoulder launched anti-armour 'rocket propelled grenade', such as the Russian RPG7.

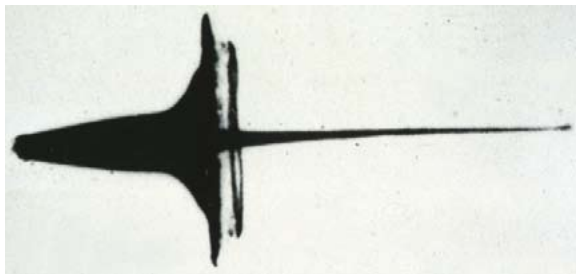


Figure 6 Collapsing Cu cone [flash X-ray photographs]

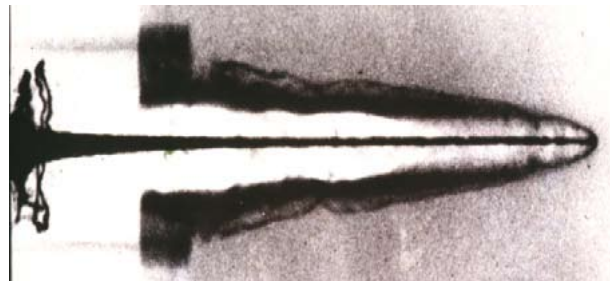


Figure 7 Jet into Al alloy target

The copper jet is squirted forward with a peak speed of $\sim 8,000\text{m/s}$ (Mach30!) as seen in Fig.6. Fig.7 shows the jet entering an Al alloy target, where it will penetrate to a depth of $\sim 20\text{CD}$ (cone diameters). For best penetration the jet should be as dense as possible, but with good ductility to give a long thin penetrator.

5. The latest multi-layered armours and applique armours

The flash X-ray photograph in Fig.8 shows an experiment with a KE long rod flying from left to right through a sloped 2 layered target. After penetrating the thinner outer layer the nose is bent, effectively blunting the penetration of the main armour behind. So multi-layering is a way of reducing penetration with no weight penalty, but fabrication is more complicated.

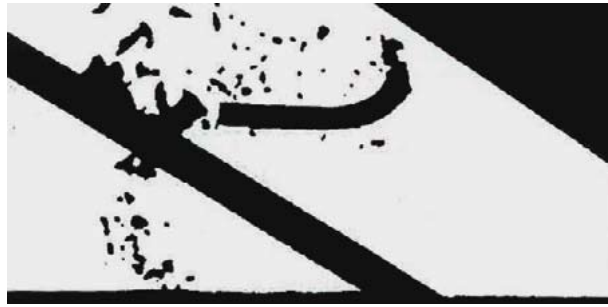


Figure 8 Long rod through 2-layered target

The next step is to fill in the air gap (glass is good against shaped charge jets) giving a 3-layered armour. Then adding an outer layer of hard material (ceramic) encourages a penetrator to shatter, and adding an inner layer of soft material (polyethylene) gives an anti-spall liner – now giving a 5-layered armour.

Applique armours come in 2 main types: 'passive' and 'reactive', and 1 example of each is shown below. Fig.9 shows ceramic tiles (to encourage shot shatter) being adhesively bonded to the steel plate.



Figure 9 Ceramic tiles applique



Figure 10 ERA on a T55 tank

Fig.10 shows 'explosive reactive armour' (ERA) elements bolted onto the steel plates. These are hollow steel boxes containing sheet explosive, designed to initiate when a shaped charge jet impinges – and then the flying plates consume much of the jet.

6. Some effects of high strain rate deformation

The conventional Instron type tensometer crosshead is not usually driven faster than $\sim 10\text{mm/s}$, giving 'quasi-static' properties at strain rates of $\sim 10^{-3}$ per second, with which we are all familiar. At Shrivenham we use an instrumented drop tower to study materials' dynamic' properties at higher strain rates (up to $\sim 10^{+3}$ per second) both in tension and in compression – and the instrument is seen in Fig.11.

Weights at up to 50kg strike the anvil at up to 20m/s, and a piezzo-crystal transducer in the striker tip feeds load values into a transient recorder.

Fig.12 shows the effect of strain rate on the tensile properties of a metal – where at higher speeds strength is raised, but at the expense of ductility. The $\dot{\epsilon}$ value for the 'static tensile test' is 10^{-3} s^{-1} , and for the 'shaped charge penetration' is 10^5 s^{-1} .



Figure 11 Drop tower

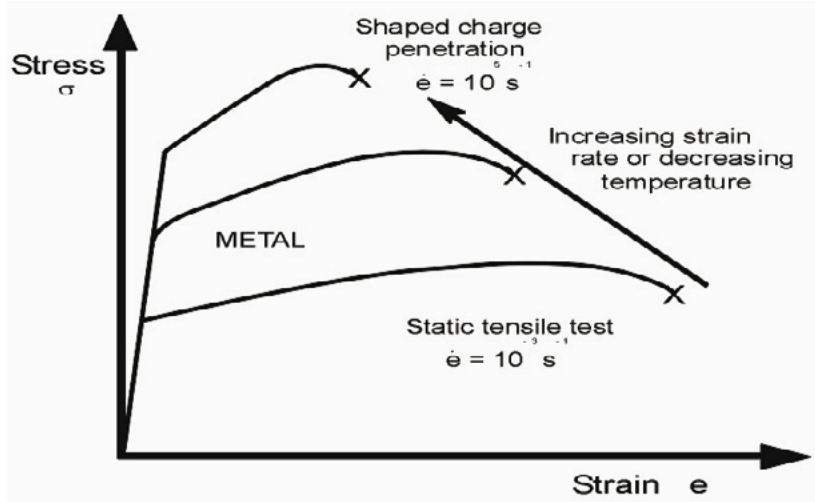


Figure 12 Tensile curves vs strain rate $\dot{\epsilon}$

Interestingly, Young's modulus and toughness (area under the curve) remain invariant with strain rate.

From dislocation theory the Holloman (or Ludwig) equation relates true stress σ to true strain ϵ and strain rate $\dot{\epsilon}$ during plastic deformation. Then at constant plastic strain (say 0.2%PS or σ_y) it can be shown [ref. 1] that:-

$$\sigma_y = \sigma_0 + K\epsilon \cdot m \quad (1)$$

Where σ_0 and K are alloy constants, and m is the strain rate sensitivity index. This gives straight line plots when using log/log axes as in Fig.13.

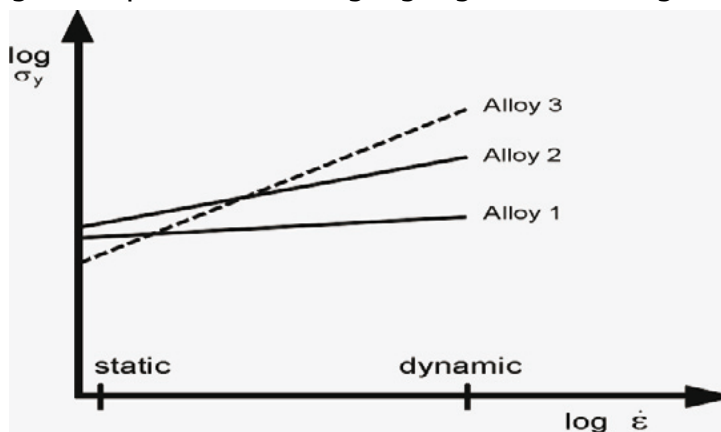


Figure 13 $\log \sigma_y$ vs $\log \dot{\epsilon}$ for 3 alloys

In reality this works well for metals - so our usual 'league table' of quasi-static σ_y values changes as strain rate increases because of differing strain rate sensitivities. This also explains the Milne de Marre graph in Fig.1 – steel is more strain rate sensitive than Al alloy, and its σ_y advantage increases with projectile speed.

Another important effect during high strain rate deformation is thermal softening from adiabatic heating – due to lack of time for Joule heating to dissipate. Fig.14 shows dynamic compression testing curves for W alloy cylinders at 3 D/L geometries all showing thermal softening, where quasi-statically work hardening would show the

curves continuing to rise during plastic deformation. Also the tall thin cylinder ($D/L = 0.5$) shows a sudden drop in load due to adiabatic shearing.

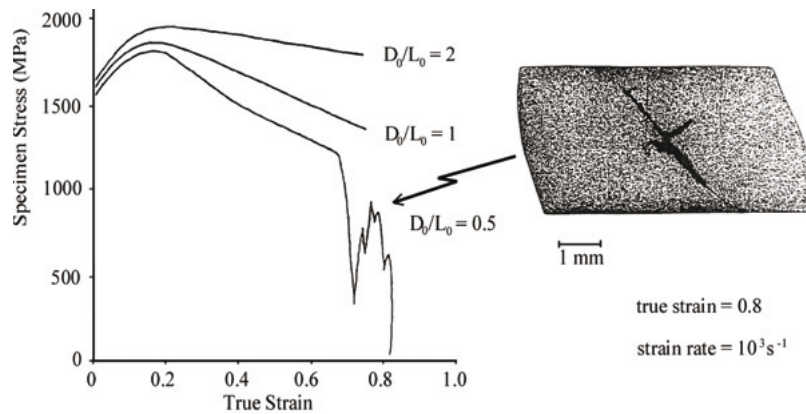


Figure 14 W alloy cylinder dynamic compression test curves

Adiabatic shear bands are interesting to study metallographically, as seen in a Ti alloy target in Fig.15. Some alloys, including Ti, are more susceptible than others – particularly if there is a relatively low temperature phase change during heating.

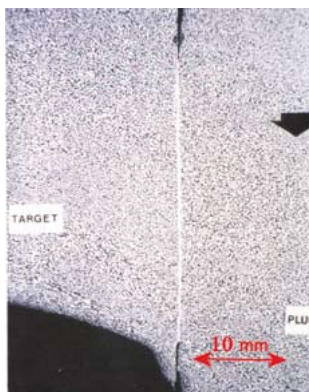


Figure 15 Adiabatic shearing in Ti

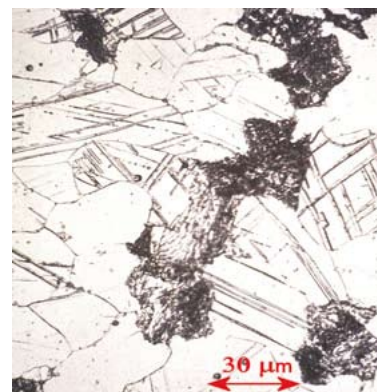


Figure 16 Deformation twins in shocked α

It is common to observe deformation twins in the ferrite of normalised steel target plates around the penetration tract after ballistic firings – a phenomenon usually only seen during cryogenic quasi-static testing.

7. Conclusion

Armour and anti-armour devices rely on good metallurgy for correct functioning. In particular, an understanding of material behaviour at high strain rate is important.

Reference

[1] Doig A.: Military Metallurgy, book 696, ISBN 1-86125-061-4, Maney Publishing, London, 2002, page 84

¹ Mr. Alistair Doig BSc Ceng MIMM MIExpE, Centre for Materials Science and Engineering, Cranfield University, Defence Academy of the UK, Shrivenham, Swindon SN6 8LA, UK. Tel: +44 1793 785390, e-mail: a.doig@cranfield.ac.uk

CURRENT POTENTIALS OF STRUCTURE ANALYSIS

Jiří Švejcar¹

Abstract

In the present paper attention is mainly focused on the relatively common methods, which have a wide range of applicability in the study of structure aspects. The aim of the paper is not describing these methods (general knowledge of their principle is assumed) but rather pointing at some of their limitations and possibilities which appears with a new development of their instrumentations. Attention is also paid to the possibility and constrains of exploiting of those methods for characterization of nano-objects.

Keywords: analytical methods, applicability, progress

1. Introduction

In view of the width of the concept of structure analysis but, above all, with a view to the number of methods that can be used for structure analysis the title of the paper is somewhat exalted. A mere list of the names of methods of structure analysis would take up at least two pages of these Proceedings. In the paper, the focus will therefore be on the most commonly used methods of structure analysis, in particular on the progress achieved in the study of morphology and local chemical analysis of structure elements. In this connection it is impossible not to mention the intense research and development in the area of nanomaterials and nanotechnologies. Manufacturers of instruments for structure analysis were quick to grasp the extent and significance of this field of science and adapted their development to the specific requirements which the characterization of nanomaterials demands. This is particularly pronounced in scanning electron microscopes but also in other types of instruments. Naturally, the content of the paper is therefore markedly influenced by this fact.

2. Light microscopy (LM)

Despite the physically conditioned relative low value of resolution and depth of sharpness in light microscopes, LM is a high-quality tool in structure analysis, in particular in morphology and also in indirect phase analysis (thanks to the exploitation of interference or polarization phase contrast, selective and colour etching, etc.). For almost 20 years, video-microscopy has been available, which in certain cases, in particular low magnifications, can even replace scanning electron microscopy, and is an excellent tool when working in field conditions (e.g. inspection of pipelines). In recent years, laser confocal microscopy has become an extremely useful method, whose main advantage is the possibility of assessing the surface

quality, inclusive of measuring roughness on the sub-micron level. Vertical resolution 20 nm, lateral resolution 120 nm, magnification range ca 100x to 17 000x, 3D display in natural colours, application of laser beam together with conventional microscopic techniques, etc., all these are a typical characteristic of modern confocal microscopes. The principle of scanning confocal microscopy has been known for more than 50 years; it was proposed in the 1950s by Minsky [1] and, independently of him, by Czech professor Petran [2], co-author of the so-called tandem confocal microscope. A simplified schematic diagram of laser confocal microscope can be seen in Fig. 1. Competing successfully with laser confocal microscopes are interference microscopes, which combine an interferometer and microscope into one instrument. Vertical scanning interferometers achieve in vertical direction a resolution of up to 0.1 nm, but lateral resolution doesn't reach the level of confocal microscope.

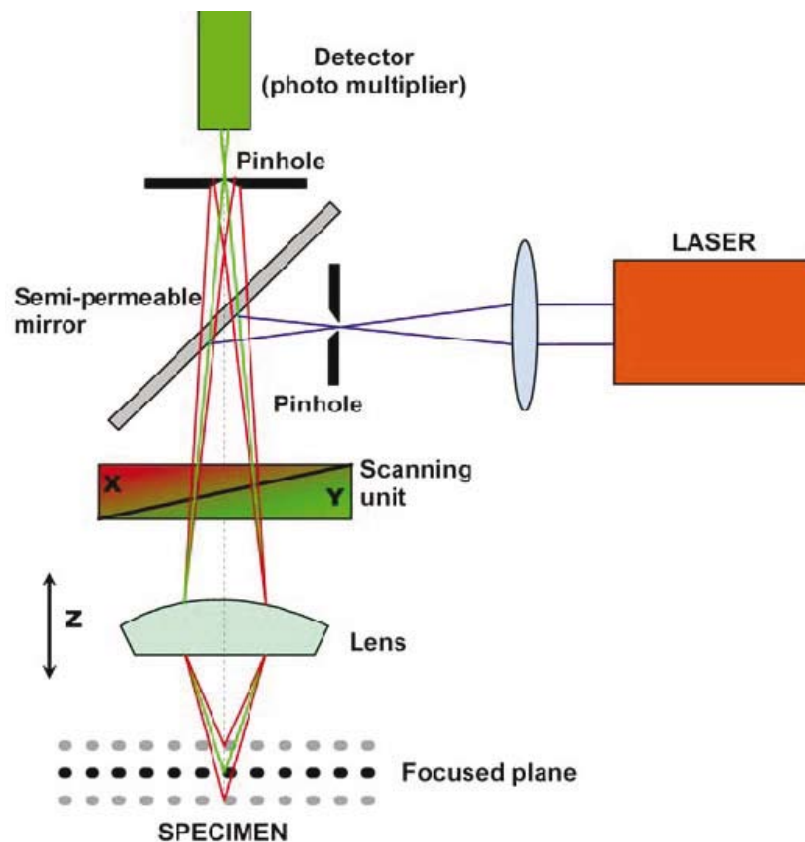


Fig. 1 Schematic diagram of laser confocal microscope

3. Electron microscopy (EM)

3.1 Scanning Electron Microscopy (SEM)

Unlike transmission electron microscopes, scanning electron microscopes relatively quickly found their way into industrial laboratories, mainly thanks to the possibility of analysing bulk samples without major requirements for their preparation. The significance of SEM increased still further thanks to the possibility of complementing them with various accessories, in particular analytical (wave and energy dispersive spectrometers) and, most recently, also the fast developing diffraction of back-scattered electrons, EBSD. The development of SEM has for long been in the direction of their computerization and, naturally, of gradual enhancement of their resolution power. There has been a marked improvement in detection by means of

back-scattered electrons. The above pressure towards characterizing nanostructured materials called for more substantial changes, in particular in the area of detecting secondary electrons (SE). Towards the end of the last century the SEM resolution in SE imaging ranged in top-class instruments between 3 and 4 nm (in instruments with conventional W cathode), in instruments equipped with FEG (Field Emission Gun), which at that time were not very common, this range was 2 to 2.5 nm. These values were obtained only at the highest acceleration voltages used in SEM, i.e. 30-40 keV. In agreement with the physical principle, at lower acceleration voltages the resolution markedly deteriorates (as is well known, resolution increases with decreasing wavelength of electrons, which decreases with increasing acceleration voltage). An analysis of nanostructures, in particular nanoparticles, requires, as will be explained in brief below, employing the lowest possible acceleration voltage, which is however in contradiction with the requirement for high resolution. As a result, it is impossible in conventional, even if high-quality SEM to obtain a good image of nanoparticles, even if they are one order larger than the guaranteed SEM resolution.

The resolution power in the case of imaging with the aid of secondary electrons greatly depends, among other things, on the ratio of secondary electrons generated directly by the incident beam from a very thin surface layer (≈ 1 nm) SE1 and secondary electrons generated by back-scattered electrons (SE2) – see Fig. 2 The latter can in fact come from places that are very distant from the place of primary beam incidence or even from outside the sample (SE3) and have a negative effect on the image quality. From the viewpoint of the requirement that secondary electrons should be generated from the thinnest surface layer possible it is optimal to use the lowest accelerating voltage possible (which is, inter alia, of advantage also in the study of poorly conducting samples, when making them conducting can be left out), but this is in contradiction with the requirement for a sufficient amount of secondary electrons and high resolution.

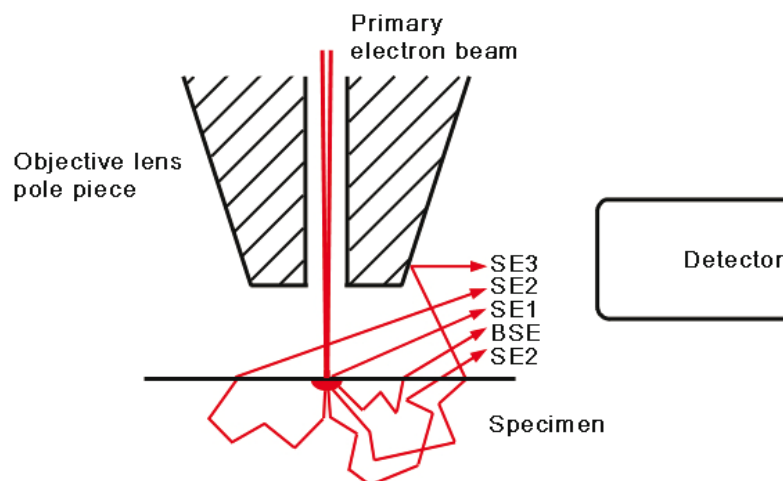


Fig. 2 Generation of secondary electrons

Most of the problems given above can be resolved by replacing the conventional W cathode by an unconventional source of electrons, preferably FEG. The value of the beam current, which is up to 4 orders higher in comparison with the conventional W cathode, enables a marked reduction of the beam diameter and thus also a higher

achievable resolution power. On top of this, low accelerating voltages (i.e. primary electrons with greater wavelength) can be used, usually up to values of 1-2 kV, while preserving a high resolution and a sufficient yield of SE (a marked improvement in the SE1/SE2 ratio). The remaining problem, i.e. suppressing the negative effect of the detection of back-scattered electrons, was resolved for the first time more than 30 years ago, when for working in the STEM and SEM modes on the transmission microscope the JEOL Company made use of the magnetic field "suction" of SE in a spiral into the detector.

Instruments suitable for work in the nanoregion (referred to by the manufacturers as High Resolution SEM, Ultra High Resolution SEM or even Nano-SEM) are thus, in addition to the indispensable unconventional source, equipped with the so-called in-lens detector (or detectors), located in the objective lens. With the most advanced of these SEMs a resolution of about 0.6 nm is recently obtained at an acceleration voltage of 5 kV, and 1 nm at 1 keV.

If we give up the requirement for extremely high resolution values, we should not fail to mention the category of microscopes that have for years been on the market as either single-purpose low-vacuum or environmental SEMs, but more frequently as one of the two working modes of current SEMs. Thanks to the special pressure-limited apertures placed under the objective, and differential exhaustion, a working pressure can be obtained in the sample chamber that is close to the value of triple point so that the difference between the pressure in the cathode space and the sample chamber is 5–6 orders. But there are also FEG-SEM in which the difference between the vacuum necessary for the FEG function and the pressure in the sample chamber is as many as 11 orders. In environmental microscopes, the sample chamber can also be filled with another medium than air, e.g. water vapour. These microscopes, the development of which was initiated by Australian sheep farmers for the purpose of analyzing sheep wool, are very useful, for example, in the study of samples containing water (e.g. biological samples) but also other types of preparations. SEM manufacturers offer instruments such as small desk SEMs, for which a special detector, EDS, was developed. It is quite interesting that there has been a return to the possibility of analyzing in SEM also transparent preparations with the aid of the STEM detector placed under the sample; this detector was long ago offered by JEOL for type 840.

3.2 Transmission electron microscopy (TEM)

The sub-nanometric (i.e. one order higher) resolution power of TEMs makes them ideally suited for the analysis of nanometric or even sub-nanometric particles. We should, of course, be aware of the fact that in conventional transmission electron microscopes (CTEMs) it is the diffraction contrast that is made use of in imaging. It arises due to local distortions of the crystal lattice (e.g. dislocations). The inner volume of nanocrystalline particles is mostly without defects (these are concentrated on particle edges). Moreover, due to the diffraction contrast, the resolution is somewhere about 1-2 nm. As a result, in objects of nanometric dimensions, CTEM actually does not provide more information than SEM does, and from the morphological viewpoint it is in practice only applicable in analyses of particle sizes and their distribution. To obtain data on the internal structure of nano-objects it is necessary to use the phase contrast, i.e. high-resolution electron microscopy (HREM).

One of the essential preconditions for a successful application of HREM is a good source of electrons and higher acceleration voltage, 200 keV at least. The greatest interest is therefore today for TEMs with an acceleration voltage of 200-300 keV. Efforts aimed at increasing the quality of imaging and resolution power have led, among other things, to providing TEMs with correctors of spherical aberration (Cs) and monochromators. Also thanks to these correctors the boundary value of 0.1 nm point resolution was overcome in 2004. A component of modern TEMs that is today taken for granted are adapters for Scanning Transmission Electron Microscopy (used for the first time as early as 1974) as well as in column energy filters, which are used not only to enhance the image quality (thanks to suppressing the undesirable effect of non-elastically scattered electrons) but also in local chemical analysis. The so-called D-STEMs (dedicated STEMs) are beginning to gain ground (the first single-purpose STEM was built already in 1937 by Manfred von Ardenne). The block diagram of such an instrument is in Fig. 3 [3]. From among the rich supply of accessories let us mention at least the facility for imaging in the HAADF mode (High Angle Anular Dark Field). This technique is sometimes referred to as Z-contrast imaging because with this technique both the diffraction and the phase contrast are suppressed and the sensitivity to chemical composition, i.e. atomic number Z, is enhanced. Using HAADF, images of particles of sub-nanometric size or even individual atoms can be obtained [4].

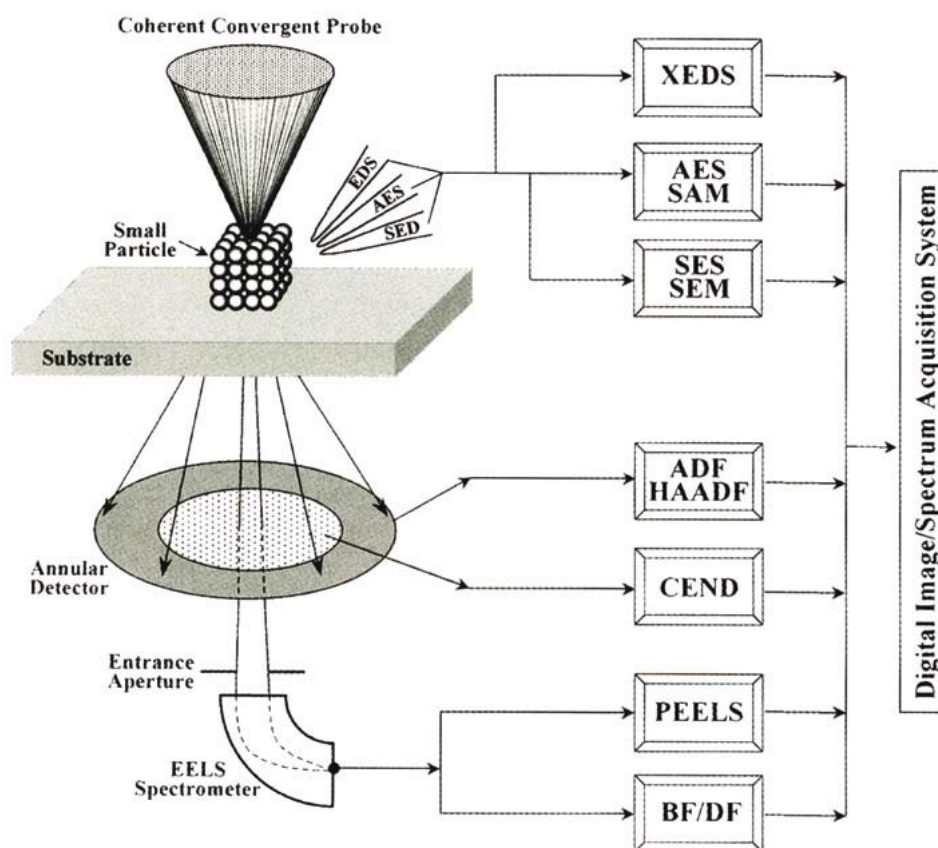


Fig. 3. Schematic diagram illustrates imaging, diffraction, and spectroscopy modes commonly used in a dedicated STEM instrument[4]

A significant advance in the useful properties of TEM can without doubt be seen in the environmental TEM presented by the FEI Company in 2008 [5]. This instrument allows conducting (S)TEM experiments in gaseous environment (in a mixture of up to four different gases at a partial pressure of up to 15 Torr, i.e. 2 kPa, possibly also at higher temperatures (Fig. 4). A similar break-through in the experimental potentials of TEM can be seen in the hardware and software accessories which enable the application of tomography, or rather micro- and nano-tomography. In combination with the analytical attachment (EDS), the space imaging of nano-objects can be complemented with their chemical characterization. An example of TEM nano-tomography is on the Fig. 5 [6]. By the way, in the last decade the family tree of micro- and nanotomography has grown significantly – Fig. 6 [7]). We should not forget to mention a technique that is closely related to TEM because, among other things, it provides the possibility to prepare transparent preparations from selected sites on the sample – FIB (Focused Ion Beam). FIB instruments (both single-purpose and in combination with SEM) are today an inherent part of modern TEM laboratories.

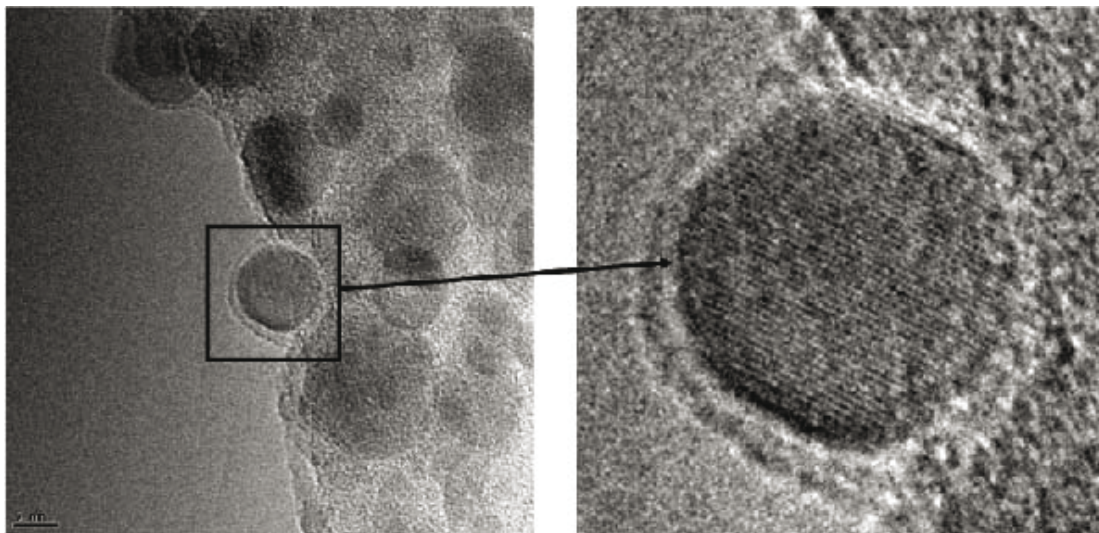


Fig. 4 HRTEM image of Fe nano particle made in gaseous environment and at temperature 680 °C [5]

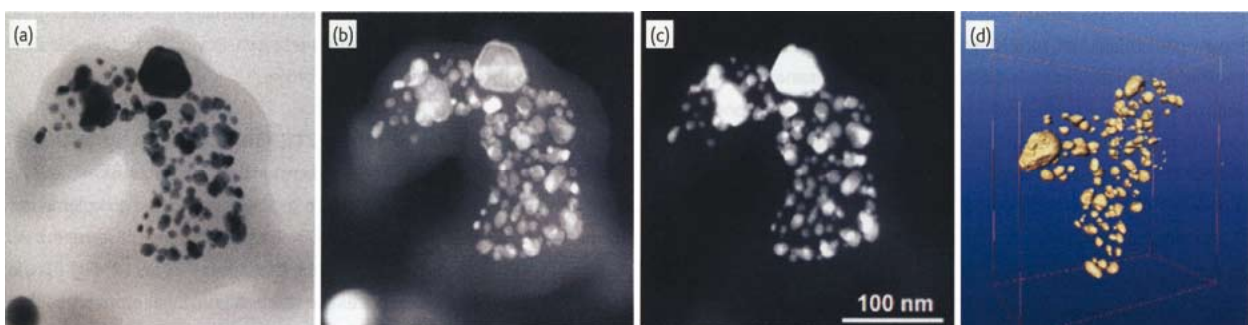


Fig. 5 Pt catalyst nanoparticles embedded in carbon matrix, (a) Bright-Field TEM, (b) ADF-STEM, (c) HAADF-STEM image, (d) 3D reconstruction from a tilt series of (c) to highlight the metal particles [6]

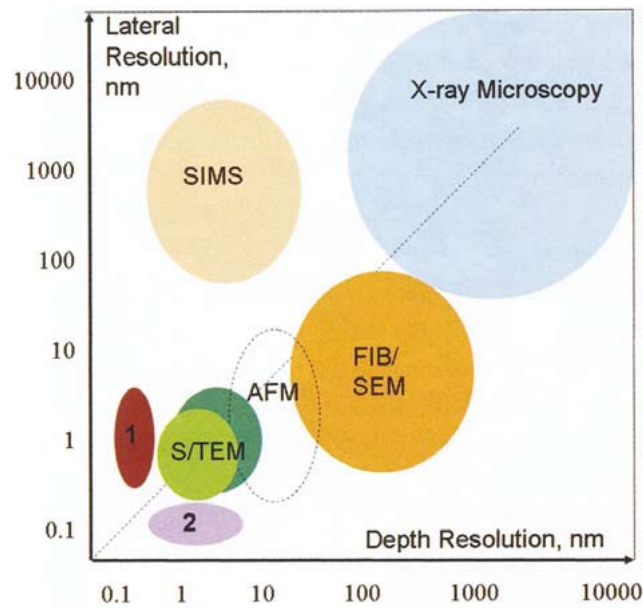


Fig. 6 Length scales of micro-/nanotomography techniques showing lateral versus depth resolution ranges [7]

3.3 Auger electron (AE) microscopy

Thanks to the well-known fact that most AE are emitted from a very small distance below the sample surface (typically 0.3 to maximally 3 nm), AE spectroscopy and microscopy belong to typically surface-sensitive methods. Problems (from the viewpoint of analysis of small volumes) arise with lateral resolution, which in classical instruments achieves under ideal conditions ca 30 nm (some 20 years ago it was a mere 500 nm; a significant improvement was elicited primarily by the need for characterizing nanoparticles). By improving the effectiveness of the detection of low-energy electrons and by other modifications of D-STEM the space resolution of Auger peak images (i.e. the map of element distribution) could recently be improved to 3 nm in bulk samples, and 1 nm in transparent samples. For example, Ag nanoparticles of < 1 nm in diameter, containing a mere 15 atoms of Ag, could be detected [4]. Thanks to the high surface sensitivity of AE the composition of multicomponent nanoparticles can be determined (qualitatively but in some cases also quantitatively).

4 Microanalysis in electron microscopes

Transmission microscopy and scanning microscopy are currently complemented with analytical attachments, which enable obtaining information about the chemical composition of micro- or nano-objects present in the structure, and thus substantially extend the morphological potentials of TEM and SEM. The most widely spread among these attachments are energy dispersive spectrometers (EDS), which are today a relatively common TEM and SEM attachment. All these attachments exploit physical processes that occur during the interaction of electrons with the sample. In the case of energy dispersive (EDS) and wave dispersive spectrometers (WDS) it is the emission of characteristic X-ray radiation resulting from the non-elastic collisions of primary electrons with the electron envelope of sample atoms. The EELS (Electron Energy Loss Spectrometry) method then measures, as its name suggests, the energy losses of the primary electrons of the beam during their interaction with the sample.

Since their appearance on the market in the early 1970s, their spectral resolution has gradually improved to the present 121-127 eV on the MnK α line (which is still two orders worse than in WDS), and, hand in hand with the advance in the area of computer technology, the speed and quality of processing the X-ray spectrum has increased. As early as the 1980s the unpleasant limitation of analyzable elements ($Z > 11$) was eliminated thanks to the beryllium window of the detector being replaced by an ultra thin plastic window. Contemporary EDSs enable analyzing also light elements ($Z > 5$). In the last few years, another disadvantage of EDSs, namely the necessity of cooling them continuously with liquid nitrogen, has been done away with. New types of detector (e.g. SDD-Silicon Drift Detectors) need to be cooled only when being used or they do not require being cooled with liquid nitrogen at all and are cooled by the Peltier phenomenon. For a simultaneous EDS/WDS analysis in particular, but also for the speed of analysis, it is important that the boundary of processable pulses has been increased from the usual 5-10 thousand to the present-day 100 thousand. An outstanding progress is evident also e.g. in the technique of element mapping (so called intelligent mapping), etc.

It follows from its principle that the EELS method can only be used for transparent preparations, i.e. in TEM. EDS and EELS are complementary methods. EELS is of greater advantage in the analysis of light elements; moreover, in high-quality analyzers even compounds, e.g. oxides, can be distinguished via analyzing the fine spectrum deviations near the respective edge. Both methods enable analyzing even very small objects. In the case of TEM/STEM with the conventional W cathode, configurations of 5-7 nm in size (on replicas in particular) can be analyzed more or less reliably. In the case of applying FEC sources the analytical potentials are even better. Analytical potentials are, of course, dependent on a number of factors, in particular the beam diameter, foil thickness, sample drift (which needs to be corrected either manually or automatically), sample contamination, etc. As published results indicate, in an optimum case, particles of ca 1 nm in size can be analyzed, and using EELS even individual atoms can be analyzed while the presence of a mere 10 atoms can be revealed if using EDS [4].

5. Notes on other methods of structure analysis

In the Introduction, the enormous number of methods of structure analysis was mentioned. There are methods that deserve separate mention, such as those designed predominantly for surface analyses, e.g. SIMS (Secondary Ions Mass Spectroscopy) or XPS (X-Ray Photoelectron Spectroscopy), methods of spectral analyses, and other methods. The today most currently used methods that have not been given here yet include methods collectively referred to as SPM (Scanning Probe Microscopy); their significance, the number of their diverse variants, their principle and their applicability are worth a separate lecture. Let us be reminded that in addition to the first method that led to the appearance of SPM methods in the 1980s (it is Scanning Tunneling Microscopy that we have in mind here) there are today tens of such methods. Some of them are only variants of well-known working modes AFM (Atomic Force Microscopy) such as phase imaging mode, torsion resonance mode, lateral force microscopy, conductive AFM, scanning capacitance microscopy, surface potential imaging, etc. Others make use of other types of "probe", e.g. sharp metal needle (scanning electrochemical potential), thermistor-based probe (scanning

thermal microscopy), dielectric tip (scanning near field optical microscopy, SNOM), and many others. Thanks to the modular set-up the user can choose only those working modes that they will use. One of the latest novelties is also the possibility to use AFM as attachment to the laser confocal microscope. STMs are known to be used with advantage as attachment to both SEM and TEM. The application range of SPM methods is vast. In view of its significance, a separate paper could be devoted to the EBSD method (Electron Backscatter Diffraction), which has become an inherent part of SEM. EBSD is based on the acquisition of diffraction pattern from bulk samples in the scanning electron microscope and rapid automated pattern analysis (Fig. 8a, b). There is no doubt that the EBSD method greatly enhances the SEM potentials, in particular by statistical analysis of orientation/misorientation, phase identification (in combination with EDS), measurement of grain-size distribution, and by the creation of the so-called orientation imaging micrographs (OIM). In some aspects the EBSD method exceeds the study potentials of TEM, e.g. [8]:

- The use of bulk samples rather than thin foils, which avoids the difficult and questionable practice of preparing thin foils which are representative of the bulk material.
- Very large areas or regions selected from large samples are readily studied.
- Data may be obtained from specific areas of interest, e.g. near surfaces, welds, etc.
- Rapid and automated acquisition and analysis of the diffraction patterns, which is not routinely available in the TEM, enable many thousands of grains/subgrains to be characterized from a single map.
- Much less expensive equipment is required than for TEM.

Last but not least, we should not forget to at least briefly mention methods that exploit X-ray radiation. Apart from the classical X-ray diffraction analysis, commonly used for tens of years and based on wide-angle elastic scattering of X-ray radiation (with excellent applicability not only in the phase analysis of nanoparticles but also in measuring their size), further experimental techniques have been developed. Worth mentioning in the nanoregion is the Extended X-Ray Absorption Fine Structure (EXAFS) method, which is in principle a spectroscopic technique based on the analysis of energy dependence of the absorption of X-ray radiation as a result of interference phenomena during the scattering of photoelectrons. Another such method is the SAXS method, which is particularly suitable in the nanoregion. SAXS, i.e. low-angle elastic scattering of X-ray radiation, provides direct information about the outer shape of nanoparticles and nanomolecules by measuring the typical magnitude of the direction of electron density (in the range of ca. 1-200 nm).

Acknowledgements

The work of J. Švejcar was supported by grant of Ministry of Education, Youth and Sports, CZ(MSM 0021630508).

References

- [1] Minski M.: Memoir on inventing the CSM, *Scanning* 10,(1998),pp.128–138
- [2] Petráň M. et al.: Tandem-Scanning Reflected-Light Microscope, *J.Opt.Soc.Am.* 58,(1968), pp.661–664
- [3] Lyman C. E.,: *J. Microscopy*,176,(1994),p. 85
- [4] Wang Z. L. (Editor): *Characterization of Nanophase Materials*,Wiley-VCH,(2000)
- [5] <http://www.edlin.cz/fei/15titan.htm> (2009)
- [6] Gontard C. et al: *J. Phys.,Conf.Ser.*(2006),26,203 (in: [7])
- [7] Möbus G., Inkson B. J: *Mater.Today*, Vol.10, 12 (2007), pp.18–25
- [8] Humphreys F. J.: *Scripta Materialia*, Vol.51, 8 (2004), p.771

¹ Prof. Ing. Jiří Švejcar, CSc., Institute of Materials Science and Engineering, Faculty of Mechanical Engineering, Brno University of Technology, Technická 2896/2, 616 69 Brno, Czech Republic, Tel.: +420 541 143 102, e-mail: svejcar@fme.vutbr.cz

THE MASTER CURVE APPROACH AS AN APPROVED FRACTURE MECHANICS TEST METHOD FOR MORE THAN ONE DECADE

Viehrig H.W.¹

Abstract

The paper gives an overview about the development of the Master Curve approach since the first version of the appropriate test standard ASTM E1921 was issued. The main focus is on the application of ASTM E1921 for the determination of fracture toughness values applied in the nuclear reactor pressure vessel integrity assessment. Test parameters influencing the reference temperature were assessed.

Keywords: fracture toughness, ductile-to-brittle transition, reactor pressure vessel steel.

Introduction

Fracture mechanics is a scientific discipline that effectively added a useful advancement to the technology of the mechanics of materials. It provides the tool to compute the capability of materials to sustain cracks under load. The linear elastic fracture mechanics provides a plain stress fracture toughness values e.g. K_{Ic} according to ASTM E399. The K_{Ic} specimen size requirements applied to structural steels of high toughness lead to impractically huge specimen size. Hence, the consideration of more plastic deformation involved in the fracture toughness development process led to the introduction of different elastic-plastic analysis procedures [Anderson-2005], of which the J-integral approach has been most widely used. However, the main use of J has been for the characterisation of ductile crack extension in terms of J-R curves and subsequently evaluated fracture toughness values like J_{Ic} according to ASTM E1820 or $J_{0.2BL}$ according to ISO 12135. Ferritic structural steels show a ductile-to-brittle transition behaviour at which the fracture mode changes from ductile to increasing amounts of brittle cleavage fracture. The estimation of the fracture toughness at brittle failure of a structure and the identification of the ductile-to-brittle transition temperature are of high importance particularly with regard to the nuclear reactor pressure vessel (RPV) integrity assessment. Modern statistical methods, and an improved understanding of elastic-plastic test methods, have been coupled to a probabilistic fracture mechanics approach, which defines both a mean transition toughness value and a distribution around that value [Mc Cabe-2005]. This approach is called "Master Curve" (MC) approach and adopted in the standard test method ASTM E1921, "Determination of Reference Temperature, T_0 , for Ferritic Steels in the Transition Range". For a specific RPV steel the reference temperature T_0 of a fracture toughness-temperature curve of

a defined fracture probability can be determined by applying of fracture toughness values measured on specimens at brittle failure. The main advantage of the MC approach is that the reference temperature T_0 can be directly determined with fracture toughness data measured on specimens at cleavage failure, K_{Jc} . However, some peculiar features of T_0 are not yet fully understood:

- specimen type and constraint (CT bend specimen),
- specimen size,
- loading rate effects,
- irradiation effects and Master Curve shape, and
- fracture mode (intergranular cleavage fracture), non homogenous steels.

The paper will present results which contribute to the clarification of this open issues in the application of the Master Curve approach to RPV steels.

Basics of the Master Curve Approach

The MC approach as adopted in the test standard ASTM E1921 examines the cleavage failure of a specimen in the lower ductile-to-brittle transition range. It is applicable to steels with a body centred cubic macroscopically uniform structure and randomly distributed fracture initiators. The model comprises following basic assumptions:

- the fracture probability cleavage model (Weibull statistics),
- the prediction of the influence of the specimen size on the failure probability, i.e. specimen thickness adjusted to 1T (25.4 mm) and
- an universal temperature dependence of cumulative fracture probability.

The transition curve definition in ASTM E1921 was originally derived from data measured on various quenched and tempered structural "ferritic" steels [Wallin-1991, Server-2009]. These data were taken from different sources and included measurements on unirradiated and irradiated RPV steels. The median MC of Eq. (1) has shown to describe the elastic-plastic K_{Jc} temperature dependence for the most structural steels independent of their yield strength and composition.

$$K_{Jc} = 30 + 70 \cdot e^{0.019 \cdot (T - T_0)}; MPa\sqrt{m} \quad (1)$$

where

K_{Jc} J integral based elastic plastic fracture toughness at cleavage failure,

T temperature in °C,

T_0 MC reference temperature in °C.

The first version of the test standard ASTM E1921 was issued in 1997 and contains the test conditions, evaluation routines and validity criteria. The following main modifications were made till the actual issue ASTM 1921-10:

- introduction of a multi temperature option,
- the validity of the MC was restricted to $T_0 \pm 50$ K,
- reduction of the quasi-static loading rate range to 0.1 to 2 MPa√m/s,
- the final stress intensity factor for the pre-cracking of the specimen is fixed to 15 MPa√m when the test temperature is below the pre-cracking temperature,
- introduction of the contribution of experimental uncertainties in the standard deviation of 4 K, and
- application of higher elevated loading rates.

As mentioned above, the basic MC method for analysis of brittle fracture test results, as defined in ASTM E1921 is intended for macroscopically homogeneous

ferritic steels only. However, there have been some limited cases where the assumed and measured K_{Ic} versus temperature dependence disagree. In general, such cases have occurred in situations where the basic assumptions of the cleavage fracture model are not fulfilled. In reality, steels are seldom macroscopically fully homogeneous. The steel's fracture toughness may depend on the specimen location in the investigated material. For example, thick plates and forgings may have very different fracture toughness at plate center and close to surface. The inhomogeneity may be deterministic or random (or a mixture of both) in nature. Deterministic inhomogeneity can be accounted for, provided that the specimen extraction histories are known and enough specimens are tested. Random inhomogeneity is much more difficult to handle. The Structural Integrity Assessment Procedures for European Industry SINTAP contains a lower tail modification of the MC analysis [Nevasmaa-1998]. This enables conservative lower bound type fracture toughness estimates even for inhomogeneous steels, which are then governed by the fracture toughness of the more brittle constituent. The problem is that the SINTAP method does not provide information about the tougher material. Therefore, a probabilistic description of the complete material is not possible. New extensions of the MC approach [Wallin-2004, Viehrig-2006] are developed for inhomogeneities governed by two separate MC distributions i.e. Bimodal Master Curve (MC-Bi) and for the analysis of inhomogeneous materials consisting of random inhomogeneities (MC-MM). The MC-Bi extension is shown to be extremely efficient in describing e.g. weld heat-affected zone (HAZ) data, whereas the MC-MM extension is perfectly adequate for data set composed of a collection of different heats of the same material, and for inherently macroscopically inhomogeneous materials. Acceptance criteria and requirements for standardizing the treatment of material inhomogeneity are under discussion and intended to be adopted in ASTM E1921.

Application of the Master Curve Approach in Reactor Pressure Vessel Integrity Assessment

Under current Nuclear Power Plant (NPP) RPV integrity assessment codes and regulations, there are no specific requirements for Master Curve testing in RPV surveillance programmes. However, the need to assess RPV fracture toughness more accurately will drive utilities to use modified surveillance specimens to measure MC fracture toughness. Current codes use an indirect and correlative approach of determining the fracture toughness of the RPV steels in the initial and irradiated condition. Procedures applied in the different countries vary in the details, but are based on the same principle. In general these procedures use results of Charpy V-notch and drop weight testing to determine the reference temperature, RT , for a fracture toughness, K_{Ic} , reference curve. The reference fracture toughness curve is based on an empirical analysis of the relationship between measured RT and K_{Ic} values and is considered to be adequately conservative. This concept has the following disadvantages [Server-2005]:

- it is not consistent since it links fracture mechanical and technological parameters, and
- margins of safety and probability estimation cannot be quantified.

There is a short-range and a long-range objective in the introduction of the MC approach in the NPP RPV integrity assessment [Rosinski-2000]. In the near future,

the intention is to use the alternative reference temperature without losing the historical link to the fracture data that was the basis of the K_{IC} reference curves of the present codes. In the United States the MC approach has been implemented in the ASME Code Case N-629 "Use of Fracture Toughness Test Data to Establish Reference Temperature for Pressure Retaining Materials for Section XI". This new parameter is adopted in the ASME K_{IC} reference curve, Eq. (2), and termed RT_{T_0} .

$$K_{Ic} = 36.5 + 22.783 \cdot \exp[0.036 \cdot (T - RT_{T_0})] \quad (2)$$

$$RT_{T_0} = T_0 + 35F \quad (19.4K) \quad (3)$$

The additional temperature increment in Eq. (3) is to account for uncertainties and the general scatter in the measured fracture toughness data. The ASME K_{IC} curve indexed with RT_{T_0} must continue to appropriately envelop the measured fracture toughness data. The benefit of ASME Code Case N-629 is that both the reference temperature for the unirradiated and irradiated state is related to a fracture mechanics parameter which can be measured on unirradiated and irradiated specimens, respectively. The ASME RT_{T_0} has also been adopted in the RPV integrity assessment codes of countries outside the USA.

The long-range objective is to apply the statistically defined MC in place of the current code reference fracture toughness curves. The MC allows predictions of the failure of a specimen on the basis of failure probabilities. For the integrity assessment, the selection of an appropriate lower confidence bound (X) needs to be made. The "Unified Procedure for Lifetime Assessment of Component and Piping in WWER NPPs - VERLIFE" [VERLIFE-2003] applies directly the MC for 5% fracture probability according to ASTM E1921 (Eq. (4) as fracture toughness reference curve.

$$K_{Ic}^{5\%}(T) = \min\{25.2 + 36.6 \cdot \exp[0.019 \cdot (T - RT_0)]; 200\} \quad MPa\sqrt{m} \quad (4)$$

$$RT_0 = T_0 + \sigma \quad (5)$$

where

σ is a margin $\sigma = \sqrt{\sigma_1^2 + \delta T_M^2}$

σ_1 standard deviation according to ASTM E1921

δT_M considers the scatter in the materials ($\delta T_M = 10$ K and 16 K for base and weld metals, respectively).

However, there are still some open questions in the application of the MC approach. Some peculiar features of T_0 are not yet fully understood. Some examples will be demonstrated with test results in the next paragraph.

Demonstration of the Influence of Test Parameters on the Reference Temperature T_0 with Selected Results

Materials and specimen

The application of the MC approach and the influence of test parameters on the evaluated T_0 is demonstrated here with a batch of different RPV base and weld metal tested at FZD:

- German RPV steel 22 NiMoCr 3-7 of the non commissioned Biblis C RPV: specimen orientation TS,
- IAEA reference RPV steel JRQ (ASTM A533B Cl. 1 type): specimen orientation TL, and

- Russian type 15Kh2MFA RPV steel of the non commissioned WWER 440 RPV of Greifswald Unit 8 (SKODA production): specimen orientation LT.

C(T) and SE(B) specimens of different thickness, fatigue pre-cracked to a/W ratios of 0.45 to 0.55 and 20% side-grooved were tested.

Testing and evaluation

Quasi-static MC tests were performed with loading rates of about $1 \text{ MPa}\sqrt{\text{m/s}}$. The specimens were monotonously loaded until they failed by cleavage. Specimen preparation and test conditions follow the test standard ASTM E1921, whereby the tests were performed and evaluated according to the 2004 to 2009 versions. Dynamic MC tests (up to $350000 \text{ MPa}\sqrt{\text{m/s}}$) were performed and evaluated according to the test standards ISO/FDIS 26843 and ASTM E1921-09a.

Influence of specimen size on the reference temperature T_0

SE(B) specimen batches of different thickness with $B=0.4T$, $0.8T$, $1.6T$ and $3T$ of RPV steel 22NiMoCr 3-7 were tested [Viehrig-2010]. The results are summarised in Table 1 and depicted in Fig. 1. For the assessment of the influence of the specimen size on T_0 , only specimens tested at temperatures close to the expected T_0 ($T_0 \pm 25 \text{ K}$) are considered in Table 1. Table 1 also contains the T_0 evaluated with additional SE(B) specimens tested beyond this temperature range. This combined evaluation results in a T_0 of -80.3°C , with which the Master Curves in Fig. 1 are indexed. However, the differences of the other specimens sizes except the $1.6T$ SE(B) specimens lie within the 1σ scatter band. Obviously, the $1.6T$ SE(B) specimens yield higher T_0 . Note that from the highest thickness $T = 3T$ only four specimens could be machined, too few to be evaluated properly with ASTM E1921-09a in which minimum six specimens are required.

Table 1: Influence of specimen thickness on quasi-static MC T_0 (specimens with fatigue-precracks to $a/W=0.5$ and 20% side-grooves, tested at temperatures within $T_0 \pm 25 \text{ K}$).

specimen thickness B in T (1T=25.4mm)	Master Curve evaluation (ASTM E1921-09a)				
	T_0 °C	σ K	$\Sigma r_i n_i$ -	r -	N -
0.4	-83.0	6.4	2.07	13	16
0.8	-85.9	7.0	1.67	10	11
1.6	-71.6	7.5	1.33	8	8
3	n.a.	n.a.	n.a.	0	4
all SE(B) specimens (0.4 to 3)	-80.3	4.9	6.57	42	63

One reason for the higher T_0 of the $1.6T$ SE(B) specimens can be seen in the low K_{Jc} measuring capacity, of the smaller specimens compared to the larger specimens. The specimen size validity criteria, $K_{Jc(\text{limit})}$, of ASTM 1921-09a contains a constraint factor M with 30 for which relatively large loss of constraint is predicted in different investigations [IWM-2005, Server-2009, Tregoning-2000]. As seen in Fig. 1 many of the tested $0.4T$ -SE(B) specimens are close to or above $K_{Jc(\text{limit})}$. The larger specimens show an increasing $K_{Jc(\text{limit})}$ as depicted in Fig. 1. Specimens with a thickness larger than $1T$ when tested around T_0 do not suffer the loss of constraint at their reported K_{Jc} values, unlike the $0.4T$ -and $0.8T$ -SE(B) specimens. The $K_{Jc(1T)}$ values of the tested SE(B) specimens with different thickness and of the $1T$ -C(T) specimens lie within the 0.02 and the 0.98 fractiles of cumulative fracture probability, Fig. 1. Even the $1.6T$ -

SE(B) and 1T-C(T) specimens which gave higher T_0 are enveloped by the 0.02 and the 0.98 fractiles.

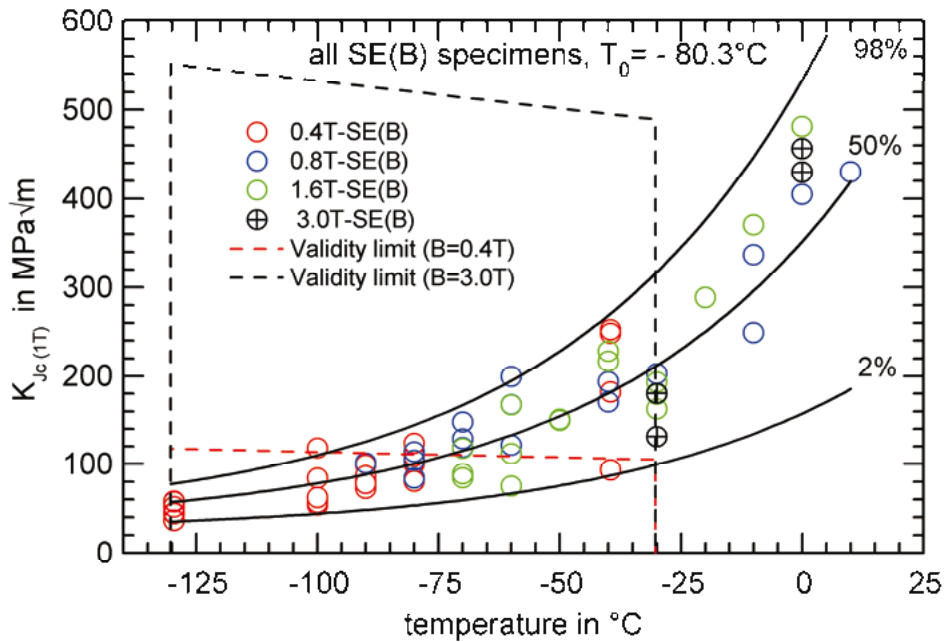


Fig. 1: Influence of the thickness B on quasi-static T_0 ($dK/dt= 0.96$ to 1.70 $MPa\sqrt{m/s}$) of fatigue pre-cracked ($a/W=0.5$) and 20% side-grooved SE(B) specimens of RPV steel 22 NiMoCr 3-7.

Influence of specimen type on the reference temperature T_0

SE(B) and C(T) specimen batches of RPV steel 22NiMoCr 3-7 and JRQ were tested [Server-2005, Viehrig-2010]. The test results are summarized in Table 2. For the RPV steel 22 NiMoCr 3-7 differences between 5 K and 12 K were determined depending on the specimen size and the test temperature range. If only the 0.4T-SE(B) and 1T-C(T) specimens tested at temperatures in the range of around $T_0 \pm 25K$ are evaluated the offset accounts 12 K. The result is graphically depicted in Fig. 2. The 0.4T-SE(B) and 1T-C(T) specimens of the JRQ block 6JRQ12 gave a difference of 12 K.

The difference in T_0 of 10 to 15 K between SE(B) and 1T-C(T) specimens as mentioned in the test standard ASTM E1921-09a was observed in the result, with the present maximum difference being 12 K. With increasing number of specimens the degree of accuracy of T_0 is higher.

Table 2: Influence of specimen type on quasi-static MC T_0 (specimens with fatigue-precracks of $a/W=0.5$ and 20% side-grooves.

material	specimen B in T (1T=25.4mm)	Master Curve evaluation (ASTM E1921-09a)				
		T_0 °C	σ K	$\Sigma r_i n_i$ -	r -	N -
22 NiMoCr 3-7	0.4T-SE(B)*	-83.0	6.4	2.07	13	16
	0.4T-SE(B)**	-82.0	6.3	2.24	14	28
	0.4-3T-SE(B)**	-80.3	4.9	6.57	42	63
	1T-C(T)*	-71.0	7.5	1.33	8	8
	1T-C(T)**	-74.0	5.6	3.21	21	21
	0.5T-C(T)*	-75.3	7.2	1.43	9	9
	1T and 0.5T-C(T)*	-73.4	5.9	2.76	17	17
	1T and 0.5T-C(T)**	-74.3	5.2	4.64	30	30
6JRQ12	0.4T-SE(B)	-68.8	6.4	1.90	13	15
	1T-C(T)	-57.1	6.6	1.93	12	12

* test temperatures $T_0 \pm 25$ K; ** all tested specimens

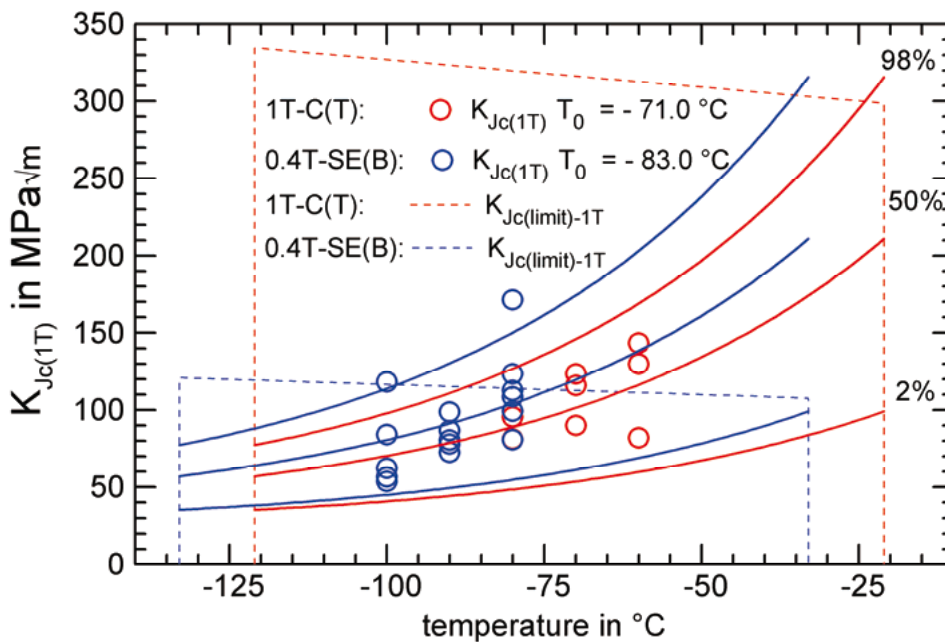


Fig. 2: $K_{Jc(1T)}$ values and MC measured on 1T-C(T) and 0.4T-SE(B) specimens of fatigue pre-cracked ($a/W=0.5$) and 20% side-grooved of RPV steel 22 NiMoCr 3-7, test temperature $T_0 \pm 25$ K.

Influence of loading rate on the reference temperature T_0

In the literature an increase of T_0 with increasing loading rate is reported [Joyce-1998, Viehrig-2001, Shutter-2001]. The actual version of ASTM E1921-10 permits testing at elevated loading rates higher than 2 MPa√m/s. The T_0 for dynamic loading can be estimated with an empirical relationship between loading rate dK/dt and increase of the reference temperature ΔT_0 (in K) based on the analysis of a large database mostly consisting of RPV steels [Wallin-1997, Hall-2003].

$$\Delta T_0 = \frac{T_{01} \cdot \ln\left(\frac{dK_I}{dt}\right)}{\Gamma - \ln\left(\frac{dK_I}{dt}\right)} \quad (6)$$

where: T_{01} reference temperature measured under quasi-static conditions (in K)
 Γ empirical function based on the Zener-Holloman Strain Rate parameter given by

$$\Gamma = 9.9 \cdot \exp\left[\left(\frac{T_{01}}{190}\right)^{1.66} + \left(\frac{R_{el}}{722}\right)^{1.09}\right] \quad (7)$$

with: R_{el} = quasi-static yield strength (in MPa).

The determination of the loading rate can be performed by applying different methods: according to ASTM E1921-09a (paragraph 8.7.1 Tab. 3), according to the HSK-AN-425 guide [Viehrig-2010], and experimentally [Lucon-1999, Server-2009]. The differences between these methods can amount up to 100%. Fig. 3 depicts the results of an IAEA Coordinated Research Project [Server-2009]. Above the 2 MPa√m/s limit, there is a clearly defined trend to increasing T_0 values with increasing loading rates. The shift of T_0 with increasing dK/dt for the JRQ steel can be estimated using Wallin's empirical relationship, Eq. (6). This correlation predicts an increase of about 52 K between the upper limit of the quasi-static loading rate (2 MPa√m/s) and an impact loading rate of about 3.5×10^5 MPa√m/s.

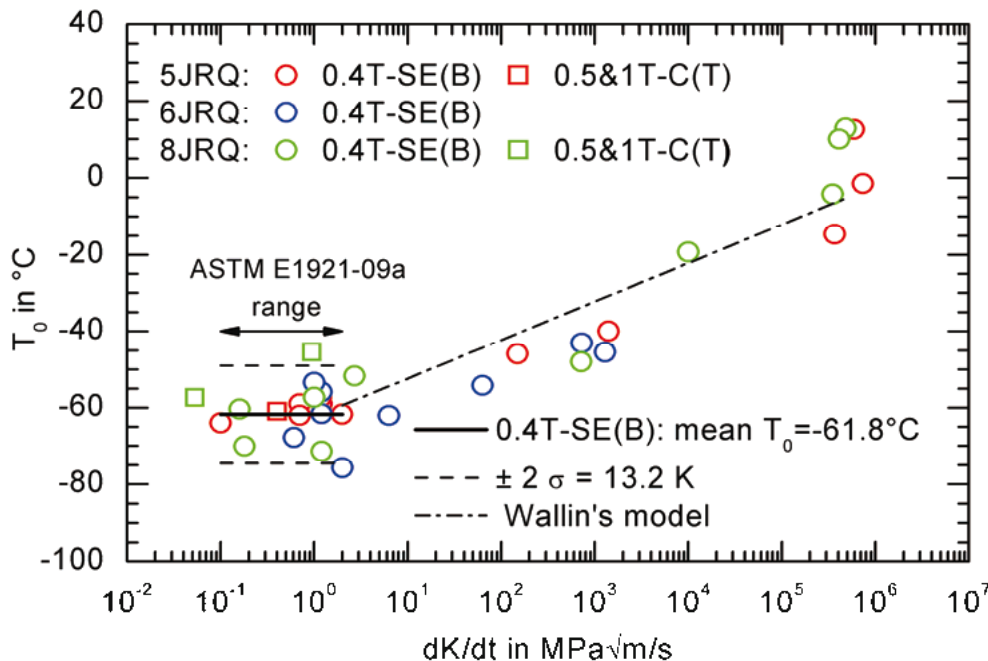


Fig. 3: Reference temperature T_0 vs. loading rate for different JRQ blocks (tested by different laboratories [Server-2009]) and comparison with the predictions of Eq. (6) (Wallin's model).

Nonhomogenous material

An example of the MC evaluation of non homogenous RPV steel is shown in Fig. 4 [Viehrig-2006]. It concerns RPV base metal of the forged ring 0.3.1. from the non-commissioned RPV of Greifswald Unit 8. The MC evaluation according to ASTM

E1921-05 was performed with K_{Jc} values measured on Charpy size SE(B) specimens from thickness locations within $\frac{1}{4}$ to $\frac{3}{4}$ thickness of the forged ring. The standard MC T_0 value amounts -113.3°C as shown in Fig. 4. Eight K_{Jc} values (about 11%) lie below the 2% probability curves indexed with the standard MC T_0 . This result and the large difference between T_0 of the standard and SINTAP evaluation are a strong indication of random inhomogeneities.

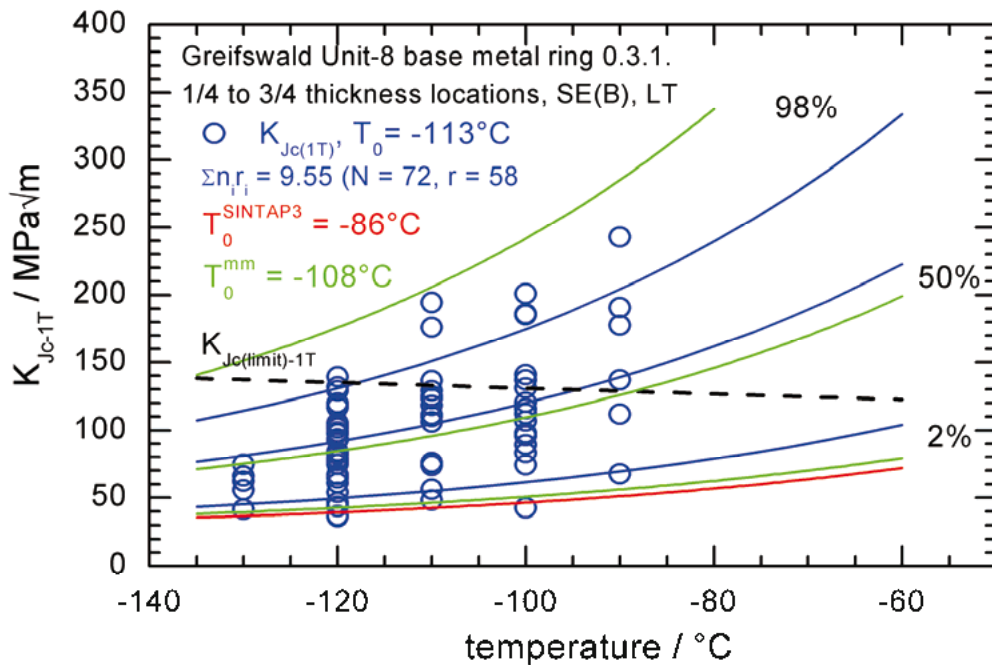


Fig. 4 K_{Jc} values and Master Curve of the standard, SINTAP and multi modal evaluation measured on Charpy size SE(B) specimens from the middle thickness locations of RPV forged ring 0.3.1.

Fractographic investigations with a scanning electron microscope (SEM) were performed to detect the initiation sites of the cleavage fracture and special features on the fractured surfaces. Fig. 5 shows SEM fractographs of a specimen tested at -120°C resulting in a low K_{Jc} value of $44 \text{ MPa}\sqrt{\text{m}}$. These fractographs display intergranular planes below and above the dashed fatigue crack front. However, the crack initiation site shows a transgranular cleavage crack.

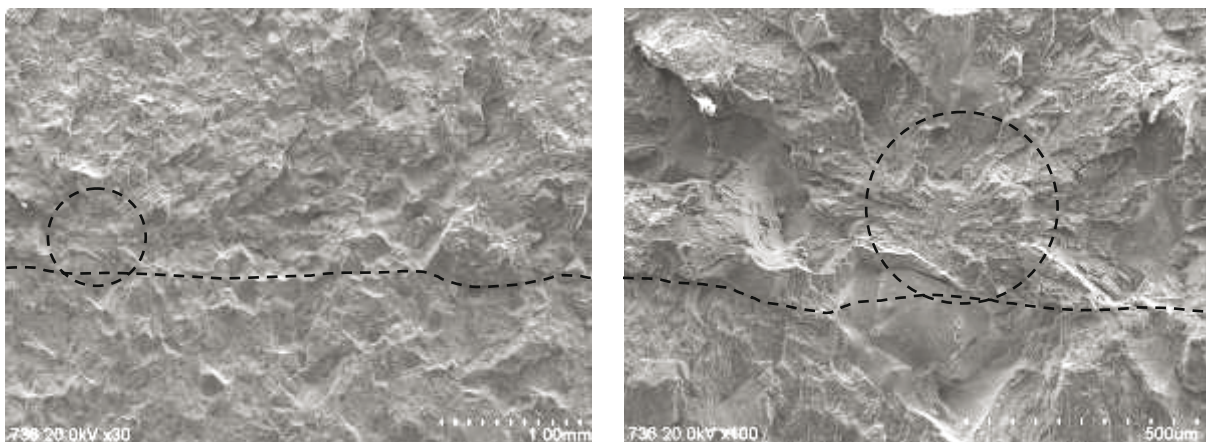


Fig. 5 SEM fractograph with the marked cleavage initiation site of a SE(B) specimen tested at -120°C , showing transgranular and intergranular cleavage planes.

The fracture appearance shown in Fig. 5 is typical for that WWER RPV base metal. The following percentages of intergranular fracture areas were measured on the crack surfaces:

- $23\% \pm 3\%$ within the surface of the fatigue crack, and
- $11\% \pm 5\%$ within the surface of the cleavage crack.

T_0 of the multi modal (MM) evaluation is 5 K higher than the standard T_0 (Fig. 4). The assessment of the standard deviations for the ASTM E1921-09a and MM suggests that both shells are inhomogeneous. As depicted in Fig. 4 the 2% and 98% MC calculated according to the MM evaluation envelop the K_{Jc} values, except 3 (about 4%) which lie below the 2% MC. In addition, the median MC separates exactly the population. Therefore, the MM MC extension is able to capture not only the lower tail but the whole data distribution.

Irradiation

For the application of the MC approach in nuclear reactor RPV integrity assessment, the universal curve shape issue may become critical if the curve shape exhibited by irradiated material deviates from that of unirradiated material. Present results from irradiation and RPV surveillance programmes strongly suggest that the curve shape issue is unlikely to become a critical issue even for highly irradiated material [Server-2009]. The neutron induced microstructural changes in the material affect not only the re-distribution of alloying and deleterious elements and the generation of precipitates, but also the fracture mode. In dependence of the embrittlement mechanism the fracture mode changes from transcrystalline cleavage to intercrystalline cleavage or a mixture of both. A literature survey [Server-2009] showed that a shape change of the fracture toughness temperature curve is generally connected with higher contents of intergranular fracture. For the assessment of the MC shape change towards higher toughness values larger specimens are necessary which are not available in the standard surveillance programmes. On the other hand toughness values above $100 \text{ MPa}\sqrt{\text{m}}$ are not relevant for the RPV integrity assessment. Because the highest stress intensity factors at measured or hypohetic crack reach maximum $100 \text{ MPa}\sqrt{\text{m}}$ during a pressurized thermal shock scenario [Server-2005], which is the most serious design-basis accident.

Fig. 6 shows an example of the MC evaluation of neutron embrittled RPV steel [Zurbuchen-2009]. Charpy size SE(B) specimens of the IAEA reference RPV steel JRQ were irradiated to different neutron fluences at the WWER-2 reactor Rheinsberg (Germany). The irradiation temperature was at 255°C . T_0 shifts to higher temperatures with increasing neutron fluence. The thermal annealing treatment led T_0 back to the temperature of the initial condition. There is no indication for a shape change for the different irradiation and the thermally annealed conditions. SEM investigations of the fractured surfaces of all conditions show transcrystalline cleavage fracture.

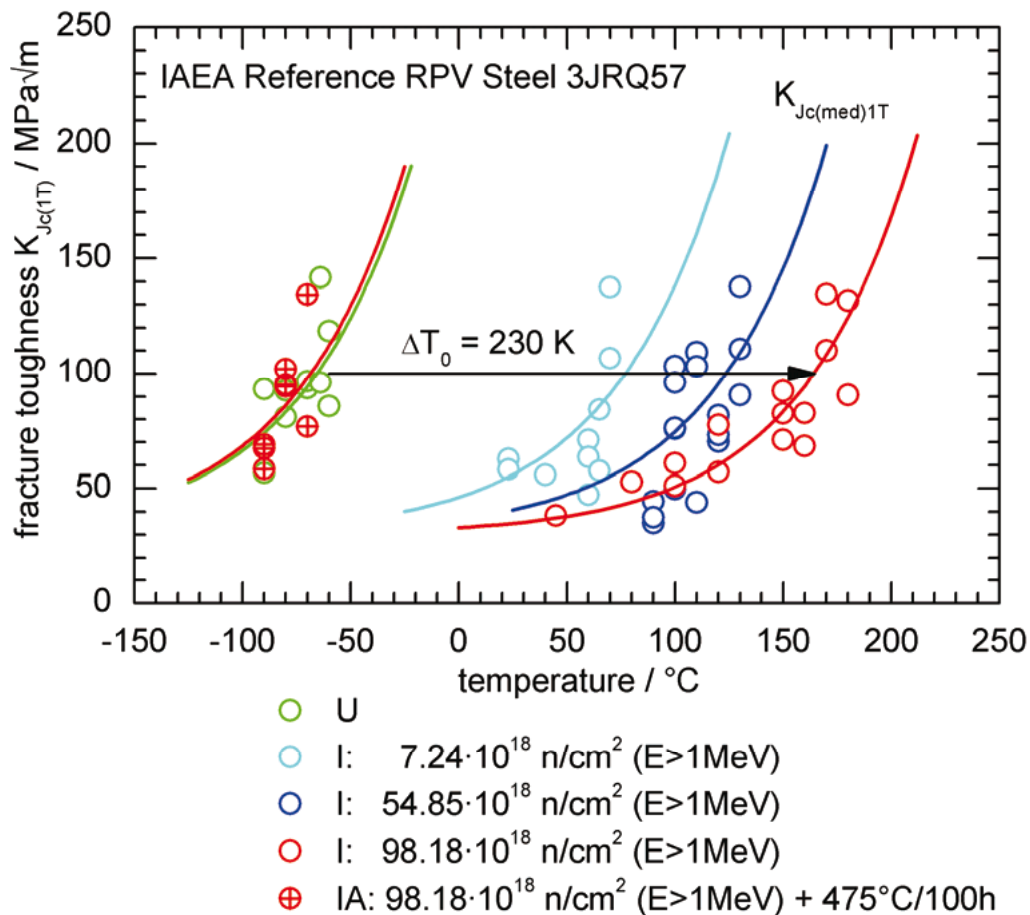


Fig. 6 K_{Jc} values and fracture toughness curves for 50% fracture probability (MC) of IAEA Reference RPV Steel 3JRQ57 irradiated on different neutron fluences and thermally annealed.

RPV integrity assessment

As an example Fig. 7 shows 1T size adjusted fracture toughness values $K_{Jc(1T)}$ measured on SE(B) and C(T) specimens of 22 NiMoCr 3-7 RPV steel [Viehrig-2010]. The Figure also depicts the ASME K_{IC} reference curves (Eq. (2)), indexed to RT_{T_0} , Eq. (3). It should be taken into account that the primary ASME- K_{IC} reference curve reflects K_{IC} values determined according to ASTM E399 which are non-size adjusted according to ASTM E1921. The reference temperature RT_{T_0} , Eq. (3), as specified in the ASME Code Case N-629 is based on T_0 calculated with size adjusted $K_{Jc(1T)}$ values, therefore the corresponding ASME- K_{IC} reference curve should envelop the measured $K_{Jc(1T)}$ values. As depicted in Fig. 7 all $K_{Jc(1T)}$ values lie above the ASME- K_{IC} reference curve indexed to $RT_{T_0} -60.9^{\circ}\text{C}$, which was evaluated with all tested SE(B) specimens. Even the $K_{Jc(1T)}$ values measured on 1T-C(T) specimens which gave approximately 6 K higher T_0 are enveloped by that curve.

Data points below the ASME- K_{IC} reference curve are considered to be acceptable as long as the number is consistent with a 5% lower tolerance bound [Server-2000]. That applies particularly to specimens of a size which is significantly larger than any real flaws that could go undetected in a reactor pressure vessel.

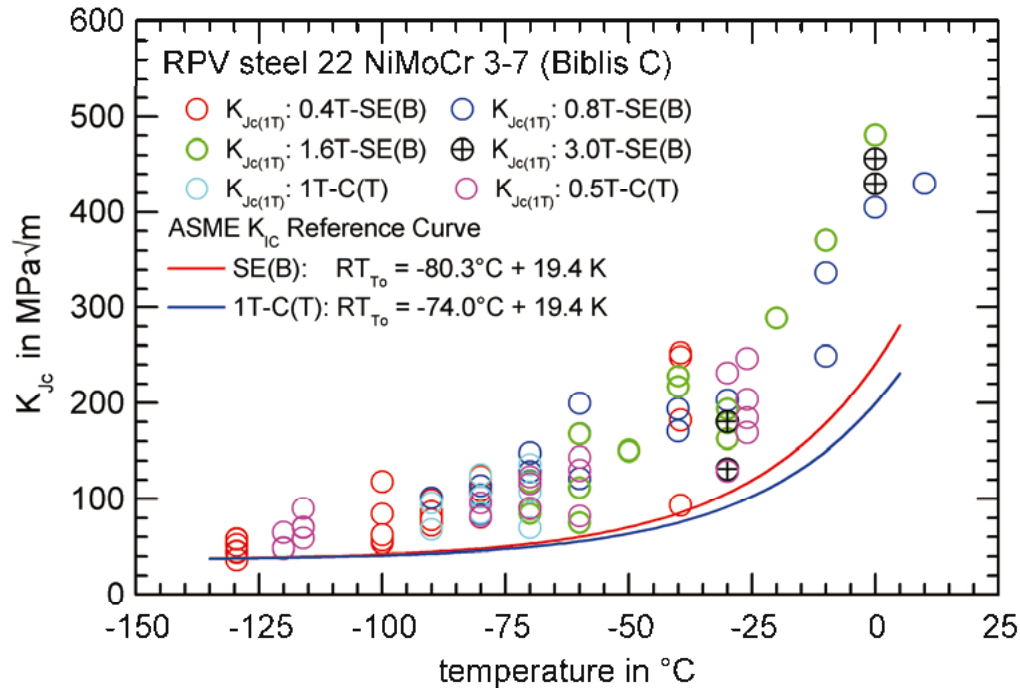


Fig. 7: $K_{Jc(1T)}$ values 1 T size adjusted measured on SE(B) and 1T-C(T) specimens and ASME- K_{Ic} reference curve indexed to RT_{T_0} according to ASME N-629.

Summary and Conclusions

The paper gives an overview about the development of the Master Curve (MC) approach since the first version of the adequate test standard ASTM E1921 was issued. The main focus is on the application of ASTM E1921 for the determination of fracture toughness values applied in the nuclear reactor pressure vessel integrity assessment. Test parameters influencing the reference temperature were assessed with selected test results. The following main results are ascertained and conclusions can be drawn:

1. The specimen size scaling procedure of test standard ASTM E1921 was confirmed. There is a trend to higher T_0 when specimens are tested close to the specimen size validity criteria of ASTM E1921. Generally, the results confirm the transferability of results from tests on 0.4T Charpy size SE(B) specimen to larger ones. With the increasing number of specimens the degree of accuracy of T_0 is higher.
2. The testing of C(T) specimens results in higher T_0 compared to SE(B) specimens, depending on the number of specimens and the test temperature range.
3. It can be stated that except for the lowest test temperature allowed by ASTM E1921-09a, the T_0 values evaluated with specimens tested at different test temperatures are consistent. The testing in the temperature range of $T_0 \pm 25$ K is recommended, because it gave the highest accuracy.
4. The MC extensions like SINTAP and multi modal procedures are applicable on inhomogeneous RPV steels. The fracture toughness vs. temperature dependency could be adequately described with these approaches.

5. A significant influence of the loading rate on the MC T_0 was observed. Increasing the loading rate from quasi-static to dynamic shifts T_0 to higher temperatures. An estimation formula proposed in ASTM E1921-09a to predict the dynamic $T_{0,d}$ from the quasi-static T_0 value is appropriate for determining an initial test temperature for dynamic tests, but shall not be used for calculating and reporting values of reference temperatures corresponding to elevated loading rates as mentioned in ASTM E1921-09a.
6. The reference temperature T_0 is eligible to define a reference temperature RT_{T_0} for the ASME- K_{IC} reference curve as recommended in the ASME Code Case N-629. An additional margin can be defined for the specific type of transient to be considered in the RPV integrity assessment and which also takes into account the level of available information of the RPV to be assessed.
7. The better option for the RPV integrity assessment is to apply the statistically defined MC in place of the current code reference fracture toughness curves, because of the consistency of the procedure. The "Unified Procedure for Lifetime Assessment of Component and Piping in WWER NPPs - VERLIFE" [VERLIFE-2003] is the first direct application. It applies directly the MC for 5% fracture probability according to ASTM E1921 as fracture toughness reference curve.

References

- [1] Anderson, T.L.: Fracture Mechanics - Fundamentals and Application, CRC Press Inc., 2000 Coporate Blvd., N.W. Boca Raton, Florida 33431, USA, 2005
- [2] Abschlussbericht Vorhaben-Nr. 1501239: Kritische Überprüfung des Mastercurve-Ansatzes im Hinblick auf die Anwendung bei deutschen Kernkraftwerken. Berichts-Nr. S8/2004. Freiburg: Fraunhofer-Institut für Werkstoffmechanik, 2005
- [3] Joyce, J. A.: On the Utilization of High Rate Pre-Cracked Charpy Test Results and the Master Curve to Obtain Accurate Lower Bound Toughness Predictions in the Ductile-To-Brittle Transition. Small Specimen Test Techniques, ASTM STP 1329, W.R. Corwin, S.T. Rosinski and E. van Walle, Eds. American Society for Testing Materials, 1998, pp. 253–273
- [4] Mc Cabe, D. E., Merkle J. G., Wallin K.: An introduction to the development and use of the Master Curve method. ASTM International, West Conshohocken, PA, USA, May 2005
- [5] Nevasmaa, P., Bannister, A., Wallin, K.: Fracture toughness estimation methodology in the SINTAP procedure, 17th International Conference on Offshore Mechanics and Arctic Engineering, ASME, OMAE98-2053, 1998
- [6] Shutter, D. M.: Dynamic Fracture Toughness Determination Using Precracked Charpy Specimens, From Charpy to Present Testing, ESIS Publication 30, D. Francois and A. Pineau (Eds.), Elsevier Science Ltd. and ESIS, 2002, pp. 237
- [7] Server, W. L., Rosinski, S.T.: Thechnical basis for application of the Master Curve approach in reactor pressure vessel integrity assessment Effects of Radiation on Materials: 19th International Symposium, ASTM STP 1366, M.L. Hamilton, A.S. Kulmar, S.T. Rosinsky, and M.L. Grossbeck, Eds., American Society for Testing and Materials, West Conshohocken, PA, 2000, pp. 127
- [8] Server, W. L. et al.: IAEA Guidelines for application of the Master Curve approach to reactor pressure vessel integrity in nuclear power plants. IAEA-Technical Reports Series 429, IAEA in Austria, March 2005
- [9] Server, B., et al: Master Curve approach to monitor fracture toughness of reactor pressure vessels in nuclear power plants. IAEA-TECDOC-1631, International Atomic Energy Agency, Vienna, 2009.

- [10] Tregoning, R. L., Joyce, J. A.: Investigation of censoring limits for cleavage fracture determination. Fourth Symposium on Small Specimen Test Techniques, Reno, Nevada, USA, 23–25 January, 2000
- [11] Brumovsky, M. et.al.: Unified procedure for lifetime assessment of component and piping in WWER NPPs "VERLIFE". European Commission, Final Report, Contract N° FIKS-CT-2001–0198, September 2003
- [12] Viehrig, H.-W., Böhmert, J. and Dzugan, J.: Use of Instrumented Charpy Impact Tests for the Determination of Fracture Toughness Values. "From Charpy to Present Impact Testing", ESIS-Publication 30, D. Francois, A. Pineau, Eds., Charpy Centenary Conference, 2–5 October 2001, Poitiers, France, Elsevier Science Ltd. and ESIS, pp. 245.
- [13] Viehrig, H.-W., Scibetta, M., Wallin, K.: Application of advanced Master Curve approaches on WWER-440 reactor pressure vessel steels. International Journal Pressure Vessel and Piping 83 (2006) Issue 8, August 2006, pp. 584.
- [14] Viehrig, H.-W., Zurbuchen, C., Schindler, H.-J., Kalkhof, D.: Effects of specimen size, initial crack acuity and test temperature on the Master Curve reference temperature. Proceedings of the 18th European Conference on Fracture, 30 August–03 September 2010, Dresden, Germany
- [15] Wallin K.: Fracture Toughness Transition Curve Shape for Ferritic Structural Steels, Proceedings of the Joint FEEG/ICF International Conference on Fracture of Engineering Materials and structures, Singapore, 6–8 August 1991
- [16] Wallin; K., Nevasmaa; P., Laukkanen, A., Planmann T. Master Curve analysis of inhomogeneous ferritic steels. Engineering Fracture Mechanics, Volume 71, Issues 16–17, November 2004, Pages 2329
- [17] Zurbuchen, C., Viehrig, H.-W.; Weiß, F.-P.: Master Curve and Unified Curve applicability to highly neutron irradiated Western type Reactor Pressure Vessel steels. Nuclear Engineering and Design 239(2009)7, 1246–1253, NED5313

¹ Dr.-Ing. Hans-Werner Viehrig, Forschungszentrum Dresden-Rossendorf, e-mail: h.w.viehrig@fzd.de

THE USE OF DCPD METHOD FOR MEASUREMENT OF GROWTH OF PHYSICALLY SHORT FATIGUE CRACKS

Ivo Černý¹

Abstract

Knowledge about resistance against fatigue growth of physically short cracks of length less than one millimetre becomes very important, particularly for advanced materials or materials manufactured using advanced technologies, containing small crack-like defects. Possibilities and limits of the use of direct current potential drop (DCPD) method for short cracks are explored in the paper. Results of sensitivity analysis on affecting parameters are shown.

Keywords: physically short cracks, direct current potential drop method, fatigue crack growth

1. Introduction

The direct current potential drop (DCPD) method represents one of the possibilities to measure crack length indirectly during experimental fatigue crack growth investigations or short-term fracture mechanics testing, like measurement of fracture toughness and J-integral. The DCPD method works on the basis of an occurrence of a potential drop caused by a discontinuity in a specimen, like cracks, when a homogeneous direct current of a sufficient value passes through the whole cross section of a sample.

A big advantage of the DCPD method is the possibility of an analytical expression of the potential drop for various configurations of electrodes, different shape and dimensions of a specimen. Johnson's formula [1] and its modification [2] is one of the most frequently used analytical description of the dependence and calculation of crack length from the potentials in specimens of a rectangular cross section with a through-thickness crack of straight crack front. A modification of the method, suitable for short specimens frequently used in laboratories, including CT-specimens, was described and discussed in [3,4]. The DCPD measurement is one of the most reliable and convenient method of automatic monitoring of crack growth process, suitable to be integrated into computer controlled monitoring systems, with no need for direct time consuming optical measurements.

The DCPD method proved its worth for measurement of usual fatigue crack growth rates and threshold values at conditions of linear elastic fracture mechanics, i.e. for ordinary long fatigue cracks according to standard recommendations (e.g. [5]). Such data are important for an assessment of residual life of components and structures containing cracks of length more than several millimetres. However, if the

material contains small crack-like defects like inclusions or pores, knowledge about resistance against fatigue growth of physically short cracks of the length less than one millimetre becomes very important. Particularly advanced fine grain steels or steels manufactured using technologies like different advanced forging methods, characteristic by very high strength and high fatigue resistance in case of no material imperfections, are usually very sensitive to small defects or short cracks. An investigation of fatigue crack growth (FCG) rates and threshold conditions of short cracks should then be an essential part of research programmes. Such data are usually missing due to experimental difficulties and labour demands (e.g. [6]).

The experimental difficulties could be significantly reduced, if an automatic indirect method could be used. The aim of the work described in this paper was to explore, analyse and verify possibilities and limits of the use of DCPD for physically short crack measurement.

2. Sensitivity analysis of DCPD method on affecting parameters

If homogenous direct current passes through a specimen with a constant rectangular cross section, the specimen contains an edge crack of the length a and potential is measured near the crack mouth at the distance y , then the crack length can be evaluated using the well known Johnson's formula:

$$\frac{V(a)}{V(a_o)} = \frac{\operatorname{arccosh} \left[\frac{\cosh(\pi y / 2W)}{\cos(\pi a / 2W)} \right]}{\operatorname{arccosh} \left[\frac{\cosh(\pi y / 2W)}{\cos(\pi a_o / 2W)} \right]} \quad (1)$$

a_o being the initial crack length, W specimen width, $V(a_o)$ the corresponding potential and y represents the distance of electrodes from crack mouth. If reference potential V_{ref} is measured in an area of specimen not affected by the growing crack, than the quotient $V(a)/V_{\text{ref}}$ instead of $V(a)$ is used in the equation. A modification of the method for short specimens, where V_{ref} is measured in the area affected by the crack was described in [3,4].

It follows from the Johnson's formula that there are two important parameters which can affect the measurement sensitivity, namely position of electrodes (distance y from the crack mouth) and specimen width W . To optimise these two parameters and explore possibilities and experimental limits, a kind of sensitivity analysis was carried out. Several situations were modelled and analytical calibration curves were calculated, namely:

- for the specimen of width $W = 15.72$ mm with three different mutual distances of potential electrodes near the crack mouth – (i) $y = 5$ mm, (ii) $y = 3$ mm and (iii) $y = 1$ mm and
- for the same three values of distances y in case of specimen width $W = 5$ mm.

Results of the sensitivity analysis are shown in Figs.1 and 2. Fig. 1 shows calibration curves for ordinary (long) cracks whilst the region of short cracks up to 1 mm is documented in detail in Fig. 2.

It follows from Fig. 1 that the DCPD measurement is significantly more sensitive for the specimen of 5 mm width in comparison with the larger one. However, the

sensitivity, i.e. the curve derivation, starts to be higher for fairly long cracks with the length at least 30% of the total specimen width. The measurement sensitivity in the region of short cracks up to 1 mm is not unfortunately increased by the reduction of specimen width. The calibration curves for short cracks as a dependence on the specimen width, either $W = 15.72$ mm or $W = 5$ mm, respectively, are almost identical – Fig. 2.

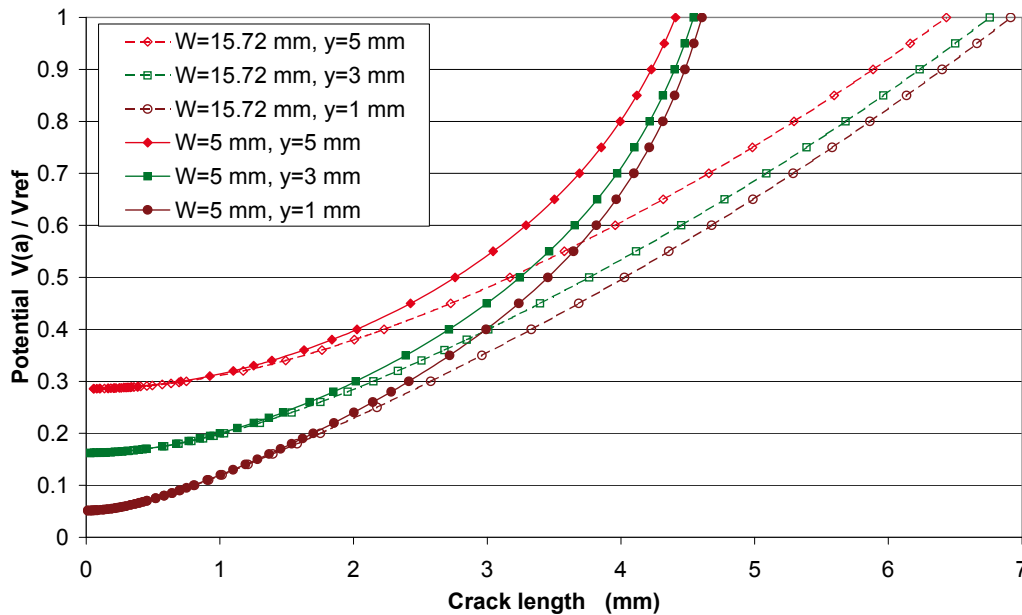


Figure 1 DCPD sensitivity analysis on specimen width and distance of measuring potential electrodes

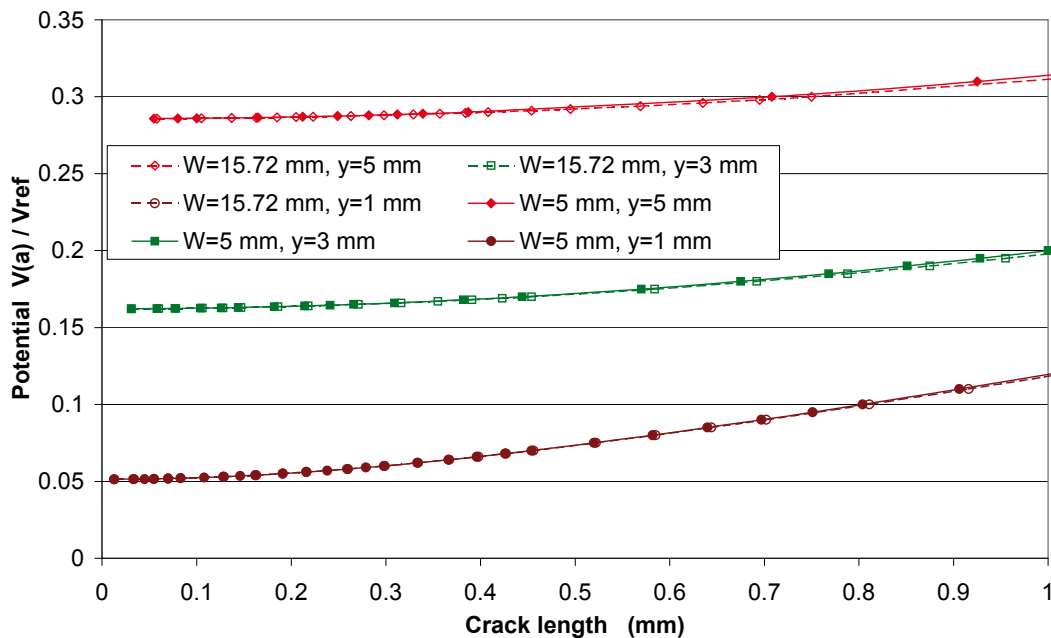


Figure 2 DCPD sensitivity analysis on specimen width and distance of measuring potential electrodes for the region of short cracks

Taking account of the low effect of the specimen dimension changes on the measurement sensitivity, the model calibration curves were further elaborated in the form of another diagram, where just specimen of the width $W = 5$ mm was considered. In addition, the curves were transformed to the form of dependence of potential increments on crack length. The diagram is in Fig. 3.

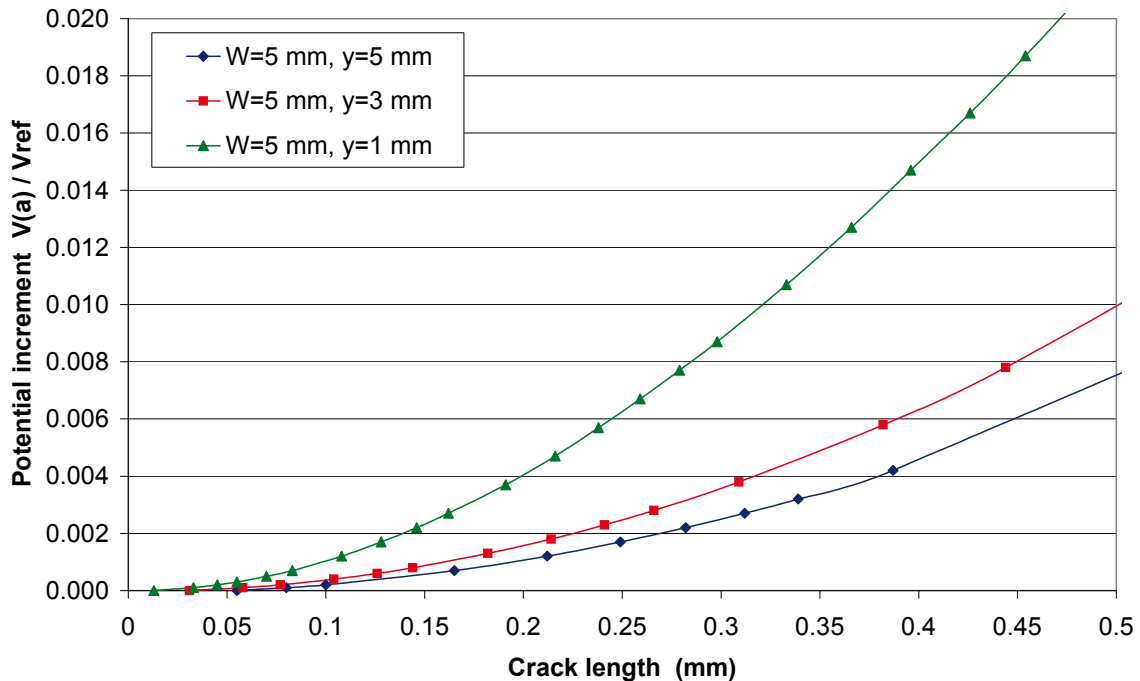


Figure 3 DCPD sensitivity analysis on distance of measuring potential electrodes for the region of short cracks

Results in Fig. 3 enable to evaluate directly the possibilities and limits of the method. The actually verified maximum resolution of the potential device is namely ± 0.001 of the potential ratio $V(a)/V_{ref}$. Fig. 3 shows that the measurement sensitivity rapidly increases for very short distances of the potential electrodes. If the distance is reduced from 5 mm to 3 mm, there is some sensitivity increase but the increase is considerably higher, when the distance is reduced from 3 mm to 1 mm. It should be, however, mentioned that connection of the electrodes at mutual distance of 1 mm, i.e. at 0.5 mm distance from the crack mouth, is already connected with rather high technical difficulties. Actually it is a very sophisticated work, On the other hand, the necessary measurement sensitivity can be then obtained.

Considering the device resolution ± 0.001 of the potential ratio $V(a)/V_{ref}$ and the diagram in Fig. 3, it can be assessed that the minimum detectable crack length corresponds to approximately 0.10 mm, 0.16 mm and 0.19 mm for the electrode distances 1 mm, 3 mm and 5 mm, respectively. This result is quite encouraging, particularly for the 1 mm distance of the electrodes. On the other hand, a serious, sufficiently precise FCG measurement should contain at least 15 – 20 experimental points in the measured region [5]. Then as an example, if short crack effect is connected with crack lengths up to 0.7 mm, the measurement resolution should be more than 0.03 mm of the crack increment. This condition is fully satisfied for the 1 mm electrode distance and crack length more than 0.2 mm, but not for the distance 3 mm or even more. For the 3 mm electrode distance, the required resolution is

reached in case of crack length more than 0.45 mm, which seems to be too much for exact investigations of short fatigue cracks behaviour. Eventually, the 5 mm mutual distance of potential electrodes looks to be insufficient at all.

3. Experimental verification – results and discussion

The DCPD sensitivity was verified using a steel specimen of the width $W = 15.72$ mm. Mutual distance of the potential electrodes was 5 mm (each electrode 2.5 mm from the crack mouth) – Fig. 4. Crack growth was experimentally modelled by gradual cutting using a thin diamond saw – Fig. 5. Data of cut depth (i.e. crack length) and corresponding potentials were gradually recorded – Fig. 6.

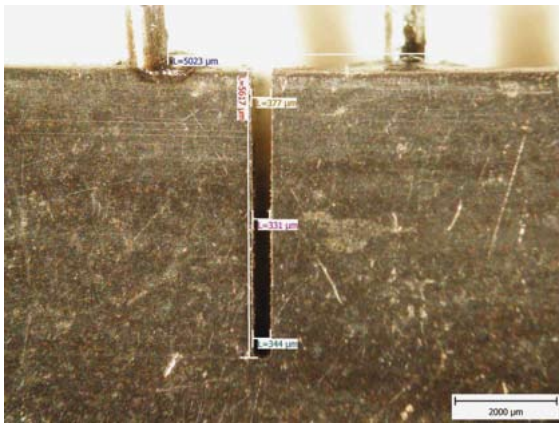


Figure 4 Verification specimen with artificial cut and electrodes at 5 mm distance

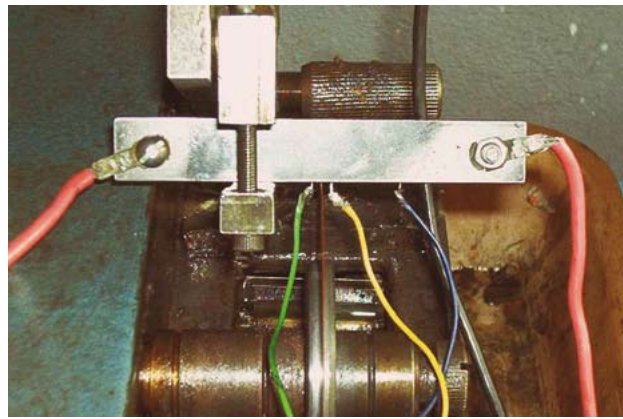


Figure 5 Verification specimen during artificial cutting using diamond saw

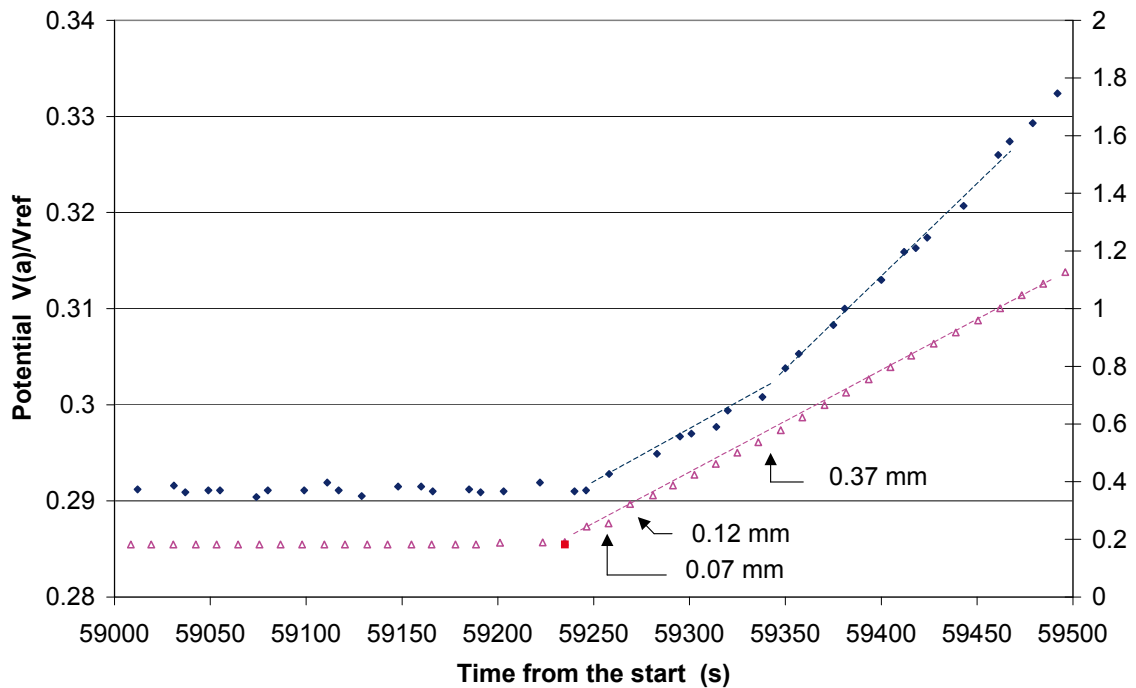


Figure 6 Verification of actual DCPD measurement sensitivity

Results of the verification in Fig. 6 confirmed that the minimum detectable crack length was even less than 0.2 mm, in spite of that the mutual electrode distance was 5 mm. This result can be interpreted as good and encouraging, confirming the potential possibility of the use of the method.

Some small discrepancies between the theoretical and actual crack lengths, not evident from the diagrams, were ascertained, actual values being somewhat higher than the theoretical ones. This effect, which has to be further verified, can be likely affected by the fact that the artificial cut had some width, about 0.35 mm, and not ideally thin like an actual crack.

3. Conclusions

The aim of the work described in the paper was to explore, analyse and verify possibilities and limits of the use of DCPD method for physically short crack measurement and for investigations of growth conditions of short fatigue cracks. Model analytical calibration curves were calculated for different parameters with the aim to perform sensitivity analysis. An experimental verification of the sensitivity and resolution was eventually made. The main results can be summarised as follows:

- Specimen dimensions, more exactly width W , do not have any significant effect on the measurement precision and resolution in case of short cracks. On the contrary, the position of potential electrodes can substantially increase the measurement precision, particularly when the electrodes are very close to the crack mouth.
- Both the sensitivity analysis and experimental verification indicated that the DCPD method can be used for short fatigue crack investigations. Limits for the position of the potential electrodes to obtain necessary precision and resolution were determined.

Acknowledgements

The work was supported by grants 1M06032 and MSM2579700001 of the Ministry of Education, Youth and Sports of the Czech Republic.

References

- [1] Johnson H.H.: Calibrating the Electric Potential Method for Studying Slow Crack Growth, *Materials Research and Standards*, Vol.5, No.9 (1965) pp. 442–445
- [2] Tada H., Paris P.C., Irwin G.R.: *The Stress Analysis of Crack Handbook*, Del Research Corporation, Hellertown, Pennsylvania (1973)
- [3] Černý I., Linhart V., Minářík J. & Hulík P.: Modification of D.C.: Potential Method for Short Specimens, *Proc. of the 2nd Int. Conf. Localized Damage, Computational Mechanics Publications*, Southampton and Boston (1992)
- [4] Černý I.: *Eng. Fract. Mech.*, Vol.71 (2004) pp.837–848
- [5] ASTM E 647 – 00 Standard Test Method for Measurement of Fatigue Crack Growth Rates
- [6] Šmíd M., Obřtlík K., Petrevec M., Polák J., Hrbáček K.: Fatigue properties of nickel-base superalloy Inconel 792-5A at 800°C. *Proc. of the Int. Conf. METAL*, 18-20 May 2010, Rožnov pod Radhoštěm, Czech Republic

¹ Ing. Ivo Černý, Ph.D., SVÚM a.s., Podnikatelská 565, 190 11 Praha 9, Czech Republic, Tel.: +420 222 724 098, e-mail: Ivo.Cerny@seznam.cz

A GEOMETRIC NONLINEAR THERMO-ELASTIC ANALYSIS WITH THE SANDWICH BAR ELEMENT

Rastislav Ďuriš¹

Abstract

This contribution deal with a two-node straight sandwich composite bar element intended to perform the non-incremental full geometric non-linear analysis. Stiffness matrix of this composite bar with constant double symmetric rectangular cross-sectional area contains transfer constants, which accurately describe polynomial uniaxially variation of the material thermo-physical properties.

In the numerical experiment weak coupled thermo-structural geometric non-linear problem was solved. Obtained results were compared with 3D model analysis made with the very fine mesh in the ANSYS programme. Findings show good accuracy of this new finite element. The results obtained with presented bar element do not depend on the element mesh density.

Keywords: geometric nonlinear analyses, bar element, sandwich structure

1. Introduction

The composite or sandwich materials are often used in many applications. By mixing two or more appropriate constituents can obtain materials with better properties than single components. These materials are characterized by non-homogeneous material properties. Effective numerical analyses of structures made from such materials require homogenization of uniaxially or spatially variable material properties. Macro-mechanical modelling of these effective material properties of composites is often based on different homogenization techniques.

In the contribution are described the equilibrium equations of the two-node sandwich bar element with constant rectangular cross-sectional area and variation of thermo-physical material properties along its axis. A new shape functions of a bar element [Kutiš, 1999] was used to accurate description of material properties variation. The composite material of this element arose from two components (matrix and fibre). Different longitudinal continuous variation of the components elasticity moduli, thermal expansion coefficient and volume fractions of the constituents is given in polynomial form in each layer. The homogenization of the material properties is made for multilayered sandwich bar using the extended mixture rule [Murín, 2007]. Effect of steady-state temperature field applied in the bar is considered too.

2. The effective material properties of the sandwich bar element

We consider sandwich material with continuously variation of elasticity moduli of both, matrix and fibre constituents along the element axis (e.g. caused by non-homogeneous temperature field in a bar) in each composite layer (Fig. 1).

Analogically vary the thermal expansion coefficient and volume fractions of the constituents. This variation of parameters defining the geometrical and mechanical properties can be expressed in polynomial form

$$p(x) = p_i \eta_p(x) \quad (1)$$

where $p(x)$ denotes uniaxially polynomial variation of fibre elasticity modulus $E_f(x)$ and the matrix elasticity modulus $E_m(x)$, the fibre $v_f(x)$ and matrix $v_m(x)$ volume fractions and thermal expansion coefficient of fibre and matrix constituents $\alpha(x)$. Parameter p_i denotes the value of listed geometric or physical properties at node i of element and $\eta_p(x)$ is the polynomial variation of selected property. For the fibre and matrix volume fractions of the constituents is valid $v_f(x) + v_m(x) = 1$ at each material point. The volume fractions and material properties are assumed to be constant through the element depth b and through its height h . The bar element is loaded in linear elastic load state.

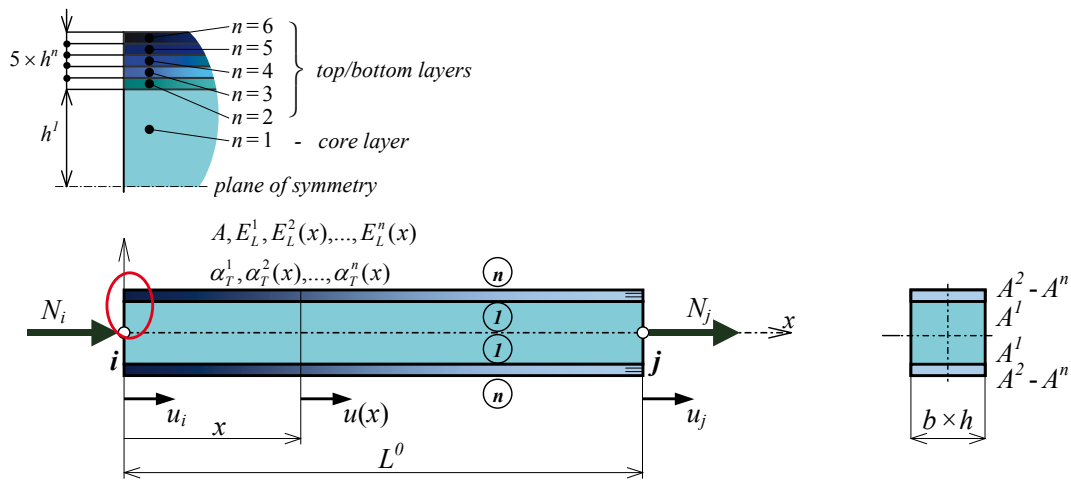


Fig. 1. Double symmetric sandwich bar element with variation of stiffness in initial state

For determination of effective longitudinal material properties of each layer of sandwich bar was extended mixture rules [Murín, Kutiš, 2007] used. The effective longitudinal elasticity modulus in the k -th layer is then given by

$$E_L^k(x) = v_f^k(x) E_f^k(x) + v_m^k(x) E_m^k(x) = E_{Li}^k \eta_{E_L}^k(x) \quad (2)$$

where $E_{Li}^k = v_{fi}^k E_{fi}^k + v_{mi}^k E_{mi}^k$ is the effective longitudinal elasticity modulus of the layer k at node i and

$$\eta_{E_L}^k(x) = 1 + \frac{\eta_{v_f}^k(x) \eta_{E_f}^k(x) + \eta_{v_m}^k(x) \eta_{E_m}^k(x)}{E_{Li}^k} \quad (4)$$

is the relation for effective longitudinal elasticity modulus variation of the layer k . The effective longitudinal thermal expansion coefficient $\alpha_{TL}^k(x)$ of the k -th layer can be calculated using expression

$$\alpha_{TL}^k(x) = \frac{v_f^k(x) \alpha_{Tf}^k(x) E_f^k(x) + v_m^k(x) \alpha_{Tm}^k(x) E_m^k(x)}{v_f^k(x) E_f^k(x) + v_m^k(x) E_m^k(x)} \quad (3)$$

Expression (3) is not polynomial and expansion to Taylor's series is necessary to be used to convert it into the polynomial form. The homogenization of the material

properties is made for n -layered sandwich bar with double symmetric rectangular constant cross-sectional area A using the laminate theory. The homogenized effective longitudinal elasticity modulus of whole element $E_L^H(x)$ in the polynomial form

$$E_L^H(x) = \sum_{k=1}^n r_A^k E_L^k(x) = E_{Li}^H \eta_{E_L^H}(x) \quad (4)$$

where E_{Li}^H is the value of homogenized effective longitudinal elasticity modulus at node i and $\eta_{E_L^H}(x)$ is the polynomial of its longitudinal variation, $r_A^k = 2A^k / A$ is a cross-sectional area ratio of k -th layer, A^k is cross-sectional area of k -th layer and A is total cross-sectional area of the bar. The homogenized effective longitudinal thermal expansion coefficient of whole element can be calculated from expression

$$\alpha_{TL}^H(x) = \frac{\sum_{k=1}^n \alpha_{TL}^k(x) E_L^k(x)}{\sum_{k=1}^n E_L^k(x)} = \frac{1}{E_L^H(x)} \sum_{k=1}^n r_A^k \alpha_{TL}^k(x) E_L^k(x) \quad (5)$$

Equation (11) can be transformed to polynomial by Taylor's series to the form

$$\alpha_{TL}^H(x) = \alpha_{TLi}^H \eta_{\alpha_{TL}^H}(x) \quad (6)$$

where α_{TLi}^H is the value of homogenized effective longitudinal thermal expansion coefficient at node i and $\eta_{\alpha_{TL}^H}(x)$ is the polynomial of its longitudinal variation.

2.1 Full geometric non-linear local stiffness matrix of the bar element

For derivation of new bar element stiffness matrix a approach to evaluation of equilibrium equations published [Rubin, 1999] is used. Thus we can obtain the new geometric non-linear non-incremental formulation of the element stiffness relations. The local FEM equilibrium equations of 2D homogenized bar element has the form

$$\mathbf{K}_u \mathbf{u} = \mathbf{F} \quad (7)$$

where $\mathbf{u} = [u_i, u_j]^T$ is the displacement vector and $\mathbf{F} = [N_i + F_i^{th}, N_j + F_j^{th}]^T$ is the load vector. By implementation of the shape functions with transfer functions and constants we get the non-linear stiffness matrix \mathbf{K}_u in the form

$$\mathbf{K}_u = \frac{AE_{Li}^H}{d'_{2E_L^H}} \left[1 + \frac{3}{2}(\lambda - 1) \frac{\overline{d'_{2E_L^H}}}{(d'_{2E_L^H})^2} + \frac{1}{2}(\lambda - 1)^2 \frac{\overline{\overline{d'_{2E_L^H}}}}{(d'_{2E_L^H})^3} \right] \begin{bmatrix} 1 & -1 \\ -1 & 1 \end{bmatrix} \quad (8)$$

where $d'_{2E_L^H} = \int_0^{L^0} d''_{2E_L^H}(x) dx$, $\overline{d'_{2E_L^H}} = \int_0^{L^0} (d''_{2E_L^H}(x))^2 dx$, $\overline{\overline{d'_{2E_L^H}}} = \int_0^{L^0} (d''_{2E_L^H}(x))^3 dx$ are the transfer

constants for homogenized effective longitudinal elasticity modulus (4), $d''_{2E_L^H}(x) = (\eta_{E_L^H}(x))^{-1}$ is the second derivative of the transfer function and $\lambda = (u_j - u_i)/L^0 + 1$ is the stretching of the bar. This local stiffness matrix can be transformed to global coordinate system by using standard transformation rules.

The temperature load is changing along the bar element length only, the effective thermal nodal forces are derived as follows [Murín et al, 2008]

$$\begin{bmatrix} F_i^{th} \\ F_j^{th} \end{bmatrix} = \begin{bmatrix} -1 \\ 1 \end{bmatrix} \frac{E_{Li}^H A \alpha_{TLi}^H \Delta T_i}{d'_{2E_L^H}} \int_0^{L^0} \eta_{\alpha_{TL}^H}(x) \eta_{\Delta T}(x) dx \quad (9)$$

where $\Delta T_i = T_i - T_{ref}$ is temperature difference at node i with respect to reference temperature, and $\eta_{\Delta T} = (T(x) + T_{ref})/\Delta T_i$ is the polynomial of the varying temperature field. Deformation of the bar due to thermal loading is

$$\Delta u_T = \int_{(L^0)} \varepsilon_0(x) dx = \alpha_{TLi}^H \Delta T_i \int_{(L^0)} \eta_{\alpha \Delta T}(x) dx \quad (10)$$

The expression for calculation of the effective longitudinal strain we get from derivation of equation (16) in the form

$$\varepsilon(x) = \frac{u_j - u_i - \Delta u_T}{\eta_{E_L^H}(x) d'_{2E_L^H}} \quad (11)$$

The effective normal stress in the homogenized bar is then

$$\sigma(x) = \varepsilon(x) E_L^H(x) \quad (12)$$

Structural stress in the k -th layer is

$$\sigma_L^k(x) = \varepsilon(x) E_L^k(x) \quad (13)$$

The thermal stresses in the bar are caused by different thermal expansion coefficient of individual layers. Thermal stress in k -th layer can be calculated from

$$\sigma_{th}^k(x) = (\alpha_{TL}^H(x) - \alpha_{TL}^k(x)) (T(x) - T_{ref}) E_L^k(x) \quad (14)$$

Total normal stress in k -th layer are equal a sum of structural and thermal stress

$$\sigma^k(x) = \sigma_L^k(x) + \sigma_{th}^k(x) \quad (15)$$

2. Numerical experiment

To show the structural behaviour of new element, we consider 12-layered two-node sandwich bar with constant cross-sectional area (see Fig. 1). Layout and geometry of layers is symmetric to neutral plane.

Table 1. Material properties of the constituents and the specimen proportions

material properties			
Tungsten (fibres)	elasticity modulus		$E_m = 400$ GPa
	thermal expansion coefficient		$\alpha_{Tf} = 5.3 \times 10^{-6}$ K ⁻¹
NiFe (matrix)	elasticity modulus		$E_f = 255$ GPa
	thermal expansion coefficient		$\alpha_{Tf} = 1.5 \times 10^{-5}$ K ⁻¹
geometrical parameters			
specimen length	$L^0 = 0.1$ m	cross-sectional area of 1 st layer	$A^1 = 0,00004$ m ²
specimen width	$b = 0.01$ m	cross-sectional area of k^{th} layer	$A^k = 0,000002$ m ²
specimen height	$h = 0.01$ m	total thickness of face layers	$t = 0,001$ m
total number of layers (incl. core)	$2n = 12$ (2×6)	thickness of 1 st layer	$h^1 = 0,004$ m
initial angle	$\alpha^0 = 7^\circ$	thickness of k^{th} layer	$h^k = 0,0002$ m
cross-sectional area	$A = 0,0001$ m ²		

Material of layers consists of two components: NiFe denoted as a matrix (index m) and Tungsten named as a fibre (index f). Geometry and material parameters for the bar chosen for numerical examples are summarized in Tab. 1.

In the numerical examples the constant linear elastic material properties of constituents are assumed ($E_f = \text{const.}$ and $E_m = \text{const.}$). Material of the middle layer

(core layer denoted as $k = 1$) is a pure matrix with constant Young's modulus E_m . Symmetric pairs of layers $k = \langle 2, \dots, 6 \rangle$ were fabricated by non-uniform mixing of both matrix and fibres components. Volume fraction of fibre is constant along the width and height of each k -th layer, but it changes linearly along the layer length i.e. mechanical properties varies along the width and length of the specimen. This longitudinal variation of volume fraction of fibre (matrix) in k -th layer is described by equation (2). At node i the volume fractions of fibre are different in each layer and at node j is this ratio considered to be constant in all layers. As a typical example of geometrically non-linear behaviour the three-hinge mechanism was analysed (Fig. 2).

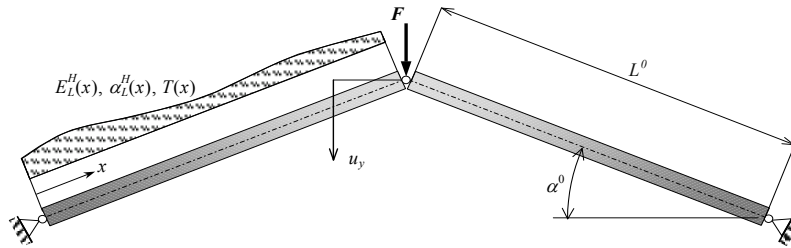


Fig. 2. Von Mises bar structure

Volume fraction of the components varies linearly along the k -th layer length in accordance with (2)

$$v_f^k(x) = 1 - v_m^k(x) = v_{fi}^k(1 + \eta_{vf1}^k x) \quad k \in \langle 2, \dots, 6 \rangle$$

List of v_{fi}^k, η_{vf1}^k parameters is given in tab. 2.

Table 2. Polynomial variation of fibre volume fraction along the x axis of the element

layer k	1	2	3	4	5	6
v_{fi}^k	0	0.6	0.7	0.8	0.9	1.0
η_{vf1}^k	0	-3/0.6	-4/0.7	-5/0.8	-6/0.9	-7/1.0

Using equation (3) we can get the effective longitudinal elasticity modulus of the individual layers in form

$$\begin{aligned} E_L^1(x) &= 2.55 \times 10^{11} \text{ [Pa]} & E_L^2(x) &= (3.42 - 4.35 x) \times 10^{11} \text{ [Pa]} \\ E_L^3(x) &= (3.56 - 5.80 x) \times 10^{11} \text{ [Pa]} & E_L^4(x) &= (3.71 - 7.25 x) \times 10^{11} \text{ [Pa]} \\ E_L^5(x) &= (3.85 - 8.70 x) \times 10^{11} \text{ [Pa]} & E_L^6(x) &= (4.00 - 1.01 x) \times 10^{11} \text{ [Pa]} \end{aligned}$$

The effective elasticity modulus of the homogenized sandwich was calculated by expression (10) and is

$$E_L^H(x) = (2.782 - 1.45 x) \times 10^{11} \text{ [Pa]}$$

Also thermal expansion coefficients of the individual layers was obtained by expression (7)

$$\alpha_{TL}^1(x) = 1.5 \times 10^{-5} \text{ [K}^{-1}\text{]} \quad \alpha_{TL}^2(x) = \frac{1.5686 \times 10^{-5}}{0.78620 - x} - 1.1758 \times 10^{-5} \text{ [K}^{-1}\text{]}$$

$$\alpha_{TL}^3(x) = \frac{1.1764 \times 10^{-5}}{0.61465 - x} - 1.1758 \times 10^{-5} \text{ [K}^{-1}\text{]} \quad \alpha_{TL}^4(x) = \frac{9.4116 \times 10^{-6}}{0.51172 - x} - 1.1758 \times 10^{-5} \text{ [K}^{-1}\text{]}$$

$$\alpha_{TL}^5(x) = \frac{7.8430 \times 10^{-6}}{0.44310 - x} - 1.1758 \times 10^{-5} \text{ [K}^{-1}\text{]} \quad \alpha_{TL}^6(x) = \frac{6.7226 \times 10^{-6}}{0.39408 - x} - 1.1758 \times 10^{-5} \text{ [K}^{-1}\text{]}$$

The effective thermal expansion coefficient of the homogenized sandwich was calculated by expression (11) and transformed to the polynomial form

$$\alpha_{TL}^H(x) = 1.2768 \times 10^{-5} + 1.2783 \times 10^{-5} x + 6.6629 \times 10^{-6} x^2 + 3.472 \times 10^{-6} x^3 + 1.81 \times 10^{-6} x^4 + 9.4341 \times 10^{-7} x^5 + 4.9171 \times 10^{-7} x^6 \text{ [K}^{-1}\text{]}$$

To compare and evaluate the numerical accuracy of new element and extended mixture rules we used four different models, three one-dimensional and one three-dimensional model:

- Beam model divided into 20 BEAM3 elements (based on hermite shape functions) in ANSYS programme
- Beam model meshed to 20 BEAM188 elements (linear isoparametric shape functions) in ANSYS programme
- Solid model with very fine mesh (10 080 SOLID45 elements) in ANSYS programme
- To examine the accuracy of the new bar element, the individual code in MATHEMATICA programme was written. Only single our new finite element was used for solution of the chosen problem.

The results obtained by this new element were compared with the beam and solid models analysis performed by ANSYS.

In all solutions steady-state temperature field was considered as a additional loading described by relation

$$T(x) = 30(1 - 2x + 4x^2) \text{ [}^\circ\text{C]}$$

The reference temperature $T_{ref} = 0^\circ\text{C}$. We used the effective longitudinal material properties of individual composite layers in ANSYS solid model. The homogenized effective material properties of sandwich were used in the new bar element (MATHEMATICA) and for the ANSYS beam models, respectively.

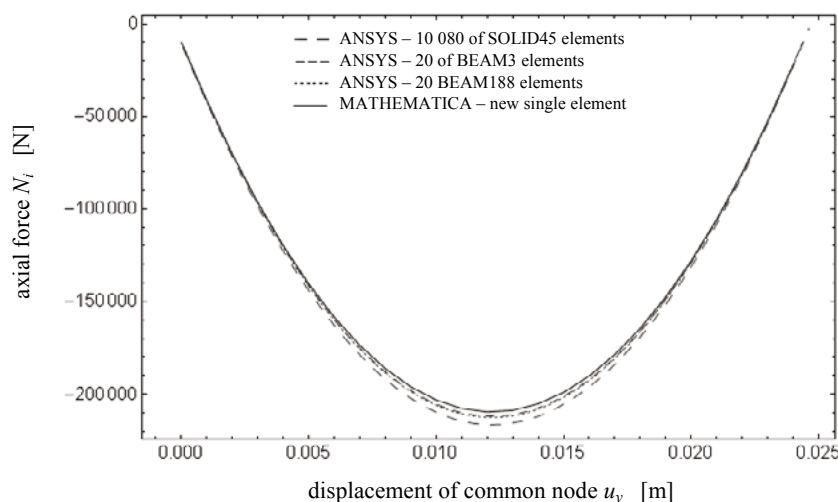


Fig. 3. Common hinge displacement vs. axial force

The first graph shows relation between common hinge displacement and axial force N (Fig. 3). Maximum intensity of axial force obtained from numerical analyses with different models are shown in the Tab. 3.

Table 3. Results of maximum forces for new bar and ANSYS solutions

axial force N [N]			
new bar element 1 element	ANSYS - BEAM188 20 elements	ANSYS - BEAM3 20 elements	ANSYS - SOLID45 20 elements
-209605	-212626	-211868	-216565
global reaction $\ F\ $ [N]			
new bar element 1 element	ANSYS - BEAM188 20 elements	ANSYS - BEAM3 20 elements	ANSYS - SOLID45 20 elements
10148.3	10248	10223.5	10420.9

Tab. 4 shows results of maximum axial stresses in the middle of each layer obtained using one new bar element and ANSYS solid analysis. Presented results corresponding the load substep when local axis x of the bar is identical with global x axis.

Table 4. Compressive stresses in middle of k -th layer in load substep $\alpha^t = 0^\circ$ (maximum of stresses in the bar)

node	k^{th} layer:	axial stress in k -th layer $\sigma_{i(i)}^k$ [MPa]					
		1	2	3	4	5	6
i	new element	-1053.15	-1342.63	-1390.86	-1439.12	-1487.36	-1535.61
	ANSYS solid	-1056.71	-1342.78	-1390.34	-1437.94	-1485.62	-1533.45
j	new element	-1098.72	-1256.82	-1256.82	-1256.82	-1256.82	-1256.82
	ANSYS solid	-1098.64	-1261.63	-1262.44	-1263.17	-1263.74	-1264.11

Distribution of total stresses in the bar layers are shown in Fig. 4. Both, results obtained by new single bar element (calculated using equation (15)) and from ANSYS solid analysis with fine mesh are presented.

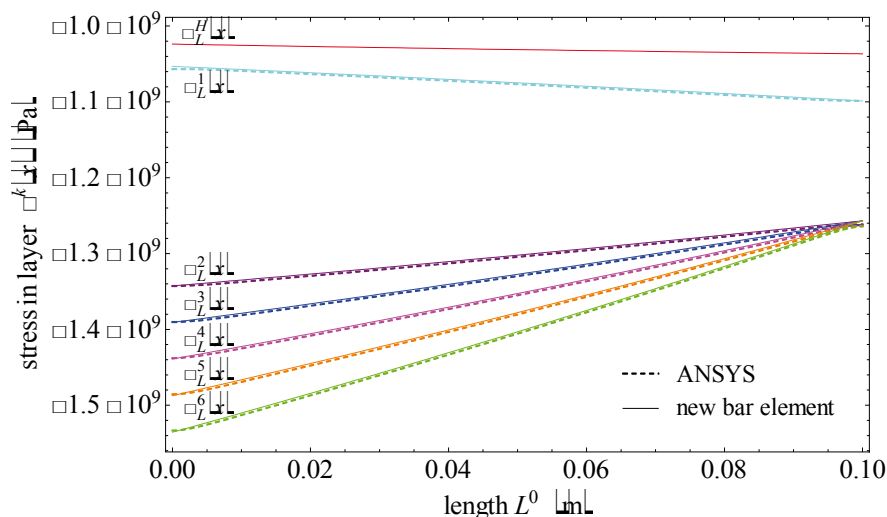


Fig. 4. Distribution of normal stresses in individual layers and homogenized normal stress in new bar element

3. Conclusion

The results of numerical experiments are presented in this contribution using the above mentioned mixture rules. All variations of material properties are included into the bar element stiffness matrix through transfer constants. The effective material properties were calculated by extended mixture rules and by the laminate theory. New finite bar element can also be used in the case when the effective material properties were obtained by other homogenization technique.

The obtained results are compared with solid analysis in the ANSYS simulation programme. Findings show good accuracy and effectiveness of this new finite element and new homogenization procedure. Difference between ANSYS solid analysis and new element results are less than 2.62% for the global reaction and 3.21% for axial force. The results obtained with this element do not depend on the mesh density.

Acknowledgements

The work has been supported by the grant projects VEGA 1/0093/10, VEGA1/0256/09. This support is gratefully acknowledged.

References

- [1] Altenbach, H., Altenbach, J., Kissing, W.: *Mechanics of Composite Structural Elements*, Springer-Verlag, 2003
 - [2] Chakraborty, A., Gopalakrishnan, S., Reddy, J.N.: A new beam finite element for the analysis of functionally graded materials, *International Journal of Mechanical Sciences* 45 (3) (2003), 519–539
 - [3] Kutiš, V.: *Beam element with variation of cross-section, which satisfies all local and global equilibrium conditions*, Ph.D. Thesis, Department of Mechanics, FEI STU (Slovak University of Technology), Bratislava, 2001
 - [4] Murín, J.: *Implicit non-incremental FEM equations for non-linear continuum*. *Strojnícky časopis*, 52, (3), 2001
 - [5] Murín, J., Kutiš, V.: *Improved mixture rules for the composite (FGM's) sandwich beam finite element*, In: *9th International Conference on Computational Plasticity COMPLAS IX, Fundamentals and Applications Part 2*, Barcelona, 2007, 647–650
 - [6] Murín, J., Kutiš, V., Masný, M.: *An effective solution of electro-thermo-structural problem of uni-axially graded material*, *Structural Engineering and Mechanics*, 28 (6), 2008, 695–714
- Rubin, H., *Bautechnik*, Ernst and Sohn, 1999

¹ Ing. Rastislav Ďuriš, Faculty of Materials Science and Technology, Slovak University of Technology in Bratislava, Paulínska 16, 917 24 Trnava, Slovak Republic. Tel.: +421 33 55 11 601, e-mail: rastislav.duris@stuba.sk

SMALL PUNCH TESTS FOR TENSILE PROPERTIES AND FRACTURE TOUGHNESS DETERMINATION

Jan Džugan¹, Pavel Konopík²

Abstract

The paper deals with the problematic of determination of mechanical properties with the use of mini-samples. Small punch test technique is employed here. Standard testing methods for tensile tests and for fracture toughness determination are used as a reference method for the SPT based results comparison. The correlation between small punch test results and results of conventional tests applied to several materials are investigated in the current paper.

Keywords: small punch test, fracture toughness, tensile test

1. Introduction

There are increasing demands on the integrity assessment of important structures in the course of their service nowadays. For that application the fracture mechanics has attained a great attention in establishing ultimate load limitations and assessing the integrity for a large number of engineering structures of multifarious types. Fracture mechanics based integrity assessment procedure of components requires fracture toughness properties of the materials which is in many cases difficult to obtain, due to lack of the experimental material. Therefore, non-destructive techniques are being developed as well as testing methods using mini-samples enabling conversion of the obtain results into conventional parameters such as tensile properties and fracture toughness parameters. One of the methods of the highest interest is small punch test (SPT).

The SPT method is using small test disc shaped samples of usual dimensions of 8mm diameter and 0,5mm thickness. The testing itself is very simple penetration of hard ball through the tests sample while the force and ball displacement is measured either at room temperature or non-ambient temperature. The problem arises when the evaluation of the tests is to be performed. There has been proposed many procedures of correlation between the SPT and various mechanical tests results such as tensile tests, Charpy impact tests, transition temperature determination, fracture toughness...

There are correlations of SPT with tensile test properties and fracture toughness proposed for example in publications [1-10]. In the current paper these correlations are investigated and applied to material investigated and performance of SPT for conventional properties evaluation is observed.

2. Experimental Materials

Experimental materials are two steels. The first one is experimental low carbon steel, designated as Steel 1 later on. The second one is 16 343 (34CrNiMo6). The steel 1 is investigated in six different states (original state, annealed at 250, 350, 440, 500 and 620°C). The steel 16 343 is tested in as delivered condition exhibiting upper shelf behaviour at room temperature and in quenched state exhibiting brittle behaviour at room temperature. Tests in the case of the steel 16 343 in as delivered condition were performed in longitudinal and transversal direction of rolled bar semi-product. Materials tensile properties are summarized in **Tab. 1**.

Tab. 1. Tensile properties

Material	State	$R_{p0,2}/R_{eH}$	R_m	A_5	Z
		[MPa]	[MPa]	[%]	[%]
Steel 1	Original	1144,8	1252,6	14,2	70,3
	250	1168,5	1365,6	13,6	67,1
	350	1166,6	1285,6	14,1	69,4
	440	981,1	1022,1	16,9	70,9
	500	816,0	863,3	17,5	71,2
	620	699,9	734,0	21,4	74,1
16 343	Longitudinal	921,3	1050,4	17,5	63,4
	Transversal	952,6	1053,3	15,7	60,0
	Quench	1219,6	1965,0	10,7	38,8

3. Fracture toughness tests

The fracture toughness tests were performed on three point bend specimens. The evaluation was done according to ASTM E 1820. Samples were machined then fatigue pre-cracked with the final stress intensity factor of about $20 \text{ MPa}\cdot\text{m}^{1/2}$. Test pieces were side-grooved after pre-cracking and subsequently tested. Tests were performed according to multiple specimen method. Crack lengths after tests were measured by digital image processing and fracture toughness values were determined for the materials investigated. There were tested at least three samples for each material state. Tests were executed at room temperature and in the case of steel 1 in the original state, tests at -20°C were also performed. Results of the fracture toughness test are summarized in **Tab. 2**. Some results of fracture toughness tests did not fulfil requirements for size independent fracture toughness. These tests are denoted as J_Q in results table

Tab. 2. Fracture toughness values

Material	State	Temperature °C	J_{IC}, J_Q kN.m	K_{IC}, K_Q MPa.m ^{0,5}
Steel 1	Original	20	----	127,1
	Original	-20	----	105,5
	250	20	----	112,6
	350	20	----	127,0
	440	20	253,5	241,9
	500	20	383	297,3
	620	20	517	345,4
34CrNiMo6	Long	20	286,8	257,3
	Trans	20	189,9	209,3
	Quenched	20	----	92,2

4. Small Punch Tests

Small punch tests were performed on servo-hydraulic testing system of 10kN capacity. Tests were carried out in testing fixture according to **Fig. 1**. Dimensions of the fixture can be found in **Tab. 3**.

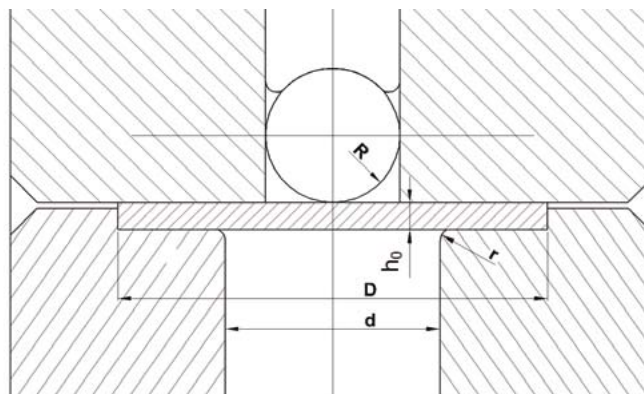


Fig. 1. Small punch test fixture

Tab. 3. Dimensions of SPT fixture

h_0	D	R	r	d
0,5	8,0	1,25	0,5	4,0

Tests were performed at room temperature as well as at -20°C. Tests at -20°C were performed in cooling chamber. Cooling medium were vapours of liquid nitrogen. Obtained curves for all materials are shown in **Figs. 2** and **3**.

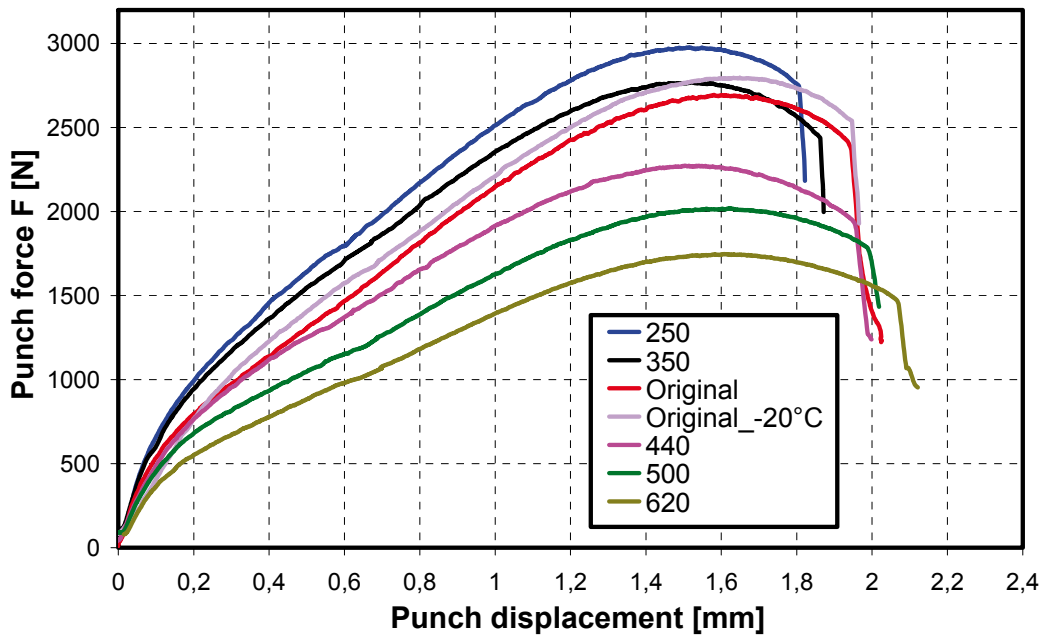


Fig. 2. SPT records - Steel 1

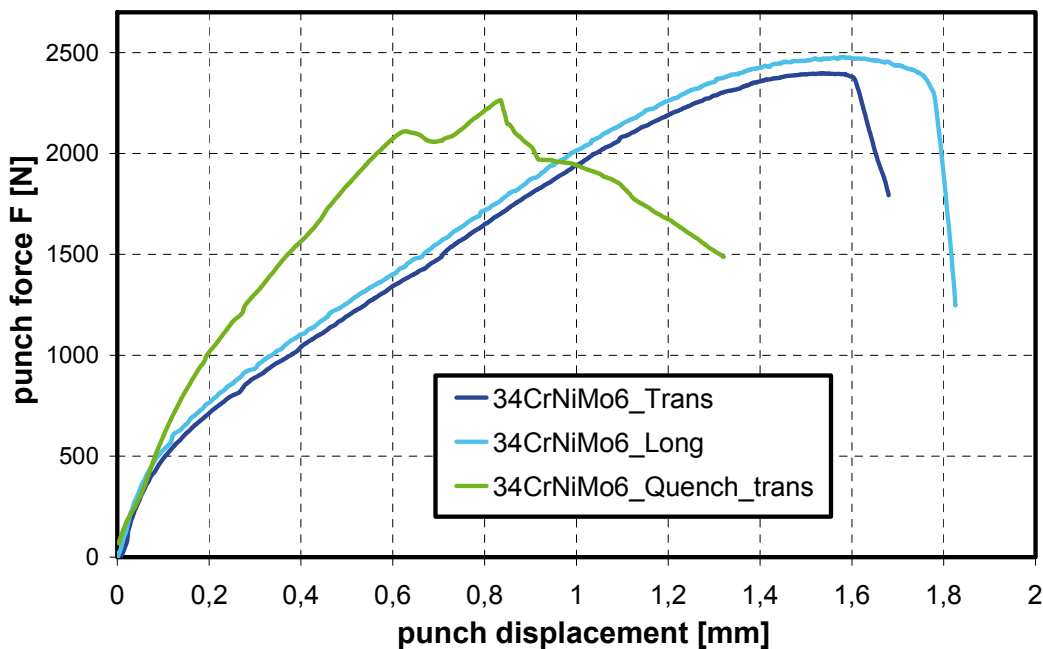


Fig. 3. SPT records – 34CrNiMo6

5. SPT tests evaluation – tensile properties

Obtained records were firstly used for the evaluation of tensile properties of the materials investigated. In order to evaluate tensile properties, distinctive points from the records were determined according to **Fig. 4**. For summarization of SPT results, normalized forces evaluated from SPT tests are used. Yield stresses and tensile strengths were evaluated. Graphical summarization of the results obtained in comparison with standard tensile test results are shown in **Figs. 5** and **6**. In both cases of comparison SPT results with tensile tests clearly linear trends can be found.

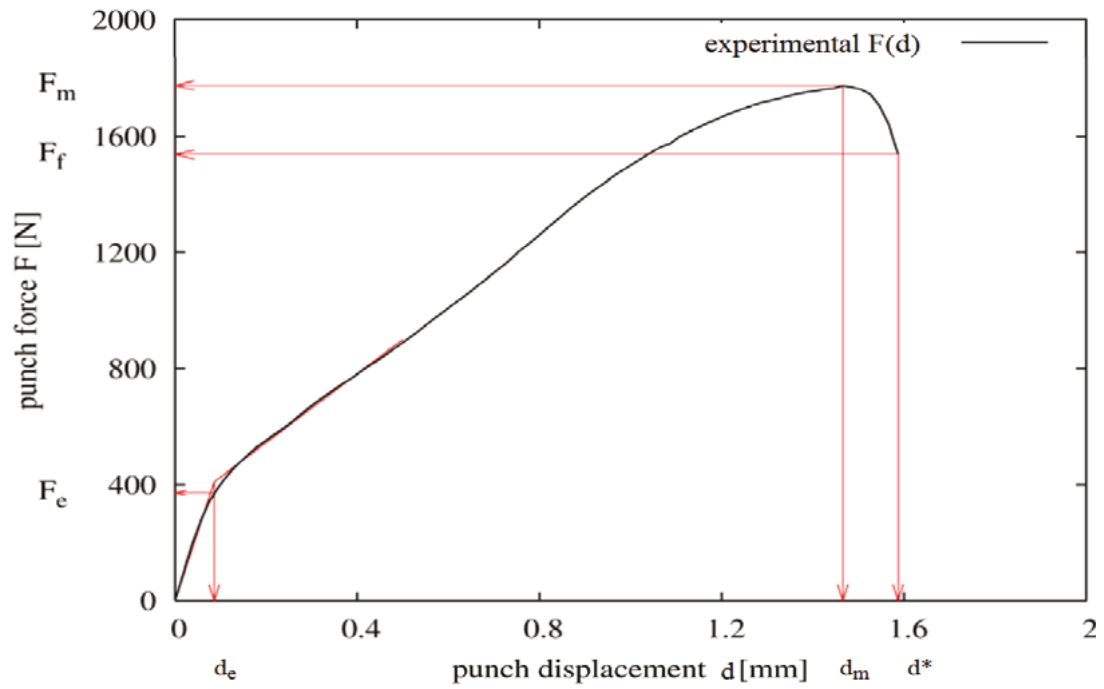


Fig. 4. Scheme of distinctive points determination from SPT record [5]

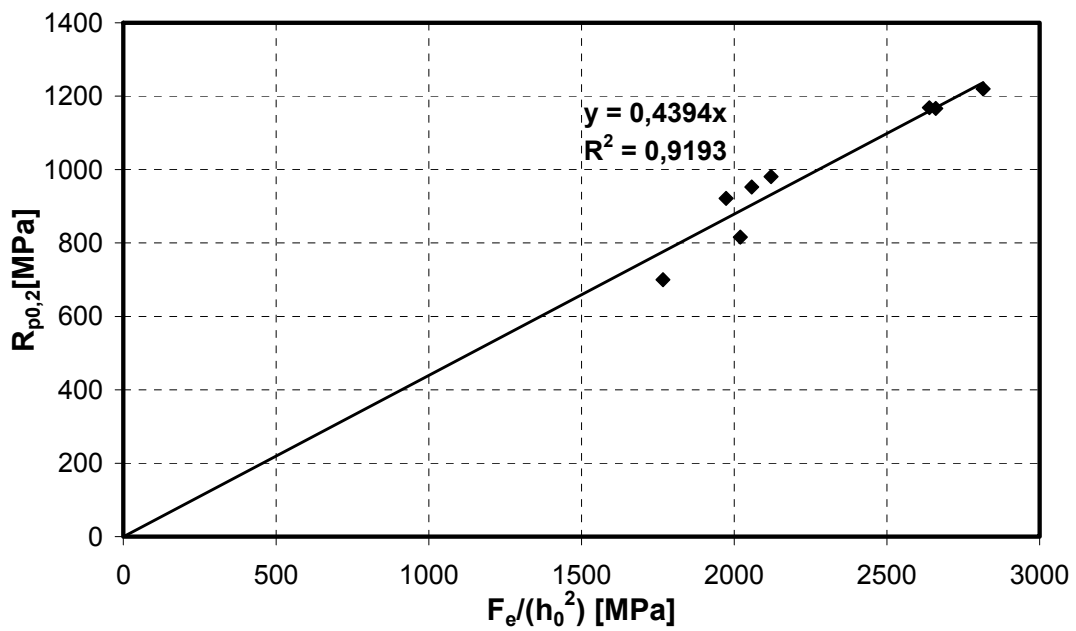


Fig. 5. Tensile Yield stress versus normalized F_e from SPT

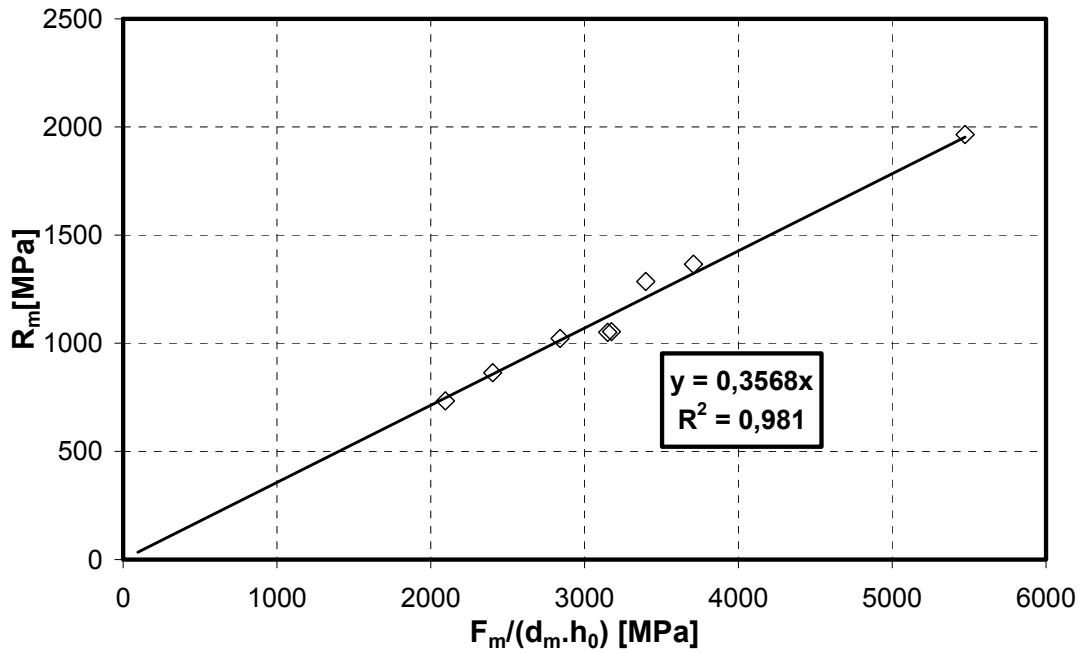


Fig. 6. Tensile strength versus normalized yielding force from SPT

6. SPT tests evaluation – fracture toughness

There are published various procedures for fracture toughness evaluation from SPT for ductile fracture [1-10]. In the case of brittle fracture there is recommended following relation [3]:

$$K_{IC} = C \cdot [\sigma_{fSP}]^{2/3} \quad (1)$$

$$\sigma_{fSP} = 130 (P_{max} / h_0^2) - 320 \quad (2)$$

where P_{max} is force at unstable crack propagation and h_0 is the initial sample thickness. C is empirically determined constant [5].

On the basis of the current results C was determined to be 1.029. The results of fracture toughness evaluated with the constant obtained here are compared with fracture toughness data evaluated from standard tests. The comparison is summarized in **Tab. 4**. Graphical summarization of the obtained results is shown in **Fig. 10**.

In the case of the upper shelf behaviour there is widely used following relation [5]:

$$J_{IC} = K \cdot \epsilon_f \cdot J_0 \quad (3)$$

$$\epsilon_f = \ln(h_0/h_f) = \beta \cdot (d^*/h_0)^x \quad (4)$$

where ϵ_f is fracture strain, h_0 initial sample thickness, h_f samples thickness in the crack region, d^* is displacement at sample fracture and β , x , K and J_0 are empirically determined constants.

There are two possibilities of ϵ_f determination as can be seen from Eq. 4. The first one is determination of fracture strain by measurement of sample thickness after fracture in the crack region according to Fig. 7. The second possibility is its determination from test records with the use of displacement at fracture (d^*). Comparison of the fracture strain determined by both methods is shown in the Fig. 8. There can be seen linear trend between fracture strains ϵ_f obtained by both methods. On the basis of this finding it can be concluded that ϵ_f can be determined directly from the tests records without need for additional experimental effort. The fracture strains obtained from graphs in used for further evaluations here.



a) Steel 1 – annealed at 500°C b) 34 CrNiMo6 – as delivered - longitudinal
Fig. 7. Determination of ϵ_f on the basis of optical measurements

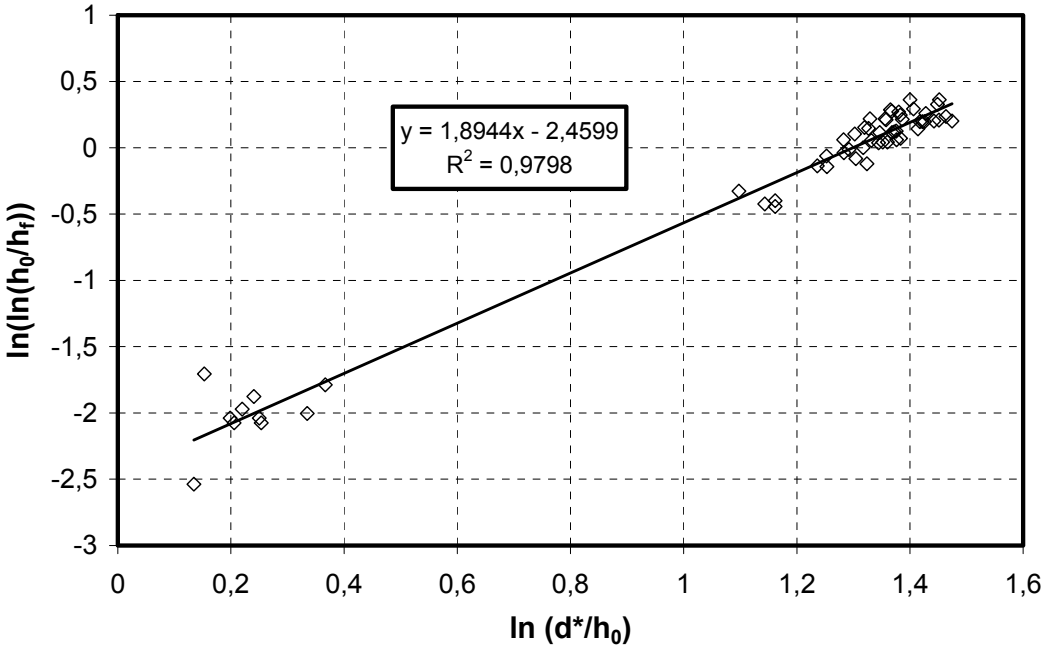


Fig. 8. Comparison of ϵ_f determined from fracture faces and from calculation

The values of constants in the **Eq. 3** and **4** for current materials were determined as $\beta = 0,111$, $x = 1,69$, $k=354,4\text{kN/m}$ and $J_0=51,4\text{kN/m}$

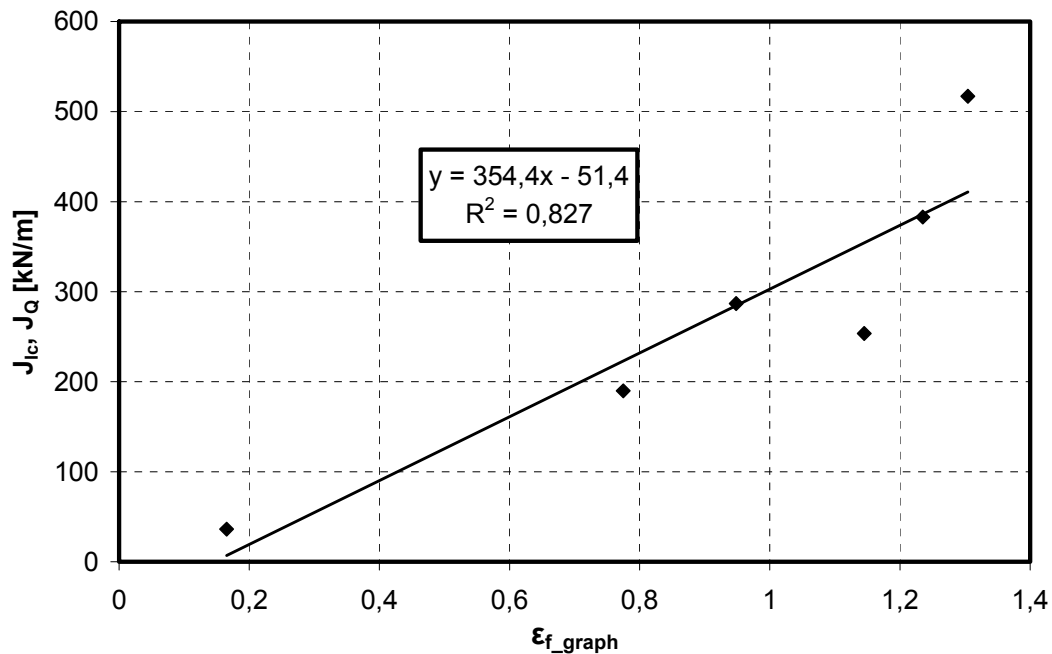


Fig. 9. SPT records - Steel 1

Obtained fracture toughness from SPT tests and from standard tests are summarized in **Tab. 4**. Graphical summarization of obtained data can be found in **Fig. 10** where $\pm 15\%$ error boundaries are shown.

Tab. 4. Results of fracture toughness evaluation

Material	State	Temperature °C	J_{IC_SPT} kN.m	J_{IC}, J_Q kN.m	K_{IC_SPT} MPa.m ^{0,5}	K_{IC}, K_Q MPa.m ^{0,5}
Steel 1	Original	20	----	----	113,7	127,1
	Original	-20	----	----	115,5	105,5
	250	20	----	----	120,3	112,6
	350	20	----	----	114,2	127,0
	440	20	354,4	253,5	286,0	241,9
	500	20	386,2	383	298,5	297,3
	620	20	410,9	517	307,9	345,4
34CrNiMo6	Long	20	284,7	286,8	256,3	257,3
	Trans	20	223,2	189,9	227,0	209,3
	Quenched	20	----	----	101,3	92,2

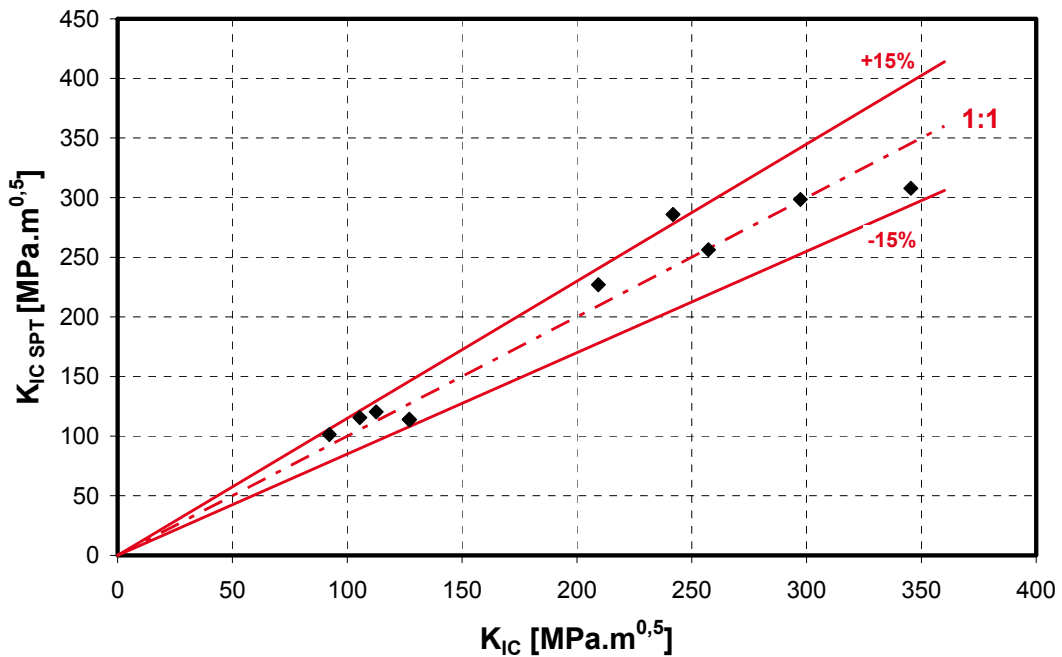


Fig. 10. Results of fracture toughness evaluation

7. Results discussion

Within the frame of the current investigations, tensile and fracture toughness properties determination with the use of SPT were performed.

Tensile tests evaluation shown very good agreement between small punch test data and results obtained by standard tensile tests. These results prove possibility of application of small punch tests for tensile properties evaluation for considered materials.

Fracture toughness tests of experimental material in lower shelf as well as in the upper shelf region were performed together with small punch tests. Separated evaluations were carried out for both regions.

In the lower shelf region, evaluation of fracture toughness from SPT was based on **Eqs. 1** and **2**. In this evaluation only one constant has to be found. The constant for current data set was obtained and good agreement between reference values and SPT values was found.

In the case of stable crack extension behaviour is fracture toughness from SPT evaluated according to **Eqs. 3** and **4**. In this case the evaluation is using fracture strain. The fracture strain can be determined on the basis of physical measurements of sample after the tests, or from obtained test record. Experimental measurement of the fracture strain requires additional effort, while direct evaluation from the graph is simple and can be automated. Analyze of current results pointed out possibility of the use of fracture strain determined from graph. With the use of this evaluation determination fracture toughness for the upper shelf behaviour was determined. Results of determined fracture toughness data are summarized in **Fig. 10**, where very good agreement of SPT based results with those obtained from standard tests is confirmed. This finding is very positive confirmation of the applicability of SPT to fracture toughness determination.

8. Conclusions

Small punch tests (SPT) were investigated in order to enable evaluation of tensile tests properties and fracture toughness. The investigation was performed on two materials, all together 10 material states.

Tensile tests evaluation shown very good agreement between small punch test data and results obtained by standard tensile tests. These results prove possibility of application of small punch tests for tensile properties evaluation.

Fracture toughness tests of material investigated exhibited very good results in comparison with fracture toughness data from standard tests. The assessment of the SPT tests pointed out following results:

- Determination of lower shelf fracture toughness and upper shelf fracture toughness has to be done separately.
- In the case of upper shelf behaviour where the evaluation is based on fracture strain, the fracture strain can be evaluated from SPT record with need for additional measurements.
- Very good agreement between reference values and SPT results is found.

SPT is potentially very powerful method in cases when limited amount of material is available e.g. for the residual life evaluation of in service components. Attention has to be paid if correct parameters and correct evaluation procedure is used for material investigated.

Acknowledgements

This work was done within the work on the project "Ductile damage parameters identification for nuclear power plants - FR-TI2/279" sponsored by Ministry of Industry and Trade of The Czech Republic.

References

- [1] Džugan, J., Konopík, P.: Evaluation of fracture toughness properties for low carbon steel in the brittle state by small punch test technique, *Hutnické listy*, 2010, Vol. LXIII, ISSN 0018-8069, ISBN 978-80-254-7994-0, pp. 119–122
- [2] Konopík, P., Džugan, J.: Small punch test application to fracture toughness determination in the upper shelf region, *Hutnické listy*, 2010, Vol. LXIII, ISSN 0018-8069, ISBN 978-80-254-7994-0, pp.123–127
- [3] Wang, Z. X. et al.: Small punch testing for assessing the fracture properties of the reactor vessel steel with different thicknesses, *Nuclear Engineering and Design*, Volume 238, Issue 12, December 2008, pp. 3186–3193
- [4] Matocha, K., Purmensky, J.: Non destructive evaluation of mechanical characteristics of in-service components materials by small punch tests, *NDT for Safety* November 07–09, 2007, Prague, Czech Republic.
- [5] Small punch test method for metallic materials, Part B: A code of practice for small punch testing for tensile and fracture behaviour, CWA 15627
- [6] Shindo, Z., Zamaguchi, Z., Horiguchi, K.: Small punch testing for determining the cryogenic fracture properties of 304 and 316 austenitic stainless steels in a high magnetic field, *Cryogenics*, Volume 44, Issue 11, November 2004, pp. 789–792
- [7] Bulloch, J. H.: A study concerning material fracture toughness and some small punch tests data for low alloy steels, *Engineering failure analysis* 11(2004), 635–653
- [8] Kupca, L., Vaclavkova, J.: Application of the small punch test methods for the mechanical properties evaluation, *METAL* 2001, 15-17.5.2001, Ostrava, Czech Republic

[9] Saucedo-Munoz, M. L. et al.: Correlation between JIC and equivalent fracture strain determined by small-punch tests in JN1 JJ1 and JK2 austenitic stainless steels, *Cryogenics* 41 (2001), 913-719

[10] Ha, J. S., Fleury, E.,: Small Punch Tests to Estimate the Mechanical Properties of Steels for Steam Power Plant: II. Fracture Toughness. *International Journal of Pressure Vessels and Piping* 75 (1998) p. 707–713

¹ Ing. Jan Džugan, Ph.D., COMTES FHT a.s., Průmyslová 955, 334 41 Dobřany, Czech Republic, Tel.: +420 377 197 350, e-mail: jan.dzugan@comtesfht.cz

² Ing. Pavel Konopík, COMTES FHT a.s., Průmyslová 955, 334 41 Dobřany, Czech Republic, Tel.: +420 377 197 351, e-mail: pavel.konopik@comtesfht.cz

CHARACTERISATION OF LOW ALLOYED STEELS USING JOMINY-PHASE-DIAGRAMS

Niko Große-Heilmann¹, Andreas Peters², Pavel Šuchmann³

Abstract

Continuous-Cooling-Transformations-Diagrams are very popular with engineers and material scientists because they are very demonstrative and the only graphical representation of relation between heat-treatment, microstructure and mechanical properties in one figure. In this publication the new Jominy-Phase-Diagram for low-alloyed steels is introduced. This new diagram is based on a single Jominy-Test and it demonstrates also the correlation between heat-treatment, microstructure and mechanical properties with less experimental effort.

Jominy-Phase-Diagrams are created for SAE 1513 and E355 steels and compared to CCT-Diagrams of the same material to test the advantages and limitations of the new method.

Keywords: Jominy-Phase-Diagram, material characterisation, CCT Diagram

1. Introduction

Continuous-Cooling-Transformation-Diagrams, abbreviated CCT-Diagrams, are well known and established in steel industry. They are commonly used to predict the mechanical properties and microstructures of heat treated components. Hundreds of steels were investigated in years of steel research and development. [1, 2]

But the application of already measured and published CCT-Diagrams in industrial purpose is often limited because of differing conditions like austenitisation temperatures, holding times or chemical compositions. Also CCT-Diagrams are often made several years ago and often from sample material created by old steel manufacturing processes, like Siemens-Martin. This is resulting in enlarged austenite grains slowing down the kinetics of transformation [3]. Because of high experimental effort and substantial relevant cost and time it is often avoided to create up-to-date and process specific CCT-Diagrams. This gap might be closed with the Jominy-Phase-Diagram.

The Jominy-Test or End-Quench-Test [4] is also a well known experiment mostly used in quality control during the steel manufacturing process or to predict the potential hardness increase by quenching and tempering. For common steel grades it is already possible to predict the hardness distribution across the sample based on the chemical composition using regression models. [5]

Publications in the 50s and 60s already showed an interrelationship between CCT diagram and Jominy-Test, as shown in figure 1. Even an interrupted Jominy-Test was used to construct CCT-Diagrams. [6, 7]

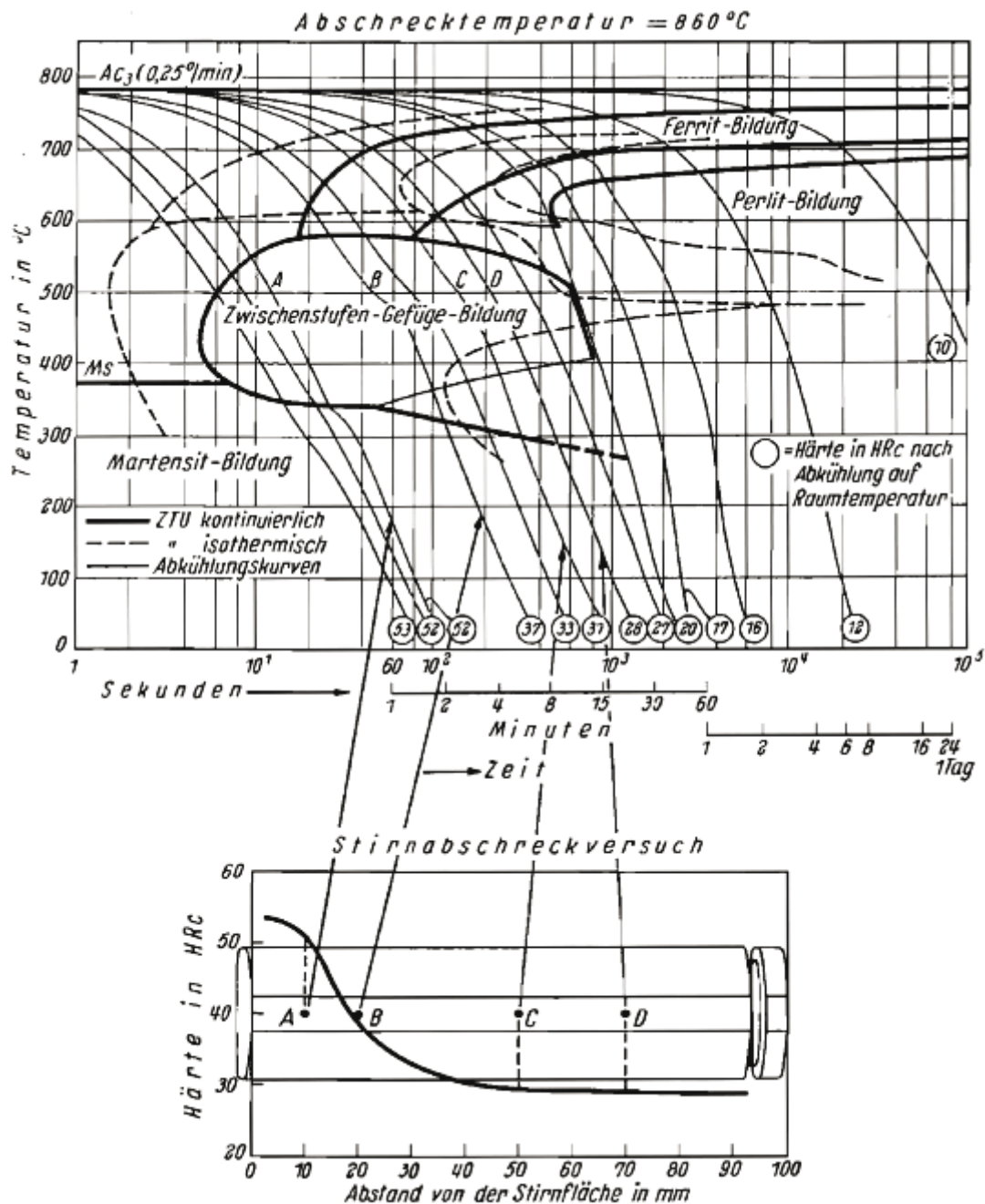


Figure 1 interrelationship between CCT-Diagram and Jominy-Test [1]

This idea of comparable cooling behaviour was used to improve the classic Jominy test to get a significant correlation between heat treatment, microstructure and mechanical properties. Therefore a two dimensional FEM Model is used to correlate the end distance and the cooling times of the Jominy-sample. Furthermore metallography is added to characterise the microstructure. All results are combined in the Jominy-Phase-Diagram.

Experimental

To avoid extensive temperature measurements with different austenitisation temperatures at lots of different positions, FEM Simulations of the simple, axially symmetric shaped, standard Jominy sample were made with software DEFORM 2D.

To compare the FEM Model of the End-Quench-Test selective temperature measurements on Jominy samples, made from standard C45 steel, were used.

Jominy-Phase-Diagrams were created for two different standard materials, SAE 1513 and E355. Therefore a Jominy-Test was performed and the resulting sample was evaluated with metallography and Rockwell-Hardness-Testing. Furthermore CCT-Diagrams according to the standard SEP 1680 [8] were measured with dilatometer for comparison.

Results and Discussion

The results of FEM Simulations at 5, 30 and 50 mm end distance are compared to the experimental cooling data of Jominy-Test samples in figure 2. The results are sufficient for a first correlation. But because of relative high cooling time differences at 400°C, especially at higher cooling rates, the FEM model should be optimized in near future.

In general it is difficult to use one model for all low-alloyed steels with differing thermal conductivity. The effect of phase transformation on the cooling behaviour will influence the results, too. It is assumed by now that cooling behaviour of low-alloyed steels is similar and the FEM Model is representative, but further work has to show whether the FEM model can become more accurate and if the deviation of common low-alloyed steels is within an acceptable tolerance.

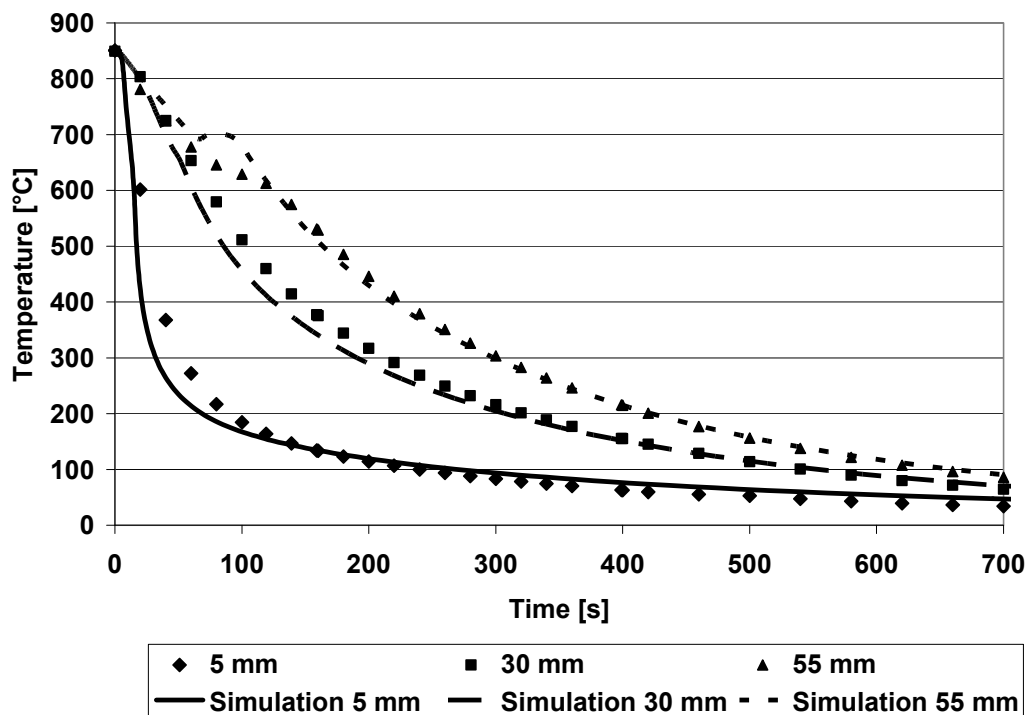


Figure 2 Comparison of simulated and measured cooling of Jominy-Test samples

Based on the FEM Model the cooling times for different end distances were calculated. From this data the Jominy-Phase-Diagrams were constructed for test materials SAE 1513 and E355 as shown in figures 3 and 5. The belonging CCT-Diagrams for comparison are represented in figures 4 and 6. Within tables 1 and 2 the interrelationships between end distance and cooling times from 950°C and 900°C to 400°C are listed.

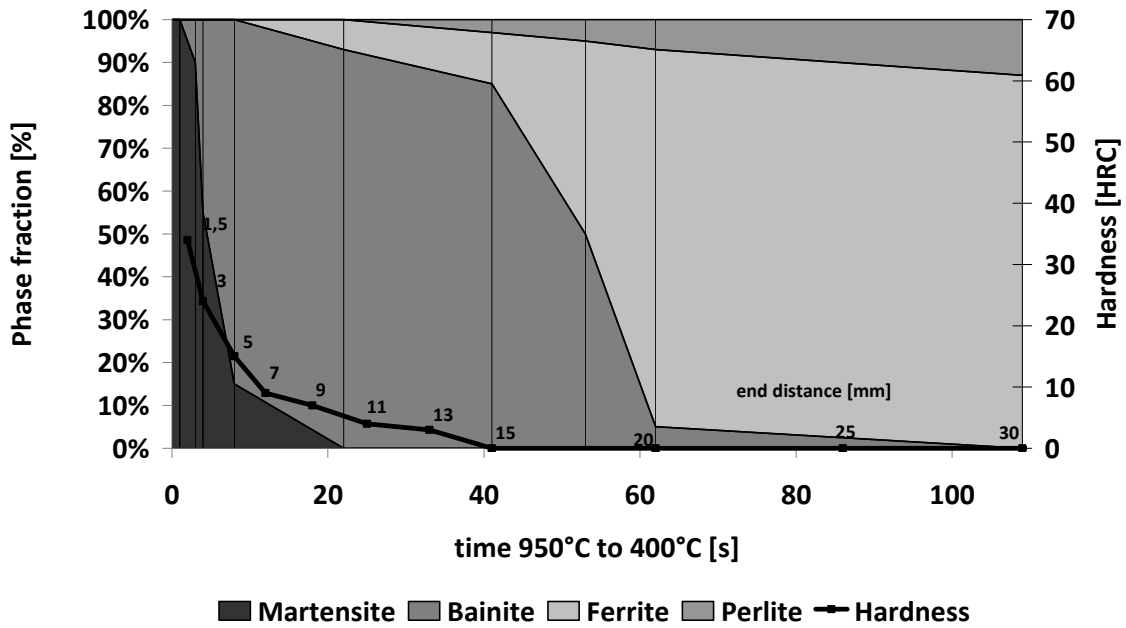


Figure 3 Jominy-Phase-Diagram of SAE1513

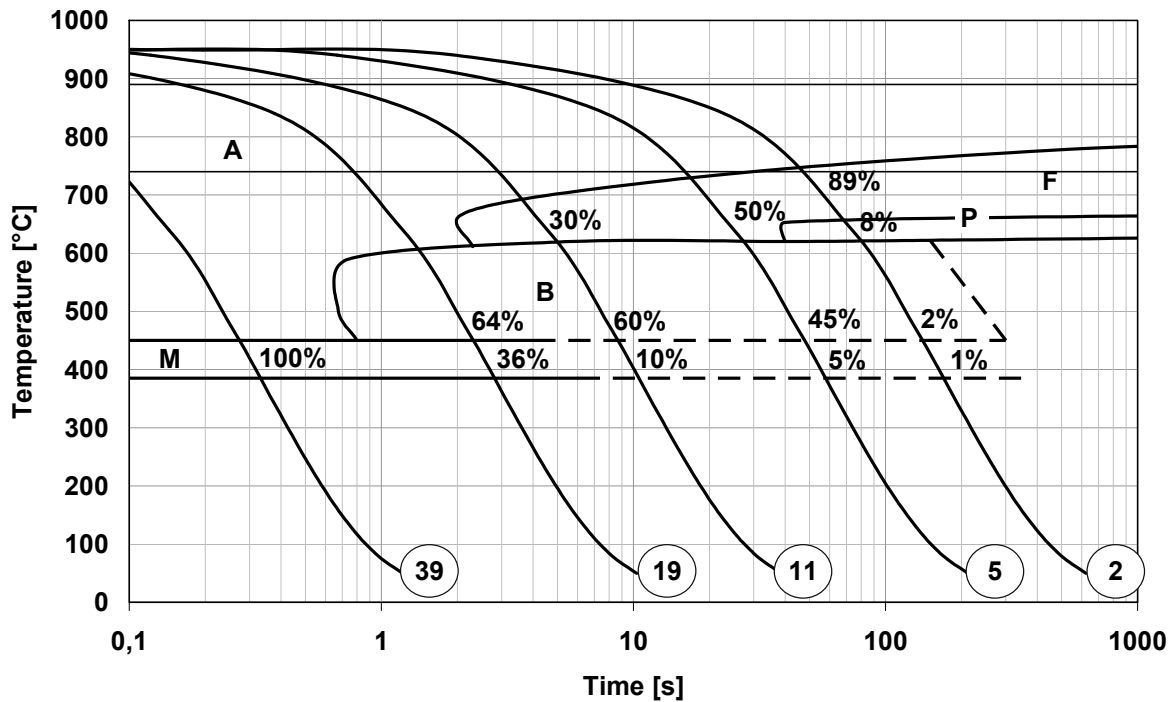


Figure 5 CCT-Diagram of SAE1513

Hardness distribution is nearly the same and the trend to form a bainitic or ferritic microstructure is also present in both diagrams. A big difference is shown in the perlitic reaction: pearlite forms much earlier in Jominy-Phase-Diagram.

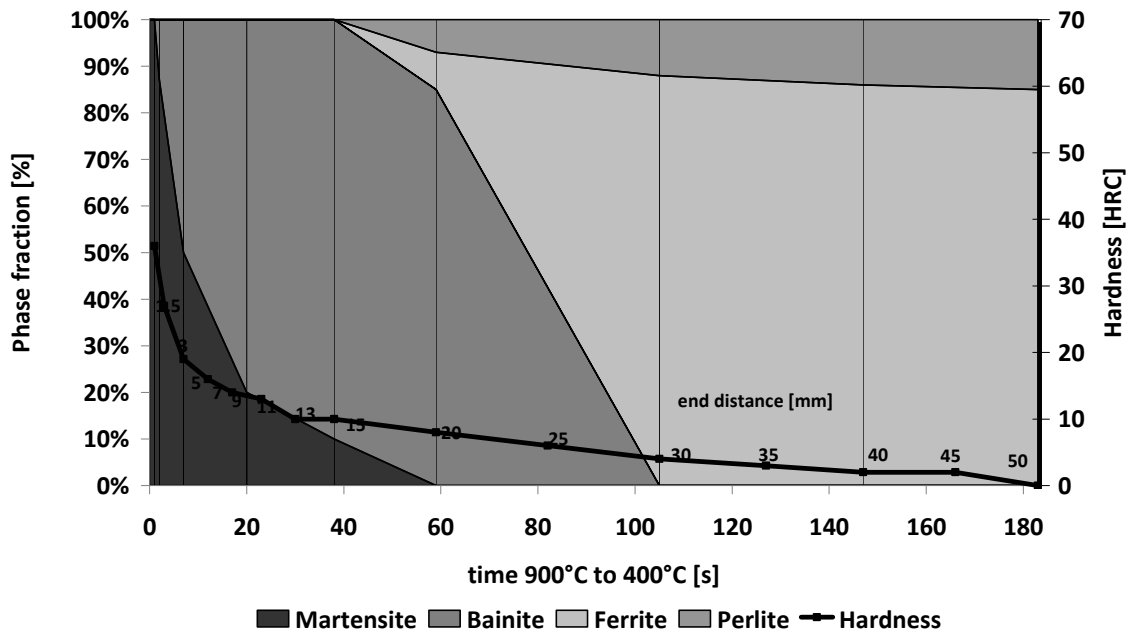


Figure 4 Jominy-Phase-Diagram of E355

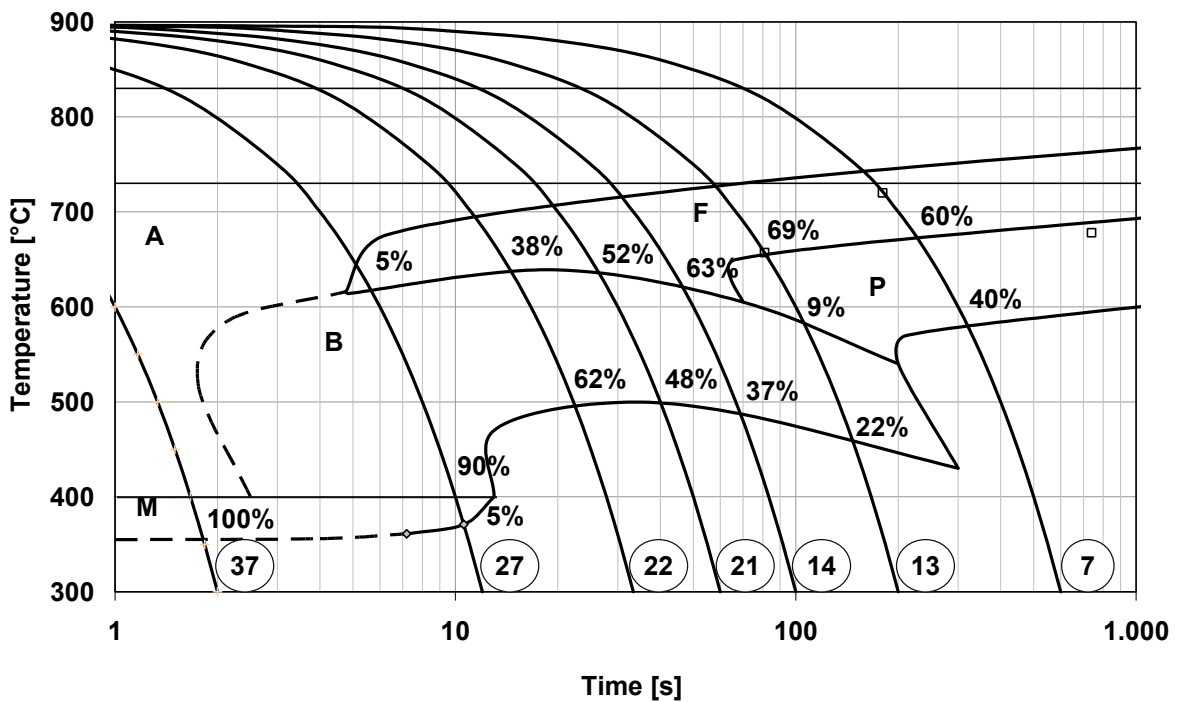


Figure 6 CCT-Diagram of E355

The construction steel E355 shows also similar hardness distributions in CCT- and Jominy-Phase-Diagram. The phase fractions after comparable heat treatment are similar in both diagrams with except of Pearlite, which forms much earlier in Jominy-Phase-Diagram, like SAE 1513.

Table 1 Jominy Sample cooling time from 950°C to 400°C

distance [mm]	1,5	3	5	7	9	11	13	15	20	25	30	35	40	45	50
Time [s]	2	4	8	12	18	25	33	41	62	86	109	132	153	172	190

Table 2 Jominy Sample cooling time from 900°C to 400°C

distance [mm]	1,5	3	5	7	9	11	13	15	20	25	30	35	40	45	50
Time [s]	1	3	7	12	17	23	30	38	59	82	105	127	147	166	183

Conclusions

The new Jominy-Phase-Diagram was introduced. First experiments with this new method were realized and compared to CCT-Diagrams. A general analogy between both diagrams was shown for martensite, bainite and ferrite. For the perlite formation a high deviation was observed.

Slow cooling rates are not achieved and transformation temperatures can not be determined with the Jominy-Phase-Diagram, therefore dilatometric measurements are still necessary.

Regular CCT-Diagrams are still more reliable and contain more information than Jominy-Phase-Diagrams, but they require high effort and substantial cost. Hence the Jominy-Phase-Diagram is a simple alternative method for basic characterisation at cooling rates down to 2 Ks^{-1} , the accuracy is less but the results are practical.

References

- [1] Wever, F.; Rose, A.; Peter, W.; Strassburg, W. & Rademacher, L. (1961), 'Atlas zur Wärmebehandlung der Stähle'
- [2] Voort, G. F. V. (1991), 'Atlas of Time-Temperature Diagrams for Iron and Steels'
- [3] DIN (2000), 'DIN EN ISO 642 - Stirnabschreckversuch (Jominy-Versuch)'
- [4] Kirkaldy, J.; Thomson, B. & Baganis, E. (1978), 'Hardenability Concepts with Applications to Steel', AIME, Warrendale
- [5] VDEh, S. (2004), 'SEP1664 - Ermittlung von Formeln durch multiple Regression zur Berechnung der Härtebarkeit im Stirnabschreckversuch aus der chemischen Zusammensetzung von Stählen'
- [6] Liedholm, C. A. (1944), Metal Progress, 94-99
- [7] Krainer, H. & Kroneis, M. (1951), Archiv für das Eisenhüttenwesen 22, 231-244
- [8] VDEh (1990), 'SEP 1680 - Aufstellung von Zeit-Temperatur-Umwandlungsschaubildern für Eisenlegierungen'

¹ Dipl.-Ing. Niko Große-Heilmann, Benteler Tube Management GmbH, Residenzstraße 1, 331 04 Paderborn, Germany, Tel.: +49 5254 81 4912, e-mail: niko.grosse-heilmann@benteler.de

² Dr.-Ing. Andreas Peters, Benteler Tube Management GmbH, Residenzstraße 1, 331 04 Paderborn, Germany, Tel.: +49 5254 81 4900, e-mail: andreas.peters@benteler.de

³ Ing. Pavel Šuchmann, COMTES FHT a.s., Průmyslová 995, Dobřany 334 41, Czech Republic, Tel: +420 377 197 330, e-mail: pavel.suchmann@comtesfht.cz

MORPHOLOGICAL AND FUNCTIONAL PATTERN OF CELLS CULTURED ON NANOSTRUCTURED TITANIUM

Daniel Hrušák¹, Lucie Hájková², Luděk Dluhoš³

Abstract

The aim of the presented study is to evaluate a standardized method for testing biocompatibility of nanostructured Titanium. Different lines of human fibroblasts were cultivated on modified titanium surfaces and their behavior observed in the following categories: cell growth, differentiation, morphology, motility, proliferation and oxidative state. The effect of material properties on cell behavior on a submicrostructural level is to be revealed.

Keywords: Nanostructured titanium, human fibroblast cell test, biocompatibility,

1. Introduction

Nanostructured commercial purity titanium produced by severe plastic deformation (SPD) is a material considered to be mechanically and biocompatibility-wise suitable for medical applications. Nanostructuring of CP titanium by SPD processing is improving the mechanical properties, especially providing sufficient mechanical strength. In our preliminary study cytocompatibility tests utilizing fibroblast mice cells L929 were undertaken to verify the biological properties of nanostructured CP titanium compared to conventionally processed grained CP Ti. The cell investigation showed that fibroblast colonization of the CP Grade 4 titanium surface dramatically increases after nanostructuring and suggested that a high osteointegration rate should be expected with nanostructured CP Grade 4 titanium. Several studies^{1,2,3} are indicating beneficial behavior of nanostructured materials for medical implants.

2.1. Material and Methods

In an effort of optimizing the biocompatibility tests for of dental implant materials, cultured cells of different human cell lines were tested with respect to their behavior on various metal substrates. In the first stage the proper shape and design of the samples according to the applied microscopy technique was evaluated. A comparative study was performed on cells cultured directly on a series of metal samples with differentially treated surfaces. Many parameters are influencing the results of cell - material interaction; the intention of the study is to develop a method for indicating implantable material properties similar to their in vivo behavior. The subsequent microscopic analyses comprised various aspects of cell morphology, adhesion, spreading, motility, viability, proliferation etc. Multiple fluorescent probes were used for the study of live cells as well as fixed preparations.

2.2. Study design

In order to achieve reproducible results while respecting the specific observation environment (e.g. inverted microscopy of live cells surface colonization), the study design required some special approach from the very beginning. The Cell line type is a crucial parameter in material testing.

Table 1 Study design: main stages of the experiment flow

- Material sample design – development of proper shape of tested material samples (5 mm diameter dish shaped disc, depth of 0,2 mm), surface finishing, sterilization, handling, ...
- Cell parameters – type of cells (CRL-1137 human osteoblast, CCL-110 human fibroblast lung, HFL-1)
- Cultivation parameters – (cell placement, cell counts, growth medium, timings etc.)
- Staining – JC 1: differential fluorescent staining of normal (red) vs. decreased (green) mitochondrial membrane potential in live cells
- Immunofluorescence of cell adhesions (anti-vinculin) in fixed cells
- Microfilament staining (labeled phalloidin) in fixed cells
- Optical observations - confocal laser scanning fluorescent microscopy; Cell-R
- Standardized method – semi quantitative measurement of material properties - desired outcome ...

2.3. Working hypothesis

There is a stochastic behavior of cell cultures – mainly in response to changing environmental parameters, simplified model of the study design includes at least two set of input variables, the ADJUSTABLE Variables and SELECTIVE INPUT Variables setup determines the threshold to de-noise the relevant signals of **Material properties Tmp**.

Table 2 ADJUSTABLE Variables representing cultivation and environmental criteria:

- „n“ - cell count
- „c“ - cell cycle duration
- „t“ - cultivation time
- „V“ - cultivation volume
- „C“ - Cell concentration (Cells/microliter)
- „S“ - cultivation surface
- „X“ – composition of cultivation solution

Table 3 SELECTIVE INPUT Variables representing cell behavior and OBSERVATION criteria

- „ Ct „ - cell type
- „ v „ - cell size
- „ a „ - cell adhesion
- „ d „ - cell differentiation
- „mo „ - cell morphology
- „mi „ - cell migration
- „ M „ - mitosis
- „ O „ - oxidative state
- „ A „ - apoptosis

Where the Tested Variable (**Tmp**) is a stochastic function of the **Material properties** influenced by the **ADJUSTABLE Variables** and **SELECTIVE INPUT Variables**. The unknown formula of this relation is still described by the expression:

$$T_{mp} = F_t(n,..c,..V,.. X,..) \quad (1)$$

All experiments were blind. The fluorescent microscopic study revealed a higher degree of beneficial modulation of cellular behavior on samples made of nanostructured titanium.



FV1000 configuration with IX81 microscope



Figure 1 Observations were made by Confocal Laser Microscopy

3. Results

Cells grown on nanostructured titanium surface exhibit typical morphological features observed in cultured cells.

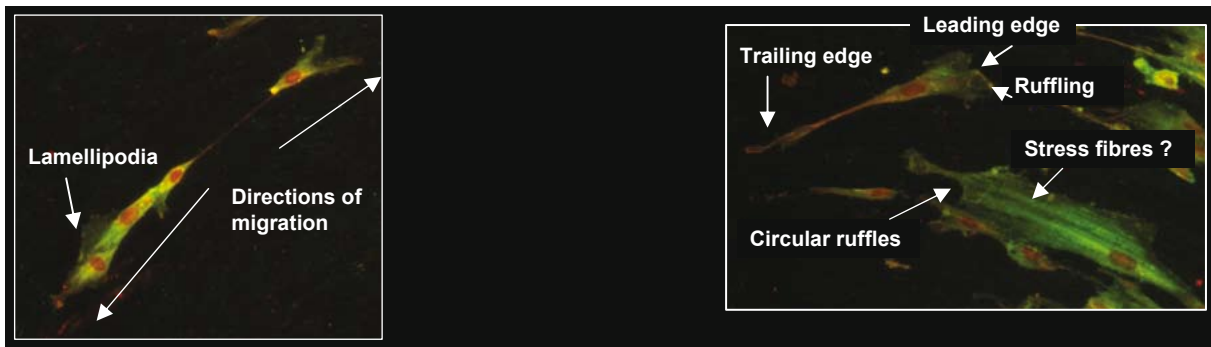


Figure 2 Observations of Cell Morphology and Migration -Immunofluorescence staining of HFL-1 primary human fibroblasts (Atto488 anti-vinculin, TRITC-phalloidin)

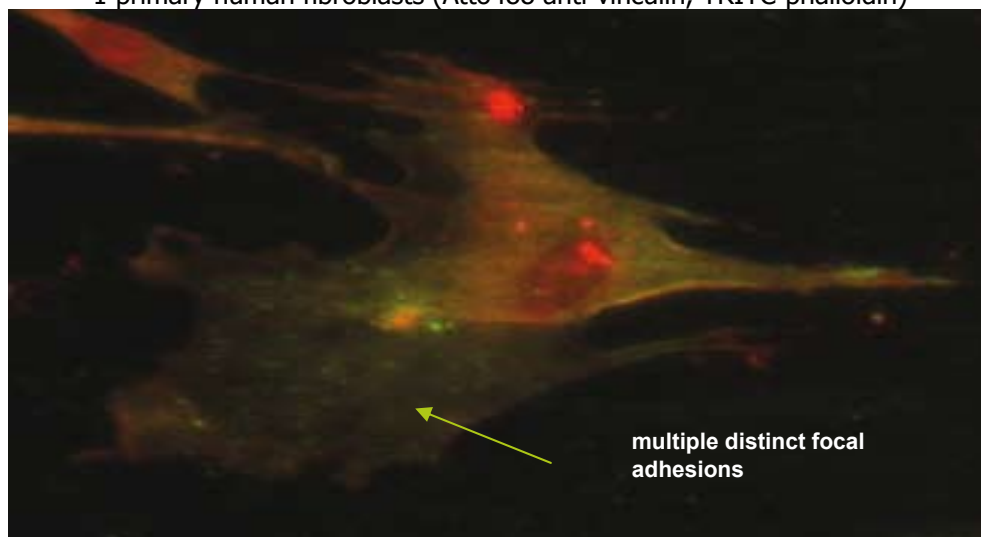


Figure 3 Observations of Cell Adhesion Immunofluorescence staining of HFL-1 primary human fibroblasts (Atto488 anti-vinculin, TRITC-phalloidin)

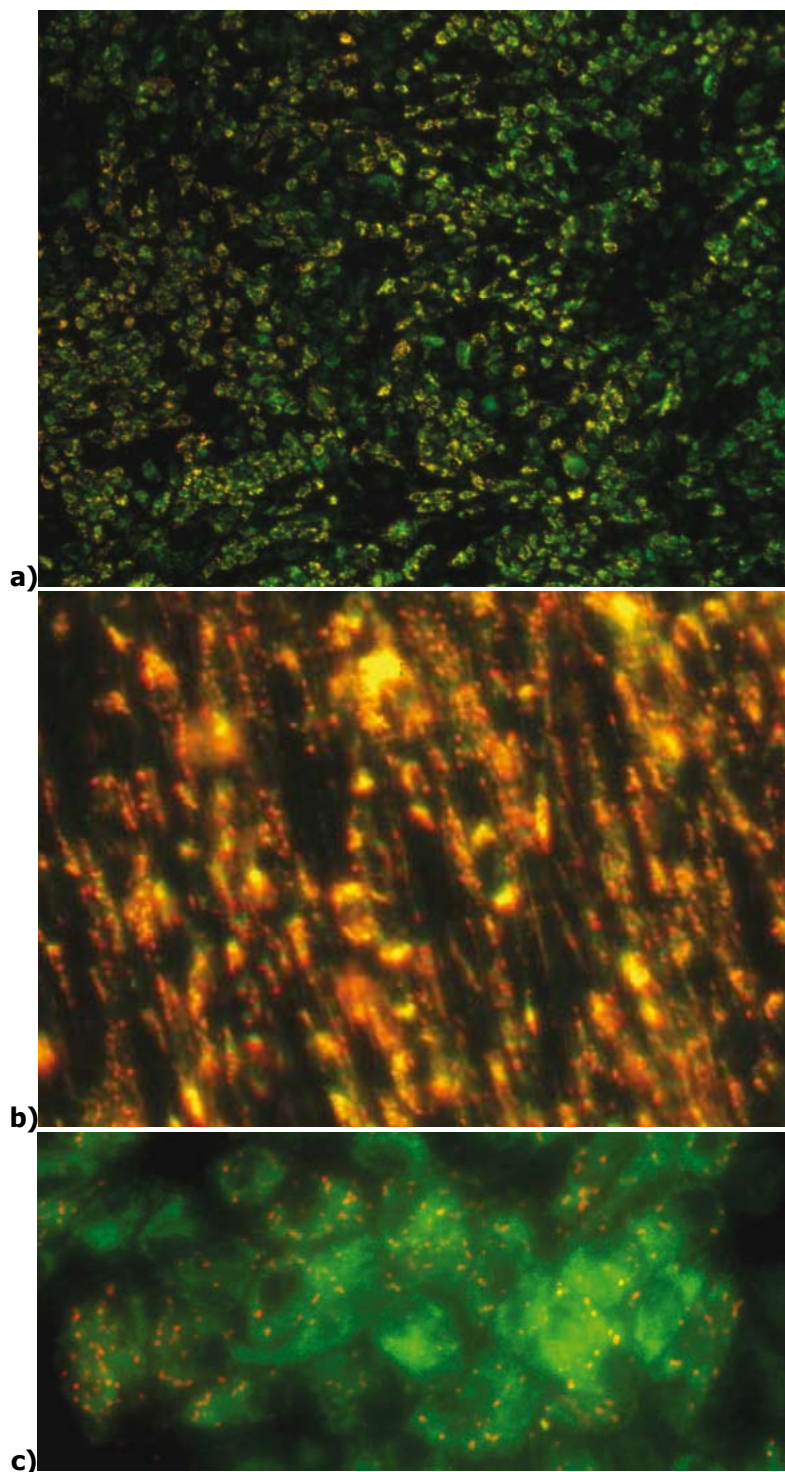


Figure 4 Observations of Oxidative State: JC-1 Stained human Cells Oxidative State represented by MTP (Mitochondrial Transmembrane Potential) JC-1 Vital Staining: **a)** differential fluorescent staining of normal (red) vs. decreased (green) mitochondrial membrane potential in live cells **b)** HFL 1 staining **c)** SW1710 staining

This paper reports the study design and some of our results of biological testing of nanostructured titanium (n-Ti). Sample preparation as well the cultivating and imaging process setup has to be standardized to maintain reproducible results, independently on parameters other than material properties. The results revealed the presence of interactions of surface colonization by human cells and raise some ideas

on possible relations based on material properties. The results of our study revealed some findings summarized:

Table 4 Types of cell interaction to surface

- Primary human fibroblasts adhere to nanostructured titanium by creating vinculin-positive focal adhesions
- Cells form F-actin-based protrusions and attain morphology typical of migration and are well spread on the surface
- In two tested human cell lines, majority of cells exhibit mitochondria with normal levels of MTP as per the JC-1 vital staining

There are some differences in the biological properties of nanostructured titanium compared to cpTi, documented by this study. Further investigations are necessary to assess the relevance of multifactorial variable environmental setup for identifying the „Material Specific Signal“ in the „noise“ of unknown parameters of materials and vital cells interactions. For routine use of biological properties material behavior to maintain reproducible results, it is mandatory to develop standard methodology and study the process of adhesion and spreading on various substrata. Known methods like time-course of focal contacts formation and microfilament rearrangement, time-lapse photomicrography should be used and there are possibly more methods to be employed.

For nanostructured titanium in this scope, the applicability for medical application and dental implants was confirmed.

References:

- [1] Choudhary, S., Berhe, M., Haberstroh, K. M., Webster, T. J.: Increased endothelial and vascular smooth muscle cell adhesion on nanostructured titanium and CoCrMo, *Nanomedicine*. 2006 March; 1(1): 41–49
- [2] Sato, M., Aslani, A., Sambito, M. A., Kalkhoran, N. M., Slamovich, E. B., Webster, T. J.: Nanocrystalline hydroxyapatite/titania coatings on titanium improves osteoblast adhesion. *J Biomed Mater Res A*. 2008 Jan; 84(1):265–72
- [3] Smith, L. J., Swaim, J. S., Chang Yao, Haberstroh, K. M., Nauman, E. A., Webster, T. J.: Increased osteoblast cell density on nanostructured PLGA-coated nanostructured titanium for orthopedic applications *Int J Nanomedicine*. 2007 September; 2(3): 493–
- [4] Hájková, L., Nyman, T., Lindberg, U., Karlsson, R.: Effects of cross-linked profilin:beta/gamma-actin on the dynamics of the microfilament system in cultured cells. *Exp Cell Res*. 2000 Apr 10;256(1):112-21
- [5] Hrušák, D., Březina, V., Dluhoš, L.: Biologické vlastnosti nanotitanu. In: *Středoevropské sympozium VIII Brněnské implantologické dny*. 8. Brno. 2006. s.18. ISBN 80-210-4150-1
- [6] Petruželka, J., Dluhoš, L., Hrušák, D., Sochová, J.: Nanostructured titanium Application in dental implants, In. *Abstract Booklet of the International Conference NANO '06*, Brno University of Technology, 1, 2006, s. 100, ISBN 80-214-3308-6
- [7] Valiev, R. Z., Semenova, I. P., Dluhoš L., a kol.: Nanostructured SPD Processed Titanium for Medical Implants, *Material Science Forum Vols. 584-586*, 2008, Switzerland, s. 49-54, IF 0,399
- [8] Použití nanostrukturního titanu pro nitrokostní implantáty, Usage of nanostructured titanium for endosteal implants, Hrušák D., Zemko M, Dluhoš L., Kraus L., konference *NANOCON 2009*, 20. –22. 10. 2009, Rožnov pod Radhoštěm, Česká Republika

¹ MUDr Daniel Hrušák, Ph.D., Stomatologická klinika LFUK a FN Plzeň, Czech Republic, e-mail: hrusak@fnplzen.cz

² MUDr. Lucie Hájková, Ph.D., Ústav Biologie, Lékařská fakulta v Plzni, Univerzita karlova v Praze, Czech Republic, e-mail: lucie.hajkova@lfp.cuni.cz.

³ Dr. Ing. Luděk Dluhoš, Timplant s.r.o., Ostrava, Czech Republic, e-mail: timplant@timplant.cz

THE EVALUATION OF CIRCUMFERENTIAL WELD OF REHEATER HEADER BY SMALL PUNCH TESTS

Karel Matocha¹

Abstract

This paper comprises the results of the determination of yield stress, tensile strength and FATT of the parent material and heat affected zone of circumferential weld of reheater header after 107 500 hours of exposure at 540°C using standard (full sized) specimens and SP tests. The disc test specimen orientation was investigated. Very good agreement was found between the results of full sized test specimens and SP Bulge tests in tensile properties of parent material regardless to the disc orientation, while tensile properties of HAZ and FATT of parent material and heat affected zone was found to be directionally sensitive.

Keywords: circumferential weld, Small Punch Test, Heat Affected Zone (HAZ)

1. Introduction

The mechanical properties of the individual regions of the welds of the fossil power plant components subjected to elevated temperatures can be affected significantly throughout the long-term operation. The knowledge of the actual mechanical properties (tensile properties, Ductile Brittle Transition Temperature (DBTT)) due to in-service degradation is very important for the residual lifetime assessment of the components. While the mechanical properties of the weld metal and parent material can be mostly determined by standardized test procedures, in the case of sufficient testing material, it is not often possible to use these methods for determination of mechanical properties of HAZ (Heat Affected Zone). In the case of small amount of the testing material, tensile and fracture characteristics of the individual regions of the welds can be determined by means of penetration tests [1-3]. In the present paper the results of standardized tensile and Charpy tests of parent material and HAZ are compared with the yield stress, tensile test and FATT determined by Small Punch Bulge tests using empirical correlations.

2. Testing material

Quadrangular prisms 130x36x11 mm in dimensions were cut off the circumferential weld of reheater header after 107 500 hours of operation at 540°C. It was manufactured of CrMoV low alloy steel. Macro- etching of the weld is shown in Fig.1. The microstructure of both parent material and HAZ is ferritic with fine precipitates. The width of HAZ is equal to 4,8 mm. A schematic illustration of the removal of the test specimen from the quadrangular prisms is shown in Fig.2. The SP

test discs for determination of tensile characteristics and FATT for parent material were oriented in accordance with CWA 15627 [4].

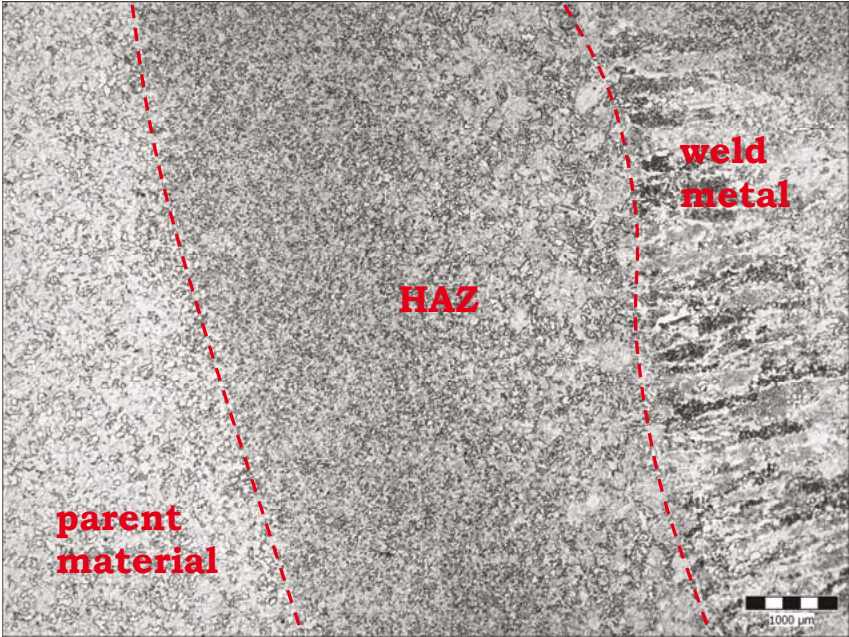


Fig.1 Macro-etching of the weld investigated

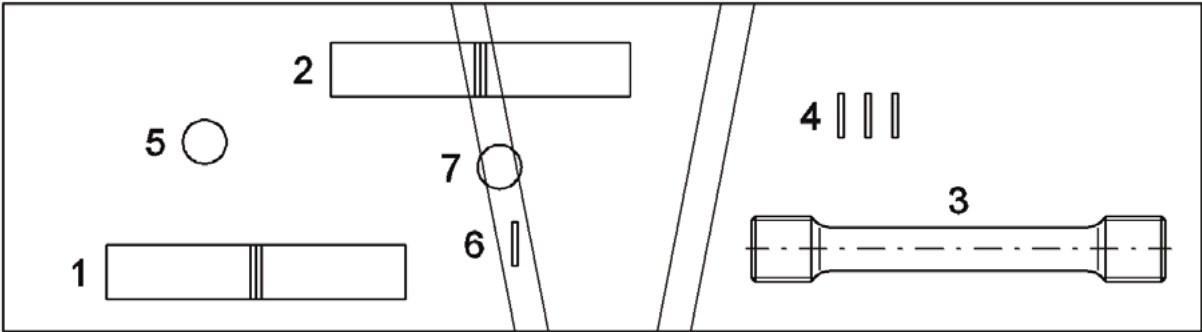


Fig.2 Location of test specimen in the testing material

3. Results of standardized and SP Bulge tests

Results of standardized tensile tests at ambient temperature are summarized in tab.I. Tensile tests were carried on electromechanical testing machine TSM 100 kN using round bar test specimens 6 mm in diameter. The values stated in the table are the average of the tree tests.

Tab. I Results of tensile tests of parent material at ambient temperature

$R_{p,0.2}$ [MPa]	R_m [MPa]	A [%]	Z [%]
376	550	27	72

FATT temperatures determined from temperature dependence of Shear Fracture Appearance of fractured Charpy test specimens are FATT = +48°C for parent material and FATT = +10°C for HAZ.

Small Punch Bulge tests at ambient and reduced temperatures were carried out on INOVA TSM10 servomechanical testing machine (see Fig.3) using disc test specimens 8 mm in diameter and 0,5 mm in thickness. All SP tests were carried out at crosshead speed 1 mm/min.



Fig. 3 INOVA TSM 10 testing machine with testing apparatus for SP tests at reduced temperatures

Table III summarizes the tensile properties (yield stress and tensile strength) of parent material determined by standardized tests procedures, the tensile properties of parent material and HAZ determined by SP Bulge tests and tensile strength converted from the hardness measurements (HV10) [5].

Tab.III Tensile properties of parent material and HAZ determined by standardized procedures, SP Bulge tests and hardness measurements

Test method	Orientace zk. tělesa	Parent material		HAZ	
		R _e [MPa]	R _m [MPa]	R _e [MPa]	R _m [MPa]
Standard. Tests	L	376	550		
SP Bulge tests	L	366	553	560	659
	T	389	565	464	576
HV10 measurements			541		648

The results of the tensile characteristics of parent material determined by SP Bulge tests are in very good agreement with the results of standardized tensile tests and hardness measurements converted to material strength.

Especially in case of parent metal the material properties are expected to be isotropic and therefore the orientation of SP specimen disc plays only minor role and

the results of SP Bulge tests correspond to the full sizes test specimens even when the direction of crack propagation is perpendicular in the respective cases.

The fracture energy for parent material as well as HAZ was determined by Small Punch Bulge tests in the temperature range -193°C to -110°C . The orientation of the specimen discs prepared from parent material was transverse, marked **T** (SP specimen disc plane parallel to the axis of tube and disc axis in tangential direction – see position 4 in Fig. 2) and longitudinal, marked **L** (SP specimen disc plane perpendicular to the axis of tube and disc axis in longitudinal direction – see position 5 in Fig. 2). Owing to the restricted area of heat affected zone, SP specimen discs were oriented transversely – see position 6 in Fig. 2. The temperature dependence of fracture energy and the method how to graphically determine T_{SP} is shown in Figures 4 to 6 for parent material in L-T and T-L directions and HAZ, respectively.

Transition temperatures T_{SP} determined in accordance with CEN CWA 15627 [4] equal to $T_{SP}=124\text{ K}$ for parent material in the transverse orientation and $T_{SP}=113\text{ K}$ for HAZ in the transverse orientation as well as parent material in the longitudinal orientation. Table IV shows the values of FATT, T_{SP} and $\alpha=T_{SP}/\text{FATT}$, which was found to be equal $\alpha=0,35$ for parent material in T-L orientation of Charpy test specimens and L orientation of SP discs, but $\alpha=0,40$ for HAZ in T-L orientation of Charpy specimens and T orientation of SP discs.

The temperature dependences of fracture energy for parent material and HAZ are summarized in Fig4 and Fig.5.

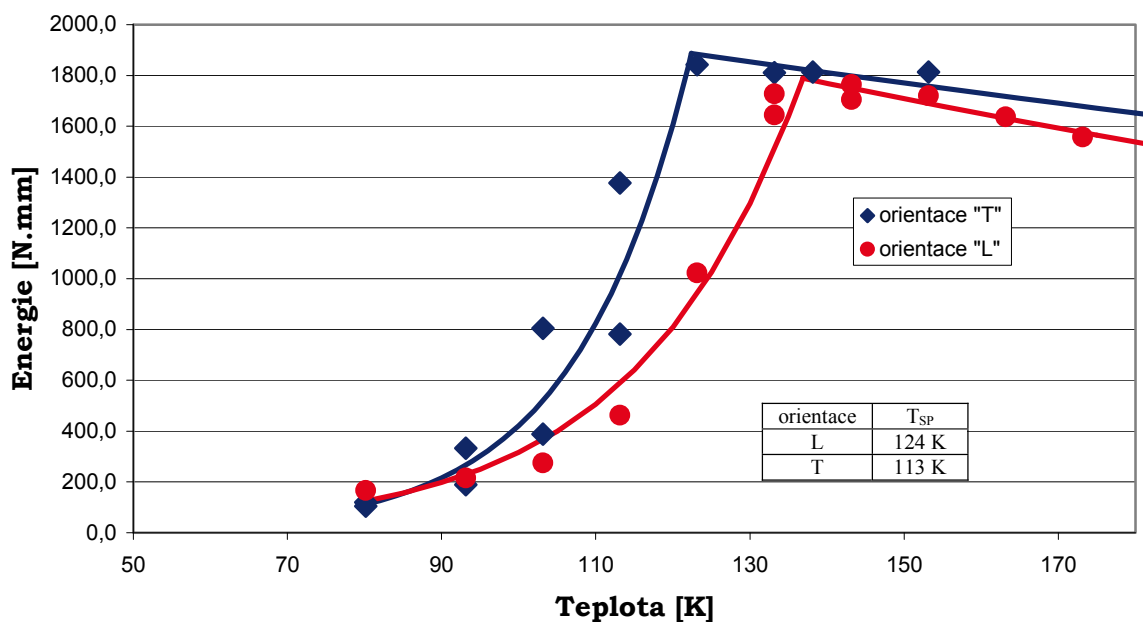


Fig. 4 The temperature dependence of fracture energy for parent material – effect of disc test specimen orientation

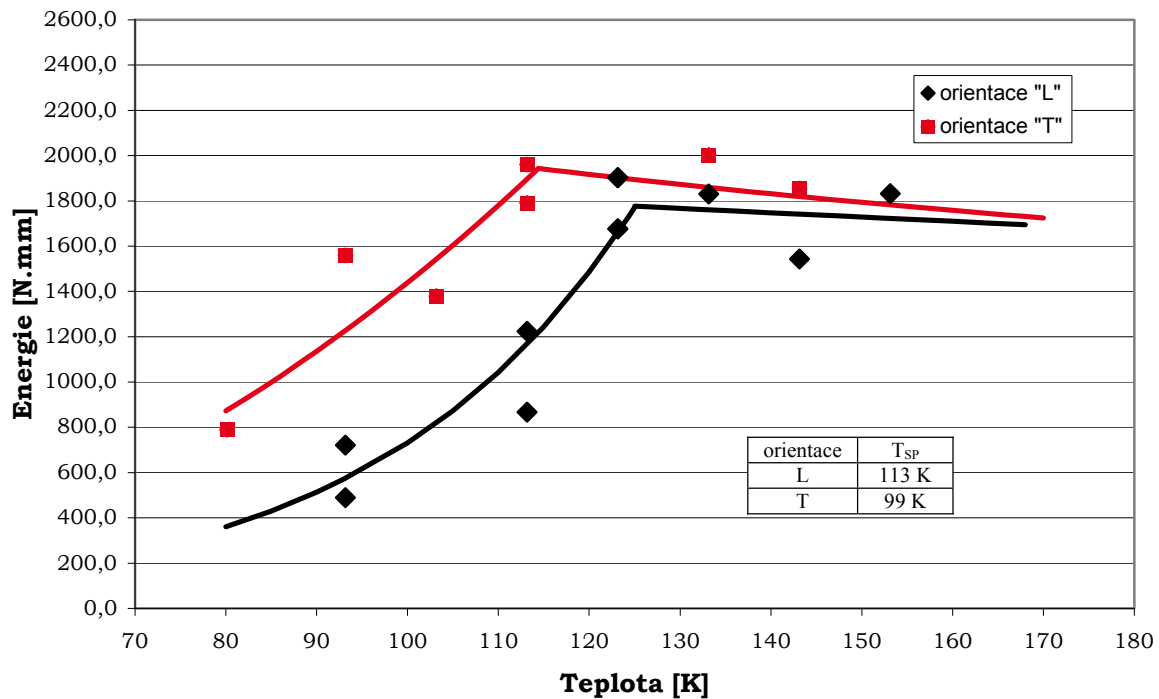


Fig.4 The temperature dependence of fracture energy for parent material – effect of disc test specimen orientation

Transition temperatures T_{SP} determined for parent material and HAZ in accordance with CEN CWA 15627 [5] is equal $T_{SP} = 113\text{K}$ for parent material and $T_{SP} = 99\text{ K}$ for HAZ. Table IV shows the values of FATT, T_{SP} and $\alpha = T_{SP}/\text{FATT}$ which was found to be equal $\alpha = 0,39$ for low alloy CrMoV steels and Charpy test specimen orientation L-T and T-L.

Table IV. FATT and T_{SP} determined for parent material and HAZ

material	Charpy orient.	Disc orient.	FATT [K]	T_{SP} [K]	T_{SP}/FATT
parent	L-T	T	321	113	0,35
	L-T	L	321	124	0,39
HAZ	L-T	T	283	99	0,35
	L-T	L	283	113	0,40

4. Conclusions

Very good agreement was found between the results of full sized test specimens and SP Bulge tests in tensile properties of parent material of the reheater header made of low-alloy CrMoV steel after long-term high temperature exposure regardless to the disc orientation, while tensile properties of HAZ and FATT of parent material and heat affected zone was found to be directionally sensitive. Therefore much attention must be paid to choose carefully the correct correlation between the results of SP samples (T_{SP}) and full sized test specimens (FATT).

Acknowledgements

The presented work has been supported by Ministry of Education, Youth and Sports of the Czech Republic under the project MSM 2587080701.

References

- [1] Gai, X., Sato, Y. S., Kokawa, H., Ichikawa, K.: Ductile – brittle transition of steel electron beam weld metal in small punch test. *Science and Technology of Welding and Joining*, 2002, Vol.7, No.4, pp. 204–211
- [2] Matocha, K., Purmenský, J.: Testing of the Exploited Weld Joints of Steel Structures, *METALLURGICAL JOURNAL* No.2/2010, Vol.LXIII, pp.51–56, ISSN 0018-8069
- [3] Karthik, V., Laha, K., Kasiviswanathan, K. V., Raj, B.: Determination of Mechanical property Gradients in Heat-Affected Zones of Ferritic Steel Weldments by Shear-Punch Tests, "*Small Specimen Test techniques*": *Fourth Volume, ASTM STP 1418*, M. A. Sokolov, J. D.Landes and G. E. Lucas, Eds., ASTM International, West Conshohocken, PA, 2002, ,pp. 380-405, ISBN: 0-8031-2897-5
- [4] Small Punch Test Method for Metallic Materials. CEN WORKSHOP AGREEMENT CWA 15627, December 2007
- [5] Metallic materials – Conversion of hardness values, ISO/CD 18265, February 2000

¹ Doc. Ing. Karel Matocha, CSc., MATERIÁLOVÝ A METALURGICKÝ VÝZKUM s.r.o., Pohraniční 31, 70300 Ostrava - Vítkovice, Czech Republic, Tel: +420 595 957 189, e-mail: karel.matocha@mmvyzkum.cz

DUCTILE DAMAGE PARAMETERS IDENTIFICATION IN FE PROGRAM ABAQUS

Jan Růžička¹, Antonín Prantl², Miroslav Španiel³

Abstract

The paper deals with identification of ductile failure parameters of models implemented in FE software Abaqus. Some original procedures identifying plastic response based on collocation and/or approximation were developed in scope of project FR-TI2/279. The following work will be focused on parameters of damage initiation criteria.

Keywords: ductile fracture, FEM

1. Introduction

Models of ductile failure implemented in the ABAQUS can be classified as empirical models. All of them use simple criteria limited according to material type, loading conditions, etc. The process of calibration of these models consists of four phases (Figure 1):

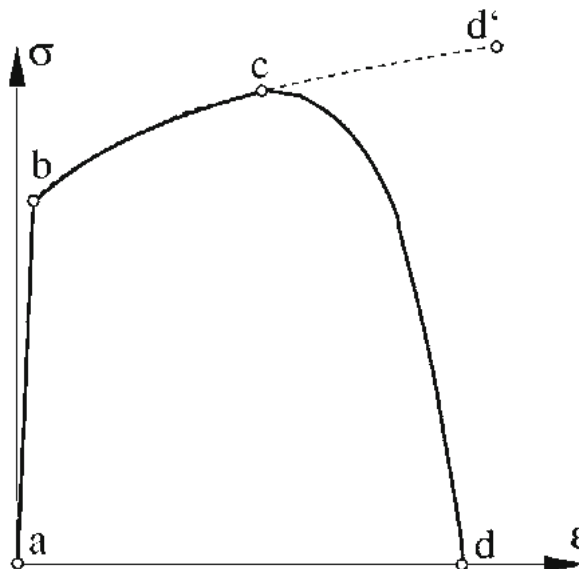


Figure 1 Tensile curve of material with damage

- elastic constants of the model calibration (a-b)
- calibration of plastic response curve (c)
- calibration of damage initiation criteria parameters (b-d')
- calibration of damage development parameters (c-d)

Development of damage in these models starts just with damage initiation and has no effect on the previous pure plastic behavior. This allows us to calibrate the purely plastic response and subsequent damage-plastic response of material separately.

Uniaxial tensile test (using smooth bar) is the most common way of identifying plastic material response in the form of true stress - logarithmic strain dependence. In the initial stage of the tensile test uniaxial stress can be considered, in the next phase of testing local necking appears which generally results in triaxial stress in the neighborhood of the neck. This stage can in principle be described using two different approaches.

- Plastic curve estimation using appropriate correction (say Bridgman's)
- Iterative calibration procedure using FE modeling of tensile test

2. Plastic response calibration

In this paper an iterative approach for the calibration of plastic curve that was developed and subsequently tested is described. It is appropriate to start the calibration process with measured plastic curve with local necking correction

Collocation alternative

The collocation alternative of calibration is based on the successive identification of individual points of the plastic curve. The output must be in tabular form containing values of stress and strain in the format of appropriate plasticity model. Therefore, collocation variant is limited to plastic models, which are defined by table in ABAQUS software (isotropic, kinematic).

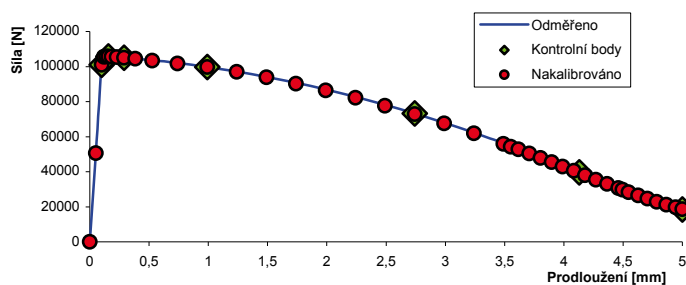


Figure 2 Tensile test, collocation points choice

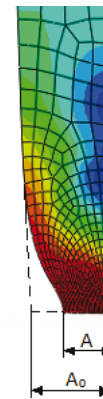


Figure 3 FE model

In the second phase of calibration first Abaqus is employed to simulate the tensile test up to displacement corresponding with collocation point. Then the difference between measured and computed load is related to the neck area (initial A_0 or actual A - Figure 3) and stress correction of plastic curve is determined. Plastic strain is expressed as average of neck forming elements (Figure 5). Then re-definition of the point of plastic response curve follows and all steps are repeated until the difference between measured and computed load is acceptable. All points defining plastic

response curve are calibrated successively the same way. Figure 2 represents the result of one of testing examples.

The calibration process rate can be partially controlled by the choice of the

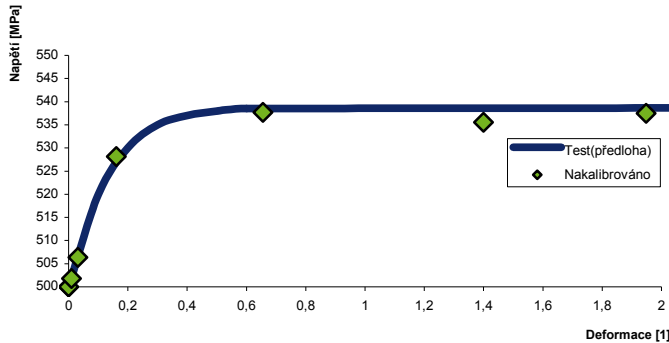


Figure 4 Final plastic response

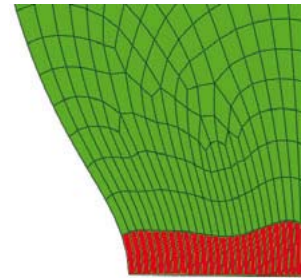


Figure 5 Elements in the neck

reference cross-section of the neck (Figure 3). If stress calculation is related with actual cross-section A , then the convergence rate is generally higher. In this case, sufficient density of control points of plastic curve is required to obtain good results. Convergence calibration is always guaranteed if the initial choice of A_0 section is made. To achieve the required accuracy, however, needs more iteration.

Advantages of collocation alternative are: 1 Possibility to interpolate the complex shape curve; 2 Calibration does not require any additional optimization schemes. Disadvantages are: 1 Collocation option requires calibration models with plastic curve in tabular form; 2 It requires a larger number of iterations.

Approximate alternative

Approximate alternative of calibration is based on searching the parameters of the curve or the plasticity model parameters minimizing suitably defined functional. Because the output of the calibration is a group of parameters, this procedure can be extended to other, parametric, models of plasticity which are restricted in collocation variant (e.g. Johnson Cook). The target functional can be defined as the area A bounded by the loading curve and calculated solution (Figure 6).

To minimize the functional method based on Newton-Raphson procedure was tested. This method requires accurate estimation of the solution and sufficient smoothness of the functional. Convergence often was unreachable and computational procedure behaved as highly instable, the calculation had led to the collapse. Using Newton-Raphson method seems to be inappropriate. An alternative way is to use an external optimization tools. Further scripts were developed to enable cooperation between the ABAQUS and Matlab, which contains the appropriate optimization tools.

Advantages: 1 Can be used for most models of plasticity; 2 Faster convergence. Disadvantages: 1 The quality of the solution is conditional and it depends on appropriate choice of approximation function; 2 Requires a sufficiently accurate estimate of the solution (the problem of local extremes).

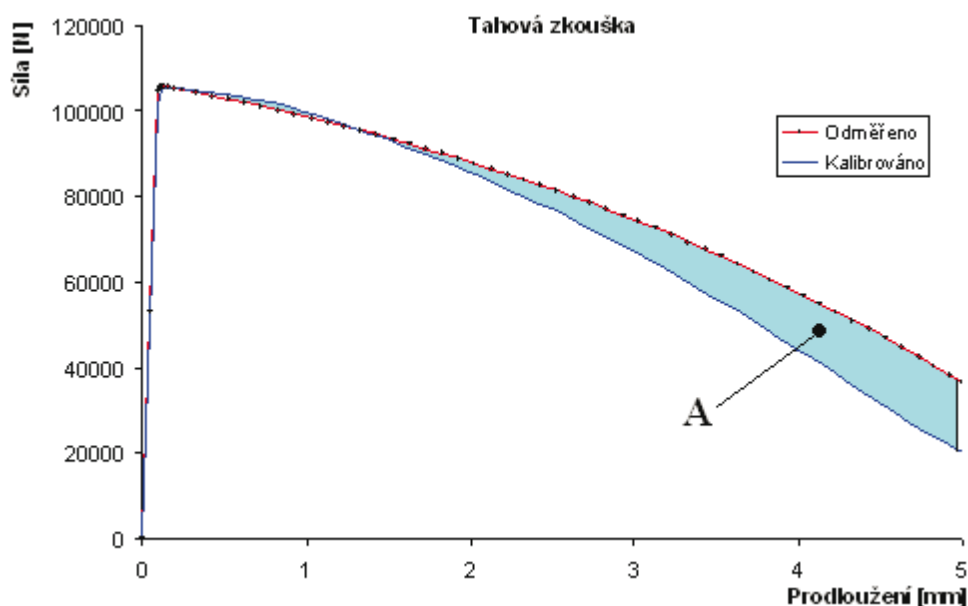


Figure 6 Target functional

3. Conclusion

In the project scope the method of plastic curves calibration was developed and tested using simple examples. The presented methods were implemented in FE program Abaqus using the scripting language Python, and Matlab. Future work is to test these procedures and to develop calibration of damage initiation.

Acknowledgement

This paper was supported by a grant MIT FR-TI2/279 Identification of parameters of ductile material failure of nuclear facilities.

References

- [1] Ling, Y.: Uniaxial True Stress-Strain after Necking. AMP Journal of Technology Vol. 5 June, 1996
- [2] ABAQUS Online Documentation: Version 6.9.
- [3] Švec, J.: Létaující cirkus. Python tutorial, 2003
- [4] NumPy User Guide. Release 2.0.0.dev8529
- [5] SciPy Reference Guide. Release 0.9.0.dev6641
- [6] Bořkovec, J.: Výpočtové modely tvárného porušování kovu v simulaci technologických procesů, Závěrečná zpráva projektu FRVŠ 2842/2006/G1

¹ Ing. Jan Růžička, FS ČVUT v Praze, Technická 4, 166 07 Praha, Czech Republic, Tel.: +420 224 352 509, e-mail: jan.ruzicka@fs.cvut.cz

² Ing. Antonín Prantl, CSc., Škoda JS, a.s., Orlík 1, 316 00, Plzeň, Czech Republic, Tel.: +420 378 048 826, e-mail: antonin.prantl@skoda-js.cz

³ Doc. Ing. Miroslav Španiel, CSc. FS ČVUT v Praze, Technická 4, 166 07 Praha, Czech Republic, Tel.: +420 224 352 561, e-mail: miroslav.spaniel@fs.cvut.cz

INFLUENCE OF HEAT TREATMENT ON THE MICROSTRUCTURE AND PROPERTIES OF CUAL10NI5FE4 ALLOY RODS

Peter Sláma¹, Kateřina Macháčková²

Abstract

The paper deals with the influence of heat treatment (annealing, quenching, and ageing) on the microstructure and mechanical properties of pressed CuAl10Ni5Fe4 bars. Their microstructures were observed in light and scanning electron microscopes. The appearance and area fractions of α and κ phases and their influence on the mechanical properties.

Keywords: Aluminium bronze, microstructure, mechanical properties

1. Introduction

CuAl10Ni5Fe4 aluminium bronze ranks among copper alloys which retain high strength even at elevated temperatures and which possess good resistance to corrosion and high wear resistance [1, 2, 3]. It has two-phase microstructure consisting of poorly formable phase α and high-temperature phase β which exhibits excellent hot formability. The alloy possesses limited cold formability (due to rapid work hardening) but excellent hot formability in the $\alpha + \beta$ region. Recommended forming temperatures are between 700 °C and 900 °C [1, 2].

Depending on the cooling rate and subsequent heat treatment, β phase may undergo martensitic transformation to the unstable phase β' which is very hard and brittle and increases the strength and reduces the ductility of the material. In addition, there are other phases in the microstructure termed κ , which consist mostly of Fe or Ni and Al [3, 4, 5], or γ_2 phases known to occur in Cu-Al binary alloys. These phases also increase the strength and reduce the ductility of the alloy. The microstructure therefore consists of the phase α and the $\alpha + \kappa + \gamma_2$ eutectoid.

Several types of the kappa phase have been classified: [6] lists 4 types denoted as κ_I , κ_{II} , κ_{III} , κ_{IV} . The phase κ_I forms large dendrite-shape particles rich in Fe, which consist of Fe₃Al with Cu and Ni. The phase κ_{II} forms smaller globular-shape particles with identical composition as κ_I . The phase (precipitates) κ_{III} are NiAl-based and have plate or lamella shape. κ_{IV} are small Fe₃Al-based precipitates.

2. Experimental

Hot-pressed bars with the diameter of 32 mm from an alloy containing 9.9% Al, 5.4% Ni and 4.5% Fe have been used for the experiment. The bars were manufactured according to the Czech Standard ČSN EN 12163. The material grade was CuAl10Ni5Fe4 (CW307G).

Specimens of bars were used for investigation of the influence of annealing between 500 and 850 °C/30 min, quenching from 930 °C and ageing of quenched specimens at 300 to 400 °C/30 min on the microstructure and mechanical properties. Attention was also paid to the influence of slow cooling in furnace and rapid cooling after removal of specimens from the furnace.

Microstructure of conventionally prepared metallographic specimens was observed in light and scanning electron microscopes. Hardness HV30 was measured on the specimens. Test bars with the parameters of M8×5×30 were used for measuring the ultimate tensile strength (UTS), the 0.2 proof stress (YS) and A₅ elongation. Impact energy KU was measured using U-notch samples.

3. Results and Discussion

3.1 Mechanical Properties

Hardness HV30 of annealed as-received specimens (AR) was measured on the heat treated specimens. The results are shown in Fig. 1. The chart shows hardness values after annealing of as-received (AR) material and hardnesses after annealing (tempering) of the quenched material. Hardness of the as-received material is 265 HV30. Quenching brings it up to 305 and ageing to 400 (tab. 3).

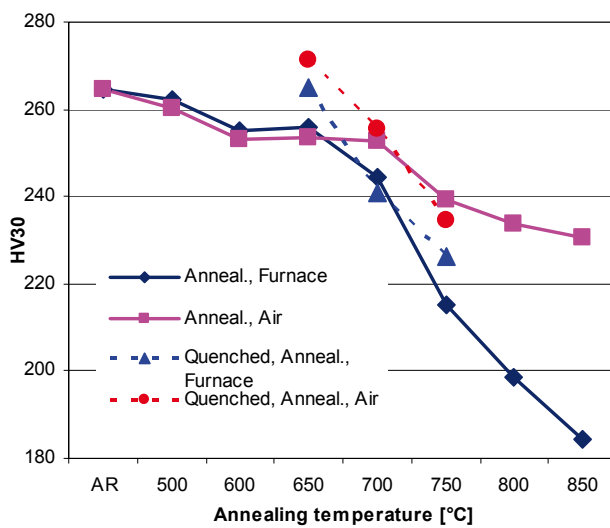


Fig. 1 HV30 hardness of annealed as-received and tempered specimens

Tab. 1 Hardness HV30

Anneal.	Annealed		Quenched and tempered	
	Furnace	Air	Furnace	Air
AR	265		305	
500 °C	262	260		
600 °C	255	253		
650 °C	256	254	265	271
700 °C	245	253	241	256
750 °C	215	239	226	235
800 °C	198	234		
850 °C	184	230		

Hardness decreases during annealing, first slowly when the temperature is below 700 °C but more rapidly when it reaches 750 °C. Greater drop in hardness was seen in specimens cooled slowly in furnace than in those cooled in air where the hardness decrease was not as high. As-received and annealed specimens showed a similar hardness drop but the difference between values after slow and rapid cooling was not as large.

Test bars were used for mechanical properties measurement (UTS, 0.2 proof stress, A₅) for specimens after annealing. The results are listed in Table 2 and in figures 2 and 3.

Mechanical properties correspond to hardness values. Largest strength and proof stress declines were found in furnace annealed and slowly cooled specimens. Elongation after annealing increases at first but drops off after the annealing temperature of 850 °C is reached (Fig. 2).

Rapidly cooled specimens showed decline of elongation with increasing annealing temperature as well.

Tab. 2 Mechanical properties of annealed specimens

	UTS [MPa]	0.2 YS [MPa]	A ₅ [%]	HV30
As-received state (AR)	911	767	14.6	265
Annealed at 750 °C, Furnace	788	591	18.9	228
Annealed at 850 °C, Furnace	681	355	16.0	182
Annealed at 750 °C, Air	844	625	11.9	236
Annealed at 850 °C, Air	823	444	10.5	219

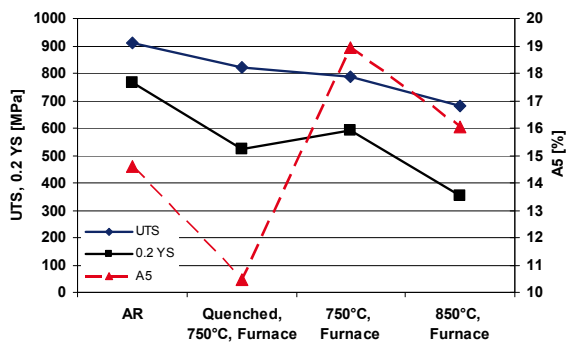


Fig. 2 Changes in mechanical properties after annealing and slow cooling in furnace

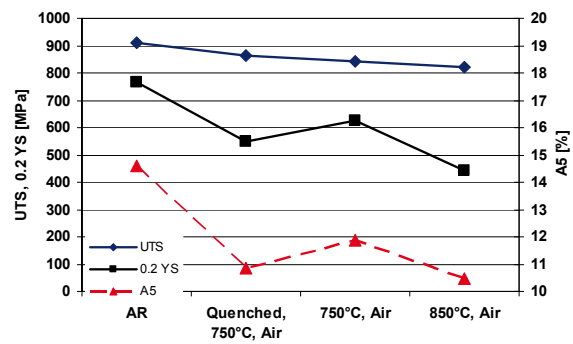


Fig. 3 Changes in mechanical properties after annealing and rapid cooling in air

Mechanical properties and hardness HV30 after quenching and ageing are listed in table 3. After quenching, the strength increases (whereas the proof stress declines) and elongation drops almost to zero. The strength of quenched specimens can be further increased by ageing to above 1,000 MPa. However, the elongation remains very low. Quenched and aged specimens are very brittle already.

Tab. 3 Properties after quenching and ageing

	UTS [MPa]	0.2 YS [MPa]	A ₅ [%]	HV30
As-received state (AR)	911	767	14.6	265
Quenched 930 °C/30 min (Q)	972	702	2	305
Aged 400 °C/30 min (Ag)	1,057	1,051	1.1	400
Quenched, tempered 750 °C, furnace	823	524	10.5	226
Quenched, tempered 750 °C, air	865	549	10.8	235

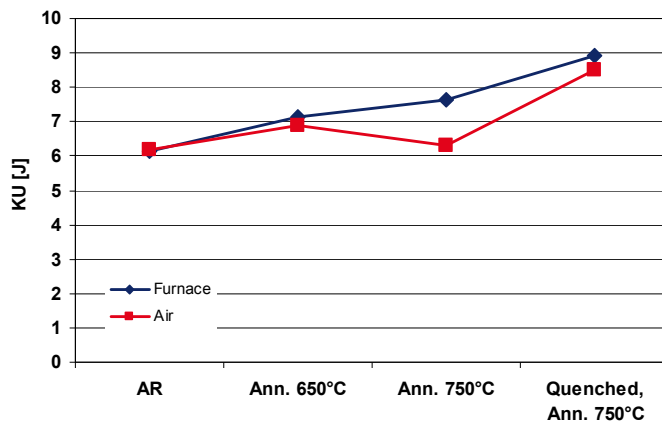
Hardness values after quenching and tempering at high temperatures (650 to 750 °C) are shown in tab. 1 and in Fig. 1. The values are comparable with those for

annealed as-received specimens. Strength is comparable as well but the elongation is lower (Fig. 2 and 3).

3.1.1 Charpy Impact Test

As-received, annealed and quenched specimens were used for measuring the impact energy KU. The results are shown in table 4 and in Fig. 4.

Impact energy values grow with the annealing temperature. Highest values were found in quenched and annealed (tempered) specimens.



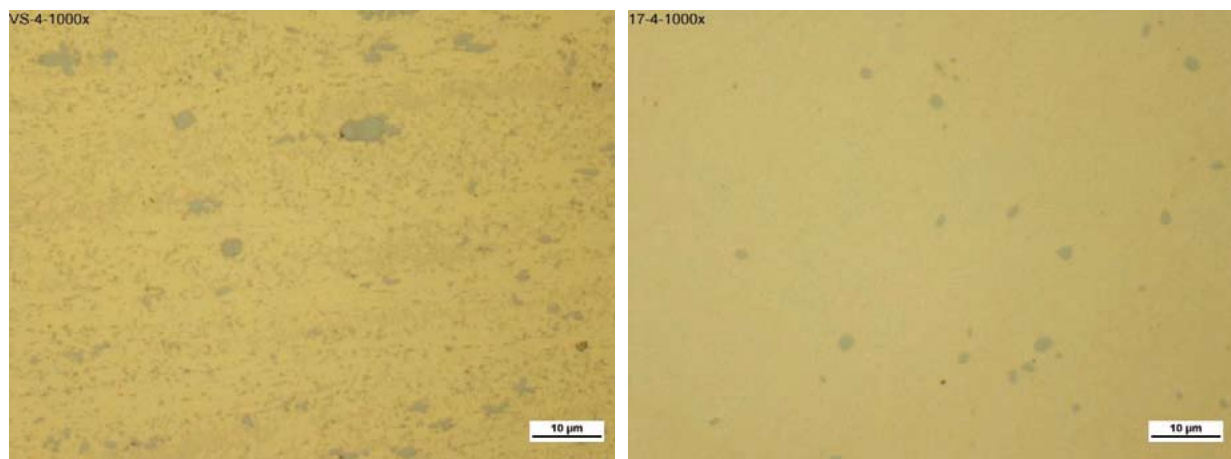
Tab. 4 Impact energy KU values

	KU [J]
As-received (AR)	6.2
Ann. 650 °C, Furnace	7.1
Ann. 650 °C, Air	6.9
Ann. 750 °C, Furnace	7.6
Ann. 750 °C, Air	6.3
Quenched, Ann. 750 °C, Furnace	8.9
Quenched, Ann. 750 °C, Air	8.5

Fig. 4 Impact energy KU for selected specimens

3.2 Microstructure

Micrographs of specimens prior to etching are shown in Fig. 5. Unetched sections show grey globular particles of κ_{II} phase (according to EDX analysis they contain 55% Fe, 11% Al and Ni, Cu, Mn and Si), light grains of the phase α and between those eutectoid consisting of $\alpha + \kappa$ or a balance of β . Annealing at the quenching temperature of 930 °C dissolves the κ phase in the eutectoid (except the globular κ_{II}) and leads to supersaturation of the solid solution α (Fig. 5b).



a) As-received state

b) 17 – After quenching

Fig. 5 Micrographs of unetched specimens

Microstructure after etching is shown in Fig. 6 and 7. Etching reveals light grains of the phase α , grey to light blue globular particles of the phase κ_{II} and the dark eutectoid. In the as-received state, the α grain size is very small: 1 to 2 μm . With increasing annealing temperature, the α grain size grows, as well as the area of the eutectoid in between. Slow furnace cooling leads to coarsening of κ precipitates (Fig. 6c, d) and formation of lamellar κ_{III} precipitates. The phase κ also precipitates along α grain boundaries.

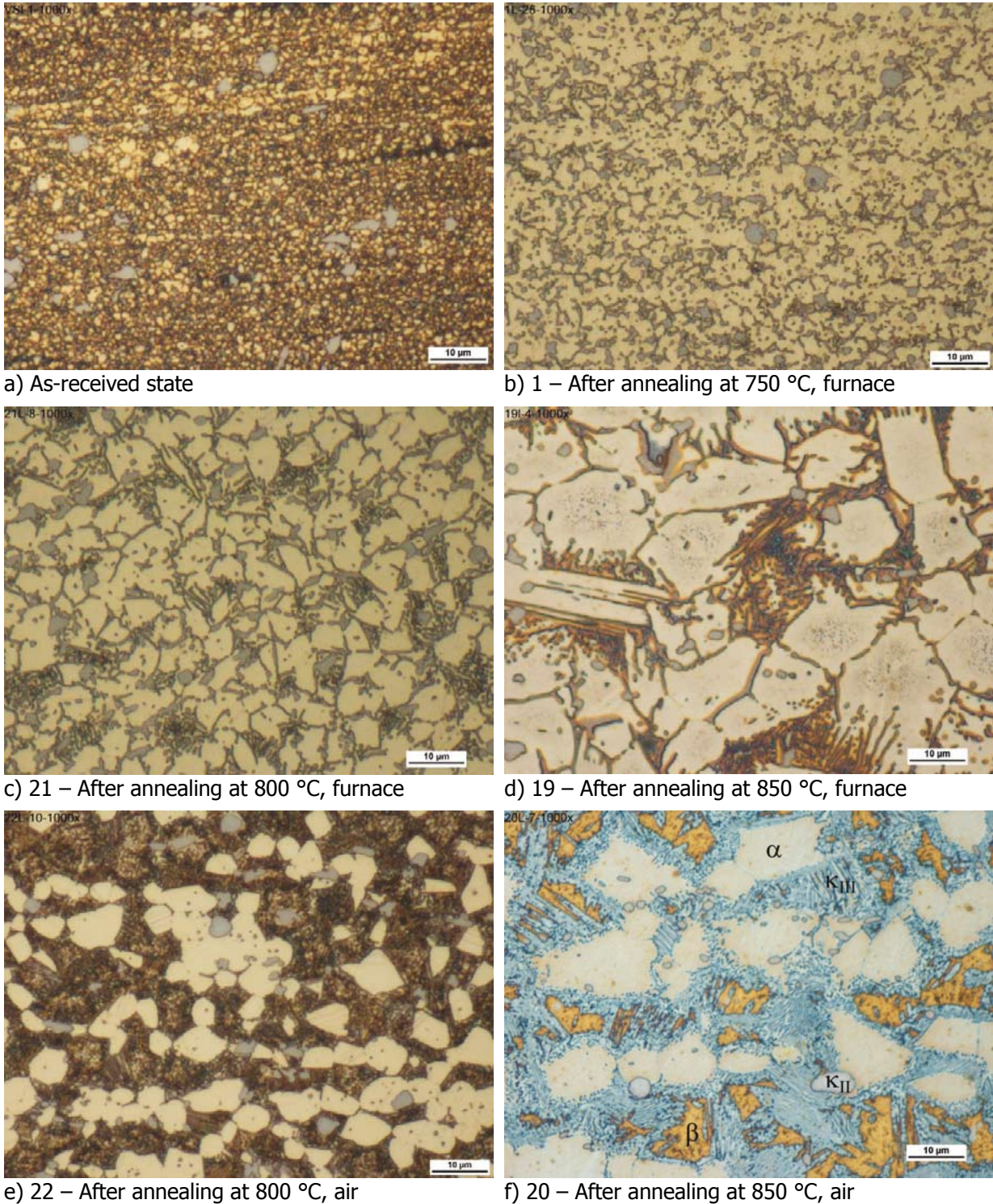


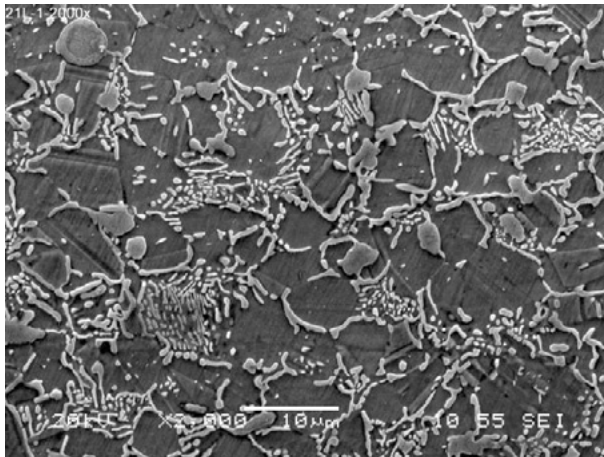
Fig. 6 Microstructure of specimens after etching with $(\text{NH}_4)_2\text{S}_2\text{O}_8$ or $\text{NH}_4\text{OH} + \text{H}_2\text{O}_2$

With increasing α grain size the strength and hardness decline. The greatest drop is seen in specimens annealed at 850 °C with slow cooling. However, the elongation decreases as well, which may be attributed to the phase κ precipitating more extensively along α grain boundaries.

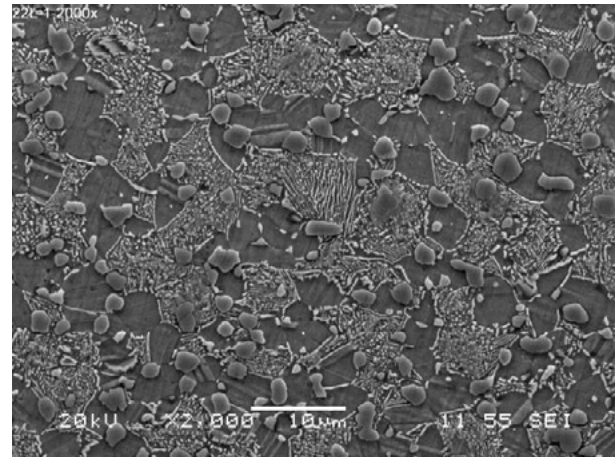
Rapid cooling leads to higher proportion of the eutectoid at the expense of the α proportion. Besides, certain fraction of the phase β is retained in the microstructure (more dark areas in the eutectoid). This is shown in Figs. 6e and 6f where short etching by $\text{NH}_4\text{OH}+\text{H}_2\text{O}_2$ revealed orange β phase, light α phase and light blue κ phase. In contrast to products of slow cooling, κ precipitates are finer. Globular precipitates of κ_{IV} have formed as well. The decrease in strength and hardness is not as great as on slow cooling which can be explained by a greater proportion of eutectoid and residual β in the microstructure.

Boundaries of recrystallized grains have only been found after annealing at 930 °C (soaking temperature for quenching). Their size is very non-uniform, reaching up to several hundreds of μm (Fig. 7c).

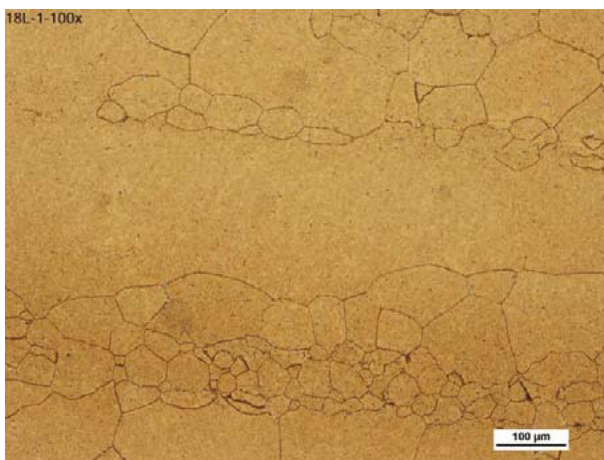
The micrographs also confirm that slow cooling leads to coarser κ precipitates than rapid cooling (Fig. 7a, b).



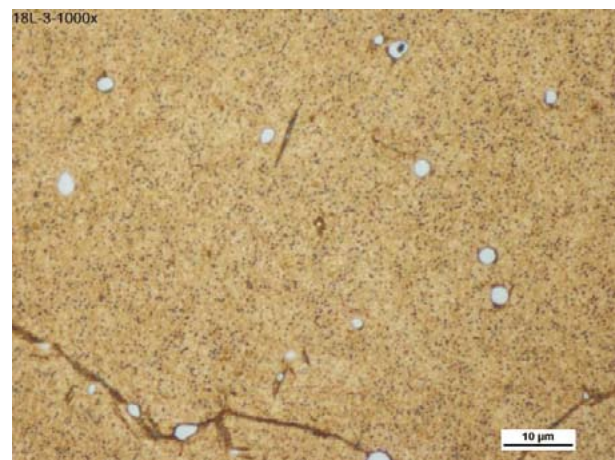
a) 21 – After annealing at 800 °C, furnace, SEM, SE



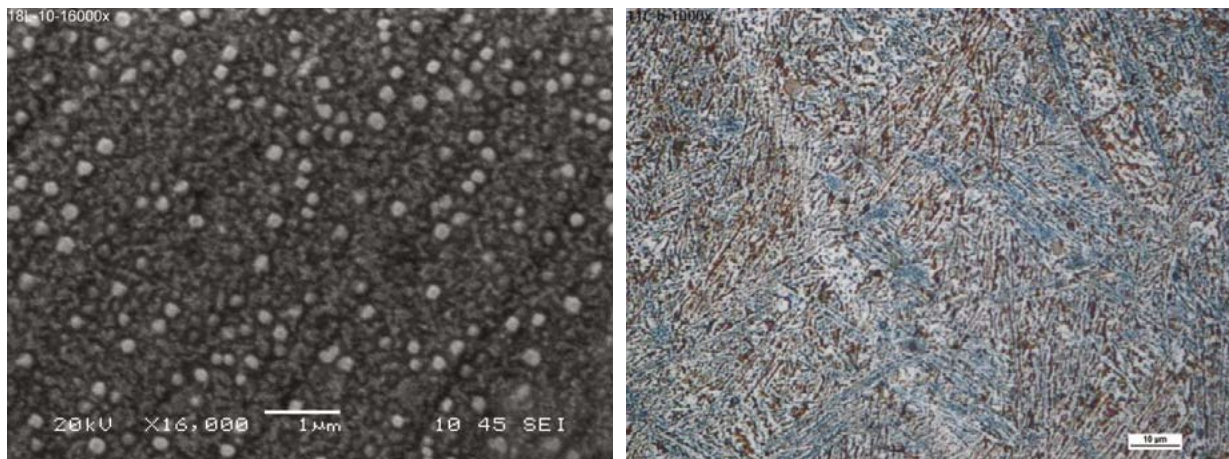
b) 22 – After annealing at 800 °C, air, SEM, SE



c) 18 – Quenched and aged at 400 °C



d) 18 – Quenched and aged at 400 °C



e) 18 – Quenched and aged at 400 °C, SEM, SE f) 11 – Quenched and annealed at 750°C, furnace

Fig. 7 Microstructure of specimens, etched

After ageing, small precipitates of κ_{IV} (Fig. 7d) are visible even in a light microscope. They are better displayed in an SEM (Fig. 7e).

Quenched specimens form the typical Widmanstätten microstructure during annealing (tempering). It consists of α needles embedded in the β' phase with blue lamellae of the κ phase in between (Fig. 7f). Hardness and other mechanical properties of specimens tempered at 750 °C do not show equally strong dependence on the cooling rate (Tab. 1 and 3).

4. Conclusions

Investigation of the effect of heat treatment on the microstructure and properties of pressed bars from CuAl10Ni5Fe4 alloy can be summarized as follows:

- Microstructure of the bars after hot pressing is very fine-grained, consisting of phase α grains with the size of 1 – 2 μm and the $\alpha + \kappa$ eutectoid. Owing to rapid cooling, the phase β may form.
- Values of mechanical properties are high and the UTS exceed 900 MPa. After quenching and ageing both strength and hardness increase but elongation drops to 1 %.
- After annealing, the grain size of the phase α increases, as well as that of the eutectoid regions. Up to 700 °C, the increase is slow, becoming more rapid above 750 °C. This is matched by the decline in hardness HV30, which is slow up to 700 °C and more rapid above 750 °C. Values of strength decrease as well. The decrease is more pronounced in slowly cooled specimens.
- During slow cooling in the furnace, the precipitates of κ begin to coarsen and formation of lamellar κ_{III} -type precipitates prevails. The phase κ also precipitates along α grain boundaries.
- Rapid cooling leads to higher proportion of the eutectoid at the expense of the phase α . In addition, certain fraction of the phase β is retained, resulting in slight decrease in strength and hardness. The microstructure of the eutectoid is finer and precipitates of the phase κ do not form along the α grain boundaries, as during slow cooling.
- During annealing at 850 °C and during slow cooling, the elongation declines, possibly due to precipitation of κ along α grain boundaries.

- Annealing of the quenched material (tempering) produces the Widmanstätten structure. Hardness and other mechanical properties of specimens do not depend on the cooling rate very strongly.

Acknowledgement

This paper was prepared in the framework of the project no. FR-TI1/473 "Industrial research and development of technology of production of the bars made from nickel and copper alloys" (Průmyslový výzkum a vývoj technologie výroby tyčí na bázi Ni a Cu) funded by the Ministry of Industry of the Czech Republic.

References

- [1] ASM Handbook Volume 02: Properties and Selection: Nonferrous Alloys and Special-Purpose Materials, ASM International, 1990
- [2] DAVIS J. R.. ASM Specialty Handbook: Copper and Copper Alloys, ASM International , 2001
- [3] Cook, M., Fentiman, W. P., Davis, E. Observations on the Structure and Properties of Wrought Copper-Aluminum-Nickel-Iron Alloys. J. Inst. Met., Vol. 80, 1951–52, pp. 419–29
- [4] Brezina, P.: Heat treatment of complex aluminum bronzes. International Metals Reviews, 1982, 27(2): pp. 77–120
- [5] Hasan, F., Jahanafrooz, A., Lorimer, G. W., Rildley, N.: The morphology, crystallography, and chemistry of phases in as-cast nickel-aluminum bronze. Metallurgical Transactions A, Vol. 13A, August 1982, pp. 1337–1345

¹ RNDr. Peter Sláma, COMTES FHT a.s., Průmyslová 955, 334 41 Dobřany, Czech Republic, Tel.: +420 377 197 344, e-mail: peter.slama@comtesfht.cz

² Ing. Kateřina Macháčková, KOVOHUTĚ ROKYCANY, a.s., Zeyerova/285, 337 01 Rokycany, Czech Republic, Tel: +420 734 510 429, e-mail: machackova@koro.cz

HEAT TREATMENT NUMERICAL SIMULATION OF SLEEVED ROLL

Marek Slováček¹, Jiří Kovařík², Josef Tejc³, Josef Bárta⁴, Petr Pustějovský⁵

Abstract

The complete numerical simulation of sleeved roll will be presented in this paper including material measurements (material measurements were done in COMTES Company) and measurements of oil quench test. The sleeved roll is manufactured from material 45Cr3MoV. Heat treatment consists of quenching in air and oil, tempering follows. The results as prediction of metallurgical phases, hardness in Vickers unit, residual stresses, distortion, plastic deformation and prediction of final yield stress will be presented.

Keywords: heat treatment numerical simulation, material 45Cr3MoC, SYSWELD

1. Introduction

The idea of sleeving is rather old. A presence of permanent tensile stress in sleeves that may lead to cracks handicapped these types of rolls. But the development in mathematical modelling, metallurgy, non-destructive metal testing and other branches enabled to produce sleeved rolls with similar or better properties than the solid ones.

A sleeved roll consists of an arbor and a sleeve that is joint by shrink fit. This produces a permanent tensile stress in the sleeve which potentially may lead to fracture.

Heat treatment and especially quenching causes distortion, residual stresses and sometimes cracking of quenched part. To eliminate these undesired side effects the whole circle of heat treatment can be also simulated by FEM (SYSWELD CODE, ESI GROUP), which makes possible a complete metallurgical, thermal and thermoplastic calculation. The goal of this simulation is to bring the whole cycle of heat treatment to optimum - to reach lowest level of residual stresses and distortion possible at its end and to meet the mechanical qualities required by the customer.

Heat treatment is a very frequently process for treating steel products before their processing to the final shapes. During the heat treatment of steel products mainly during quenching non-uniform thermal distribution and structural metallurgical transformation take place. These two phenomena originate internal stresses and due to a change in crystal lattice volume during transformation changes in steel also transformation plasticity originates in steel. Total internal stresses and structural distribution after substantially the resulting properties as e.g. deformed work shape, resulting mechanical properties, hardness, possibility of crack initiation, fatigue life. To be able to quantify the assumption of some results properties (hardness,

distribution of metallurgical phases, residual stresses, distortion etc.) we need to perform a complete numerical simulation of the whole heat treatment process.

2. Heat treatment numerical simulation

SYSWELD software from ESI Group company, using finite element method base, enables complete numerical solution of quenching, tempering, it means complete heat treatment process

The complete heat treatment numerical simulation can be also divided into three following stage:

1. During the first stage a complete diagram of anisothermic decomposition (CCT diagram) is entered by special pre-process module. The results of this stage are coefficients describing the kinetic of transformation process depending on cooling rate at individual areas of heat-affected zone. The coefficients depend on the temperature and on the metallurgical phase of particular material and are used as direct input to the second phase. In this stage the complete material properties should be prepared.

2. The second stage is a thermo metallurgical solution. This part needs complete thermo physical and thermo metallurgical material properties. There is applied a classical equation of the heat conduction extended with the transformation of latent heat during change of phase and during melting of material. Coupling between phase transformation and heat conductivity is used. The results of the first stage are non-stationary temperature fields, percentage distribution of individual phases, size of primary austenitic grain, hardness.

3. The results of the second stage (mainly non stationary temperature fields and distribution of material structure) are applied as a loading condition in the third stages, the structural analysis. The complete mechanical properties are needed. The mechanical properties (thermal expansion, yield stress, hardness, Young modulus etc.) depend on the temperature and individual phases. Resulting mechanical properties are calculated on the basis of individual material structure distribution and their mechanical properties. The results of the third stage are, total deformation (consist of elastic part, thermal part, convectional plastic part, viscoplastic part and transformation plasticity), residual stresses and distortion.

One of the most important parameters for heat treatment numerical simulation is heat transfer coefficient, mainly for quenching process. The heat transfer coefficient can be taken from SYSWELD internal database for different media (water, several types of oils, polymers, air, salt etc.). The heat transfer coefficient can be prepared based on the results from real "quenched test".

The material data which are needed for heat treatment numerical simulation can be found in literature, measured or taken from internal SYSWELD database.

The advantage of numerical simulation is that there are visible parameters as material structure, hardness, residual stresses, plastic deformation and distortion during whole process. These stated parameters can be measured only at the end of the process.

3. Heat treatment numerical simulation of sleeved roll

The main aim of numerical simulation [2] of sleeved roll was optimisation of heat treatment temperature regime to obtain requirement material structure, hardness, mechanical properties, lowest level of residual stresses and distortion.

The sleeved roll is manufactured from steel 45Cr3MoV. The accuracy of calculated results is also depending on quality of input data. The detail material measurements of steel 45Cr3MoV were done [1]. The CCT diagram and tensile tests and hardness of basic materials, martensite, bainite and tempered structure were measured. Results of material measurements were used as input material data for numerical simulation.

The "quench" test of oil which is using for quenching of sleeved roll was done. The "quench" test was done for oil temperature 25°C, 40°C and 60°C. The results of the quench test are shown in fig.1. The complete "quench" test was simulated by SYSWELD software and appropriate heat transfer coefficient for used oil was found out. The heat transfer coefficient for oil 40°C is shown in Fig. 2.

Heat treatment of sleeved roll consists of normalization, oil quenching and tempering follows.

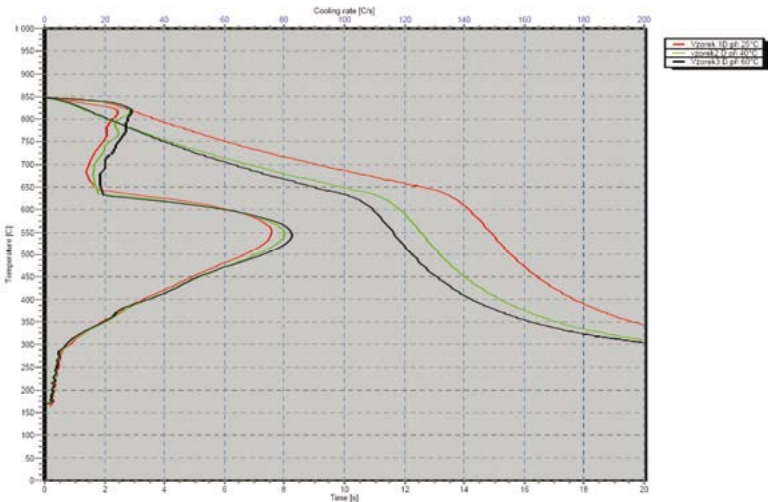


Figure 1 Quench test results

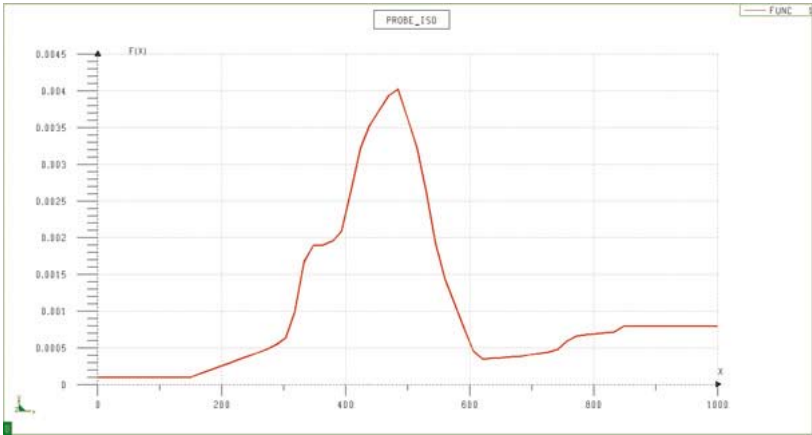


Figure 2 Heat transfer coefficient

The two axis-symmetrical computational models were prepared and used, Fig.3. The first one was used for the first part of heat treatment process (two air cooling and one tempering) before rough machining. After rough machining the calculated results were projected on second model and oil quenching and second tempering was numerical simulated.

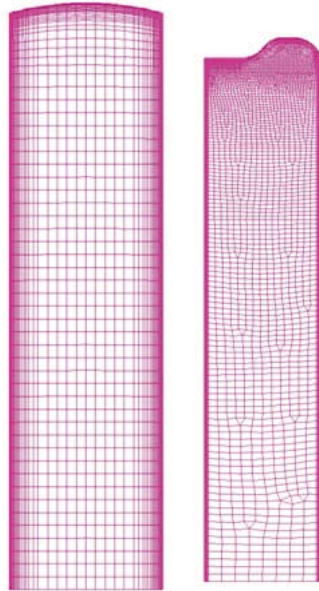


Figure 3 Computational model

The VITKOVICE HEAVY MACHINERY Company delivered draft of heat treatment regime and based on the calculated results the parameters as cooling and heating velocity, soaking time, temperature of soaking time etc. the heat treatment regime was modified. The percentage of martensite and bainite after oil quenching is shown in Fig. 4. The hardness in Vickers unit is shown in Fig.5. The residual stresses, as mean stress and VON MISE equivalent stress, are shown in Fig.6. The total distortion (deformation) and total plastic deformation at the end of the heat treatment process is shown in Fig.7. The residual stresses are not so high due to slow cooling across 300°C where martensite structure is created and also due to high mechanical properties of martensite and bainite structure (yield stress of martensite is approximately 1300 MPa and yield stress of bainite is approximately 1100 MPa). Also there is not appearing big plastic deformation on sleeved roll after complete heat treatment process.

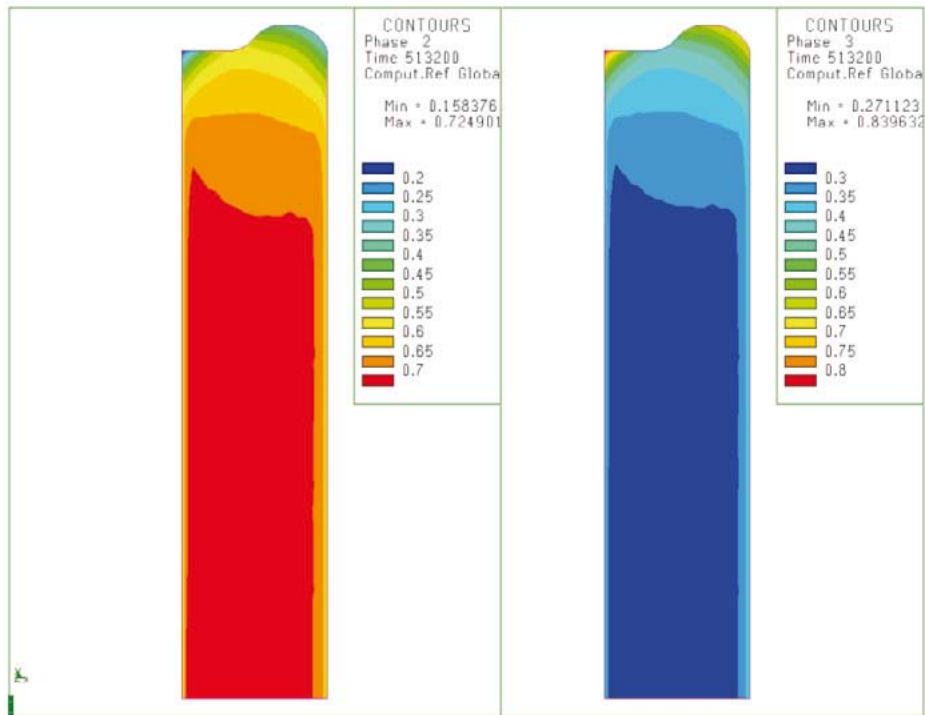


Figure 4 Martensite (left) and bainite (right) distribution after oil quenching

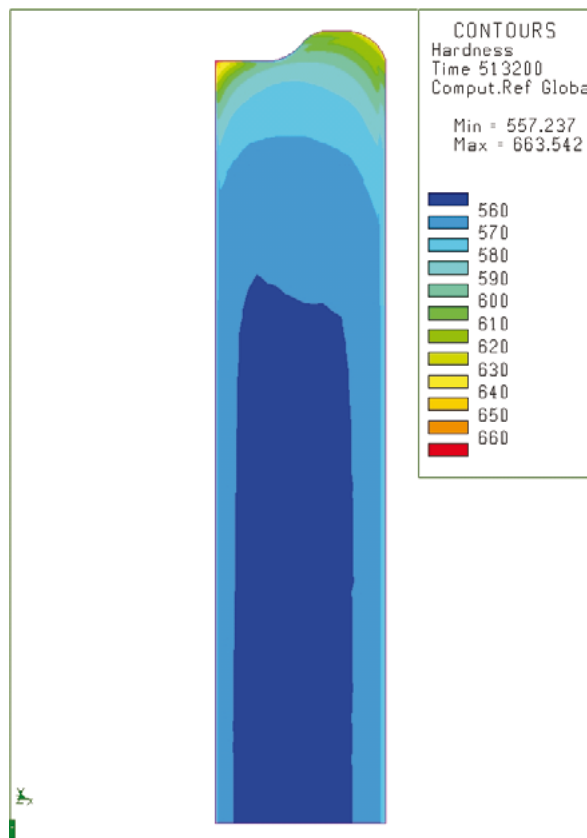


Figure 5 Hardness in Vicker unit after oil quenching

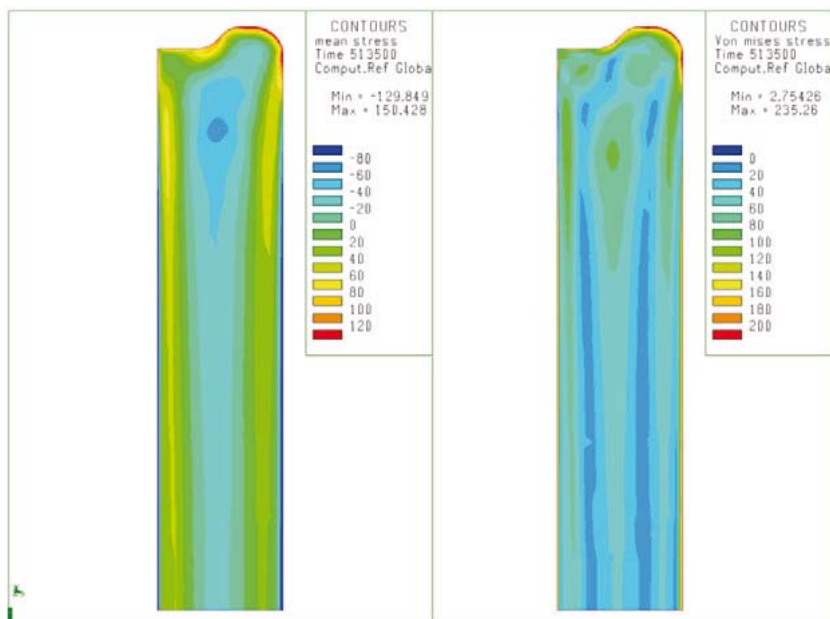


Figure 6 Residual stresses after oil quenching

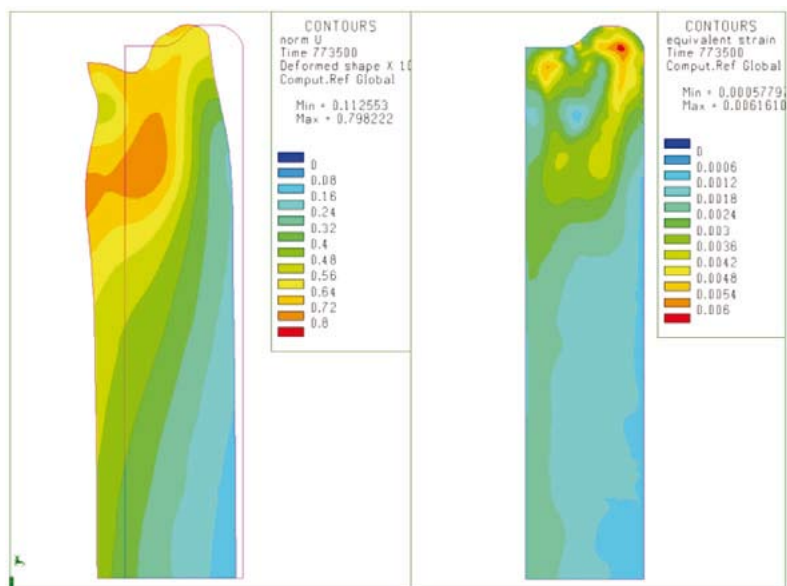


Figure 7 Distortion (left) and plastic deformation (right) at the end of the heat treatment process

During the experimental part, the hardness of quenched and tempered marteniste and bainite was measured. In table 1 there is a comparison between calculated and measured hardness.

Table 1

	Hardness HV, centre of the model	
	Measured value	Calculated value
After oil quenching	588	569
At the end of the process	481	487

4. Conclusion

The main aim in the industry is cost reduction with increasing product quality. The very detail knowledge about the process and product are needed to keep the customer requirements. The reduction of the cost and time for design and technology preparation can be done to decrease the experiments or repairing before the finalization of the product and technology. The numerical simulations of the heat treatment process are very modern and productive tool. The recent rapid progress in modeling techniques provides researchers and engineers with more information to achieve a better understanding of the residual stresses and distortion during heat treatment process. This paper demonstrates how numerical solutions can give some very important and interesting information about heat treatment process. The results can be used as one of the basis during the proposal of a new product, new technology validation or optimization of current heat treatment technology.

Possibility of using heat treatment numerical simulation was demonstrated on case of heat treatment of sleeved roll.

References

- [1] Motyčka, P.: Fázové transformace a mechanické vlastnosti oceli 45Cr3MoV, zpráva č. 2009-82 COMTES FHT a.s., Listopad 2009
- [2] J.Pokorný, J.Tejc: Numerická analýza tepelného zpracování bandáží, zpráva MECAS ESI s.r.o., č. M_Z_09_022_r01, únor 2010
- [3] Hajduk, D. Hanel, I., Zapoměl, J.: Výpočty bandáží válců, Kalibrace válců 2005, Beskydy – Čeladná, 15.16.6.2005, 93–98
- [4] Tvrdy, M., Hryzlak, J., Bembenek, Z., Molinek, B.: Sleeving of backed-up rolls as method of renovation and development, ROLLS 2007, Birmingham
- [5] Yanaka, T.: Manufacture of Roll Sleeves, Rolls for the metalworking industries, Ed.: R. B. Corbett, 1990, ISBN 0-932897-46-0, 121–134

¹ Ing. Marek Slováček, Ph.D., MECAS ESI s.r.o., Brojova 2113/16, 326 00 Plzeň, Czech Republic, e-mail: marek.slovacek@mecasesi.cz

² Ing. Jiří Kovařík, CSc., MECAS ESI s.r.o., Brojova 2113/16, 326 00 Plzeň, Czech Republic, e-mail: jiri.kovarik@mecasesi.cz

³ Ing. Josef Tejc, MECAS ESI s.r.o., Brojova 2113/16, 326 00 Plzeň, Czech Republic, e-mail: josef.tejc@mecasesi.cz

⁴ Ing. Josef Bárta, CSc., VÍTKOVICE HEAVY MACHINERY a.s., Ruská 2887/101, 706 00 Ostrava - Vítkovice, Czech Republic, e-mail: josef.barta@vitkovice.cz

⁵ Ing. Petr Pustějovský, Ph.D., VÍTKOVICE HEAVY MACHINERY a.s., Ruská 2887/101, 706 00 Ostrava - Vítkovice, Czech Republic, e-mail: petr.pustejovsky@vitkovice.cz

FRACTURE-MECHANICAL CHARACTERIZATION OF STEEL TUBES USING ARC-SHAPED SPECIMENS

Benedikt Wiedemeier¹, Manuela Sander², Hans Alber Richard³, Andreas Peters⁴

Abstract

The increasing importance of lightweight structures leads to a higher relevance of fracture-mechanical parameters. Concerning the according characterization of steel tubes one must be aware of the thermo-mechanical conditioning during the production process. Thus, meaningful tests must be conducted at the finished product. This contribution deals with the development of a specially adapted specimen for the fracture-mechanical characterization of steel tubes.

Keywords: Steel tubes, fatigue crack growth, fracture toughness

1. Introduction

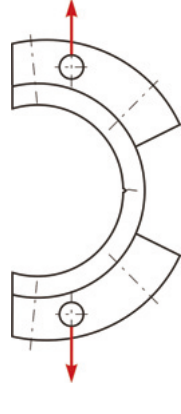
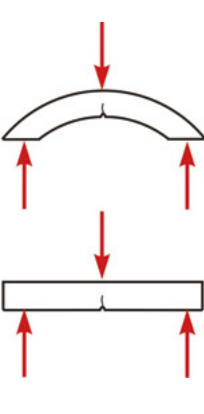
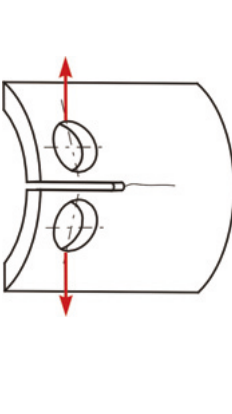
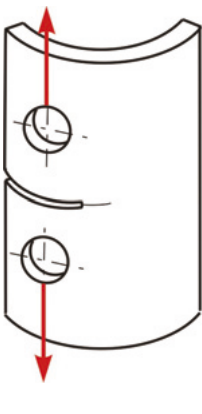
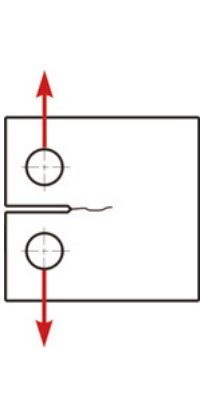
The incipient climate change probably caused by carbon dioxide emission and the strong efforts to save energetically significant resources lead to an increasing importance of lightweight constructions. High-strength steel tubes have excellent properties as components of lightweight structures as the specific strength is high and the geometry is optimal, if it is loaded by torsion and bending. However, the increasing importance of lightweight structures also leads to a higher relevance of fracture-mechanical parameters.

Due to flaws and small cracks, which exist in every real tube product, not only the strength values of the material but also its fracture-mechanical properties concerning static and cyclic loading must be considered to obviate failure during service life.

Concerning the fracture-mechanical characterization of steel tubes one must be aware of the thermo-mechanical conditioning during the production process as it strongly influences the material properties. Thus, meaningful tests must be conducted at the finished product using specially adapted specimens, which match the restricting tube geometry.

Possible specimen concepts for this goal in conjunction with a scheme for their adaptation are given in [1]. The actual concepts are also presented in Table 1.

Table 1 Specimen concepts for the fracture-mechanical characterization of high-strength steel tubes

				
Enforced C-specimen	Bending specimens	Axial specimen	Circumferential specimen	(Mini-)CT specimen
C-R orientation; Enforcements limit deformation	Orientations between C-R and L-R	Curved CT specimen	Curved CT specimen	For tubes with sufficient dimensions

2. Specimen Design

In this contribution the enforced C-specimen shall be particularly discussed, including its adaptation to the tube geometry and application for the characterization of steel tubes.

Basically this specimen concept is given in [2] as standard specimen for the determination of fracture toughness. There it is denominated as arc-shaped tension specimen. The application of the size recommendations of this standard is not completely possible, if a typical steel tube with an outer diameter of about $D = 130$ mm and a wall thickness of $t_r = 10$ mm has to be examined. Moreover a quiet erratic wall and an enormous eccentricity of about $e \approx 0,15$ can be found at hot rolled tubes.

Besides this, the relatively small wall of such a tube leads to strong deformations. Using CASTIGLIANO's theorem, a displacement for the point of force transmission $u = 2$ mm can be estimated. This calculation bases on a crack-length $a = 1$ mm and a stress-intensity $K_I = 22 \text{ MPa}\sqrt{\text{m}}$. Its reduction to an acceptable value $u = 0,3$ mm can be achieved by enforcing the specimen. Moreover side grooves in the region of the crack plane are expedient to optimise the stiffness. Without these measures the limited power of a servo-hydraulic testing machine leads to unacceptable low test frequencies.

The enforcements are fixed on the outer surface of the tube specimen by screws. Possible deviations of the pre-load have no effect on the resulting stress intensities. This could be shown with a FE-analysis, varying for each screw the pre-load between $0,2\sigma_S$ and σ_S , which is the nominal value for the pre-tension of the screw. The stress intensity was determined with the MVCCI-method using a sub model for determining the stresses along the crack front [3].

Between all simulated variants with their differing pre-tension the stress intensity differs less than 0,1%.

Figure 1 gives a contour plot of the stresses in the 2-direction for the unloaded model with pre-stressed screws.

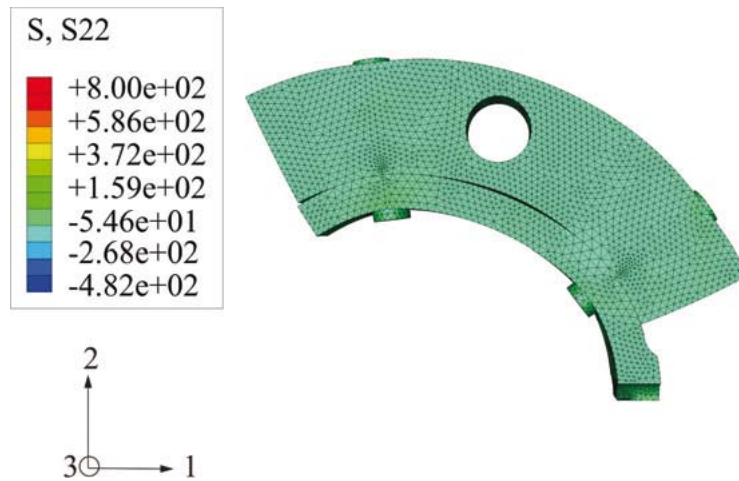


Figure 1 Contour plot of the stresses in the 2-direction for the unloaded model with nominal pre-tension for all screws

It has already been mentioned that side grooves are useful for the reduction of the deformation of the C-specimen. As they also should be designed in a way that straight crack fronts occur, three-dimensional fatigue crack growth simulations with differing notch radii were necessary to optimise their shape [4-5].

Figure 2 depicts the crack fronts simulated with ADAPCRACK3D for different side groove radii. Very straight crack fronts can be expected for $r_{Sk} = 5$ mm.

Side grooves with this geometry are relatively mild notches compared with V-notches with a radius of 0,5 mm recommended in [6].

During the actual design process care has to be taken to assure that sufficient accuracy could be realized during the fabrication of the specimens.

For example the joint area for the enforcements can be fabricated by an eroding process leading to high accuracy and having no effects on the microstructure and the resulting mechanical properties. Moreover the crack ligament is maximized to reduce possible size effects.

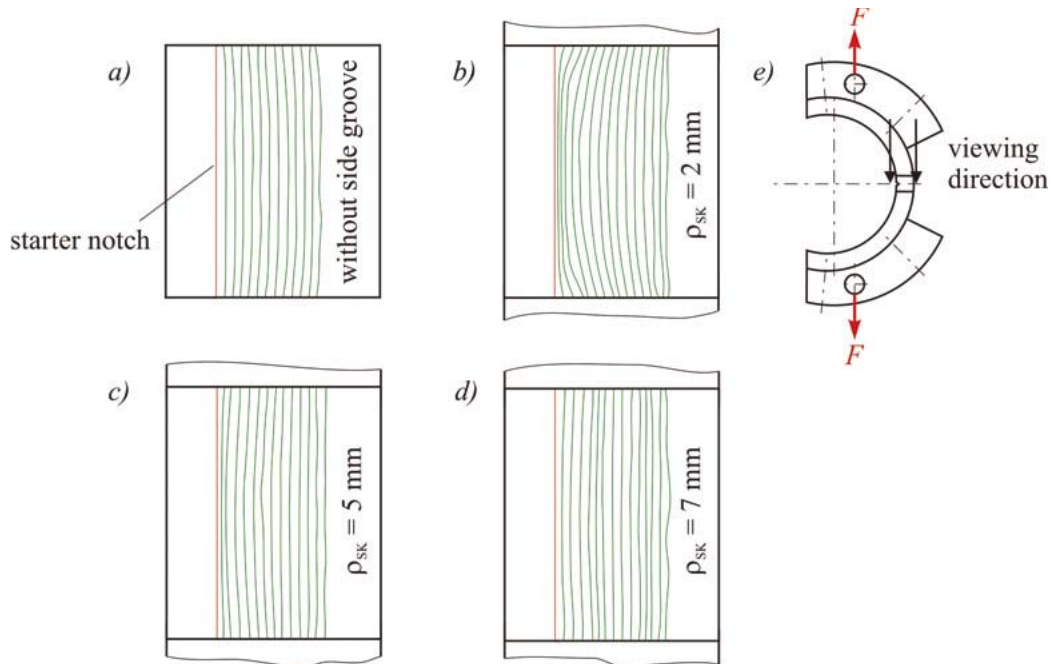


Figure 2 Fatigue crack fronts simulated with ADAPCRACK3D for: C-specimen a) without side grooves, b) $r_{sk} = 2$ mm, c) $r_{sk} = 5$ mm, d) $r_{sk} = 7$ mm; e) viewing direction

3. Experimental Validation

Experiments for the basic validation of the enforced C-specimen have been conducted. The applied experimental procedure bases on [7] and is described in [8]. The K -calibration has been determined numerically by means of two-dimensional crack growth simulation with FRANC/FAM giving discrete values for the stress intensities [9-10]. The graph of this function is given in Figure 3. An additional analytically calculated data point has been generated to fit a polynomial of sixth order. In order to find this analytical point for a crack with crack length $a = 0,1$ mm, the maximum nominal normal bending stress in the ligament has been treated as boundary stress on an infinite plate with a surface crack. This yields a value $Y = 1,12$.

This value has finally been transformed according to the definition of Y used for the purpose of these examinations:

$$Y = \frac{K_I}{\sigma_{z,Lig} \sqrt{\pi a}} = \frac{K_I}{\frac{F}{B_N w} \sqrt{\pi a}} \quad (1)$$

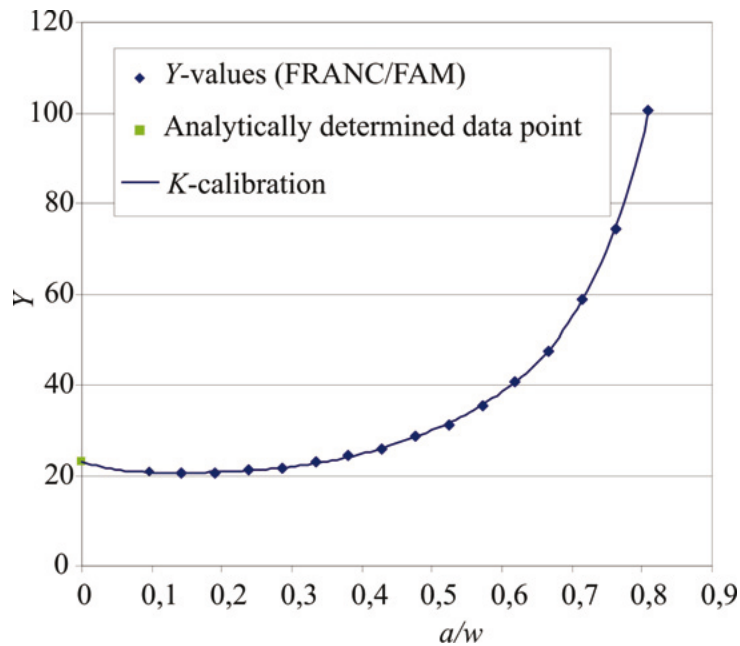


Figure 3 *K*-calibration for enforced C-specimen

In order to validate the new specimen concept, fatigue crack growth rates have been measured and compared using the same material 34CrNiMo6 ($R_m = 1050$ MPa, $R_{p0,2} = 921$ MPa) but applying standard CT specimens with $w = 72$ mm matching the requirements in [8] and enforced C-specimens. The material reveals a static fracture toughness $K_{J02Bl} = 210 \text{ MPa}\sqrt{\text{m}}$ measured with standard three point bending specimens following the multi specimen procedure given in [6]. Figure 4 shows the fatigue crack growth rates of this material for $R = 0,1$. The curves are in good agreement. This is surprising, especially as the curves do not show discrepancies in the region near the fracture toughness, where a non-conservative behavior of the smaller specimen could be expected due to a lower degree of constraint. In spite of this, the special specimen with its side grooves shows a more brittle behavior, so that the results for high propagation rates are even conservative compared with the results of the CT specimen.

However, the standard specimen reveals clear influences of the specimen size. Therefore the crack growth rates depend on the crack length and not only on the stress intensity, which finally leads to the kink in the curve given for the standard specimen in Figure 4.

The fracture surface of the special specimen is shown in Figure 5. Only very small shear lips can be observed. The brittle material behavior can be explained by the side grooves, which seem to lead to a comparably high constraint though being not as sharp as V-notches. Therefore the results drawn from Figure 4 are confirmed.

Moreover the results of the simulations with ADAPCRACK3D are affirmed as a very straight crack front occurs.

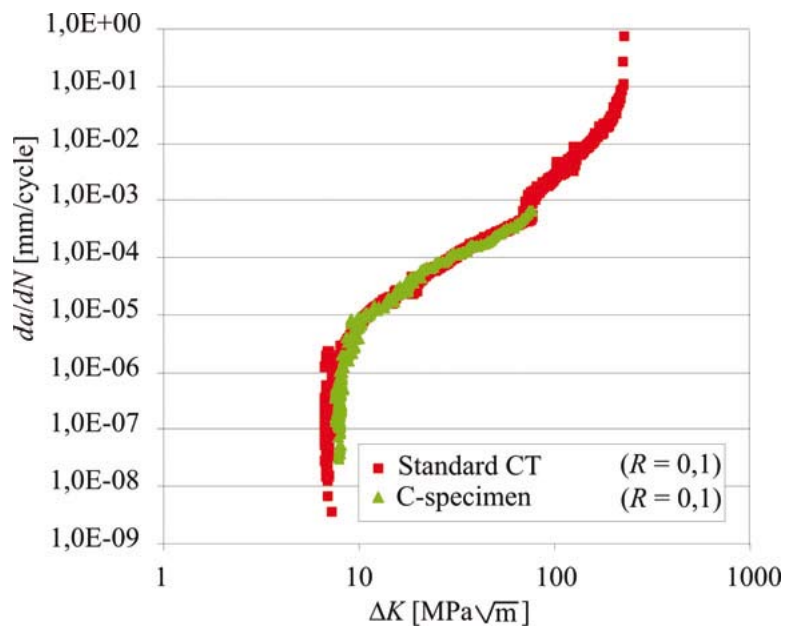


Figure 4 Comparison of fatigue crack growth rates determined with CT specimen and C-specimen

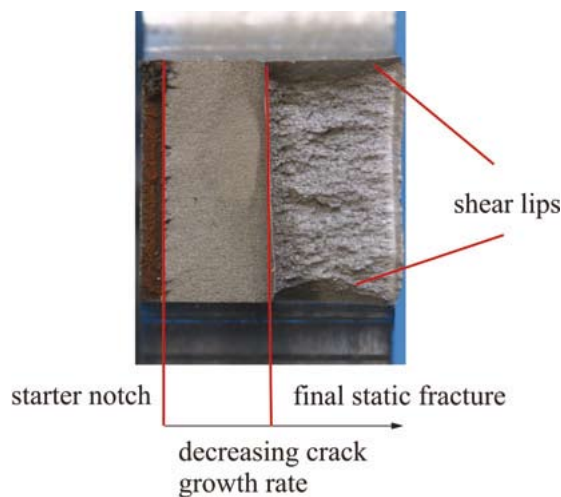


Figure 5 Fracture surface of C-specimen

Experimental data from constant amplitude fatigue crack growth tests with $R = 0,5$ is given in Figure 6. The higher R -ratio leads to non-conservative results near ΔK_{th} , if the results of the C-specimen are considered. This is due to the higher degree of plastification compared to $R = 0,1$ at the beginning of fatigue crack growth in conjunction with the K -gradient $C = -0,35 \text{ mm}^{-1}$. This extreme value is necessary to stop the fatigue crack within the small ligament of the C-specimen.

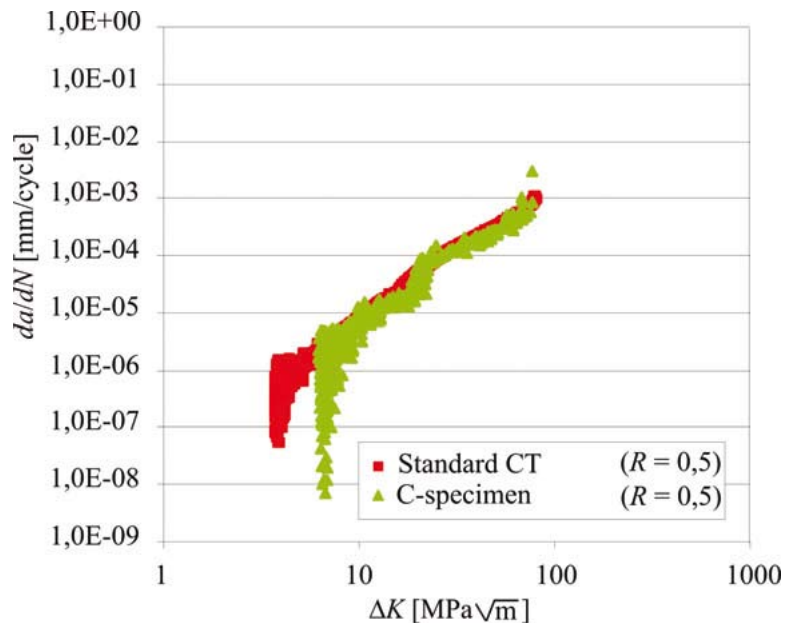


Figure 6 Comparison of fatigue crack growth rates determined with CT specimen and C- specimen

4. Conclusions

This contribution deals with specimens for the fracture-mechanical characterization of high-strength steel tubes. The design process of a specially adapted arc-shaped specimen is presented containing analytical and numerical methods.

Experimental results show the applicability of this specimen concept for the determination of fatigue crack growth rates. However, the results deviate from the ones determined with standard specimens, if tests at higher R -ratios are conducted.

Moreover it is surprising that the relatively mild side grooves of the special specimen lead to a high degree of embrittlement. In order to get a better understanding of their influence numerical analyses have to be conducted. On their basis constraint parameters can be determined, which gives more information about the influence of the side groove geometry on the state of stress in the fracture-mechanical specimen.

References

- [1] Wiedemeier, B.; Sander, M.; Džugan, J.; Richard, H. A.; Peters, A.: *Probenkonzepte zur bruchmechanischen Charakterisierung hochfester Stahlrohre*. In: Bruchmechanische Werkstoff- und Bauteilbewertung: Beanspruchungsanalyse, Prüfmethode und Anwendungen, Tagungsband zur 42. Tagung des DVM-Arbeitskreises Bruchvorgänge, Berlin, 2010, pp. 237–246
- [2] American Society for Testing and Materials: *E399 - Standard Test Method for Linear-Elastic Plane-Strain Fracture Toughness K_{Ic} of Metallic Materials*. ASTM International, West Conshohocken, 2008
- [3] Fulland, M.; Richard, H. A.: *Application of the FE-Method to the simulation of fatigue crack growth in real structures*. In: Steel Research, Vol. 74, 2003, pp. 584–90

- [4] Fulland, M.; Schöllmann, M.; Richard, H. A.: *ADAPCRACK3D - Development of the program for simulation of three-dimensional crack propagation processes*. In: Atluri, S.N., Brust, F.W. (eds.): *Advances in Computational Engineering & Sciences*, Vol. 1, 2000, pp. 948–953
- [5] Schöllmann, M.; Richard, H. A.; Kullmer, G.; Fulland, M.: *A new criterion for the prediction of crack development in multiaxially loaded structures*. In: *International Journal of Fracture*, Vol. 117, 2002, pp. 129–141
- [6] American Society for Testing and Materials: *E1820 - Standard Test Method for Measurement of Fracture Toughness*. ASTM International, West Conshohocken, 2008
- [7] American Society for Testing and Materials: *E647 - Standard Test Method for Measurement of Fatigue Crack Growth Rates*. ASTM International, West Conshohocken, 2008
- [8] Sander, M.; Richard, H. A.: *Automatisierte Ermüdungsrissoausbreitungsversuche*. In: *Materialprüfung*, Vol. 46, 2004, pp. 22–26
- [9] Wawrzynek, P. A.; Ingraffea, A. R.: *Interactive finite element analysis of fracture processes: an integrated approach*. In: *Theoretical and Applied Fracture Mechanics*, Vol. 8, 1987, pp. 137–50
- [10] Wawrzynek, P. A.; Ingraffea, A. R.: *An interactive approach to local remeshing around a propagating crack*. In: *Finite Elements in Analysis and Design*, Vol. 5, 1989, pp. 87–96

¹ Dipl.-Ing. Benedikt Wiedemeier, Benteler Tube Management GmbH, Residenzstraße 1, 331 04 Paderborn, Germany, Tel.: +49 5254 81 4911, e-mail: benedikt.wiedemeier@benteler.de

² prof. Dr. Manuela Sander, Chair of Structural Mechanics, University of Rostock, Albert-Einstein-Straße 2, 18051 Rostock, Germany, Tel.: +49 381 4989341, e-mail: manuela.sander@uni-rostock.de

³ Prof. Dr. Hans Albert Richard, Institute of Applied Mechanics, University of Paderborn, Pohlweg 47-49, 330 98 Paderborn, Germany, Tel.: +49 5251 60 5323, e-mail: richard@fam.upb.de

⁴ Dr. Andreas Peters, Benteler Tube Management GmbH, Residenzstraße 1, 33104 Paderborn, Germany, Tel.: +49 5254 81 4900, e-mail: andreas.peters@benteler.de